Technical Report
TR-21-06
December 2022

Post-closure safety for the final repository for spent nuclear fuel at Forsmark

Data report, PSAR version

SVENSK KÄRNBRÄNSLEHANTERING AB

SWEDISH NUCLEAR FUEL
AND WASTE MANAGEMENT CO

Box 3091, SE-169 03 Solna
Phone +46 8 459 84 00
skb.se

ISSN 1404-0344
SKB TR-21-06
ID 1896821

December 2022
Updated 2024-04

Post-closure safety for the final repository for spent nuclear fuel at Forsmark

Data report, PSAR version

Svensk Kärnbränslehantering AB

Keywords: KBS-3, Spent fuel repository, Safety assessment, SR-Site.

This report is published on www.skb.se

Updated 2024-04

The original report, dated December 2022, was found to contain editorial errors which have been corrected in this updated version.

Contents

1 Introduction

1.1 Role of this Data report in the PSAR

This report compiles, documents, and qualifies input data identified as essential for the post-closure safety assessment in SKB's Preliminary Safety Assessment Report (PSAR) for a final repository for spent nuclear fuel at the Forsmark site.[1] The input data concern the repository system, broadly defined as the deposited spent nuclear fuel, the engineered barriers, the host rock, and the biosphere in the proximity of the repository. The input data also concern external influences acting on the system, in terms of climate related data. Data are provided for a selection of relevant conditions and are qualified through traceable standardised procedures.

The report is an update of the Data report for the safety assessment SR-Site (SKB 2010a). The extent of the update is described in Section 1.2.1.

1.1.1 Assessment methodology in eleven steps

As described in Section 2.5 of the **Post-closure safety report**,[2] the current safety assessment consists of eleven main steps. We refrain from outlining the steps here, except for the step concerning the Data report, and instead refer to the detailed description in the **Post-closure safety report.** Figure 1-1 is a graphical illustration of the steps, with the present step highlighted.

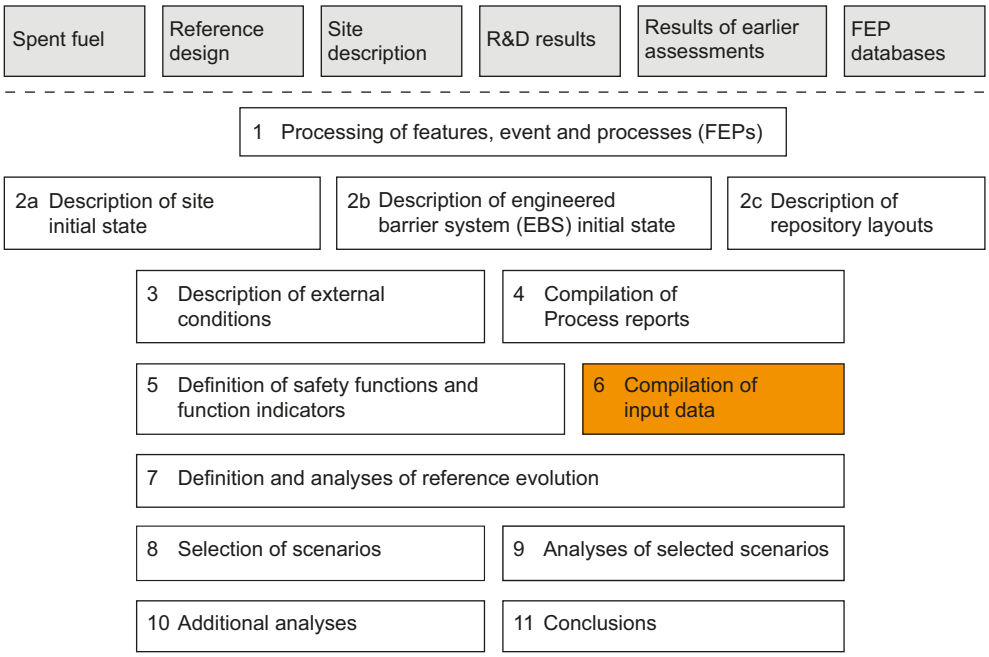

Figure 1-1. *The assessment methodology in eleven steps, with the Data report step highlighted.*

[1] The present report is published some time before the submission of the PSAR. In case the need for any changes of the contents of this report arises between its publication and the submission of the PSAR, a report of these changes will be provided in the PSAR.

[2] Abbreviated names in **bold** are used for a number of key references, see Table 1-1. The **Post-closure safety report** is the top-level document of the assessment.

The following is stated concerning step 6 “Compilation of input data” in Section 2.5 of the **Post-closure safety report**:

“In this step, data to be used in the quantification of repository evolution and in dose calculations are selected using a structured procedure. The process of selection and the data values adopted are reported in a dedicated Data report. The process follows a template developed and applied in the SR-Site assessment for discussion of input data uncertainties. The template… and the selected data are provided in the Data report. The models for which data are required are given in the AMF described in step 4.

While the data types used in the PSAR are essentially the same as those used in the SR-Site assessment, data values or value intervals differ between the assessments for some data types. For data types where new values are used in the PSAR, the full template is reported in the PSAR Data report. For data types where it has been assessed that the same values as in SR-Site can be used, the data qualification from the SR-Site is reproduced.”

The structured procedures and the template referred to are described in detail in Section 2.3.

1.1.2 Key reports referenced

Several of the steps carried out in the safety assessment result in specific reports that are of central importance for the conclusions and analyses in the **Post-closure safety report**. These specific reports, referred to as main references. Besides the main references, there are additional references, treating more narrow issues, supporting the **Post-closure safety report** and/or one or more of the main references. The report hierarchy is illustrated in Figure 1-2.

In addition to the reports mentioned above, references are made to a variety of documents, articles, and publications, either from SKB or from other organisations, or as part of the open literature. SKB reports that deserve mentioning are those from previous safety assessments, and those from site investigations and site descriptions. A report produced outside the safety assessment framework, but that still is fundamental input to the safety assessment, is the SDM-Site version of the site-descriptive model of the Forsmark site, see the **Site description Forsmark**.

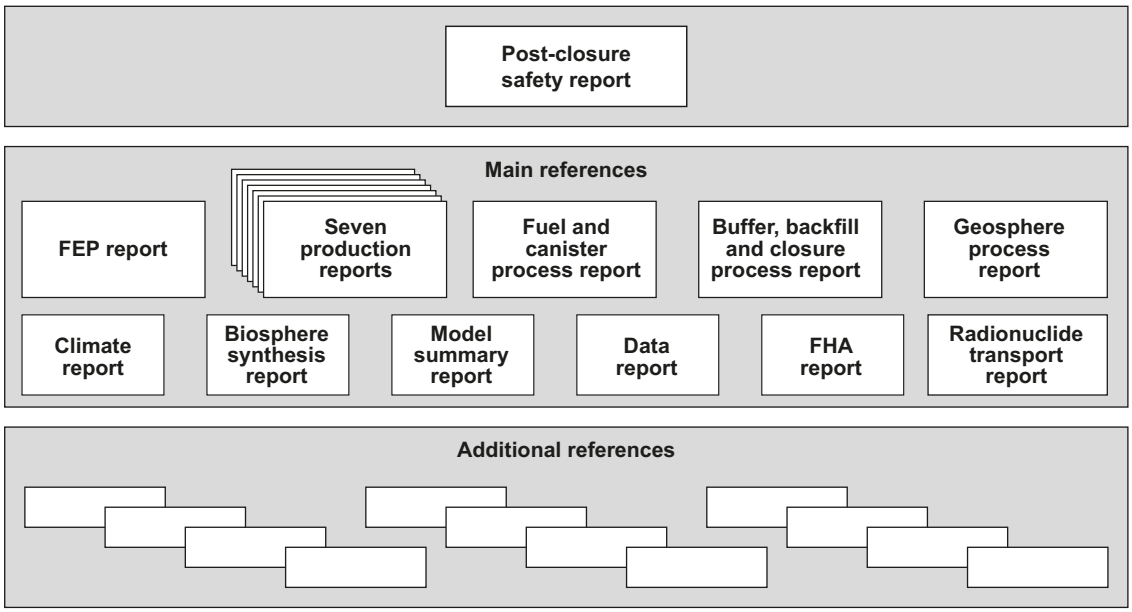

Figure 1-2. *The hierarchy of the main and additional references. The main references support the Post-closure safety report. The additional references may either support the Post-closure safety report directly or the main references. The seven production reports include the Spent fuel report and the Underground openings construction report.*

The Post-closure safety report and main references, as well as the site-descriptive model of the Forsmark site, are referenced by using abbreviations. The abbreviations as well as their full references, are given in Table 1-1.

Table 1-1. Abbreviations and full references of SKB reports, used in this Data report.

Abbreviation used when referenced in this Data report	Full reference, as given in the reference list
Backfill production report	**Backfill production report, 2022.** Produktionsrapport Återfyllning, SKBdoc id 1525864 ver 4.0, Svensk Kärnbränslehantering AB. (In Swedish.) (Internal document.)
Biosphere synthesis report	**Biosphere synthesis report, 2010.** Biosphere analyses for the safety assessment SR-Site – synthesis and summary of results. SKB TR-10-09, Svensk Kärnbränslehantering AB.
Buffer, backfill and closure process report	**Buffer, backfill and closure process report, 2022.** Post-closure safety for the final repository for spent nuclear fuel at Forsmark – Buffer, backfill and closure process report, PSAR version. SKB TR-21-03, Svensk Kärnbränslehantering AB.
Buffer production report	**Buffer production report, 2022.** Produktionsrapport Buffert, SKBdoc id 1392269 ver 5.0, Svensk Kärnbränslehantering AB. (In Swedish.) (Internal document.)
Canister production report	**Canister production report, 2022.** Produktionsrapport Kapsel, SKBdoc id 1407944 ver 2.0, Svensk Kärnbränslehantering AB. (In Swedish.) (Internal document.)
Climate report	**Climate report, 2020.** Post-closure safety for the final repository for spent nuclear fuel at Forsmark – Climate and climate-related issues, PSAR version. SKB TR-20-12, Svensk Kärnbränslehantering AB.
Closure production report	**Closure production report, 2022.** Produktionsrapport Förslutning, SKBdoc id 1387771 ver 3.0, Svensk Kärnbränslehantering AB. (In Swedish.) (Internal document.)
Fuel and canister process report	**Fuel and canister process report, 2022.** Post-closure safety for the final repository for spent nuclear fuel at Forsmark – Fuel and canister process report, PSAR version. SKB TR-21-02, Svensk Kärnbränslehantering AB.
Geosphere process report	**Geosphere process report, 2022.** Post-closure safety for the final repository for spent nuclear fuel at Forsmark – Geosphere process report, PSAR version. SKB TR-21-04, Svensk Kärnbränslehantering AB.
Model Summary Report	**Model Summary Report, 2022.** Post-closure safety for the final repository for spent nuclear fuel at Forsmark – Model summary report, PSAR version, SKB TR-21-05, Svensk Kärnbränslehantering AB.
Post-closure safety report	**Post-closure safety report, 2022.** Post-closure safety for the final repository for spent nuclear fuel at Forsmark – Main report, PSAR version. SKB TR-21-01, Svensk Kärnbränslehantering AB.
Radionuclide transport report	**Radionuclide transport report, 2022.** Post-closure safety for the final repository for spent nuclear fuel at Forsmark – Radionuclide transport report, PSAR version. SKB TR-21-07, Svensk Kärnbränslehantering AB.
Site description Forsmark	**Site description Forsmark, 2008.** Site description of Forsmark at the completion of the site investigation phase, SDM-Site Forsmark. SKB TR-08-05, Svensk Kärnbränslehantering AB.
Spent fuel report	**Spent fuel report, 2021.** Använt kärnbränsle att hantera i KBS-3-systemet. SKBdoc id 1380282 ver 3.0, Svensk Kärnbränslehantering AB. (In Swedish.) (Internal document.)
Underground openings construction report	**Underground openings construction report.** Produktionsrapport Bergutrymmen, Svensk Kärnbränslehantering AB. (In Swedish.) (Internal document.) *In prep*.

1.2 Objective and scope of the Data report

1.2.1 Compilation and qualification of essential input data

This Data report is based on the SR-Site Data report (SKB 2010a) that was part of the application to construct, own and operate a nuclear facility for the final disposal of spent nuclear fuel and nuclear waste.

In the report, essential input data are compiled and qualified. These data are intended for use in subsequent safety assessment modelling. The compiled data are divided on five different chapters concerning the:

- Spent fuel (Chapter 3).
- Copper canister (Chapter 4).
- Buffer and backfill (Chapter 5).
- Geosphere (Chapter 6).
- Surface system (Chapter 7).

The set of input parameters for the safety assessment is very large. Some "input data uncertainties" (including both data uncertainty and natural variability) will have a substantial influence on safety related output uncertainty, which ultimately leads to uncertainty in assessed radiological risk. Other data may range over orders of magnitude but still not influence the assessed radiological risk. An example of the latter are transport properties in the geosphere of those radionuclides that will never exit the engineered barrier.

It is therefore appropriate to identify input data to which safety related output is sensitive, and use these insights in allocating resources to the determination and, where feasible, reduction of input data uncertainties. It is also important to have a high degree of confidence in the data that are used to conclude that particular processes, nuclides, etc will never contribute to radiological risk. The identification of essential input data is discussed in the next section, and in Chapter 2.

The data presented in the Data report are either compiled from supporting reports and documents, as part of previous tasks or as part the safety assessment project or produced and justified in this Data report. The majority of data are compiled from background reports, such as the **Site description Forsmark**, **Production reports**, or other reports produced as part of the assessment, etc and in those cases the justification of data is mainly done in the supporting documents. In such a case, the qualifying role of the Data report is to control that the suggested data are traceable and applicable for prevailing conditions, and to some extent to suggest their role in the safety assessment. For example, a set of data suggested in the site descriptions may only be valid for a certain climate domain of the glacial cycle, or at some other specified condition. Furthermore, estimates of uncertainties as well as of natural variability should be delivered by the Data report, so that the data can be properly used in the subsequent safety assessment modelling. It is part of the qualifying role to make sure that reasonable, quantitative, and usable uncertainty estimates are delivered.

The way of qualifying data is through traceable standardised procedures where extra effort is put into documenting the data qualification process, and to discuss uncertainty in data originating from conceptual uncertainty, data uncertainty, and natural variability. These standardised procedures are detailed in Section 2.3.

The compiled and qualified data are found in Section x.x.12 of each section in Chapter 3 to 7. In this section, clear referencing to tables in the preceding sections may substitute duplication of the data. Data that cannot be tabulated in this report, for example the co-ordinates of thousands of exit locations for groundwater flow paths, are stored in referenced databases.

In the PSAR version of the Data report, only data that has been updated since the SR-Site are qualified. For data that has not been updated the material from the SR-Site Data report is reproduced, and an indication of this is given in the heading of a reproduced text. Note that the text may still be slightly modified in that references to the PSAR report hierarchy rather than to that of SR-Site may occur as appropriate. Also, experiences from the modelling in SR-Site have been taken into account when evaluating all data sets, irrespective of whether they are updated or not. Details are as follows:

- Spent fuel (Chapter 3). This chapter contains sections on radionuclide inventory, instant release fraction and corrosion release fraction, fuel dissolution and solubility data. Due to new results regarding inventory calculations the section on radionuclide inventory has been updated. Due to the new radionuclide inventory the section on Instant release fraction and corrosion release fraction has been updated to reflect these new results. Due to new information concerning irregular fuel types the section on fuel dissolution has been updated to include these results. As discussed in Section 3.4, the Solubility data recommended for use in the PSAR are the same as those recommended for SR-Site and texts on data qualification have been reproduced from the SR-Site Data report (SKB 2010a).
- Copper canister (Chapter 4). This chapter contains section on data of intact canister and evolving canister defect. Due to new supporting documents the sections on initial canister thickness and resistance to mechanical loads has been updated to reflect the new results, though the qualified data are unaltered. As discussed in each section some sections have been reproduced from the SR-Site Data report (SKB 2010a). The data recommended for use in the PSAR are the same as the data recommended for SR-Site.
- Buffer and backfill (Chapter 5). This chapter contains sections on density and porosity of buffer and backfill, hydraulic properties of buffer and backfill and migration data of buffer and backfill. Since the Production reports have been updated for the PSAR texts related to the initial state have been updated. The data recommended for use in the PSAR are the same as the data recommended for SR-Site.
- Geosphere (Chapter 6). This chapter contains sections on ground water chemical composition, bedrock thermal properties, Discrete-Fracture Network (DFN) models, rock mechanics, spalling and the excavation damaged zone, quantities for groundwater flow modelling and non-flow related migration properties. As discussed in each section, the data recommended for use in the PSAR are the same as the data recommended for SR-Site and sections on data qualification have been reproduced from the SR-Site Data report (SKB 2010a).
- Surface system (Chapter 7). This chapter contains a section on Climate and climate related data and a section on Landscape dose conversion factors. The section on climate and climate related data has been modified to reflect updates of the **Climate report**. The section on landscape dose conversion factors includes updates due to experiences obtained from other safety assessment projects. With few exceptions, the data recommended for use in the PSAR are the same as the data recommended for SR-Site.

1.2.2 Identification of essential input data

The identification of essential input data has been performed in two ways. The primary approach is through analysing assessment model flow charts, AMFs, (see Section 7.5 of the **Post-closure safety report** and Section 2.1 of this present report). AMFs are produced based on information from the other steps of the eleven step methodology (cf Figure 1-1), experience from previous safety assessments, as well as on other recent information. This approach has been generally used for identifying the input data of this report and is described in Section 2.1. There are limitations in this approach resulting in a situation where peripheral data that may be of importance for the safety assessment are not included in the Data report, but are reported elsewhere. Such an example is the biosphere data constituting the background for estimating Landscape dose conversion factors. In this specific case, a decision has been taken to limit the scope of the Data report to include the estimated Landscape dose conversion factors as the only biosphere related data.

One of the purposes of the Data report has been to deliver qualified data for radionuclide transport calculations. Therefore, all input parameters of the radiuonuclide transport codes COMP23 (Romero et al. 1999, Cliffe and Kelly 2006, Vahlund and Hermansson 2006) and FARF31 (Norman and Kjellbert 1990, Elert et al. 2004) have been closely examined. Many of the associated data are qualified in this Data report, while some inputs are taken from other sources, as outlined in Section 2.2 and as detailed in the **Radionuclide transport report**. The data inventory for the PSAR corresponds to the SR-Site inventory.

1.2.3 Relation to specific sites

The PSAR builds on site-specific data for, and site-descriptive models of, the selected Forsmark site, i.e. the location of the repository facility to which the PSAR applies. Parallel to the site investigation at Forsmark in the municipality of Östahammar, also the Laxemar site in the municipality of Oskarshamn was thoroughly investigated. Knowledge gained for the latter site, and other relevant sites, is sometimes used in the present report, e.g. to illustrate general conditions in granitic rock in Sweden.

1.2.4 Intended audience of this report

This report is written by, and for, experts in the concerned scientific fields. It should be possible for generalists in the area of post-closure safety of geologic nuclear waste repositories to comprehend the content of the report. However, it may be a difficult task for laymen to grasp the details of this report. This report is an important part of the documentation of safety assessment.

1.3 Participating parties in this Data report

The data recommended are generally based on measurements, modelling, or interpretation. Therefore, there is always a component of expert judgment involved in choosing the recommended data (as stated in Section 1.2, trivial data are not handled in this report). The work of producing much of the data, as well as of compiling the data and writing this report, has been done by experts working at, or on behalf of, SKB. Therefore, formally the expert should not be considered as independent. The experts could have their expertise in a narrow subject area, such as thermal properties of the rock, or as generalists in the safety of spent nuclear fuel (which indeed could also be considered as a narrow field of expertise).

The structure of the Data report separates the views of experts supplying the data (either directly or through supporting documents) from the views of experts of the assessment team. This works well when the supplied data are independent from assumptions made in the safety assessment (e.g. the rock porosity). However, when the supplied data have been produced in close cooperation with the assessment team, such a separation is difficult to obtain. Examples of the latter data are exit locations of flow paths during repository evolution, or the groundwater composition during the glacial cycle.

For the current report, the vocabulary used for separating the teams or persons supplying the data, the groups or persons within the assessment team responsible for the data, and the assessment team as a whole were:

- Supplier
- Customer
- Assessment team

This may appear to be an odd choice of vocabulary, which was not used in safety assessments prior to SR-Site. The terms supplier and customer were adopted from standard quality assurance systems (e.g. the ISO 9001 standard), and was a response to the authorities overall review comment that the degree of quality assurance in the SR-Site safety assessment needed to be increased, as compared to in SR-Can (Dverstorp and Strömberg 2008, e.g. summary).

These roles of the parties involved in producing the Data report as well as the current are further described in Section 2.3. The individuals involved in authoring each subject area section, and their role in the supplier team or assessment team, are documented according to SKB's quality assurance system. Experts which have participated indirectly in producing the data, by way of authoring supporting document, are identified by standard referencing.

1.4 Repository design

In the following a very short description of the engineered repository is given for orientation, with the purpose of outlining the framework for data in individual subject area sections. Details on the engineered system are found in a multitude of other documents, for example the **Post-closure safety report**. The engineered repository can be divided on the fuel, the copper canister, the buffer surrounding the canister, the backfill of deposition tunnels and other underground openings, and the closure.

1.4.1 The spent fuel and fuel assemblies

The fuel and the fuel assemblies are described in the **Spent fuel report**. The spent fuel is predominantly UOX fuel (Uranium OXide), but smaller amount of MOX fuel (Mixed OXide) and fuel residues from research will also be deposited. There will be ca 8 300 tonnes of BWR fuel and about 3 100 tonnes of PWR fuel that will need to be deposited. Here BWR and PWR are abbreviations for Boiling light water reactors and Pressurised light water reactors, respectively. The fuel is deposited as fuel assemblies with construction materials comprised of zirconium alloys, nickel alloys and stainless steel. Furthermore, some additional material such as control rods will be deposited together with the fuel assemblies.

1.4.2 The copper canister and cast iron insert

The copper canister and the cast iron insert are described in the **Canister production report**. Figure 1-3 (upper left) shows the reference canister, over 4.8 m in length, about one metre in diameter, and 5 cm in copper thickness.

The reference canister design comprises two different inserts, one for 12 BWR fuel assemblies and one for 4 PWR fuel assemblies. Figure 1-3 (middle and upper right) shows the differences between the two. The loaded canister weights between 24.6–26.8 tonnes, where the copper shell weights 7.5 tonnes, the cast iron insert with lid between 13.7–16.4 tonnes, and the fuel between 2.6–3.5 tonnes, depending on the type (cf Table 3-1 of the **Canister production report**).

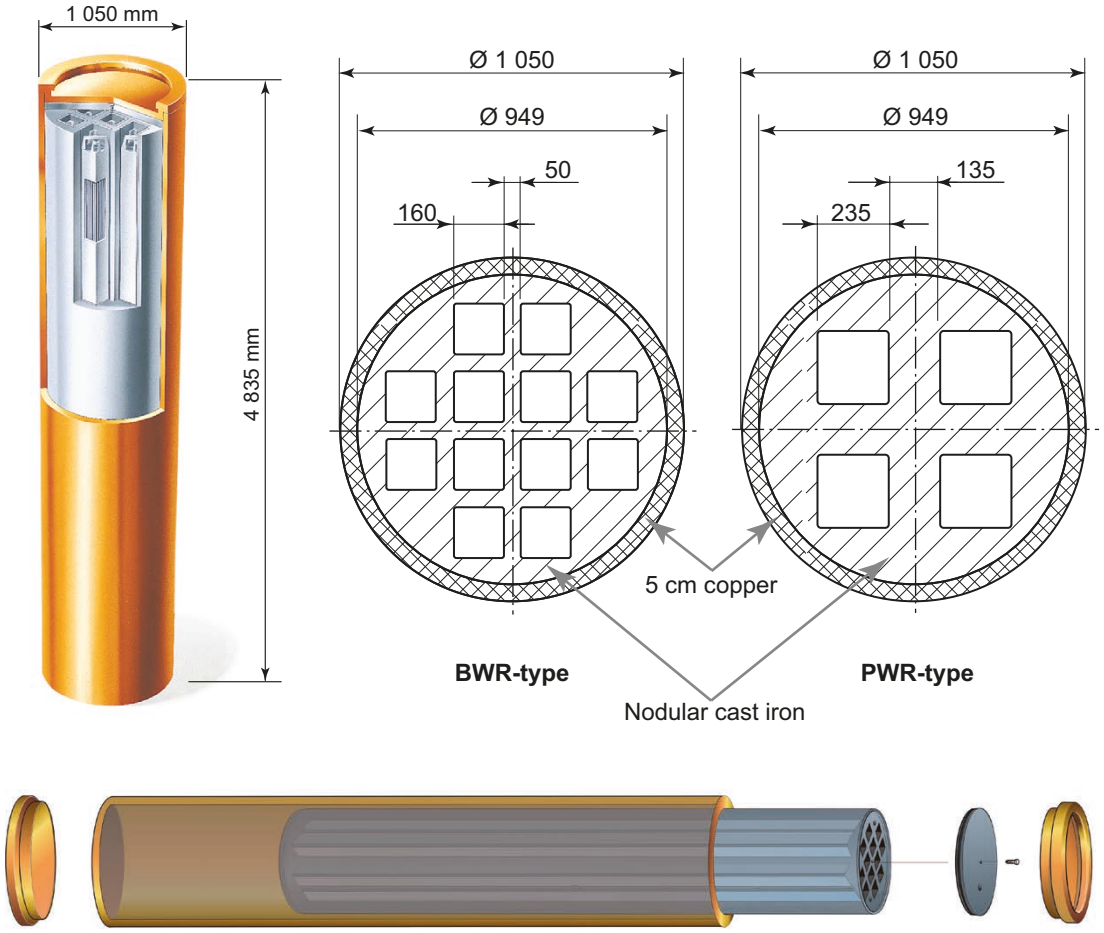

Figure 1-3. *Upper left: SKB's reference canister with an outer corrosion barrier of copper and an insert of nodular cast iron. Upper middle and right: Basic differences between the BWR and PWR cast iron inserts. Lower: Exploded view of the reference canister and its components (from the left: copper base, copper tube, insert, steel lid for insert and copper lid). Modified and reproduced from Figures 3-1 to 3-3 of the Canister production report.*

1.4.3 The buffer and backfill

The buffer surrounding the canister is described in the **Buffer production report** while the backfill of the deposition tunnels is described in the **Backfill production report**. The reference material of the buffer is bentonite clay, where examples of commercial bentonites given in the **Buffer production report** is MX-80. The buffer is manufactured as blocks and pellets that are placed around the canister with the aim at achieving a specified density. The installed buffer with the reference geometry, as given in the **Buffer production report,** is illustrated in Figure 1-4.

The reference material of the backfill of the deposition tunnels is low grade bentonite clay, where Asha 2012 is given as an example in the **Backfill production report**. The backfill is manufactured as blocks and pellets that are placed in the deposition tunnel with the aim at achieving a specified density.

1.4.4 The underground openings

In the **Underground openings construction report,** the construction of deposition holes and tunnels, the ramp and shafts, main and transport tunnels, and central area rock caverns is discussed. Figure 1-5 shows an illustration of the reference layout, where different underground openings are indicated.

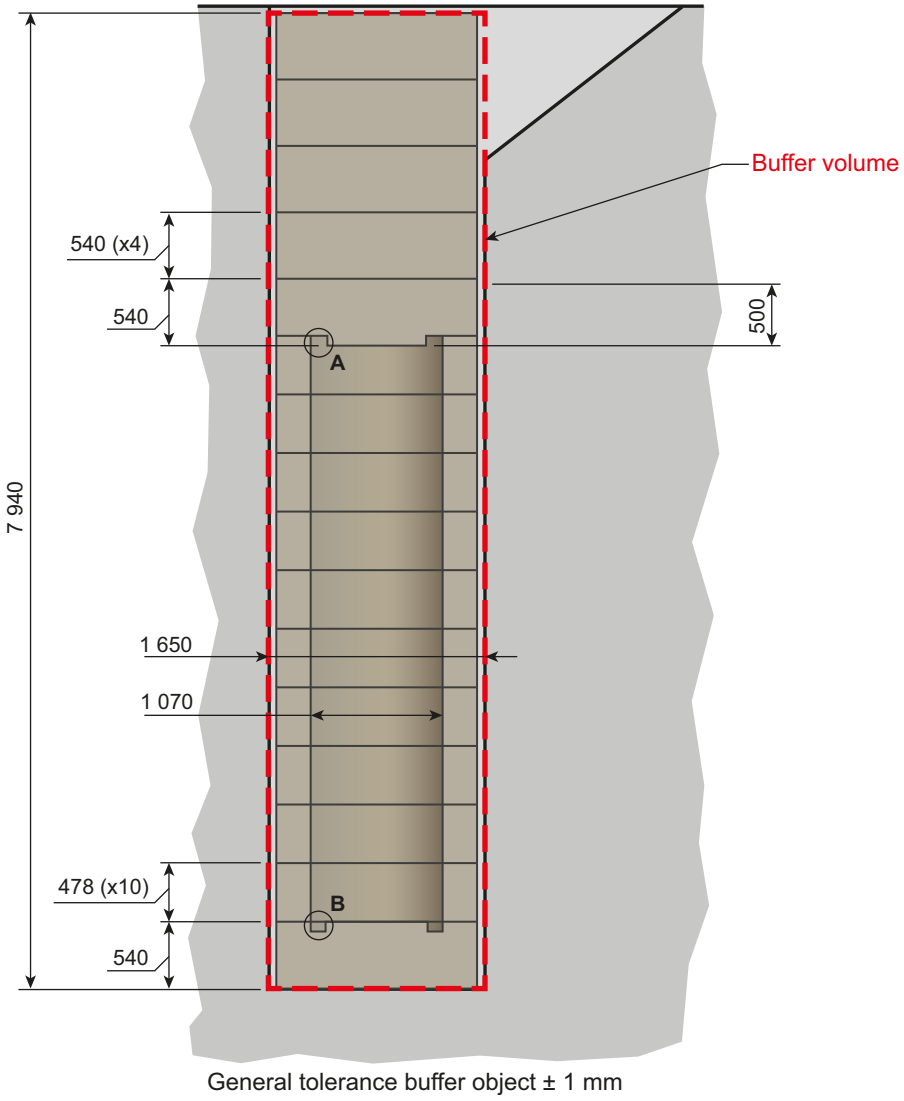

Figure 1-4. *Reference geometry of the installed buffer and the nominal dimensions given as design premises.*

1.4.5 The closure

In the **Closure production report**, the backfilling of main and transport tunnels, the central area, the ramp and shafts, and boreholes is outlined. The closure, see Figure 1-5 includes:

1. Main tunnels and transport tunnels.
2. Central area.
3. Ramp and shafts below the top sealing.
4. Top seal.
5. Plugs (other than deposition tunnel plugs).
6. Investigation boreholes from the ground surface and boreholes from the underground openings in the repository.

The purpose and function of the closure is to limit groundwater flow and migration of radionuclides through the tunnels and other openings to significantly obstruct unintentional intrusion into the final repository, to prevent collapse of the rock structure and also to prevent the expansion of bentonite into connecting rock spaces. This means that all rock spaces need to be backfilled.

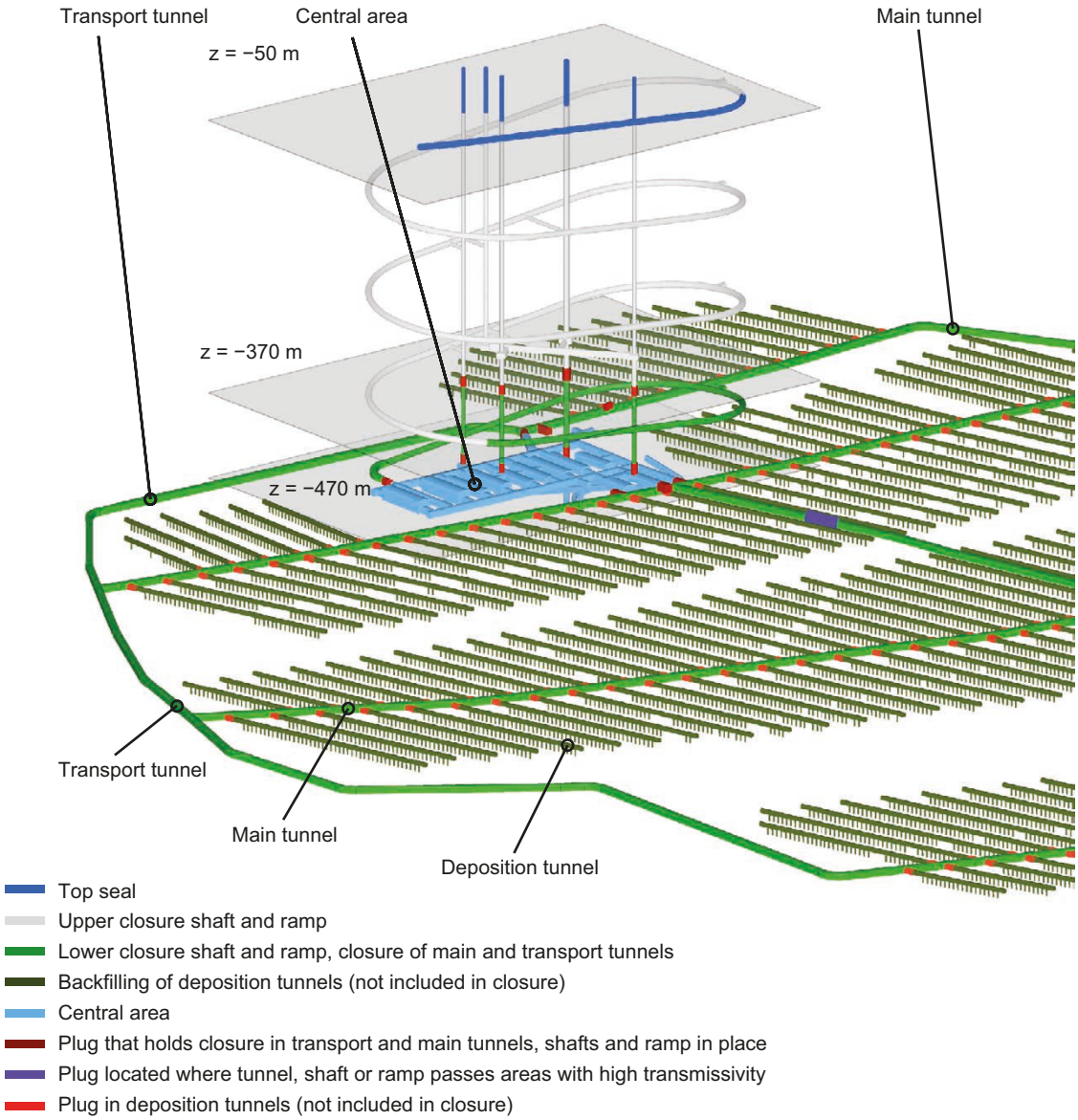

Figure 1-5. *Outline of the reference designs of closure and plugs in the underground openings.*

1.5 The Forsmark site

This section does not aim to give a short summary of the Forsmark site, but merely to provide maps and graphic information so that the reader can orientate when site specific nomenclature is used in the subject area sections. For a detailed description of the surface system of Forsmark, Lindborg (2008) is recommended.

Site description Forsmark is based on the surface-based investigations that were completed in 2007. Since then, some sampling and investigations of the surface system as well as monitoring in some existing boreholes have continued. In addition, investigations in preparation for the construction of the repository facility have been carried out (Follin 2019). These preparatory investigations were conducted in the area where the access ramp and shafts of the repository facility are planned to be located. Data from eleven core-drilled boreholes and from three percussion-drilled boreholes, each less than 200 m deep, were collected with the focus to evaluate geological and hydrogeological conditions in the shallow bedrock. To gain more information from depth in the access area, investigations have also been conducted in a core-drilled borehole reaching a depth of 540 m. The evaluation and modelling of the results from these investigations conducted since the completion of the surface-based investigations have added more detailed information to the description of the area where the investigations were conducted, but have not justified an update of the site descriptive model (Follin 2019). Therefore, the analyses of post-closure safety in the PSAR is, likewise to SR-Site, based on **Site description Forsmark.**

1.5.1 The locations of the Forsmark site, drill sites, and boreholes

The Forsmark site is located in northern Uppland within the municipality of Östhammar, about 120 km north of Stockholm (see Figure 1-6). The candidate area for site investigation, approximately 6 km long and 2 km wide, is located along the shoreline of Öregrundsgrepen, a bay of the Baltic Sea. The candidate area is encircled by the red line in Figure 1-6.

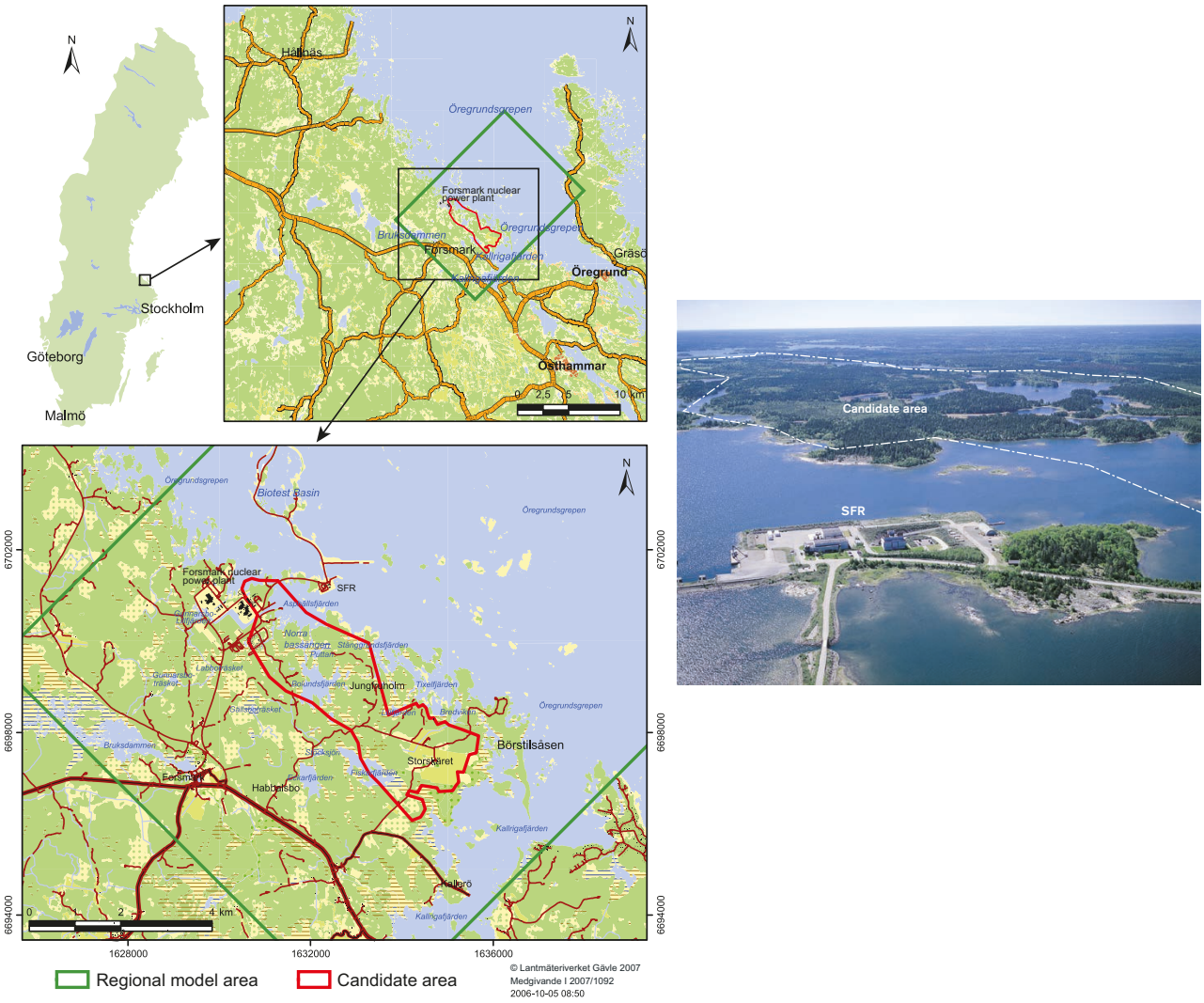

Figure 1-6. *Upper left: The location of the Forsmark site. Lower left: The regional model area and the candidate area. Right: Photo of the Forsmark candidate area. Reproduced from Figures 1-3 and 1-6 of the Site description Forsmark.*

A key aspect of collecting data in the site investigation has been drilling boreholes and performing downhole surveys and investigations. Two types of boreholes have been drilled into the bedrock, core-drilled boreholes extending down to a depth of 1 000 m and shorter percussion-drilled boreholes. Core-drilled boreholes are drilled from specific drill sites, and labelled so that the drill site (DS) can be easily identified. For example, borehole KFM01A and KFM12A are drilled from DS1 and DS12, respectively. Figure 1-7 shows the drill sites and boreholes of the Forsmark candidate area. Core-drilled boreholes are marked by purple dots and percussion-drilled borehole by blue dots. The yellow tube corresponding to each dot shows the direction and 2-D extension of the borehole. The yellow dots in the right figure mark soil pipes. Especially core-drilled boreholes are referenced in tables and figures providing data in Chapter 6.

As can be seen, the density of boreholes is increased in the north–western part of the candidate area where the target area has been selected for the repository.

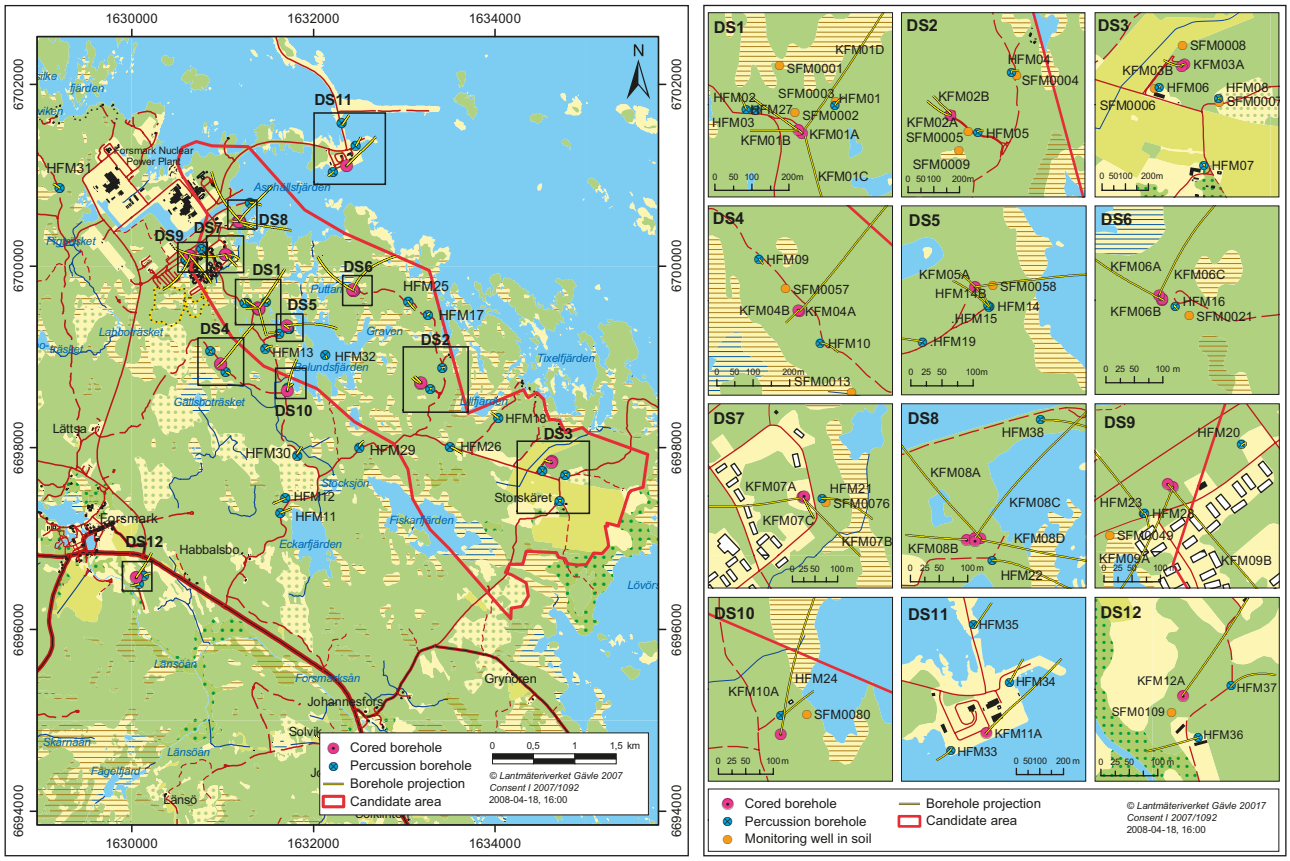

Figure 1-7. *Drill sites and boreholes of Forsmark. Reproduced from Figures 2-1 and 2-2 of the Site description Forsmark.*

1.5.2 The locations of rock domains

In the site-descriptive model, the host rock surrounding the repository has been divided into numerous volumes, which are often referenced in figures and tables providing data in this Data report. The rock lithology is described by rock domains, defined on the basis of composition, grain size, homogeneity, and style and degree of ductile deformation. Figure 1-8 shows the rock domains of the Forsmark candidate area. The rock domains can be identified by the numbers. Two rock domains of special importance for the target area are RFM029 and RFM045, marked by the numbers 29 and 45 in the figure. According to repository layout D2 (SKB 2009a), the repository should be located in these two domains.

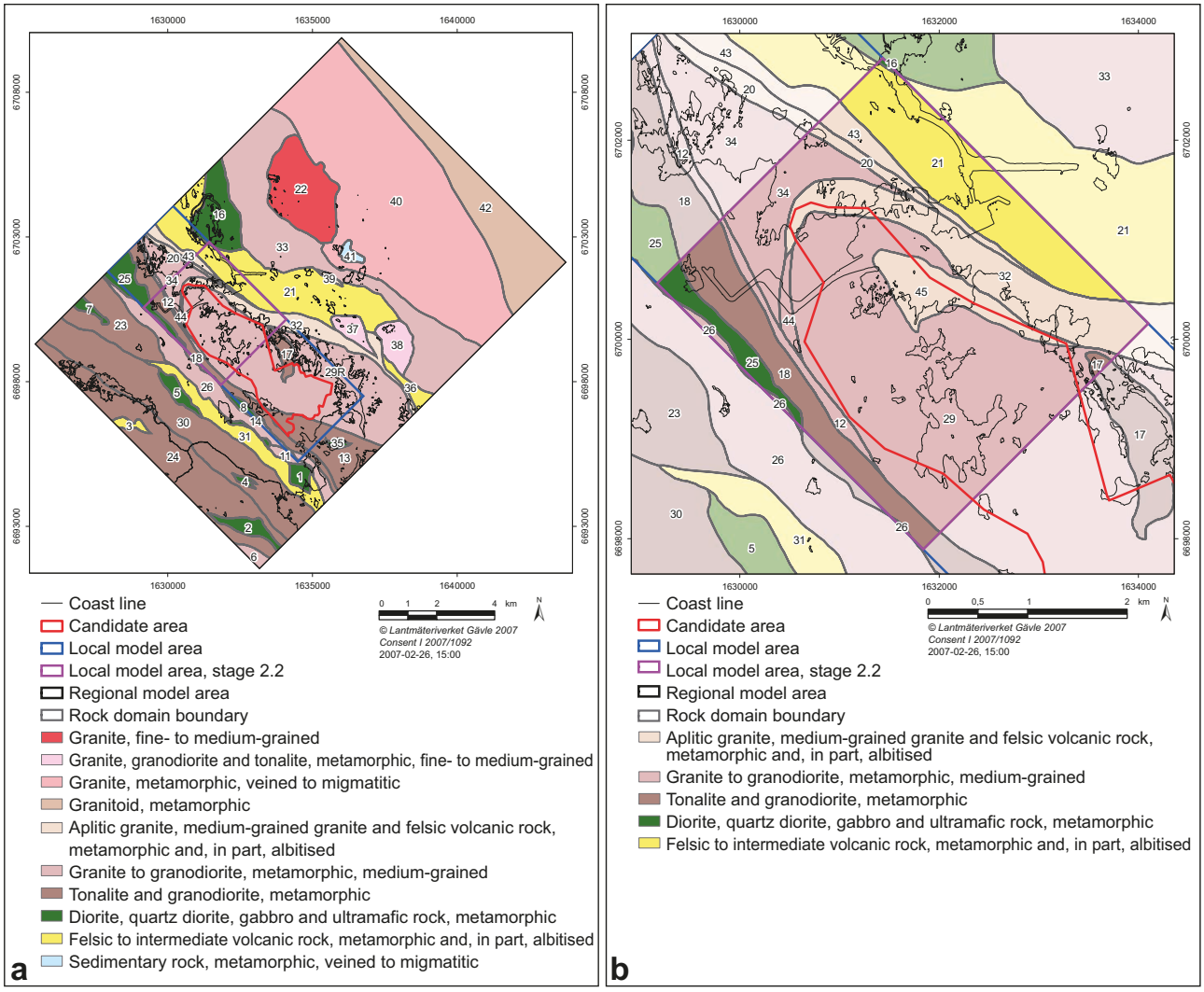

Figure 1-8. *Rock domains included in the two dimensional models at the ground surface. a) Model inside the regional model area. b) Model inside the local model area (darker colours). The different colours represent the dominant rock type in each domain. Reproduced from Figure 5-24 in the Site description Forsmark.*

1.5.3 The locations of deformation zones and fracture domains

The rock domains are divided into the mutually exclusive volumes deformation zones and fracture domains. Deformation zones of the north–western part of the target area are shown in Figure 1-9. The figure illustrates the two dimensional horizontal surface at –500 m elevation in the local model volume.

Figure 1-10 shows the modelled deformation zones along a WNW–ESE cross-section through the candidate volume, as well as boreholes.

Six different fracture domains, FFM01–FFM06, are defined within the candidate area, whereof FFM01–FFM03 and FFM06 are found within the target area. Figure 1-11 shows a 3-D model of the fracture domains of the north–western part of the target area. The figure also shows some of the deformation zones of the area. Note that in the illustrations, north faces left.

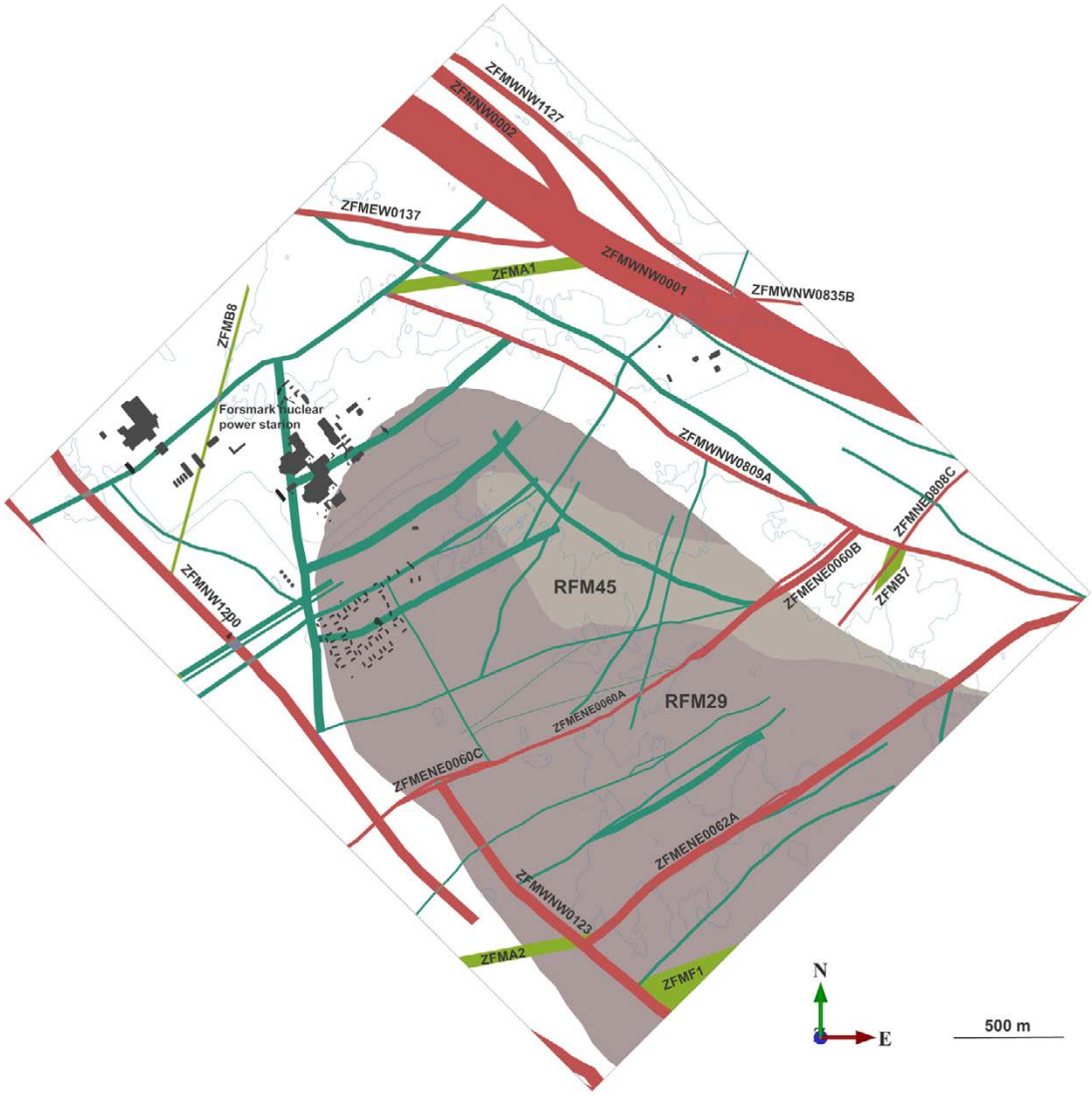

Figure 1-9. *Distribution of the two rock domains RFM029 and RFM045, and all deformation zones with L > 1 000 m, on a surface at 500 m depth within the local model volume (model stage 2.2). Zones marked in red are steeply dipping or vertical and have a trace length at the surface longer than 3 000 m. Zones marked in blue-green are steeply dipping or vertical and are less than 3 000 m in length. Zones marked in green are gently dipping. Reproduced from Figure 5-13 in Stephens et al. (2007).*

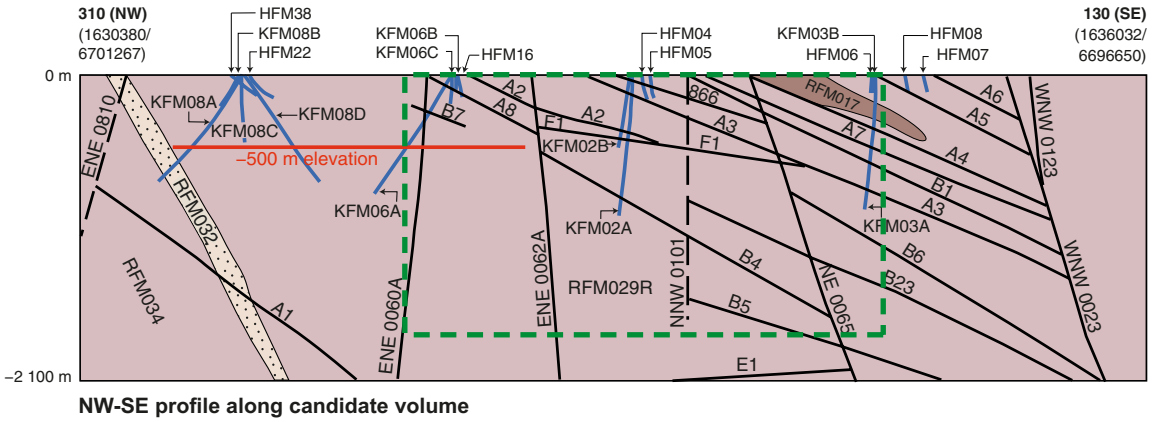

Figure 1-10. *WNW–ESE cross-section through the candidate volume in the structural model showing rock domains and deformation zones. Reproduced from Figure 11-13 of the Site description Forsmark.*

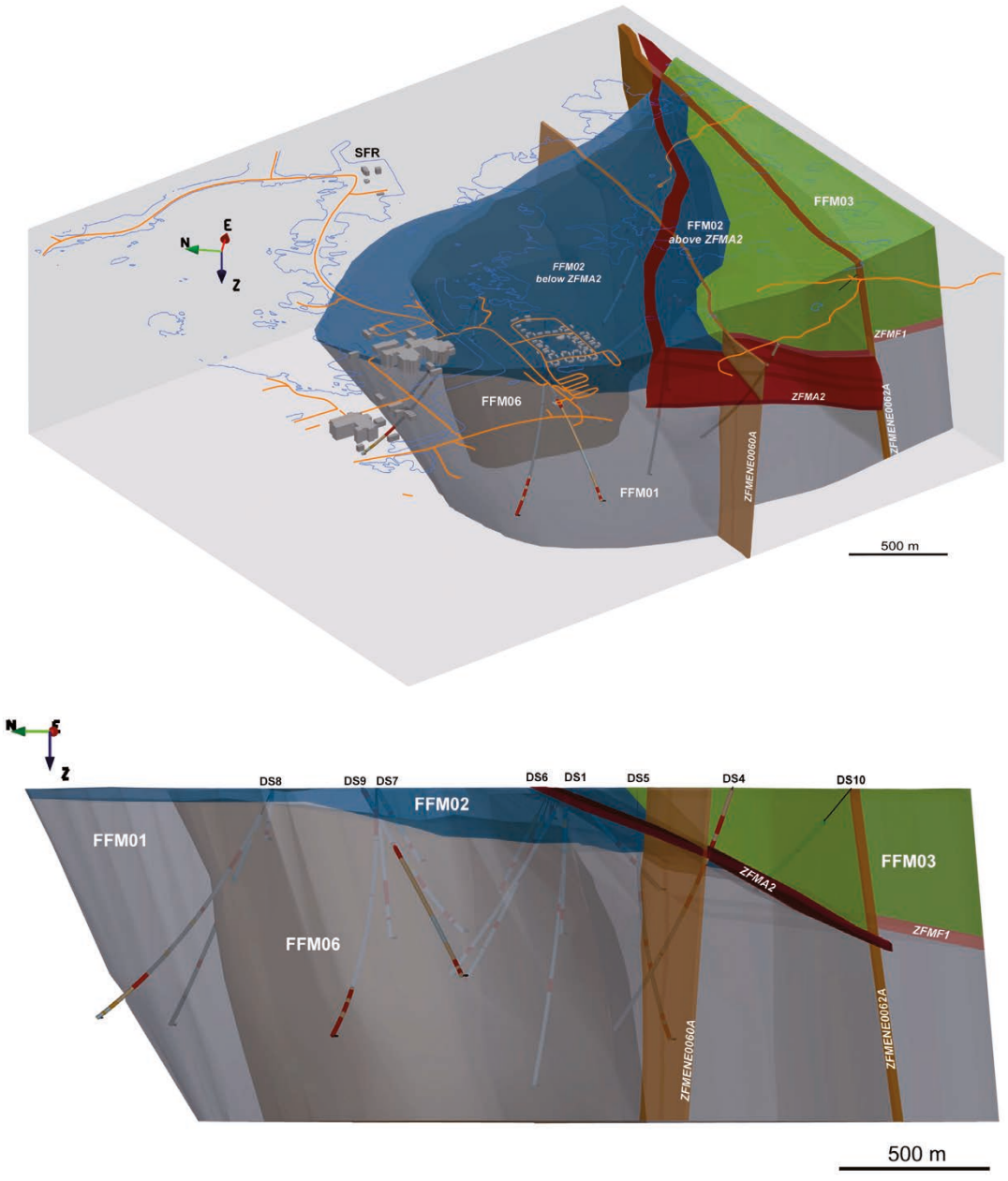

Figure 1-11. *Three dimensional views of fracture domains in the target area of Forsmark. Images reproduced from Figures 5-4 and 5-7 of Olofsson et al. (2007).*

2 Methodology for identifying and qualifying data

As mentioned in Section 1.2.2, the identification of essential data to be qualified in this Data report is primarily performed by using the AMF approach. A parallel approach has been used in the case of radionuclide transport modelling, where the input data needs of the computational codes COMP23 and FARF31 have been closely examined. These two approaches are outlined in Sections 2.1 and 2.2. Once a set of data has been identified it is qualified according to a standardised procedure, as detailed in Section 2.3.

2.1 Identifying data via assessment model flowcharts

Assessment model flowcharts (AMFs) give an overview of models used in the evaluation of repository evolution and safety, the dependencies/interactions between the models, and data used in the modelling. Two assessment model flowcharts have been developed. One AMF represents the excavation/operation and initial temperate period (cf Figure 2-1) and one represents periglacial and glacial conditions (cf Figure 2-2). The role of AMFs in the safety assessment is further described in the **Post-closure safety report** (Section 7.5).

In the AMFs, each blue box represents one or more subject area sections of this Data report, and is either labelled according to the section title or the concerned data. The section number is given in the parentheses. The modelling activities and assessments that use the data as inputs are represented by the yellow rounded rectangles and white rounded rhombuses, respectively. Modelling tasks are presented in the **Model summary report**.

The couplings between subject area sections and modelling activities and assessments are summarised in Table 2-1 to Table 2-5. An example of such a coupling is between the solubility data qualified in Section 3.1 and the solubility modelling of radioelements inside the canister, using the data as inputs. This coupling is shown in the lower corner of Figure 2-1 by the arrow from the blue box “Solubility data (DR 3.4)” to the yellow modelling activity “solubilities (TR-10-50[3])”. The solubility data are indirectly propagated to subsequent modelling activities, for example “Radionuclide transport, near field”. In Table 2-1 to Table 2-5, however, only the direct couplings of the AMFs are given.

There are also couplings between blue boxes in the AMFs. For example, “Inventory for RN transport (DR 3.1)” feeds into “IRF and CRF (DR 3.2)”. In such a case, data qualified in one section function as direct inputs to another section. Table 2-1 to Table 2-5, data that feeds more or less directly into other sections are indicated at a greater level of detail than in the AMFs. In should be noted that neither the AMFs nor the tables aim to present the complete picture of how data and models are coupled in the safety assessment.

Data concerning the spent fuel are dealt with in Chapter 3, and are primarily used as inputs when assessing the source term in near-field radionuclide transport modelling. The couplings between the data in Chapter 3 and the AMFs are given in Table 2-1. It should be noted that a large quantity of spent fuel data are also qualified in the **Spent fuel report**.

A majority of the data concerning the canister is qualified in the **Canister production report**, wherein dimensions, geometries, material data, etc are found. As a result there is a limited set of canister data that needs to be qualified in this Data report, as presented in Chapter 4. The couplings between data in Chapter 4 and the AMFs are given in Table 2-2.

[3] The number, in this case TR-10-50, refers to the SKB report where the modeling activity is reported.

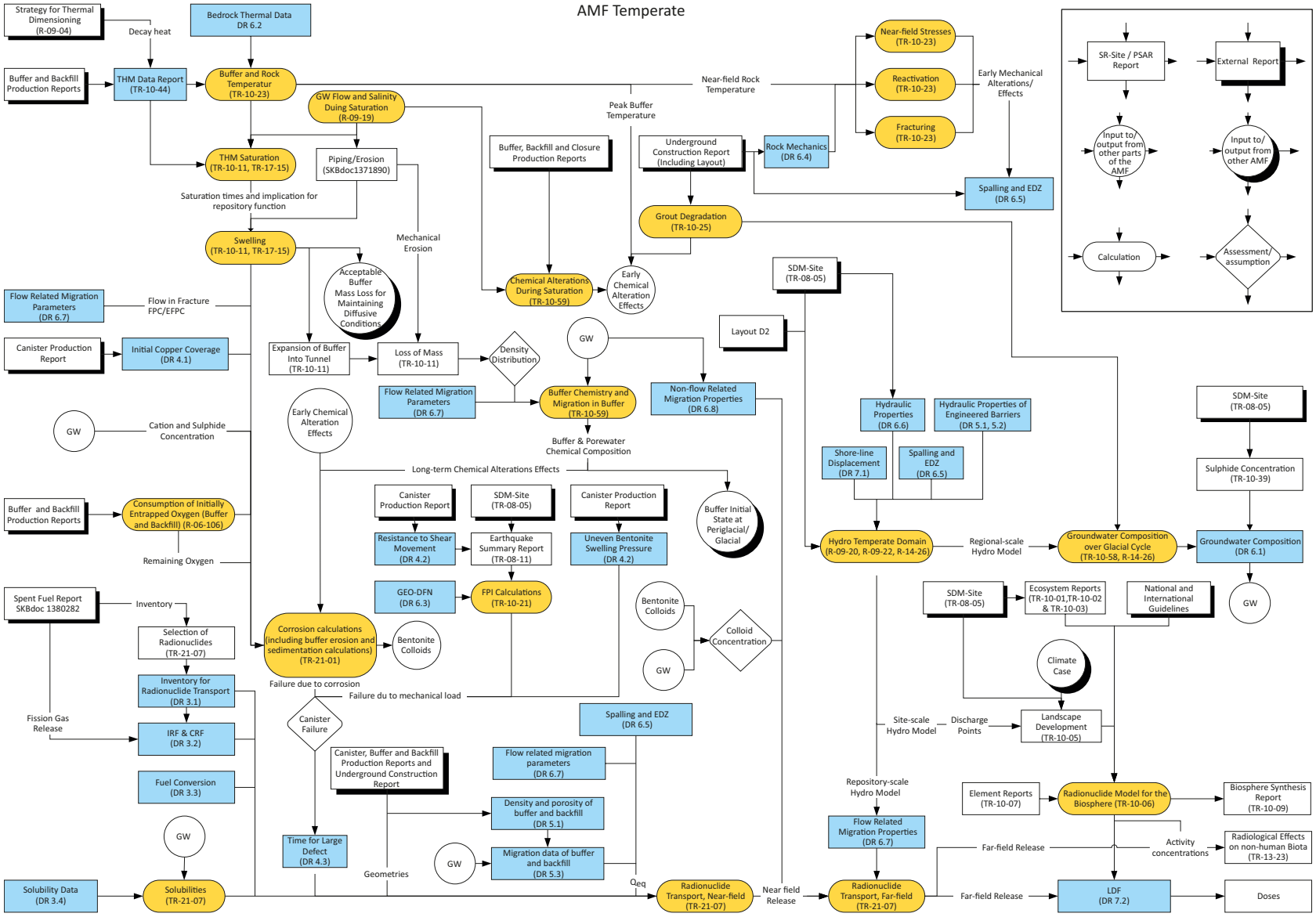

Figure 2-1. *The assessment model flowchart for the excavation/operation period and the initial temperate period after closure.*

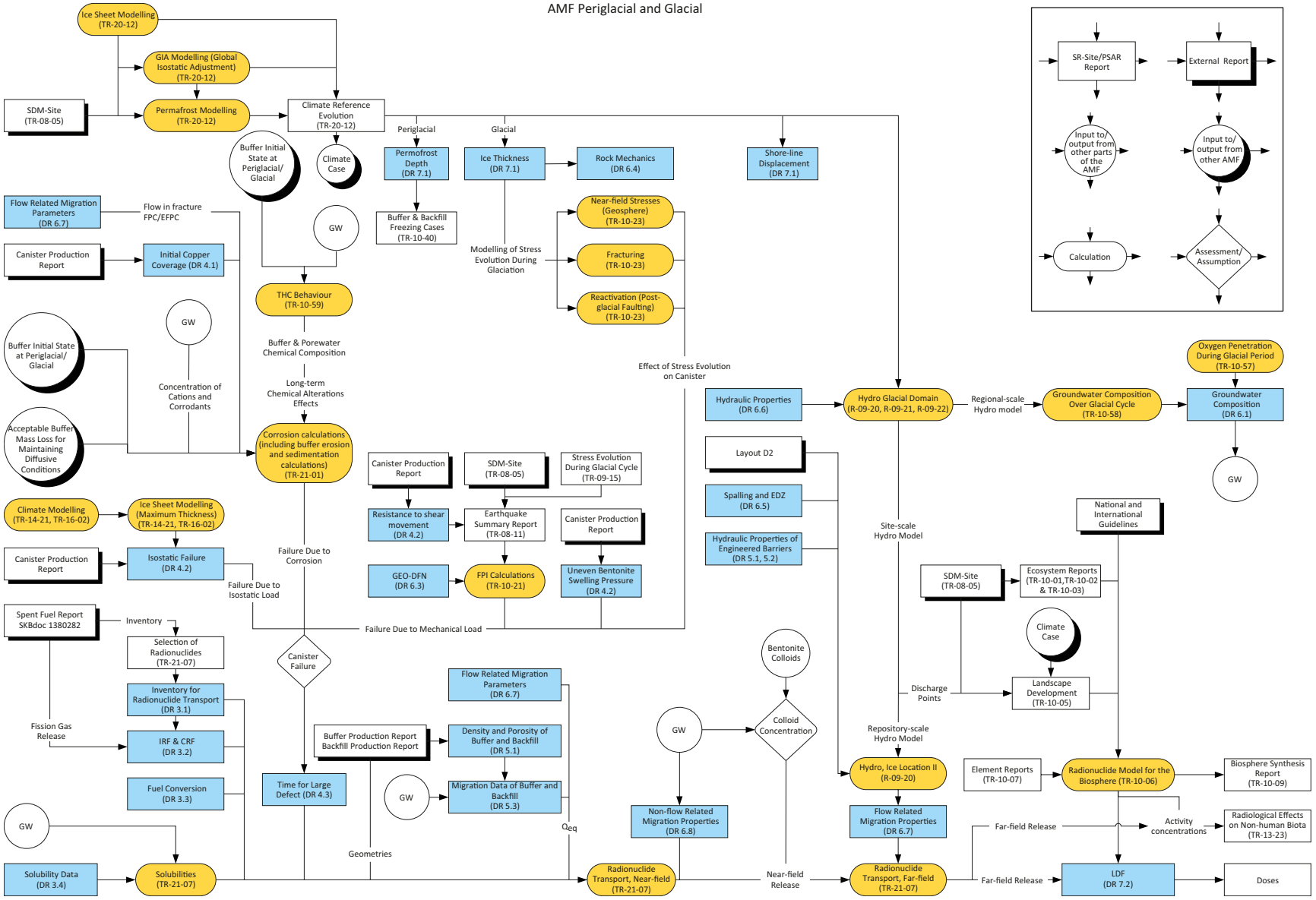

Figure 2-2. *The assessment model flowchart for periglacial and glacial conditions.*

Data concerning the buffer and backfill are provided in Chapter 5 and are primarily inputs to near-field radionuclide transport modelling, copper corrosion calculations, and hydrogeological modelling. This is outlined in Table 2-3. Other buffer and backfill data, such as geometries and compositions, are qualified in the **Buffer production report** and the **Backfill production report**.

Table 2-1. Couplings between subject area sections of Chapter 3 and items in the assessment model flowcharts (AMF1 and AMF2) and other Data report sections (DR).

Section number/title	Data provided	Primarily supports
3.1 Selected inventory.	Radionuclide inventories of the BWR and PWR type canisters and average canister, and half-lives and specific activities.	AMF1: Radionuclide transport, near-field. AMF2: Radionuclide transport, near-field. DR: 3.2
3.2 Instant release fraction and corrosion release fraction.	Instant release fraction, corrosion release fraction, fission gas releases, and corrosion time for the BWR and PWR type canisters and average canister.	AMF1: Radionuclide transport, near-field. AMF2: Radionuclide transport, near-field.
3.3 Fuel conversion.	The fuel conversion rate for the UO2 fuel matrix.	AMF1: Radionuclide transport, near-field. AMF2: Radionuclide transport, near-field.
3.4 Solubility data.	Solubility limiting phases with associated reactions and thermodynamic data. For use inside the canister.	AMF1: Solubilities. AMF2: Solubilities.

AMF1 = Figure 2-1, AMF2 = Figure 2-2.

Table 2-2. Couplings between subject area sections of Chapter 4 and items in the assessment model flowcharts (AMF1 and AMF2) and other Data report sections (DR).

Section number/title	Data provided	Primarily supports
4.1 Data of the intact canister.	Initial minimum copper thickness, canister void volumes, and canister's resistance to mechanical loads.	AMF1: Corrosion calculations and buffer erosion. FPI calculations. Canister failure. Radionuclide transport, near-field. AMF2: Corrosion calculations and buffer erosion. FPI calculations. Canister failure. Radionuclide transport, near-field. DR: 4.2
4.2 Evolving canister defect.	Delay time, defect radius, and tlarge for the different failure modes.	AMF1: Radionuclide transport, near-field. AMF2: Radionuclide transport, near-field.

AMF1 = Figure 2-1, AMF2 = Figure 2-2, void volume is input to Radionuclide transport, near-field, not shown in AMFs.

Table 2-3. Couplings between subject area sections of Chapter 5 and items in the assessment model flowcharts (AMF1 and AMF2) and other Data report sections (DR).

Section number/title	Data provided	Primarily supports
5.1 Density and porosity of buffer and backfill.	Dry density, saturated density, and physical porosity of the buffer and backfill.	AMF1: Hydro temperate domain. AMF2: Hydro, ice location II. DR: 3.2, 3.3
5.2 Hydraulic properties of buffer and backfill.	Hydraulic conductivity of the buffer and backfill.	AMF1: Hydro temperate domain. AMF2: Hydro, ice location II. DR: 4.2, 6.6
5.3 Migration data of buffer and backfill.	Sorption partitioning coefficient, effective diffusivity, and diffusion available porosity of the buffer and backfill.	AMF1: Radionuclide transport, near-field. Corrosion calculations and buffer erosion. AMF2: Radionuclide transport, near-field. Corrosion calculations and buffer erosion.

AMF1 = Figure 2-1, AMF2 = Figure 2-2.

In Chapter 6, geosphere data are presented. discussing a variety of subject areas providing geochemical, thermo-hydro-mechanical, geological, hydrogeological, and solute transport data. The couplings between the geosphere data of Chapter 6 and the AMFs are given in Table 2-4. What is not shown in the table is that geosphere data in Appendix A supports hydrogeological modelling as well as Section 6.6.

Chapter 7 concerns surface system data including climate related data and landscape dose conversion factors. Couplings between surface system data and the AMFs are given in Table 2-5.

Table 2-4. Couplings between subject area sections of Chapter 6 and items in the assessment model flowcharts (AMF1 and AMF2) and other Data report sections (DR).

Section number/title	Data provided	Primarily supports
6.1 Groundwater chemical composition.	Groundwater chemical composition data for main cations, anions, pH, and redox potential over the glacial cycle.	AMF1: Corrosion calculations and buffer erosion. Solubilities. Buffer chemistry and migration. Colloid concentration. AMF2: Corrosion calculations and buffer erosion. Solubilities. THC behaviour. Colloid concentration. DR: 3.2, 3.3, 5.3, 6.6, 6.8
6.2 Bedrock thermal properties.	Thermal properties of different rock volumes, temperature margin, in situ temperature, internal heat generation, and geothermal flow.	AMF1: Buffer and rock temperature. AMF2: Permafrost modelling. DR: 6.4, 6.5, 7.1
6.3 Discrete-Fracture Network (DFN) models.	Parameters of the geological DFN model for different fracture sets.	AMF1: FPI calculations. AMF2: FPI calculations. DR: 6.6
6.4 Rock mechanics.	Mechanical properties of the rock mass and of fractures, as well as in situ stresses during the glacial cycle and the stress-transmissivity relation.	AMF1: Near-field stresses. Reactivation. Fracturing. AMF2: Near-field stresses. Reactivation. Fracturing. Hydro glacial domain. DR: 6.5, 6.6

Table 2-4. Continued.

Section number/title	Data provided	Primarily supports	
6.5 Spalling and the excavation damaged zone.	Potential for spalling, and hydraulic and migration properties of the spalled zone and excavation damaged zone.	AMF1:	Corrosion calculations and buffer erosion. Hydro temperature domain. Radionuclide transport, near-field.
		AMF2:	Corrosion calculations and buffer erosion. Hydro, ice location II. Radionuclide transport, near-field.
		DR:	6.6
6.6 Quantities for groundwater flow modelling.	Parameters of the hydrogeological DFN model, ECPM model, and CPM model, including fracture aperture.	AMF1:	Hydro temperate domain. Corrosion calculations and buffer erosion.
		AMF2:	Hydro glacial domain. Corrosion calculations and buffer erosion.
		DR:	6.1, 6.7
6.7 Flow related migration properties.	Data from hydrogeological modelling including Darcy fluxes, equivalent flow rates, advective travel times, and flow related transport resistance. Also dispersion and maximum penetration depth for matrix diffusion.	AMF1:	Radionuclide transport, near-field. Radionuclide transport, far-field. Corrosion calculations and buffer erosion. Buffer chemistry and migration.
		AMF2:	Radionuclide transport, near-field. Radionuclide transport, far-field. Corrosion calculations and buffer erosion. Oxygen penetration.
		DR:	6.1
6.8 Non-flow related migration properties.	Sorption partitioning coefficient, effective diffusivity, diffusion available porosity, and connectivity of the rock matrix.	AMF1:	Radionuclide transport, far-field.
		AMF2:	Radionuclide transport, far-field. Oxygen penetration.
		DR:	6.1, 6.6, 6.7

AMF1 = Figure 2-1, AMF2 = Figure 2-2, requirements of oxygen penetration modelling not shown in AMFs.

Table 2-5. Couplings between subject area sections of Chapter 7 and items in the assessment model flowcharts (AMF1 and AMF2) and other Data report sections (DR).

Section number/title	Data provided	Primarily supports	
7.1 Climate and climate related data.	Air and ground-surface temperatures, ice thickness and ice surface gradients, shore-level changes, and permafrost and ground-freezing depths over the glacial cycle.	AMF1:	Hydro temperate domain Biosphere landscape model.
		AMF2:	Hydro glacial domain Biosphere landscape model.
		DR:	6.1, 6.4, 6.6, 7.2.
7.2 Landscape dose conversion factors.	Landscape dose conversion factors, LDF, for the different periods of the glacial cycle and LDF pulse for the temperate period.	AMF1:	Dose assessment.
		AMF2:	Dose assessment.

AMF1 = Figure 2-1, AMF2 = Figure 2-2.

2.2 Identifying data for radionuclide transport modelling

A special effort has been undertaken in the **Radionuclide transport report** to identify input data needed in radionuclide transport modelling. This effort concerns:

1. Identifying the radionuclides that may be of any significance for the safety assessment, and the needs of data that are radionuclide or radioelement specific.
2. Identifying what input data should be taken from the Data report, and what input data should be taken from other sources.

2.2.1 Selected inventory

Some of the data provided in this Data report are radionuclide or radioelement specific. The spent fuel is comprised of numerous of radionuclides whereof only a fraction is of importance for the assessment results. In the **Radionuclide transport report** (Appendix D), the radionuclides that may be of any significance for the safety assessment have been identified. These radionuclides comprise the selected inventory, as listed in Table 2-6.

In Table 2-6, the radionuclides are sorted into the three categories “Important”, “Less important”, and “Needs only inventory and half-lives”, as justified in the **Radionuclide transport report** (Appendix D). Based on this categorisation, there are different demands on the delivery from this Data report. For the important radionuclides, the entire set of nuclide or element specific data are provided. This full set of data comprises:

- Inventory data and half-lives (Section 3.1).
- Instant release fraction and corrosion release fraction (Section 3.2).
- Solubility data (Section 3.1).
- Diffusion available porosity, effective diffusivity, and sorption partitioning coefficient in the buffer and backfill (Section 5.3).
- Diffusion available porosity, effective diffusivity, and sorption partitioning coefficient in the fractured rock (Section 6.8).
- Landscape dose conversion factors (Section 7.2).

For the less important radionuclides, all of the above data have been requested from the supplier, but in some instances the suppliers have not provided the data. For each such instance the assessment team have recommended data for use in radionuclide transport modelling, often by means of recommending pessimistic data. A note on each instance is given in the corresponding subject area section. For the radionuclides for which only the inventory and half-life are required, such data are found in Section 3.1.

A set of nuclide specific data that is not listed in the above bullet list is *LDF pulse* (Section 7.2), which is only provided for radionuclides that may be released as a pulse, together with the prerequisite that they may be of any significance for the safety assessment.

Table 2-6. Selected radionuclides for which data are needed in radionuclide transport modelling. Based on Table D-6 of the Radionuclide transport report.

Important	Less important[1]	Need only inventory and half-lives[2]
Fission and activation products		
C-14	Ag-108m	
Cl-36	Cd-113m	
Cs-135	Eu-152	
Cs-137	H-3	
I-129	Nb-93m	
Nb-94	Ni-63	
Ni-59	Sm-151	
Pd-107	Sn-121m	
Se-79	Ho-166m	
Sn-126	Mo-93	
Sr-90		
Tc-99		
Zr-93		
Decay chains		
4n		
Pu-240	Cm-244	
U-236		
Th-232		
4n+1		
Cm-245	Pu-241	U-237
Am-241		Pa-233
Np-237		
U-233		
Th-229		
4n+2		
Cm-246	Am-242m	Am-242
Pu-242	Pu-238	Cm-242
U-238		Np-238
U-234		Th-234
Th-230		Pa-234m
Ra-226		
Pb-210		
4n+3		
Am-243	Cm-243	Np-239
Pu-239		
U-235		
Pa-231		
Ac-227		

[1] Radionuclides that might be of importance in the hypothetical cases of initial or early defects in the canister.

[2] Radionuclides with such short half-life that their contribution in safety assessment modelling is through decay products.

2.2.2 Input to radionuclide transport modelling

All input parameters to the radionuclide transport modelling codes COMP23 (Romero et al. 1999, Cliffe and Kelly 2006, Vahlund and Hermansson 2006) and FARF31 (Norman and Kjellbert 1990, Elert et al. 2004) are listed in Table 3-2 and Table G-1 of the **Radionuclide transport report**. Out of all these parameters, those qualified in the Data report are listed in Table 2-7. In the leftmost column the parameter name in the computational code is given. In the right part of the table, the concerned section in the Data report is given together with the symbol used.

Table 2-7. Input parameters for the probabilistic calculations for the corrosion, shear load, isostatic load and pinhole scenarios. The first four columns are reproduced from the Radionuclide transport report (Table 3-2) for selected rows concerning the Data report. NF = near field (COMP23), FF = far field (FARF31).

Parameter name in code	Parameter	Unit	NF/FF	Data report section, symbol, and comment		
HALFLIFE	Half-life.	Yr	NF/FF	3.1	$t_{½}$	
INVENTORY	Radionuclide inventory.	mol/can	NF	3.1		a
FDMC	Fuel dissolution time.	Yr	NF	3.3		b
IRF	Instant release fraction of inventory.	-	NF	3.2	*IRF*	
CRF	Corrosion release fraction of inventory.	-	NF	3.2	*CRF*	
TCORR	Corrosion time.	Yr	NF	3.2	t_{corr}	
TDELAY	Delay time for onset of radionuclide transport.	Yr	NF	4.2	t_{delay}	
TLARGE	Time for large canister defect.	Yr	NF	4.2	t_{large}	
ADELAY, ALARGE	Canister defect sizes.	m	NF	4.2	r_{defect}	
CSOL	Solubility limits.	mol/m^3	NF	3.4		c
KDB	Buffer sorption partitioning coefficients.	m^3/kg	NF	5.3	K_d	
DEB	Buffer effective diffusivities.	m^2/s	NF	5.3	D_e	
EPSB	Buffer porosities (diffusion available porosity).	-	NF	5.3	ε	
RHO for material 2	Buffer density (density of the solid particles).	kg/m^3	NF	5.1	ρ_s	
KDBF	Backfill sorption partitioning coefficients.	m^3/kg	NF	5.3	K_d	
DEBF	Backfill effective diffusivities.	m^2/s	NF	5.3	D_e	
EPSBF	Backfill porosity (diffusion available porosity).	-	NF	5.3	ε	
RHO for material 3	Backfill density (density of the solid particles).	kg/m^3	NF	5.1	ρ_s	
QEQ_1	Equivalent flow from deposition hole to fracture(s) intersecting deposition hole.	m^3/yr	NF	6.7	Q_{eq1}	
QEQ_2	Equivalent flow to EDZ.	m^3/yr	NF	6.7	Q_{eq2}	
QEQ_3	Equivalent flow to fractures intersecting deposition tunnel.	m^3/yr	NF	6.7	Q_{eq3}	
U0_1	Darcy flux at deposition hole.	m^3/m^2,yr	NF	6.7	q	
Wzone	Width of spalling zone.	m	NF	6.5	W_{zone}	
Lzone	Length of spalling zone.	m	NF	6.5	L_{zone}	
dzone	Thickness of spalling zone.	m	NF	6.5	d_{zone}	
epszone	Porosity of spalling zone.	-	NF	6.5	ε_{zone}	
Dp	Diffusion coefficient in spalling zone (damaged zone).	m^2/s	NF	6.5		d
Dw	Diffusivity in water.	m^2/s	NF	6.8	D_w	
KDR	Rock sorption partitioning coefficients.	m^3/kg	FF	6.8	K_d	
DER	Rock effective diffusivities.	m^2/s	FF	6.8	D_e	
EPSR	Rock porosities (diffusion available porosity).	-	FF	6.8	ε	
	Rock density (solid density).	kg/m^3	FF	6.4	ρ	
F_1, F_2, F_3	Rock transport resistance for paths beginning at Q1, Q2 and Q3.	yr/m	FF	6.7	F	
TW_1, TW_2, TW_3	Rock advective travel time for paths beginning at Q1, Q2 and Q3.	Yr	FF	6.7	t_w	
PE	Rock Peclet number.	-	FF	6.7	Pe	
DPEN	Max. penetration depth in rock matrix.	m	FF	6.7	L_D	
LDF	Biosphere LDF factors.	Sv/y per Bq/y	FF	7.2	*LDF*	
	Void volume.	m^3	NF	4.1	V	e

a. Inventory provided and used as mol/canister, although the unit in Table 3-2 is given as mol.

b. The Data report provides the Fuel dissolution rate (yr^{-1}).

c. The Data report provides input data to solubility limit calculations, but not solubility limits.

d. Dp is not provided in the Data report, but can be calculated from D_w/τ_y^2, *where* τ_y is the zone tortuosity.

e. Void volume is not included in Table 3-2 but requested in Table G-1 of the Radionuclide transport report.

2.3 Qualification of input data – instruction to the supplier and customer

The final objective of the Data report is at performing data qualification including estimates of both conceptual and data uncertainty, as well as of natural variability, for various subject areas. In addition, the traceability of the data is examined. The qualified data are intended for use as input data in the safety assessment modelling.

The Data report does not concern all data used in the safety assessment, but those which are identified to be of particular significance for assessing repository safety (see Sections 2.1 and 2.2). Data may concern both measured data from the laboratory and from the field, as well as output from detailed modelling where measured data are interpreted, depending on the subject area. Even though the data may represent both parameters and entities, in this instruction the word "data" is generally used.

It should be pointed out that in the process of qualifying data, the traceability that is the focus of many quality assurance systems is only one aspect. An equally important aspect is the scrutinising of the scientific adequacy of the data.

Each data set provided in this report is categorised into one of many different subject areas. For each subject area, the data qualification process comprises a sequence of stages resulting in a text of a standard outline. The sequence of stages and the standard outline are shown in Figure 2-3.

Below the parties involved in the Data report and the sequence of stages shown in Figure 2-3 are discussed. The standard outline is described in Sections 2.3.1 to 2.3.12. For each subject area, the Data report team identifies the customer and supplier of data, and assigns a customer representative and a supplier representative that co-author the subject area section[4].

The customer is in broader terms the assessment team that is responsible for performing the safety assessment. However, the entire team is generally not involved in each subject area but it is rather embodied by a group of persons with special knowledge and responsibility. The customer representative should represent the assessment team, and not rely solely upon own opinions.

The suppliers are the teams originating the sources of data, for example the site-descriptive model reports, production reports, and other supporting documents. The supplier representative should represent the team, and not rely solely upon own opinions.

The intended chronology of the writing of a subject area section is the following.

Stage A: The customer writes the first two sections defining what data are requested from the supplier, how the data will be used in safety assessment modelling, and how similar data were used in previous assessments.

Stage B: The supplier writes the following eight sections that are the core of the data qualification. This is done according to a standard outline where a number of issues such as traceability, data uncertainty, and natural variability should be dealt with. These sections should result in sets of qualified data that are the delivery to the customer.

Stage C: The customer, representing the entire assessment team, writes the last two sections making judgements upon the delivery and recommending data for use in the safety assessment modelling. The text is produced in close cooperation with other persons within the assessment team with special knowledge and responsibility. The text should reflect upon the formal decision taken in Stage D (accordingly, it may need to be revised after Stage D).

The text of each stage should be made available in good time to the person or persons responsible for writing the text of the subsequent stage. Upon completion of Stage C, a data qualification meeting is held (Stage D) and the text is subjected to factual review (Stage E). If case the subject area text has been well communicated during its preparation, and the customer and supplier share the views of the text, the data qualification meeting (Stage D) may be held after the factual review (Stage E), to get an external input on the data delivered.

[4] The terms customer and supplier come from standard quality assurance terminology.

Stage D: For each subject area, a data qualification meeting is held where the customer and supplier representatives, and at least one member of the Data report team are invited. Appropriate members of the assessment team and supplier team may also be are invited. At the meeting, the data delivery to the safety assessment is formally decided upon and the decision is recorded in minutes (documented according to SKB's quality assurance system). For the PSAR, data qualification meetings have only been conducted when the recommended data has been updated (Sections 3.1, 3.2 and 3.3).

Stage E: The subject area section is subjected to a factual review according to standard procedures.

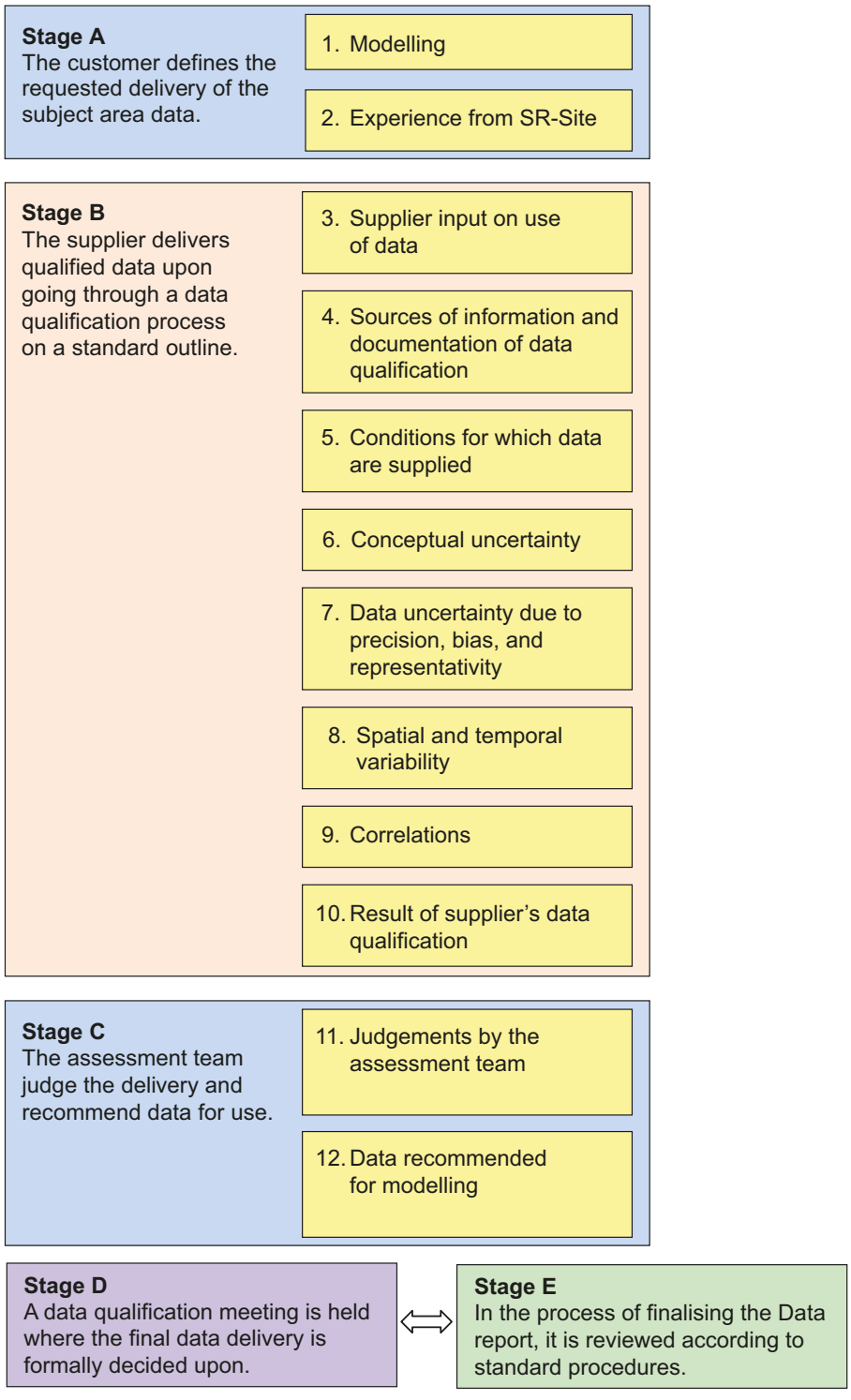

Figure 2-3. *Stages of writing and reviewing the Data report. The standard outline of a subject area is shown in the yellow boxes.*

Finally, within the assessment project but outside the scope of the Data report team, a follow-up is made where it is controlled that the correct data are used. This could be seen as Stage F in the data qualification process, but its falls upon the modellers using the data to carry this stage through. It is therefore not shown in Figure 2-3.

In the following sections, the outline shown in the yellow boxes in Figure 2-3 is described in detail. The text is based on an SKB quality assurance document "Supplying data for the SR-Site Data report" which was used in SR-Site. However, to fit the format of this SKB report, editorial modifications have been made. To limit the number of editorial modifications, the grammatical tense of the instruction has been kept.

Based on the experiences from SR-Site (stage A in Figure 2-3 and presented, for each subject area, in Sections x.x.1 to x.x.2), the majority of the modelling activities in the currents safety assessment use the same data and models as in SR-Site. For many of these, the qualification process is reproduced from the SR-Site Data report (stage B in Figure 2-3 is presented, for each subject area, in Sections x.x.3 to x.x.10). The justification for using this data (stage C in Figure 2-3 is presented, for each subject area, in Sections x.x.11 to x.x.12).

2.3.1 Modelling

In this section, the customer should define what data are requested from the supplier, and give a brief explanation of how the data of the subject area are intended to be used in modelling activities.

Defining the data requested from the supplier

Here, the customer should define the data (parameters) that should be part of the supplier's delivery, in a bullet list. If applicable, the parameter symbol and unit should be provided in this list. If the supplier should focus on providing data of certain ranges, or for certain conditions, this should be specified. This text should not only facilitate the task of the supplier, but also assist the reader of the Data report in understanding the scope of the subject area section.

Modelling activities in which data will be used

Here the customer should give a brief explanation of how the data are intended to be used in different modelling activities. This explanation should cover both how the data are used in specific models, and in the model chain (unless evident from the assessment model flowcharts). Differences from the use of this type of data in SR-Site should be highlighted. The justification for the use of these models in the assessment is provided in other documents, such as the **Post-closure safety report** and process reports.

As a result of the extensive work that will be conducted up to near completion of the SR-Site safety assessment, details of the models and the model chain may be modified. As a result, this text may have to be finalised in a late stage of the Data report project. Thus only a preliminary version is provided early on to the supplier.

2.3.2 Experience from SR-Site

In this section the customer should give a brief summary on how data of the subject area were used in SR-Site. The experience from SR-Site should function as one of the bases for defining the input data required. It should be noted that the teams undertaking the safety assessments largely are the same, so transferring experience from previous assessments should not present any substantial problem. The summary of how the data were used in SR-Site should conform to the following outline:

- Modelling in SR-Site.
- Conditions for which data were used in SR-Site.
- Sensitivity to assessment results in SR-Site.
- Alternative modelling in SR-Site.
- Correlations used in SR-Site modelling.
- Identified limitations of the data used in SR-Site modelling.

More detailed guidance regarding what should be included in the summary in relation to each of these bullets is given below.

Modelling in SR-Site

The use of the data in specific SR-Site models, as well as in the SR-Site model chain, should be described. The summary should be kept short and focus upon differences between the use of data in SR-Site and the current assessment. Repetitions from the section "Modelling" should be avoided. If there is no difference between the SR-Site and the current assessment modelling approaches, it is sufficient to state this.

Conditions for which data were used in SR-Site

In this section, the relevant conditions to which the subject area data were subjected to in SR-Site modelling should be outlined. Relevant conditions are only those conditions that significantly influence the data, in the context of demonstrating repository safety. Different subject area data are affected by different conditions. For example, the sorption partition coefficient K_d may be strongly influenced by groundwater salinity. Thus, in characterising the conditions under which K_d values were used, it is likely to be appropriate to give the salinity range during repository evolution, for example as assessed in the SR-Site hydrogeochemical modelling. Other types of conditions may include gradients, boundary conditions, initial states, engineering circumstances, etc.

It is sufficient to state the relevant conditions used in SR-Site modelling (including those applied in sensitivity analyses, various initial states, different scenarios, and evolution within scenarios) and to refer to SR-Site documents for background information. Justification as to why those conditions were studied is not required. Where appropriate, the relevant conditions should be tabulated. It should be noted that the stated conditions do not restrict qualification of data for use under other conditions, but merely underline the conditions considered appropriate within the modelling context of SR-Site. If conditions of SR-Site were similar to those of the current assessment, it is sufficient to state this.

Sensitivity to assessment results in SR-Site

Where appropriate, an account should be given of results from sensitivity analyses performed as part of, or prior to, the SR-Site safety assessment. Such analyses were made in order to prioritise uncertainty assessments for those data and conditions judged to be potentially important for performance, both for overall end-points such as risk and for conditions affecting the state of the system. If such sensitivity analysis was performed, the following issues may be outlined:

- For what ranges of the data was the impact on the SR-Site safety assessment significant and are there ranges where the impact was negligible? If sensitivity analyses show that only part of the range has an impact on repository safety, less effort may be given to quantifying parameter values outside this range.
- Was the impact monotonic, i.e. is there a unidirectional relationship between the data value and performance, is there an "optimal" value, or is the impact dependent in a complicated manner upon the values of other input data?
- What degree of variation in the data is needed to have an impact on safety assessment results (this may be different for different data ranges)?
- Were the results applicable to all conditions of interest – or only to some?

In discussing the above, the customer should consider if the cited sensitivity analyses were sufficiently general to provide definitive answers.

Alternative modelling in SR-Site

Whenever it applies, the customer should summarise alternative modelling in SR-Site focusing on the concerned data. The following issues should be reflected upon:

- What alternative models exist and what influence did they have on the safety assessment?
- Were conceptual uncertainties, related to the models in which the data were used, identified in SR-Can? In that case, what was the impact on assessment results?

Correlations used in SR-Site modelling

A correct treatment of probabilistic input data requires that any correlations between those data are identified and quantified. The correlations associated with the subject area data, as accounted for in SR-Site, should be briefly described. This includes internal correlations within the subject area and correlations with data of other subject area sections. If the same correlations were used as will be used in the current assessment, it is sufficient to state this.

Identified limitations of the data used in SR-Site modelling

If limitations or shortcomings of the data used in SR-Site have been identified, which may significantly have affected the assessment, such should be accounted for. The limitations or shortcomings can be due to, for example, lack of site-specific data or lack of data obtained at conditions representative for the repository. The limitations and shortcomings may have been identified by the regulatory authorities, by SKB, or by other parties.

2.3.3 Supplier input on use of data in SR-Site and the current assessment

In this section the supplier has the opportunity to comment on the two above sections. The focus for the supplier should be to help the SR-Site team in choosing appropriate data and modelling approaches, and avoid repeating errors and propagating misconceptions from SR-Site or from earlier safety analyses. Even if a single individual has the roles as both supplier and customer representative, he or she may still make comment upon the use of data in SR-Site and the current assessment.

2.3.4 Sources of information and documentation of data qualification

This section is devoted to presenting the most important sources of data, as well as categorising different data sets on the basis of their traceability and transparency, and scientific adequacy. Sources of data may include SKB reports, SKB databases, and public domain material. Documents of importance for the data qualification may also consist of SKB internal documents. All underlying documents should be properly cited throughout the Data report.

Sources of information

The supplier is asked to tabulate the most prominent references used as sources of data. In addition, the references of important documents describing the process of acquiring, interpreting, and refining data may be listed.

If the data qualification process is well documented in supporting documents, it is sufficient to reference these documents and to only briefly summarise the data qualification process. If not, the Data report gives the supplier a chance to appropriately document the data qualification process of the subject area data.

Concerning sources of information, the supplier should:

- Fully cite all sources of information throughout the text. It is necessary to keep in mind that the text may have readers with limited in-depth knowledge of the subject. Therefore, what normally would seem as trivial may deserve references for further reading. It is strongly recommended to make an extra effort to refer to the open literature where possible, and not only to SKB documents.
- In case of referring to a document of many pages, for example a site-descriptive model report, give detailed information on the section, figure, table, etc where the relevant information can be found.

- Properly cite databases, SKB internal documents, etc even though they may not be available to the general reader. In the case of referring to databases, the precise reference should be given to the individual data set used. For example, it is not sufficient to refer to the SKB database Sicada if not also giving detailed information, such as the activity or the number of a Sicada delivery note. This is to ensure traceability.
- Fully cite advanced modelling tools where the underlying code may have implications for data qualification.

Categorising data sets as qualified or supporting

The supplier should categorise data as either qualified data or supporting data. Qualified data has been produced within, and/or in accordance with, the current framework of data qualification, whereas supporting data has been produced outside, and/or in divergence with, this framework. Data taken from peer-reviewed literature take a special position in that they may be considered as qualified even though they are produced outside the SKB framework of data qualification. However, such data are not by necessity categorised as qualified, as they may be non-representative or lack in some other aspect.

Data recently produced by SKB, for example in the site investigations, should a priori be considered as qualified. However, before the data are formally categorised as qualified, a number of considerations need to be made as described below. Data produced outside the data qualification framework should a priori be considered as supporting data. This could for example be data produced by SKB prior to the implementation of its quality assurance system, or data produced by other organisations. Before formally categorise the data as supporting, a number of considerations need to be made as described below.

Data taken from widespread textbooks, engineering handbooks, etc, which are considered to be established facts, need not to be scrutinised. Well-known data that should be excluded from the Data report need not to be categorised as qualified or supporting data, although their exclusion may need to be justified.

It is outside the scope of the Data report to deal with individual data. Instead the supplier should characterise data sets as qualified or supporting. The supplier should decide to what extent various data can be included in a single data set for the specific case. The following examples of natural barrier data sets could be used for inspiration:

- Data, or part of data, obtained by a specific method at a site, rock volume, borehole, etc.
- Data, or part of data, obtained by various methods at certain conditions (e.g. saline water) at a site, rock volume, borehole, etc.
- Data, or part of data, taken from an external publication.

Qualified data

The following considerations should be made for data that a priori are identified as qualified, before formally categorising them as qualified. Most of the data that is delivered to the Data report are refinements and interpretations of observed data. Such refinements and interpretations are performed both for engineered and natural barrier data. For example, the multitude of data acquired within the site investigation are normally refined within the site-descriptive modelling by use of more or less complex models. The supplier should judge whether data acquisition and refinement, and associated documentation, are in accordance with the implemented data qualification framework. The following considerations may form the basis for the judgement.

Considerations concerning data acquisition:

- Is the acquisition of observed data performed in conformance with a widely adopted quality management system (e.g. the ISO 9000 series or equivalent)?
- Is it possible to trace relevant quality assurance documents (for example method descriptions, field notes, etc) for the measurements? It should be noted that even though the quality assurance documents may not be available for the general reader, they are accessible for the SR-Site team.

- Is it possible to extract relevant information on the data quality, variability, and representativity from documents reporting the acquisition of data?
- Are concerns associated with the observed data and nonconformities of the measurements transparently described?
- Is the undertaken data acquisition programme sufficient to determine the full range of data uncertainty and natural variability, and do the acquired data appropriately characterise the intended aspect of the system (site, rock domain, copper canister, population, etc)?

Considerations concerning data refinement:

- Are concerns and nonconformities described in the supporting documents propagated to, and addressed in, the data refinement?
- In refining observed data by use of more or less complex modelling, is this done in accordance with documented methods?
- In case of more complex modelling, which may have implication for data qualification, is the details of the modelling described in either a task description or the document reporting the modelling results? Furthermore, is the modelling tool developed in accordance with a widespread quality assurance system and/or is its quality tested in other ways?
- Has comparative/alternative modelling been performed to evaluate artefacts induced in the modelling, and to evaluate whether the modelled interpretation of the data is reasonable?

Going through these questions in detail for each data set may be a too extensive task. Accordingly, the sorting of data to some degree is based on expert judgement. However, in making this judgment, it may be helpful to revisit the above bullet lists.

If appropriate data qualification has been performed and documented in supporting documents, or can be performed and documented as part of the delivery, the data should be formally categorised as qualified data. If the documentation of the data qualification process is inadequate in supporting documents, and appropriate data qualification cannot be performed as part of the delivery, the data must be demoted to the category supporting data.

As mentioned before, data taken from peer-reviewed literature takes a special position in that they may be considered as qualified even though they are produced outside the SKB framework of data qualification. However, before formally categorising them, one needs to judge whether they are representative for the intended KBS-3 repository system and the Forsmark site. A prerequisite for making such a judgement is often that the documents are transparently written. In case the data are non-representative for Swedish conditions, or their degree of representativity is difficult to evaluate, the data may be categorised as supporting instead of as qualified.

Supporting data

The following considerations should be made for data that a priori are identified as supporting, before formally categorising them as supporting. Such data are produced by SKB outside the framework of data qualification, or by other organisations. The supplier should:

- Consider how well the method used to acquire the data is described? The greater the transparency with which the method is described in the supporting document, the greater the value should be ascribed to the data.
- Consider how well the method used to interpret and refining the data is described? The more transparently the interpretation and refinement is described in the supporting document, the greater the value should be ascribed to the data.
- Consider if it is possible to identify and evaluate the data qualification process used in acquiring and refining the data? If it is shown that a sound data qualification process has been used, the data should be ascribed greater value.
- Judge, based on the above, whether the data can be used as part of the basis for recommending data to SR-Site safety assessment modelling, as comparative data for other qualified data, or should not be used at all. In some cases the transparency of a document is so poor that crucial information

concerning data qualification cannot be extracted. If this renders an assessment of the data's scientific adequacy and their representativity for Swedish conditions impossible, the supplier should recommend that the data are dismissed. This can be done even if the numerical values of the data are consistent with other, qualified data.

In case data that a priori are assumed to be supporting are acquired, interpreted, and refined according to a similar data qualification framework as implemented by SKB, and the data are accurate and representative, the supplier can promote the data to the category qualified data.

It should be noted that data taken from peer-review literature can be categorised as supporting data. This can be done if, for example, data are only partially representative for the Swedish repository concept and the Forsmark site.

Upon formally categorising the data sets as qualified or supporting, they should be tabulated as exemplified in Table 2-8. As can be noted, justifications for the sorting are given in the same table for the numbered items.

Table 2-8. Qualified and supporting data sets (for parameter Y).

Qualified data sets	Supporting data sets
1. (SKB, 20xx), Section 4.5: All data on parameter Y obtained for rock domain RFM029. 2. Data presented in the **Underground openings construction report** in Figure x. 3. (Svensson, 20xx), Table 2: Data between the borehole length 400–452 m in KFM01D, indicating an average value of 2 650 m^3/kg. 4. All parameter Y data stored in SKB Database X, with the identity number xxx-yyy-zzz.	5. (Nilsson, 19xx), Table 1. Data obtained in the pH range 6–9 in sedimentary rock.
1–2, 4. These data have been produced within the site investigation (item 1), within a production report (item 2), or as part of the site-descriptive modelling (item 4). These data are produced within the SKB data qualification framework and are judged as qualified. 3. (Svensson, 20xx) is a peer-review article and the data are obtained at the Forsmark site and are judged as representative. The data set is judged as qualified. 5. (Nilsson, 19xx) is a peer-review article that is transparent and scientifically sound. However, the data are predominantly representative for sedimentary rock. Accordingly they are judge as supporting.	

Excluded data previously considered as important

Within the field of nuclear waste management, there are large quantities of data that are of little significance for the safety assessment, as they are less representative for the Forsmark site, the KBS-3 repository concept, etc than other available data. In general, excluding such data from subsequent use in the assessment does not require justification. The exception is if the data constitutes a well-known part of the basis of previous safety assessments (or equivalent tasks), and/or have a significant impact on the perception of the appropriate choice of data values. If it could be seen as a significant inconsistency or omission not to use the data, their exclusion should be explicitly justified. Providing an appropriate justification is particularly important if the excluded data disagree with the presently used data.

2.3.5 Conditions for which data are supplied

The data of the different subject areas are likely affected by different conditions. Conditions refer to initial conditions, boundary conditions, barrier states, and other circumstances, which potentially may affect the data to be estimated. In the process of qualifying data for subsequent use in safety assessment, an important part is to account for the conditions for which data were acquired, and to compare these conditions with those of interest for the safety assessment.

In the section "Experience from SR-Site" it is stated for what conditions data were used in SR-Site. These conditions should not limit the conditions for which data are examined, but merely point out conditions that are likely to be of importance for a safety assessment. The supplier may have been given instructions from the assessment team, or may have opinions about important conditions, which lead to modifications of the SR-Site conditions.

In this section, the conditions for which the data have been obtained should be discussed and, as appropriate, justified as relevant to the assessment. Such a condition is often a single value (e.g. temperature), a range (e.g. salinity range), or a gradient (e.g. hydraulic gradient). Other factors of relevance for repository safety may be included as conditions, at the discretion of the supplier. Conditions that are deemed to be of particular importance for repository safety should be highlighted. Other conditions that do not significantly relate to repository safety, but may be of importance for data qualification, are also important to note. Such information is valuable when, for example, crosschecking data sets with those of other studies or evaluations. The supplier may list ranges of applied conditions during data acquisition, excluding conditions that are both general and self-evident (such as the gravitation).

In many cases, it is expected that the conditions for which data are supplied will differ from those assumed in the safety assessment. For example, a set of supplied data may not represent the full temperature range required, or may have been obtained at a different pressure than expected *in situ*. The differences identified by the supplier should be outlined in this section. Furthermore, for each deviating condition of importance for the assessment results, the implications should be discussed.

2.3.6 Conceptual uncertainty

This section concerns conceptual uncertainty of the subject area data. Two types of conceptual uncertainty should be discussed. The first concerns how well the data, and the models wherein they are used, represent the physical reality, and the second concerns conceptual uncertainties introduced in the acquisition, interpretation, and refinement of the data. Generally data are included in models that represent an idealised reality, which to some degree differs from the physical reality. Therefore, one can expect that a degree of conceptual uncertainty is associated with all data compiled in this Data report.

To the extent possible, the supplier should describe such conceptual uncertainty. This should be done in the context of the models in which the data are used, intended to describe certain postulated processes. Also, it may be appropriate to discuss alternative conceptualisations in which the data may be used in different ways. If comprehensive discussions on the subject have already been documented, such documents may be referred to and a short summary of the conceptual uncertainty will suffice. Aspects of the conceptual uncertainty that are obviously unrelated to repository safety may be disregarded.

Conceptual uncertainty may also be introduced in the acquisition, interpretation, and refinement of the data. For example the data may have been obtained by inverse modelling of experimental results, where conceptual uncertainty is introduced by the model. The data may also have been obtained by using some correlation relationship, where there is conceptual uncertainty in the correlation. Many other sources of conceptual uncertainty are conceivable and may be discussed at the discretion of the supplier. In doing this, the supplier should carefully differentiate between uncertainties introduced due to conceptual issues and data uncertainty introduced by measurement errors, etc. Data uncertainty should be discussed in the following section.

2.3.7 Data uncertainty due to precision, bias, and representativity

In this section data uncertainty should, if possible, be discussed in terms of precision, bias, and representativity, in the context of their application in SR-Site. Such uncertainty is associated both with the acquisition of data, for example in the site investigations, and subsequent refinement of data, for example in the site-descriptive modelling. Data uncertainty includes neither conceptual uncertainty nor natural variability.

If comprehensive discussions on these matters are documented elsewhere, such documents should be referred to, and a short summary of the discussion will suffice. The supplier should begin with discussing the precision of the supplied data. To the extent possible, data spread due to the precision should be separated from data spread due to natural variability. Precision issues are both associated with the method used in acquiring the raw data and subsequent interpretation of data. Concerning acquiring raw data, limitations in precision are not only associated with the equipment and method used when performing the measurements, but also with the sampling procedure, sample preparation, etc. Precision issues associated with interpretation of the data depend to a large degree on the procedure used, and should be discussed at the discretion of the supplier. As an example, it may not be straight forward to estimate the precision of data that are a function of other acquired data, with their intrinsic limitations in precision.

Thereafter, the supplier should discuss the bias of the supplied data. Similar considerations apply as when discussing precision, both for bias associated with the acquisition of raw data and with their subsequent interpretation. Bias in observed data is often associated with the method used for acquiring data and its calibration, and with effects of sample preparation. Bias is also associated with the sampling procedure, sample size, and differences in conditions for example between those in the laboratory and *in situ*. Bias issues associated with data interpretation depend to a large degree on how the interpretation is made, and should be discussed at the discretion of the supplier.

Finally the supplier should discuss the representativity of the supplied data, both in terms of data acquisition, and data interpretation and refinement. Issues associated with the representativity of acquired data often concern the sampling procedure, the sample size relative to natural variability and correlation length, and differences in conditions between, for example, those in the laboratory and *in situ*.

An important issue is whether the data are generic or site and/or technique specific. In the case of access to generic data only, the supplier should discuss whether, and to what degree, the lack of site and/or technique specific data influences the data uncertainty. Representativity issues associated with data interpretation and refinement depend much on the specific interpretation and refinement process, and should be discussed at the discretion of the supplier.

As well known, the precision, bias, and degree of representativity often depend on a mixture of the above-suggested sources for data uncertainty, and may not be easily separated. However, the supplier is asked to reflect carefully on these issues, as an assessment of data uncertainty is central for the data qualification. In case data uncertainty cannot be discussed in terms of precision, bias, and representativity, for example as the resolution in data does not allow for such separation, it will suffice to make a general data uncertainty discussion.

Comprehensible illustrations of different data sets are of high value. The objective of the illustrations is not necessarily to provide a detailed basis and description of the numerical values of the individual data. Sometimes the objective may be to give the reader an understanding of how much, and in what ways, the data varies and the data sets differ from each other. An example of presenting different data sets is given in Figure 2-4, where the reader can get an immediate perception about differences between the data sets. Examples of other illustrations are given in subection 2.3.10.

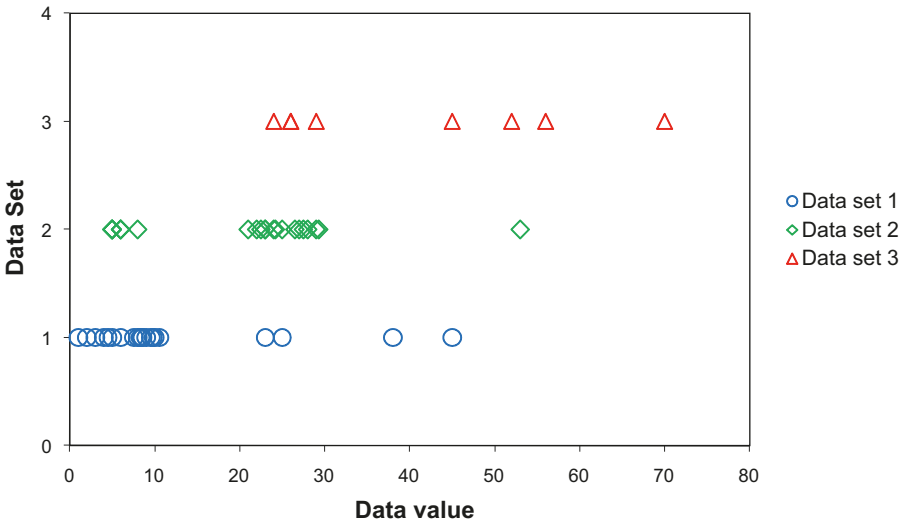

Figure 2-4. *Example of presenting differences in data sets.*

2.3.8 Spatial and temporal variability of data

In this section the supplier should discuss the spatial and temporal variability of the subject area parameters. The natural variability should as far as possible be separated from data uncertainty, discussed in the above section.

The supplier should describe what is known about the spatial variation, sometimes referred to as heterogeneity, of the subject area data. This may result in different data sets for different volumes or elements of the repository system, or for different time periods. If comprehensive discussions on the natural variability are documented elsewhere, such documents should be referred to and a short summary of the natural variability will suffice.

In the process of describing the spatial variability, it may be helpful to reflect on the following line of questions.

- Is there spatial variability of the data, and if so is it of consequence for the safety assessment?
- Is the spatial variability scale dependent? If so, can an appropriate approach of upscaling to safety assessment scale be recommended?
- What is known about correlation lengths from, for example, variograms?
- Can the spatial variability be represented statistically as a mean of data qualification and, if so, how is this done?
- Is there any information about the uncertainty in the spatial variability?

In the process of describing the temporal variability, it may be helpful to reflect on the following line of questions.

- Is there temporal variability of the data, and if so is it of consequence for the safety assessment?
- What processes affect the temporal variability of the data and how is the temporal variability correlated with these processes?
- Does the temporal variability follow any pattern, for example a cyclic pattern?
- Could the temporal variability be represented statistically as a mean of data qualification and if so, how is this done?
- Is there any information about the uncertainty in the temporal variability?

In addition, other relevant issues concerning the natural variability may be addresses at the discretion of the supplier. Comprehensible illustrations of different data sets from different volumes, elements, or time periods are of high value.

2.3.9 Correlations

An appropriate treatment of probabilistic input data requires that any correlations and functional dependencies between those data are identified and quantified. In the extensive work with the FEP database and the Process reports, most correlations and functional dependencies between parameters have been identified. Where appropriate, these correlations and functional dependencies should also be implemented in the safety assessment models. It should be an aim to aid those performing stochastic modelling, by giving well defined and usable information on how to handle correlations between input data.

Correlations and functional dependencies may also have been used when acquiring, interpreting, and refining data. For example, concerning sorption partition coefficients, data have not been acquired for all relevant radioelements. For species for which there is a lack in observations, the supplied sorption partition coefficient will have been estimated from data obtained for one of more analogue species. This has implications for how to correlate input data in stochastic safety assessment modelling.

In this section the supplier is requested to address the following questions:

- Are there correlations or functional dependencies between parameters within the subject area, or with parameters of other subject areas? If so, account for these and if possible also outline the consequences for subsequent modelling.
- If correlations have been used in acquiring, interpreting, and refining data, how is this done? Furthermore, is the outcome based solely upon correlations, or on both measurements and correlations?
- If the data varies in space and time – is anything known about its autocorrelation structure?
- Is there any other reason (apart from already cited correlations and functional dependencies) to suspect correlations between parameters considered as input to SR-Site modelling?

2.3.10 Result of supplier's data qualification

In this section the supplier is requested to present data that are considered to be appropriate as a basis for suggesting input data for use in the safety assessment. Comprehensive information relating to each parameter requested in the bullet list under the heading "Defining the data requested from the supplier" (cf Section 2.3.1) should be given. Only one set of data should be delivered for each specified condition, volume, element, time period, alternative modelling approach, etc.

The general process of reducing and interpreting data, valuing different data sets, and finally selecting the recommended data for delivery to the assessment team should be fully accounted for, if not already accounted for in the previous sections or in supporting documents. In the latter case, it is sufficient to briefly summarise, or refer to, the process of selecting the delivered data.

In case the data presented in supporting documents need reinterpretation and further refinement, in the light of this instruction and/or other information, this should be fully documented. In case the supporting documents give more than one data set for a specified condition, volume, element, time period, etc, further data reduction is required. Such data reduction may include the merging of data sets, and there may be a need to give different weight to different data sets. Much weight should be given to peer-reviewed data judged as representative for the Swedish site and repository system. Generally, more weight should be given to qualified data than to supporting data. The degree to which the data are representative in the context of their application in the assessment should also be a factor in the weighting. Exactly how much weight should be given to individual data sets must be decided upon by the supplier. The process of further reinterpretation, refinement, and data reduction should be fully documented. If it increases the readability of the text to also utilise other sections for such documentation, this is allowed. Also, if this requires much space, some information may be appended.

The data sets that the supplier recommends to the assessment team should be in the form of single point values, probability distributions, mean or median values with standard deviations, percentiles, ranges, or as otherwise appropriate.

If the data have significant variability and/or uncertainty, the spread in data could be described as a range. However, the meaning of the range has to be provided, e.g. does it represent all possible values, all "realistically possible" values or just the more likely values? The supplier may provide more than one range, representing different probabilities, as exemplified below:

- The range wherein the likelihood of finding the data is high.
- The range for which the likelihood of finding data outside this range is very low.

All data should be recommended in the context of input data to safety assessment modelling. Accordingly the final uncertainty estimate should encompass conceptual uncertainty, data uncertainty, and natural variability (cf Sections 2.3.6, 2.3.7, and 2.3.8). If the supplier has used some kind of mathematically expression to account for the uncertainty and natural variability, this expression should be provided and justified.

If the data are suggested to be described by a well-defined probability distribution, it should be justified on statistical grounds that the data indeed are (sufficiently well) distributed accordingly. The usage of standard deviation is often perceived to imply that the data are normally distributed; even through the definition of standard deviation is unrelated to specific probability distributions. Therefore, when giving the standard deviation, it should be remarked upon whether or not the normal distribution appropriately describes the data. If there are obvious differences between how the data set at hand is actually distributed, and the probability distribution (or range) finally recommended, the reasons for, and implications of, this should be discussed. Outliers should not be dismissed without justification.

It should be noted that in many cases, at some stage probability distributions must be assigned to numerical data being the input to probabilistic safety assessment modelling. If the supplier feels inadequate to deliver a defined distribution, but for example delivers a best estimate, an upper, and a lower limit for data, it may fall on the SR-Site team to transform such information into probability distributions. This is justified as the SR-Site team may have a better understanding of how the shape of the assigned distributions (especially in their tails) affects the assessment results. The SR-Site team may also, in some cases, have a better understanding of the underlying statistics of the suggested distribution.

The above instructions are not applicable to all data, as all data are not necessarily in the form of numerical values. Examples are exit locations for groundwater flowpaths, given as co-ordinates, or information on solubility limiting phases, given as chemical species and reactions.

For a spatially varying function well described by a given stochastic process, e.g. through a variogram or as realised in a Discrete Fracture Network, a potential statement may be that all realisations of this spatially varying function are equally probable.

Finally, it may be impossible to express the uncertainty by other means than a selection of alternative data sets. There are a number of uncertainties that cannot be managed quantitatively in any other rigorous manner, from the point of view of demonstrating compliance, than by pessimistic assumptions. This is allowed, as long as the supplier clearly documents this together with the justification for adopting this approach.

Comprehensible illustrations and tables of the suggested data sets are of high value. Figure 2-5 shows some examples, taken from the SR-Can Data report (SKB 2006b), displaying how data may be represented. Figure 2-5a shows a histogram of formation factor data and also a fitted log-normal probability distribution (SKB 2006b, Figure 6-20). The distribution parameters are displayed in the figure. Figure 2-5b shows an excerpt of a table displaying sorption partitioning coefficients (SKB 2006b, Table A-43). Here a median value is given as the best estimate value. In addition two ranges are given, one range wherein 50 % of the data are estimated to be found, and one wherein roughly 99 % of the data are estimated to be found. Figure 2-5c, which is an excerpt of SKB (2006b, Table A-6) shows an example where no numerical data is given. Instead solubility limiting phases, used in the analysis of the solubility limits, are shown.

For data which are impractical to tabulate in the Data report (for example the co-ordinates of thousands of exit locations for groundwater flowpaths), it is sufficient to precisely refer to a database or equivalent. However, if possible the data should be illustrated in figures or excerpts of tables.

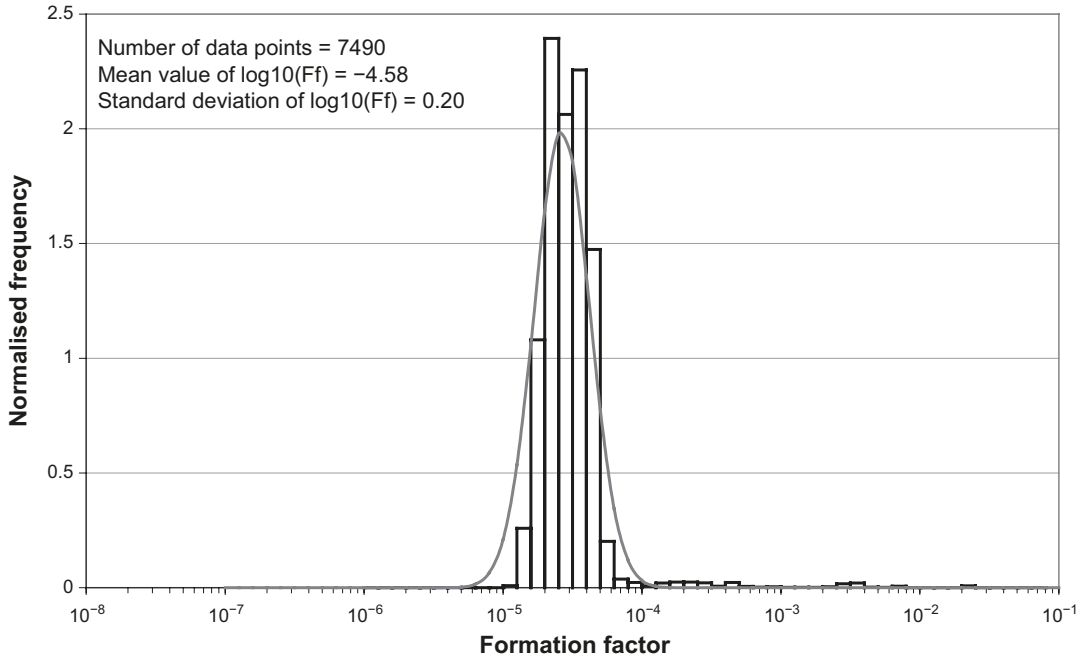

a

b

Nuclide/redox state		Non-saline K_d (m^3/kg)
Ni(II)[1]	best estimate	1.2×10^{-1}
	$K_{d,25\%} - K_{d,75\%}$	$5.5 \times 10^{-2} - 3.0 \times 10^{-1}$
	$K_{d,low} - K_{d,high}$	$1.8 \times 10^{-2} - 5.4 \times 10^{-1}$
Sr(II)[1]	best estimate	1.3×10^{-2}
	$K_{d,25\%} - K_{d,75\%}$	$6.5 \times 10^{-3} - 4.1 \times 10^{-2}$
	$K_{d,low} - K_{d,high}$	$1.0 \times 10^{-3} - 6.1 \times 10^{-1}$

c

	Limiting specie	Reaction
Ag(0)	Ag(s)	$Ag(s)+H^{+}+0.25O_2 = Ag^{+}+0.5H_2O$
Ag(I)	AgCl(cr)	$AgCl(cr) = Ag^{+}+Cl^{-}$
Am(III)	$Am(OH)_3(am)$	$Am(OH)_3(am)+3H^{+} = Am^{+3}+3H_2O$

Figure 2-5. *Examples of representations of recommended data. Reproduced from, or excerpts of, Figure 6-20, Table A-5, and Table A-43 of the SR-Can Data report (SKB 2006b).*

2.3.11 Judgements by the assessment team

In this section, the customer representative, on behalves of the SR-Site team, should document the examination of the delivery provided by the supplier, and make judgment on the data qualification process and on the qualified data. This text should be produced in close cooperation with persons of the assessment team with special knowledge and responsibility. In case of unresolved issues, the final phrasing should be decided upon by the assessment team. Comments should be made on all the sections listed below:

- Sources of information and documentation of data qualification.
- Conditions for which data are supplied.
- Conceptual uncertainty.
- Data uncertainty due to precision, bias, and representativity.
- Spatial and temporal variability of data.
- Correlations.
- Result of supplier's data qualification.

If appropriate, a response to the section "Supplier input on use of data in SR-Site and SR-Can" may also be warranted.

Concerning the section "Sources of information and documentation of data qualification" the customer should judge if appropriate documents are referenced, and if the categorisation of data sets into qualified or supporting is adequately performed and justified.

Concerning the section "Conditions for which data are supplied" the customer should focus upon whether the conditions given by the supplier are relevant for assessment modelling. If not, it should be accounted for how this is handled in the current assessment (for example by extrapolating data, using generic data, or assuming pessimistic values) and what degree of uncertainty such a procedure induces.

Concerning the section "Conceptual uncertainty" the customer should judge whether the discussion provided by the supplier is reasonable and sufficiently exhaustive. If the customer sees the need to include additional sources of conceptual uncertainty, such should be described and if possible quantified. Finally, where necessary the impact of the conceptual uncertainty on the assessment should be discussed, as well as how conceptual uncertainty is handled in assessment modelling (for example by applying pessimistic corrections factors to the data).

Concerning the section "Data uncertainty due to precision, bias, and representativity", the customer should make a judgment on the account provided by the supplier. Also, if the customer sees the need to include additional sources of data uncertainty, these should be described and if possible quantified. If necessary the impact of the data uncertainty on the assessment should be discussed, as well as how data uncertainty is handled in SR-Site modelling (for example by applying data uncertainty distributions or using corrections factors for the data).

Concerning the section "Spatial and temporal variability of data" the customer should focus upon whether the spatial and temporal variability are adequately characterised and whether they are of relevance for the modelling. Also, if the customer sees the need to include additional sources of spatial and temporal variability, such should be described and if possible quantified. In necessary, the impact of the spatial and temporal variability on the assessment should be discussed, as well as how this is handled in assessment modelling (for example by applying data distributions or different data for different model times and volumes).

Concerning the section "Correlations" the customer should scrutinise the correlations and functional relationships suggested by the supplier. Also, if correlations other than those suggested by the supplier are identified in the SR-Site project (for example in Process reports) these should be briefly described where necessary. If appropriate, a summary could be provided concerning which correlations are of actual importance for safety assessment modelling and results.

Concerning the section “Result of supplier’s data qualification” the customer should make judgement on the choice of data by the supplier, based on scientific adequacy, usefulness for the safety assessment, and the data qualification process. Comments could be made on the delivered estimates of data uncertainty and natural variability, as well as on the data reinterpretation/refinement/reduction process. Furthermore, the delivered distributions, data ranges, etc should be scrutinised from a statistical point of view. It should be judged whether the suggested way of representing data, for example by a log-normal distribution, is adequate for SR-Site modelling. If the assessment team chooses to promote other data than those suggested by the supplier, the choice should be fully documented.

For all the sections listed above, supplier statements or supplied data believed to be extra uncertain, dubious, or even erroneous should be highlighted by the customer. These matters should be raised with the supplier and, if possible, resolved and accounted for in this section.

2.3.12 Data recommended for use

The main delivery of the Data report is recommendations of data that generally are numerically well defined. Such recommended data should be given in this section.

Based on all the available information, but also on the needs from assessment modelling, the customer representative and assessment team should make a final choice of data in form of single point values, ranges, or well-defined probability distributions, encompassing natural variability, data uncertainty, and other uncertainty. These data should be clearly tabulated (or otherwise presented) in this section. Alternatively, precise referencing to tables or equivalent in previous sections can be made. For data which are impractical to tabulate in the Data report it is sufficient to precisely refer to a database or equivalent.

Also short guidelines for how to use the data in subsequent modelling should be given, as required. Justifications and guidelines should be kept short so that this section mainly contains tabulated data that are easily extractable for safety assessment modelling.

3 Spent fuel data

3.1 Radionuclide inventory

The inventory of a canister is the quantity of radionuclides in the canister. The data presented represent the inventory of an average canister, as well as the inventory of six different hypothetical canisters with different average burnup. The inventory of an average canister is obtained by dividing the total inventory expected at the time of repository closure by the estimated total number of canisters.

In this section the term selected inventory is used. The inventory of a canister is comprised of a great number of radionuclides. However, only a handful of them are relevant for the safety assessment, as they have long enough half-life, large enough radiotoxicity, exist in large enough amounts, and/or produce decay products of the above standing attributes. One can through very basic calculations screen out the great majority of the radionuclides as obviously insignificant for the safety assessment. The result of such a screening is presented in Section 2.2.1, in form of a list of selected radionuclides of potential importance for the safety assessment.

As a result of radioactive decay, the inventory varies over time. If the inventory is known at one specified time, one can through decay chain calculations determine the inventory at other times. The inventory presented here is that for a selection of radionuclides expected in year 2045, at the time for shut down of the last nuclear power plant according to Table 2-1 in the **Spent fuel report**.

3.1.1 Modelling

This section describes what data are needed, and in what modelling activities the data are to be used.

Defining the data need

The data encompass:

- The total inventory in activity per canister (Bq/canister) for an average canister, for the radionuclides of the selected inventory.
- The total inventory in activity per canister (Bq/canister) for hypothetical canisters of average varying burnup, for the radionuclides of the selected inventory.
- The inventory in activity per canister (Bq/canister) for hypothetical canisters of average varying burnup, as distributed on the UO_2 pellet inventory[5], construction material[6] inventory, crud inventory, and control rod inventory.
- The half-lives, $t_{½}$ (yr), and specific activity (Bq/mol) for the radionuclides of the selected inventory.

If there are tabulated inventory data in the **Spent fuel report** that would take numerous pages to reproduce, they could instead be properly referred to. In Section 2.2.1, the radionuclides of the selected inventory are listed.

For radionuclide transport modelling, the inventory is needed in amount of substance per canister (mol/canister). Therefore, the assessment team should at the end of this section give:

- The supplied inventories in amounts per canister (mol/canister).

[5] In this report the term UO_2 pellet also includes the small fraction of fuel that has (U,Pu)O2 pellets, ie MOX pellets.

[6] The fuel cladding, the control rod cladding, and metal parts of the fuel assemblies.

Modelling activities in which data will be used

In radionuclide transport modelling, the selected inventory is used for assessing the source term (see the **Radionuclide transport report)**. In the near-field modelling it is used as one of the bases for calculating concentrations and quantities of radionuclides that can leave a breached canister. As the inventory is constantly evolving due to radioactive decay, inventories at later times must be assessed. This is done by standard methods using the Bateman equations.

3.1.2 Experience from SR-Site

This section briefly summarises experience from the SR-Site safety assessment, which may be of direct consequence for the data qualification.

Modelling in SR-Site

For SR-Site, the radionuclide inventory in UO_2 pellets was calculated with the computer program Origen-S in the Scale 5.1 package (Agrenius 2010) , while the inventory in construction materials and crud was estimated from calculations with the computer programs IndAct and CrudAct (Eriksson 2009).

Using these models, the total radionuclide inventory was estimated for the average age of the fuel assemblies in the year 2045. For the radionuclide transport modelling, this inventory was recalculated using the COMP23 program to the year 2070 which for SR-Site corresponded to repository closure.

Conditions for which data were used in SR-Site

In SR-Site, the total radionuclide inventory was based on the BWR (boiling water reactor), PWR (pressurised water reactor) and a smaller number of MOX (Mixed-Oxide) fuel. The total inventory was then used to estimate the inventory in an average canister. In addition, radionuclide inventories in canisters with different possible fuel configurations were calculated. The canisters contained BWR, PWR and MOX fuels of different burnup and decay time, i.e. time after final irradaition (Agrenius 2010). From these various fuel configurations, eight type canisters were selected (SR-Site Spent fuel report SKB 2010e). The type canisters were used to illustrate variation in radionuclide inventory between canisters.

Sensitivity to assessment results in SR-Site

In SR-Site, the inventories of Ra-226 and some of its decay parents in the *4n+2* decay chain (Th-230, U-234, and U-238 were relevant) were of great consequence for the assessment results. However, the assessment results were not sensitive to uncertainties in the U-238 inventory.

In the SR-Site shear load scenario, when an early canister failure cannot be ruled out, C-14 and Nb-94 dominated the radiological risk. However, compared to the regulatory limit the risks were small.

Alternative modelling in SR-Site

No alternative modelling with regard to the inventory was performed.

Correlations used in SR-Site modelling

Many of the radionuclides are correlated through decay chains. No other correlation with regard to the inventory was used.

Identified limitations of the data used in SR-Site modelling

No major limitation of the inventory data used in SR-Site was identified.

3.1.3 Use of data in the PSAR and SR-Site

For SR-Site, the data in the SR-Site Spent fuel report (SKB 2010e) was obtained in dialogue with the SR-Site team. There were remaining issues concerning the half-life of Ag-108m and Se-79 that the SR-Site team was suggested to investigate further. 6 103 canisters were needed, as described in the **Spent fuel report**. In the PSAR, this number has decreased to 5 689 due to a change in the prognosis for future operation of the nuclear reactors (**Spent fuel report**).

Fuel residues from research performed at Studsvik was, for SR-Site, estimated to generate about 25 special boxes that will be placed in PWR canisters (see Table 2.3 of the **Spent fuel report**), and the contribution to the total inventory from these canisters was deemed to be negligible. For the PSAR, this number is 37: 20 boxes for PWR canisters and 17 boxes for BWR canisters. In addition, special containers have been developed for leaking fuel rods and taken into use. It is estimated to result in 33 special containers. Neither the final number nor the detailed radionuclide inventory of these boxes and containers has been established for the PSAR and they are not part of the radionuclide inventory presented in this report. However, their potential contribution to radiological risk based on available data and assumption is estimated for the PSAR (**Fuel and canister process report**).

3.1.4 Sources of information and documentation of data qualification

Sources of information

For SR-Site, the only source of inventory data was the **Spent fuel report**, and data for the SR-Site calculations were qualified there. For the PSAR, the only source of data for the radionuclide inventory is the **Spent fuel report** (see Table 3-1). The scrutinising of lower level references is part of the qualification process of that report and is not dealt with in this Data report**.**

Table 3-1. Main sources of information used in data qualification.

Spent fuel report, Använt kärnbränsle att hantera i KBS-3 systemet, Svensk Kärnbränslehantering AB.

Categorising data sets as qualified or supporting data

Table 3-2 shows the qualified data sets and a justification for the sorting of the items is given.

Table 3-2. Qualified and supporting data sets.

Qualified data sets	Supporting data sets
1. Total inventory of the repository: Table D-2, Appendix D in **Spent fuel report**.	None.
2. Inventory of canisters with varying average burn-up: Tables E-1 to E-6, Appendix E in **Spent fuel report**.	
3. Total number of canisters: 5689, Section 8.3 in **Spent fuel report**.	
4. Radionuclide half-lives and specific activity: Table D-1, Appendix D in **Spent fuel report**.	
1–4. Data delivered in **Spent fuel report** are qualified in that report in accordance with the SKB quality assurance system. This qualification is found to be in compliance with the requirements of the Data report.	

Excluded data previously considered as important

No such data has been excluded. However, the half-life for Se-79 is still being studied in the scientific community and new data are successively being published.

3.1.5 Conditions for which data are supplied

Conditions of importance for the radionuclide inventory are discussed in, for example, Section 5.1 in **Spent fuel report**. In summary, from a repository perspective, the burnup is the fuel parameter that has the largest impact on the radionuclide inventory. The burnup reflects the amount of nuclear fission and neutron radiation that has occurred in the assembly, and thus the content of fission and activation products and transuranium elements. High burnup leads to higher content of fission products and, due to neutron capture, higher content of activation products and altered content of transuranium elements. The burnup and total radionuclide inventory in the final repository will ultimately depend on the total energy output from the nuclear power plants.

Except for the burnup, the radionuclide inventory is to some extent also affected by the irradiation and power history of the assemblies. Also the fuel type (either uranium oxide fuel or mixed oxide fuel), affects the inventory.

Part of the inventory will be in the construction materials of the fuel assemblies. When construction material is exposed to neutron radiation in the reactor vessel, neutron capture will lead to formation of activations products. The amount and composition of the construction materials, and the time that the fuel assembly has been in the reactor, will determine the content of activation products in the construction material. Radionuclides are also found as surface deposits (crud).

The canister specific inventory depends on the above mentioned issues, on the stored spent fuel type (PWR, BWR or MOX), the number of assemblies, and whether they include control rods and inserts such as start-up neutron sources, boron glass rods, and plugs.

3.1.6 Conceptual uncertainty

This section concerns existing spent fuel, as well as a prognosis of spent fuel that will be produced in the coming years. The amount of spent fuel to be deposited in the repository is assumed to be in accordance with the scenario for the future operation of the nuclear power plants (Section 5.2.1 of **Spent fuel report**). There is conceptual uncertainty in this scenario that can only be handled through sensitivity analysis. Other sources of uncertainty on the borderline of conceptual uncertainty/data uncertainty are treated as data uncertainty.

3.1.7 Data uncertainty due to precision, bias, and representativity

At the time of closure of the final repository, the burnup, irradiation history, power history, and age of the assemblies in each canister will be known. From this information the radionuclide inventory of each individual canister can be calculated.

However, it is not possible to do this today. To handle uncertainties in the inventory of the individual canisters, results from two approaches are propagated to the safety assessment modelling.

- In the first approach, the total inventory associated with the prognosis for future reactor operation is divided by the estimated total number of canisters, to obtain the inventory of an average canister.
- The second approach is to assess the inventory of canisters containing BWR- and PWR fuel with varying burnup. This approach facilitates comparisons between BWR- and PWR canisters as well as the inventory ranges from low to high burnup. The major uncertainty concerns how representative the data obtained through this simplified approach are for the canisters to be deposited, since in practice, canister will contain fuel elements with varying burnup. The rationale and uncertainty connected with this approach is discussed in the **Spent fuel report**.

This section concerns data applicable for the prognosis for the future operation of nuclear reactors in Sweden. The main source of deviations from this would be changes in the total energy output from the nuclear power plants, which is treated as conceptual uncertainty. However, the consequence of operating a reactor for one year longer is illustrated by the increase of total activity for all spent fuel generated by the Swedish nuclear programme. For BWR, an extra year results in 0.3 % of the total activity, while for PWR, this number is 0.8 % (see Table 5-5 in **Spent fuel report**).

Inventory per average canister

In Table D-2 of **Spent fuel report**, the total inventory based on the number of assemblies for all spent fuel generated by the Swedish nuclear programme, as well as 217 MOX assemblies irradiated in Germany, is given. This total inventory is divided by the estimated total number of canisters, to get the inventory per average canister. The estimated total number of canisters is 5 689 (of which 3 982 are BWR canisters and 1 707 PWR canisters) based on the **Spent fuel report**, No uncertainty range based on this approach is specified. MOX fuel, fuel from Ågesta and Fuel Assembly skeletons will be placed in BWR- and PWR-canister depending on their design. These fuel types are included the calculation of total number of canisters. Therefore they are also included in the calculation of the total inventory. In addition to the listed fuel types, there will also be a few canisters with containers with fuel residues and fuel with failed cladding. The exclusion of these low activity fuel types in the calculation of the inventory per average canister is however conservative since they would decrease the activity of the average canister. The risk contribution from these fuel types is instead calculated separately, see the **Radionuclide transport report.**

Inventory in canisters with varying burnup

There is a large number of ways in which the assemblies can be combined in individual canisters. However, variation is somewhat limited by a requirements that the decay power of any individual canister, is not allowed to exceed 1 700 W at the time of deposition. This has been employed in encapsulation simulations estimating the number of canisters required. These simulations provide a basis for estimates of how average burnup in the canisters, or canister burnup, may vary. The distribution of BWR and PWR canister burnups are illustrated in Figure 3-1.

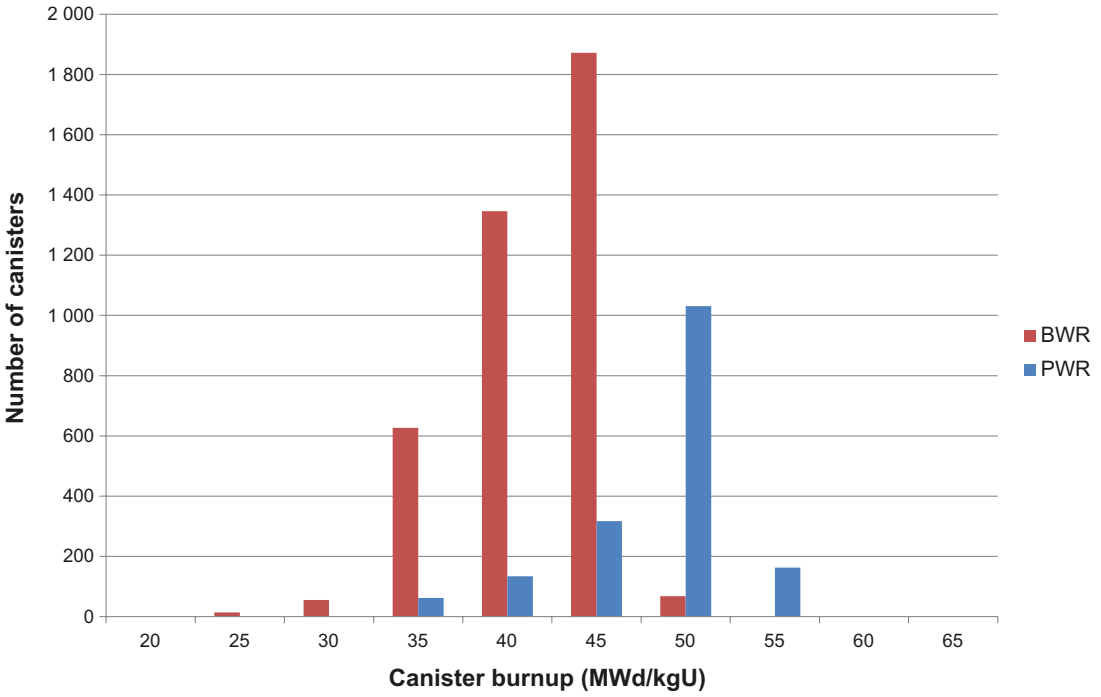

Figure 3-1. *Canister burnup according to the encapsulation simulation. This is based on the adopted scenario for future operation of the nuclear power plants.*

- **BWR Low** (12 × 30 MWd/kgU) represents a canister with low average burnup of 30 MWd/kgU. In the encapsulation simulation, these canisters are often filled with a set of fuel elements with a low burnup and a set with high burnup. The inventory of BWR Low is however calculated assuming 12 fuel elements with burnup 30 MWd/kgU.
- **BWR Medium** (12 × 40 MWd/kgU) represents a canister with medium average burnup of 40 MWd/kgU. Most of the BWR canisters will have an average burnup around this value (see Figure 3-1), and in the encapsulation simulation the burnups of individual fuel elements are more normally distributed around the average than the BWR Low canister.
- **BWR High** (12 × 50 MWd/kgU) represents a canister with average burnup of 50 MWd/kgU. The highest average burnup for BWR-type canisters is 47.5 MWd/kgU. A canister with such a high average burnup is likely to be filled mostly by high burnup fuel elements late in the encapsulation process.
- **PWR Low** (4 × 35 MWd/kgU) represents a PWR canister with an average burnup of 35 MWd/kgU, and is according to the encapsulation simulation likely to be filled by two fuel elements with low burnup and two with high burnup.
- **PWR Medium** (4 × 45 MWd/kgU) represents a PWR canister with a medium average burnup of 45 MWd/kgU, and as for BWR Medium, one can expect a more normal distribution of the burnup of individual fuel elements in this kind of canister.
- **PWR High (**4 × 55 MWd/kgU) represents a PWR canister with a high average burnup of 55 MWd/kgU. In the encapsulation simulation these kinds of canisters are produced late in the encapsulation process and filled with a set of fuel elements with equal burnup.

In Appendix E (Tables E-1 to E-6) of **Spent fuel report** the inventories of the different canisters listed above are given. For many important radionuclides, the inventory per canister is similar for the different canisters. For some radionuclides, the activity is much higher in certain canisters than in others. In Figure 3-2 Figure 3-1, the examples of I-129 and Nb-94 are shown. As can be seen, Nb-94 is predominantly associated with PWR canisters, while the activity of I-129 is similar for all canisters; the variation is correlated with burnup.

The spread in all inventory data for the different canisters is shown in Figure 3-3 where the inventory per canister is normalised to the inventory per average canister.

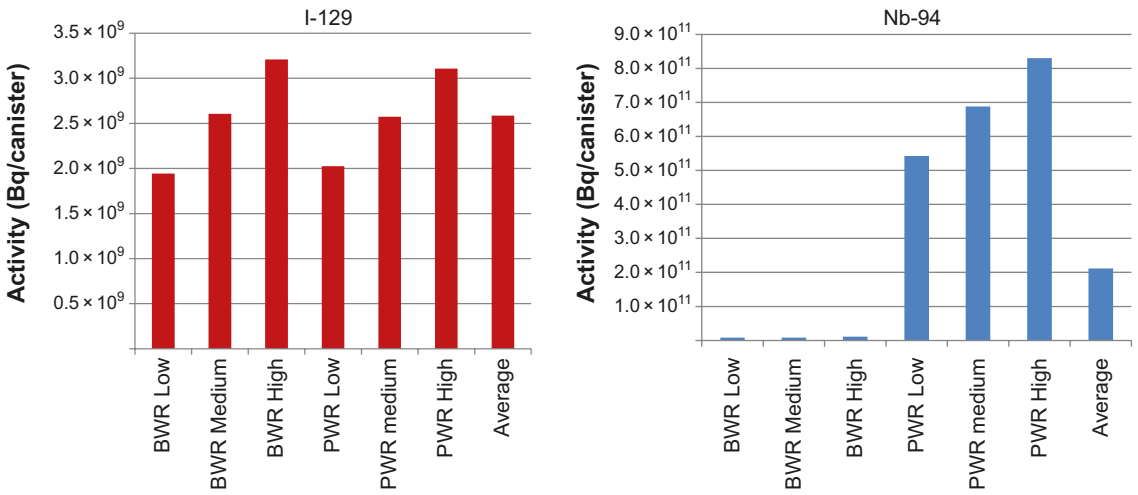

Figure 3-2. *Total I-129 and Nb-94 inventories in terms of activity per canister for the different canisters. Data taken from Appendix D and E in Spent fuel report.*

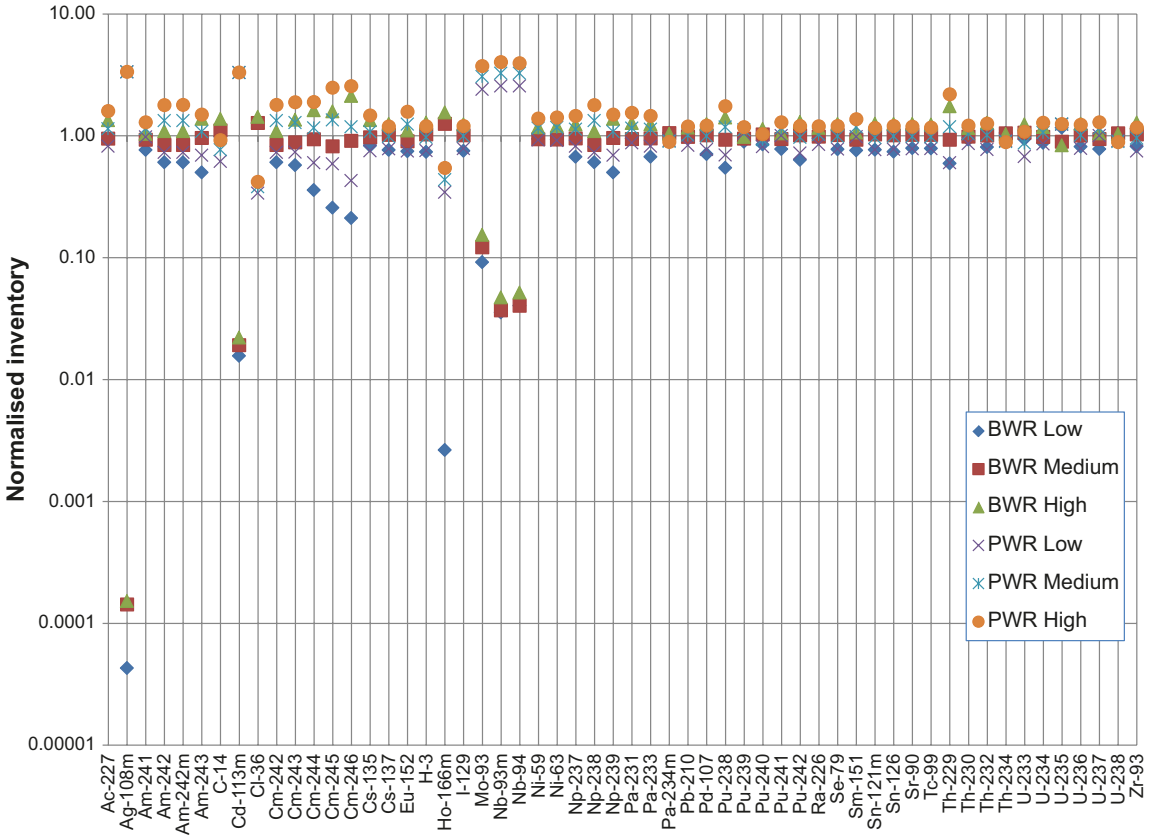

Figure 3-3. *Spread in data of inventory per canister, as normalised with the inventory per average canister. All data taken from Appendix D and E in Spent fuel report.*

As can be seen, for most of the radionuclides the spread of data is limited (within the same order of magnitude) while for some radionuclides the spread is over one or more orders of magnitude.

In Tables E-1 to E-6 of **Spent fuel report** the inventories of low, medium and high burnup canisters are distributed on different sources. These sources are the:

- Total (sum of all sources).
- UO_2-pellets (including the gap and grain boundary inventory, see Section 3.2).
- Construction material.
- Crud.
- Control rods (in case of PWR canisters).

Here a note is needed on the term UO_2-pellets. When discussing the instant release fraction in Section 3.2, a terminology is used where the UO_2 matrix inventory and gap and grain boundary inventory are mutually exclusive. The source of both is, however, from the irradiated UO_2-pellets. Therefore, in the remaining of this report, we will use the term UO_2 pellet inventory for the inventory including both the matrix and gap and grain boundary inventories.

For most radionuclides, the UO_2 pellets is the dominating source, while for a few nuclides, other sources dominate. Figure 3-4 shows the inventory for the BWR Medium and PWR Medium canisters, as distributed among these sources. The sorting of the radionuclides is based on descending inventory of the BWR Medium canister. As can be seen from Figure 3-4 only for a few nuclides the inventory is significantly affected by the inventory of the construction material, crud, or control rods. The radionuclides where the inventory of the construction material, crud, and control rods comprises more than 1 % of the total inventory are for BWR Medium: Ag-108m, C-14, Cl-36, Mo-93, Nb-93m, Nb-94, Ni-59, Ni-63, Sn-121m, U-233, and Zr-93. For PWR Medium , the same radionuclides apply with the addition of Cd-113m. For these radionuclides, uncertainty in the inventory estimate in the construction material, crud, and control rods may add to the total uncertainty. For the other radionuclides, the total uncertainty depends on the uncertainty of the UO_2 pellet inventory.

3.1.8 Spatial and temporal variability of data

Spatial variability of data

As there is variability in the inventory of different canisters, there will be a spatial variability that depends on where the canisters are deposited. If it is assumed that there is no trend in the canister deposition locations, spatial variability may be discussed as data uncertainty. This is the approach taken in this text.

Temporal variability of data

The temporal variability in data, due to decay, can be accounted for by decay chain modelling. The inventory is given for year 2045.

3.1.9 Correlations

Radionuclides, as decay parents and daughters, are correlated through the decay chains.

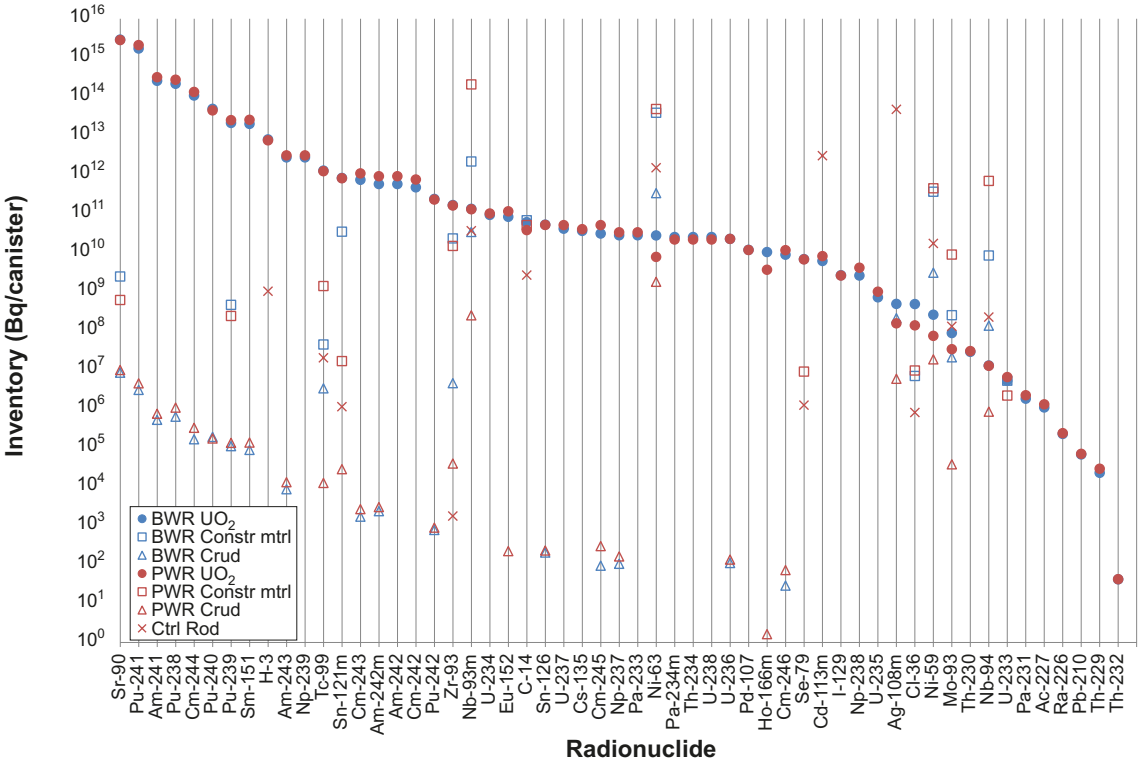

Figure 3-4. *Inventory per canister of the BWR Medium and PWR Medium canisters, distributed among UO_2 pellets, construction material, crud, and control rods. All data from Appendix E in Spent fuel report.*

3.1.10 Result of data qualification

The inventory is given in two ways, either as the inventory per average canister or as the inventory in canisters of different type (BWR or PWR) and burnup.

Inventory per average canister

The total inventory is given in Table D-2 in **Spent fuel report**. In Table 3-3 of the present report, this inventory is reproduced, together with the activity per average canister. Based on the **Spent fuel report**, the total number of canisters is 5 689. The data apply for the year 2045, which is the year the last Swedish nuclear power plant is closed.

Table 3-3. Total activity for the repository, and activity in Bq per average canister. Total activity data reproduced from Table D-2 of Spent fuel report. Activity per average canister based on 5 689 canisters.

Nuclide	Total activity of spent fuel (Bq)	Activity per average canister (Bq/canister)	Nuclide	Total activity of spent fuel (Bq)	Activity per average canister (Bq/canister)
Ac-227	6.36×10^{9}	1.12×10^{6}	Pa-231	1.08×10^{10}	1.89×10^{6}
Ag-108m	2.74×10^{16}	4.81×10^{12}	Pa-233	1.66×10^{14}	2.92×10^{10}
Am-241	1.56×10^{18}	2.74×10^{14}	Pa-234m	1.36×10^{14}	2.39×10^{10}
Am-242	3.85×10^{15}	6.76×10^{11}	Pb-210	3.84×10^{8}	6.75×10^{4}
Am-242m	3.86×10^{15}	6.79×10^{11}	Pd-107	6.63×10^{13}	1.17×10^{10}
Am-243	1.63×10^{16}	2.86×10^{12}	Pu-238	1.31×10^{18}	2.30×10^{14}
C-14	6.57×10^{14}	1.15×10^{11}	Pu-239	1.27×10^{17}	2.23×10^{13}
Cd-113m	1.81×10^{15}	3.18×10^{11}	Pu-240	2.69×10^{17}	4.73×10^{13}
Cl-36	2.15×10^{12}	3.79×10^{8}	Pu-241	1.03×10^{19}	1.82×10^{15}
Cm-242	3.18×10^{15}	5.59×10^{11}	Pu-242	1.34×10^{15}	2.35×10^{11}
Cm-243	4.74×10^{15}	8.33×10^{11}	Ra-226	1.29×10^{9}	2.26×10^{5}
Cm-244	6.45×10^{17}	1.13×10^{14}	Se-79	3.83×10^{13}	6.73×10^{9}
Cm-245	2.13×10^{14}	3.75×10^{10}	Sm-151	1.22×10^{17}	2.15×10^{13}
Cm-246	5.52×10^{13}	9.69×10^{9}	Sn-121m	4.75×10^{15}	8.34×10^{11}
Cs-135	2.10×10^{14}	3.70×10^{10}	Sn-126	2.93×10^{14}	5.15×10^{10}
Cs-137	2.51×10^{19}	4.41×10^{15}	Sr-90	1.62×10^{19}	2.85×10^{15}
Eu-152	5.21×10^{14}	9.16×10^{10}	Tc-99	7.09×10^{15}	1.25×10^{12}
H-3	4.43×10^{16}	7.78×10^{12}	Th-229	1.37×10^{8}	2.40×10^{4}
Ho-166m	4.69×10^{13}	8.24×10^{9}	Th-230	1.63×10^{11}	2.87×10^{7}
I-129	1.47×10^{13}	2.59×10^{9}	Th-232	2.34×10^{5}	4.11×10^{1}
Mo-93	1.65×10^{13}	2.91×10^{9}	Th-234	1.36×10^{14}	2.39×10^{10}
Nb-93m	3.59×10^{17}	6.32×10^{13}	U-233	5.55×10^{10}	9.75×10^{6}
Nb-94	1.20×10^{15}	2.11×10^{11}	U-234	5.36×10^{14}	9.42×10^{10}
Ni-59	2.22×10^{15}	3.91×10^{11}	U-235	4.49×10^{12}	7.89×10^{8}
Ni-63	2.36×10^{17}	4.15×10^{13}	U-236	1.26×10^{14}	2.22×10^{10}
Np-237	1.66×10^{14}	2.92×10^{10}	U-237	2.48×10^{14}	4.35×10^{10}
Np-238	1.74×10^{13}	3.06×10^{9}	U-238	1.36×10^{14}	2.39×10^{10}
Np-239	1.63×10^{16}	2.86×10^{12}	Zr-93	1.04×10^{15}	1.84×10^{11}

Inventory in canisters of varying type and burnup

In the **Spent fuel report**, in Tables E-1 to E-6, the inventories of six different hypothetical canisters are given in terms of activity per canister. The referenced table associated with each hypothetical canister is given in Table 3-4. In addition to giving the total activity per canister, the activity is distributed among different sources for each canister (cf Figure 3-4). The different sources are the UO_2 pellets, the construction material, and the crud. In addition, in the case of PWR canister, inventory data for the control rods are given. All data of the referenced tables are qualified.

Table 3-4. Sources for where inventory data for hypothetical canisters of varying average burnup are found.

Hypothetical Canister name	Short description	Table in the Spent fuel report
BWR Low	12 BWR assemblies Burnup 30 MWd/kgU Age 35 years	Table E-1
BWR Medium	12 BWR assemblies Burnup 40 MWd/kgU Age 35 years	Table E-2
BWR High	12 BWR assemblies Burnup 50 MWd/kgU Age 35 years	Table E-3
PWR Low	4 PWR assemblies Burnup 35 MWd/kgU Age 35 years	Table E-4
PWR Medium	4 PWR assemblies Burnup 45 MWd/kgU Age 35 years	Table E-5
PWR High	4 PWR assemblies Burnup 55 MWd/kgU Age 35 years	Table E-6

* HM = Heavy metal i.e. uranium and plutonium.

Half-lives and specific activity of radionuclides

The half-lives and specific activities in Table 3-5 are reproduced from Table D-1 of **Spent fuel report**.

There are ongoing investigations and discussions concerning the half-life of Se-79 in the scientific community.

Table 3-5. Half-lives and specific activities of selected radionuclides. Data reproduced from Table D-1 in Spent fuel report.

Nuclide	Half-life [years]		Specific activity [Bq/mol]	Nuclide	Half-life [years]		Specific activity [Bq/mol]
Ac-227	21.8		6.06×10^{14}	Pa-231	3.28×10^{4}		4.02×10^{11}
Ag-108m	439		3.01×10^{13}	Pa-233	27.0	d)	1.78×10^{17}
Am-241	433		3.05×10^{13}	Pa-234m	1.2	m)	6×10^{21}
Am-242	16	h)	7.21×10^{18}	Pb-210	22.2		5.95×10^{14}
Am-242m	141		9.36×10^{13}	Pd-107	6.50×10^{6}		2.03×10^{9}
Am-243	7.37×10^{3}		1.79×10^{12}	Pu-238	87.9		1.5×10^{14}
C-14	5.71×10^{3}		2.31×10^{12}	Pu-239	2.41×10^{4}		5.48×10^{11}
Cd-113m	14.1		9.36×10^{14}	Pu-240	6.56×10^{3}		2.01×10^{12}
Cl-36	3.01×10^{5}		4.39×10^{10}	Pu-241	14.3		9.23×10^{14}
Cm-242	163	d)	2.95×10^{16}	Pu-242	3.74×10^{5}		3.53×10^{10}
Cm-243	29.1		4.54×10^{14}	Ra-226	1.60×10^{3}		8.25×10^{12}
Cm-244	18.2		7.25×10^{14}	Se-79	2.95×10^{5}		4.49×10^{10}
Cm-245	8.52×10^{3}		1.55×10^{12}	Sm-151	90.1		1.47×10^{14}
Cm-246	4.77×10^{3}		2.77×10^{12}	Sn-121m	43.9		3.01×10^{14}
Cs-135	2.30×10^{6}		5.74×10^{9}	Sn-126	2.30×10^{5}		5.74×10^{10}
Cs-137	30.1		4.39×10^{14}	Sr-90	28.8		4.58×10^{14}
Eu-152	13.6		9.71×10^{14}	Tc-99	2.11×10^{5}		6.26×10^{10}
H-3	12.3		1.07×10^{15}	Th-229	7.35×10^{3}		1.8×10^{12}
Ho-166m	1.20×10^{3}		1.1×10^{13}	Th-230	7.55×10^{4}		1.75×10^{11}
I-129	1.57×10^{7}		8.41×10^{8}	Th-232	1.41×10^{10}		9.36×10^{5}
Mo-93	4×10^{3}		3.3×10^{12}	Th-234	24.1	d)	2×10^{17}
Nb-93m	16.2		8.15×10^{14}	U-233	1.59×10^{5}		8.3×10^{10}
Nb-94	2.03×10^{4}		6.5×10^{11}	U-234	2.46×10^{5}		5.37×10^{10}

Table 3-5. Continued.

Nuclide	Half-life [years]		Specific activity [Bq/mol]	Nuclide	Half-life [years]		Specific activity [Bq/mol]
Ni-59	7.60×10^{4}		1.74×10^{11}	U-235	$7.04E \times 10^{8}$		1.88×10^{7}
Ni-63	101		1.31×10^{14}	U-236	2.34×10^{7}		5.64×10^{8}
Np-237	2.15×10^{6}		6.14×10^{9}	U-237	6.7	d)	7.14×10^{17}
Np-238	50.8	h)	2.28×10^{18}	U-238	4.47×10^{9}		2.95×10^{6}
Np-239	56.5	h)	2.05×10^{18}	Z-r93	1.53×10^{6}		8.63×10^{9}

m) Minutes.

h) Hours.

d) Days.

3.1.11 Judgements by the assessment team

Sources of information and documentation of data qualification

The supplier suggests that the only source of information, the **Spent fuel report**, is qualified. The assessment team agree.

Conditions for which data are supplied

The supplier has described different conditions in terms of fuel, burnup, etc. The way of handling these different conditions is by defining a number of hypothetical canisters containing fuel of variable type (BWR or PWR) and burnup. The assessment team agree with this handling.

Conceptual uncertainty

The main conceptual uncertainty identified by the supplier is uncertainty in the prognosis for future operation of Swedish nuclear power plants. However, although the amount of spent fuel, and therefore also the total radionuclide inventory and the number of canisters needed, depends on the future operation of the Swedish nuclear power plants, the *average* inventory of a canister is not particularly sensitive to uncertainties in this prognosis.

Data uncertainty due to precision, bias, and representativity

The supplier has handled data uncertainty by giving the inventory of six different hypothetical canisters, together with the inventory of an average canister. The inventories of these different canisters can be used for estimating the spread in the inventory data of deposited canisters. The assessment team agree with this handling.

Spatial and temporal variability of data

The supplier suggests that spatial variability can be treated as data uncertainty, in case the canisters are deposited without a trend (i.e. random deposition). It is cautioned that the use of data on inventory per average canister is restricted, if there is an uneven distribution of canisters with different average burnup in the repository. The assessment team agree.

Correlations

The supplier has identified correlations in data through the decay chains, as well as a correlation between half-life and specific activity. The assessment team agree.

Result of data qualification

The supplier has given total inventories for the average canister (Table 3-3), and references to tabulated data for the six hypothetical canister inventories (Table 3-4). For the hypothetical canisters, the referenced tables include the inventory distribution amongst the UO_2 pellets, construction material, crud, and control rods. The assessment team accept these data.

The supplier has given half-lives and specific activities in Table 3-5. The assessment team accept the data for all radionuclides except for Se-79. For this nuclide, the most recently published recommended value for its half-life is recommended for use in the PSAR. For Se-79 the recommended half-life is 3.27×10^5 years (Singh 2016).

In addition to the radionuclides listed above the modelling activities require data for Rn-222. Recent data for the nuclide is provided by Singh et al. (2011).

The publications by Singh (2016) and Singh et al. (2011) are sources to the data chosen in the IAEA Chart of the Nuclides, which in turn base their selection on the ENSDF (Evaluated Nuclear Structure Data File). ENSDF is an internationally used data base that contains recently evaluated experimental data on the structure and decay of nuclei.

For radionuclide transport modelling, the inventory is needed in amount of substance per canister [mol/canister], wherefore the assessment team has converted the supplied inventory data. This is done by dividing the inventory in terms of activity per canister by the specific activity, for each radionuclide.

3.1.12 Data recommended for use in modelling

Half-life and specific activity of radionuclides

All the data in Table 3-5, except for Se-79, are recommended for use in modelling. In addition, the half-life and specific activity Rn-222 is relevant for radionuclide transport calculations, even if it is not significant for the initial radionuclide inventory and therefore not included in Table 3-5. For Rn-222 and Se-79, the half-lives and specific activities in Table 3-6 are recommended for use in modelling.

Table 3-6. Half-lives of Rn-222 and Se-79, recommended for use in the PSAR.

Nuclide	Half-life [years]	Specific activity (Bq/mol)
Rn-222	1.05×10^{-2} a)	1.26×10^{18}
Se-79	3.27×10^{5} b)	4.04×10^{10}

a) (Singh et al. 2011).
b) (Singh 2016).

Inventory per average canister

The data in Table 3-7 are recommended for use in modelling. The data are produced by dividing the activity per canister data in Table 3-3 with the specific activity of Table 3-5, for each radionuclide. The suggested inventory is valid for year 2045.

To illustrate the total inventory of the selected radionuclides in the average canister, the data in Table 3-7 are illustrated in Figure 3-5.

Table 3-7. Inventory in mol per average canister at year 2045, recommended for use in the PSAR. Based on the total number of 5689 canisters.

Radionuclide	Amount per average canister (mol/canister)	Radionuclide	Amount per average canister (mol/canister)
Ac-227	1.85×10^{-9}	Pa-231	4.71×10^{-6}
Ag-108m	1.60×10^{-1}	Pa-233	1.64×10^{-7}
Am-241	8.98	Pa-234m	3.98×10^{-12}
Am-242	9.37×10^{-8}	Pb-210	1.13×10^{-10}
Am-242m	7.25×10^{-3}	Pd-107	5.74
Am-243	1.60	Pu-238	1.53
C-14	4.99×10^{-2}	Pu-239	40.8
Cd-113m	3.40×10^{-4}	Pu-240	23.5
Cl-36	8.64×10^{-3}	Pu-241	1.97
Cm-242	1.89×10^{-5}	Pu-242	6.66
Cm-243	1.84×10^{-3}	Ra-226	2.74×10^{-8}
Cm-244	1.56×10^{-1}	Se-79	1.67×10^{-1}
Cm-245	2.42×10^{-2}	Sm-151	1.47×10^{-1}
Cm-246	3.50×10^{-3}	Sn-121m	2.77×10^{-3}
Cs-135	6.45	Sn-126	8.97×10^{-1}
Cs-137	10.1	Sr-90	6.21
Eu-152	9.44×10^{-5}	Tc-99	19.9
H-3	7.25×10^{-3}	Th-229	1.34×10^{-8}
Ho-166m	7.49×10^{-4}	Th-230	1.64×10^{-4}
I-129	3.08	Th-232	4.39×10^{-5}
Mo-93	8.81×10^{-4}	Th-234	1.20×10^{-7}
Nb-93m	7.75×10^{-2}	U-233	1.17×10^{-4}
Nb-94	3.25×10^{-1}	U-234	1.76
Ni-59	2.25	U-235	42.1
Ni-63	3.18×10^{-1}	U-236	39.3
Np-237	4.75	U-237	6.10×10^{-8}
Np-238	1.34×10^{-9}	U-238	$8.11 \times 10^{+3}$
Np-239	1.39×10^{-6}	Zr-93	21.3

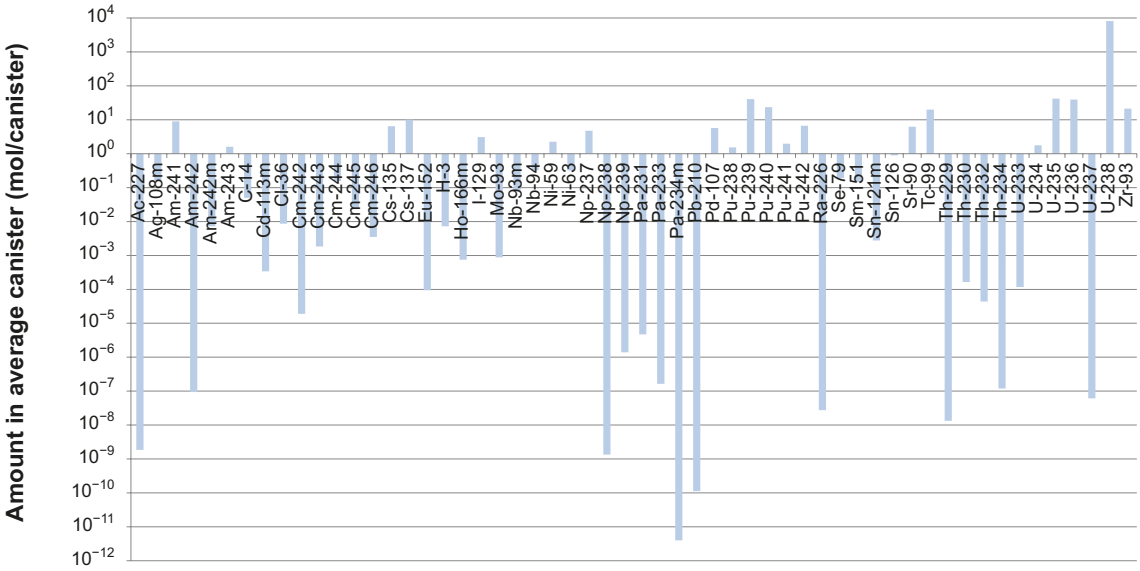

Figure 3-5. *Amount of substance of selected radionuclides in the average canister at year 2045.*

3.2 Instant release fraction and corrosion release fraction

The Instant Release Fraction *IRF* represents the fraction of the total radionuclide inventory that is modelled to be instantly released to the interior of the canister, upon contact with water. While nuclides embedded in the fuel matrix (including the higher actinides) will be released at the conversion rate of the fuel matrix, a fraction of the nuclides located in the fuel-clad gap and grain boundaries will be released more rapidly. On a safety assessment time scale this release is considered to occur instantaneously, as described in the **Fuel and canister process report**. In addition to gap and grain boundary inventory, the inventory of the crud[7] (a deposit on the outer surface of the cladding) is included in the *IRF*. Also, for the particular case of C-14, part of the inventory in the fuel cladding is included in the *IRF*.

The Corrosion Release Fraction *CRF* represents the inventory fraction that is modelled to be released on a relatively short time scale, as a result of corrosion of construction material upon contact with water. This corrosion is likely to take place over thousands of years after the canister is breached. The construction material includes the fuel cladding, the control rod cladding, and metal parts of the fuel assemblies.

The radionuclide inventory in the Ag-In-Cd alloy of the irradiated PWR control rods includes Ag-108m and Cd-113m. Due to de-alloying, the Cd is expected to be released more rapidly than Ag. Therefore, Cd-113m is included in the IRF, while Ag-108m is released at a separate, experimentally determined, slow rate.

In order to estimate the *IRF* and *CRF*, knowledge of the full radionuclide inventory is essential and this is discussed in Section 3.1.

3.2.1 Modelling

This section describes what data are expected from the supplier, and in what modelling activities the data are to be used. Furthermore, for this particular section it falls upon the customer (the assessment team) to provide certain data.

Defining the data need

For each radionuclide of the selected inventory, the *IRF* represents the fraction of the radionuclide inventory that is assumed to be instantly released. The *IRF* is in the interval 0 to 1, depending on the characteristic of the nuclide. In case *IRF* = 0, the radionuclide is completely entrapped in the UO_2 matrix and/or in the construction material, and will not be instantly released. In case *IRF* = 1, the entire inventory of the radionuclide is, or is pessimistically assumed to be, instantly released. In case of $0 < IRF < 1$, part of the radionuclide inventory is entrapped in the UO_2 matrix[8] and/or the construction material, and part is instantly released. The *IRF* is generally calculated according to the following equation:

$$IRF = \frac{\left(F_{GGB} \times I_{UO2}\right) + I_{Crud}}{I_{Tot}} \qquad 3\text{-}1$$

where *IRF* (-) is the instant release fraction, F_{GGB} (-) is called the gap and grain boundary fraction and is the fraction of the UO_2 pellet inventory comprised of gap and grain boundary inventory, I_{UO2} (mol/canister) is the inventory in the UO_2 pellets, I_{Crud} (mol/canister) is the crud inventory, and I_{Tot} (mol/canister) is the total inventory of the canister. In the particular cases of C-14, and Cd-113m, an additional term is needed in the numerator of Equation 3-1, stemming from assumed instant release from the fuel cladding or from the Ag-In-Cd alloy of the control rods. The gap and grain boundary fraction of some volatile radionuclides is correlated to the Fission Gas Release, *FGR* (-), while for other radionuclides there is no evident correlation. For most nuclides of the selected inventory, the gap and grain boundary inventory is negligible or non-existing.

[7] Originally the abbreviation for Chalk River Unidentified Deposits.

[8]

The terms I_{UO2}, I_{Crud}, and I_{Tot} of Equation 3-1 are delivered from the supplier as part of Section 3.1 and in the **Spent fuel report**. For this present section the supplier should deliver the:

- Fission gas releases, *FGR* (-), representative for BWR and PWR canisters.

The assessment team should deliver the:

- The gap and grain boundary fraction, F_{GGB} (-), either as correlated to *FGR* or based on leaching data, representative for BWR and PWR canisters, and for an average canister.
- Instant release fraction, *IRF* (-), as calculated from Equation 3-1, representative for BWR and PWR canisters, and for an average canister.

The average canister should be based the total inventory and total number of canisters as described in Section 3.1 in this report.

For each radionuclide of the selected inventory, the *CRF* represents the fraction of the inventory that is assumed to be released on a relatively short time scale, as result of corrosion of construction material of the fuel assemblies. (The cast iron insert and the copper canister are not considered in this section.) The *CRF* is defined to be in the interval 0 to 1, where the value 0 means that the nuclide does not exist in the construction material and the value 1 means that the total inventory is entrapped in the construction material. In case $0 < CRF < 1$, part of the radionuclide inventory is entrapped in the construction material, and part in the UO_2 matrix and/or the *IRF*. The *CRF* is calculated according to the following equation:

$$CRF = \frac{I_{Constr.Mtrl} + I_{Ctrl.Rods}}{I_{Tot}} \qquad 3\text{-}2$$

Where $I_{Constr.Mtrl}$ (mol/canister) is the inventory of the construction material excluding the control rods, and $I_{Ctrl.Rods}$ (mol/canister) is the inventory of the steel cladding of the control rods, excluding the Ag-In-Cd alloy inventory. These two inventories are given in the **Spent fuel report**. It should be noted that control rods are only included in a fraction of the PWR canisters, since an estimated 586 PWR fuel assemblies of an estimated total of 6 793 will be encapsulated with a control rod cluster. In the particular case of C-14, only part of the construction material inventory should be accounted for when estimating the *CRF*, as part of it is assumed to be instantly released.

The assessment team should deliver the:

- Corrosion release fraction, *CRF* (-), as calculated from Equation 3-2, representative for BWR and PWR canisters, and for an average canister.
- The corrosion time, t_{corr} (years) over which the construction material fully corrodes. This time may be cautiously set as the minimum time over which full corrosion is possible to occur, or as a distribution of possible corrosion times.
- A statement on whether the corrosion rate can be assumed to be uniform in time, or follows some functional relationship.

The requested *IRF* and *CRF* data should be delivered with uncertainty estimates for all radionuclides of the selected inventory (see Section 2.2.1), where applicable. These data are only significant for radionuclides where release due to *IRF* and/or *CRF* is not overshadowed by release due to fuel conversion.

Modelling activities in which data will be used

The instant and corrosion release fractions are used in radionuclide transport modelling in the near-field to calculate the release rates of radionuclides from the fuel and from breached canisters (see the **Radionuclide transport report**). In the conceptual model used, it is assumed that the radionuclides may either be released instantly, on a relatively short time scale, or slowly at the dissolutionrate of the UO_2 matrix. The total *IRF* is pessimistically assumed to be released instantaneously to the intruding water in the canister, in case there is no solubility limit. For radioelements that are solubility limited, the total *IRF* is not dissolved instantly in the intruding water, but only that fraction that correpond to the concentration at the solubility limit in the canister interior. Further release from the fuel is then governed by the water flow in the canister. The *CRF* is assumed to be released relatively fast on a

safety assessment time scale, but not instantaneously. This release is treated in a similar way as release due to fuel conversion, although the time it takes for the construction material to fully corrode is much shorter than the time it takes for the spent fuel to fully convert.

In case the corrosion release rate (mol/ year) is assumed to be uniform, it is calculated for each radionuclide by taking the product of the *CRF* and the total inventory, and dividing it by the corrosion time. For assessing the release rate of solutes to the intruding water, solubility limits need to be taken into account.

The silver in the PWR control rods is expected to be released much slower than the other metals in the construction materials due to dealloying effects. A slow, experimentally determined release rate is therefore used in the modelling.

The conceptual model used in the PSAR differs from that used in SR-Site in the way that the silver release rate is different than that from both *CRF* and *IRF*.

3.2.2 Experience from SR-Site

Some of the experience gained from previous work with the SR-Site safety assessment is useful for the data qualification in this Data report. This is briefly summarised below.

Modelling in SR-Site

The modelling activities of SR-Site using the *IRF* differ from those in the PSAR in that Ag-108m was assumed to be released with the IRF, and solubility limited (due to the inclusion of all silver in the calculation). In an additional calculation (Evins 2013), the inhomogeneous distribution of the radioactive silver in the silver alloy was taken into account, and it was estimated that this would increase dose and risk from the Ag-108m with about a factor of 3. Due to the low peak dose from Ag-108m, the overall assessment results still yields a dose that is more than two orders of magnitude below the risk limit.

Conditions for which data were used in SR-Site

The *IRF* data used in SR-Site were based on estimates of fission gas release of the BWR and PWR assemblies of the December 2007 fuel inventory in Clab (SKB 2010e) and the leaching data presented for individual radionuclides in the SR-Site Data report (SKB 2010a). For BWR and PWR spent fuel, the average burnup was 40.4 MWd/kg U and 44.8 MWd/kg U, respectively. For both fuel types, the maximum burnup was 60 MWd/kg U.

Sensitivity to assessment results in SR-Site

In SR-Site, two scenarios contributed to the estimated risk and were thus of particular importance: one where canister failure occurs through shearing of the canister due to earthquakes, and one where failure occurs through enhanced corrosion following loss of the bentonite buffer due to erosion. In these scenarios, the actinide daughter Ra-226 dominated the risk at times of maximal mean annual effective dose. For all actinides the *IRF* was in SR-Site assumed to be 0, based on conceptual understanding. For the central corrosion case, the IRF pulse is only included in deterministic calculations since this pulse yields negligible contributions to the probabilistically calculated mean dose. The IRF radionuclides with highest contribution to dose from the pulse release were I-129 and Se-79 (SR-Site Radionuclide transport report, SKB 2010c, p 63). The IRF radionuclides are also important in the analysis of so called risk dilution, see Section 13.9.4 in SR-Site Main report (SKB 2011). Here, the most important IRF contributors were I-129, Se-79 and Tc-99.

The CRFs of a few nuclides play an important role especially in scenarios where the canister is breached early. Of the two scenarios contributing to the calculated risk, early failures occurred only in the shear load scenario. There, the mean annual effective dose is first dominated by the CRF of C-14, and later by that of Nb-94, but their contribution to risk are very low compared to regulatory limits (SR-Site Radionuclide transport report, SKB 2010c, p 119).

Alternative modelling in SR-Site

No alternative modelling was performed in SR-Site, with regard to the *IRF*.

Correlations used in SR-Site modelling

In SR-Site, the instant release fractions of Cl-36, Cs-135, Cs-137, I-129 and Se-79 were correlated to fission gas release. No other correlation was used.

Identified limitations of the data used in SR-Site modelling

In SR-Site the *IRF* was for some nuclides calculated from the *FGR*, while for other nuclides it was based on leaching data, crud inventory or for a few nuclides, also parts of the inventory in the control rods or construction materials. This approach is part theoretical, and in part based on experimental results. Availability of experimental data was limited for many radionuclides.

In the SSM report (SSM 2018) it is observed that there are few available data for radionuclides that form part of the IRF, and that more data for especially Se-79, Nb-94 and I-129 would be beneficial for a better estimate of the IRF.

3.2.3 Use of data in the PSAR and SR-Site

The instant release fraction, which is defined here as it was defined in SR-Site, is based on the gap and grain boundary inventory and the crud inventory. The fuel cladding and/or the control rods are other sources for the *IRF* of Ag-108m, C-14, and Cd-113m. The instant release fraction is released instantaneously in radionuclide transport modelling and superimposed on the release due to fuel conversion. If there are solubility limits, this inventory can however not be dissolved instantly.

Concerning the part of the *IRF* that originates from the crud, the following should be considered: fuel conversion is postulated to take place at all times, upon contact with water. For most radionuclides of concern for the current safety assessment, the crud inventory is insignificant compared to the inventory in the UO_2 pellets. Thus, fuel dissolution will very quickly release much more of the radionuclide than what is contained in the crud. Only nuclides where 10 years of fuel dissolution occurring with a steady rate of 10^{-7} year^{-1} (cf Section 3.3.12), will release less than the crud inventory, are deemed significant for inclusion in the IRF. For Ag-108m, Mo-93, Nb-93m, Nb-94, Ni-59, Ni-63, Sn-121m, and Zr-9 the inventory of the crud outweighs the inventory of the fuel dissolved over ten years.

In this comparison, the inventories of the BWR and PWR hypothetical canisters of medium burnup (cf Tables CE-2 -and E-2 in **Spent fuel report**) were used. The crud inventory of all other radionuclides falls below the threshold where it is of any consequence for the post-closure safety of the repository, and is therefore disregarded.

The corrosion release fraction originates from corroding construction material, which includes the steel cladding of the control rods (excluding the Ag-In-Cd alloy), the zircaloy cladding, and other metal parts of the fuel assemblies. To evaluate which nuclides have a significant CRF, the amount released from the metals is compared to the amount released from 100 years of spent fuel dissolution occurring with a steady rate of 10^{-7} year^{-1} (cf Section 3.3.12). For C-14, Cl-36, Mo-93, Nb-93m, Nb-94, Ni-59, Ni-63, Se-79, Sn-121m, Tc-99, U-233, and Zr-93 the release due to corrosion of metallic parts outweighs the release due to 100 years of fuel dissolution.

It is suggested that the *CRF* is set to zero for all other radionuclides.

3.2.4 Sources of information and documentation of data qualification

Both the supplier and customer provide data in this Data report. Therefore, it is noted whether the referred documents are the supplier's or the customer's sources of information.

Sources of information

For the supplier, the main source of information is the **Spent fuel report**, which provides inventories and fission gas release data.

For the customer a number of documents are listed as main sources of information in Table 3-8. The main source of information is the SR-Site Data report (SKB 2010a). In addition, information regarding IRF is provided in later publications from the EU project First-Nuclides. The main sources are used to estimate the *IRF*, *CRF*, and corrosion time.

Table 3-8. Main sources of information used in data qualification.

Spent fuel report, Använt kärnbränsle att hantera i KBS-3-systemet. SKBdoc 1380282 ver 2.0, Svensk Kärnbränslehantering AB.
SKB, 2010a. Data report for the safety assessment SR-Site. SKB TR-10-52, Svensk Kärnbränslehantering AB.
Johnson L Günther-Leopold I, Kobler Waldis J, Linder H P, Low J, Cui D, Ekeroth E Spahiu K, Evins L Z, 2012. Rapid aqueous release of fission products from high burn-up LWR fuel: Experimental results and correlations with fission gas release. Journal of Nuclear Materials 420, 54–62. Kienzler B, Duro L, Lemmens K, Metz V, De Pablo J, Valls A, Wegen D H, Johnson L, Spahiu K, 2017. Summary of the Euratom Collaborative Project FIRST-Nuclides and conclusions for the safety case. Nuclear Technology 198, 260–276.
Lemmens K, Gonzalez-Robles E, Kienzler B, Curti E, Serrano-Purroy D, Sureda R, Martínez-Torrents A, Roth O, Slonszki E , Mennecart T, Günther-Leopold I, Z. Hozer H, 2017. Instant release of fission products in leaching experiments with high burnup nuclear fuels in the framework of the Euratom project FIRST- Nuclides. Journal of Nuclear Materials 484, 307–323.

Categorising data sets as qualified or supporting data

Different data sets used can be categorised as qualified or supporting. This is done in Table 3-9. In Table 3-10 justifications for the sorting are given.

Table 3-9. Qualified and supporting data sets.

Qualified data sets	Supporting data sets
1. Spent fuel report, Använt kärnbränsle att hantera i KBS-3-systemet. SKBdoc 1380282 v. 2.0. Svensk Kärnbränslehantering AB, Tables D-2 and E-1 to E-6.: Inventory data for the total repository and in hypothetical canisters with fuel of varying burnup. Inventory data is distributed on the sources UO_2 matrix, construction material, crud, and control rods. Average FGR data, with uncertainty estimates, for BWR assemblies and PWR assemblies are given here.	
2. SR-Site Data report Section 3.2.10: IRF for radionuclides correlated to fission gas release; IRF for radionuclides based on leaching data; IRF of radionuclides that require special treatment; CRF for nuclides that mainly originate from activation of construction materials; Corrosion time for the construction materials.	
3. Johnson et al. 2012: Instant release of I-129, Cs-137 and Se-79 from high-burnup fuels and correlation to fission gas release.	
4. Lemmens et al. 2017: Instant release of I-129 and Cs-137 from medium to high-burnup fuels and correlation to fission gas release and linear power rating.	
5. Kienzler et al. 2017: Instant release of Sr-90, Tc-99, I-129, Cs-137 (Figure 7) from medium to high-burnup fuels and correlation to fission gas release.	

Item number 1 are data sets provided by the supplier while the rest are data sets provided by the customer.

Table 3-10. Justifications to the sorting of items in Table 3-9.

1. Data provided in the **Spent fuel report** are qualified in accordance with the SKB quality assurance system. This qualification is found to be in compliance with the demands of this Data report.
2. Data provided in the SR-Site Data report (SKB 2010a) are qualified in accordance with the SKB quality assurance system and were selected and qualified during the SR-Site safety assessment.
3–5. (Johnson et al. 2012, Lemmens et al. 2017, Kienzler et al. 2017) are peer-reviewed scientific journal articles and the data presented are considered to be qualified.

3.2.5 Conditions for which data are supplied

The data are applicable to reactor operations used in the past as well as foreseen future operations in accordance with the scenario presented in the **Spent fuel report**. The data are applicable for year 2045.

For estimating the corrosion time, the conditions in the breached canister are needed. One could expect elevated temperatures in case the canister is breached relatively early. However, in the more likely case of late canister breach, the temperature should resemble that of the host rock. The groundwater compositions should correspond with those given in Chapter 6. However, it is assumed that the corrosion of the cast iron insert and construction materials will assure anoxic conditions in the canister. Information on the parts comprising the construction material is given in the **Spent fuel report**.

3.2.6 Conceptual uncertainty

The data of this section, which are used as input to radionuclide transport modelling, are consistent with the needs of the present modelling approach. However, as there is a large portion of pessimism included when estimating the data, they are not intended to in detail represent the conceptual view on these issues.

Instant release fraction, IRF

The radionuclide transport modelling approach concerning the *IRF* is pessimistic in assuming that the *IRF* is released instantaneously. In reality, the release of this fraction of the inventory is likely to occur during a more or less prolonged time period. In addition to the gap and grain boundary inventory, the *IRF* includes the crud inventory. The properties of crud are largely unknown, consequently instantaneous release is assumed. All in all, the conceptual uncertainties associated with the *IRF* are handled by pessimistically assuming instantaneous release, which may lead to an overestimation of the initial release rate.

Corrosion release fraction, CRF

Conceptual uncertainties associated with the *CRF* include the questions whether all construction material becomes fully corroded during the repository evolution, and whether corroded construction material releases its entire radionuclide inventory. Concerning the latter issue it is conceivable that the corrosion products may sorb or otherwise immobilise a fraction of the corrosion released nuclides. This uncertainty is handled by cautiously assuming that the full inventory of the construction material is released to the surrounding water during the corrosion time. This simplified conceptualisation may lead to an overestimation of the corrosion release rate.

Corrosion time, t_{corr}

Conceptual uncertainties associated with the corrosion time include the questions of:

- At what rates do different parts of the construction material corrode?
- What is the range of conceivable conditions in the canister?
- Will the corrosion itself increase the corrosion time, as corrosion products may pose a transport resistance for the corrodants?
- How does one assess a corrosion time from a great number of different corrosion rates and geometries?

The approach taken in the PSAR is to pessimistically assume that all parts corrode at the same rate as the fastest corroding material, which is stainless steel. Furthermore, all parts are assumed to be fully corroded at the time the thinnest part has corroded. This has two consequences. The first is that the release rates from thick metallic parts become unrealistically high. The second is that the release rate from relatively slowly corroding alloys becomes unrealistically high. It is important to notice that this is due to the pessimistic modelling approach taken, and not a consequence of the conceptual view. Other uncertainty, such as the corrosion rate at the conditions in the canister, is treated as data uncertainty. In the PSAR, the release rate of Ag-108m from the silver alloy in the PWR control rods deviates from the assumed release rate of the CRF of other metallic construction parts. Since silver is a noble metal, and corrosion would only be relevant in conditions with oxygen or sulphur available for electron transfer, it is conceptually sound to assume a lower release than the rest of the CRF. Nevertheless, the approach taken in the PSAR, with a defined, albeit low, corrosion rate for silver, involves uncertainties regarding the corrosion behaviour of the Ag-In-Cd alloy under repository conditions.

Fission gas release, FGR

The calculated fission gas release is used to estimate the *IRF* for some of the radionuclides. The *FGR* values are results of first principles calculations based on best available input data, such as diffusion data of fission gases. Such calculations are currently being performed and validated for the utilities in order to ensure that fuel failure will not occur and that the reactors can be operated safely. The calculations show a large span of fission gas releases for different fuel rods in the core. Even though there is a conceptual element in how to handle such a large span of *FGR* in safety assessment, this is treated as data uncertainty.

Gap and grain boundary fraction, F_{GGB}

A main conceptual uncertainty in determining the *IRF* for some nuclides lies in establishing a relationship between the *IRF* and *FGR*, via the F_{GGB}. The F_{GGB} relates to the segregation of fractions of certain radionuclides in the fuel, during operation, to the fuel-clad gap and grain boundaries. The concept of a gap and grain boundary fraction that is instantly released is based on the transfer of certain radionuclides to parts of the fuel from where they can be released much faster than through fuel conversion or dissolution. For the fuel-clad gap there is no significant uncertainty. However, an element of this uncertainty lies in establishing which part of the spent fuel is easily accessible to water, thus enabling instant releases of the radionuclides. There are also questions on how to handle the rim of the spent fuel pellet, as discussed below.

It has been discussed (see e.g. (Johnson et al. 2004, 2005, Ferry et al. 2008)) whether the radionuclide inventory in the rim of the irradiated fuel pellet should be included in the gap and grain boundary inventory. Experimental studies, however, have not shown any preferential release from the rim region (Clarens et al. 2008). In fact several studies have shown that the releases do not increase with burnup, i.e., within the accuracy of the experiments there is no evidence for an increasing contribution from the fuel rim (Jégou et al. 2004, Ekeroth et al. 2009, Hanson 2008). In this section, the estimations of F_{GGB} include the gap and grain boundary inventory but do not involve the rim inventory.

For the grain boundaries it is uncertain to what degree they are accessible to water. Furthermore, the radionuclides associated with the grain boundary inventory is mainly found as insoluble metallic alloy aggregates and is therefore not likely to be instantly released to water (Ramebäck et al. 2000, Cui et al. 2004).

3.2.7 Data uncertainty due to precision, bias, and representativity

Generally the resolution in the data does not allow for separating what part of the data uncertainty relates to precision, bias, and representativity. Data concerning the inventories of the different hypothetical canisters of variable average burnup are discussed in Section 3.1, where also an uncertainty discussion is given.

Ågesta fuel, Swap MOX and Fuel assembly skeletons are part of the total inventory and therefore also part of the calculation of the average canister inventory. These fuel types are not expected to affect the FGR, CRF and corrosion data uncertainty discussed here. Boxes with fuel residues and failed fuel are treated separately, se Section 3.1.7.

Fission gas release, FGR

This Data report presents *FGR* estimations for the average canister, based on the existing and estimated future BWR and PWR inventories of the scenario for nuclear power plant operation adopted by SKB that also includes high burnup fuel. Data from high burnup fuel are now available for both BWR and PWR fuel (Johnson et al. 2012, Kienzler et al. 2017, Lemmens et al. 2017).

Fission gas releases were calculated for both PWR and BWR fuel with burnup up to 60 MWd/kgU. Complete data sets including uncertainties are accounted for by Oldberg (2009) for the BWR cases and by Nordström (2009) for the PWR cases. The results of those calculations are used by Agrenius (2010) to calculate an average *FGR* for the BWR and PWR inventories used in SR-Site. The resulting data, with uncertainties, are representative also for the current spent fuel inventory relevant for the PSAR. These numbers, including uncertainties, are thus used in the estimations of *IRF* performed by the customer. Details regarding FGR calculations are given in the SR-Site data report.

In the SR-Site Data report the *FGR* is given as following (arithmetic mean ± one standard deviation):

- For spent BWR fuel: 0.019 ± 0.011
- For spent PWR fuel: 0.043 ± 0.031

These estimations are the results of the calculations by Agrenius (2010) in which data from all the cases presented by Nordström (2009) and Oldberg (2009) are used.

The fission gas release of a fuel pin depends on the location of the fuel pin in the reactor core. This is reflected in a wide span of data from the whole core. Furthermore, the *FGR* depends on the burnup and linear power rating (Kienzler et al. 2017, Lemmens et al. 2017). The estimated *FGR* averages given above take this into account, thereby assuring the representativity of the data.

Gap and grain boundary fraction, F_{GGB}

The leaching data available in the literature have been used to estimate the gap and grain boundary fraction of relevant nuclides (SR-Site Data report and references therein). The leaching data indicate variable correlation between F_{GGB} and *FGR* for different radionuclides. For some nuclides, no correlation at all could be seen and for these, the F_{GGB} is directly estimated from available leaching data or from conceptual understanding.

A few radionuclides of the selected inventory are considered to be mobile in the fuel, in a similar way as the fission gases during reactor operation (high temperature). These are I-129, Cs-135, Cs-137, Ag-108m, and Cd-113m. Existing leaching data for iodine and caesium indicate that the *FGR* constitutes an upper limit for F_{GGB} (Kienzler et al. 2017, Lemmens et al. 2017); for caesium in particular, correlations of *FGR* versus F_{GGB} have been shown to be ca 3:1 (Johnson et al. 2012). Thus, for these radionuclides, a 1:1 correlation is used as a bounding case in safety assessment. There is no fuel leaching data for Ag-108m and Cd-113m; however, their physical and chemical properties have been utilised in model calculations to show that they are likely to transfer to the fuel-clad gap in a similar way as I and Cs (Cubicciotti and Sanecki 1978, Johnson and Tait 1997). In PWR canisters containing control rods, the significant sources for Ag-108m and Cd-113m are the control rods; consequently the gap and grain boundary fraction is negligible in comparison. Nevertheless, for the average canister, it is relevant to consider this fraction.

At the time of the SR-Site safety assessment, the existing leaching data for Se-79 was limited to failed attempts to measure Se-79 in solutions (Wilson 1990a, b), which resulted in the conclusion that the amount leached was less than the detection limit for the method used. This suggests that there is no real evidence for Se-79 segregation to the gap at low to moderate burnup. The dearth of information regarding the behaviour of Se-79 advocates comparisons with other, chemically similar elements. Based on the observation of Te in the fuel-clad gap of a fuel with *FGR* of 10–13 % (Cubicciotti and Sanecki 1978), one may suggest that Se-79 could also be somewhat mobile in the fuel at high temperatures. The available data (Wilson 1990a, b) indicate that Se release is less than 0.15 times *FGR,* and the correlation $F_{GGB} = 0.15 \cdot FGR$ is cautiously adopted here. The data uncertainty regarding F_{GGB} (and *IRF*) for Se-79 is thus related to the uncertainty in the *FGR* values used in the correlation, as well as the fact that the correlation factor 0.15 is based on the upper limit of leached Se-79 given by the detection limit of Wilson (1990a). Later efforts to improve the knowledge and data base for Se-79 have been

produced varying and to some extent discrepant results (Johnson et al. 2012, Curti et al. 2015, Kienzler et al. 2017). Curti et al. (2015) indicates that selenium Se-79 is stabilized to sparingly soluble Se(-II) in the spent fuel matrix. Further investigations concerning the gap and grain boundary inventory of Se is warranted. In light of this, for the PSAR the previously adopted method of estimating the F_{GGB} is kept.

Two radionuclides are considered to be more mobile than the fission gas in the fuel matrix. The first is H-3, which is formed in the fuel but where the full inventory is expelled from the fuel matrix during reactor operation and found in the surrounding material (fuel-clad gap and cladding). The second most mobile radionuclide is Cl-36, which is expected to be very mobile in the fuel matrix (Pipon et al. 2007). There are no leaching data for Cl-36 release from light water reactor fuels. The estimates of the F_{GGB} are therefore based on the CANDU fuel data of Tait et al. (1997). A best available estimate (Tait et al. 1997) indicates a three-to-one correlation between the F_{GGB} and *FGR* for Cl-36.

For radionuclides where available data indicate a one-to-one correlation between *FGR* and F_{GGB}, the values and uncertainties in the corresponding *FGR* are adopted. For Cl-36 and Se-79, the values and uncertainties are multiplied by a factor of three and 0.15, respectively. There is also uncertainty in the correlation factor through which the F_{GGB} and *FGR* are correlated. However, this uncertainty is judged to be small in comparison to the spread in the *FGR* and is not propagated.

For a number of the concerned radionuclides there is no scientific evidence for a correlation between the gap and grain boundary fraction and the *FGR*. These radionuclides are C-14, Sr-90, Tc-99, Pd-107, Sn-121m, and Sn-126. For these radionuclides, leaching data available in the literature have been consulted. Leaching data published after the SR-Site assessment (Johnson et al. 2012, Lemmens et al. 2017, Kienzler et al. 2017) indicate approximately the same values as was used in SR-Site (SR-Site Data report) and do not warrant any change from the previous values recommended for use in SR-Site. The reader is therefore referred to SR-Site Data report for details regarding the leaching data for these nuclides. Best estimate values for IRF of these nuclides together with and upper and lower estimates of the distributions are provided in Section 3.2.

Instant release fraction, IRF

The sources of the *IRF* are the gap and grain boundary inventory, crud and, in the case of C-14, the fuel cladding. In addition, for PWR canisters Cd-113m inventory of the control rods is pessimistically assumed to be instantly released.

While F_{GGB} is the fraction of the UO_2 pellet inventory I_{UO2} that is comprised of gap and grain boundary inventory, the *IRF* is the fraction of the total inventory I_{Tot} that is instantly released (cf Equation 3-1). Therefore, for nuclides where part of the inventory is in the construction material and/or crud, *IRF* values will not be the same as the F_{GGB} values.

For Cl-36, Cs-135, Cs-137, I-129, Pd-107, Se-79, Sn-126, Sr-90, and Tc-99, the gap and grain boundary inventory is the only significant source of the *IRF*:

For Cl-36, Cs-135, Cs-137, I-129, and Se-79 the I_{UO2}/I_{Tot} ratio is close to unity (> 97 %); consequently the values and uncertainties of the F_{GGB} are adopted. For these nuclides, the values and uncertainties of the F_{GGB} are in turn adopted from those of the *FGR*.

FGR values are only suggested for BWR and PWR fuel by Agrenius (2010), but not for the average canister. If combining two populations, and if having their means and variances, the mean and standard deviation of the combined population can be calculated:

$$\mu_{XY} = \frac{N_X \mu_X + N_Y \mu_Y}{N_X + N_Y} \qquad 3\text{-}3$$

$$\sigma_{XY} = \sqrt{\frac{N_X\left(\sigma_X^2 + \mu_X^2\right) + N_Y\left(\sigma_Y^2 + \mu_Y^2\right)}{N_X + N_Y} - \mu_{XY}^2} \qquad 3\text{-}4$$

where μ_{XY} and σ_{XY}^2 are the mean and variance of the new distribution, μ_X and μ_Y and σ_X^2 and σ_Y^2 are the means and variances of the distributions to be combined. Furthermore, N_X and N_Y are the number of data points in the populations to be combined (that is 3 982 BWR canisters and 1 707 PWR canisters).

If using $\mu = 0.019$ and $\sigma = 0.011$ for BWR canisters and $\mu = 0.043$ and $\sigma = 0.031$ for PWR canisters, the *IRF* for the average canister becomes distributed according to $\mu = 0.026$ and $\sigma = 0.022$. These values correspond to the data uncertainty for the *IRF* of Cs-135, Cs-137, and I-129. For Cl-36 these numbers are multiplied by a factor of three, and for Se-79, they are multiplied with a factor of 0.15.

For Pd-107, Sn-126, Sr-90, and Tc-99 the I_{UO2}/I_{Tot} ratio is close to unity (> 99 %). The data and uncertainty estimate for the F_{GGB}, is adopted for these nuclides. As the F_{GGB} is estimated based on leaching data, the uncertainty estimates are given as a range and a best estimate value. In the background sources (e.g. Werme et al. 2004), triangular distributions in the normal space were assigned based on the range and best estimate value. However, from a risk analysis perspective it may not be optimal to use an asymmetric triangular distribution (unless this is expressly warranted). In this text we assume that the best estimate value is set in such manner that it is of equal probability (50 %) that the "true" value is above as below this best estimate value. Therefore, we recommend the double triangle distribution (e.g. AACE 2008). The double triangle distribution is illustrated in Figure 3-6.

The resolution in data from the background sources does not allow for assigning different data sets or distribution to different fuel types or canister types for these nuclides.

For Mo-93, Nb-93m, Nb-94, Ni-59, Ni-63, and Zr-93, the crud inventory is the only source of *IRF*:

For these nuclides, the Best Estimate for the *IRF* of the average canister is estimated by weighting the *IRF*s of the BWR and PWR fuel elements by the number of each fuel element according to:

$$IRF = \frac{\sum_i N_i \frac{I_{Crud,i}}{I_{Tot,i}}}{\sum_i N_i} \qquad 3\text{-}5$$

Where $I_{Crud,i}$, $I_{Tot,i}$, and N_i are the crud inventory, total inventory, and number of fuel elements for the BWR and PWR elements, respectively. The uncertainty range of the *IRF* is here constrained by the highest and lowest *IRF* values of fuel elements of low and high burnup. For BWR, the low burnup is set to 30 MWd/kgU and the high burnup is set to 50 MWd/kgU. For PWR, corresponding burnups are 35 and 55 MWd/kgU. However, in doing so care must be taken when assigning distributions to the data, so that the approach does not give rise to risk dilution. This is achieved by recommending the double triangular distribution.

For a few nuclides, Ag-108m, C-14, Cd-113m, H-3, and Sn-121m, individual treatment is required.

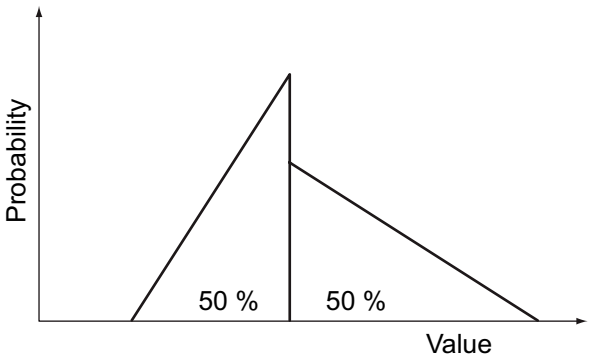

Figure 3-6. *Illustration of the double triangular distribution, where the integral of each triangle holds 50 % probability.*

The inventory of Ag-108m differs dramatically between BWR and PWR canisters, where only a minute fraction (~ 10^{-5}) is associated with BWR canisters. For PWR canisters, practically all Ag-108m is located in the Ag-In-Cd alloy of the control rods. Available unpublished in-reactor data indicate a potential de-alloying and release of In and Cd. The Cd-content of the control rods is therefore pessimistically assumed to be released instantaneously and, as a result, the recommended *IRF* for PWR fuel for this nuclide is one. In BWR fuel, Cd-113m exists only in the UO_2 fuel pellets, and the gap and grain boundary fraction is assumed to have a one-to-one correlation with the *FGR*.

Published Data are now available showing very slow release of Ag-108m from irradiated control rods (Askeljung et al. 2019). This fraction is therefore not included in the IRF but rather released with a slow rate (see next section on Corrosion Release Fraction). For BWR fuel, crud contains ca half of the total Ag-108m inventory is assumed to be the Ag-108m inventory (cf Table D-2 in **Spent fuel report**). The contribution from the gap and grain boundary inventory is on the order of one percent and is added. A recommended IRF is still provided in Table 3-11.

For C-14, the IRF fraction is based both on the fraction found in the gap and grain boundaries (F_{GGB}) and the inventory found in oxidized cladding of the fuel rods. For SR-Site the assumed F_{GGB} was 10 % and 20 % if the $I_{Constr.Mtrl}$..(SKB 2010a) The same fractions are adopted here for the PSAR. The recommended *IRF* (F_{GGB}) for the average canister is calculated by weighted average of IRF in BWR and PWR fuel and is reported in Table 3-11.

For H-3, almost the entire inventory originates from the fuel matrix. As the mobility of H-3 is so high, the full inventory is expelled from the fuel matrix and may therefore be instantly released. Therefore, for the average canister, the *IRF* is set to one.

For Sn-121m, the *IRF* stems both from the gap and grain boundary inventory and the crud inventory. Thus the F_{GGB} and I_{Crud} from BWR and PWR fuels are calculated, and the weighted average of the BWR and PWR fuels is used to calculate the recommended best estimate IRF for the average canister. The range of data is limited by the upper and lower estimates, that are calculated similarly but with low and high burnup fuels. The recommended distribution is that of a double triangle, and the values are provided in Table 3-11.

Corrosion release fraction, CRF

Based on the reasoning in Section 3.2.3, the *CRF* is only meaningful for C-14, Cl-36, Mo-93, Nb-93m, Nb-94, Ni-59, Ni-63, Se-79, Sn-121m, Tc-99, U-233, and Zr-93.

In addition, for the PSAR, Ag-108m is assumed to be part of the CRF rather than the IRF, due to new experimental data.

By using Equation 3-5, but exchanging I_{Crud} for $I_{Constr.Mtrl} + I_{Ctrl.Rods}$, the weighted average of the *CRF* for BWR and PWR fuels is obtained. This value is recommended as best estimate for the average canister. The here assumed uncertainty range is contained by the highest and lowest *CRF* of all fuels with low and high burnup. These *CRF*s gives the upper and lower limit of the suggested double triangle distribution for each radionuclide. Regarding Nb-93m and Nb-94, ca 97 % of the inventory is found in PWR fuel, where the CRF fraction is 100 %. In the BWR fuel, the lower limit is close to 80 % ; this is the lower limit used for the distribution.

The main source of Ag-108m is the PWR Control rods. In SR-Site, all silver in the control rods was assumed to be released instantaneously (SKB 2010a). This handling was based on lack of experimental data, and was during the review of SR-Site considered questionable. By assuming instant release of all silver, radioactive and stable, the solubility limit for silver was reached, resulting in a reduced release rate of Ag-108m from the canister. Additional information was requested in which it was shown that even if the radionuclide is found only in a 1 mm thick surface layer of the silver alloy, the dose and risk posed by the corrosion of the alloy would only increase by a factor of 3 (Evins 2013). In PSAR, the Ag-108m is modelled to be part of the CRF, however, with a slower rate than the rest of the CRF (see next section).

Corrosion time, t_{corr}

For the PSAR, recommended corrosion time for construction materials containing the CRF have not changed since SR-Site. Thus, for the corrosion time, a triangular distribution is suggested in the $\log_{10}$-space with the lower, best estimate, and upper values of 10^2, 10^3, and 10^4 years, respectively (SKB 2010a).

For the corrosion time, a triangular distribution is suggested in the $\log_{10}$-space with the lower, best estimate, and upper values of 10^2, 10^3, and 10^4 years, respectively.

Corrosion time is assumed to be different for silver in the PWR control rods. Based on new experimental data, the best estimate of the corrosion time is 5.9×10^7 years (Askeljung et al. 2019). The recommended distribution is triangular in the $\log_{10}$-space ranging from 5.9×10^8 to 5.9×10^6 years.

3.2.8 Spatial and temporal variability of data

Spatial variability of data

The *IRF* and C*RF* of each canister depend on the spent fuel type, and on other factors, such as whether the canister contains control rods or not. In the PSAR, the variability is estimated by use of low, medium and high burnup fuels in BWR and PWR canisters (Appendix E in the **Spent fuel report**). From these data one can assess the variability in the *IRF* and *CRF* for each radionuclide. However, as there is presently no strategy on how the canisters will be placed in the repository, this variability is treated as data uncertainty.

Furthermore, by taking a pessimistic approach in estimating the corrosion time, potential spatial variability is dwarfed by the pessimism.

Temporal variability of data

There is no temporal variability of the *IRF* and C*RF* data of interest for safety assessment.

For the radionuclide transport modelling, the corrosion rate of the construction material is suggested to be uniform over time within a canister, although different canisters may have different corrosion times. This is a simplification where one disregards the fact that corrosion products may pose a transport resistance for corrodants on their way towards the corrosion surface.

3.2.9 Correlations

As discussed in Section 3.1, the radionuclides are correlated through decay chains. As discussed in this section, the *IRF* is assumed to correlate with the *FGR* and/or F_{GGB} for a few nuclides. Functional relations concerning the parameters of this section are given in Equations 3-1, 3-2, and 3-5.

In terms of the data used as input to probabilistic radionuclide transport modelling, the *IRF* of Cl-36, Cs-135, Cs-137, I-129, and Se-79 should be correlated. The *IRF* of all other radionuclides could be kept uncorrelated. The C*RF*s of the different radionuclides do not need to correlate to each other.

3.2.10 Result of data qualification

The *IRF* is given for the following radionuclides:

- Cl-36, Cs-135, Cs-137, I-129, and Se-79,
- Pd-107, Sn-126, Sr-90, and Tc-99,
- Mo-93, Nb-93m, Nb-94, Ni-59, Ni-63, and Zr-93,
- Ag-108m, C-14, Cd-113m, H-3, and Sn-121m.

The bullet list above represents four different categories. The first category features radionuclides for which the *IRF* is equal to the F_{GGB}, which is for these radionuclides, assumed to be correlated to the fission gas release. For the radionuclides of the second bullet the *IRF* is also based on the F_{GGB}, but without correlation to *FGR*; instead, experimental data from leaching experiments are used to establish

the F_{GGB}. For the third bullet, the *IRF* is solely based on the crud inventory. For the fourth bullet, the *IRF* is based both on the F_{GGB}, on the crud inventory, and part of the inventory of the construction material and control rods, as specified for the particular cases.

The *CRF* is given for the following radionuclides:

- Ag-108m, C-14, Cl-36, Mo-93, Nb-93m, Nb-94, Ni-59, Ni-63, Se-79, Sn-121m, Tc-99, U-233, and Zr-93.

For more detailed discussions and justifications of data and uncertainty ranges, please turn to Section 3.2.7.

IRF: Cl-36, Cs-135, Cs-137, I-129, and Se-79

As discussed above, the *IRF* of Cl-36, Cs-135, Cs-137, I-129, and Se-79 is equal to the F_{GGB}, which in turn correlates to the *FGR*. The FGR values for BWR and PWR canisters, and the average canister, have been estimated to:

- For spent BWR fuel: $\mu = 0.019$, $\sigma = 0.011$.
- For spent PWR fuel: $\mu = 0.043$, $\sigma = 0.031$.

For the average canister: $\mu = 0.026$, $\sigma = 0.022$.

- For Cs-135, Cs-137, and I-129 a one-to-one correlation with FGR is recommended, while for Cl-36 a three-to-one correlation is recommended.
- For Se-79, the *IRF* is assumed to be 0.15 times the *FGR*.

The resulting recommended IRFs for these nuclides are presented in Table 3-11.

IRF: Pd-107, Sn-126, Sr-90, and Tc-99

The recommended *IRF* for Sn-126 is the same as in SR-Site (SKB 2010a). It is suggested to use the double triangle distribution in the normal space and for each radionuclide; lower, upper, and best estimate values are supplied in Table 3-11.

IRF: Mo-93, Nb-93m, Nb-94, Ni-59, Ni-63, and Zr-93

For these radionuclides the only source of the *IRF* is the crud inventory. The recommended data are based upon inventory data in Appendix D and E of **Spent fuel report**. Double triangle distributions in the normal space with lower, best estimate, and upper values are recommended for the Average canister, see Table 3-11.

IRF: Ag-108m, C-14, Cd-113m, H-3, and Sn-121m

These nuclides require special treatment, as discussed in detail in Section 3.2.7. In short, the *IRF* of Ag-108m for BWR canisters originates from the crud and gap and grain boundary inventory while in the PWR fuel assembly, Ag-108m from the control rods dominates the inventory. For Cd-113m the situation is similar, with the exception that it is not found in the BWR crud inventory. For C-14, the *IRF* originates both from the UO_2 pellet and from the cladding. H-3 is so mobile in the fuel matrix that the *IRF* is considered to be unity on conceptual grounds. Finally, Sn-121m is found both in the gap and grain boundary inventory and in the crud.

Depending on the nuclide, different distributions are recommended for the average canister. For Cd-113m, a single point value is recommended. The same applies for H-3. For the other discussed nuclides, the double triangle distributions in the normal space with lower, best estimate, and upper values are recommended. The recommended data for the average canister are presented in Table 3-11.

Table 3-11. Recommended IRFs.

Radionuclide	μ	Σ		Distribution
Cl-36	0.078	0.066		Normal
Cs-137	0.026	0.022		Normal
Cs-137	0.026	0.022		Normal
I-129	0.026	0.022		Normal
Se-79	0.0039	0.0033		Normal
Radionuclide	**Lower**	**Best estimate**	**Upper**	**Distribution**
Ag-108m	3.0×10^{-5}	3.0×10^{-4}	6.0×10^{-4}	Double triangle, normal space
C-14	9.1×10^{-2}	9.2×10^{-2}	9.3×10^{-2}	Double triangle, normal space
Cd-113m		1.0		Single point value
H-3		1.0		Single point value
Mo-93	4.0×10^{-3}	4.8×10^{-3}	6.2×10^{-3}	Double triangle, normal space
Nb-93m	3.7×10^{-4}	4.7×10^{-4}	2.5×10^{-2}	Double triangle, normal space
Nb-94	4.3×10^{-4}	5.4×10^{-4}	2.9×10^{-2}	Double triangle, normal space
Ni-59	4.4×10^{-3}	5.4×10^{-3}	5.8×10^{-3}	Double triangle, normal space
Ni-63	4.4×10^{-3}	5.6×10^{-3}	6.0×10^{-3}	Double triangle, normal space
Pd-107	0	0.002	0.01	Double triangle, normal space
Sn-121m	7.6×10^{-5}	4.8×10^{-4}	1.1×10^{-3}	Double triangle, normal space
Sn-126	0	3.00×10^{-4}	0.001	Double triangle, normal space
Sr-90	0	0.0025	0.01	Double triangle, normal space
Tc-99	0	0.002	0.01	Double triangle, normal space
Zr-93	1.4×10^{-5}	1.7×10^{-5}	2.1×10^{-5}	Double triangle, normal space

CRF: Ag-108m, C-14, Cl-36, Mo-93, Nb-93m, Nb-94, Ni-59, Ni-63, Se-79, Sn-121m, Tc-99, U-233, and Zr-93

The *CRF* is based on the inventory of the construction material and control rods, with the exception of the Cd-113m inventory in the Ag-In-Cd alloy. Double triangle distributions in the normal space with lower, best estimate, and upper values are recommended. Data are given for the average canister. The best estimate values are weighted averages of the *CRF* for BWR and PWR fuel. The ranges are given by the lowest and highest *CRF* of the low and high burnup fuel. The data are presented inTable 3-12.

Table 3-12. Recommended CRFs.

Radionuclide	Lower	Best estimate	Upper	Distribution
Ag-10m		1		
C-14	4.4×10^{-1}	4.9×10^{-1}	5.3×10^{-1}	Double triangle, normal space
Cl-36	1.1×10^{-2}	2.0×10^{-2}	7.2×10^{-2}	Double triangle, normal space
Mo-93	7.2×10^{-1}	9.7×10^{-1}	9.9×10^{-1}	Double triangle, normal space
Nb-93m	7.7×10^{-1}	1.0	1.0	
Nb-94	7.9×10^{-1}	1.0	1.0	
Ni-59	8.2×10^{-1}	9.9×10^{-1}	9.9×10^{-1}	Double triangle, normal space
Ni-63	7.9×10^{-1}	9.9×10^{-1}	9.9×10^{-1}	Double triangle, normal space
Se-79	0	3.9×10^{-4}	1.3×10^{-3}	Double triangle, normal space
Sn121m	2.1×10^{-5}	2.9×10^{-2}	4.3×10^{-2}	Double triangle, normal space
Tc-99	3.7×10^{-5}	3.6×10^{-4}	1.2×10^{-3}	Double triangle, normal space
U-233	2.2×10^{-1}	4.4×10^{-1}	5.5×10^{-1}	Double triangle, normal space
Zr-93	8.4×10^{-2}	1.1×10^{-1}	1.3×10^{-1}	Double triangle, normal space

3.2.11 Judgements by the assessment team

Only part of the data and discussion delivered in this section are produced by the supplier, while the assessment team has produced the remaining part. In this section the judgment is limited to the part supplied by the supplier, which is the *FGR*. The supplier has also supplied the inventory on which calculations are based. However, judgment on these inventories has been delivered in Section 3.1.11.

Sources of information and documentation of data qualification

The assessment team agrees with selection and categorisation of the different sources of information and data sets made by the supplier.

Conditions for which data are supplied

The conditions for which the data are supplied have been described as in accordance with the scenario for the future operation of the nuclear power plants as described in the **Spent fuel report**. This is accepted by the assessment team.

Conceptual uncertainty

The supplier argues that there is little conceptual uncertainty concerning the calculations on which the *FGR* are based, and that the existing uncertainty in the *FGR* should be handled as data uncertainty. The assessment team agrees.

Data uncertainty due to precision, bias, and representativity

The description of the *FGR* allows for interpreting the spread in the data. The assessment team accept the supplier's interpretations.

Spatial and temporal variability of data

The supplier suggests that there is significant spatial variability of the *FGR* within a canister. However, for the PSAR the spatial variability of concern is between canisters. This must be handled as data uncertainty, as there currently is no strategy for how different canisters will be placed in the repository. As the *IRF* is assumed to be instantly released, there is no temporal component of the *FGR* of interest (after the fuel is taken out of the reactor).

Correlations

The supplier gives no correlation related to the supplier data. Correlations given between the parameters of this section are suggested by the customer.

Result of data qualification

The supplier has only provided a limited part of the data delivered in this section, namely data and uncertainties of the *FGR* for BWR and PWR fuels. The assessment team agree with these data.

3.2.12 Data recommended for use in modelling

The *IRF* and CRF data presented in Table 3-11 and Table 3-12 are recommended to be used in the PSAR modelling. Where normal distributions are suggested, they should be truncated at zero and one. For all radionuclides of the selected inventory that are not displayed in these tables, the *IRF* and CRF are insignificant and is recommended to be set equal to zero.

As the corrosion rate is assumed to be uniform, the corrosion release rate for each radionuclide should be calculated by taking the product of the *CRF* and total inventory and dividing it by the corrosion time. The corrosion time distribution for all CRF radionuclides except Ag-108m is shown in Table 3-13. Each canister should be given a single corrosion time in radionuclide transport modelling.

Table 3-13. Distribution of corrosion time t_{corr}.

Lower limit (yr)	Best estimate (yr)	Upper limit (yr)	Distribution
10^2	10^3	10^4	Triangular distribution, $\log_{10}$-space

For Ag-108m, the recommended corrosion time is given in Table 3-14.

Table 3-14. Distribution of corrosion time t_{corr} for silver (Ag-108m).

Lower limit (yr)	Best estimate (yr)	Upper limit (yr)	Distribution
5.9×10^6	5.9×10^7	5.9×10^8	Triangular distribution, $\log_{10}$-space

3.3 Fuel dissolution rate

In case of canister failure, groundwater may come in contact with the UO_2 matrix inside the canister. If so, this will cause the fuel matrix to dissolve or become otherwise altered. As a result, uranium and radionuclides embedded in the fuel matrix will be released in the intruding water. The process is controlled primarily by the chemical environment of the intruding water and by the fuel composition (see the **Fuel and canister process report**).

The release rate of radionuclides embedded in the UO_2 fuel matrix is assumed to be the same as the dissolution rate of the UO_2 matrix. For the expected reducing conditions inside a breached canister, the solubility limit of reduced uranium species will rapidly be reached. This would prevent a further dissolution of the UO_2 fuel matrix. However, radiolysis is known to cause oxidative dissolution (corrosion) of the UO_2 fuel matrix. The effect will be continuous release of radionuclides at the rate of oxidative dissolution. This process will be relevant close to the fuel surface, while the bulk environment of the canister interior is expected to be reducing. Therefore, reduction and precipitation of the dissolved uranium species in the canister interior occurs at the same rate as the oxidation. The water is thereby kept at the solubility limit for reduced uranium.

In the conceptual model for fuel dissolution, when the transport rate of uranium species out of the canister is low, only the oxidative fuel dissolution component contributes to fuel dissolution. For these cases, the fuel dissolution rate is practically equal to the rate of oxidative fuel dissolution. For larger out flows, the component for upholding the solubility limit of uranium may become important. However, as Ekeroth et al. (2020) points out, the flows required for this to cause a dissolution rate higher than the oxidative dissolution rate are unrealistically large.

A small fraction of the spent fuel will be spent fuel residues from the Studsvik operations and containers with failed fuel, i.e. fuel with failed cladding. The dissolution rate relevant for these irregular fuel types require special treatment and recommended dissolution rates are given in this document.

3.3.1 Modelling

This section describes what data are expected from the supplier, and in what modelling activities the data are to be used.

Defining the data need

The radionuclide transport modelling activities need the following fuel dissolution rate data:

- The fuel dissolution rate of the UO_2 matrix under reducing conditions, in fractions per year (yr^{-1}). The fuel dissolution rate should, if possible, be given with uncertainties, implicitly encompassing different relevant conditions, such as water and fuel compositions.

- The fuel dissolution rate of spent fuel residues and in special containers. As for the regular fuel, this should be relevant for reducing conditions and given in fractions per year (yr^{-1}).
- The fuel dissolution rate of failed spent fuel rods in special containers. As for the regular fuel, this should relevant for reducing conditions and given in fractions per year (yr^{-1}).

To clarify the expression "fuel dissolution rate in fractions per year", this is the amount of UO_2 dissolved per year, divided by the initial total amount of UO_2.

Modelling activities in which data will be used

The fuel dissolution rate is used when calculating the release of radionuclides from the fuel matrix to the water that has intruded into the canister (see the **Radionuclide transport report)**.

The near-field radionuclide transport code used within the PSAR is the same as the one used in SR-Site. For details, see the **Model summary report**. In the model the fuel dissolution rate is constant and independent of the degree of saturation of uranium species in the intruding water. Fuel dissolution due to the upholding of the uranium concentration at the solubility limit is only relevant if the transport rate out of the canister is higher than the rate of oxidative fuel dissolution. For lower transport rates, the solubility limit will be reached and, consequently, uranium precipitates will form. In this situation, the component representing fuel dissolution due to the upholding the uranium concentration will be negligible. If the transport rate out of the canister is larger than the fuel dissolution rate, the non-oxidative fuel dissolution will become more important. The fuel dissolution rate is set to balance the fuel dissolution and transport rates in the model. The conceptual model agrees with that used in previous assessments.

3.3.2 Experience from SR-Site

This section briefly summarises experience from the SR-Site safety assessment, which may be of direct consequence for the data qualification in this Data report.

Modelling in SR-Site

The handling of regular fuel dissolution in SR-Site agrees with the handling in the PSAR. In SR-Site the fuel dissolution rate was given as a triangular probability density function in the $\log_{10}$ space with the central value at 10^{-7} yr^{-1}, and minimum and maximum values at 10^{-8} yr^{-1} and 10^{-6} yr^{-1}, respectively. Irregular spent fuels, such as spent fuel residues and failed fuels, were considered negligible and were not included in the modelling.

Conditions for which data were used in SR-Site

The data provided in SR-Site were relevant for the December 2007 inventory of fuel stored at the Clab interim storage facility as well as for the prognosis including the future spent fuel. Besides the different fuel types, also linear power rating and burnup were considered. The experimental data considered were obtained in a reducing environment.

Sensitivity to assessment results in SR-Site

The radiological risk was, for important SR-Site scenarios, dominated by Ra-226 at times of maximal mean annual effective dose. For these times, the release rate of Ra-226 was assumed to be directly dependent on the fuel dissolution rate.

Alternative modelling in SR-Site

No alternative modelling of the fuel dissolution process was used in SR-Site.

Correlations used in SR-Site modelling

The fuel dissolution rate was not directly dependent on any other data in SR-Site. However, the release rate of matrix bound radionuclides was correlated to the fuel dissolution rate.

Identified limitations of the data used in SR-Site modelling

The fuel dissolution data delivered to SR-Site modelling could be used for all required conditions and modelling activities. Concerning the data in SR-Site, the regulatory authorities found that additional information was requested concerning fuel residues and as a response, amounts, characteristics and potential contribution to risk were assessed (Johansson and Evins 2013). To estimate the contribution to risk, fuel dissolution rates were provided for different types and fractions of the fuel residues (Evins and Hedin 2013). One identified limitation was therefore that the dissolution rate used was only relevant for the regular fuel. Additional information was also requested concerning the background to the chosen distribution for the fuel dissolution rate and the justification for using the same distribution for the full assessment time was questioned (SSM 2018). Additional data and arguments were provided during the review phase (Spahiu and Evins 2014, Spahiu 2012).

3.3.3 Use of data in the PSAR and SR-Site

The fuel dissolution rate data used in SR-Site is the same as in the PSAR. This is supported by results published after SR-Site, discussed in the **Fuel and canister process report**,

For the PSAR, the assessment includes estimates of risk contribution from irregular spent fuels, i.e. spent fuel residues and failed fuel. The fuel dissolution rates given for these irregular spent fuels are mainly based on cautious assumptions and in many cases overly pessimistic. This approach is taken due to the lack of relevant experimental data and as more relevant data are available and published, the pessimism may be reduced.

3.3.4 Sources of information and documentation of data qualification

Sources of information

The main source of information is the SR-Site Data report (SKB 2010a). In the **Fuel and canister process report** (Section 2.5.5), recent publications supporting the chosen dissolution rates, or even suggesting lower dissolution rates, are discussed. Additional sources of information are the documents submitted to the regulatory authorities during the review phase of SR-Site, and a recent report concerning risk contributions from failed fuels. The main sources of information are tabulated inTable 3-15. Some of the supporting publications discussed in the **Fuel and canister process report** are given in Table 3-16.

Table 3-15. Main sources of information used in data qualification.

SKB 2010a Data report for the safety assessment SR-Site. SKB TR-10-52, Svensk Kärnbränslehantering AB.
Fuel and canister process report. **Fuel and canister process report for the final repository for spent nuclear fuel at Forsmark – PSAR version. SKB TR-21-02, Svensk Kärnbränslehantering AB.**
Evins L Z, Hedin A, 2013. Uppskattning av riskbidrag från bränslerester. SKBdoc 1395834 ver 1.0, Svensk Kärnbränslehantering AB.
Evins L Z, Hedin A, 2020. Failed fuel in special containers: potential contribution to risk calculated in the post-closure safety for the spent nuclear fuel repository. SKBdoc 1872793 ver 1.0, Svensk Kärnbränslehantering AB.

Categorising data sets as qualified or supporting data

The main source of information for the regular spent fuel is the SR-Site Data report which is qualified (produced within the current SKB framework for data qualification). References within the **Fuel and canister process report** are either considered to be qualified or supporting. Data sets that are sorted as qualified or supporting are summarised in Table 3-16. The rationale for the sorting is discussed below the listed items.

Table 3-16. Qualified and supporting data sets.

Qualified data sets	Supporting data sets
1. SR-Site Data report (SKB 2010a), Section 3.3.12 Recommended distribution of fuel dissolution rates. 2. **Fuel and canister process report**, Section 2.5.5: Review of recent publications supporting the chosen fuel dissolution range. 3. Evins and Hedin 2013: Assumed fuel dissolution rates from spent fuel residues. 4. Evins and Hedin 2020: Estimated fuel dissolution rates from spent fuel with failed cladding. 5. Puranen et al. (2017): Anoxic iron corrosion suppressing oxidative dissolution of spent fuel. 6. Puranen et al. (2018): Hydrogen suppressing oxidative dissolution of high-burnup fuel. 7. Ollila et al. (2013): Dissolution rates of alpha-doped UO_2 in natural groundwater. 8. Odorowski et al. (2017) Fe(II) produced by iron corrosion suppresses the oxidative dissolution of highly doped, unirradiated MOX pellets. 9. Bauhn et al. (2018a, b) Data supporting reaction between hydrogen and hydrogen peroxide at the spent fuel surface. 10. Liu et al. (2017) Model incorporating hydrogen effect showing corrosion rates decreasing with time to negligible levels. 11. Ekeroth et al. (2020). Hydrogen suppressing oxidative effect of radiolysis on the spent fuel surface.	12. Evins L Z et al. (2014). Fuel dissolution rates for alpha doped samples in natural groundwater.

1-4. Reports produced within the current SKB framework for data qualification.

5–11. Peer reviewed journal or conference articles. Furthermore, they are all considered as relevant for the fuel in the Swedish programme, and for Swedish repository conditions.

12. Final report from the REDUPP project published as Posiva Workreport according to the review process connected to this publication type at Posiva at the time.

Excluded data previously considered as important

No data previously considered as important has been excluded.

3.3.5 Conditions for which data are supplied

The fuel dissolution rate suggested for regular spent fuel in this section, with its uncertainty range, should encompass all relevant fuel types and water compositions under reducing conditions, expected in a KBS-3 repository. The conditions for which the data are supplied are described in the SR-Site Data report (SKB 2010a) and these have not changed for the PSAR.

The spent fuel to be deposited is described by the scenario for the operation of Swedish nuclear power plants and consists predominantly of UOX spent fuel but to some extent also of MOX spent fuel. The burnup ranges from somewhat above 10 MWd/kgHM to somewhat below 60 MWd/kgHM (**Spent fuel report**). For regular fuels, data provided in the SR-Site Data report SKB 2010a) are judged as relevant for the PSAR, since there has been no change in fuel type and maximum burnup since then. Modern fuel types that are doped with Cr and Al display similar leaching behaviour as the standard UOX fuel (Fidalgo et al. 2020). In addition, for irregular fuels, new fuel types including fuel residues and failed fuel are included in the PSAR. Fuel residues mainly originate from the hot cell examination and experiments performed in Sweden. Fuel rods with failed cladding originate from fuel used in Swedish nuclear power plants.

3.3.6 Conceptual uncertainty

For regular fuels, the conceptual uncertainty connected to spent fuel dissolution remains essentially the same since SR-Site (SR-Site data report, SKB 2010a). Further work has been performed that reduces the conceptual uncertainty connected to the spent fuel dissolution process has been published since then (e.g. Puranen et al. 2017, 2018, Bauhn et al. 2018a, b, Ekeroth et al. 2020).

For irregular fuels, much less research is available and the conceptual uncertainty is significant. In the case of spent fuel residues, there is uncertainty concerning effect of degradation of epoxy and formation of potential complex formation. For oxidized fuel matrix, stemming from either exposure to air in a Hot Cell environment or from interaction with coolant in nuclear reactors or in storage pools, there is uncertainty in the formation of secondary phases, radionuclide content in these, and the rate at which the secondary phases dissolve in repository conditions. In these cases, a pessimistic approach is taken.

3.3.7 Data uncertainty due to precision, bias, and representativity

For regular fuels, the uncertainties in the experimental data upon which the recommended dissolution rates are based are discussed in the original publications, which are generally peer-reviewed articles. However, the fuel dissolution rate is based on total uranium or releases and cautious assumptions. It disregards a large body of experimental data which show decreasing release rates, or alternatively no release, as well as modelling results that suggests lower releases. The large uncertainty (a span of two orders of magnitude) in the recommended dissolution rates is intended to capture all uncertainties, including conceptual uncertainties. For irregular fuels, there are various sources of uncertainties associated with data used to estimate dissolution rates. These are discussed below.

Data uncertainty due to precision

As the chosen range of fuel dissolution rates for regular fuel is cautious (as discussed above), data uncertainty due to precision issues in measurements or models is judged as subordinate.

Dissolution of various fractions (oxidized, powders, epoxy-encased samples) of the fuel residues have been assumed to instant, so for these data uncertainty due to precision is not relevant. In the case of oxidized fuel fractions in failed fuel, dissolution data is connected with uncertainty due to precision. The estimated rates depend on parameters which are likely to vary within certain ranges, such as pH. This uncertainty is captured by assigning a distribution between an upper and lower estimate.

Data uncertainty due to bias

There are experimental results suggesting much lower fuel dissolution rates than those suggested (e.g. Carbol et al. 2005, Cui et al. 2008, Muzeau el al. 2009, Spahiu et al. 2000, 2004). In this sense the degree of pessimism in SR-Site could be seen as a bias.

Bias is likely one source of data uncertainty for the dissolution data connected to oxidized fuel matrix in failed fuel. There is very a limited number of experimental data, which means there is risk the data may cluster above or below the true value. This bias is expected to be covered by the uncertainty range given by the suggested distribution.

Data uncertainty due to representativity

The experimental data that forms a basis for the recommended dissolution rates for regular fuels have been obtained both with relatively fresh spent fuel and α-doped UO_2. Spent fuel represents the real properties of the fuel matrix, but has an unrealistically high radiation field with large contribution of β- and γ- radiations. For this reason it is tested under relatively high hydrogen concentrations (> 1 mM). On the other hand, α-doped UO_2 represents better the radiation field of the spent fuel expected to contact groundwater, but does not represent other properties of the spent fuel matrix. In this case the data have been obtained with low concentrations of reductants, or no reductants present. Most of the spent fuel leaching tests have been carried out in bicarbonate containing solutions, known to enhance dissolution. Cations such as Ca or Mg, which are reported to decrease dissolution rates (Wilson and Gray 1990, Santos et al. 2006), have often been excluded in order to obtain cautious rates. The analysis

includes data obtained in solutions with average or high chloride concentrations, variable pH, as well as synthetic groundwaters. Thus the rates analysed should be cautious and representative for all possible conditions in the repository.

Regarding irregular fuels, the underlying experimental results are collected on certain oxidized phases that may not be fully representative of the actual phases in the failed fuel. This constitutes an uncertainty with regards to representativity. This uncertainty is also expected to be covered by the suggested range of the distribution.

3.3.8 Spatial and temporal variability of data

No spatial or temporal variability is considered. The fuel dissolution rates are assumed constant in time and valid for all canisters.

Spatial variability of data

As the burnup and linear power for the fuel is increasing (due to the increased power outtake in the power plants), it is not unlikely that the deposition tunnels built in the later part of the deposition period will contain fuel with higher burnup than that deposited in the initial part. However, within the accuracy of several recent experiments there is no evidence for increased dissolution rates from high burnup fuel. For this reason, spatial effects on fuel dissolution rates are disregarded. They are assumed to be captured by the uncertainty range in the fuel dissolution rates.

Irregular fuels may or may not be encapsulated together with regular fuels. If they are encapsulated separately and these canisters are deposited near each other in the repository, this would constitute a spatial variability. However, no decision is taken concerning encapsulation strategy for irregular fuels, and the approach in the PSAR is to disregard this potential spatial variability. For the final estimation of risk, the spatial variability is of no consequence.

Temporal variability of data

No temporal variability of dissolution rates are taken into account. The dissolution rates for both regular fuel and for the oxidized part of the failed fuel are given with wide uncertainty ranges that are expected to cover any potential change in rates over time. The argument for keeping a constant dissolution rate over the full assessment time is given in the SR-Site Data report (SKB 2010a) and in Spahiu and Evins (2014).

3.3.9 Correlations

No correlations were assigned in SR-Site Data report (SKB 2010a) Based on this and the results from recent studies, it is concluded that fuel dissolution is not a function of fuel burnup and no correlation with the instant release fraction exists.

The release rate of matrix bound radionuclides is correlated to the fuel dissolution rate.

3.3.10 Result of data qualification

The dissolution rates for regular fuels (including MOX) qualified in the SR-Site Data report SKB 2010a). are the same as the rates resulting from the current qualification. Based on data reported from experiments using spent nuclear fuel and α-doped UO_2 , reviewed in the **Fuel and canister process report**, a dissolution rate with a triangular probability density function in the log10-space is suggested. The lower limit, best estimate, and upper limit are suggested to be 10^{-8}, 10^{-7}, and 10^{-6} yr^{-1}. The fuel conversion rate is suggested not to vary in time.

The dissolution rates for spent fuel residues and failed fuels are qualified here for the PSAR. Based on the data provided in Evins and Hedin (2013, 2020), the following dissolution rates assumed for the different fractions are given in Table 3-17.

Table 3-17. Dissolution rates suggested for various fractions of fuel in spent fuel residues and failed fuel.

Irregular fuel type	Dissolution rate (yr^{-1}), triangular distribution in log10-space		
Spent fuel residues:	Upper estimate	Best estimate	Lower estimate
Unaltered fuel matrix	1.0×10^{-6}	1.0×10^{-7}	1.0×10^{-8}
Air-oxidized fuel matrix		Instant release	
Fuel powder		Instant release	
Fuel samples in epoxy		Instant release	
Failed fuel:			
Unaltered fuel matrix	1.0×10^{-6}	1.0×10^{-7}	1.0×10^{-8}
Oxidized/altered fuel matrix	2.9×10^{-3}	2.9×10^{-4}	2.91×10^{-5}

3.3.11 Judgements by the assessment team

According to the instruction given in Section 2.3, the assessment team should comment on Sections 3.3.4 to 3.3.10. The assessment team agrees with the statements and suggestions made in these sections.

3.3.12 Data recommended for use in modelling

The probability density function of the fuel dissolution rate recommended for use in the PSAR modelling is the same that for SR-Site, and is given in Table 3-18. The distribution should apply for all types of regular fuel, and for all reducing conditions and time periods.

Table 3-18. Distribution of fuel dissolution rates suggested for use in modelling.

Lower limit (yr^{-1})	Best estimate (yr^{-1})	Upper limit (yr^{-1})	Distribution
10^{-8}	10^{-7}	10^{-6}	Triangular distribution, $\log_{10}$-space.

For modelling dissolution of irregular fuel types containing spent fuel residues and failed fuel, the data in Table 3-17 is recommended.

3.4 Solubility data

In case of canister failure, groundwater will enter the void inside the canister and come in contact with the spent fuel and metal parts inside the canister. As a result, radionuclides will be released into this water as dissolved species. If the concentrations of the dissolved species get high enough, radionuclides will precipitate as solid phases. The solubility of the precipitated phases will determine the maximum concentration of a radioelement inside the canister. These concentrations are used as the source term for the radionuclide transport calculations.

The solubility concentration in the assessment is radioelement specific and dependent on:

1. The assumed solubility limiting phase.
2. The geochemical conditions inside the void.
3. The thermodynamic database used.

The selection of solubility limiting phases is done for the purpose of safety assessment.

3.4.1 Modelling

This section describes what data are expected from the supplier, and in what modelling activities the data are to be used. The PSAR is based on the same modelling as SR-Site.

Defining the data requested from the supplier

The output from this section should include solubility limiting phases and associated reactions assumed to occur in the aqueous phase inside a failed canister, as well as associated thermodynamic data. The supplier should deliver:

- A list of solubility limiting phases and associated reactions including the elements requested in Section 2.2.1, as well as relevant groundwater species.
- Thermodynamic data for each of the listed reactions, including uncertainty estimates. The data should be delivered in form of equilibrium constants, $log_{10}(K^0_r) \pm \Delta log_{10}(K^0_r)$.

The elements for which data are requested (see Section 2.2.1) are: H, C, Cl, Ni, Se, Sr, Mo, Zr, Nb, Tc, Pd, Ag, Cd, Sn, I, Cs, Sm, Eu, Ho, Pb, Ra, Th, Ac, Pa, U, Np, Pu, Am, and Cm. The choice of relevant groundwater components should be justified. The groundwater composition is handled in Section 6.1 of this report. As part of the uncertainty discussion, supporting data from natural systems, laboratory experiments, and previous assessments may be useful.

The process of co-precipitation process for Ra-Ba sulphate is considered. Thus, the supplier should deliver:

- A formula for the $(Ra,Ba)SO_4$ co-precipitate, as well as guidance on how to incorporate co-precipitation in the safety assessment.

The reactions and thermodynamic data delivered in this section are inputs to the Simple Functions spreadsheet (Grivé et al. 2010a), which is used to assess the solubility limits of radioelements in the canister. As a second step of the radionuclide transport modelling, the assessed solubility limits are used to determine the concentration of dissolved radioelements inside the canister, and thus to determine the source term (see the **Radionuclide transport report**).

Except for the data delivered here, the Simple Functions spreadsheet requires input data on the groundwater composition, in terms of the major ions, pH, redox potential, and ionic strength. Such data are presented in Section 6.1.

3.4.2 Experience from SR-Site

For the two main canister failure scenarios in SR-Site, shear due to an earthquake and corrosion following bentonite erosion, solubility limits were only applied in the shear scenario. The reason is that when the bentonite buffer is eroded, advective flow can keep the concentration of radionuclides lower than the solubility limits, alternatively, if colloidal species have precipitated, there is no bentonite to provide transport resistance. Since the shear scenario only contributes to a small degree to the overall calculated risk, radionuclide solubilities do not contribute significantly to the overall result of the safety assessment. SSM commented on this in the review of SR-Site, suggesting that this may reflect an overly pessimistic approach regardring solubility limits in the safety assessment overall (SSM 2018). Some important aspects of the solubility calculations are discussed below. The discussion is based on experience both during the SR-Site project, and experience gained during the review phase.

Thermodynamic data

The thermodynamic data included in the solubility calculations for the PSAR are the same as for SR-Site. Considering the assignment and treatment of uncertainties , Grivé et al. (2013a) provides a background and discussion on the uncertainty values in the Simple Functions tool, as well as giving examples for a few radionuclides. The conclusion of the extended reasoning of the uncertainty assignment approach is that it seems sufficiently accurate and appropriate for the purpose.

One issue regarding the calculations concerns the excusion of phosphate in the calulations, and what effects this may have on the results. New calculations including phosphate were therefore performed and results were compared with calculations that excluded phosphate solubilities (Grivé et al. 2013b). Important conclusions are that excluding phosphate is conservative, i.e. even low phosphate concentrations in the water would lower the solubility significantly for many radionuclides, and that no change is observed for the radionuclides dominating risk. Thus, the total risk is unaffected by the inclusion of phosphate in the solubility calculations.

In addition, the effect of temperature on thermodynamic data was pointed out and clarifications were requested that would illustrate the difference at low and high temperature. Temperature affects solubilities; however, the calculations perfomed in SR-Site are only valid for 25 ºC. Since temperature will be higher than that for some time in the respository, Grivé et al. (2013b) performed some calculations in response to this request. This work highlights that the solubility of most radionuclides will be higher at 90 ºC than at 25 ºC, but also that these temperature corrections are relying on available enthalpy data, which for casesfew, or none. For uranium, the solubility changes with several orders of magnitude; however, this is related to the lack of enthalpy data for the selected solid phase. Finally, it can be concluded that solubility is strongly dependent on temperature and it is doubtful to use solubilities for 25 ºC for cases where the expected temperature is higher. However, in the PSAR, as in SR-Site, 25ºC is expected to be reached ca 3 000 years after closure of the repository. During this early stage, there is no risk for failure of the canister due to corrosion, and the probability for a failure due to shear is very low. In the case of early shear failure, the dose is dominated by C-14 and no solubility limit is assigned for this radionuclide. Thus, in the current assessment, the same solubility data as in SR-Site, valid for 25ºC, is used.

Ra-Ba co-precipitation

The consequence calculatiosn show that Ra, originating from decay of ^{238}U, is an important radionuclide, responsible for the highest risk far in the future. Therefore the the solubility of Ra is important in the consequence calculations; in SR-Site solubility of Ra was assumed to be controlled by Ra-Ba co-precipitation. Since the solubility of Ra was then calculated using an assigned Ra/Ba ratio), this triggered further investigations concerning potential transport of Ba out of the canister. Additionally the availability of Ba in the fuel matrix, effect of timing of canister failure, actual Ba inventory in the fuel, potential effect of Sr, and apparent correlation between Ra and Ca concentrations in natural ground waters was also contemplated. Grandia (2013) provides an extended discussion on all these issues along the following lines of argument. At the time of canister failure, Ba (and Ra) may diffuse out of the canister if there is a concentration gradient. Considering the expected concentration in the bentonite pore waters and the concentration in the canister, there will be a very weak driving force for diffusion. It is also argued that the assumed Ra/Ba is acceptable as a maximum also for early times of canister failure. The amount of Ba in fuel, and thus the Ra/Ba ratio is also shown to not be sensitive to fuel type. A number of research results relating to the effect of Sr on formation of the (Ra, Ba)SO_4 solid solution show that Ra will eventually fixed as ternary (Ba,Sr,Ra)SO_4 solid solution. Thus, dissolved Sr inside a failed canister is not expected to significantly affect the Ra co-precipitation with barite. Regarding the observed correlations between Ra and Ca, Grandia (2013) provides a detailed discussion showing that equilibrium of Forsmark deep ground waters with barite is clearly observed, and that the Ra solubility limiting phase in the deep ground waters at Forsmark is likely a set of Ba-Ra sulphate solid solutions.

Recent and on-going research regarding the Ra-Ba co-precipitation process is presented and discussed in the **Fuel and canister process report.** None of the results warrants any change from the handling in SR-Site, and thus no change has been made regarding input data for the PSAR.

3.4.3 Supplier input on use of data (text reproduced from SR-Site Data report)

The supplier will not deliver solubility data or reactions for the radioelements Mo, Cd, Eu, and Ac. These elements are not included in the Simple Functions Spreadsheet and no solubility assessment has been made.

The supplier agrees with the use of data in SR-Site. It is noted that the exclusion of other co-precipitates than (Ra,Ba)SO_4 from the safety assessment is pessimistic, but that it is up to the safety assessment team to choose the degree of pessimism. With the chosen degree of pessimism in SR-Can (the exclusion of all co-precipitates) the supplier agrees with the use of data.

3.4.4 Sources of information and documentation of data qualification

Sources of information

The main sources of information on solubility limits are (Duro et al. 2006a, b), which are reports dedicated for SR-Can. The solubility limiting phases and reactions are taken from Duro et al. (2006a), while the thermodynamic database (TDB) is taken from Duro et al. (2006b). A supplement to Duro et al. (2006a) has been recently produced (Grivé et al. 2010b). A major reference in Duro et al. (2006b) is the NAGRA-PSI 01/01 TDB, reported in Hummel et al. (2002). For data on Pb, an element that was not included in Duro et al. (2006a, b), the main reference is Grivé et al. (2010b). The main source of information on the performance of the Simple Functions spreadsheet is Grivé et al. (2010a). In addition, Grivé et al. (2013a, b) are sources of information concerning effects of temperature, phosphate and uncertainties on calculated solubility limits. The main sources of information on (Ra,Ba)SO_4 co-precipitation are Grandia et al. (2008) and Bosbach et al. (2010). Additional sources of information regarding Ra-Ba co-precipitation are Grandia (2013), Weber et al. (2017). All these sources of information are shown in Table 3-19.

Table 3-19. Main sources of information used in data qualification.

Duro L, Grivé M, Cera E, Gaona X, Domènech C, Bruno J, 2006a. Determination and assessment of the concentration limits to be used in SR-can. SKB TR-06-32, Svensk Kärnbränslehantering AB.
Duro L, Grivé M, Cera E, Domènech C, Bruno J, 2006b. Update of a thermodynamic database for radionuclides to assist solubility limits calculation for performance assessment. SKB TR-06-17, Svensk Kärnbränslehantering AB.
Hummel W, Berner U, Curti E, Pearson F J, Thoenen T, 2002. Nagra/PSI chemical thermodynamic data base 01/01. Boca Raton: Universal Publishers.
Grivé M, Domènech C, Montoya V, García D, Duro L, 2010a. Simple Functions Spreadsheet tool presentation. SKB TR-10-61, Svensk Kärnbränslehantering AB.
Grivé M, Domènech C, Montoya V, García D, Duro L, 2010b. Determination and assessment of the concentration limits to be used in SR-Can. Supplement to TR-06-32. SKB R-10-50, Svensk Kärnbränslehantering AB.
Grandia F, Merino J, Bruno J, 2008. Assessment of the radium-barium co-precipitation and its potential influence on the solubility of Ra in the near-field. SKB TR-08-07, Svensk Kärnbränslehantering AB.
Bosbach D, Böttle M, Volker M, 2010. Experimental study of Ra^{2+} uptake by barite (BaSO4). Kinetics of solid solution formation via $BaSO_4$ dissolution and $Ra_xBa_{1-x}SO_4$ (re) precipitation. SKB TR-10-43, Svensk Kärnbränslehantering AB.

Categorising data sets as qualified or supporting data

The different data sets used as inputs to this section are categorised as qualified or supporting in Table 3-20. The reasoning behind the sorting is given in Table 3-21.

Table 3-20. Qualified and supporting data sets.

Qualified data sets	Supporting data sets
1. Duro et al. (2006a): Selected solubility limiting phases and rationale for their selection. 2. Duro et al. (2006b): Thermodynamic database used in SR-Can (tables in Chapters 2 to 18). Formation reactions of aqueous species and solubility constants for solid phases. One chapter of the report is dedicated to each element or group of elements. 3. Hummel et al. (2002), NAGRA-PSI 01/01 thermodynamic database: Reference thermodynamic database modified for the SR-Can solubility assessment. 4. Grivé et al. (2010b): Updated thermodynamic database, as supplement to SKB TR-06-32. Includes the element Pb. 5. Original thermodynamic database published by the OECD NEA-TDB project and discussion on the selection of the thermodynamic data. Rand et al. (2009) TDB of Thorium. Brown et al. (2005) TDB of Zirconium. Olin et al. (2005). TDB of Selenium. Gamsjäger et al. (2005). TDB of Nickel. Guillaumont et al. (2003). TDB of Uranium, Neptunium, Plutonium, Americium and Technetium. Lemire et al. (2001). TDB of Neptunium and Plutonium. Rard et al. (1999). TDB of Technetium. Silva et al. (1995). TDB of Americium. Grenthe et al. (1992a). TDB of Uranium. 6. References (Chapter 19) in Grivé et al. (2010b): Papers and reports used to update thermodynamic data included in the Simple functions spreadsheet. 7. Results in Bosbach et al. (2010) showing that re-crystallisation kinetics of barite as well as (Ra, Ba) sulphate co-precipitation are relatively fast processes. 8. Inventory data in Appendix C, Table C-15 of SR-Site Spent fuel report (SKB 2010c).	9. Figure 3-2 in Grandia et al. (2008) and conclusions stating that the relative amount of Ra with respect to Ba in the precipitating system will be at least 1 000 times lower (e.g. page 33 of Grandia et al. 2008). 10. Duro et al. (2006a), Chapter 4.1 and Appendix A: Data of measured radionuclide solubilities from laboratory experiments. 11. Duro et al. (2006a), Chapter 4.2 and Appendix B: Data of measured radionuclide solubilities from natural systems. 12. Duro et al. (2006a), Appendix C: Data of recommended solubility limits from other national performance assessments exercises. 13. Grivé et al. (2013a). Data from update of Simple Functions to assess effects of phosphate and temperature. 14. Grivé et al. (2013b). Supporting information concerning uncertainties in thermodynamic data. 15. Grandia (2013). Additional information regarding Ra-Ba co-precipitation supporting the handling of Ra solubility. 16. Weber et al. (2017). Data supporting the uptake of Ra in barite to form (Ba,Ra) SO_4 solid solution.

Table 3-21. Justifications to the sorting of items in Table 3-20.

1. (Duro et al. 2006a) was written and reviewed according to the SKB quality assurance system. It is considered as qualified, as it is a dedicated SR-Can document and produced in accordance with the current framework for data qualification. In Duro et al. (2006a), the solubility limiting phases and associated reactions are selected with an expert judgement methodology. The selection of the aqueous species considered in the solubility calculations for each radio-element is based on the sensitivity analyses presented in Chapter 6 of Duro et al. (2006a).

2. Duro et al. (2006b) is considered as qualified, as it is a dedicated SR-Can document and produced in accordance with the current framework for data qualification. The report delivers equilibrium constants as well as enthalpy data for the chemical reactions of interest. The aim of that report was to take data from a thermodynamic database (NAGRA-PSI 01/01 TDB (Hummel et al. 2002)) for solubility calculations and to complete the database in case data were lacking, where considered appropriate. Several changes, updates and checks for internal consistency and completeness to the NAGRA-PSI 01/01 database were conducted when needed. Most modifications incorporated to the NAGRA-PSI 01/01 database are reported in Duro et al. (2006b).

3. The thermodynamic database “NAGRA-PSI 01/01 database” was prepared by PSI and NAGRA and reported in Hummel et al. (2002). This work has undergone a peer review by an independent reviewer, according to NAGRA’s QA procedures. Furthermore, the data are relevant for the Swedish repository concept and can therefore be considered as qualified.

4. Since the publication of Duro et al. (2006b) several experimental programmes and scientific literature works have been devoted to the improvement of the thermodynamic databases for the elements of interest. All modifications needed for the implementation of the newly appeared databases until 2009 are reported in Grivé et al. (2010b). Most modifications reported in Grivé et al. (2010b) refer to the implementation of the thermodynamic data published in the “Chemical Thermodynamics” series of books from the OECD NEA. Thermodynamic data for Pb system has been included in the Simple Functions spreadsheet in 2009.

5. The OECD NEA “Chemical Thermodynamics” series of books, as well as articles and reports from the scientific literature, were used to update the thermodynamic data included in the Simple Functions spreadsheet and are properly referenced in Grivé et al. (2010b). These data are considered as qualified given that they are peer reviewed and constitute the highest quality thermodynamic databases on radioelements relevant for the Swedish repository.

6. Papers and reports used to update thermodynamic data included in the Simple Functions spreadsheet are qualified, given that they have been submitted to a peer review process before considering them. References are given in Grivé et al. (2010b).

7. The SKB report (Bosbach et al. 2010) is written and reviewed in accordance with the SKB quality assurance system.

8. SKB (2010b) is written and reviewed in accordance with the SKB quality assurance system. The data are used for calculate ing the Ba/Ra ratio in the canister for BWR and PWR spent fuel.

9. The SKB report (Grandia et al. 2008) is written and reviewed in accordance with the SKB quality assurance system. However, the spent fuel for which numerical data are given is ATM-104 spent fuel (PNL 1991), which is not identical with the Swedish spent fuel (but very similar). These data are sorted as supporting, and it should be noted that recommended data are based on similar calculations for Swedish fuel (cf Figure 3-8).

10. Data of measured radioelement solubilities from laboratory experiments are reported in Section 4.1 and Appendix A of Duro et al. (2006a). These are supporting data used in the expert judgement for the solubility assessment presented in Duro et al. (2006a).

11. Data of measured radioelement solubilities from natural systems are reported in Section 4.2 and Appendix B of Duro et al. (2006a). These are supporting data used in the expert judgement for the solubility assessment presented in Duro et al. (2006a).

12. Data of recommended solubility limits from other national performance assessment exercises are included in Appendix C of Duro et al. (2006a). These data are used as supporting information to compare the current solubility assessment with other assessments of the same type, conducted by different nuclear waste management organisations.

13. Grivé et al. (2013a) provides data that supports the exclusion of phosphate from the calculation by showing that this is a pessimistic approach. The solubilities calculated for temperatures up to 90 °C show that for calculation cases involving elevated temperatures it is doubtful to use solubilities calculated for 25 °C.

14. Grivé et al. (2013b) provides additional information supporting the treatment of uncertainties in thermodynamic data.

15. Grandia (2013) supports the treatment of Ra-Ba co-precipitation and the coice of Ra/B ratio to calculate the Ra solubility.

16. Weber et al. (2017) supports the treatment of Ra-Ba co-precipitation by showing proof of Ra uptake in barite.

Excluded data previously considered as important

No such data has been identified.

3.4.5 Conditions for which data are supplied (text reproduced from SR-Site Data report)

The conditions under which the radioelement solubility assessment has been done are described in Duro et al. (2006a).

They are briefly summarised as follows:

- The assessment of radioelement concentration limits considers the vicinity of the spent nuclear fuel, in the void between the spent fuel and the canister. The solid phases, selected as likely to precipitate, apply only to the conditions in the void between the spent fuel and canister (Chapter 5 of Duro et al. 2006a).
- The temperature for which solubility limits are assessed, by using the Simple Function spreadsheet, is 25 °C. The code is currently not designed to return solubility limits for any other temperatures. For the time periods where solubility limits are most likely to be of consequence for the safety assessment, that is when the canister has failed and water has intruded, the ambient temperature is expected to be lower than this.
- The selected solubility limiting phases and thermodynamic data support calculations of solubilities for all relevant redox conditions, i.e. from pH_2 = 10 MPa (100 atm of H_2 derived from steel anoxic corrosion) to pO_2 = 20 kPa (equilibrium with atmospheric pO_2). Inside the canister, corrosion of the cast iron insert and stainless steel construction material will give rise to production of H_2 gas, wherefore reducing conditions are expected.
- Sensitivity analyses of radioelement concentration limits have been done to study both the influence of the groundwater composition on the geochemistry of the selected radioelements, and to identify the main solid phases thermodynamically able to precipitate in the system.
- The selection of thermodynamic data and solubility limiting phases has been done for a pH range of 6 to 11. The assumptions may not be valid outside of this range.
- The activity correction used (Debye-Hückel theory) is not valid for an ionic strength of > 0.2 M and it would have been preferable to use the Specific Interaction Theory instead, since the ionic strength of the waters considered may be as high as 2 M, or more. However, this approach has not yet been implemented in the geochemical codes that are available. Comparisons between both approaches have been conducted, when possible, and show small differences.

Concerning (Ra,Ba)SO_4 co-precipitation, sufficient amounts of Ba^{2+} and SO_4^{2-}, or $BaSO_4$, is generally expected to exist for the co-precipitate to form in the void between the spent fuel and canister. The co-precipitate is also expected to form within the expected temperature range and range of water compositions (Grandia et al. 2008).

3.4.6 Conceptual uncertainty

The solubility assessment reported in Duro et al. (2006a) is focused on the very-near field, when water enters the canister void and interacts with the spent fuel.

The most significant conceptual uncertainties concerning to the capacity of the data and model used to represent the reality are presented below.

The composition of the interacting groundwater

Although this could be seen a priori as data uncertainty, there is a non-trivial conceptual component associated with the water composition. It is very likely that groundwater interacts with the engineering barriers before contacting the spent fuel. In the currect assessment the reaction between the groundwater and the buffer is suggested to be neglected in the solubility calculations. The justification for this is:

- Elemental solubilities are active for very long time frames. “Conditioning” of the groundwater by accessory minerals (carbonates) in the buffer is expected have relatively short duration, or to have small impact on the overall composition.
- Ion-exchange reactions will have limited impact on solubilities.

The reaction between the cast iron insert and the groundwater is considered throughout the assessment. This is done by an adjustment of the redox conditions in the interior of the canister, based on the equilibrium of magnetite/goethite. The corrosion products of the cast iron insert can be expected to control the redox potential for all timescales.

Precipitation of pure solid phases and mixed solid phases

Except for $(Ra,Ba)SO_4$ co-precipitate, calculations implying the formation of mixed solid phases have not been conducted. This approach may be seen as non-realistic given the expected low concentrations of the elements originating from the spent fuel matrix, but it is based on the following facts:

- The solubility assessment applies to the void between the spent fuel and the canister which implies low water volumes; so that even limited radioelement release can result in concentrations high enough as to reach the solubility limit with respect to pure solid phases.
- No presence of major minerals frequently occurring in geochemical systems is expected inside the canister, except for minerals produced by corrosion. This a priori excludes the possibility that calcite and fracture filling material can act as substrates for radionuclide co-precipitation.
- Although phases produced by the canister corrosion may act as substrates for retention and co-precipitation of radionuclides, the uncertainty associated with assessing the formation of mixed solid phases is much higher than the uncertainty associated with the assumption of pure solid phases governing the individual radioelement concentrations.

The co-precipitation of Ra-Ba sulphate is a very well-known process. The affinity of radium to barium sulphate was first reported by Marie Curie in her radium discovery work (Curie et al. 1898). The fact that the process occurs in nature is undisputed (Grandia et al. 2008). There are two main potential scenarios for $(Ra,Ba)SO_4$ co-precipitation in the vicinity of the spent fuel.

- Co-precipitation of primary Ra-226 as generated and released contemporaneously with Ba from spent fuel and the sulphate present.
- Surface precipitation of Ra-226 on existing $BaSO_4(s)$. This initial surface precipitate would evolve towards a Ra(II)-Ba(II) sulphate solid solution by re-crystallisation and/or Ra^{2+} diffusion into the $BaSO_4(s)$ lattice.

Within the canister, the second scenario is primarily of interest. Although the thermodynamics favours co-precipitate, there is still the question of kinetics. Grandia et al. (2008, Section 4.5) states that even if all the direct and indirect evidence points towards a fast incorporation of Ra(II) onto an existing Ba(II) sulphate structure, there is a need to perform a devoted mechanistic study to fully back up the macroscopic findings. Such a study was carried out by Bosbach et al. (2010) and the results indicate for a relatively rapid incorporation of Ra in the barite structure. Further studies by Weber et al. (2017) provides insight into the mechanism on Ra uptake in barite, highlighting the importance of pores and defects in the pre-existing barite crystals for the observed rapid kinetics.

Crediting amorphous over crystalline phases

Amorphous or less crystalline solid phases have been credited over crystalline phases. This assumption may not necessarily be true for high temperatures and long time periods, when crystalline phases may form. As crystalline phases have lower solubility than amorphous ones, this assumption is pessimistic.

Metallic and native phases

No metallic phases have, in principle, been considered, given the very slow kinetics of precipitation of this type of phases under the conditions of interest. This approach is, nevertheless, associated with a certain level of uncertainty and in some cases (e.g. Pd, Ag, Se, and Tc) the role of a metallic phase as a solubility limiting phase has been discussed in Duro et al. (2006a).

The process of reduction of sulphate to sulphide

This process has not been considered in the reference case. The abiotic (thermochemical) reduction of sulphate to sulphide is such a slow process that it has not been observed at temperatures below ~ 200 °C (e.g. Goldstein and Aizenshtat 1994). The reduction is accelerated with the presence of sulphate reducing bacteria (SRB). Having SRB present will assist this reaction and will have impact on the solubility limit for elements limited by sulphate solids. For the SRB to be active, they need electron donors, for example hydrogen, as well as a carbon source. Assuming a carbon source will be available, the effect of SRB on the sulphate concentration inside the failed canister depends on the relative concentrations of sulphate and hydrogen (or other electron donors). The sulphide produced could give very low solubilities for certain radioelements (e.g. nickel), but no sulphide phases are considered in the solubility assessment.

The process of reduction of carbonate to methane

This process has not been considered in the reference case. However, it is thermodynamically plausible if temperature increases and/or biological activity is present. Kudo and Komatsu (1999) studied the reduction of metal carbonates to methane and concluded that the yield of methane generation reach a maximum (only of 17 %) at 400 °C and does not occur in the absence of biological activity if the temperature is below 150–200 °C.

Summary

All these uncertainties do not affect the solubility assessments of the different radioelements in the same degree. Table 3-22 summarises the conceptual uncertainties identified for each individual radioelement, as further discussed in Chapter 5 of Duro et al. (2006a).

Table 3-22. Sources of conceptual uncertainty identified for each one of the radioelements under study (Duro et al. 2006a). No uncertainties of this type have been identified for radioelements not included in the list.

Element	Associated uncertainty
C	Reduction to $CH_4(g)$.
Sr	SO_4^{2-} to HS^- reduction. Possibility of co-precipitation with other elements' carbonates.
Ra	SO_4^{2-} to HS-reduction. Possibility of co-precipitation with other elements' carbonates.
Sn	SO_4^{2-} to HS^- reduction.
Pb*	SO_4^{2-} to HS^- reduction.
Se	Formation of native Se^0. SO_4^{2-} to HS^- reduction.
Zr	Crystallinity of the solid phase.
Tc	Formation of metallic Tc^0.
Ni	SO_4^{2-} to HS^- reduction.
Pd	Formation of metallic Pd^0.
Ag	Formation of metallic Ag^0. SO_4^{2-} to HS^- reduction.
Th	Crystallinity of the solid phase.
U	Silicate solid precipitation.
Np	Crystallinity of the solid phase.
Pu	SO_4^{2-} to HS^- reduction.

* Uncertainty concerning Pb is discussed in Grivé et al. (2010b).

3.4.7 Data uncertainty due to precision, bias, and representativity

In Chapter 6 of Duro et al. (2006a) a discussion on data uncertainty is given, where the contributions from precision, bias, and representativity to the overall data uncertainty have been identified.

Concerning the matter of $(Ra,Ba)SO_4$ co-precipitation, this is discussed under a separate heading at the end of this section.

Precision

Precision of solubility data reported from laboratory and field measurements is described in the original sources from which data have been extracted. The influence of the precision of the measurements is included in the sensitivity analyses conducted for the solubility assessment of each radioelement in Chapter 6 of Duro et al. (2006a).

The uncertainty of solubility limits, as calculated in the SR-Site safety assessment, is affected by the precision of the input data used in the calculations. This mainly concerns groundwater compositions and SKB-TDB thermodynamic data. Precision of groundwater data compositions is discussed in Section 6.1. Precision of thermodynamic data is specifically reported in Duro et al. (2006b) and in Grivé et al. (2010b), and further discussed in Grivé et al. (2013b).

Bias

Data on concentrations of elements obtained from spent fuel dissolution experiments, gathered in Chapter 4 of Duro et al. (2006a), are biased due to the variability in the experimental conditions and to the difficulty of maintaining reducing conditions in the experiments. This would result in reported measured values in different publications that are higher than the actual solubility values expected to prevail under reducing conditions. This is especially relevant for the concentrations measured for uranium, due to its redox sensitivity. Experimental data of solubilities for other radioelements can be more importantly biased due to the high ionic strengths used in some of the experiments. Bias due to the data scarcity must be also considered.

Representativity

The data presented should be representative for a canister in a KBS-3 repository, under ambient conditions. In Duro et al. (2006a) different categories of data have been used as sources of information:

- Radioelement inventory and occurrence in rocks and minerals.
- Radioelement concentrations from laboratory spent fuel experiments.
- Radioelement concentrations in natural waters.
- Radioelement inventories and aqueous concentrations in natural analogue sites.

The way these data have been acquired varies and depends on several factors: the study performed; the institution doing it; the measured radioelement; natural variability; etc. The individual acquisition and treatment procedure is described in the original source. However, these sets of data have been selected after a critical revision of both the quality of data and their usefulness for the solubility assessment of the very-near field of a KBS-3 repository. Data of poor or uncertain quality, or data obtained under conditions far from those expected, have not been used.

Each category of data relies on data compiled from several authors, obtained at different conditions and for different purposes. Data selection has been done, thus, with the aim to cover the whole range of conditions expected in the studied scenarios, ensuring the representativity of each of these categories of data.

One specific uncertainty affecting representativity of the solubility data concerns the phosphate concentration in groundwaters. This uncertainly is now reduced by strutinizing the effects of a range of relevant phosphate concentrations on the radioelements investigated (Grivé et al. 2013a). Previous work indicated phosphate complexes would not be important for speciation, and that it was doubtful

whether phosphate phases could control radioelement solubilty (Duro et al. 2006a). The new analyses by Grivé et al. (2013a) show that this was a correct conclusion for the many of the of analysed radioelements. However, in some conditions, including phosphate in the caluclations will lower the solubility limits for some trivalent lanthanides and actinides. This means that excluding phosphate from the calculations is a conservative approach.

In Duro et al. (2006b) the procedure for both *logK* selection and uncertainty assignment is fully documented. Further discussion and supporting arguments concerning existing and assigned uncertainty to the thermodynamic data is provided by Grivé et al. (2013a). The database used in the calculations considers the most relevant aqueous species and solid phases in a KBS-3 repository environment.

A major representativity issue is the effect of temperature on the stability of aqueous species and solid compounds. The input data to, and output data from, the Simple Functions spreadsheet apply at 25 °C. Due to the presence of the spent fuel, it is foreseen that the temperature initially can reach up to 100 °C. However, after longer time periods, when canister failure may occur, the activity of the spent fuel has substantially decreased wherefore elevated temperatures are not expected. Therefore, the ambient temperature is likely to be lower than 25 °C. At temperate climate the ambient temperature is expected to be around 15 °C, while at periglacial conditions the temperature may drop to just above freezing (cf Section 7.1).

It would have been preferable to be able to correct all *logK* data, so that they represent a range of temperatures. However, due to lack of enthalpy data this has not been possible in the Simple Function spreadsheet. To investigate the data uncertainty introduced by this limitation, a sensitivity study was performed in Grivé et al. (2010a) including the radioelements Ni, Np, Se, Th, and U. The data delivered from the Simple Functions spreadsheet was compared with data delivered from the program HYDRO-MEDUSA (Puigdomenech 2002), at 0 °C, 10 °C, 25 °C, 40 °C, 70 °C, and 100 °C. A comparison is shown in Figure 3-7, in terms of dissolved radioelement concentration at the solubility limit.

The (limited) sensitivity study indicates that for most radioelements, the solubility limits delivered by the Simple Functions spreadsheet are adequate or overestimated for temperatures at or below 2 °C. However, nickel shows that there are exceptions where the solubility increases with decreasing temperature.

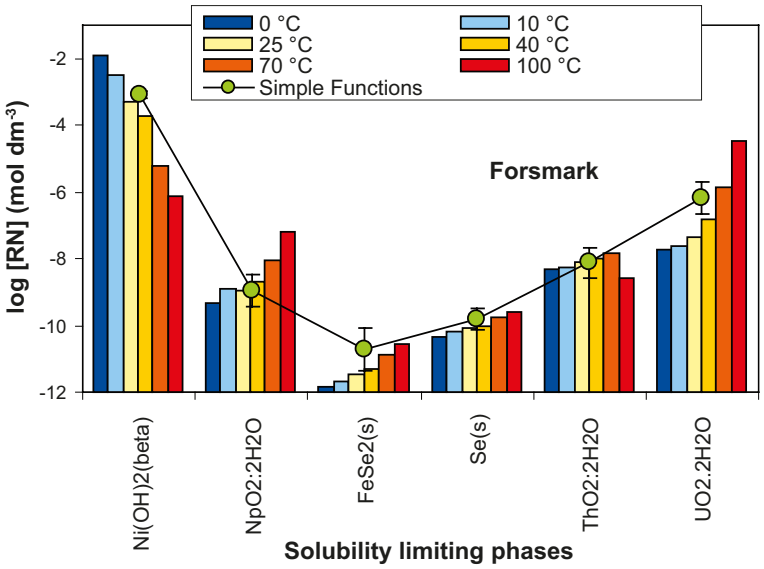

Figure 3-7. *Results from a sensitivity study on the influence of temperature on the solubility limit. Image reproduced from Figure 4-5 of Grivé et al. (2010a).*

The issue of temperatures was further investigated by Grivé et al. (2013b). The conclusions of this deeper analysis, looking at a temperature range from 0 to 90 ºC , are that radionuclide solubilities might differ up to two orders of magnitude from that at 25 ºC. Due to scarcity on enthalpy data, specifically lack of enthalpy data for the selected solid phase, U is an exception and this strongly affects the calculated solubilities at different temparatures. The data for U therefore presents differences of up to five orders of magnitude. The effect of availability of enthalpy data is clear when observing the results for Np, where enthalpy data does exist for the selected solid phase, the increase in solubility at higher temperature is within one order of magnitude. For other elements, such as Sm, Ho, Pu, and Am, large variations are observed for some conditions. The results can be explained both in terms of predicted domainant speciation in the aqeuous solution, and lack of enthalpy data for a number of relevant species.

Ionic strength activity corrections have been considered in the calculation of radioelement solubility. Although the most appropriate procedure to conduct activity corrections in the ionic strength range studied (10^{-3} to 2 mol/dm^3) is the Specific Interaction Theory (SIT), as recommended by the NEA guidelines, this approach is not yet implemented in the geochemical codes used in Duro et al. (2006a). The codes used in Duro et al. (2006a), which are HYDRA-MEDUSA and PhreeqC, both use the extended Debye-Hückel approach. Therefore, Debye-Hückel is used in the calculations of solubility (cf Section 3.3.1 of Duro et al. 2006a). Nevertheless, calculations have been done with both approaches whenever possible and results consistently compare. The largest differences are found in solubilities calculated at saline water composition, and in the case the aqueous speciation is dominated by highly charged species which stability is much dependent on the ionic strength, e.g. silver chlorides.

Table 3-23 summarises sources of representativity uncertainties identified for each individual radioelement. These uncertainties are discussed in Chapters 5 and 6 of Duro et al. (2006a).

Table 3-23. Sources of identified representativity uncertainties No uncertainties of this type have been identified for radioelements not included in the list.

Element	Associated uncertainty
Ra	Temperature dependence of solubility limit
Ni	Temperature dependence of solubility limit
Nb	Scarcity of data in TDB.
Se	Temperature dependence of solubility limit
Sm	Effect of phosphates in water. Stability of the solid hydroxo-carbonate. Lack of enthalpy data for aqueous species. Temperature dependence of solubility limit
Ho	Effect of phosphates in water. Stability of the solid hydroxo-carbonate. Lack of enthalpy data for aqueous species. Temperature dependence of solubility limit
Th	Uncertain thermodynamic data for aqueous carbonates.
Pa	Lack of thermodynamic data.
U	TDB data on solid stability. Temperature dependence of solubility limit
Pu	Effect of phosphates in water. Stability of the solid hydroxo-carbonate. Temperature dependence of solubility limit
Am/Cm	Effect of phosphates in water. Stability of the solid hydroxo-carbonate. Cm: Lack of thermodynamic data Temperature dependence of solubility limit

* Uncertainty concerning Pb is discussed in Grivé et al. (2010b).

Radium barium co-precipitation

Special attention is given to the matter of co-precipitation, as new data are presented in this Data report that has not been presented in supporting documents. The approach taken to account for co-precipitation is simplistic and delivers for most time periods pessimistic results. In essence the Ra/Ba ratio inside of the canister is estimated based on inventory data and radioactive decay calculations. The calculation carried out in Chapter 3 of Grandia et al. (2008) for ATM-104 spent fuel was repeated for the spent fuels of the two type canisters PWR I and BWR I SKB (2010b) For these fuels, the Ra/Ba ratio varies with time from extremely low values ($\sim 10^{-9}$ after about 40 years when the fuel is placed in the canisters) to a peak value of about 3×10^{-4} years after 100 000 years, as illustrated in Figure 3-8. The Ra/Ba ratios calculated using the different fuels (ATM-104, BWR I, PWR I) are very similar (Grandia 2013).

A safety margin is added to this peak value and the Ra/Ba ratio of 10^{-3} is pessimistically assumed during the entire repository evolution period. As is shown by Grandia (2013), only limited, if any, Ba transport out of the canister is expected and therefore this process cannot significantly change the ratio. It is clear from Figure 3-8, that this ratio best represents the situation at ca 100 000 years, while the ratio is much smaller at earlier times. This ratio is recommended to be used as a correction factor that is multiplied with the Ra^{2+} concentration, as calculated from the Simple Function spreadsheet when disregarding co-precipitation, using $RaSO_4(s)$ as the solubility limiting phase.

3.4.8 Spatial and temporal variability of data (text reproduced from SR-Site Data report)

Natural heterogeneity is considered by determining the solubility limits and solubility limiting phases for the entire range of different groundwater compositions, which in turn represent different spatial and temporal conditions expected in the repository over long timescales.

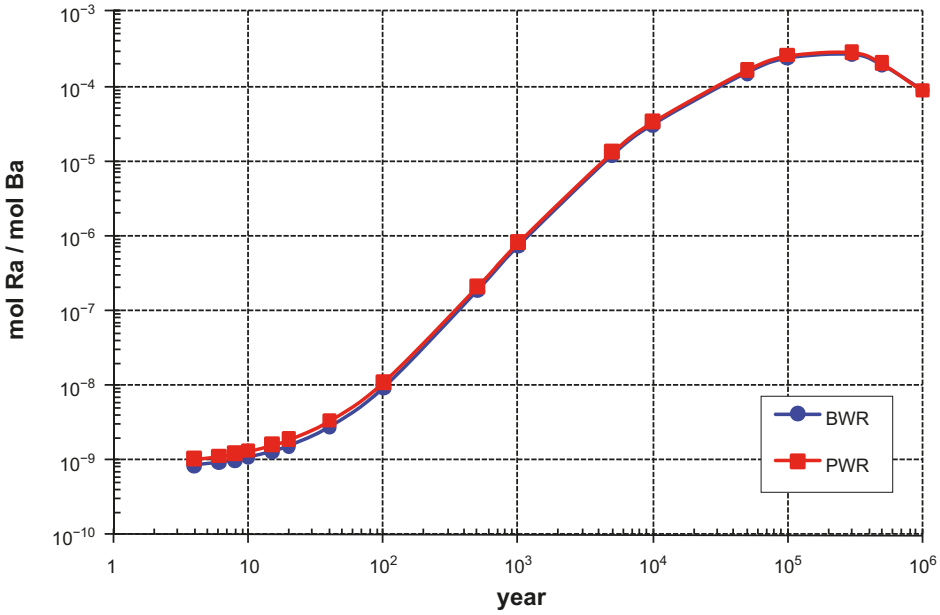

Figure 3-8. *Time evolution of the molar ratio between Ra and Ba in unaltered spent fuel calculated for BWR I and PWR 1 type canisters.*

3.4.9 Correlations

Geochemical calculations are by themselves a set of closely related correlations between different parameters, usually named primary parameters. The simple calculation of the aqueous speciation of a chemical element is thus the solution of a set of equations in which different parameters, such as pH, redox conditions, or ligand concentrations are correlated. Because of that, geochemical codes that are especially devoted to solve this type of complex equations have been used. Therefore, it is evident that dependences between parameters have been used to identify the solid phases controlling the elements' solubility under the selected conditions.

The main correlations used are:

- Equilibrium reactions between aqueous species.
- Equilibrium reactions between solid phases and aqueous solutes.
- Calculation of the ionic strength corrections by means of the extended Debye-Hückel reaction.

More information about the treatment of these correlations can be found in the code manuals and descriptions (Parkhurst and Appelo 2001, Puigdomenech 2002) and in general chemical and geochemical literature.

Not all the correlations between parameters have the same importance. Table 3-24, which includes Table 3-4 of Duro et al. (2006a), indicates the main parameters affecting the behaviour of the studied radioelements. Special attention was paid to these parameters in Duro et al. (2006a).

Table 3-24. Main geochemical parameters affecting the geochemical behaviour of each radioelement under study. Shadowed cells indicate that the element in the row is sensitive to pH and/or pe, within the range of variability of the parameter studied. All information from Duro et al. (2006a) and Grive at al. (2010b), except for Ra-Ba co-precipitation where information is taken from Grandia et al. (2008).

Element [a)]	pH	pe	Ligand/species
C			Ca^{2+}
Cs			Cl^-
Sr			CO_3^{2-}, SO_4^{2-}
Ra			CO_3^{2-}, SO_4^{2-}, Cl^-, Ba^{2+}, $BaSO_4$ [b)]
Sn			Ca^{2+}
Pb			CO_3^{2-}, Cl^-
Se			Fe(II)
Zr			-
Nb			-
Tc			-
Ni			-
Pd			Cl^-
Ag			Cl^-
Sm			CO_3^{2-}
Ho			CO_3^{2-}
Th			CO_3^{2-}
Pa			-
U			CO_3^{2-}, Ca^{2+}, $Si(OH)_4$
Np			CO_3^{2-}
Pu			CO_3^{2-}
Am and Cm			CO_3^{2-}

a) The excluded elements H, Cl, and I are suggested to have no solubility limit in safety assessment modelling.

b) The two components Ba^{2+} and $BaSO_4$ are not directly included in the assessment. They are only included by way of determining the correction factor for co-precipitation.

As mentioned also in in the Radionuclide transport report, calculations using thermodynamic data should ideally take into account correlated uncertainties, since in general, equilibrium constants are correlated. However, necessary correlation data required for the calculations is rarely published, and therefore this kind of correlation is not included in the calculations. This generally results in pessimistic overestimates of the uncertainties in the calculated solubilities.

3.4.10 Result of supplier's data qualification

The customer has requested that a list of relevant solubility limiting phases and associated reactions are supplied, together with thermodynamic data in form of equilibrium constants. These data are inputs to the Simple Functions spreadsheet.

In addition, the customer has requested that an expression for (Ra,Ba)SO_4 co-precipitate should be delivered, together with guidance on how to incorporate this information in the safety assessment.

Solubility limiting phases

The solubility limiting phases for the radioelements, selected according to the expert judgement procedure presented in Duro et al. (2006a), are found in Table 3-25. The solubility assessment for Pb is reported in Grivé et al. (2010b).

Table 3-25. Recommended solubility limiting phases. All data taken from Duro et al. (2006a), except for Pb data taken from Grivé et al. (2010b).

Radioelement	Recommended solubility limiting phase
H	Suggested to have no solubility limit in Safety assessment modelling.
C	Suggested to have no solubility limit in Safety assessment modelling.
Cl	Suggested to have no solubility limit in Safety assessment modelling.
Ni	$NiCO_3$(s), $Ni(OH)_2$(s).
Se	FeSe(s), $Fe_{1.04}Se$(s), Se(s).
Sr	Celestite ($SrSO_4$(s)), Strontianite ($SrCO_3$(s)).
Zr	$Zr(OH)_4$(s).
Nb	Nb_2O_5(s).
Tc	$TcO_2 \cdot 1.6H_2O$(s), Tc(s).
Pd	$Pd(OH)_2$(s).
Ag	AgCl(s).
Sn	SnO_2(s), Ca[SnO_6].
I	Suggested to have no solubility limit in Safety assessment modelling.
Cs	Suggested to have no solubility limit in Safety assessment modelling.
Sm	$Sm_2(CO3)_3$(s), $Sm(OH)_3$(am), $SmOHCO_3$(s).
Ho	$Ho_2(CO3)_3$(s), $Ho(OH)_3$(am).
Pb	$PbCO_3$(s), $Pb_3CO_3(OH)_2$(s), PbClOH(s).
Ra	$RaSO_4$(s), $RaCO_3$(s), $Ra_xBa_{(1-x)}SO_4$(s).
Th	$ThO_2 \cdot 2H_2O$(s).
Pa	Pa_2O_5(s).
U	$UO_2 \cdot 2H_2O$(s), Coffinite, Schoepite, $CaUO_4$(s), Becquerelite, Uranophane.
Np	$NpO_2 \cdot 2H_2O$(s), Np_2O_5(s), $NaNpO_2CO_3$(s).
Pu	$Pu(OH)_4$(s), $Pu(OH)_3$(s), $PuCO_3OH$(s).
Am	$AmOHCO_3$(s), $Am(OH)_3$(am), $Am_2(CO_3)_3$(s), $Am(CO_3)_2Na \cdot 5H_2O$(s).
Cm	$CmOHCO_3$(s), $Cm(OH)_3$(am).

Reactions and thermodynamic data

The reactions and thermodynamic data presented in Table 3-26 to Table 3-29 are recommended as input data to the Simple Function spreadsheet.

Table 3-26. Reactions and equilibrium constants recommended for use in the Simple Functions spreadsheet, valid at 25 °C (1/4).

	Species	Reaction	$\log K^0$	$\Delta \log K^0$
Groundwater species	$CaOH^+$	$Ca^{2+} + H_2O = CaOH^+ + H^+$	–12.78	0.30
	$FeOH^+$	$Fe^{2+} + H_2O = FeOH^+ + H^+$	–9.50	0.10
	$Fe(OH)_3(aq)$	$Fe^{2+} + 0.25O_2(g) + 2.5H_2O = Fe(OH)_3(aq) + 2H^+$	–4.80	1.06
	$Fe(OH)_4^-$	$Fe^{2+} + 0.25O_2(g) + 2.5H_2O = Fe(OH)_4^- + 3H^+$	–13.84	0.08
	Calcite	$Ca^{2+} + CO_3^{2-} = CaCO_3$	8.48	0.02
	HCO_3^-	$H^+ + CO_3^{2-} = HCO_3^-$	10.33	0.02
	$CaCO_3(aq)$	$Ca^{2+} + CO_3^{2-} = CaCO_3$	3.22	0.14
	$CaHCO_3^+$	$Ca^{2+} + CO_3^{2-} + H^+ = CaHCO_3^+$	11.44	0.09
	$NaCO_3^-$	$Na^+ + CO_3^{2-} = NaCO_3^-$	1.27	0.30
	$NaHCO_3$	$Na^+ + CO_3^{2-} + H^+ = NaHCO_3$	10.08	0.30
	$FeCO_3(aq)$	$Fe^{2+} + CO_3^{2-} = FeCO_3(aq)$	4.38	1.31
	$FeHCO_3^+$	$Fe^{2+} + CO_3^{2-} + H^+ = FeHCO_3^+$	12.33	0.30
	HSO_4^-	$H^+ + SO_4^{2-} = HSO_4^-$	1.98	0.25
	$CaSO_4(aq)$	$Ca^{2+} + SO_4^{2-} = CaSO_4$	2.30	0.30
	$NaSO_4^-$	$Na^+ + SO_4^{2-} = NaSO_4^-$	0.70	0.30
	$FeHSO_4^+$	$Fe^{2+} + SO_4^{2-} + H^+ = FeHSO_4^+$	3.07	0.30
	$FeSO_4(aq)$	$Fe^{2+} + SO_4^{2-} = FeSO_4(aq)$	2.25	0.05
	$FeCl^+$	$Fe^{2+} + Cl^- = FeCl^+$	0.14	0.23
Sr	$SrOH^+$	$Sr^{2+} + H_2O = SrOH^+ + H^+$	–13.29	0.30
	$SrCO_3(aq)$	$Sr^{2+} + CO_3^{2-} = SrCO_3(aq)$	2.81	0.05
	$SrHCO_3^+$	$Sr^{2+} + CO_3^{2-} + H^+ = SrHCO_3^+$	11.51	0.05
	$SrSO_4$	$Sr^{2+} + SO_4^{2-} = SrSO_4(aq)$	2.29	0.26
	$SrCl^+$	$Sr^{2+} + Cl^- = SrCl^+$	0.32	0.12
	$SrCO_3$(strontianite)	$SrCO_3(s) = Sr^{2+} + CO_3^{2-}$	–9.27	0.30
	$SrSO_4$(celestite)	$SrSO_4(s) = Sr^{2+} + SO_4^{2-}$	–6.63	0.30
Ra	$Ra(OH)^+$	$Ra^{2+} + H_2O = Ra(OH)^+ + H^+$	–13.50	0.25
	$RaCO_3(aq)$	$Ra^{2+} + CO_3^{2-} = RaCO_3$	2.50	0.40
	$RaSO_4(aq)$	$Ra^{+2} + SO_4^{2-} = RaSO_4$	2.75	0.10
	$RaCl^+$	$Ra^{+2} + Cl^- = RaCl^+$	–0.10	0.30
	$RaCO_3(s)$	$RaCO_3(s) = Ra^{2+} + CO_3^{2-}$	–8.30	0.30
	$Ra(SO_4)(s)$	$Ra(SO_4)(s) = Ra^{2+} + SO_4^{2-}$	–10.26	0.09
Zr	$Zr(OH)_4(aq)$	$Zr^{4+} + 4H_2O = Zr(OH)_4(aq) + 4H^+$	–2.19	1.70
	$Zr(OH)_4$(am,fresh)	$Zr(OH)_4(s) + 4H^+ = Zr^{4+} + 4H_2O$	–3.24	0.10
	$Zr(OH)_4$(am,aged)	$Zr(OH)_4(s) + 4H^+ = Zr^{4+} + 4H_2O$	–5.55	0.20
Nb	$Nb(OH)_4^+$	$NbO_3^- + 2H^+ + H_2O = Nb(OH)_4^+$	6.90	0.02
	$Nb(OH)_5(aq)$	$NbO_3^- + H^+ + 2H_2O = Nb(OH)_5(aq)$	7.34	0.02
	$Nb_2O_5(s)$	$Nb_2O_5(s) + H_2O = 2NbO_3^- + 2H^+$	–24.34	0.04
Tc	TcO^{2+}	$TcO(OH)_2 + 2H^+ = TcO^{2+} + 2H_2O$	4.00	1.42
	TcO_4^-	$TcO(OH)_2 + 0.75\ O_2 = TcO_4^- + 0.5\ H_2O + H^+$	32.94	2.05
	$TcO(OH)^+$	$TcO(OH)_2 + H^+ = TcO(OH)^+ + H_2O$	2.50	0.30
	$TcO(OH)_3^-$	$TcO(OH)_2 + H_2O = TcO(OH)_3^- + H^+$	–10.90	0.40
	$Tc(CO_3)(OH)_2$	$TcO(OH)_2 + CO_3^{2-} + 2H^+ = Tc(CO_3)(OH)_2 + H_2O$	19.30	0.30
	$Tc(OH)_3(CO_3)^-$	$TcO(OH)_2 + CO_3^{2-} + H^+ = Tc(OH)_3(CO_3)^-$	11.00	0.60
	$TcO_2 \cdot 1.63H_2O$	$TcO_2\ 1.63H_2O = TcO(OH)_2 + 0.63\ H_2O$	–8.40	0.50
Ni	$NiOH^+$	$Ni^{2+} + H_2O = NiOH^+ + H^+$	–9.54	0.14
	$Ni(OH)_2(aq)$	$Ni^{2+} + 2H_2O = Ni(OH)_2(aq) + 2H^+$	–18.00	0.30
	$Ni(OH)_3^-$	$Ni^{2+} + 3H_2O = Ni(OH)_3^- + 3H^+$	–29.20	1.70
	$NiCl^+$	$Ni^{2+} + Cl^- = NiCl^+$	0.08	0.60
	$NiCO_3(aq)$	$Ni^{2+} + CO_3^{2-} = NiCO_3(aq)$	4.20	0.40
	$Ni(OH)_2(s)$	$Ni(OH)_2(s) + 2H^+ = Ni^{2+} + 2H_2O$	11.03	0.28
	$NiCO_3{:}5.5H_2O(s)$	$NiCO_3{:}5.5H_2O(cr) = Ni^{2+} + CO_3^{2-} + 5.5H_2O$	–7.52	0.24

Table 3-26. Continued.

	Species	Reaction	logK⁰	ΔlogK⁰
Pd	$Pd(OH)^+$	$Pd^{2+} + H_2O = Pd(OH)^+ + H^+$	–1.86	0.30
	$Pd(OH)_2$	$Pd^{2+} + 2H_2O = Pd(OH)_2 + 2H^+$	–3.79	0.30
	$Pd(OH)_3^-$	$Pd^{2+} + 3H_2O = Pd(OH)_3^- + 3H^+$	–15.93	0.30
	$Pd(OH)_4^{2-}$	$Pd^{2+} + 4H_2O = Pd(OH)_4^{2-} + 4H^+$	–29.36	0.04
	$PdCl^+$	$Pd^{2+} + Cl^- = PdCl^+$	5.10	0.01
	$PdCl_2$	$Pd^{2+} + 2Cl^- = PdCl_2$	8.30	0.04
	$PdCl_3^-$	$Pd^{2+} + 3Cl^- = PdCl_3^-$	10.90	0.07
	$PdCl_4^{2-}$	$Pd^{2+} + 4Cl^- = PdCl_4^{2-}$	11.70	0.09
	$Pd(OH)_2(s)$	$Pd(OH)_2(s) + 2H^+ = Pd^{2+} + 2H_2O$	–1.61	1.16
Ag	AgCl(aq)	$Ag^+ + Cl^- = AgCl(aq)$	3.27	0.17
	$AgCl_2^-$	$Ag^+ + 2Cl^- = AgCl_2^-$	5.27	0.37
	$AgCl_3^{2-}$	$Ag^+ + 3Cl^- = AgCl_3^{2-}$	5.29	0.39
	$AgCl_4^{3-}$	$Ag^+ + 4Cl^- = AgCl_4^{3-}$	5.51	1.71
	AgOH	$H_2O + Ag^+ = AgOH + H^+$	–12.00	0.30
	$Ag(OH)_2^-$	$2H_2O + Ag^+ = Ag(OH)_2^- + 2H^+$	–24.00	0.10
	AgOH(s)	$AgOH + H^+ = Ag^+ + H_2O$	6.30	0.05
	AgCl(cr)	$AgCl(cr) = Ag^+ + Cl^-$	–9.75	0.04

Table 3-27. Reactions and equilibrium constants recommended for use in the Simple Functions spreadsheet, valid at 25 °C (2/4).

	Species	Reaction	logK⁰	ΔlogK⁰
Sn	$Sn(OH)^+$	$Sn^{4+} + 2H_2O = Sn(OH)^+ + 0.5O_2(g) + 3H^+$	–40.28	0.39
	$Sn(OH)_2(aq)$	$Sn^{4+} + 3H_2O = Sn(OH)_2(aq) + 0.5O_2(g) + 4H^+$	–44.28	0.39
	$Sn(OH)_4(aq)$	$Sn^{4+} + 4H_2O = Sn(OH)_4 + 4H^+$	–0.53	0.67
	$Sn(OH)_5^-$	$Sn^{4+} + 5H_2O = Sn(OH)_5^- + 5H^+$	–8.53	0.73
	$Sn(OH)_6^{2-}$	$Sn^{4+} + 6H_2O = Sn(OH)_6^{2-} + 6H^+$	–18.93	1.00
	$SnO_2(am)$	$SnO_2(am) + 4H^+ = Sn^{4+} + 2H_2O$	–6.77	0.73
	$Ca[Sn(OH)_6](s)$	$Ca[Sn(OH)_6](s) + 6H^+ = Sn^{4+} + 6H_2O + Ca^{2+}$	8.54	0.74
Se	HSe^-	$SeO_4^{2-} + H^+ = HSe^- + 2O_2$	–84.61	0.44
	SeO_3^{2-}	$SeO_4^{2-} = SeO_3^{2-} + 0.5O_2$	–13.50	0.34
	Se^{2-}	$SeO_4^{2-} = Se^{2-} + 2O_2$	–99.52	0.77
	H_2Se	$SeO_4^{2-} + 2H^+ = H_2Se + 2O_2$	–80.76	0.67
	$HSeO_3^-$	$SeO_4^{2-} + H^+ = HSeO_3^- + 0.5O_2$	–5.15	0.41
	H_2SeO_3	$SeO_4^{2-} + 2H^+ = H_2SeO_3 + 0.5O_2$	–2.51	0.43
	$HSeO_4^-$	$SeO_4^{2-} + H^+ = HSeO_4^-$	1.75	0.10
	$CaSeO_4$	$SeO_4^{2-} + Ca^{2+} = CaSeO_4$	2.00	0.10
	$FeSe_2(s)$	$FeSe_2(s) + 3.5O_2 + H_2O = 2SeO_4^{2-} + Fe^{2+} + 2H^+$	110.55	2.80
	$Fe_{1.04}Se(s)$	$Fe_{1.04}Se(s) + 2.02O_2 + 0.08H^+ = SeO_4^{2-} + 1.04Fe^{2+} + 0.04H_2O$	82.87	0.92
	Se(s)	$Se(s) + 1.5O_2 + H_2O = SeO_4^{2-} + 2H^+$	35.44	0.56
Th	$Th(OH)^{3+}$	$Th^{4+} + H_2O = Th(OH)^{3+} + H^+$	–2.50	0.50
	$Th(OH)_2^{2+}$	$Th^{4+} + 2H_2O = Th(OH)_2^{2+} + 2H^+$	–6.20	0.50
	$Th(OH)_4$	$Th^{4+} + 4H_2O = Th(OH)_4 + 4H^+$	–17.40	0.70
	$Th(CO_3)(OH)_3^-$	$Th^{4+} + CO_3^{2-} + 3H_2O = Th(CO_3)(OH)_3^- + 3H^+$	–3.70	0.70
	$Th(CO_3)(OH)_4^{2-}$	$Th^{4+} + CO_3^{2-} + 4H_2O = Th(CO_3)(OH)_4^{2-} + 4H^+$	–15.60	0.60
	$Th(CO3)_5^{6-}$	$Th^{4+} + 5CO_3^{2-} = Th(CO_3)_5^{6-}$	31.00	0.70
	$Th(OH)(CO_3)_4^{5-}$	$Th^{4+} + 4CO_3^{2-} + H_2O = Th(OH)(CO_3)_4^{5-} + H^+$	21.60	0.50
	$Th(CO_3)_2(OH)_2^{2-}$	$Th^{4+} + 2CO_3^{2-} + 2H_2O = Th(CO_3)_2(OH)_2^{2-} + 2H^+$	8.80	0.50
	$Th(SO_4)^{2+}$	$Th^{4+} + SO_4^{2-} = Th(SO_4)^{2+}$	6.17	0.32
	$Th(SO_4)_2$	$Th^{4+} + 2SO_4^{2-} = Th(SO_4)_2$	9.69	0.27
	$Th(SO_4)_3^{2-}$	$Th^{4+} + 3SO_4^{2-} = Th(SO_4)_3^{2-}$	10.75	0.07
	$ThCl^{3+}$	$Th^{4+} + Cl^- = ThCl^{3+}$	1.70	0.10
	$ThO_2{\cdot}2H_2O$(am, aged)	$ThO_2{\cdot}2H_2O(am) + 4H^+ = Th^{4+} + 4H_2O$	8.50	0.90

Table 3-27. Continued.

	Species	Reaction	logK⁰	ΔlogK⁰
Pa	$PaO_2(OH)(aq)$	$PaO_2^+ + H_2O = PaO_2(OH)(aq) + H^+$	–4.50	0.20
	$Pa_2O_5(s)$	$Pa_2O_5(s) + 2H^+ = 2PaO_2^+ + H_2O$	–4.00	1.00
U	UO_2OH^+	$UO_2^{2+} + H_2O = UO_2OH^+ + H^+$	–5.25	0.24
	$UO_2(OH)_2(aq)$	$UO_2^{2+} + 2H_2O = UO_2(OH)_2(aq) + 2H^+$	–12.15	0.07
	$UO_2(OH)_3^-$	$UO_2^{2+} + 3H_2O = UO_2(OH)_3^- + 3H^+$	–20.25	1.05
	$UO_2(OH)_4^{2-}$	$UO_2^{2+} + 4H_2O = UO_2(OH)_4^{2-} + 4H^+$	–32.40	0.68
	$(UO_2)_3(OH)_5^+$	$3UO_2^{2+} + 5H_2O = (UO_2)_3(OH)_5^+ + 5H^+$	–15.55	0.12
	$(UO_2)_3(OH)_7^-$	$3UO_2^{2+} + 7H_2O = (UO_2)_3(OH)_7^- + 7H^+$	–32.20	0.80
	$UO_2CO_3(aq)$	$UO_2^{2+} + CO_3^{2-} = UO_2CO_3(aq)$	9.94	0.03
	$UO_2(CO_3)_2^{2-}$	$UO_2^{2+} + 2CO_3^{2-} = UO_2(CO_3)_2^{2-}$	16.61	0.09
	$UO_2(CO_3)_3^{4-}$	$UO_2^{2+} + 3CO_3^{2-} = UO_2(CO_3)_3^{4-}$	21.84	0.04
	$(UO_2)_2CO_3(OH)_3^-$	$2UO_2^{2+} + CO_3^{2-} + 3H_2O = (UO_2)_2CO_3(OH)_3^- + 3H^+$	–0.86	0.50
	UO_2^+	$UO_2^{2+} + 0.5H_2O = UO_2^+ + 0.25O_2 + H^+$	–19.30	0.02
	$U(OH)_3^+$	$UO_2^{2+} + 2H_2O = U(OH)_3^+ + H^+ + 0.5O_2$	–37.22	1.00
	$U(OH)_4(aq)$	$UO_2^{2+} + 3H_2O = U(OH)_4(aq) + 2H^+ + 0.5O_2$	–42.52	1.40
	$U(CO_3)_4^{4-}$	$UO_2^{2+} + 4CO_3^{2-} + 2H^+ = U(CO_3)_4^{4-} + 0.5O_2 + H_2O$	2.60	0.93
	$UO_2{\cdot}2H_2O(am)$	$UO_2{\cdot}2H_2O(am) + 2H^+ + 0.5O_2 = UO_2^{2+} + 3H_2O$	34.02	1.09
	Coffinite	$USiO_4(s) + 2H^+ + 0.5O_2 + H_2O = UO_2^{2+} + H_4SiO_4$	31.02	6.57
	Schoepite	$UO_3{\cdot}2H_2O(s) + 2H^+ = UO_2^{2+} + 3H_2O$	5.96	0.18
	$CaU_2O_7{:}3H_2O(s)$	$CaU_2O_7{:}3H_2O + 6H^+ = 2UO_2^{2+} + Ca^{2+} + 6H_2O$	23.40	1.00
	Becquerelite	$Ca(UO_2)_6O_4(OH)_6{\cdot}8H_2O + 14H^+ = Ca^{2+} + 6UO_2^{2+} + 18H_2O$	29.00	1.00
	Uranophane	$Ca((UO_2)_2SiO_3OH)_2{\cdot}5aq + 6H^+ = Ca^{2+} + 2UO_2^{2+} + 2H_4SiO_4 + 5H_2O$	9.42	5.06

Table 3-28. Reactions and equilibrium constants recommended for use in the Simple Functions spreadsheet, valid at 25 °C (3/4).

	Species	Reaction	logK⁰	ΔlogK⁰
Np	$Np(OH)_3^+$	$Np^{4+} + 3H_2O = Np(OH)_3^+ + 3H^+$	–2.80	1.00
	$Np(OH)_4$	$Np^{4+} + 4H_2O = Np(OH)_4 + 4H^+$	–8.30	1.10
	$Np(CO_3)_4^{4-}$	$Np^{4+} + 4CO_3^{2-} = Np(CO_3)_4^{4-}$	36.68	1.03
	$Np(OH)_4(CO_3)^{2-}$	$Np^{4+} + CO_3^{2-} + 4H_2O = Np(OH)_4(CO_3)^{2-} + 4H^+$	–6.83	1.13
	$NpCO_3(OH)_3^-$	$Np^{4+} + CO_3^{2-} + 3H_2O = NpCO_3(OH)_3^- + 3H^+$	3.82	1.13
	$Np(OH)_2(CO_3)_2^{2-}$	$Np^{4+} + 2CO_3^{2-} + 2H_2O = Np(OH)_2(CO_3)_2^{2-} + 2H^+$	15.17	1.50
	NpO_2^+	$Np^{4+} + 0.25O_2 + 1.5H_2O = NpO_2^+ + 3H^+$	10.57	0.12
	NpO_2OH	$Np^{4+} + 0.25O_2 + 2.5H_2O = NpO_2OH(aq) + 4H^+$	–0.73	0.71
	$NpO_2(OH)_2^-$	$Np^{4+} + 0.25O_2 + 3.5H_2O = NpO_2(OH)_2^- + 5H^+$	–13.03	0.51
	$NpO_2(CO_3)^-$	$Np^{4+} + 0.25O_2 + CO_3^{2-} + 1.5H_2O = NpO_2CO_3^- + 3H^+$	15.53	0.13
	$NpO_2(CO_3)_2^{3-}$	$Np^{4+} + 0.25O_2 + 2CO_3^{2-} + 1.5H_2O = NpO_2(CO_3)_2^{3-} + 3H^+$	17.10	0.16
	$NpO_2(OH)_2$	$Np^{4+} + 0.5O_2 + 3H_2O = NpO_2(OH)_2(aq) + 4H^+$	–0.45	1.51
	$NpO_2(CO_3)_2^{2-}$	$Np^{4+} + 0.5O_2 + H_2O + 2CO_3^{2-} = NpO_2(CO_3)_2^{2-} + 2H^+$	28.28	0.74
	$NpO_2(CO_3)_3^{4-}$	$Np^{4+} + 0.5O_2 + H_2O + 3CO_3^{2-} = NpO_2(CO_3)_3^{4-} + 2H^+$	31.13	0.24
	$NpO_2{\cdot}2H_2O(am)$	$NpO_2{\cdot}2H_2O(am) + 4H^+ = Np^{4+} + 4H_2O$	–0.70	0.50
	NpO_2OH (am, aged)	$NpO_2OH(am) + 4H^+ = Np^{4+} + 0.25\ O_2 + 2.5H_2O$	–5.87	0.23
	NpO2(CO3)Na·3.5aq	$NpO_2CO_3Na{\cdot}3.5H_2O + 3H^+ = Np^{4+} + 0.25O_2 + 5H_2O + CO_3^{2-} + Na^+$	–21.57	0.27

Table 3-28. Continued.

	Species	Reaction	logK⁰	ΔlogK⁰
Pu	$PuOH^{2+}$	$Pu^{3+} + H_2O = PuOH^{2+} + H^+$	–6.90	0.30
	$Pu(OH)_2^+$	$Pu^{3+} + 2H_2O = Pu(OH)_2^+ + 2H^+$	–15.90	1.00
	$Pu(OH)_3(aq)$	$Pu^{3+} + 3H_2O = Pu(OH)_3(aq) + 3H^+$	–25.30	1.50
	$PuCO_3^+$	$Pu^{3+} + CO_3^{2-} = PuCO_3^+$	7.64	0.86
	$Pu(CO_3)_2^-$	$Pu^{3+} + 2CO_3^{2-} = Pu(CO_3)_2^-$	12.54	0.86
	$Pu(CO_3)_3^{3-}$	$Pu^{3+} + 3CO_3^{2-} = Pu(CO_3)_3^{3-}$	16.40	1.40
	$PuSO_4^+$	$Pu^{3+} + SO_4^{2-} = PuSO_4^+$	3.91	0.66
	$Pu(SO_4)_2^-$	$Pu^{3+} + 2SO_4^{2-} = Pu(SO_4)_2^-$	5.70	0.91
	$Pu(OH)_3^+$	$Pu^{3+} + 0.25O_2 + 2.5H_2O = Pu(OH)_3^+ + 2H^+$	0.79	0.73
	$Pu(OH)_4(aq)$	$Pu^{3+} + 0.25O_2 + 3.5H_2O = Pu(OH)_4(aq) + 3H^+$	–5.41	0.84
	$Pu(CO_3)_4^{4-}$	$Pu^{3+} + 0.25O_2 + 4CO_3^{2-} + H^+ = Pu(CO_3)_4^{4-} + 0.5H_2O$	40.09	1.29
	PuO_2^+	$Pu^{3+} + 0.5O_2 + H_2O = PuO_2^+ + 2H^+$	6.42	0.96
	$PuO_2CO_3^-$	$Pu^{3+} + 0.5O_2 + CO_3^{2-} + H_2O = PuO_2CO_3^- + 2H^+$	11.54	0.97
	$PuO_2(OH)_2(aq)$	$Pu^{3+} + 0.75O_2 + 2.5H_2O = PuO_2(OH)_2(aq) + 3H^+$	–1.82	1.91
	$PuO_2CO_3(aq)$	$Pu^{3+} + 0.75O_2 + CO_3^{2-} + 0.5H_2O = PuO_2CO_3(aq) + H^+$	20.88	1.29
	$PuO_2(CO_3)_2^{2-}$	$Pu^{3+} + 0.75O_2 + 2CO_3^{2-} + 0.5H_2O = PuO_2(CO_3)_2^{2-} + H^+$	26.08	1.29
	$PuO_2(CO_3)_3^{4-}$	$Pu^{3+} + 0.75O_2 + 3CO_3^{2-} + 0.5H_2O = PuO_2(CO_3)_3^{4-} + H^+$	29.38	1.29
	$Pu(OH)_3(s)$	$Pu(OH)_3(cr) + 3H^+ = Pu^{3+} + 3H_2O$	15.80	1.50
	$PuCO_3OH(s)$	$PuCO_3OH(s) + H^+ = Pu^{3+} + CO_3^{2-} + H_2O$	–5.94	1.26
	$Pu(OH)_4(s)$	$Pu(OH)_4(s) + 3H^+ = Pu^{3+} + 0.25O_2 + 3.5H_2O$	–3.89	1.47
	$PuO_2(OH)_2{:}H_2O$	$PuO_2(OH)_2{:}H_2O + 3H^+ = Pu^{3+} + 0.75O_2 + 3.5H_2O$	–5.85	1.55
Am	$Am(OH)^{2+}$	$Am^{3+} + H_2O = Am(OH)^{2+} + H^+$	–7.20	0.50
	$Am(OH)_2^+$	$Am^{3+} + 2H_2O = Am(OH)_2^+ + 2H^+$	–15.10	0.70
	$Am(OH)_3$	$Am^{3+} + 3H_2O = Am(OH)_3 + 3H^+$	–26.20	0.50
	$Am(CO_3)^+$	$Am^{3+} + CO_3^{2-} = Am(CO_3)^+$	8.00	0.40
	$Am(CO_3)_2^-$	$Am^{3+} + 2CO_3^{2-} = Am(CO_3)_2^-$	12.90	0.60
	$Am(CO_3)_3^{3-}$	$Am^{3+} + 3CO_3^{2-} = Am(CO_3)_3^{3-}$	15.00	1.00
	$AmHCO_3^{2+}$	$Am^{3+} + H^+ + CO_3^{2-} = AmHCO_3^{2+}$	13.43	0.30
	$Am(SO_4)^+$	$Am^{3+} + SO_4^{2-} = Am(SO_4)^+$	3.30	0.15
	$Am(SO_4)_2^-$	$Am^{3+} + 2SO_4^{2-} = Am(SO_4)_2^-$	3.70	0.15
	$AmCl^{+2}$	$Am^{3+} + Cl^- = AmCl^{2+}$	0.24	0.03
	$AmCl_2^+$	$Am^{3+} + 2Cl^- = AmCl_2^+$	–0.74	0.05
	$Am(OH)_3$ (am)	$Am(OH)_3(am) + 3H^+ = Am^{3+} + 3H_2O$	16.90	0.80
	$Am(CO_3)(OH)(s)$	$Am(CO_3)(OH)(s) + H^+ = Am^{3+} + CO_3^{2-} + H_2O$	–6.20	1.00
	Am2(CO3)3(s)	$Am_2(CO_3)_3(s) = 2Am^{3+} + 3CO_3^{2-}$	–33.40	2.20
	$Am(CO_3)_2Na{\cdot}5H_2O(s)$	$Am(CO_3)_2Na\ 5H_2O(s) = Am^{3+} + 2CO_3^{2-} + 5H_2O + Na^+$	–21.00	0.50
Cm	$Cm(OH)^{2+}$	$Cm^{3+} + H_2O = Cm(OH)^{2+} + H^+$	–7.20	0.50
	$Cm(OH)_2^+$	$Cm^{3+} + 2H_2O = Cm(OH)_2^+ + 2H^+$	–15.10	0.70
	$Cm(OH)_3$	$Cm^{3+} + 3H_2O = Cm(OH)_3 + 3H^+$	–26.20	0.50
	$Cm(CO_3)^+$	$Cm^{3+} + CO_3^{2-} = Cm(CO_3)^+$	8.00	0.40
	$Cm(CO_3)_2^-$	$Cm^{3+} + 2CO_3^{2-} = Cm(CO_3)_2^-$	12.90	0.60
	$Cm(CO_3)_3^{3-}$	$Cm^{3+} + 3CO_3^{2-} = Cm(CO_3)_3^{3-}$	15.00	1.00
	$CmHCO_3^{2+}$	$Cm^{3+} + H^+ + CO_3^{2-} = CmHCO_3^{2+}$	13.43	0.55
	$Cm(SO_4)^+$	$Cm^{3+} + SO_4^{2-} = Cm(SO_4)^+$	3.30	0.15
	$Cm(SO_4)_2^-$	$Cm^{3+} + 2SO_4^{2-} = Cm(SO_4)_2^-$	3.70	0.15
	$CmCl^{2+}$	$Cm^{3+} + Cl^- = CmCl^{2+}$	0.24	0.03
	$CmCl_2^+$	$Cm^{3+} + 2Cl^- = CmCl_2^+$	–0.74	0.05
	$Cm(OH)_3$ (am)	$Cm(OH)_3(am) + 3H^+ = Cm^{3+} + 3H_2O$	16.90	0.80
	$Cm(CO_3)(OH)(s)$	$Cm(CO_3)(OH)(s) + H^+ = Cm^{3+} + CO_3^{2-} + H_2O$	–6.20	1.00
	$Cm_2(CO_3)_3(s)$	$Cm_2(CO_3)_3(s) = 2Cm^{3+} + 3CO_3^{2-}$	–33.40	2.20

Table 3-29. Reactions and equilibrium constants recommended for use in the Simple Functions spreadsheet, valid at 25 °C (4/4).

	Species	Reaction	logK⁰	ΔlogK⁰
Sm	$SmOH^{2+}$	$Sm^{3+} + H_2O = SmOH^{2+} + H^+$	–7.90	0.10
	$Sm(OH)_2^+$	$Sm^{3+} + 2H_2O = Sm(OH)_2^+ + 2H^+$	–16.50	0.20
	$Sm(OH)_3$	$Sm^{3+} + 3H_2O = Sm(OH)_3 + 3H^+$	–25.90	1.00
	$Sm(OH)_4^-$	$Sm^{3+} + 4H_2O = Sm(OH)_4^- + 4H^+$	–36.90	1.00
	$SmCO_3^+$	$Sm^{3+} + CO_3^{2-} = SmCO_3^+$	7.80	0.50
	$Sm(CO_3)_2^-$	$Sm^{3+} + 2CO_3^{2-} = Sm(CO_3)_2^-$	12.80	0.60
	$SmHCO_3^{2+}$	$Sm^{3+} + CO_3^{2-} + H^+ = SmHCO_3^{2+}$	12.43	0.50
	$SmSO_4^+$	$Sm^{3+} + SO_4^{2-} = SmSO_4^+$	3.50	0.20
	$Sm(SO_4)_2^-$	$Sm^{3+} + 2SO_4^{2-} = Sm(SO_4)_2^-$	5.20	0.10
	$SmCl^{2+}$	$Sm^{3+} + Cl^- = SmCl^{2+}$	0.40	0.10
	$Sm(OH)_3$(am)	$Sm(OH)_3(am) + 3H^+ = Sm^{3+} + 3H_2O$	18.60	1.00
	$Sm_2(CO_3)_3$(s)	$Sm_2(CO_3)_3(s) = 2Sm^{3+} + 3CO_3^{2-}$	–34.50	2.00
	$SmOHCO_3$(s)	$SmOHCO_3(s) + H^+ = Sm^{3+} + CO_3^{2-} + H_2O$	–7.70	0.30
Ho	$HoOH^{2+}$	$Ho^{3+} + H_2O = HoOH^{2+} + H^+$	–7.90	0.20
	$Ho(OH)_2^+$	$Ho^{3+} + 2H_2O = Ho(OH)_2^+ + 2H^+$	–16.10	0.10
	$Ho(OH)_3$	$Ho^{3+} + 3H_2O = Ho(OH)_3 + 3H^+$	–24.50	0.10
	$Ho(OH)_4^-$	$Ho^{3+} + 4H_2O = Ho(OH)_4^- + 4H^+$	–33.40	0.20
	$HoCO_3^+$	$Ho^{3+} + CO_3^{2-} = HoCO_3^+$	8.00	0.40
	$Ho(CO_3)_2^-$	$Ho^{3+} + 2CO_3^{2-} = Ho(CO_3)_2^-$	13.30	0.60
	$HoHCO_3^{2+}$	$Ho^{3+} + CO_3^{2-} + H^+ = HoHCO_3^{2+}$	12.50	0.50
	$HoSO_4^+$	$Ho^{3+} + SO_4^{2-} = HoSO_4^+$	3.40	0.30
	$Ho(SO_4)_2^-$	$Ho^{3+} + 2SO_4^{2-} = Ho(SO_4)_2^-$	4.90	0.30
	$HoCl^{2+}$	$Ho^{3+} + Cl^- = HoCl^{2+}$	0.30	0.50
	$Ho(OH)_3$(am)	$Ho(OH)_3(am) + 3H^+ = Ho^{3+} + 3H_2O$	17.80	0.30
	$Ho_2(CO_3)_3$(s)	$Ho_2(CO_3)_3(s) = 2Ho^{3+} + 3CO_3^{2-}$	–33.80	1.00
Pb	$PbOH^+$	$Pb^{2+} + H_2O = PbOH^+ + H^+$	–7.51	0.50
	$Pb(OH)_2$	$Pb^{2+} + 2\ H_2O = Pb(OH)_2 + 2\ H^+$	–16.95	0.20
	$Pb(OH)_3^-$	$Pb^{2+} + 3\ H_2O = Pb(OH)_3^- + 3\ H^+$	–27.20	0.70
	$Pb(OH)_4^{2-}$	$Pb^{2+} + 4\ H_2O = Pb(OH)_4^{2-} + 4\ H^+$	–38.90	0.80
	$PbCO_3$	$Pb^{2+} + CO_3^{2-} = PbCO_3$	7.00	0.50
	$PbCl^+$	$Pb^{2+} + Cl^- = PbCl^+$	1.55	0.30
	$PbCl_2$	$Pb^{2+} + 2Cl^- = PbCl_2$	2.00	0.30
	$PbCl_3^-$	$Pb^{2+} + 3Cl^- = PbCl_3^-$	2.01	0.30
	PbClOH (s)	$PbClOH(s) + H^+ = Pb^{2+} + Cl^- + H_2O$	0.62	0.30
	$PbCO_3$ (Cerussite)	$PbCO_3\ (s) = Pb^{2+} + CO_3^{2-}$	–13.29	0.69
	Hydrocerussite	$Pb_3(CO_3)_2(OH)_2 + 2\ H^+ = 3\ Pb^{2+} + 2\ CO_3^{2-} + 2\ H_2O$	–17.91	1.94

Radium barium co-precipitation

As discussed in Section 3.4.7, the Ra/Ba ratio in the PWR and BWR canister will throughout repository evolution be below 10^{-3}. It is suggested to pessimistically assume that this ratio is valid during the entire time period, resulting in the formula $Ra_{0.001}Ba_{0.999}SO_4(s)$. It is furthermore suggested to handle Ra-Ba co-precipitation by calculating the Ra solubility limit with the Simple Function spreadsheet, using $RaSO_4(s)$ as the solubility limiting phase, and multiplying the outcome by a factor of 0.001. This treatment is a simplification since it basically means that thermodynamic data for barium is identical to data for radium, and it is actually the solubility of barium that is calculated.

Recommendations for elements not included in the Simple Functions spreadsheet

The flowing elements are (for the purpose of safety assessment) suggested not to be solubility limited, and are thus not included in the Simple Functions spreadsheet:

- H, C, Cl, I, and Cs.

The following elements of the selected inventory have not been studied by the supplier, and no recommendation is given:

- Ac, Cd, Eu, and Mo.

These elements are not included in the Simple Functions spreadsheet.

3.4.11 Judgements by the assessment team

Sources of information and documentation of data qualification

The supplier has listed a number of sources of information and sorted numerous of data sets as either qualified or supporting. The supplier has also justified the sorting. The assessment team agree with this handling.

Conditions for which data are supplied

The supplier has listed a number of conditions, such as pH, temperature, pH_2, etc, for which data are supplied. As result of the corrosion of iron inside the canister, the redox conditions of the intruding water is determined by the magnetite/goethite equilibrium, which is used as a condition in the Simple Functions spreadsheet. The assessment team agree with this handling.

Conceptual uncertainty

The supplier has in detail discussed conceptual uncertainty, and referred to even more detailed discussions. The assessment team agree with this handling.

Data uncertainty due to precision, bias, and representativity

The supplier has in detail discussed data uncertainty, in terms of precision, bias, and representativity, and referred to even more detailed discussions. The assessment team agree with this handling. An identified limitation of the data is that solubility limits can only be assessed for 25 °C. It is noted that while the ambient temperature at the time of canister failure most likely is ca 10 °C lower, the variability on $\log(K_{sol})$, as a result of a 10 °C temperature difference, is less than the uncertainty of the constant. For time periods of elevated temperatures, the solubility may be several orders of magnitude higher for some radionuclides; however, this often is a result of lacking enthalpy data. Since canister failure during times of significantly elevated temperatures can be excluded, this is only relevant for postulated "what if" calculation cases. The supplier has investigated the effects of phosphate complexes with the results showing that excluding phosphate is a pessimistic approach. The aseessment team agree.

Spatial and temporal variability of data

For solubility limits, the supplier argues that accounting for various groundwater compositions handles spatial and temporal variability. The assessment team agree.

Correlations

The supplier argues that the geochemical calculations by themselves are a set of closely related correlations. The asessment team agree. Due to lack of correlation data for equilibrium constant uncertainties, no correlations have been used to calculate uncertainties. The assessment team agrees with this handling.

Result of supplier's data qualification

The supplier delivers a number of solubility limiting phases and numerous relevant reactions and equilibrium constants. For radioelements not included in the Simple Functions spreadsheet, recommendations on how to assess their solubility limit are given. The assessment team agree with the handling.

The supplier gives no data and no recommendation for Ac, Cd, Eu, and Mo. Ac will not be solubility limited, and the other elements are of minute significance for assessment results, wherefore one can pessimistically assume that they are not solubility limited.

The supplier recommends that Ra-Ba co-precipitation is handled by assessing the Ra solubility limit using the Simple Functions spreadsheet (with $RaSO_4$ (s) as the solubility limiting phase) and multiplying the outcome by a factor of 0.001. The assessment team agree.

3.4.12 Data recommended for use in the assessment

The solubility limiting phases recommended for use in the Simple Functions spreadsheet are given in Table 3-25.

The reactions and equilibrium constants recommended for use in the Simple Functions spreadsheet are given in Table 3-26 to Table 3-29. Due to the corrosion of iron inside the canister, the redox condition should correspond to that determined by the magnetite/goethite equilibrium.

The recommended way of handling radioelements of the selected inventory that are not included in the Simple Functions spreadsheet, which are Ac, C, Cd, Cl, Cs, Eu, Mo, and I, is to assume that they are not solubility limited.

The recommended ways to assess the solubility limit of Ra is to use the Simple Functions spreadsheet with $RaSO_4$ (s) as the solubility limiting phase, and to multiplying the outcome by a factor of 0.001.

4 Canister data

4.1 Data of the intact canister

This section concerns non-trivial geometric data associated with the intact canister. These data are the initial minimum copper thickness and the void volume of the average canister. The former is used in copper corrosion calculations while the latter is used mostly for assessing data relevant for radionuclide transport modelling. Trivial geometric canister data are given in the **Canister production report**.

This section also concerns the canister's resistance to mechanical loads (isostatic load, shear loads due to shear movement of the rock mass surrounding the deposition hole, and asymmetric loads due to uneven swelling of the bentonite). Of specific concern is the data for the modelling of the response to shear loads as this is further modelled within the assessment.

4.1.1 Modelling

This section describes what data are needed, and in what assessment modelling activities the data are to be used.

Defining the data need

The data encompass:

- The initial minimum copper thickness d_{Cu} (m) of the installed canister.
- The void volumes V (m^3) for the fully loaded and the average BWR type canister, for the fully loaded and the average PWR type canister, and for the average canister.
- Resistance to mechanical loads, in terms of whether the canister complies with the design premises (Posiva SKB 2017).

Modelling activities in which data will be used

The initial minimum copper thickness is used as input to the PSAR corrosion calculations, as described in SKB (2010d). In the corrosion calculations it is assumed that corrosion may occur where the copper thickness is the least. The copper shell may have a varying thickness due to the design, imperfections induced in the manufacturing and welding, and defects induced by the handling up until, and in, the installation in the repository.

The void volume is used for assessing the delay time (cf Section 4.2) associated with the onset of radionuclide transport from a defect canister. This onset occurs as the void volume is filled with water intruding into the canister. The void volume is also used for assessing the source term (cf the **Radionuclide transport report**). In case the concentration of the dissolved radioelement is below its solubility limit, a larger void volume dilutes the concentration compared to a smaller void volume, if the same amount of the radioelement is dissolved. And opposite, if the concentration is at its solubility limit, a larger void volume gives rise to a larger amount of the dissolved radioelement. The void volume is further used in an assessment of the canister internal overpressure from both accumulated He and initial gas and water (Lilja 2012).

The resistance to mechanical loads are input to the choice of scenarios. The resistance to shear movement is the coupling to the seismic modelling (cf Munier 2010, Fälth et al. 2010). In this modelling, the probability is assessed that the shear magnitude and velocity in the rock volume surrounding the deposition holes are larger than specified in the canister design premises. In case a seismic event gives rise to such shear, it is assumed that the affected canisters fail. This probability is used as input in the radionuclide transport modelling (cf the **Radionuclide transport repor**t).

4.1.2 Experience from SR-Site

Modelling in SR-Site

Concerning the initial minimum copper thickness, it is used in the copper corrosion calculations in the same way in PSAR as in SR-Site (and SR-Can).

Concerning the void volume, no new insights or results have been obtained during SR-Site or during the ensuing work addressing review comments on SR-Site. The void volume is used in the same way in PSAR as in SR-Site (and SR-Can), both for assessing the source term and delay time (Section 4.2 is referred to for further information on the delay time).

In SR-Site the effect on the canister due to mechanical loads was modelled as a 3D finite element model using the ABAQUS code (Hernelind 2010, Raiko et al. 2010). Variables that were varied for the shear load cases included the angle with which the fracture intersected the deposition hole and the buffer density.

Conditions for which data were used in SR-Site

The conditions concerning the initial minimum copper thickness and void volume are the same in PSAR as in SR-Site (and SR-Can), i.e. they apply for the installed but intact canister. The conditions for the resistance to shear movement generally agree in SR-Site and SR-Can, and correspond to the *in situ* conditions of the installed canister at the upper limit of the buffer density. However, the criterion for maximum shear magnitude is 5 cm in SR-Site, compared to 10 cm in SR-Can.

Sensitivity to assessment results in SR-Site

Concerning the initial minimum copper thickness it was shown in SR-Site that there will be no initial defects penetrating through the copper shell. For no canister the defects reduce the initial minimum copper thickness to less than 25 mm (cf Table 5-9 in SKB 2011). The time needed to corrode through the copper shell (approximately) scale inversely proportional to the copper thickness. Accordingly there is only a difference in corrosion time of a factor 2 between 25 mm and 50 mm minimum copper thicknesses. Also, in Section 14.2 in SKB (2011) it was concluded that the number of failed canisters increased the by a factor about 2, when halving the thickness to 25 mm. Therefore, the analysis was rather insensitive to this parameter.

In SKB (2011, Section 10.4.5) it was concluded that the copper canister could withstand a shear movement with a magnitude of 5 cm, but that for a shear movement of 10 cm, failure of the copper shell cannot be totally excluded. It was recognised that the study was limited and that the creep model needed improvement. In SKB (2011, Section 10.4.9) it was concluded that no canister failures at the expected maximum over-pressure at the Forsmark site are expected.

Alternative modelling in SR-Site

No alternative modelling of importance for the initial minimum copper thickness, void volume, or resistance to mechanical loads was performed in SR-Site.

Correlations used in SR-Site modelling

No correlation was used in subsequent SR-Site modelling concerning the initial minimum copper thickness, the void volume, or the resistance to mechanical loads.

Identified limitations of the data used in SR-Site modelling

No limitation has been identified in the data on, and usage of, the initial minimum copper thickness or void volume.

Concerning the resistance to shear movement, limitations in the study was recognised in SKB (2006a, Section 9.4.5), giving rise to suggestions for further modelling (cf SKB 2006a, Table 9-14). The regulatory authorities also recognised limitations in the SR-Can modelling and found that the arguments for the 10 cm criterion need to be reinforced in order to demonstrate the validity of SKB's strategy for overall handling of the earthquake problem (Dverstorp and Strömberg 2008).

In SR-Site only BWR insert mechanical data was available, and this data was therefore also used for PWR insert modelling. Also only crack-like defects were analysed.

4.1.3 Use of data in the PSAR

Underlying data on the initial minimum copper thickness and the resistance to shear movement are supplied by the Canister production report team. Prior to supplying these data there has been much communication with the assessment team and as result, the supplier has no further input.

The void volumes supplied in this section have been produced by the assessment team; hence no supplier formally exists. None the less, the text is written according to the standard outline of the Data report.

4.1.4 Sources of information and documentation of data qualification

Sources of information

The assessment of the initial minimum copper thickness is based on data in the **Canister production report**. The analysis of the canister's resistance to mechanical loads is made in the **Canister production report** and the Mechanical design analysis for the canister (Jonsson et al. 2018), supported with deterministic calculations in the reports of Alverlind (2016), Hernelind (2010), Dillström (2015), and Unosson (2016). The full references to the main sources of information are given in Table 4-1.

Table 4-1. Main sources of information used in data qualification.

Canister production report, 2020. Produktionsrapport Kapsel. SKBdoc 1407944 ver 1.0, Svensk Kärnbränslehantering AB.
Jonsson M, Emilsson G, Emilsson L, 2018. Mechanical design analysis for the canister. Posiva SKB Report 04, Posiva Oy, Svensk Kärnbränslehantering AB.

Categorising data sets as qualified or supporting

The input data for the assessment on the initial minimum copper thickness mainly come from Sections 5.5.4, 5.7.3 and 7.1.1 of the **Canister production report**. The input data for the void volume calculations mainly come from the **Canister production report** and SKB (2010b). For the resistance to mechanical loads, the judgement in the **Canister production report** on whether or not the canister can withstand the loads according to the design premises is used.

These data sets are sorted as qualified or supporting in Table 4-2. The justification to the sorting of each item is given in the table.

Table 4-2. Qualified and supporting data sets.

Qualified data sets	Supporting data sets
1. **Canister production report**, Table 3-6: Geometric data on the BWR and PWR type canisters, for void volume calculations. 2. **SKB (2010b)**, Table 2-4: Weights of components of fuel assemblies, for void volume calculations. 3. **Canister production report**, Sections 5.5.4, 5.7.3 and 7.1.1 : Minimum thicknesses of the copper shell after machining. 4. **Canister production report**, Sections 7.2.1–7.2.3: Statement that canisters manufactured according to the reference design will fulfil the design premises related to mechanical loads.	5. Densities of materials in fuel assemblies from CRC (2008) and Slagle et al. (1994, Appendix A), for void volume calculations.
1, 3–4. These data have been qualified in the **Canister production report**, in accordance with the SKB quality assurance system. This qualification is found to be in compliance with the demands of this data report. 2. These data have been qualified in SKB (2010b), in accordance with the SKB quality assurance system. Thisqualification is found to be in compliance with the demands of this data report. 5. These density data are taken from the open literature but are judged as supporting as the data may not be representative for the exact materials used in the fuel assemblies. It is judged, however, that this potential lack of representativeness would give rise to very minor deviations in the supplied void volume data.	

Excluded data previously considered as important

Concerning the initial minimum copper thickness, the concept of an initial pinhole penetrating the copper shell has been abandoned, due to improved welding methods. Concerning the resistance to shear movement, the design premises analysis has been set to 5 cm shear , while 10 cm shear magnitude was used in SR-Can (see further discussion in Section 2.3 of SKB (2009b)).

4.1.5 Conditions for which data are supplied

Initial minimum copper thickness

The copper shell may have a varying thickness due to the design, imperfections induced in the manufacturing and welding, and defects induced by the handling up until, and in, the installation. The entire chain from production to installation is described in the **Canister production report**. The data applies for the installed canister, but before corrosion and major mechanical loads influence the copper thickness.

Void volume

The void volume is calculated for the SKB spent fuel reference scenario and for the SKB canister reference design. Changes in volumes due to varying temperature have been disregarded. The void volume is calculated for an intact canister, and does not include a potential reduction of the void volume due to the formation of corrosion products upon water intrusion in a defect canister.

Resistance to mechanical loads

The behaviour of the canister and its parts due to static and dynamic loads has been simulated with finite element (FE) models, and in addition possible failure mechanisms as plastic collapse and crack growth have been evaluated. The load cases, material plasticity and damage modes, geometries, postulated defects, and FE-solvers are summarized in Jonsson et al. (2018). Canisters for BWR and PWR have different internal designs and have therefore been modelled separately; most importantly the PWR canister design has a larger cross section mass which results in a more efficient load distribution. Even minor differences in material properties have been accounted for between the models. The effects of compromise between geometric complexity and model simplification have been investigated in Dillström (2015).

The static strength of the canister varies with the cast iron elasticity, strain hardening, fracture properties, and cross section centricity of channels for fuel elements. The mechanical data and geometric variations have been modelled on the data from heavy section ductile cast iron manufactured in full dimensions for SKB described in the **Canister production report.** The safety factor for plastic collapse is shown to be at least 1.5 and is set to the square root of 10 which equals 3.16 for crack growth.

Variables that were varied for the shear load cases include the angle with which the fracture intersects the deposition hole and the buffer density. Results corresponding to the shear magnitude of 5 cm are reported in Jonsson et al. (2018). However, results are available also for larger shear magnitudes in Hernelind (2010) and Dillström and Bolinder (2010). The design analysis is valid for canisters that have not been subjected to heavy corrosion. For detailed conditions of the modelling Jonsson et al. (2018), Hernelind (2010) and Dillström and Bolinder (2010) are referred to.

4.1.6 Conceptual uncertainty

Initial minimum copper thickness

There is no conceptual uncertainty associated with the initial minimum copper thickness. However, there is some uncertainty associated with how this copper thickness should be used in corrosion calculations. In case of defects, these occur at a very local area of the copper shell (most importantly in the welds). In the advection/corrosion scenario it is assumed that the buffer has eroded at the fracture intersecting the deposition hole, but not that the entire buffer in the deposition hole has been removed. This means that only a limited area of the copper surface is subjected to increased corrosion rates, while other copper surface areas are still protected by the buffer. There is only a certain probability that the area featuring the initial minimum copper thickness is exposed to advection/corrosion.

Void volume

The void volume is calculated using elementary geometrical considerations. Accordingly, there is no conceptual uncertainty. In subsequent modelling, however, there is the question of to what degree the void volume is utilised by water intruding into the canister. There is also the question of how efficiently radionuclides can be transported from different parts of the void volume.

Resistance to mechanical loads

An uncertainty discussion concerning the design analysis of the canister is given in Chapter 7 of Jonsson et al. (2018). An uncertainty discussion is also given in Chapter 10 of Hernelind (2010).

Conceptual uncertainty is associated with how well the models represent the intended cases (for example the size of the mesh in the finite element modelling). Conceptual uncertainty is also associated with how the output from one modelling is used as input in subsequent modelling. The nature of the conceptual uncertainty is not such that it jeopardises the validity of the conclusions from the analyses.

4.1.7 Data uncertainty due to precision, bias, and representativity

Initial minimum copper thickness

Uncertainties in the initial minimum copper thickness are associated with how well one can produce the copper shell components, how well it can be welded and the subsequent handling until the canister is installed. This chain of events is discussed at length in the **Canister production report**. In Chapter 3 of the **Canister production report**, the reference design is discussed. In Sections 5.5.4, 5.7.3 and 7.1.1 the probability of different deviations from this design, as well as of defects in the welds and shell, are given. These data and probabilities are used in Section 4.1.10 of this present text to justify an initial minimum copper thickness for subsequent use in PSAR corrosion calculations.

Void volume

The void volume is calculated using elementary geometrical considerations (cf Section 4.1.10). The tolerances in the canister and cast insert dimensions are very small, wherefore little uncertainty is induced in the geometrical calculations. The total volume of typical fuel assemblies is calculated from the weights and densities of different materials of the fuel assembly. In doing this, density data on similar, but not the exact, materials have been used. However, the uncertainty induced is judged to be insignificant. When calculating the void volume of the average canister, it is necessary to make a few assumptions regarding this hypothetical average canister (cf Section 4.1.10 for details on these assumptions). The uncertainty introduced as result of these assumptions is judged to be minor.

Resistance to mechanical loads

According to the **Canister production report** the major uncertainties in the shear load case are that the calculations are based on pessimistic assumptions, mainly on the material properties of the bentonite. Resulting from deterministic damage tolerance analyses, the acceptable defect size for the cast iron insert is 7–9 mm at shear movement depending on the buffer density. At 2 050 kg/m^3 buffer density the acceptable defect size is 7 mm (Jonsson et al. 2018). In probabilistic analyses the acceptable defect size is 4 mm (Dillström 2014). Such defects can be detected by standard inspection techniques such as ultrasonic testing in cast iron (Ahmad and Bond 2018).

An uncertainty discussion is given in Sections 7.6 and 7.7 of Jonsson et al. (2018) and Chapter 10 of Hernelind (2010), concerning load on the canister due to rock shear movement. Among the mentioned sources of data uncertainty are uncertainty in the stress-strain relationship of the canister material and the bentonite; natural scattering in the material data and in the fracture toughness; uncertainties in the copper creep model and in the creep strain rate; and assumption made for the coefficient of friction between the copper and the surrounding materials. For a full account of the uncertainties Jonsson et al. (2018), Hernelind (2010) and Dillström and Bolinder (2010) are referred to.

4.1.8 Spatial and temporal variability of data

Initial minimum copper thickness

The recommended initial minimum copper thickness is intended for the general canister, which could be deposited at any canister position in the repository. In this respect there is no component of spatial variability. It is noted that the initial minimum copper thickness is more likely to be found in the welds than in the tube, base or lid, but this should have little consequence for subsequent modelling. The data applies at the initial state.

Void volume

For the void volume of the average canister, spatial variability is of no concern. For individual canisters the void volume depends on how many channel tubes are occupied by fuel assemblies. This is handled by supplying void volumes for canisters filled with different numbers of fuel assemblies (cf Table 4-3 in Section 4.1.10). Temporal variability due to changes in temperature is judged as insignificant and is accordingly disregarded. The void volume is valid for the intact canister, and does not account for the formation of corrosion products, upon intrusion of water in a defect canister.

Resistance to shear movement

The design analysis is general and there is no component of spatial variability when (indirectly) applying its result on different canister positions in the repository. The metal manufacturing introduces some variability to the mechanical properties of each canister, but the variations of the strength and ductility are limited and within the requirements. The temporal variability is handled by accounting for the additional load due to the ice sheet during glaciation. Different sequences of glacial loads and earthquakes have been analysed (Hernelind 2010).

4.1.9 Correlations

Initial minimum copper thickness

The supplied data should be used for the general canister and there are no correlations of concern for subsequent modelling.

Void volume

The supplied data should be used for the general canister and there are no correlations of concern for subsequent modelling.

Resistance to mechanical loads

The design analysis is general and gives a judgement on whether or not the canister can withstand the specified mechanical loads. There is no correlation that needs to be used when applying this in subsequent analyses (other than the combinations of mechanical loads already specified in the design premises (Posiva SKB 2017)).

4.1.10 Result of data qualification

Initial minimum copper thickness

The production and inspection of copper components are described in the **Canister production report**, Sections 5.5.4, 5.7.3 and 7.1.1, and the following can be derived:

Machining is a well-known and proven industrial process. The dimensions, including the copper wall thickness, can be measured either by conventional laser tracker systems or by use of ultrasonics. In Section 5.5.4 in the **Canister production report** the resulting wall thicknesses for a number of manufactured copper components are presented. Based on these data, the minimum copper thickness after machining in normal operations is judged to be 48.1 mm for the tube, 48.9 for the base, 48.3 for the lid, including a 1 mm deep identity marking, and 47.5 mm for the welds. Therefore the overall minimum thickness in normal operation is 47.5 mm.

Furthermore, it can not be excluded that one percent of the canisters might have areas where the minimal copper thickness is reduced to 45 mm due to disturbed operation. This value is based on the fact that larger deviations will be detected when the components are handled and assembled and the canister is sealed and these deviations will thereby lead to rejection of the canister. Experience indicates that such large deviations in dimensions will be detected by by testing. The probability that any canister will have a minimum thickness after machining of less than 45 mm is therefore judged as negligible.

The occurrences of defects in the copper shell are one cause for further reduction of the corrosion barrier. Occurrences of defects in the welds have been investigated based on the results of welding demonstration series under normal operational conditions performed at the Canister Laboratory. Normal operation during welding means that both input and output welding variables are within a defined "process window" that must be met in order for a weld to be considered approved. The only type of defect that has been detected in the welds made in normal operation is joint line hooking (a tight, crack like discontinuity with extension radially with a gap of < 10 μm) and incomplete pentration. The cavity type of defect (near-surface discontinuity) has only been seen outside normal operations for the weld.

In the first demonstration series, the largest detected defects were of the order of a few millimetres with the largest one being 5.4 mm in radial direction. The second series was performed with an improved welding tool and resulted in smaller defects with the largest one being 1.5 mm.

The probability for disturbed operations resulting in one or more of the process parameters being outside the process window is estimated to be low: 97 % of the welds are free from joint line hooking defects (Cederqvist et al. 2018). The results from probability-of-detection studies of the NDT methods show a 90 % detection capability for a 5 mm joint line hooking defect and a capability of almost 100 % for defects lager than 10 mm.

The probability that the process parameters are such that they cause defects that exceed 5 mm and this occurs simultaneously with a failure of the control system,, is at the present stage of development judged to be less than 3 % of the canisters. This statement is based on the fact that the developed welding process is very reliable and reproducible. If these disturbed operations do occur, the maximum reduction of the copper thickness is estimated not to exceed 10 mm.

For the copper shell components (the base, the lid and the tube), there are few possible defects, forging laps being one example. Such defects can be avoided by proper manufacturing. Further, the defects can be detected by non-destructive testing (van den Bos 2018). Forging laps can be detected by magnetic (eddy current) testing. The results of inspections of manufactured copper components indicate that there will remain no defects in the extruded tubes or forged lids and bases that remain after the final machining.

Since the possible defects in the copper components are expected to mainly extend perpendicularly to the corrosion barrier and since no real manufacturing defects have been found in the canister components, the welds are presently considered to be the potentially thinnest parts of the copper shell.

Reductions may also occur as a result of surface damage during transportation, handling and deposition of the canister. Available information on the occurrence of surface damage during these stages is limited since full-scale tests, which focus on this issue using relevant handling equipment and transport casks, remain to be performed. The probability for critical reduction of the corrosion barrier due to transportation damages is, however, considered negligible since the canister is protected by a transport cask. In addition, the canister is inspected for surface damage when it is lifted from the transport cask into the radiation shield of the deposition machine in the reloading station at repository depth.

To derive a minimum copper thickness to be used in the corrosion calculations the starting point is that the machined canister surface area has 48.1 mm thickness of copper, while the weld areas have at least 47.5 mm (for > 99 % of the canisters). A cautious statement would thus be to say that a large majority of the canisters would have at least 47.5 mm, over the entire surface.

The further reductions of this minimum copper thickness regard few canisters and/or small areas. It is estimated 1 % of the canisters could have a minimum machined thickness of the welds of 45 mm, covering some percents of the canister surface area. The maximum reduction of the copper thickness

due to defects from the hot-forming and welding processes (occurring only under disturbed operation) is given as 10 mm for 3 % of the canisters. Also this reduction regards a small area of the surface, which could pessimistically be assumed to be the whole weld area.

The absolute lower limit in the ranges given for the welds would be 35 mm (45 mm, lowest value for machined weld, minus 10 mm, for a maximum defect). It is though totally unrealistic to base the corrosion calculations that should reflect the status for the whole canister surface, on this value for the weld areas.

It is suggested that, built on the experience from the pilot production of canister, a copper thickness of 47 mm (rounded from the 47.5 mm given above) is used as a reference value in the corrosion calculations.

Void volume

According to the **Spent fuel report** the estimated number of canisters to be deposited is 5 689, whereof 3 982 hold BWR and BWR-MOX spent fuel and 1 707 hold PWR and PWR-MOX. Figure 4-1 shows the BWR cast iron insert with 12 channel tubes and the PWR cast iron insert with 4 channel tubes.

The length and diameter of both types of cast iron inserts are 4 573 mm and 949 mm, respectively. The BWR insert holds 12 channel tubes, each 160 × 160 mm wide and 4 463 mm in length (cf Tables 3-6 of the **Canister production report**). This gives a BWR insert volume of about 1.87 m^3 (if disregarding minor details in the design, such as the curvature of the channel tubes). The PWR insert (with channel tubes 235 × 235 mm) has the volume 2.25 m^3 (cf Tables 3-6 of the **Canister production report**).

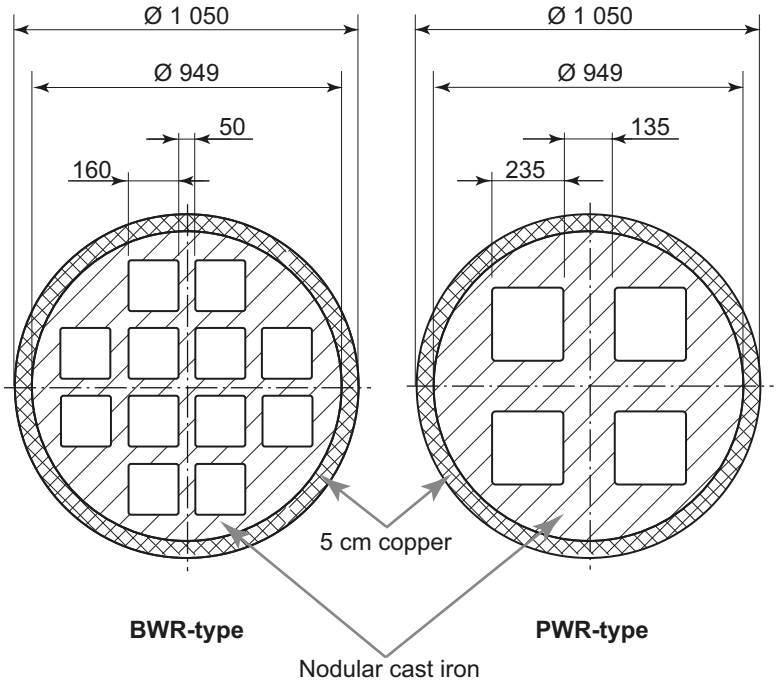

Figure 4-1. *SKB's reference canister with an outer corrosion barrier of copper and an insert of nodular cast iron. Basic differences between the BWR and PWR insert design.*

A typical BWR fuel assembly holds 198 kg UO_2, 78 kg zirconium alloys, 13 kg stainless steel, and 1 kg nickel alloys (cf Table 2-4 of SKB 2010b). The corresponding volumes can be calculated from the following densities: $UO_2 = 1.05 \times 10^4$ kg/m^3; stainless steel = 7.9×10^3 kg/m^3; zirconium alloy = 6.5×10^3 kg/m^3; and nickel alloy = 8.25×10^3 kg/m^3 (Slagle et al. 1994, CRC 2008). This results in the total volume of one typical BWR fuel assembly of 0.033 m^3.

A typical PWR fuel assembly holds 526 kg UO_2, 129 kg zirconium alloys, 15 kg stainless steel, and 2 kg nickel alloys (cf Table 2-4 of SKB 2010b). In addition, in about one fourth of the PWR fuel assemblies a control rod cluster will be deposited, with a typical weight of 16.3 kg stainless steel and 51.4 kg AgInCd alloy[9] (Section 2.2.1 and Table B-5 of SKB 2010b). The volume of a typical control rod cluster can be calculated to 0.0071 m^3. This results in the total volume of one typical PWR fuel assembly (with one fourth of a control rod cluster) of 0.074 m^3.

From the data given in the above paragraphs, the void volumes of BWR and PWR type canisters with all channel tubes occupied by typical fuel assemblies can be calculated. For the BWR and PWR type canisters the void volume becomes 1.0 m^3 and 0.71 m^3, respectively.

As described in SKB (2010b)., there will be canisters deposited with empty channel tubes. According to the SKB reference scenario, in total 47 904 BWR and BWR-MOX assemblies, as well as 6 049 PWR and PWR-MOX assemblies will be deposited in 4 451 BWR type canisters and 1 652 PWR type canisters (cf Tables C-2 and C-5 of SKB 2010b)[10]. This means that on average, a BWR type canister will have 10.8 occupied and 1.2 empty channel tubes. Each empty BWR channel tube adds 0.11 m^3 to the void volume. The average PWR type canister will have 3.66 occupied and 0.34 empty channel tubes. Each empty PWR type channel tube adds 0.25 m^3 to the void volume. If assuming that the volume of each fuel assembly is described by either the typical BWR or PWR fuel assembly, described above, the void volume of the average canister can be calculated. Firstly, the void volumes of the average BWR type canister and PWR type canister are calculated to 1.1 and 0.79 m^3, respectively. Based on the weighted average of the 4 451 BWR type canisters and 1 652 PWR type canisters, the void volume of the average canister is calculated to 1.0 m^3. All the void volumes for the different canisters are summarised in Table 4-3. To illustrate extreme void volumes, the half-full BWR and PWR type canisters are also included in the table.

Table 4-3. Void volume of different canister types.

Canister	Void volume (m^3)
Full BWR type canister (12 fuel assemblies)	1.0
Full PWR type canister (4 fuel assemblies)	0.71
Average BWR type canister (10.8 fuel assemblies)	1.1
Average PWR type canister (3.66 fuel assemblies)	0.79
Half-full BWR type canister (6 fuel assemblies)	1.7
Half-full BWR type canister (2 fuel assemblies)	1.8
Average canister	1.0

[9] The density of 10.20 g/cm^3 of the AgInCd alloy is taken from a product sheet on "Neutron Absorber – AgInCd 80/15/5" from Umicore Technical Materials. For comparison the density of Ag is 10.50 g/cm^3.

[10] Due to updates in the prognosis of future operation of the power plants, the estimated total number of canister has changed from 6 103 in SR-Site to 5 683 in the PSAR (3 982 BWR canisters and 1 707 PWR canisters), see further Section 3.1 or the **Post-closure report**. The number of BWR and PWR type canisters discussed here are based on the prognosis used in SR-Site. The influence on the calculation of average void volume is deemed insignificant. The text from SR-Site have therefore been reproduced.

Resistance to mechanical loads

According to the **Canister production report**, Section 7.1.2 the strength analysis shows that canisters manufactured according to the reference design will fulfil the design premises related to shear loads. However, the damage tolerance analysis gives acceptable defects sizes that put rigorous requirements on manufacturing and NDT (non-destructive testing) capability. It is further stated that the copper shell will have sufficient ductility to remain intact also after shear loads as long as the insert remains intact.

According to the **Canister production report**, Section 7.1.2 the probability for the canister not to fulfil the design requirement related to isostatic load and uneven pressure from the bentonite respectively, is deemed to be insignificant. This also accounts for the load from an ice sheet during a glaciation.

4.1.11 Judgements by the assessment team

The data on the initial minimum copper thickness and void volume has been produced or modified by the assessment team, based on data from the supplier. The resistance to mechanical loads is justified by the supplier.

Sources of information and documentation of data qualification

Input data for the assessment of the initial minimum copper thickness and void volume are found in the **Canister production report** and SKB (2010b). The discussion on the resistance to mechanical loads is found in the **Canister production report** and references therein.

The references cited in the data qualification are judged to be relevant and the citing is judged to be sufficiently precise. The data sets used are judged to be adequately categorised into qualified and supporting data sets.

Conditions for which data are supplied

The conditions for which the data are supplied are sufficiently well described, and have been chosen to represent those of the repository.

Conceptual and data uncertainties

There is little conceptual uncertainty associated with the geometric data on the initial minimum copper thickness and the void volume. There is detailed information on uncertainties associated with the resistance to mechanical loads in the supporting documents.

Data uncertainty due to precision, bias, and representativity

The data uncertainty concerning the initial minimum copper thickness and void volume is small and bounded in rather narrow ranges by extreme values. The supplier has provided probabilities for minimum copper thicknesses for different canister components. Importantly, the supplies suggest that the probability is zero that an initial defect penetrates the copper shell. The assessment team agree with this handling. Concerning the resistance to mechanical loads, most of the data uncertainty is dealt with by modelling different isostatic and rock shear cases.

Spatial and temporal variability of data

The canister data supplied for the canister are general and should be applicable to all canisters in the repository. The variation of the mechanical properties is limited and within the requirements. Therefore, in terms of canister positions, the data have no spatial variability. The initial minimum copper thickness and void volume represent the initial state. Temporal variability associated with the resistance to mechanical loads is handled by the design premises stating the long-term loads in the repository.

Correlations

There is no correlation that needs to be propagated to subsequent handling.

Result of supplier's data qualification

Concerning the initial minimum copper thickness and void volume the final data have been produced by the assessment team, based on underlying data supplied by the **Canister production report** and SKB (2010b). The assessment team find these underlying data adequate.

The supplier argues that the canisters that are manufactured according to the reference design will fulfil the design premises related to mechanical loads. For the shear load case the calculated acceptable defects sizes in the insert are small and puts rigorous requirements on the manufacturing and NDT capability.

4.1.12 Data recommended for use in assessment modelling

For the initial minimum copper thickness it is recommended to use the thickness 47 mm in PSAR copper corrosion calculations. For PSAR radionuclide transport modelling, it is recommended that the void volume of 1.0 m^3 is used for the average canister. Concerning the resistance to mechanical loads, it is judged that all canisters can withstand the loads according to the design premises, also accounting for the additional load from an ice sheet during a glaciation. These data are summarised in Table 4-4.

Furthermore, for the evaluations of corrosion in the safety assessment, the area exposed to corrosion and the number of canisters involved need to be taken into account in an evaluation of whether the low probabilities given in Section 4.1.10 of less than 47 mm copper thickness could influence the results. Here, also the geometries of the defects need to be considered. For example, while a defect in the form of a small void located near the outer surface of the canister can, for geometrical reasons, be argued to have no impact on the time for breakthrough by corrosion, the same defect in contact with the inner surface could reduce the effective thickness for a corrosion calculation by the projected length of the defect along the canister radius.

Table 4-4. Data recommended for use in PSAR.

Parameter	Data
Initial minimum copper thickness	47 mm
Void volume	1.0 m^3
Resistance to mechanical loads	Canister will withstand the mechanical loads as specified in the design premises.

4.2 Evolving canister defect

This section concerns data needed in safety assessment modelling regarding potential penetrating canister defects. Before dissolved radionuclides can migrate from a failed canister, a continuous water pathway needs to be established between the spent fuel and the canister exterior. This requires a defect through the copper shell and the size of this defect is of importance for the water intrusion rate, as well as for the radionuclide release rate once the continuous water pathway has formed. Before the pathway can form, sufficient amounts of water need to intrude the canister so that its void becomes filled. As water intrudes into the canister, the cast iron insert will corrode, forming hydrogen gas that will limit the pressure gradient constituting the driving force for water to intrude into the canister. In addition, the corrosion reaction consumes water and corrosion products may block the void that would otherwise constitute the pathway (cf the **Fuel and canister process report**).

The hydromechanical evolution of canisters with a minor initial defect was given substantial attention in the SR 97 safety assessment (SKB 1999b). The conclusion was that the processes in the canister internals add a considerable delay time before a continuous water pathway between the spent fuel and the buffer is formed. This is mainly related to the slow ingress of water into the canister, due to the low permeability of the buffer, the limited size of the defect, and the generation of a gas pressure inside the canister. In case of a minor defect, the canister internal would basically remain dry until the pressure from the corrosion products would physically damage the copper shell, causing a larger defect (SKB 1999b, Section 9.6).

This section deals with the time it takes from canister failure, i.e. when a defect penetrating the copper shell is formed, to the formation of a continuous water pathway. This time is called the delay time. Furthermore, this section deals with the defect size in the copper shell, which has implications for the cross-section area over which radionuclide release can occur, as well as for the diffusive transport pattern in the buffer. Finally this section deals with the point in time, denoted $t_{large,}$ when the defect becomes so large that it constitutes no hindrance to mass transfer. Before such unhindered mass transfer can occur, a continuous water pathway needs to have formed. It should be noted that even for a large defect, it may take some time to fill the canister with water.

The PSAR is based on the same modelling of Evolving canister defect as SR-Site. In the following sections, the modelling strategy is described (Section 4.2.1) followed by an account of the experiences from the SR-Site safety assessment (Section 4.2.2). Since the PSAR is based on the same data as SR-Site, the data qualification (Sections 4.2.3 to 4.2.10) is reproduced from the SR-Site Data report. In Section 4.2.11 the formal judgement by the assessment team to use the qualified data is presented followed by Section 4.2.12 where the recommended data is presented.

4.2.1 Modelling

This section describes what data are needed, and in what assessment modelling activities the data are to be used. These are the same modelling activities as in the SR-Site assessment.

Defining the data need

This section should supply data for three of the canister failure modes in the safety assessment:

- The postulated growing pinhole failure, with an initial defect radius of 2 mm.
- Canister failure due to corrosion.
- Canister failure due to shear load.

For these three failure modes, the supplier should deliver the following data:

- The defect radius r_{defect} (m). In case of a circular defect the defect radius should be given. In case of a non-circular defect, the equivalent defect geometry should be provided, unless the defect is so large that the canister poses no transport resistance for escaping radionuclides. If the circular or non-circular defect is so large that the canister poses no transport resistance, r_{defect} can be set as unlimited.
- The delay time t_{delay} (yr) between canister failure (penetrated copper shell) and the establishment of a continuous water pathway from the fuel to the exterior of the canister.
- The time t_{large} (yr) from repository closure to when r_{defect} is set to unlimited.

In case there are large uncertainties in the t_{delay} and t_{large} data, it may be justified to only supply the orders of magnitudes for these data. It may also be justified to supply pessimistic values, where the most pessimistic value of t_{delay} is zero, and of t_{large} is equal to the time for failure.

Modelling activities in which data will be used

Modelling of radionuclide release in the near-field is done with the transport simulation code COMP23 (Romero et al. 1999, Cliffe and Kelly 2006, Vahlund and Hermansson 2006), as detailed in the **Radionuclide transport report.** In this code the canister interior is pessimistically assumed to possess no transport resistance and no sorbing capacity. Rather, as soon as the canister is filled with water, a continuous pathway between the spent fuel and the canister exterior is assumed, and the canister interior is represented as a water volume in which radionuclides are dissolved and diffuse freely. This occurs after the delay time. Transport resistances or barrier functions of the inner structural parts of the canister and the fuel, including the fuel cladding, are disregarded once the transport pathway is established.

In case the canister is surrounded by the buffer, which is assumed in the failures modes growing pinhole failure and canister failure by shear load, the defect radius and t_{large} are input data to modelling diffusive transport of radionuclides through the buffer. The defect radius is used to calculate both the diffusion resistance in the hole and an additional transport resistance, resulting from the fact that radionuclides exiting a small defect diffuse in a three-dimensional pattern in the buffer. This is illustrated in Figure 4-2, showing the copper shell with a minor defect, the buffer, and the surrounding rock where a fracture intersects the deposition hole (Neretnieks et al. 2010).

In the radionuclide transport model, the additional transport resistance at the canister/buffer interface is immediately lost as t_{large} has been reached. This does not necessarily mean an onset of radionuclide transport, as this also requires that the canister is filled with water. The additional transport resistance would in the real cases gradually decrease as the defect radius increases, so this must be compensated for by setting the value of t_{large} sufficiently small, so that the additional transport resistance is neglected as soon as the defect radius significantly increases from that of the original defect.

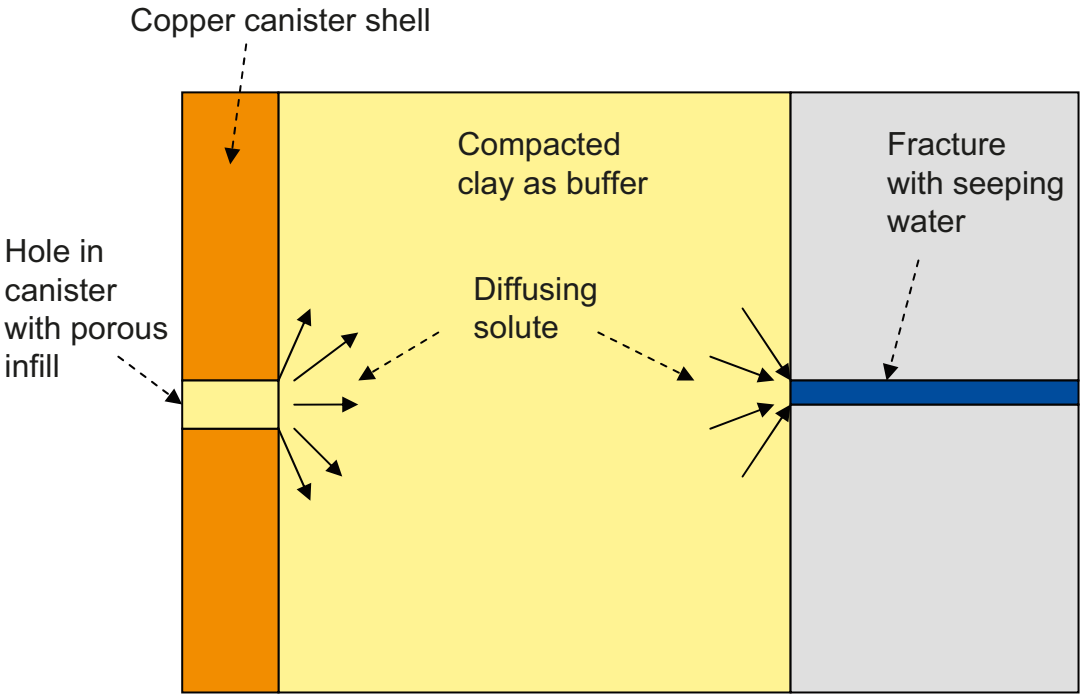

Figure 4-2. *Illustration of the diffusion profile in the buffer, where radionuclides spread out at the defect and converge at the fracture. Excerpt from Figure 5-1 of Neretnieks et al. (2010).*

4.2.2 Experience from SR-Site

Defect radius

No new insights or results have been obtained on defect radius during SR-Site or during the ensuing work addressing review comments on SR-Site.

Delay time

No new insights or results have been obtained on delay time during SR-Site or during the ensuing work addressing review comments on SR-Site.

Time from repository closure to when the defect radius is set to unlimited

No new insights or results have been obtained on defect the time from repository closure to when the defect radius is set to unlimited during SR-Site or during the ensuing work addressing review comments on SR-Site.

Based on these experiences, there has been no need to update these data for the PSAR. Therefore, the data qualification in Sections 4.2.3 to 4.2.10 are, in large, reproduced from the SR-Site Data report. The judgement, by the PSAR assessment team, to use the data for the PSAR is presented in Section 4.2.11 followed by a compilation of the recommended data in Section 4.2.12.

4.2.3 Supplier input on the use of data (text reproduced from SR-Site Data report)

The data supplied in this section have been produced by the SR-Site team; hence no supplier formally exists. None the less, the text is generally written according to the standard outline of the Data report.

In this section, t_{delay} will pessimistically be set to zero for the canister failure due to corrosion, and t_{large} will be set to the time of failure. Because of using this highest degree of pessimism, it is judged that there is no need to qualify these data. Accordingly, the standard outline of the Data report will not be followed for the data for canister failure by corrosion. This failure mode will not be mentioned until in Section 4.2.10 in SR-Site Data report (SKB 2010a), where the data are tabulated.

4.2.4 Sources of information and documentation of data qualification (text reproduced from SR-Site Data report)

Sources of information

For the growing pinhole failure, the sources of information on the delay time and t_{large} are the SR-Site Fuel and **c**anister process report (SKB 2010e) and the SR-Can Data report (SKB 2006b, Section 4.4). Other sources of information are the SR-97 Main report (SKB 1999b, Section 9.6) and its supporting documents (Bond et al. 1997, Takase et al. 1999).

For the canister failure due to shear load, the geometry of the defect is discussed in this section, but there is very limited information on the properties of a shear failure defect. Therefore, pessimistic defect geometries are propagated, which are used to estimate the delay time. This is done by using the same approach as in Bond et al. (1997), by using an equation describing the water inflow into the canister (Wikramaratna et al. 1993). The main sources of information are listed in Table 4-5.

Table 4-5. Main sources of information used in data qualification.

Bond A E, Hoch A R, Jones G D, Tomczyk A J, Wiggin R M, Worraker W J, 1997. Assessment of a spent fuel disposal canister. Assessment studies for a copper canister with cast steel inner component. SKB TR 97-19, Svensk Kärnbränslehantering AB.

SKB, 1999b. SR 97 – Deep repository for spent nuclear fuel. SR 97 – Post-closure safety. Main report – Vol. II. SKB TR-99-06, Svensk Kärnbränslehantering AB.

SKB, 2006b. Data report for the safety assessment SR-Can. SKB TR-06-25, Svensk Kärnbränslehantering AB.

SKB, 2010e. Fuel and canister process report for the safety assessment SR-Site. SKB TR-10-46, Svensk Kärnbränslehantering AB.

Wikramaratna R S, Goodfield M, Rodwell W R, Nash P J, Agg P J, 1993. A preliminary assessment of gas migration from the copper/steel canister. SKB TR 93-31, Svensk Kärnbränslehantering AB.

Categorising data sets as qualified or supporting data

The growing pinhole failure is only used as a hypothetical residual scenario, as there will be no initial pinhole (cf Section 4.1 in the SR-Site Data report (SKB 2010a)). Therefore, the data recommended for SR-Site are based upon the corresponding SR-Can data. However, before qualifying this data set, the argumentation of SR 97 and SR-Can is reviewed. In doing this the argumentation given in Bond et al. (1997), and Wikramaratna et al. (1993) is examined and Equation 3-1 of Bond et al. (1997) is used for calculating the water inflow rate into the canister.

For the canister failure due to shear load, little data exist on the extent of the defect. Therefore, it is assumed to be a circumferential crack where the aperture is varied up to pessimistic values. Based on these apertures the delay time is calculated by using Equation 3-2 of Bond et al. (1997), neglecting any effects of corrosion gases.

The important data sets used in this data qualification are shown in Table 4-6, where also justifications to the sorting of the items are given.

Table 4-6. Qualified and supporting data sets.

Qualified data sets	Supporting data sets
1. SKB (2006b, Table 4-2): Radius of initial defect = 2 mm, t_{delay} = 1 000 years, t_{large} = right triangular distribution in log space with lower value, upper value, and peak value at 0, 10^5, and 10^5 years, respectively.	6. Best estimate corrosion rate for the cast iron insert of 0.1 µm/yr and lower limit corrosion rate of 0.01 µm/yr (Bond et al. 1997).
2. Equation 3-1 in Bond et al. (1997), for calculating the water inflow rate into the canister in case of a pinhole defect.	7. Estimate in Bond et al. (1997) that corrosion consumes intruding water at a matching rate if the defect radius is at or below 1.62 mm.
3. Equation 3-2 in Bond et al. (1997), for calculating the water inflow rate into the canister in case of a circumferential crack defect (it is the same as Equation 6.1.2 in Wikramaratna et al. (1993)).	
4. Canister geometry data from Section 4.1 of the SR-Site Data report (SKB 2010a): canister radius = 0.525 m, void volume = 1.0 m^3.	
5. Hydraulic conductivity of the buffer taken from Section 5.2.12 in the SR-Site Data report (SKB 2010a). Best estimate K = 5×10^{-14} m^2 m/s, upper K = 1×10^{-13} m^2 m/s.	

1. The data given in the SR-Can Data report is considered as qualified. However, as the authorities found the reporting in Section 4.4 unclear, an effort is made to revisit the data.

2–3. Equation 3-1 in Bond et al. (1997) is used for revisiting the delay time for the pinhole case given in SR-Can Data report. Equation 3-2 in Bond et al. (1997) is used for estimating the delay time for canister failure due to shear load. Although Bond et al. (1997) in general is considered as supporting, the equations are judged as qualified.

4–5. These data are used in Equations 3-1 and 3-2 in Bond et al. (1997). The geometry data in item 4 are qualified in the SR-Site Fuel and Canister production report (SKB 2010e) (canister radius) and Section 4.1 of the SR-Site Data report (SKB 2010a) (void volume). The hydraulic conductivity of the buffer is qualified in Section 5.2 of the SR-Site Data report (SKB 2010a).

6–7. Bond et al. (1997) is generally considered as supporting, as the report is written prior to the implementation of the present data qualification framework.

4.2.5 Conditions for which data are supplied (text reproduced from SR-Site Data report)

The delay time is dependent on the time it takes to fill the canister with water, so that a continuous water pathway is established between the spent fuel and the canister exterior. The water inflow rate through a pinhole can be calculated by Wikramaratna et al. (1993) and Bond et al. (1997):

$$Q = 2\pi r_{defect} \frac{\kappa}{\mu} \Delta p \qquad 4\text{-}1$$

where Q (m^3/s) is the water inflow rate, κ (m^2) is the buffer permeability, μ (Pa·s) is the dynamic viscosity of the water, and Δp is the pressure drop over the buffer (i.e. between the rock mass and the interior of the canister). The hydrostatic pressure in the rock mass at 500 m depth is about 5 MPa.

The equivalent equation for a circumferential crack, as in the shear load scenario, is (Bond et al. 1997):

$$Q = -2\pi^2 \frac{\kappa}{\mu} \frac{r_c}{\ln\left(\frac{b}{l}\right)} \Delta p \qquad 4\text{-}2$$

where r_c (m) is the canister radius, b (m) is the buffer thickness, and l (m) is the crack aperture.

As can be seen in Equations 4-1 and 4-2 the water inflow rate is proportional to the permeability of the buffer, which in turn depends on the degree of compaction of the buffer. The permeability can be calculated from the hydraulic conductivity K (m/s) of the buffer, which is given in Section 5.2:

$$\kappa = \frac{K\mu}{\rho g} \qquad 4\text{-}3$$

where ρ (kg/m^3) is the density of water and g is the gravity. For a typical hydraulic conductivity for the buffer of 5×10^{-14} m/s at 20 °C (cf Section 3.2.12 of the SR-Site Data report (SKB 2010a)), the corresponding permeability[11] is 5.1×10^{-21} m^2.

As can be seen in Equations 4-1 and 4-2 the water inflow rate is also proportional to the pressure drop over the buffer. As water intrudes the canister, the cast iron insert will corrode and hydrogen gas will form. According to the SR-Site Fuel and canister process report (SKB 2010e) and Bond et al. (1997) this hydrogen will build up a counter pressure that will more or less match the pressure in the rock, and the water inflow rate will decrease and eventually become zero. Therefore, the way one accounts for corrosion and build-up of a hydrogen pressure are important conditions for the calculation of the delay time.

A simplistic way of calculating the delay time is by dividing the canister void volume V (m^3) by the water inflow rate:

$$t_{delay} = \frac{V}{Q} \qquad 4\text{-}4$$

For a minor defect this is pessimistic, as water is consumed in the corrosion process as it flows into the canister. Bond et al. (1997) estimated that corrosion consume intruding water at a matching rate if the defect radius is at, or below, 1.62 mm. In this estimate a cast iron corrosion rate of 0.1 µm/yr was assumed together with a pressure drop of 5 MPa, which means that the pressure build-up due to hydrogen gas was neglected. Therefore, using Equation 4-4 for the growing pinhole failure, where the initial defect radius is 2 mm, is most likely pessimistic. In case of a major defect, the water inflow rate may be much higher than the consumption rate (at least if neglecting the hydrogen gas pressure build-up).

Concerning t_{large}, this parameter is more dependent on the corrosion rate of the cast iron insert than of the copper corrosion rate. As the cast iron corrodes, the corrosion products will be more voluminous than the metallic cast iron. This will create a stress from the inside of the canister, which could eventually rupture. This was modelled in Bond et al. (1997) and it was found that this is a very slow process. In SR 97 it was assumed that a larger canister failure due to this process would take about 200 000 years (SKB 1999b, Section 9.6.4). In Smart et al. (2002a, b) a series of different corrosion experiments are reported. Part of the study was to investigate the influence of corrosion products and water chemistry on the corrosion rates. The mean corrosion rates were low and generally less than 1 µm per year. The uncertainties in the corrosion rates are further discussed in the SR-Site Fuel and canister process report (SKB 2010e, Section 3.5.1).

[11] Calculated by using $\mu = 1.00 \times 10^{-3}$ Pa·s, $\rho = 1.00 \times 103$ kg/m^3 (Coulson et al. 1990), and g = 9.81 m/s^2.

4.2.6 Conceptual uncertainty (text reproduced from SR-Site Data report)

The processes occurring upon canister failure are described in detail in the SR-Site Fuel and canister process report (SKB 2010e). For the delay time, the description of hydraulic processes is essential (Section 2.3 of the SR-Site Fuel and canister process report (SKB 2010e)). For a small defect, inflowing water is to various degrees consumed by corrosion reactions, which results in a hydrogen pressure build-up that halts further inflow. Accordingly, further transport of water in the defect can only occur by gas phase diffusion of water vapour. For a larger defect, enough water may have flown into the canister before the hydrogen pressure reaches the ambient pressure, and a continuous water pathway between the spent fuel and the canister exterior can be established.

The conceptualisation of the hydraulic situation has very little bearing on the numerical data for the delay time suggested in this section, as one pessimistically neglects any hindrance of water flow into the canister due to the pressure build-up in the canister.

4.2.7 Data uncertainty due to precision, bias, and representativity (text reproduced from SR-Site Data report)

Delay time

By using Equations 4-1, 4-3, and 4-4, the delay time of the growing pinhole failure can be calculated. In doing this, one pessimistically neglects that water is consumed in the corrosion reaction. The hydrogen pressure build-up which would decrease, or even halt, the water inflow is also neglected.

In the following two examples, best estimate and lower delay times are calculated for a 2 mm pinhole, under the prerequisite that realistic buffer properties are used and that the hydrogen pressure build-up is pessimistically neglected. In Section 3.2.12 of the SR-Site Data report (SKB 2010a), the best estimate hydraulic conductivity of the buffer is given as 5×10^{-14} m/s, which translates to a permeability of 5.1×10^{-21} m^2. For the pressure drop over the canister the value 5 MPa is assumed, which equals the external water pressure at repository depth. The void is assumed to be the total void of 1.0 m^3, as suggested for the average canister in Table 4-3 of the SR-Site Data report (SKB 2010a). The viscosity depends on the water temperature and in our calculations a relatively high water temperature of 75 °C is assumed, with a corresponding viscosity of 3.8×10^{-4} Pa·s (Coulson et al. 1990). By inserting all the above data into Equations 4-1, 4-3, and 4-4, the delay time equals about 3.8×10^4 years. If, in a second example, instead using the lowest hydraulic conductivity suggested in Section 5.2 of the SR-Site Data report (SKB 2010a) (1×10^{-13} m/s), and assuming a water temperature of 100 °C (thereby decreasing the water viscosity to the lowest possible), the delay time becomes[12] about 1.4×10^4 years.

In SR-Can, the pessimistic delay time of 1 000 years was suggested for the pinhole case. This low value would encompass a buffer hydraulic conductivity much lower than the range specified in the design premises, alternatively a much larger defect radius than 2 mm (about 70 mm if using the same data as in the first example above). As seen in Section 4.2.10 of the SR-Site Data report (SKB 2010a), this unrealistically low delay time is suggested to be adopted also for SR-Site, justified by the fact that the scenario is only residual and as there in the real case will be no pinhole. Accordingly, the accuracy of the used data is of lesser concern. In light of this, data uncertainty becomes subordinate.

For the canister failure due to shear load giving rise to a circumferential crack, the delay time can be calculated by Equations 4-2, 4-3, and 4-4. The pessimism of neglecting the hydrogen pressure build-up is adopted from the above case. For the permeability, the best estimate value of 5.1×10^{-21} m^2 is adopted together with the dynamic viscosity at 75 °C. The buffer thickness is assumed to be reduced to 25 cm, as a result of the shear movement.

Finally, for the defect aperture the values 1 mm and 10 mm are suggested. For these values the delay time becomes on the order of 100 years (147 years for the larger aperture and 252 years for the smaller aperture). Also in this case data uncertainty is overshadowed by the degree of pessimism adopted in neglecting the hydrogen pressure build-up. (If the shear movement instead would induce a circular defect, the defect radius corresponding to a delay time of about 100 years would be very large; on the decimetre scale.)

[12] Calculated by using $\mu = 0.287 \times 10^{-3}$ Pa·s (Coulson et al. 1990).

Defect radius and t_{large}

For the growing pinhole failure the defect radius is initially set to 2 mm. It is assumed to be of constant radius until the time t_{large}, when the defect radius becomes sufficiently large to offer no transport resistance (r_{defect} set to unlimited).

In Bond et al. (1997), t_{large} was assessed for a pinhole case where it was assumed that water vapour could diffuse into the canister, but that water flow was hindered as the hydrogen pressure in the canister matches the external water pressure. According to the calculations, it takes at least 100 000 years from the time of the initial penetration before more extensive damage occurs on the copper canister. On the other hand, if pessimistically assuming that water can flow into the canister unhindered, thus neglecting the hydrogen pressure build-up, one could argue for a considerably lower t_{large}. In SR-Can this uncertainty was handled by suggesting a right triangular distribution in the log-space for t_{large}, with one year as the lower limit and 100 000 years as the upper limit and peak value. By setting the peak value at 100 000 years, instead of in the middle of the range, it was implicitly stated that one considers it more reasonable, from a process understanding point of view, that the water ingress is diffusion controlled and much less probable than that water flows into the canister. For SR-Site modelling, only a single point values is requested. The arithmetic mean of the SR-Can distribution is around 1.6×10^4 years. For SR-Site this is suggested to be cautiously rounded to 1×10^4 years.

For the canister failure due to shear load, the initial circumferential crack is assumed to be so large that the canister immediately loses its transport resistance. Accordingly it is suggested to set t_{large} equal to the time of failure and r_{defect} to unlimited.

In the above example, the degree of pessimism overshadows any effect of data uncertainty in input data.

4.2.8 Spatial and temporal variability of data (text reproduced from SR-Site Data report)

Spatial variability of data

The description of the canister failure is general and no spatial variability is accounted for.

Temporal variability of data

The temporal variability concerning the onset of radionuclide transport is handled by assuming no radionuclide transport prior to t_{delay}, while radionuclide transport subsequent to t_{delay} takes place.

The temporal variability concerning the growing pinhole defect is handled by assuming a constant defect radius until the time t_{large}, when the defect momentarily becomes infinitely large.

4.2.9 Correlations (text reproduced from SR-Site Data report)

This section only supplies single point values. Accordingly there is no need to account for correlations in subsequent modelling.

4.2.10 Result of supplier's data qualification (text reproduced from SR-Site Data report)

The growing pinhole failure

For the growing pinhole failure, the following pessimistic values are suggested:

- $t_{delay} = 1 \times 10^3$ yr
- $t_{large} = 1 \times 10^4$ yr
- $r_{defect} = 2$ mm prior to t_{large} and unlimited subsequent to t_{large}

The t_{delay} and t_{large} values are justified in Section 4.2.7 of the SR-Site Data report (SKB 2010a).

Canister failure due to corrosion

For the canister failure due to corrosion, the most pessimistic values are suggested:

- $t_{delay} = 0$
- t_{large} = same as time of failure (penetrated copper shell)
- r_{defect} = unlimited subsequent to failure

Canister failure due to shear load

For the canister failure due to shear load, the following cautious values are suggested:

- $t_{delay} = 1 \times 10^2$ yr
- t_{large} = same as time of failure (penetrated copper shell)
- r_{defect} = unlimited subsequent to failure

The values are justified in Section 4.2.7 of the SR-Site Data report (SKB 2010a). It should be noted that in this case the onset of radionuclide transport is governed by the time of failure plus the delay time.

4.2.11 Judgement by the assessment team

Defect radius

Since no new information or data has been obtained, the judgement is to use the same data as in SR-Site.

Delay time

Since no new information or data has been obtained, the judgement is to use the same data as in SR-Site.

Time from repository closure to when the defect radius is set to unlimited

Since no new information or data has been obtained, the judgement is to use the same data as in SR-Site.

4.2.12 Data recommended for use in assessment

The following data are recommended for use in radionuclide transport modelling.

Table 4-7. Data recommended for use in the PSAR.

Canister failure due to	t_{delay} (yr)	t_{large} (yr)	r_{defect} (m)
Growing pinhole	1×10^3	1×10^4	0.002 priori to t_{large} Unlimited subsequent to t_{large}
Corrosion	0	Same as time of failure.	Unlimited subsequent to failure.
Shear load	1×10^2	Same as time of failure.	Unlimited subsequent to failure.

5 Buffer and backfill data

5.1 Density and porosity of buffer and backfill

This section concerns the density and physical porosity of the reference buffer and backfill. In PSAR, MX-80 bentonite serves as an example of a buffer material while the reference backfill is a lower grade bentonite, with Asha-2012 as an example. Since SR-Site, the reference design of both the buffer and backfill has been updated and as a consequence also the initial state for the PSAR as further discussed in the **Post-closure safety report**.

For SR-Site, an assessment of the performance of buffer and backfill was reported in Åkesson et al. (2010a). As shown later in this section, the difference between the initial state used in Åkesson et al. (2010a) and the initial state used in the PSAR will have limited impact on the results of that assessment. Åkesson et al. (2010a) as well as some other SR-Site assessment calculations that are based on the density and porosity of buffer and backfill have therefore not been updated for the PSAR.

The **Buffer production report** presents the technical design requirements, the reference design of a bentonite buffer, verifying analyses showing that the reference design fulfils the design premises requirements and the production and control procedures selected to achieve the reference design. The report also includes an account of the achieved results from test manufacturing and buffer installation.

To guide the design and production of the buffer, technical design requirements on characteristics that can be inspected and verified in the production are stated (Posiva SKB 2017). The technical design requirements are based on the assessment of the post-closure evolution of the buffer in the repository and available technology and shall be fulfilled at initial state.

- The following shall be *determined* for the selected buffer material:
  - the maximum dry density yielding a swelling pressure < 10 MPa when determined with a specified laboratory test procedure,
  - the minimum dry density yielding a swelling pressure > 3 MPa when determined with a specified laboratory test procedure,
  - the minimum dry density yielding a hydraulic conductivity in saturated state < 10^{-12} m/s when determined with a specified laboratory test procedure,
  - the maximum dry density yielding an unconfined compressive strength at failure < 4 MPa at a deformation rate of 0.8 %/min when determined with a specified laboratory test procedure, and for material specimens in contact with waters with less favourable characteristics than site-specific groundwater, i.e. deionised water and water with a salinity of 1 M $CaCl_2$ respectively to cover uncertainties with a margin.
- The buffer volume shall be cylindrical and determined from its cross sectional area in the deposition hole and its height, i.e. the sum of its thickness above and below the canister and the distance between the surface of the canister lid and bottom, minus the canister volume.
- The buffer thickness shall be
  - at least 50 cm below the canister
  - at least 50 cm above the canister
  - at least 30 cm around the canister.
- The installed buffer material mass shall in average in the buffer volume result in
  - a dry density ≥ the lowest required material-specific dry density determined for the specific buffer material,
  - a dry density ≤ the highest allowed dry density determined for the specific buffer material.
  - The installed dry density shall be > 1 000 kg/m^3, to filter colloids.
- Acceptable contents of impurities:
  - organic carbon should be less than 1 wt-%,
  - sulphide should not exceed 0.5 wt-% of the total mass, corresponding to approximately 1 wt-% of pyrite,
  - total sulphur (including the sulphide) should not exceed 1 wt-%.

Furthermore, the thermal conductivity over the installed buffer shall, given the allowed decay power in the canister, the thermal properties of the canister and the rock and the canister spacing, yield a buffer temperature < 100 °C.

The reference design of the buffer is described by a set of *design parameters* for which nominal values and acceptable variations are given. The design parameters will be inspected in the production to confirm that the installed buffer conforms to the reference design and to provide an estimate of the actual properties of the buffer at the initial state.

The initial state represents the installed buffer blocks and pellets with dry densities given by the manufacturing process. The parameters in the initial state should produce a saturated buffer that lies within the required swelling pressure, hydraulic conductivity and compressive strength after saturation for every cross-section that mechanically can affect the canister in the deposition hole, neglecting the effects of incomplete homogenization.

When adapting the design of the buffer it is generally the swelling pressure which is the governing parameter and a design is made aiming at approximately 10 MPa. Blocks and ring are given starting dry densities which is applied in a simulation of 10 000 deposition holes including the tolerances of the rock excavation (deposition hole), buffer components (blocks, rings and pellets) and the canister volume (which is set as a constant). The calculations result in an average installed buffer dry density including standard deviation data. A 95 % confidence is applied and the calculations are iterated until appropriate block and ring dry densities can be decided. The results are presented in Table 5-1. The swelling pressure is within the acceptance interval (3–10 MPa) in the ring section around the canister. The swelling pressure in the block section above the canister will be higher, which is acceptable.

Table 5-1. Results of simulation of variation between deposition holes of average key buffer properties within a hole. Resulting dry densities with standard deviation and 95 % confidence. Corresponding maximum (1M $CaCl_2$ solutions) and minimum (deionised water) swelling pressures are given (Table 2-5 in the Buffer, backfill and closure process report).

Without heave	Dry density (kg/m^3)	Std dev	Dry density min (kg/m^3)	Dry density max (kg/m^3)	Swelling pressure min, $CaCl_2$ (kPa)	Swelling pressure max, Deion (kPa)
Average deposition hole	1547.1	3.3	1540.5	1553.6	6906	9711
Block section	1584.0	3.7	1576.8	1591.3	9772	12664
Ring section	1509.3	4.0	1501.6	1517.0	4756	7504

In the **Buffer production report** it is concluded that the methods for producing the buffer will yield installed average densities that fulfil the specification of the reference design.

The **Backfill production report** presents the technical design requirements, the reference design, verifying analyses that the reference design does fulfil the design requirements, the production and control procedures selected to achieve the reference design, verifying analyses that these procedures do achieve the reference design and an account of the achieved initial state of the deposition tunnel backfill.

The installed dry density in the backfill shall be > 1 361 kg/m^3 on average between two deposition holes. The average installed backfill dry density will depend on the density and dimensions of the installed blocks and pellets, i.e. the installed buffer mass and the backfill geometry which is dependent on the excavated tunnel volumes. The dimensions of the tunnel and the installed mass will be registered during installation and the average installed dry density calculated to ensure that the properties at initial state fulfil the reference design.

Based on the initial state values of the design parameters of the backfill and the deposition tunnel volumes the installed dry density, mass and porosity to be used in the PSAR have been calculated, the results are presented in Table 5-2. The reference design values are given as comparison.

During operation some backfill material in already completed and plugged deposition tunnels may be lost by piping and erosion. Material may also be lost in the future during the assessment period both during and after saturation of the backfill. Countermeasures related to piping erosion during installation due to water inflow has been taken in the reference design of the pellets surrounding the block pile, see the **Backfill production report**.

Table 5-2. The backfill design parameters at the initial state (Table 2-16 in the Buffer, backfill and closure process report).

Design parameter	Reference design and initial state	Acceptable tolerances
Dry density of blocks (Asha 2012) (kg/m^3)		
– Tunnel section	1 725	≥ 1 650
Dry density of pellet filling (kg/m^3)	900	≥ 850
– Bottom bed		
– Between blocks and rock wall		
– Bevel in deposition hole		
Geometry	Nominal: Figure 2-8 in the **Buffer, backfill and closure process report**	
Average dry density in deposition tunnel (Asha 2012)*	1 437* – 1 488	≥ 1 361

** Interval is given by variations in the tunnel volume (18 to 30 % overbreak).*

The porosity and density are inputs to Sections 5.2 and 5.3, where hydraulic and solute transport properties of the buffer and backfill are discussed. The physical porosity can be assessed by knowing the dry or the saturated density of the clay material, and the density of the solid clay particles.

5.1.1 Modelling

This section describes what data are expected from the supplier, and in what modelling activities the data are to be used. Due to a revision of the requirements (Posiva SKB 2017) the material density has changed since SR-Site. The average dry density for the buffer in a deposition hole in SR-Site was 1 562 kg/m^3 while it is 1 550 kg/m^3 in PSAR. However, since the changes are small and that the results are relative insensitiv to the parameters, the modelling activities have not been updated which is further described in the following section.

Defining the data requested from the supplier

The qualification of buffer density data is performed within the **Buffer production report**. For the installed reference buffer, the supplier should deliver:

- Data showing that the installed buffer, upon saturation, has a dry density ρ_s (kg/m^3) within the design premises interval

Based on this information, a saturated density as well as a physical porosity can be derived.

The qualification of backfill density data is performed within the **Backfill production report**. Furthermore, the justification that the reference design complies with the design premises is given in the **Backfill production report.** For the reference backfill, the supplier should deliver:

- Dry density data ρ_d (kg/m^3) of the installed backfill showing that the backfill can be produced and installed in such a way that it conforms to design premises.

Based on this information a saturated density as well as a physical porosity can be derived. The relation used to calculate physical porosity from dry density is:

$$n = 1 - \frac{\rho_d}{\rho_s} \qquad 5\text{-}1$$

Where ρ_s (kg/m^3) is the specific density of solid particles (grain density), where the value 2.78 kg/m^3 can be used for MX-80 (Svensson et al. 2019). The equation used to calculate the saturated density from dry density is:

$$\rho_m = \rho_d + n \cdot \rho_w \qquad 5\text{-}2$$

Where ρ_w (kg/m^3) is the water density of the typical value 1 000 kg/m^3.

Modelling activities in which data will be used

Buffer and backfill porosities and densities qualified in the SR-Site Data report were used in hydrogeological modelling as summarised in Selroos and Follin (2010), these calculations have has not been updated for the PSAR.

Buffer and backfill porosities and densities, qualified in the SR-Site Data report are also used for radionuclide transport calculations presented in the **Radionuclide transport report**. It should be noted that the diffusion-available porosity, delivered in Section 5.3, should be used when modelling diffusive transport in the buffer and backfill, and not the physical porosity delivered in this section.

5.1.2 Experience from SR-Site

This section briefly summarises experience from the SR-Site safety assessment, which may be of direct consequence for the data qualification in this Data report.

Modelling in SR-Site

Buffer and backfill porosities and densities qualified in the SR-Site Data report were used for hydrogeological modelling and Radionuclide transport calculations.

Conditions for which data were used in SR-Site

For the buffer, the same reference material was use in SR-Site as in the PSAR. However, for the backfill, the reference material has been changed, but the relevant properties are expected to be similar.

Except for the material itself, the degree of compaction influences the density and porosity data. Similar degrees of compactions were of concern for SR-Site as for the PSAR. No other condition significantly affects the data.

Sensitivity to assessment results in SR-Site

As long as the buffer density conforms to the design premises interval, and as long as the backfill density is high enough so that other design premises (hydraulic conductivity etc) conform to design premises, the actual values of the buffer and backfill densities have little effect on repository safety. In this respect the assumed densities for the buffer and backfill had little influence on assessment results in SR-Site.

If the buffer erodes to the point where advective conditions prevail in the deposition hole, this has major consequences for assessment results. However, this section concerns the installed buffer and backfill, prior to potential post-closure buffer and backfill removal. When assessing buffer erosion, it is rather the composition of the buffer material, as well as the advective flow and the groundwater composition, that are of importance, whereas the initial density of the buffer should be of little consequence.

In the backfill, advective flow was of some importance in SR-Site. The hydraulic conductivity is dependent on the backfill density in a non-linear but monotonic fashion. In case of a too low density, the hydraulic flow field in the repository may change, which may significantly affect the safety assessment. This is especially true if also other tunnels than the deposition tunnels are filled with a backfill of too low density. However, the backfill densities considered in SR-Site were not low enough to substantially impact the assessment results in this way.

Alternative modelling in SR-Site

No alternative modelling of the porosity and densities was used in SR-Site.

Correlations used in SR-Site modelling

The correlations (or functional relationships) between the density and porosity (e.g. Equations 5-1 and 5-2) used in the PSAR and SR-Site agree. A number of parameters of different subject areas were in SR-Site correlated to the density, such as swelling pressure and hydraulic conductivity. Similar correlations are used in the PSAR.

Identified limitations of the data used in SR-Site modelling

For the reference buffer of SR-Site, there remained issues on how it should be produced and installed, which affected the data.

5.1.3 Supplier input on the use of data

The supplier has no additional input on the use of data, but points out that the data in the Buffer production report and the Backfill production report have been produced in communication with the assessment team.

5.1.4 Sources of information and documentation of data qualification

Sources of information

The data presented in the **Buffer production report and the Backfill production report** are qualified in these reports**.** Therefore, only these reports are sources of information for the Data report. The scrutinising of lower level references is part of the qualification process of the production reports and is not dealt with in the Data report**.**

Table 5-3. Main sources of information used in data qualification.

Buffer production report, 2022. Produktionsrapport Buffert. SKBdoc 1392269 ver 5.0, Svensk Kärnbränslehantering AB. (In Swedish.) (Internal document.)
Backfill production report, 2022. Produktionsrapport Återfyllning. SKBdoc 1525864 ver 4.0, Svensk Kärnbränslehantering AB. (In Swedish.) (Internal document.)

Categorising data sets as qualified or supporting

Table 5-4 shows the data sets of the production reports that are used as bases for this section. The table also gives the motivation for the sorting of the data sets as qualified.

Table 5-4. Qualified and supporting data sets.

Qualified data sets	Supporting data sets
1. **Buffer production report** Section 2.3.1 for “Results of simulation of variation between deposition holes of average key buffer properties within a hole “, reproduced in Table 5-1.	
2. **Backfill production report**, Section 4.2 Table 4-2 “Reference design of installed backfill”. Reproduced in Table 5-6.	
1–2. Data delivered in the **Buffer production report** are qualified in the **Buffer production report**. Data delivered in the **Backfill production report** are qualified in the **Backfill production report**. This is in accordance with the SKB quality assurance system and comply with the demands of the Data report.	

Excluded data previously conidered as important

No such data have been excluded for the considered materials.

5.1.5 Conditions for which data are supplied

The reference buffer material is described in the **Buffer production report**. Example of the reference buffer material is MX-80 bentonite. The reference backfill material is described in the **Backfill production report**. An example of the backfill material is Asha 2012.

An important condition is the degree of compaction. Methods of production and installation are discussed in the production reports.

When the buffer and backfill are installed, they are only partly saturated. As an effect of the saturation, the buffer and backfill will swell and there should be no gap between the deposition hole or tunnel wall and the clay material. The data supplied should represent homogenised cross section areas of the deposition hole and tunnel, respectively.

The density and porosity are not expected to be significantly affected by groundwater chemistry, temperature, or other conditions. There may be anion exclusion effects in the porous system, but these are discussed in Section 5.3. In case the clay material is removed, for example through buffer erosion, the density and porosity may be altered. However, such post-closure removal is not a focus of attention in this section.

5.1.6 Conceptual uncertainty

There is no significant conceptual uncertainty regarding the saturated and dry densities, or the physical porosity, of the installed buffer and backfill. Conceptual uncertainty related to how the porous system affects hydraulic properties of, and the migration in, the buffer and backfill is discussed in Sections 5.2 and 5.3.

5.1.7 Data uncertainty due to precision, bias, and representativity

The data uncertainty associated with the buffer and backfill mainly concerns the degree of accuracy with which the buffer and backfill can be produced and installed. The precision, bias, and representativity of experimental measurement add little to the data uncertainty, compared to uncertainties in how well production and installation can be performed. In this case, the data uncertainty has not been separated from spatial variability.

Buffer density

The initial state represents the installed buffer blocks and pellets with dry densities given by the manufacturing process. The parameters in the initial state should produce a saturated buffer that lies within the required swelling pressure, hydraulic conductivity and compressive strength after saturation for every cross-section that mechanically can affect the canister in the deposition hole, neglecting the effects of incomplete homogenization.

The average installed buffer dry density will depend on the density and dimensions of the installed blocks and pellets, i.e. the installed buffer mass, and the volumes of the deposition hole and canister. The impact of the variations of volume of the canister and dimensions of the blocks on the installed buffer density can be neglected. The important parameters are the installed density of the blocks and pellets and the volume of the deposition hole.

When adapting the design of the buffer it is generally the swelling pressure which is the governing parameter and a design is made aiming at approximately 10 MPa. Blocks and ring are given starting dry densities which is applied in a simulation of 10 000 deposition holes including the tolerances of the rock excavation (deposition hole), buffer components (blocks, rings and pellets) and the canister volume (which is set as a constant). The calculations result in an average installed buffer dry density including standard deviation data. A 95 % confidence is applied and the calculations are iterated until appropriate block and ring dry densities can be decided. The results are presented in Table 5-1. The swelling pressure is within the acceptance interval (3–10 MPa) in the ring section around the canister. The swelling pressure in the block section above the canister will be higher, which is acceptable, since this part will have a smaller impact on the canister. It will also allow for some expansion into the backfill.

Backfill density

The installed dry density of the backfill will depend on the volume of the deposition tunnel and the mass of backfill material installed in the tunnel. The installed density is calculated per tunnel section, defined as the average distance between two deposition holes, i.e. about 6 m. The calculated installed density for the reference design of backfill components according to Table 5-5 and the installed backfill according to Table 5-6, are set out in Table 5-7.

The calculated average dry density in a backfilled tunnel section is reported in the **Backfill production report**. The calculated dry density of Asha 2012 is 1 488 kg/m^3 if the design parameters for the backfill have their nominal values and the excavated tunnel volume including the expected average of 18 % overbreak. At 30 % overbreak, the corresponding calculated average density is 1 437 kg/m^3. At both these values, the interval of acceptance for Asha 2012 on installed dry density is achieved. Even the lowest calculated density that can be obtained with the present design, that is when all design parameters have their lowest accepted value, meets the interval of acceptance.

Table 5-5. Reference blocks and pellets ready for installation, based on Asha 2012 (Table 2-10 in the Buffer, backfill and closure process report).

Design parameter	Nominal design	Accepted variation
Blocks		
Dry density Asha 2012 (kg/m^3)	1 725	≥ 1 650
Water content (%)	20 (As in the material ready for compaction)	± 1.5 (As in the material ready for compaction)
Dimensions (mm^3)	500 × 571 × 400	± 1 × 1 × 2
Tensile strength (kPa)	-	> 200
Pellets		
Dry density Asha 2012 (kg/m^3)	900	≥ 850
Dimensions (mm^3)	∅ 6 L: 6-22	-
Water content		< 20
Pellet durability		Sufficient to have less than 10 % fine material in the pellets filling

Table 5-6. Reference design of installed backfill, based on Asha 2012 (Table 2-11 in the Buffer, backfill and closure process report).

Design parameter	Nominal design	Accepted variation
Blocks		
Geometry	According to Figure 2-8 in the **Buffer, backfill and closure process report**	The number of blocks must not be changed
Free space between blocks and nominal tunnel profile (mm)	100	≥ 100
Pellet filling in gap between blocks and tunnel walls		
Pellet-filled proportion of free space between block and tunnel wall (%)	94	≥ 90
Percentage of fine material in the installed pellet filling (%)	-	< 10
Pellet bottom bed		
Thickness (above theoretical floor above deposition hole (mm)	100	± 20
Surface roughness (mm)	Perfectly even	± 5
Calculated installed average dry density between deposition holes		
Dry density Asha 2012 (kg/m^3)	1 488	≤ 1 361

1) In the reference design buffer blocks are used and the design parameters are the ones specified for solid blocks in the **Buffer production report***, Table 3-4.*

2) In the reference design the same kind of pellets are used for the bottom bed and the gap between the blocks and tunnel walls. This may be changed.

Table 5-7. Calculated average installed backfill dry density for reference design with Asha 2012 (Table 2-12 in the Buffer, backfill and closure process report).

Design parameter	Value, average overbreak (V_t = 136.5 m^3)	Value, highest acceptable overbreak (V_t = 150.4 m^3)
Dry density blocks	1 725 kg/m^3	1 725 kg/m^3
Volyme, block stack incl. space between blocks	100.7 m^3	100.7 m^3
Dry density, pellets	980 kg/m^3	980 kg/m^3
Volume, free space between blocks and tunnel profile	30.2 m^3	44.1 m^3
Volume, pellets bottom bed	5.6 m^3	5.6 m^3
Volume, pellets bevel in deposition hole	1.9 m^3	1.9 m^3
Degree of filling, pellets between block stack and rock	94 %	94 %
Degree of filling, pellets bottom bed and bevel	100 %	100 %
Average dry density in tunnel section with one deposition hole	1 488 kg/m^3	1 437 kg/m^3

Buffer and backfill porosity

The estimation of porosities is based on the installed densities from SR-Site. No new assessment has been made for the PSAR.

For the buffer, the porosities corresponding the saturated densities 1 950 and 2 050 kg/m^3 are estimated to 0.46 and 0.41, respectively**.** This estimate depends on the assumed density of solid particles ρ_s. This density is suggested to be within the range 2.75–2.78 kg/m^3.

For the backfill, the porosities corresponding to the dry densities 1 458, 1 504, and 1 535 kg/m^3 are estimated to 0.44, 0.46 and 0.48, respectively. The density of solid particles ρ_s is assumed to be 2 780.

The uncertainty in the porosity is equally affected by uncertainties in the dry and saturated densities of the buffer and backfill, as by the uncertainty in the density of solid particles. All in all, the porosity ranges are narrow, and the overall uncertainty in the porosity is small.

5.1.8 Spatial and temporal variability of data

The spatial variability of the data in the different cross sections of deposition holes and tunnels depends on the production and installation of the buffer and backfill. In this case, variation in data due to spatial variability has not been separated from other data uncertainty. Therefore, Section 5.1.7 is referred to.

There will be temporal variability in the data as the buffer and backfill becomes saturated. Furthermore, erosion and other possible processes of buffer and backfill removal may cause temporal variability. However, such processes are to be studied within the PSAR and are not accounted for in this Data report. The data delivered here concern the buffer and backfill at the time of installation.

5.1.9 Correlations

Examples of functional relationships between densities and the porosity used in the PSAR modelling are shown in Equation 5-1 and 5-2. Other data, for example hydraulic conductivity, swelling pressure, etc are correlated to the density.

5.1.10 Result of supplier's data qualification

Buffer

It is suggested that the buffer can be produced and installed in such a way that the design premises are fulfilled. Thus the dry density ρ_d is in the interval:

$1\,544\ kg/m^3 < \rho_d < 1\,556\ kg/m^3$

However, hydrogeological and readionuclide transport modelling from SR-Site has not been updated. Consequently data from SR-Site Data report (SKB 2010a) are used. This means that the saturated density ρ_m is in the interval:

$1\,950\ kg/m^3 < \rho_m < 2\,050\ kg/m^3$

This corresponds to the porosity interval:

$0.41 < n < 0.46$

Furthermore, experimental data suggest that one can produce and install the buffer in such a way that it is more likely to obtain buffer densities and porosities in the centre of the interval, than at the boundaries.

Backfill

The dry density of the installed backfill is given as an average value, and as upper and lower limits, according to Table 5-8. In the table, the corresponding porosities are also given. The values in the table are from SR-Site and do not correspond to the reference design in the PSAR.

Table 5-8. Dry density and physical porosity data used for the for the backfill in PSAR. (Data are taken from SR-Site and are not consistent with the data presented in Section 5.1.7).

	Dry density (kg/m^3)	Porosity (–)
Lower limit density	1458	0.48
Average density	1504	0.46
Upper limit density	1535	0.44

5.1.11 Judgement by the assessment team

As a result of development work of buffer and backfill conducted after SR-Site the reference design as, presented in the PSAR **Buffer production report** and **Backfill production report** has been updated. There are differences in the target dry density for the buffer compared to SR-Site. The relative difference in mass and porosity is however minor and the data set from SR-Site is therefore still used in assessment calculations.

5.1.12 Data recommended for use in assessment

Table 5-9 compiles the dry and saturated densities, as well as the porosity, recommended for use in the assessment for the reference buffer. Table 5-10 compiles the dry and saturated densities, as well as the porosity, recommended for use in the assessment for the reference backfill. As previously menitioned, the recommended data set is identical to that of SR-Site and has not been updated to reflect to updated reference design in the PSAR.

Table 5-9. Data for the reference buffer, recommended for usethe the PSAR.

Data	Values	Distribution
Saturated density ρ_m	Lower boundary = 1950 kg/m^3 Peak value = 2000 kg/m^3 Upper boundary = 2050 kg/m^3	Triangular distribution in normal space
Porosity n	Lower boundary = 41 % Peak value = 43.5 % Upper boundary = 46 %	Triangular distribution in normal space
Dry density ρ_d	Lower boundary = 1484 kg/m^3 Peak value = 1562 kg/m^3 Upper boundary = 1640 kg/m^3	Triangular distribution in normal space

Table 5-10. Data for the reference backfill, recommended for use in the PSAR.

Data	Values	Distribution
Saturated density ρ_m	Lower boundary = 1 921 kg/m^3 Peak value = 1 963 kg/m^3 Upper boundary = 1 983 kg/m^3	Double triangular distribution in normal space
Porosity n	Lower boundary = 44 % Peak value = 46 % Upper boundary = 48 %	Triangular distribution in normal space
Dry density ρ_d	Lower boundary = 1 458 kg/m^3 Peak value = 1 504 kg/m^3 Upper boundary = 1 535 kg/m^3	Double triangular distribution in normal space

5.2 Hydraulic properties of buffer and backfill

This section describes the hydraulic properties of the buffer and backfill used in the hydrogeological modelling. It also describes the hydraulic conductivity of the buffer used in calculations of water ingress into failed canisters.

After SR-Site, the development work on buffer and backfill has continued and the reference design has been updated as presented in the **Buffer production report** and the **Backfill production report**. The target hydraulic properties (presented as *better than*) that were used in SR-Site hydrogeological simulation have not been updated for the PSAR. However, since the PSAR is based on an updated reference design the data qualification in this PSAR Data raport has been revisited.

5.2.1 Modelling

Defining the data requested from the supplier

For the installed and saturated reference buffer, the data required are:

- The hydraulic conductivity K (m/s) corresponding to the target value of the dry density 1 556 kg/m^3, and its lower boundary values 1 544 kg/m^3.

For the installed reference backfill of the deposition tunnels, the data required are:

- The hydraulic conductivity K (m/s) corresponding to the lower boundary value for the dry density of 1 437 kg/m^3.

For the filled deposition holes, backfilled tunnels and underground openings data are required for the hydraulic conductivity K (m/s) used in hydrogeological modelling.

In SR-Site "crown space" was assessed as a variant (Joyce et al. 2010). Once the repository has been closed, the deposition tunnels will be backfilled with low permeability material, typically bentonite, which may consolidate over a period of time. This settlement of the backfill may leave a crown space between the top of the backfill and the top of the tunnel. The crown space may lead to extra flow in the repository and provide additional transport pathways for particles. A variant considers a case with a crown space included, but it is expected that there will always be a swelling pressure of the backfill such that a crown space will not develop in reality (Åkesson et al. 2010b).

Modelling activities in which data will be used

The primary use for the hydraulic conductivity of the buffer is to assess whether diffusion is the dominant transport mechanism. This is the case when the buffer hydraulic conductivity is $< 10^{-12}$ m/s (e.g. Table 2-3 of the **Buffer, backfill and closure process report**). This assessment has been revisited for the PSAR.

The hydraulic conductivity of the backfill is used in groundwater flow modelling of periods with temperate climate conditions using the ConnectFlow software (Joyce et al. 2010, Selroos and Follin 2010). In this modelling the repository with its backfilled deposition tunnels, and other underground openings, is included (cf Section 6.6). To account for the groundwater flow in these tunnels and underground openings, the hydraulic conductivity of the backfill is required. These simulations have not been updated for the PSAR.

In Section 4.2 of this Data report, the water ingress rate into a failed canister is used to calculate the delay time, which is the time it takes from canister failure to the formation of a continuous water pathway between the fuel and canister exterior. This calculation uses the hydraulic conductivity of the buffer as input.

5.2.2 Experience from SR-Site

This section briefly summarises experience from the SR-Site safety assessment, which may be of direct consequence for the data qualification in this Data report.

Modelling in SR-Site

Backfilled tunnels were explicitly included in the hydrogeological modelling in SR-Site in a similar manner as in the PSAR. The chosen hydraulic conductivity values were 1×10^{-10} m/s for the backfill and 1×10^{-11} m/s for the buffer.

The hydraulic conductivity of the buffer was indirectly used as background information when assigning the delay time in SR-Site, although the delay time was set pessimistically in a manner that did not reflect on the precise values of the estimated hydraulic conductivity.

Conditions for which data were used in SR-Site

For the buffer, the same reference material with a similar degree of compaction was use in SR-Site as in the PSAR. For the backfill, the material has been changed, but the properties are assumed to be simular.

Sensitivity to assessment results in SR-Site

A degraded tunnel backfill case was considered in SR-Site. For this case, the only change was to use a hydraulic conductivity of 1×10^{-8} m/s. The sensitivity to the backfill properties was limited since the system of deposition tunnels was arranged orthogonal to the head gradients.

The hydraulic conductivity of the buffer had little effect on the chosen delay time in SR-Site, as very pessimistic values were suggested. For the probable failure modes included in the main scenario, the delay time was set to zero. Accordingly, the hydraulic conductivity was of no consequence.

Alternative modelling in SR-Site

No alternative way of modelling or representing the hydraulic properties of the buffer and backfill was used in SR-Site.

Correlations used in SR-Site modelling

Similar correlations and functional relationships were used in SR-Site as are used in the PSAR.

Although the experiences from SR-Site does not warrant an update of the data qualification for the PSAR the updated reference design as presented in the **Buffer production report** and the **Backfill production report** is based on further studies which are also included in the data qualification in the following sections.

5.2.3 Supplier input on the use of data

The realistic data presented for the buffer and backfill are based on measurements, as compiled in Svensson et al. (2019) and Fritzell (2017). As stated in the **Buffer, backfill and closure process report** (Sections 3.3.2 and 4.2.2, Section "Handling in the PSAR") the suggested data on the hydraulic conductivity of the buffer and backfill should be based on empirical data.

5.2.4 Sources of information and documentation of data qualification

Sources of information

The main sources of information are Svensson et al. (2019) and Fritzell (2017) which are supporting documents to the **Buffer production report** and the **Backfill production report.** The recommended data in Åkesson et al. (2010a) for the reference buffer are based on Börgesson et al. (1995) and Karnland et al. (2000, 2006, 2009). In Johannesson et al. (2010) data for the reference backfill are supplied. The buffer and backfill materials are described in the **Buffer production report** and the **Backfill production report**. The hydraulic conductivities of the buffer and backfill actually used in hydrogeological modelling are compiled in Joyce et al. (2010). The full references to Åkesson et al. (2010a), Johannesson et al. (2010) and Joyce et al. (2010) are given in Table 5-11.

Table 5-11. Main sources of information used in data qualification.

Åkesson M, Börgesson L, Kristensson O, 2010. SR-Site Data report. THM modelling of buffer, backfill and other system components. SKB TR-10-44, Svensk Kärnbränslehantering AB.
Johannesson L-E, Sandén T, Dueck A, Ohlsson L, 2010. Characterization of a backfill candidate material, IBECO-RWC-BF. Baclo Project – Phase 3. SKB R-10-44, Svensk Kärnbränslehantering AB.
Joyce S, Simpson T, Hartley L, Applegate D, Hoek J, Jackson P, Swan D, Marsic N, Follin S, 2010. Groundwater flow modelling of periods with temperate climate conditions – Forsmark. SKB R-09-20, Svensk Kärnbränslehantering AB.
Fritzell A, 2017. KBP1012 Verifiering av återfyllningens utformning avseende funktion i KBS-3-förvaret. SKBdoc 1531424 ver 1.0, Svensk Kärnbränslehantering AB.
Svensson D, Eriksson P, Johannesson L-E, Lundgren C, Bladström T, 2019. Development and testing of methods suitable for quality control of bentonites as KBS-3 buffer and backfill. SKB TR-19-25, Svensk Kärnbränslehantering AB.

Categorising data sets as qualified or supporting

Table 5-12 shows the data sets that are used as bases for this section. The table also gives the justification of the sorting of the data sets as qualified.

Table 5-12. Qualified and supporting data sets.

Qualified data sets	Supporting data sets
1. Åkesson et al. (2010a): Experimental data compiled in Figure 10-3 and associated empirical relations.	-
2. Johannesson et al. (2010): Data from experiments performed in IBECO-RWC-BF.	
3. Joyce et al. (2010, Table 4-2): Hydraulic conductivities assumed for the buffer and materials of backfilled tunnels and underground openings.	
4. Joyce et al. (2010, Table 5-3): Hydraulic conductivity of crown space in variant case.	
5. Figure 4-2 in **Buffer production report**, reproduced in Figure 5-1 (originally from Svensson 2019).	
6. Figure 4-1 in **Backfill production report**, reproduced in Figure 5-2 (originally from Fritzell 2017).	

Table 5-12. Continued.

1. Åkesson et al. (2010a) is a complement to the SR-Site Data report and data are qualified on a similar outline as in the SR-Site Data report.

2. Johannesson et al. (2010) is a dedicated report investigating the properties of the candidate backfill material IBECO-RWC-BF.

3. The data on hydraulic properties of the buffer and backfill used in hydrogeological modelling are difficult to sort as qualified or supporting. These data are used as qualified in hydrogeological modelling. However, they are pessimistic and do not reflect on the actual properties of the buffer and backfill.

4. The assumed properties of the crown space given in Joyce et al. (2010) are considered as qualified. It should be noted that the crown space is only included in the hydrogeological variant case, as it is expected that there will always be a swelling pressure of the backfill and that such a crown space will not develop in reality (Åkesson et al. 2010b).

5. Data delivered in the **Buffer production report** are qualified in the **Buffer production report**, in accordance with the SKB quality assurance system. This qualification was found to be in compliance with the demands of the Data report.

6. Data delivered in the **Backfill production report** are qualified in the **Backfill production report**, in accordance with the SKB quality assurance system. This qualification was found to be in compliance with the demands of the Data report.

Excluded data previously considered as important

No such data have been excluded for the considered materials. However, the reference design described in the production reports has been updated for the PSAR.

5.2.5 Conditions for which data are supplied

The conditions of importance can be divided on conditions for the buffer and backfill materials, and conditions for the ground/pore water. These conditions, including the degree of compaction, are further described in Section 5.1. Based on knowledge of the installed buffer and backfill, the permeability can be assessed.

When assessing the hydraulic conductivity also characteristics of the fluid are needed, where the dynamic viscosity is the governing parameter (cf Equation 4-3). The dynamic viscosity is mainly affected by the fluid temperature, where a higher temperature increases the viscosity and as a result, also the hydraulic conductivity.

5.2.6 Conceptual uncertainty

There is no conceptual uncertainty concerning the hydraulic conductivity that is of significant consequence for data and safety assessment calculations. Even though there may be aspects of groundwater transport through a highly charged matrix that are not fully understood, data are not based upon modelling. Instead, data are based upon measurements in the reference buffer and backfill materials at relevant conditions (such as degree of compaction). The data can thus be considered as empirical. If extrapolating data to other temperatures, minor uncertainty may be introduced as other parameters than those of Equation 4-3 may affect the hydraulic conductivity. Such other parameters may, for example, be associated with charge interactions of the ground/pore water and its solutes with clay mineral surfaces.

5.2.7 Data uncertainty due to precision, bias, and representativity

In Åkesson et al. (2010a) experimental results from Karnland et al. (2000, 2006, 2009) for the MX-80 bentonite buffer are compiled (cf Figure 5-1). The measurement data are detailed in the supporting documents while the empirical relations are described in Section 10.2.2 of Åkesson et al. (2010a).

As can be seen from Table 5-10, the dry density range of interest for the installed buffer is 1 484–1 640 kg/m^3. Within this range, measurement results suggest hydraulic conductivities in the range 10^{-14} – 10^{-13} m/s.

Figure 5-2 shows measurement data from the reference backfill material Asha 2012, using water of different compositions Fritzell (2017).

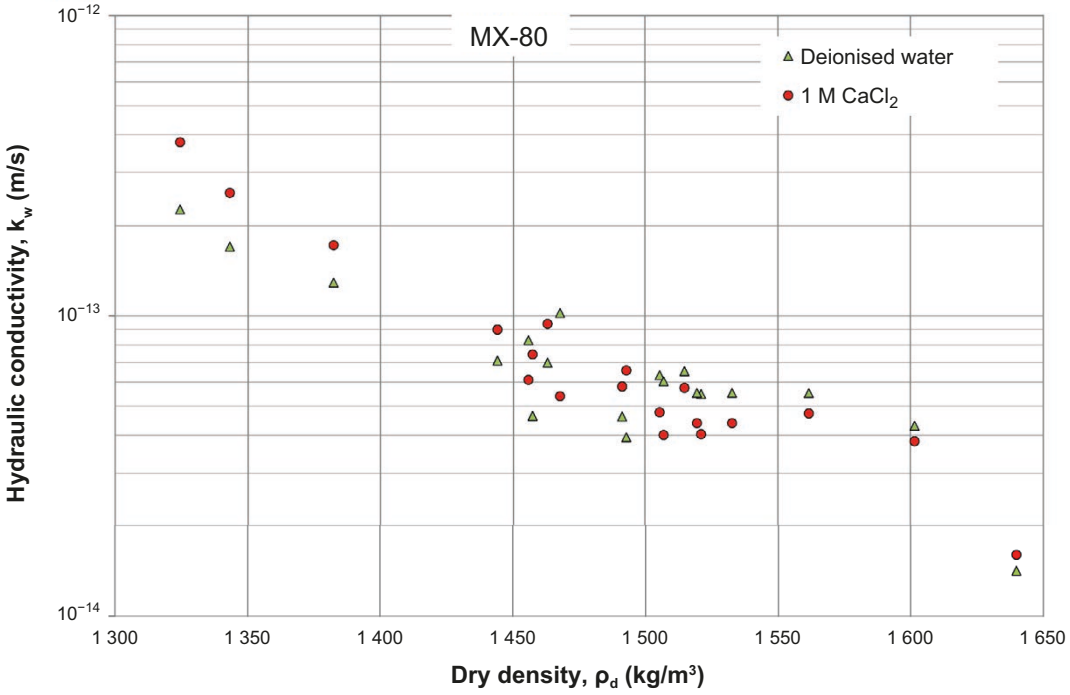

Figure 5-1. *Example of relationship between dry density and Hydraulic conductivity based on measured values for the example material MX-80 bentonite (Svensson et al. 2017). The green dots correspond to the hydraulic conductivity measured in deionized water. The red dots correspond to the hydraulic conductivity measured and 1 M $CaCl_2$.*

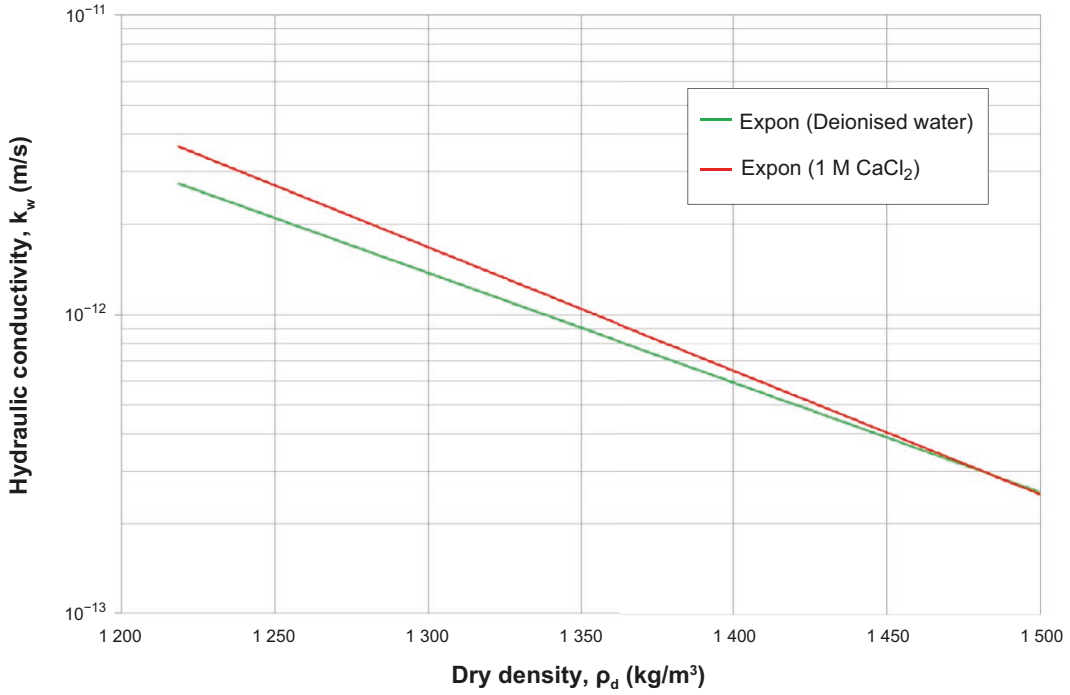

Figure 5-2. *Relationship between dry density and hydraulic conductivity for Asha 2012 based on data from Fritzell (2017). The curve in the figure is fitted with an exponential function to data from measurements performed according to Section 6.2 in* ***Backfill production report****. The requirement for hydraulic conductivity, $< 10^{-10}$ m/s, is met for all measured dry densities.*

As can be seen from Figure 5-2, the dry density range of interest for the installed backfill is 1 458 –1 535 kg/m^3. Within this range, measurement results suggest hydraulic conductivities in the approximate range $1 \times 10^{-13} – 3 \times 10^{-13}$ m/s. As can be seen, the spread in the data is limited, indicating limited data uncertainty. It is interesting to note that there is a wide margin to the minimum hydraulic conductivity (1×10^{-10} m/s) of the backfill specified in the design premises.

5.2.8 Spatial and temporal variability of data

The spatial variability of the buffer and backfill properties is handled by the uncertainty ranges suggested in Section 5.2.7 and in Table 5-9 and Table 5-10.

The data concern the fully saturated system. Accordingly, the temporal variability associated with the saturation process is of no concern for this section. Furthermore, temporal variability associated with post-closure removal (erosion) of the buffer and backfill is not handled in this section. Temporal variability due to the changing temperature in the repository can be approximately handled by correcting for the water dynamic viscosity (cf Equation 4-3).

5.2.9 Correlations

These data have been estimated from measurements on the concerned materials under appropriate conditions. Accordingly, no correlation exist that needs to be propagated to subsequent modelling.

5.2.10 Result of supplier's data qualification (text reproduced from SR-Site Data report)

Realistic hydraulic conductivities

Section 5.2.7 provides reasonable ranges for the hydraulic conductivity of the buffer and backfill at room temperature. From these ranges, the hydraulic conductivity of 5×10^{-14} m/s is recommended as best estimate value in subsequent modelling. As an upper value 1×10^{-13} m/s is recommended. As an upper hydraulic conductivity for the backfill, 3×10^{-13} m/s is recommended.

The hydraulic conductivities used in hydrogeological modelling (Joyce et al. 2010, Table 4-2) are tabulated in Table 5-13. As can be seen, the data pessimistically assumed in hydrogeological modelling are orders of magnitudes higher than those of the actual buffer and backfill. Due to the large discrepancy, temperature corrections become subordinate.

Table 5-13. Hydraulic conductivities used in hydrogeological modelling. Data reproduced from Table 4-2 of Joyce et al. (2010).

Underground opening	Material	*K* (m/s)
Deposition hole	Bentonite	1.0×10^{-12}
Deposition tunnel	Low-grade bentonite	1.0×10^{-10}
Main tunnel	Low-grade bentonite	1.0×10^{-10}
Transport tunnel	Low-grade bentonite	1.0×10^{-10}
Ramp	Low-grade bentonite	1.0×10^{-10}
Elevator shaft	Low-grade bentonite	1.0×10^{-10}
Skip shaft	Low-grade bentonite	1.0×10^{-10}
Air intake shaft	Low-grade bentonite	1.0×10^{-10}
Air exhaust shaft	Low-grade bentonite	1.0×10^{-10}
Deposition area air exhaust shaft	Low-grade bentonite	1.0×10^{-10}
Central area tunnel	Crushed rock	1.0×10^{-5}
Top sealing	Rock blocks	0.10
Crown space	Gap	1.0×10^{-3}

5.2.11 Judgement by the assessment team

There are differences in the target dry density for the buffer and backfill compared to SR-Site. The data used in the assessment was however not derived from the actual components, but pessimistic assumptions to represent an upper bound. Since hydrogeological simulations have not been updated after SR-Site the same data are consequently used in PSAR.

5.2.12 Data recommended for use in assessment

For the buffer the best estimate hydraulic conductivity of 5×10^{-14} m/s is recommended. As an upper value 1×10^{-13} m/s is recommended.

An upper realistic value of the hydraulic conductivity of the backfill is 3×10^{-13} m/s. This value has not been used in subsequent SR-Site modelling as hydrogeological modelling is based on pessimistic values. These pessimistic values are tabulated in Table 5-13 and accepted for use in SR-Site, and hence also PSAR, hydrogeological modelling.

5.3 Migration data of buffer and backfill

This section concerns migration data for the buffer and backfill, or more specifically the effective diffusivity, sorption partitioning coefficient, and the diffusion-available porosity. The migration data are to be used in the PSAR solute transport modelling.

The data are given for the reference buffer, described in the **Post-closure safety report.** The examples of reference buffer material is MX-80 bentonite and the reference backfill is a low grade bentonite, with Asha 2012 as an example.

The dry density and physical porosity of the buffer and backfill are given in Section 5.1.

5.3.1 Modelling

Defining the data requested from the supplier

Diffusion in bentonite has been studied thoroughly in conjunction with radionuclide transport. Despite the substantial experimental and theoretical challenges arising from the inaccessibility of the pore space in compacted clay, to date there is a good phenomenological (macroscopic) understanding of the diffusion of trace constituents in compacted clays. Similarly, robust values for the diffusion rates of many radionuclides through clays under various conditions and the corresponding diffusion coefficients are available. On a macroscopic level, well-established equations are available for describing and quantifying the observable results of tracer diffusion and for linking diffusion with other macroscopic parameters, (K_d, density, porosity).

The following data are needed for the assessment:

- Effective diffusivity D_e (m^2/s) for the reference buffer and backfill for the elements of the selected inventory, dissolved oxygen, sulphide, and sulphate. The supplied effective diffusivities should be valid for an appropriate range of pore water compositions, and for the appropriate bentonite density range.
- Sorption partitioning coefficients K_d (m^3/kg) for the reference buffer and backfill for the elements of the selected inventory, dissolved oxygen, sulphide, and sulphate. As sorption partitioning coefficients are only valid for a particular set of conditions, values should be supplied for an appropriate range of pore water compositions. In PSAR, the system is assumed to be open with regard to exchange of CO_2. For redox-sensitive elements, all relevant oxidation states should be considered for data selection.
- The diffusion-available porosity ε (–) for all elements of interest in the reference buffer and backfill.

The elements of the selected inventory, for which transport parameters are required, are provided in Section 2.2.1. For clarification tritium should be assumed to be in the form of tritiated water (HTO), and data on carbon should be provided for inorganic and organic compounds. The dry densities and physical porosities are given in Table 5-9 for the reference buffer and in Table 5-10 for the reference backfill.

The system is assumed to be open with regard to CO_2 exchange, as opposed to being closed. This assumption results in a calculated pore water pH that is about 0.8 units higher than in the case of a hypothetical closed system. It is noted that the pore water compositions differ from the groundwater compositions delivered in Section 6.1, and that it is the pore water composition that is relevant with respect to all retention processes in the buffer/backfill. Furthermore it is noted that it is too big of a task to model pore water compositions based on all site specific groundwater compositions expected during the glacial cycle, and thereafter assessing the associated migration data. Therefore, it is allowed to use appropriate reference pore water compositions that span the likely conditions. However, the appropriateness of the chosen reference pore waters should be commented upon, in the light of the site specific groundwater.

Modelling activities in which data will be used

The modelling of radionuclide transport in SR-Site is described in the **Radionuclide transport report**. Radionuclide migration in the buffer and backfill is modelled in the near-field transport simulation code COMP23 (Romero et al. 1999, Cliffe and Kelly 2006) as diffusive and advective transport through the porous network, in combination with sorption of radionuclides. The modelling parameters that are not flow related, used to describe these processes, are the effective diffusivity, the diffusion-available porosity, the sorption partitioning coefficient, and the dry density of the clay material. The magnitudes of these entities depend on physical properties of the buffer and backfill, on the pore water composition, and on the migrating species. From the entities listed above, an apparent diffusivity D_a (m^2/s) may be derived (Ochs and Talerico 2004):

$$D_a = \frac{D_e}{\varepsilon + K_d \rho_d} \qquad 5\text{-}3$$

Solute transport in bentonite is also modelled to estimate copper corrosion (SKB 2010b) and SKB (2019a), where the corrodants are either dissolved oxygen or sulphide (cf Section 6.1).

5.3.2 Experience from SR-Site

This section briefly summarises experience from the SR-Site safety assessment, which may be of direct consequence for the data qualification in this Data report.

Modelling in SR-Site

The modelling performed in SR-Site generally agree with the SR-PSAR modelling. No significant difference with bearing to the parameters of this section has been identified.

Conditions for which data were used in SR-Site

In SR-Site the MX-80 and the Deponit-Can bentonites were used as the reference buffer material, and migration parameters were evaluated based on a buffer dry density of 1 562 kg/m^3 and porosity 0.435. The same values are used in PSAR, but only the MX-80 bentonite is evaluated.

Sensitivity to assessment results in SR-Site

In SR-Site it was shown that the scenarios giving the highest dose were associated with a situation where the buffer had eroded. In such a situation the data delivered in this section lose their importance.

In cases where the buffer remained uncompromised, the general copper corrosion rate was assumed to increase monotonically with increasing effective diffusivity of dissolved oxygen and/or sulphide in the buffer.

In cases where the buffer remained uncompromised but the canister was breached, the release rate was assumed to increase monotonically with increasing effective diffusivity, and decrease monotonically with increasing sorption partitioning coefficient.

Alternative modelling in SR-Site

No alternative modelling of relevance to this section was used in SR-Site.

Correlations used in SR-Site modelling

The correlations used in SR-Site are identical to those used in the PSAR.

Identified limitations of the data used in SR-Site modelling

Some of the identified limitations in data used in SR-Site remain for data to be used in PSAR. These limitations are highlighted in the remaining of this section. The identified limitations did not give rise to general changes in the approach of collecting data for the PSAR. The limitations in data most likely had a small effect on the assessed radiological risk in SR-Site. Most of the data used was extracted already for SR-Can (Ochs and Talerico 2004) and the limitations has remained since then.

A few limitations were identified in the SKI report (Stenhouse et al. 2008). For example, there were differences between the reference solid and waters used by Ochs and Talerico (2004) and data recommended in the SR-Can Data report (SKB 2006b). Most significantly concerning the clay material, there were differences in percentage of minor constituents, for example calcite. However, even traces of calcite in the bentonite are enough to establish solubility equilibrium between dissolved Ca ions and calcite, due to the high solid/water ratio in compacted material and the solubility limit of calcite. The only relevant variation would be complete absence of calcite, which was tested in the pore water calculations for SR-Site. Furthermore, there were small differences in the CEC of the clay materials. These may have a small influence on radionuclides sorbing only through ion exchange (Cs, Sr, Ra), but this uncertainty can be assumed to be small compared to the overall uncertainty. In case of radionuclides sorbing by surface complexation, the influence of differences in the CEC is not significant in comparison to other uncertainties that were considered for SR-Site.

Concerning the groundwater, saline Beberg water (BFI01B) was used as the reference groundwater, as defined in SR-97 and based on investigations at Finnsjön. This reference water was used as a basis when modelling the pore water composition.

On a general note, Stenhouse et al. (2008) found that a relatively small number of batch sorption datasets were used as the basis for the different K_d recommendations, and that the treatment of uncertainty could be improved.

Although there are some differences in the PSAR initial state and the SR-Site initial state (the materials and material properties as presented in the SR-Site Buffer production report and the SR Site Backfill production report and the materials and material properties presented in the **Buffer production report** and the **Backfill production report)**, these differences are of minor importance to the migration data for buffer and backfill. Therefore, the PSAR is in large based on the same data qualification as the SR-Site and the majority of the text in Sections 5.3.3 to 5.3.10 has been reproduced from the SR-Site Data report.

5.3.3 Supplier input on the use of data

As part of SR-Can, a major review was made on migration parameters for the bentonite buffer (Ochs and Talerico 2004). As part of SR-Site, a minor update of the data presented in Ochs and Talerico (2004) was made. All the of the data recommended for SR-Site are also recommended for the PSAR.

The following main changes should be noted.

- Several additional sets of effective diffusion coefficients (D_e) obtained in through-diffusion experiments with compacted bentonite and, especially, in argillaceous rocks have become available since the publication of Ochs and Talerico (2004). Therefore, new data are included in the figures compiling D_e data from various publications. The new data do not significantly deviate from the recommendations given in Ochs and Talerico (2004) but are still implemented as a basis for recommending slightly modified data.
- In SR-Site the reference backfill was based on the properties of a material from Milos, Greece, while a material from India is used in the PSAR (Asha 2012)., All backfill data are however kept from Sr-Site since the difference is assumed to be small.

Concerning the request to comment on the appropriateness of the chosen reference pore water compositions, in the light of the site specific groundwater; such comments are based on groundwaters given in SR-Can (Auqué et al. 2006).

5.3.4 Sources of information and documentation of data qualification

Sources of information

The main sources of information on migration properties in buffer and backfill are given in Table 5-14. Among the references considered to be of major importance in Ochs and Talerico (2004) the following deserves mentioning: A Nagra report on selected K_d values for MX-80 (Bradbury and Baeyens 2003), and original data sources cited therein; SKB reports on K_d, D_e, and D_a (Yu and Neretnieks 1997) and groundwater composition (Laaksoharju et al. 1998), and original data sources cited therein; Japan Atomic Energy Agency (JAEA, formerly JNC) reports and databases on diffusion in Kunigel-V1 and Kunipia-F bentonites as a function of dry density.

Table 5-14. Main sources of information used in data qualification.

Auqué L F, Gimeno M J, Gómez J B, Puigdomenech I, Smellie J, Tullborg E-L, 2006. Groundwater chemistry around a repository for spent nuclear fuel over a glacial cycle. Evaluation for SR-Can. SKB TR-06-31, Svensk Kärnbränslehantering AB.
Ochs M, Talerico C, 2004. SR-Can. Data and uncertainty assessment. Migration parameters for the bentonite buffer in the KBS-3 concept. SKB TR-04-18, Svensk Kärnbränslehantering AB.
A number of recent peer reviewed scientific publications and technical report from the open literature, as referred to in the present text.
A great number of peer reviewed scientific publications and technical report from the open literature, as referred to in Ochs and Talerico (2004).

Categorising data sets as qualified or supporting

A great majority of the data recommended for use is taken directly from Ochs and Talerico (2004). This is a dedicated report for the SR-Can Safety Assessment and the data therein are considered as qualified. However, before judging the data as qualified, the conditions of the report (buffer and backfill dry density and groundwater composition) have been compared with the PSAR conditions. Properties of the buffer and backfill, such as density, CEC, etc, are taken from the SR-Site Data report.

Migration data for a number of species not covered by Ochs and Talerico (2004), including H-3, Mo, Cd, Ac, HS^-, SO_4^{2-} and O_2, have been estimated. This estimate is based on analogues and data in the open scientific literature, e.g. Bazer-Bachi et al. (2007).

Qualified and supporting transport data sets for the buffer and backfill are displayed in Table 5-15 and numbered from 1 to 9. Detailed comments to the data sets are given in Table 5-16.

Table 5-15. Qualified and supporting data sets.

Qualified data sets	Supporting data sets
1. Ochs and Talerico (2004, Table in Section 5-4): Summary of D_e values.	8. Ochs and Talerico (2004, Appendix A). Groundwater compositions including the reference groundwater saline Beberg water (BFI01B).
2. Ochs and Talerico (2004, Tables in Section 5-4): K_d data for reference pore water, reference pore water for closed system with respect to CO_2, and highly saline pore water.	9. A great number of data sets taken from scientific publications and technical report from the open literature, as referred to in this present text or in Ochs and Talerico (2004).
3. Ochs and Talerico (2004): Reduction factor of 2.5 for diffusion-available porosity for anions, as compared to the physical porosity. Text in association with Equation 5.9 (page 52).	
4. Auqué et al. (2006, Table 3-3): Modelled groundwater compositions at repository depth at Forsmark at different times.	
5. Bazer-Bachi et al. (2007): Sulphate sorption on Callovo-Oxfordien argillites.	
6. van Loon et al. (2003a, b): The diffusion available anion porosity is selected based on the findings of van Loon et al. (2003a, b), who made an explicit effort to distinguish D_e from ε in their data interpretation.	
7. CEC data for the buffer in the **Buffer production report** (Table 3-2) and for the backfill in the **Backfill production report** (Table 3-2).	

Excluded data previously considered as important

For the buffer, no data previously considered as important is excluded.

Table 5-16. Justification of the sorting of items in Table 5-15.

1. Concerning D_e and K_d for the buffer and backfill, this present text can be seen as an updated supplement to the SR-Can report (Ochs and Talerico 2004), wherein a full reference list can be found. The SR-Can data presented in Ochs and Talerico (2004) are considered to be qualified, as the report was written on a structure similarly to the present structure for data qualification. This means that the report is written on a similar outline as this present text, handling data uncertainty and variability in a robust fashion. Original experimental data reported in a large number of peer-reviewed publications constitute the main data source. Many of these publications are cited in a Nagra report on selected K_d values for MX-80 (Bradbury and Baeyens 2003); in an SKB report on selection of diffusion data (Yu and Neretnieks 1997); and reports and databases by JAEA. The D_e values are given for the dry density values that correspond well to specifications of the SR-Site reference buffer and backfill.

2. The K_d values in Ochs and Talerico (2004) are given for a range of pore waters corresponding to groundwaters with different salinities based on Beberg water, as given in the SR-97 safety assessment. All K_d values used were derived on the basis of primary information (original experimental sorption data); i.e., no interpreted information was used. After having confirmed that these groundwater compositions are in line with site specific groundwater (see Section 6.1 of this present report) the K_d values were judged as qualified.

3. The reduction factor presented in Ochs and Talerico (2004) is considered as qualified. Neither the buffer and backfill dry density or the groundwater composition differs considerable between SR-Site and SR-Can.

4. The modelled groundwater compositions at repository depth in Forsmark at different times (Auqué et al. 2006) are judged as qualified for this purpose, as they were acquired as part of SR-Can. These compositions are compared with the groundwaters used in Ochs and Talerico (2004).

5–6. Bazer-Bachi et al. (2007) and van Loon et al. (2003a, b) are peer reviewed scientific journal articles and the data presented are be considered to be relevant and qualified.

7. Data delivered in the Buffer production report and the Backfill production report are qualified in these two reports, in accordance with the SKB quality assurance system. This qualification is found to be in compliance with the demands of the Data report.

8. The saline Beberg water BFI01B presented in Laaksoharju et al. (1998) and used as reference groundwater in Ochs and Talerico (2004) is not site specific for Forsmark. It is judged as supporting data.

9. In this text, a number of articles and documents from the open literature are referred to. In addition, in Ochs and Talerico (2004) a great number of articles and documents from the open literature are referred to. These are generally peer-reviewed and sorting them as qualified or supporting often depends on how representative data are. It is considered to be too voluminous to handle each article or document in this list. Comments are instead given, when necessary, where the reference is made.

5.3.5 Conditions for which data are supplied

Buffer and backfill density and composition

The reference buffer is MX-80 bentonite. The reference backfill in the PSAR is Asha 2012, but migration data are taken from the backfill in SR-Site.

In Ochs and Talerico (2004) migration data are compiled for MX-80 bentonite of the dry density 1 590 kg/m^3. As stated in Section 5.1 of this present report, for the PSAR the buffer dry density should be within the range 1 544–1 566 kg/m^3, with the best estimate somewhere in the centre of that range (set to 1 550 kg/m^3). The discrepancy between the SR-Can and the PSAR dry densities is judged to be insignificant in the light of K_d values, and no correction is needed.

While bentonites other than MX-80 (e.g. Asha 2012) have not been considered explicitly in Ochs and Talerico (2004), the following variations in bentonite composition were considered:

- Bentonite converted completely to the Ca-form.
- Bentonite completely depleted of soluble impurities and some accessory minerals (NaCl, KCl, gypsum, calcite).

With regard to K_d, a difference in bentonite composition (smectite content or measured CEC) would require a re-calculation on formal grounds (i.e. based on the procedures used for K_d derivation in SR-Can). However, MX-80 and Asha 2012 are similar in terms of these parameters. It can be assumed that the concentration of clay edge sites (which are responsible for the sorption of most radionuclides via surface complexation) are the same for all three materials within the assumed uncertainties. (It should be noted that it is not finally established whether edge site density is directly proportional to the measured CEC (NEA 2005)).

Concerning the backfill, the dry density of the PSAR should range between 1 361 and 1 488 kg/m^3. This is somewhat below the dry density of SR-Can (Ochs and Talerico 2004), but the discrepancy is judged to be small in comparison with other uncertainties regarding K_d.

In the case of radionuclides sorbing predominantly or exclusively through ion exchange (Cs, Ra, and Sr), scaling according to the CEC of the clay can be performed, as sorption of these elements can be assumed to be directly related to this parameter. CEC scaling is also applicable for sulphate, which is assumed to sorb as outer sphere complex. The CEC of the buffer and backfill materials are shown in Table 5-17.

Table 5-17. CEC of bentonites in SR-Can and PSAR.

Bentonite	SR-Can CEC (meq/100 g)	PSAR CEC (meq/100 g)
MX-80	85	85
ASha 2012		85

References: Svensson et al. (2019), Fritzell (2017).
MX-80, SR-Can (Ochs and Talerico 2004, Appendix B).

Groundwater

The data delivered in this section apply at fully saturated buffer and backfill. The buffer and backfill will be affected by a range of geochemical conditions, such as groundwater composition, redox potential, and pCO_2 (partial pressure of carbon dioxide). The groundwater has an indirect influence on migration parameters, through its interaction with the pore water (see discussion below). While K_d data are clearly affected by the pore water composition, the effective diffusivity and diffusion-available porosity are less affected.

In Ochs and Talerico (2004) the reference groundwater used for pore water modelling was saline Beberg water (BFI01B). Variants included a non-saline and highly saline groundwater, as well as two saline groundwaters having alkaline to highly alkaline pH (up to pH 13.15). None of these groundwaters are specific for the Forsmark site.

In Auqué et al. (2006), the groundwater composition at repository depth at the Forsmark site at different time periods was modelled. A comparison in terms of the major ions is given in Figure 5-3 for the three main groundwaters of Ochs and Talerico (2004, Appendix A) and three modelled Forsmark groundwaters during the temperate period (Auqué et al. 2006, Table 3-3). The error bars for the modelled Forsmark groundwaters represent the 99.9 % confidence limits.

Extracting information by visual inspection of Figure 5-3, with the aim at understanding how K_d values will differ for the different groundwaters, would be extremely difficult. This is especially true as the groundwater only indirectly affects the sorption. The figure should rather be used to demonstrate that the groundwater chemical composition at Forsmark is expected to vary significantly. This is especially true if taking the entire glacial cycle into account (the Forsmark data in Figure 5-3 only represent the initial temperate period).

K_d values are conditional data, in other words they only apply at a certain set of conditions. The varying geochemical conditions over the glacial cycle make it very difficult to estimate a K_d, with its associated uncertainty range, that should encompass the likely geochemical conditions.

The saline Beberg water used in Ochs and Talerico (2004) is based upon measurements in Finnsjön, a site located a few tens of kilometres inland from the Forsmark site (see Figure 5-4).

As the Finnsjön site is located nearby the Forsmark site, and in a broader sense has about the same geological settings, it is suggested to be acceptable to use the K_d data of Ochs and Talerico (2004). Especially as the variant groundwaters used in Ochs and Talerico (2004) span a good portion of reasonable, and even less reasonable, groundwaters at depth.

One could have chosen to perform new pore water modelling, based on a few site specific groundwater compositions from arbitrarily chosen points in time of the glacial cycle. However, it is suggested that performing such a task would not reduce data uncertainty at any greater extent. Due to the conditional nature of K_d, and the varying geochemical conditions at the site, any approach chosen will be associated with large uncertainties.

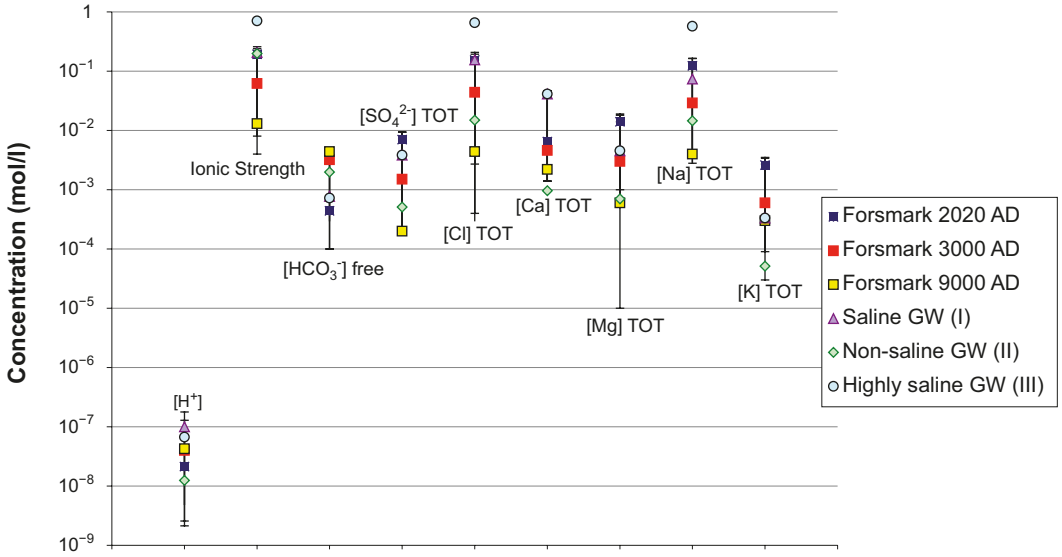

Figure 5-3. *Concentration of important groundwater constituents of three modelled groundwaters during the temperate period in Forsmark (squares) (Auqué et al. 2006) and the three main groundwaters used in Ochs and Talerico (2004).*

Figure 5-4. *The locations of the Finnsjön and Forsmark sites. Reproduced from Figure 2-3 of SKB (1999a).*

Pore water

The pore water compositions used as the basis for the derivation of K_d data in SR-Can, SR-Site and teh PSAR are the result of thermodynamic modelling of clay-water interactions. The use of models is necessitated by the experimental and conceptual uncertainties in extracting and determining the composition of pore water in compacted bentonite. The modelling results depend on the composition of clay material and contacting groundwater, on assumptions regarding boundary conditions (e.g., imposed redox conditions, and whether or not the system is open or closed to CO_2 gas exchange with the host rock), as well as on the actual modelling approach. This needs to be kept in mind when the influence of individual conditions is discussed.

The effect of uncertainties in the pore water compositions differs between the various migration parameters. K_d depends strongly on the pore water composition and therefore indirectly on the groundwater composition. D_e and ε depend comparatively little on the pore water composition, although extremely high salinity can have an influence on anion exclusion effects.

In Ochs and Talerico (2004, Section 5.4) K_d values are tabulated for three different pore waters (and various conditions in terms of bentonite composition and pCO_2) within a reasonable range in terms of salinity and pH. In Ochs and Talerico (2004, Appendix C), the modelled pore waters are described. The different pore waters are: reference pore water (RPW) based on saline groundwater and an open system with respect to CO_2; highly saline pore water (HSPW), based on highly saline groundwater and an open system; and RPWC, based on saline groundwater but for a closed system. This latter pore water is of lesser concern for the PSAR, where an open system is assumed. No K_d values that formally correspond to a non-saline groundwater are tabulated in Ochs and Talerico (2004). However, pore water conditions were calculated by Ochs and Talerico (2004) using a non-saline groundwater as well. The resulting pore water compositions proved to have intermediate values of the most relevant solution parameters (pH, carbonate concentration) in comparison to the pore waters used for K_d derivation. At the same time, the resulting ionic strength in the pore water is almost identical in case of the non-saline and saline groundwater, because the pore water in compacted bentonite is to a large degree controlled by the soluble constituents of the bentonite itself. Thus, it can be expected that K_d for the non-saline groundwater will lie within the range given by the saline groundwater.

As K_d values for many radioelements are very sensitive with regard to pore water composition, the validity of the selected data is bounded by the ranges of conditions covered by the pore water compositions considered. It is not advisable to extrapolate K_d values to conditions outside these ranges. Special remarks are made below for carbonate, pH, and salinity:

- *Carbonate:* Different open systems were considered in Ochs and Talerico (2004) with a pCO_2 of $10^{-2.6}$ atm, giving pH values of about 7 to 7.4. A host-pCO_2 above 0.1 atm would lead to pH values below 6.6 and K_d values below the range considered in Ochs and Talerico (2004), even if taken into account the K_d values estimated for the closed system.
- *pH:* The groundwater and bentonite compositions that may lead to a low pore water pH have been investigated in Ochs and Talerico (2004). The calculations show that the carbonate buffer system in the bentonite is the main factor controlling pH. In an open system, as considered for SR-Site, calcite from the bentonite and pCO_2 imposed by the host rock will prevent low pH values. The porewater compositions are the result of model calculations, where bentonite of a defined composition is equilibrated with a defined groundwater composition and an external (fixed by the host formation) pCO_2 (Ochs and Talerico 2004). Due to its surface properties and the presence of dissolved impurities, bentonite (and other compacted clays) exerts an important buffer effect. This means that pH and other solution parameters are buffered towards a common value in case of many different groundwaters. Still, groundwater with extreme pH values or salinities will strongly influence porewater composition.
- *Salinity:* The salinity does not have a pronounced effect on K_d for most species, because of the comparative "inertness" of Na^+ and Cl^-. For species sorbing by complexation it is expected that an increase of salinity to more than 1 M will have a very small effect on K_d. This effect is likely encompassed by the uncertainty range of K_d already considered. However, under conditions where sorption is already very low (e.g. near lower limits and/or at lower end of pH range considered), K_d values could fall outside of the range given in Ochs and Talerico (2004) in the case of Cl^- concentrations significantly above 1 M. This is in all likelihood only relevant when the pH is already low; i.e. if the system is closed with respect to CO_2 exchange.

For elements whose migration behaviour is dominated by ion exchange (Cs, Sr, and Ra), an increase of salinity above the values considered in Ochs and Talerico (2004) will lead to a decrease of K_d. According to Ochs and Talerico (2004), an increase in pore water ionic strength from about 0.3 M to 0.8 M leads approximately to a 5-fold decrease of K_d. The lower limits of K_d are a factor of about 5 lower than the best estimates. This means that an increase of ionic strength from about 0.8 M to about 4 M would be required to give a K_d that falls below the respective lower limit. Based on the groundwater salinities indicated in Auqué et al. (2006), this is not to be expected.

Depending on the type of clay-water model used, an increase of ionic strength due to high salinity is predicted to cause lower pore water pH, which could lead to K_d values outside of the range considered. This is in all likelihood only relevant when pH is already low; i.e. if the system is closed with respect to CO_2 exchange.

Double layer effects in the pores of compacted bentonite will be decreased by high pore water salinity; therefore anion exclusion effects will be less important at high salinity. However, no significant effect is expected in comparison to the uncertainties already considered on the basis of the available experimental data.

Concerning the pCO_2 of the groundwater, values reported from the Forsmark site investigation in Gimeno et al. (2008, Figure 3-14) are either in line with, or lower than, those assumed in Ochs and Talerico (2004). In Auqué et al. (2006, Section 3.4.3) it is estimated that the pCO_2 of the groundwater will increase with time during the temperate period.

For an approximate estimation of the possible effects of variations in the pore water composition, the diagrams in Section 5.3.5 of Ochs and Talerico (2004) can be used. Interpolation between the three reference pore water conditions is easily possible for salinity, but should to be done with care for parameters that are directly linked to others (pH, pCO_2).

The influence of the different composition of exchangeable cations between MX-80, Deponit CA-N, and Milos backfill on pore water composition (and therefore on K_d) is considered to be negligible, based on the available information.

Temperature

The selected data are valid for 25 °C. An increase to 50 °C is expected to lead to a twofold increase of D_e. A decrease in temperature to just above freezing is expected to lead to about a twofold decrease in D_e. The temperature influence on D_e is also discussed in Section 6.8.5. Based on the data presently available, it is not possible to assess the influence of temperature on K_d with any certainty. No effect on diffusion-available porosity is expected for this temperature range.

5.3.6 Conceptual uncertainty

For the derivation of buffer and backfill migration parameters, the conceptual uncertainties discussed below were identified.

- Conceptual uncertainties are introduced when interpreting experimental data into recommended diffusion and sorption values. Several related conceptual uncertainties exist regarding the interpretation of, and self-consistency among, batch K_d values and diffusivities of sorbing radionuclides on the one hand, and of diffusivities and diffusion available porosities of anions and certain mobile cations, such as Cs, on the other hand. Both issues are discussed to some detail in the **Buffer and backfill process report**. In the case of diffusion coefficients, uncertainties correspond to the experimental error as well as to any uncertainty introduced in the required modelling for raw data reduction.
- For K_d, the most significant conceptual uncertainties, in terms of representing reality, are related to the description of pore water composition as a function of conditions. There are still some scientific shortcomings regarding the derivation of pore water composition in compacted bentonite (such as effects of the electrical double layers in the pore space on e.g. the amount of "free" water, water activity, etc), and its evolution over time under repository conditions. As the pore water composition of compacted bentonite cannot be determined experimentally with any certainty, it is calculated through thermodynamic surface chemical models. Several published models are available for this purpose. While they are based on the same principles, they differ in a number of details regarding e.g. the treatment of specific surface chemical equilibria. Because of the limited accessibility of the pore space of compacted bentonite, a direct comparison of pore water model and experimental results is not possible. The comparisons of experimental and model-derived macroscopic migration parameters in compacted bentonite in Ochs and Talerico (2004) and Ochs et al. (2001) indicate that the available models are sufficient for describing the effect of bentonite and groundwater properties on pore water composition and radionuclide migration within experimental uncertainties.
- Conceptual uncertainties are introduced when converting suggested data obtained at a specific set of conditions through models or estimation procedures into data applicable at conditions relevant for safety assessments. These are largely included in the uncertainty factors applied by Ochs and Talerico (2004).
- If there are significant uncertainties associated with the application conditions themselves, it is critical to take the conditional nature of the relevant migration parameters into account. K_d values in particular are highly conditional and need to be derived for each specified set of (expected) conditions. In Ochs and Talerico (2004), variability of geochemical conditions was addressed by deriving K_d values separately for several sets of possible geochemical conditions.
- There are some open questions regarding the fundamental, underlying chemistry of radionuclides in aqueous solutions. This is also acknowledged in recent TDB (thermodynamic database) compilations (e.g. Hummel et al. 2002). For example, the stability of actinide(III)-silicate or mixed actinide(IV)–OH-CO_3 complexes is not established to date. There are also uncertainties regarding the solution speciation of many of the less well researched elements, such as Nb, Zr, etc. The TDB used for the present data derivation is indicated for each element in Appendix F of Ochs and Talerico (2004). Use of different TDBs, or future updates in SKB's reference TDB, could lead to different migration parameters.

5.3.7 Data uncertainty due to precision, bias, and representativity (text reproduced from SR-Site Data report)

As discussed in the following (see also Ochs and Talerico (2004) for details), the uncertainty of the selected sorption and diffusion parameters depends on uncertainties in the underlying data, but also on uncertainties that are introduced in the process of synthesizing and scaling these data to the specified safety assessment conditions. Therefore, data uncertainty is discussed together with descriptions of the derivation of sorption and diffusion parameters, as well as the basic results of data derivation. The numerical results are summarised in Section 5.3.10.

Effective diffusivity

Diffusion experiments are (in comparison to sorption batch experiments) more difficult to perform in terms of controlling chemical and other boundary conditions. On the other hand, the conditions in diffusion experiments are very similar to the actual conditions anticipated for the buffer and backfill. Further, effective diffusivities are representative for steady-state conditions; i.e. chemical processes and in particular sorption do not play a role anymore during the actual data acquisition (or can be factored out). To actually obtain D_e values requires a relatively complex processing of the raw experimental data (fitting of models that have to be chosen as a function of boundary conditions). Because of the effort and time requirements associated with diffusion experiments, D_e values are typically available only for mobile but not for sorbing elements, and are only in a few cases available as a function of systematic variations of chemical conditions.

Following this situation, D_e values presented here are compiled from various publications, and selected values and uncertainties are evaluated directly from plots of reported D_e versus clay dry density. Uncertainties related to the influence of conditions on diffusion-relevant bentonite characteristics (pore size, etc) are assumed to be included in the uncertainties given for D_e in each case, as these data are derived based on numerous experimental measurements that already cover a range of different conditions.

Following the approach taken in Ochs and Talerico (2004), D_e was evaluated separately for neutral diffusants on the one hand, and anions showing anion exclusion effects on the other hand. In addition, a distinction was made between Cs, which exists practically always as simple cation in aqueous solutions, and all other cations which exist mainly in hydrolysed form or in the form of ion pairs (i.e, where all species taken together typically give a near-neutral average charge).

Neutral diffusants (HTO)

The effective diffusivity for most elements (hydrolysable cations, cations existing mainly as neutral ion pairs, neutral molecules) are in this section based on the diffusion of HTO. Many of these elements are moderately or strongly sorbing, and if any element specific D_e data exist, they are isolated. Therefore it is preferred to rely on data for HTO.

Figure 5-5 shows reported D_e data from a number of publications, obtained on compacted clays of relevance for the buffer and backfill materials.

The data for HTO and CH_4 show good agreement, as do data for MX-80 and the crude bentonite Kunigel-V1. This means that the effective diffusivity of HTO is consistent among different bentonites with low to intermediate smectite content. Furthermore, the diffusion behaviours of HTO and CH_4 do not appear to differ significantly. On the other hand, it can be seen that (purified) bentonites with high smectite content (especially Kunipia-F consisting of almost pure smectite) lead to lower values of D_e for HTO.

As can be seen in Figure 5-5, the best estimate dry densities of the backfill and buffer are indicated by the brown and orange lines at 1 504 and 1 562 kg/m^3, respectively. For the dry density range of interest (1 458–1 640 kg/m^3), the experimental D_e values ranges over about one order of magnitude for the different clay materials. Some of the spread is due to differences in clay materials, and possibly also due to differences in conditions (addition of sand, salinity). The variation of conditions does not appear have a clear effect on D_e of neutral tracers, however. Experimental uncertainties and uncertainties in the reduction of the raw data will also contribute to the spread in data.

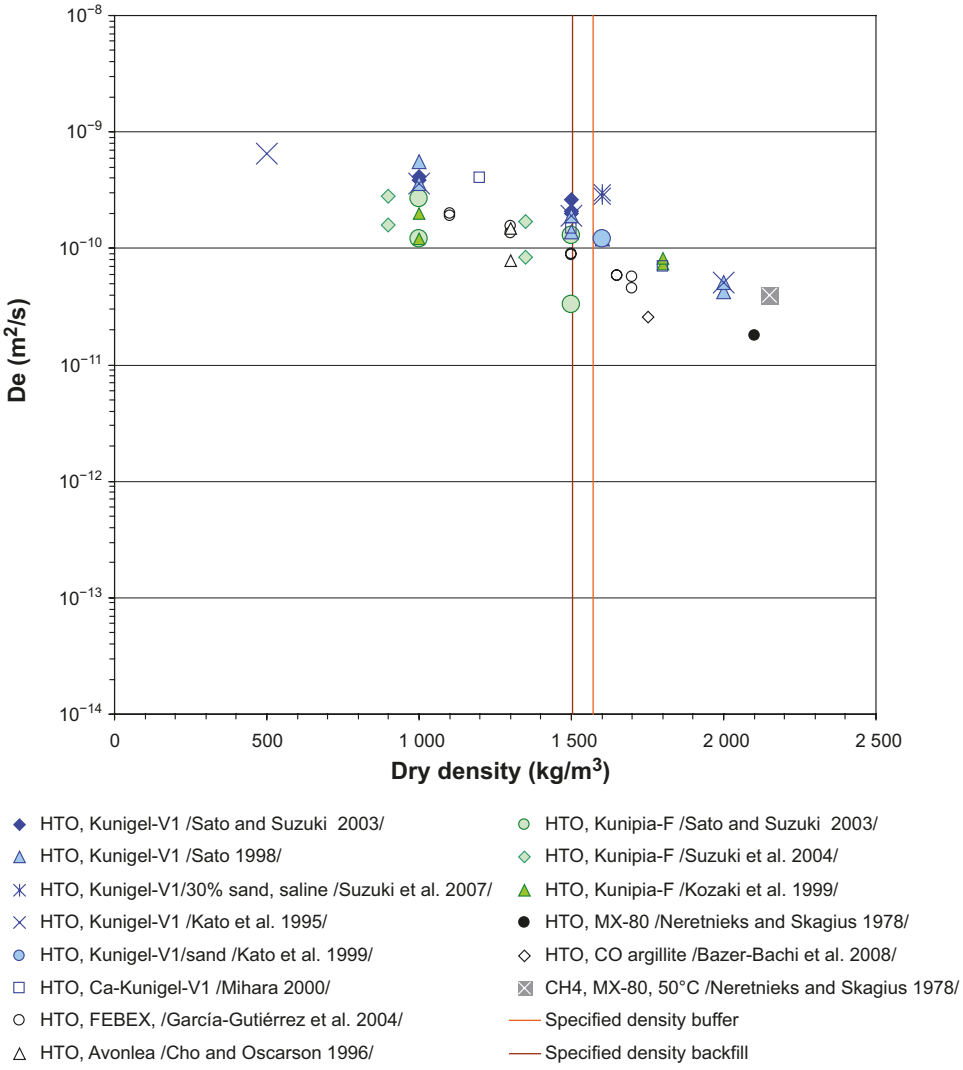

Figure 5-5. *Effective diffusivities obtained in compacted clays using non-charged tracers (HTO: blue symbols – Kunigel-V1, black – MX-80, green – Kunipia-F, black open – other; grey: CH_4/MX-80). Dry densities specified for the reference buffer and backfill are indicated by the orange and brown line, respectively. The scale is chosen to allow direct comparison with data for anions and Cs.*

Recommended D_e values are based on a regression analysis including all HTO data for Kunigel-V1 and MX-80 (Figure 5-6). The standard error of the regression analysis (standard error for predicted values) is indicated on the brown and orange lines at the best estimate dry densities of the backfill and buffer. The regression is not valid at low clay densities, as this would suggest that D_e becomes higher than the diffusivity in unconfined pore water D_w (m^2/s), which is about 10^{-9} m^2/s.

The regression parameters are shown in Equation 5-4.

$$D_e = 3.48 \times 10^{-9} \cdot e^{(-0.00205 \cdot \rho_d)} \qquad 5\text{-}4$$

The resulting best estimate D_e values are 1.4×10^{-10} m^2/s for the buffer (ρ_d = 1 562 kg/m^3) and 1.6×10^{-10} m^2/s for the backfill (ρ_d = 1 504 kg/m^3). These values are based on the densties from the SR-Site assessment. The in the PSAR would yield somewhat higher diffusivities, but the effect is marginal.

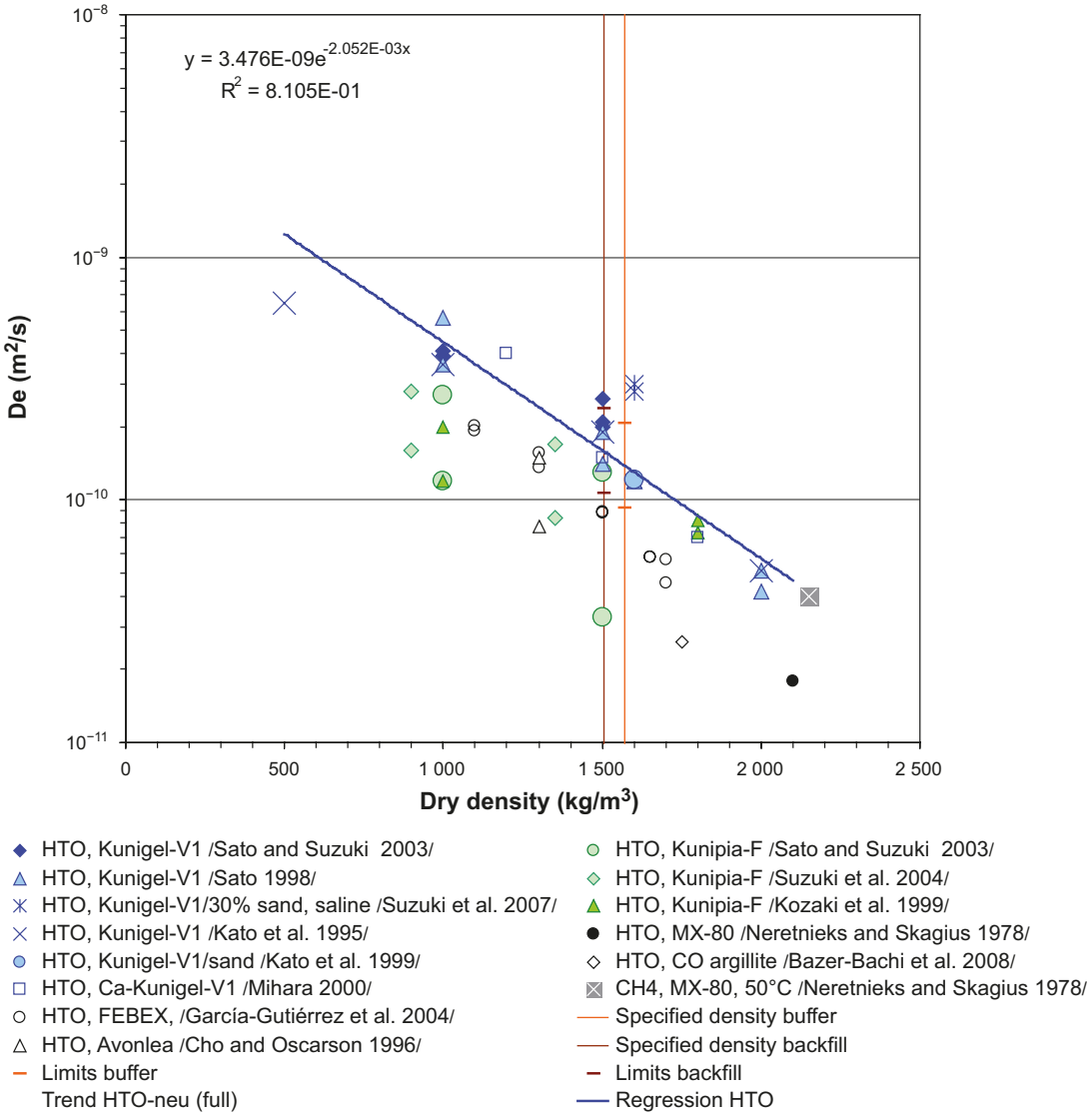

Figure 5-6. *Same data as in Figure 5-5. Indicated are the regression analysis of D_e for HTO (based on all data for Kunigel-V1 and MX-80) as well as the standard error at the dry densities specified for the reference buffer and backfill. Note that scale is different from in Figure 5-5.*

Possible additional uncertainties are introduced by assuming that the D_e values obtained using certain non-charged tracers also apply for other non-charged tracers. An obvious bias in assuming this is that differences in diffusivities in unconfined pore water D_w between species are not accounted for. Theoretically, this bias could be compensated for by scaling the D_e data with D_w values of all individual species including the concerned element occurring in the pore water, using a weighted average. However, this would be very cumbersome, and the usefulness of such a procedure would be limited due to uncertainties regarding *a)* the calculated speciation of a given element in the pore water and regarding *b)* the D_w value of complex species (such as hydrolysed actinide elements). In general, differences in D_w are considered as small in comparison to the overall uncertainty.

Anions

The effective diffusivity for anions is estimated from experimental data on compacted clays using anionic tracers and independent model predictions. Figure 5-7 shows compiled D_e data versus dry density.

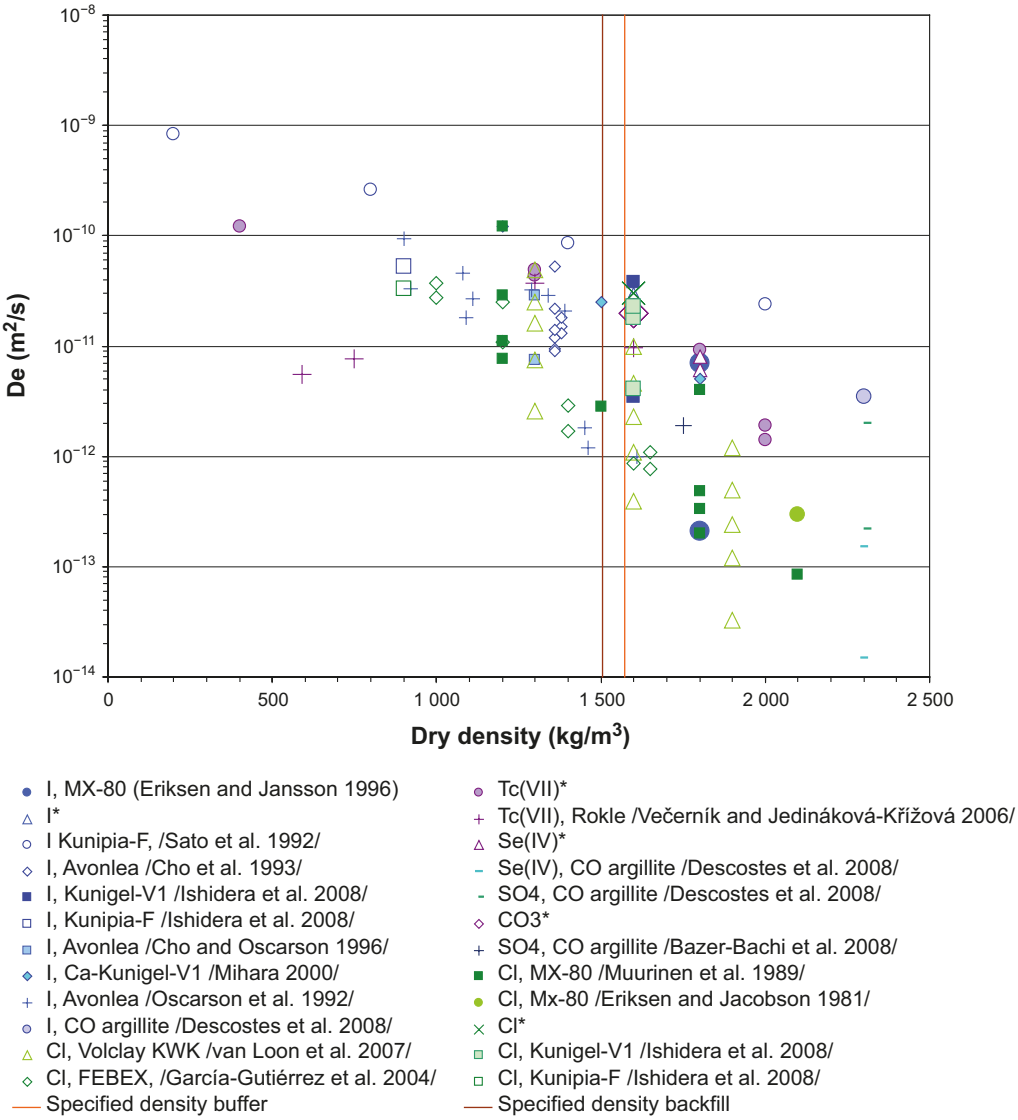

Figure 5-7. *Effective diffusivities obtained in compacted clays using anionic tracers. All data marked * are for Kunigel-V1 (Sato 1998). The specified reference buffer and backfill dry densities are indicated.*

Figure 5-8 shows the same data, but includes the regression for HTO from Figure 5-6, as well as independent predictions for chloride in MX-80 and Tc(VII) in Kunipia-F by Ochs et al. (2001).

The effective diffusivity of anions is on average lower than for the non-changed species, indicating anion exclusion effects. Note that the predicted dependency of D_e versus dry density for chloride diffusion in MX-80 (green line) (Ochs et al. 2001) corresponds nearly exactly to the slope of the regression for HTO data (blue line).

The D_e values close to the dry densities of the reference buffer and backfill ranges over at least two orders of magnitude. The data points are however obtained on a number of different clay materials. It can further be seen that the spread appears to increase with the degree of compaction. This may at least in part be due to basic difficulties of separating the raw diffusion data into D_e and diffusion-available porosity in case of anions (see Ochs and Talerico (2004) for a more detailed discussion). The data indicate a spread over at least one order of magnitude for MX-80 bentonite (see for example data points from Muurinen et al. (1989)).

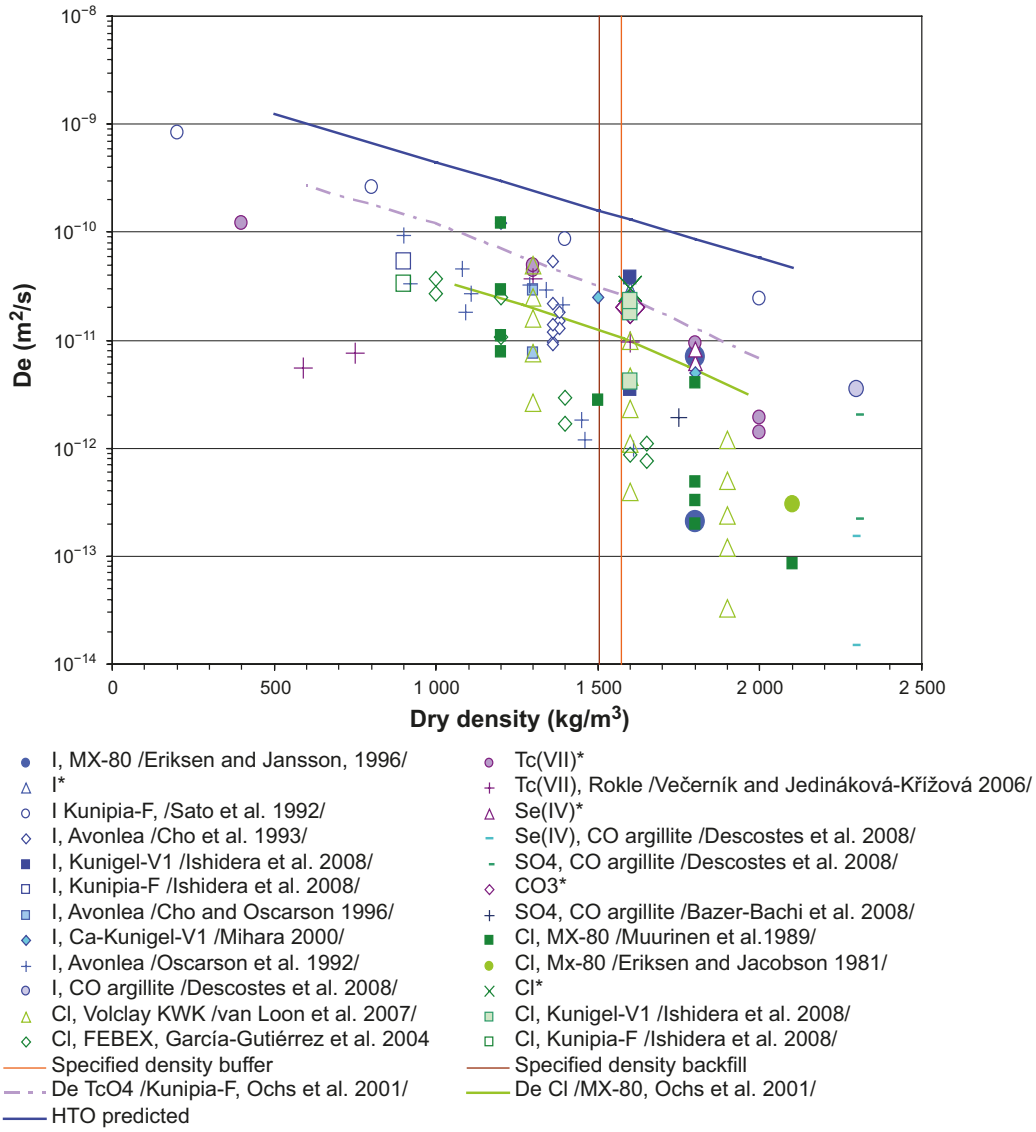

Figure 5-8. *Same data as in Figure 5-7, but including regression for HTO and independent predictions for chloride in MX-80 and Tc(VII) in Kunigel-V1 by Ochs et al. (2001).*

Because of the scatter of the data, and because of the basic uncertainty of assigning the experimentally observable anion diffusion effects to D_e and available porosity, recommended D_e is based on the following approach (instead of purely on a regression analysis):

- Accepting the argumentation in Ochs and Talerico (2004), it is suggested that the model prediction by Ochs et al. (2001) for the diffusion of chloride in MX-80 is representative for the range of dry densities considered here. This prediction is used for obtaining best estimates of D_e for the buffer and backfill at the dry densities corresponding to the brown and orange lines in Figure 5-8. The resulting best estimate D_e values are 1.1×10^{-11} m^2/s for the buffer and 1.2×10^{-11} m^2/s for the backfill.
- Upper and lower limits are somewhat subjectively based directly on the available experimental data, by drawing an area including the great majority of the data points. This is done in Figure 5-9, where an upper and lower green line mark the boundaries wherein it is most likely to find experimental D_e data. Note that at zero dry density, D_e equals D_w in accordance with process understanding.

Based on visual inspection, the lower green line is estimated to intercept the buffer dry density at $D_e = 6 \times 10^{-13}$ m^2/s and the backfill dry density at $D_e = 1 \times 10^{-12}$ m^2/s. The upper green line is estimated to intercept the buffer dry density at $D_e = 6 \times 10^{-11}$ m^2/s and the backfill dry density at $D_e = 7 \times 10^{-11}$ m^2/s.

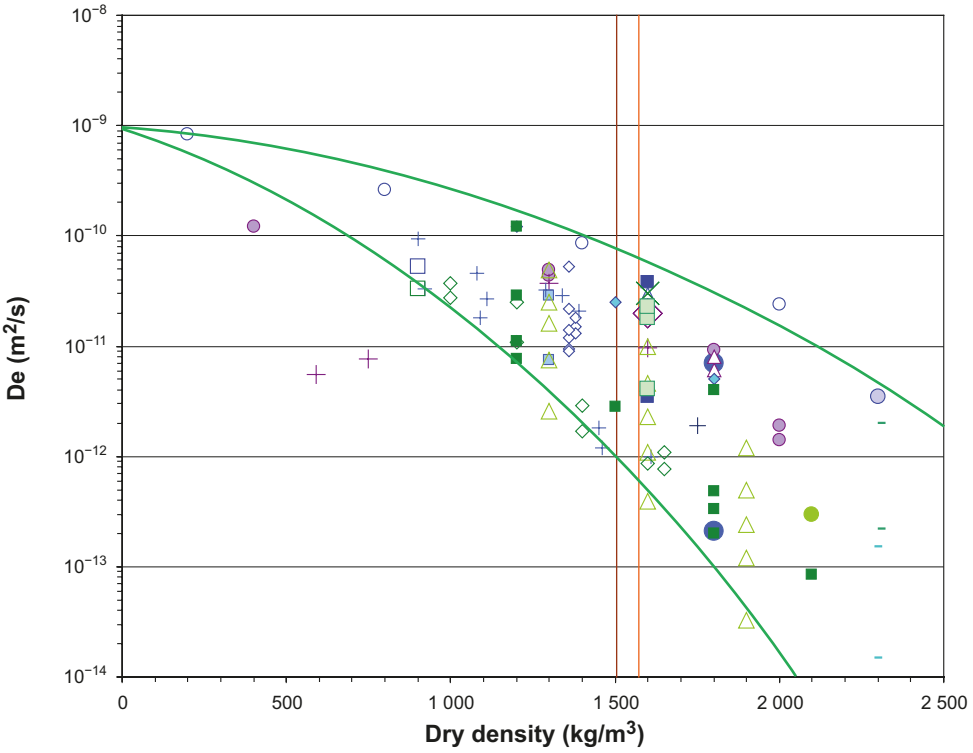

Figure 5-9. *Subjectively set area, bounded by the green lines, wherein D_e data are likely to be found. The data are the same as in Figure 5-7.*

By taking this approach, the uncertainty ranges become rather large. It is therefore suggested that they also encompasses the minor deviations in dry density estimated for the buffer and backfill.

Caesium

The effective diffusivity for Caesium is estimated from experimental data on compacted clays using Caesium as the tracer. Figure 5-10 shows the D_e data versus dry density.

In contrast with non-charged tracers (see Figure 5-6), it is less clear whether the D_e values for Cs correlate with the dry density. While the data by Sato (1998) show a clear trend, the D_e values measured by different researchers at densities close to the dry densities of the reference buffer and backfill range over two orders of magnitude. We refrain from speculating whether this spread is due to errors (experimental, raw data interpretation, etc). It is interesting to note that the range in D_e values cannot be entirely attributed to differences in the clay materials, as separate measurements on MX-80 at the same dry density give very different data.

Most weight is given to the data by Sato (1998), because they were measured for a range of dry densities and the raw data were interpreted without using a separate surface diffusion coefficient. The value for Cs is evaluated as follows, using again the same reasoning and approach as given in Ochs and Talerico (2004). In comparison to the regression line for HTO, the values measured by Sato (1998) are at most a factor 3 higher. Therefore, both the best estimate and upper limit of D_e for Cs are taken as three times higher the best estimate value for HTO, which becomes 4.2×10^{-10} m^2/s for the buffer and 4.8×10^{-10} m^2/s for the backfill. The lower limit is set equal to the lower limit for HTO.

Diffusion-available porosity

The diffusion-available porosity for neutral species and cations is suggested to equal the physical porosity. The diffusion-available porosity for anions is estimated by reducing the physical porosity by a reduction factor. This factor is based on the findings of van Loon et al. (2003a, b), who made an explicit effort to distinguish D_e from ε in their data interpretation. Their data for chloride suggest a reduction of the diffusion-available porosity (from HTO to anions) by a factor of 1.8–3.5, if a K_d

of zero is assumed. Based on this finding, a reduction factor of 2.5 is proposed. Suggested limiting values for the reduction factor are 1.8 and 3.5. These reduction factors are found to be reasonable for anionic tracers in bentonite, as shown in Ochs and Talerico (2004, Figure 5-6) and corresponding text. The range in the reduction factor is considered to be so large that it encompasses minor uncertainty in the physical porosity. Thus, for estimating the range of diffusion-available porosity for anions, the limiting values of the reduction factor can be applied to the best estimate physical porosity.

There is not enough resolution in background data to separately discuss precision, bias, and representativity.

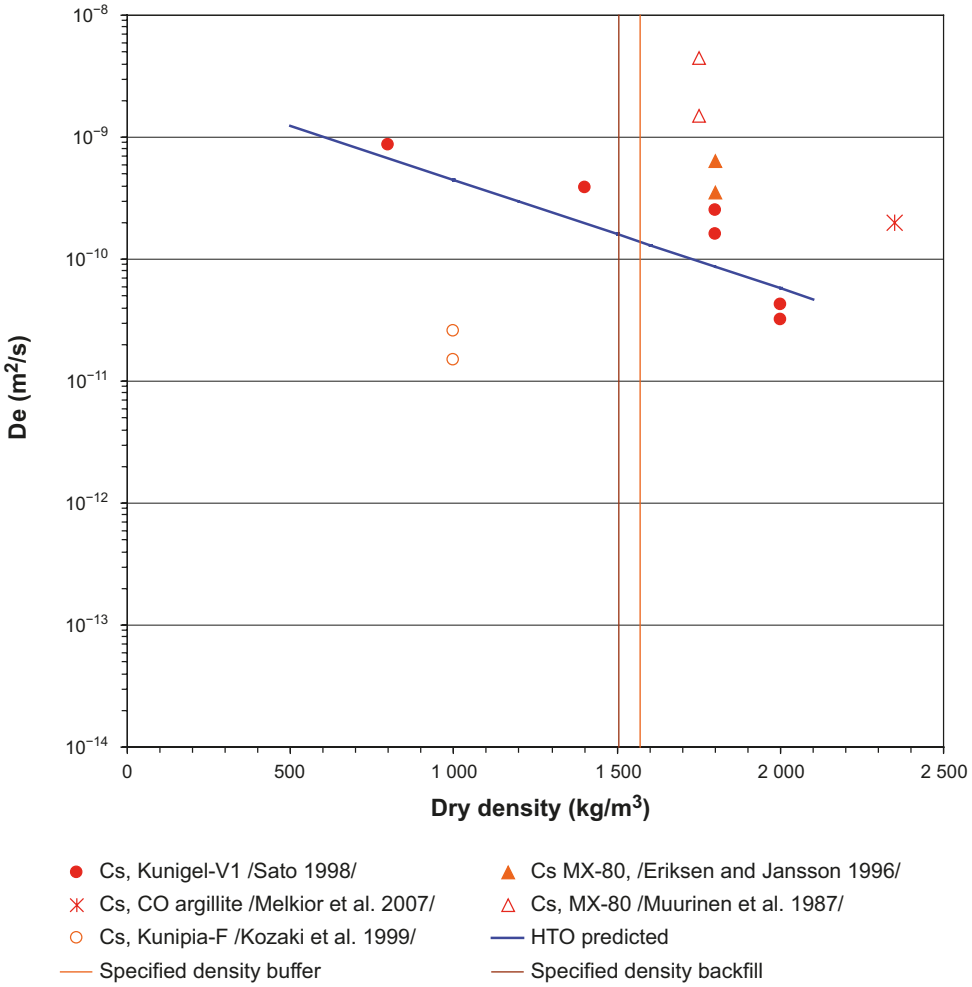

Figure 5-10. *Effective diffusivities obtained in compacted clays using Cs^+ as tracer. The specified reference buffer and backfill dry densities are indicated. The regression for HTO is shown for comparison.*

Sorption partitioning coefficient

Overview and general considerations

Sorption batch experiments are comparatively easy to control in terms of the applied boundary conditions. The interpretation of the experimental raw data is straightforward in well-designed experiments and K_d values can be obtained by simple arithmetic. As a single experiment requires relatively little effort, data are often obtained in large series, ideally as a function of an important parameter such as pH or radionuclide concentration. The resulting trends allow good evaluation of the consistency of various data sets. The embedding in a series of related data lends additional confidence to the individual data points in terms of both representativeness and absence of bias. Uncertainties for experimental K_d values, as well as for the related experimental key parameters (pH, CEC), were estimated in Ochs and Talerico (2004).

Batch sorption data obtained in typical laboratory systems need to be interpreted and re-calculated to correspond to the relevant site-specific conditions, because they are typically not obtained under chemical conditions matching those of the pore water in the bentonite. Because of the pronounced dependency of K_d on chemical conditions, uncertainties introduced during the transfer of data from experimental to site-specific conditions may make up the larger part of overall uncertainties (NEA 2005). For each step in such data transfer calculations, Ochs and Talerico (2004) estimated the respective uncertainties. Overall uncertainties were then calculated on the basis of estimated uncertainties for both experiments and data transfer.

Based on the available data, the compositions of Deponit CA-N and Milos bentonites are relatively similar to that of MX-80. Therefore, it can be expected that calculated pore water compositions will be similar, in particular under conditions where carbonate equilibria are controlled by an external pCO_2 (open system). Considering the uncertainties in pore water derivation discussed above, the modelling of pore water compositions for Deponit CA-N and Milos backfill is not seen as meaningful, as it would suggest a higher precision than can actually be achieved. Instead, the pore water compositions given in Ochs and Talerico (2004) are accepted for the present purpose.

Uncertainty factors

Below, the uncertainty factors introduced in Ochs and Talerico (2004) are briefly summarised. For a full account the reader should turn to Ochs and Talerico (2004, Section 5.1.4). The derivation of K_d values corresponding to the desired conditions in compacted bentonite from experimental data almost invariably involves an extrapolation step. Where possible, this extrapolation was done with the help of an appropriate thermodynamic sorption model. Where such a model is not available, semi-quantitative conversion procedures were applied, based on (Bradbury and Baeyens 2003). The conversion procedures include scaling/conversion for differences in CEC of the clay, in pH of the pore water (which determines surface speciation and radionuclide hydrolysis) and additional radionuclide complexation effects. In each conversion, uncertainty is introduced, which is handled by also introducing uncertainty factors. There is no obvious reason for choosing between quantifying uncertainties as an error on a linear scale (i.e, $K_d \pm$ error) versus a logarithmic scale (i.e. log $K_d \pm$ log error). Because several careful sorption studies (e.g. Bradbury and Baeyens 1997) report errors that are symmetric on a log scale, the latter type of representation was adopted for the present purpose. The following uncertainty factors (UF) are considered:

UF-starting K_d: There is always some uncertainty associated with the starting K_d value obtained through experiments or through modelling. For good quality experimental data an uncertainty of K_d of $\pm$ 0.2 $\log_{10}$ units is proposed, based on the findings of Bradbury and Baeyens (1997). An extensive modelling exercise (NEA 2005) showed that good sorption models are able to reproduce experimental data very closely, and we propose to use the same uncertainty as for experimental data. Where a K_d is derived using sorption data for an analogue element, but the speciation is evaluated directly for the element under investigation, the UF-starting K_d is set to $\pm$ 0.4 $\log_{10}$ units. In case of more questionable analogues, the UF-starting K_d is set to $\pm$ 0.6 $\log_{10}$ units.

UF-CEC: When scaling the K_d based on different CEC values, uncertainty is introduced. It is estimated that CEC can be measured within an uncertainty of ca 10 %, and that S-OH site density can be scaled via CEC within an uncertainty of ca 20 %. This gives an overall uncertainty of $\pm$ 30 %, or $\pm$ 0.15 $\log_{10}$ units.

UF-pH: If performing a conversion based on pH, this introduces uncertainty. When performing such conversion, two K_d values are needed, one at the source pH and one at the application pH. Because the conversion contains the uncertainties of two K_d values, UF-pH is set to 0.4 $\log_{10}$ units (two times UF-starting K_d). Because of the predominance of ion exchange for Cs sorption, the pH-conversion factor is replaced in this case by a CF-cation conversion factor with a UF-cation conversion of ± 0.4 $\log_{10}$ units.

UF-speciation: If performing conversion due to different speciation (pore water composition), uncertainty is introduced. Following the evaluation by Hummel and Berner (2002), who propose a factor of 2 between highest and lowest value, a UF-speciation of ± 0.3 $\log_{10}$ units is used. Note, however, that this is the uncertainty associated with the use of a given complete TDB. If certain species are missing or erroneous, uncertainties could be much higher. Also, this uncertainty factor does not take into account any inappropriate evaluation of the conversion factor for speciation.

UF-batch: The conversion from dispersed batch system to a compacted system does not introduce significant uncertainty. However, an additional uncertainty factor is introduced to acknowledge possible uncertainties in the application conditions (i.e. in the pore water composition, resulting from model uncertainties and effects from variations in the amount of impurities present in bentonite samples). The uncertainty factor was set to ± 0.3 $\log_{10}$ units.

The validity of this approach was in Ochs and Talerico (2004, Section 5.3.5) evaluated for each radionuclide by comparing D_a values, calculated from K_d values derived for compacted bentonite and D_e using Equation 5-3, with independent experimental data for D_a. Figure 5-11 shows an example of such a comparison, where the D_a data of Am as estimated from thermodynamic modelling for three different pore waters are compared with independent D_a obtained from experiments.

In Ochs and Talerico (2004) it is judged as extremely likely that that any K_d for Am under the specified scenario would be within the indicated ranges.

Here a caution is warranted. In this section the recommended uncertainty is distributed symmetrically around a central value, which may give rise to higher upper K_d values than experimentally observed in experiment. When using the data in subsequent radionuclide transport modelling, it must be carefully considered how the large uncertainty ranges of K_d affect the estimate of radiological risk. Generally this should not give rise to non-conservatism in probabilistic modelling, as it is the lower tail of the K_d distribution that affects assessment results.

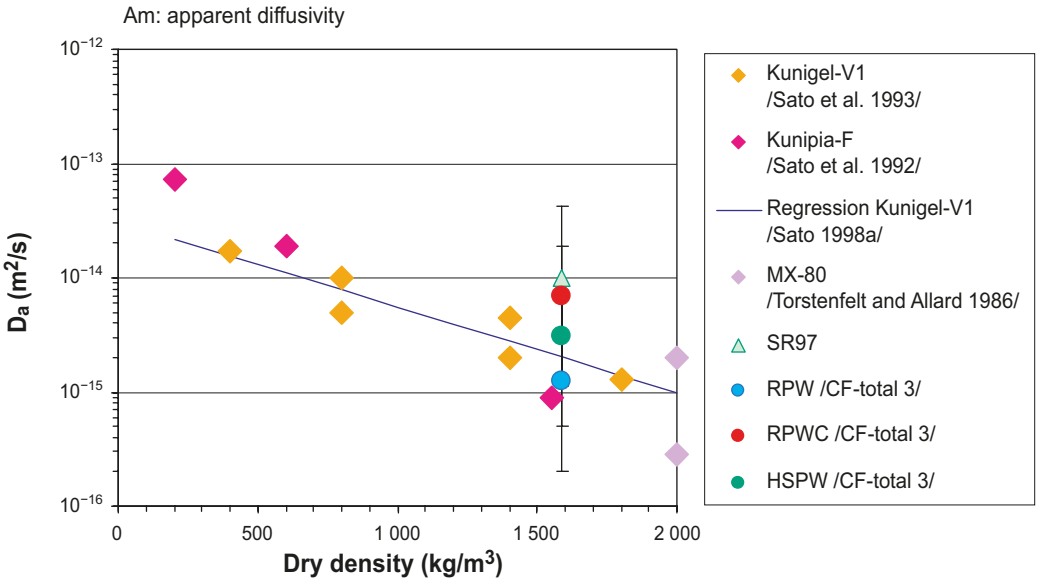

Figure 5-11. *Example of comparison between modelled D_a and D_a obtained from experimental values (reproduced from Ochs and Talerico (2004, Figure 5-8)).*

Elements not considered in SR-Can

For some of the elements of interest for the PSAR, no K_d data was delivered in Ochs and Talerico (2004). These elements are Mo, Cd, Ac, S, dissolved O_2, and H (tritium, assumed in the form of HTO). K_d values for these elements are derived based on the following considerations.

- HTO corresponds to water in the chemical sense, and is therefore considered non-sorbing.
- Dissolved oxygen is also considered as non-sorbing (as methane or radon).
- Based on Brookins (1988) and Hummel et al. (2002), MoO_4^{2-} and the respective protonated forms (where Mo is present in +VI-valent form) are considered as the only relevant aqueous species. Therefore, sorption is considered to be identical to that of selenate; i.e. $K_d = 0$.
- Ac exists only in +III valent form. It is treated in analogy to the lanthanide elements (Eu, Ho, Sm). This is pessimistic, since the chemistry of Ac may be closer to that of the actinide elements. To be consistent with the approach used by Ochs and Talerico (2004) an additional uncertainty factor of 2.5 is used to account for uncertainties introduced in the analogy consideration.
- Based on the systematics regarding hydrolysis discussed in Baes and Mesmer (1976), it is assumed that the main sorption process (surface complexation) is very similar in case of Cd and Ni. Therefore, Cd is treated by using the analogy with Ni and an additional UF of 4 (see Ochs and Talerico (2004) for the selection of UF).
- For sulphur, relevant and stable oxidation states in aqueous solutions include -II and VI, with HS^- and SO_4^{2-} as the only important species in typical solutions (sulphite is not considered relevant under the present conditions and timeframes). Following the handling of uncertainties for redox-sensitive elements proposed in Ochs and Talerico (2004), if variable redox conditions need to be taken into account, the overall uncertainty for the K_d of S would encompass the combined data range for all oxidation states predicted to be present.
  - For sulphide, no reliable data could be found and a K_d of zero is proposed.
  - Relatively little is known regarding the sorption of sulphate on mineral surfaces. Most information is available for the sorption of sulphate on (hydrous) iron oxides (see Davis and Kent 1990) and RES^{3}T database (Brendler et al. 2003)). Sorption of sulphate on metal oxides is weak and strongly influenced by the presence of background electrolyte anions; it is typically interpreted as formation of outer-sphere complexes (Davis and Kent 1990).
  - Regarding sorption on smectite or bentonite under relevant conditions, only one systematic study has been found. Bazer-Bachi et al. (2007) measured sulphate sorption on Callovo-Oxfordien argillites by batch, column, and diffusion studies. Due to the weak sorption of sulphate, only one of several batch experiments can be interpreted to show sorption different from zero. As this result is corroborated by column experiments, it is accepted for the present purpose. Sorption data derived from diffusion are not used, because they are not consistent and may suffer from uncertainties in the interpretation of diffusion-available porosity. On this basis, an average K_d of 5×10^{-4} m^3/kg can be extracted, based on both batch and column experiments. This value has been obtained under conditions that are similar to the calculated pore water conditions in MX-80. Conversion factors have been applied to account for the relatively large differences in the CEC of the substrates and the difference in total dissolved [sulphate + chloride] concentration, based on the expected outer-sphere complex sorption of sulphate. The resulting values and uncertainties are plotted in Figure 5-12. The final results are compiled in Table 3-19 in Section 3.3.10.

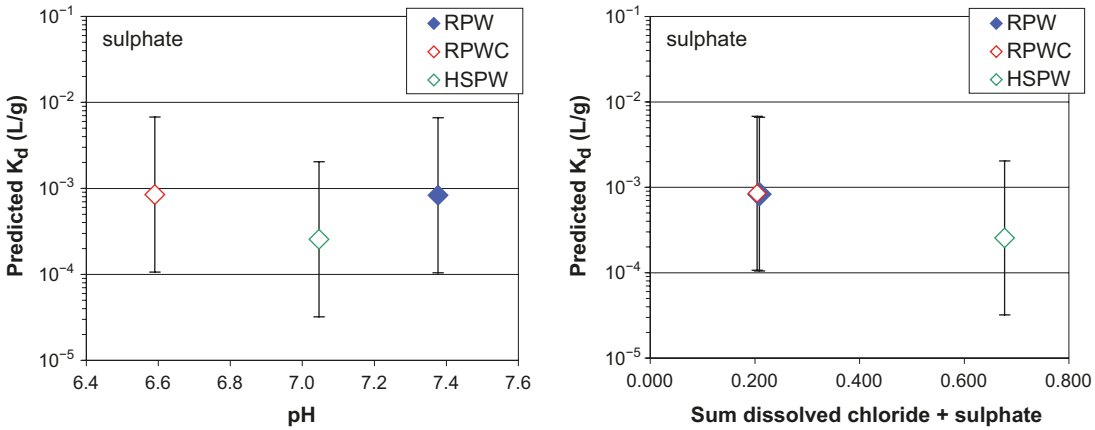

Figure 5-12. *K_d values for sulphate derived for different conditions based on the experimental data by Bazer-Bachi et al. (2007).*

5.3.8 Spatial and temporal variability of data (text reproduced from SR-Site Data report)

The following remarks concern saturated conditions, and may not necessarily apply during the saturation phase.

Spatial variability of data

On the scale of a deposition hole and tunnel, the buffer and backfill can be considered as homogeneous. Therefore, spatial variation is not considered relevant.

Temporal variability of data

Temporal variation becomes important when the evolution of clay material and pore water is being considered. This has to be assessed through models, and is of special importance in light of evolving geochemical conditions and post-closure removal of the buffer and backfill, e.g. due to erosion. If the post-closure removal is limited, K_d data reported in this text can be used, and D_e and ε data can be scaled to new appropriate clay densities. If the post-closure removal is extensive, which is conceivable in deposition holes, one may have to assume advective conditions where there is limited or no retention in the buffer. In such case, the data in this section are of little importance (although K_d principally still applies in advective transport).

In this section, temporal variability due to evolution of the groundwater chemistry is to some extent dealt with by supplying data corresponding to a few different groundwaters, which may be encountered during a glacial cycle. However, one must be humble to the fact that the temporal variability in geochemical conditions evokes large uncertainty.

5.3.9 Correlations (text reproduced from SR-Site Data report)

Following their chemical characteristics, the radionuclides considered can be organised into groups (correlation groups) of elements and oxidation states whose migration behaviour will generally show a similar response to variations in pore water composition, as caused by variations in groundwater composition, bentonite evolution, etc. Moreover, elements handled via chemical analogies correlate with the respective analogues. Overall, the following grouping is used, where analogies are also indicated in the following way. X/Y: both elements were treated identically in the data derivation; X(Y): X was derived based on analogy with Y. Groups 1 to 7, as well as 10, should be seen as correlation groups.

1. Alkaline and alkaline earth elements: Cs, Ra/Sr.
2. Other di-valent elements Pb, Ni, Cd(Ni).

3. Tri-valent elements: Am, Cm(Am), PuIII(Am), Sm/Ho/Ce/Ac(Eu).
4. Tetra-valent elements and Zr: Th, UIV(Th), PuIV(Th), NpIV(Th), TcIV(Th), Zr(Th), Sn(Th). Due to lack of reliable element-specific data, Tc(IV), Zr, and Sn(IV) were also evaluated on the basis of data for Th, and the derived K_d values show therefore some correlation (because Th is not an ideal analogue for these elements, additional uncertainties are associated with the resulting K_d values).
5. Penta-valent elements: NpV, PuV(NpV).
6. Hexa-valent cationic elements: UVI, PuVI(UVI).
7. Non-sorbing anions: $Cl^-/I^-/TcO_4^-/SeO_4^{2-}/HSe^-/HS^-/MoO_4^{2-}$/HTO/simple organic anions.
8. Some elements are not known well enough to assess correlations Pa, Nb, Pd, Ag.
9. The weakly sorbing anions SeO_3^- and carbonate will not correlate. Carbonate is proposed to be handled via isotope exchange. In case of the weakly sorbing anion SO_4^{2-}, not enough information is available to exactly define correlations, but a rough correlation with SeO_3^- is considered more reasonable than assigning no correlation at all.
10. Dissolved gasses: Rn, CH_4, O_2.

Furthermore Ochs and Talerico (2004) points out that:

- Redox-sensitive radionuclides will take on higher oxidation states if oxidising conditions are considered, generally leading to lower K_d values. Notable exceptions are Se(-II→IV) and S(-II→VI).
- A lower pore water pH (within the range considered) will decrease the K_d of most radionuclides (actinides, lanthanides, transition elements, heavy metals) in a similar way. Exceptions are penta- and hexavalent actinides that form oxo-cations: U(VI), Np(V), Pu(VI/V).
- An increase in major cation concentration will lower K_d values for alkaline and alkaline earth elements.
- A lower density of the buffer will lead to higher D_e and D_a values.

5.3.10 Result of supplier's data qualification (text reproduced from SR-Site Data report)

Concerning solute transport parameters of the buffer, the major work was done in a dedicated SR-Can report (Ochs and Talerico 2004), and it has not been an aim of this present work to reproduce that work. Only in cases where there are obvious differences in conditions between SR-Can and the PSAR or where new data have been compiled, the supplied data have been changed from those recommended in SR-Can.

For the backfill, the suggested data are based on data for MX-80 taken from Ochs and Talerico (2004), and modified by performing scaling with regards to dry density (for D_e and ε) and CEC (for K_d for Cs, Ra, Sr).

Diffusion-available porosity

For neutral species and cations, the diffusion-available porosity is suggested to equal the physical porosity.

Concerning the diffusion-available porosity for anions, the reduction factors suggested in Ochs and Talerico (2004) are suggested for use also in SR-Site. The reduction factors are given as a best estimate at 2.5, an upper limit reduction factor at 3.5 and a lower limit reduction factor at 1.8. The range in the reduction factor is suggested to be large enough to encompass minor uncertainty in the physical porosity. Thus, for estimating the range in diffusion-available porosity for anions, the best estimate and limiting values of the reduction factor can be applied to the best estimate physical porosity. This is done in Table 5-18.

Table 5-18. Diffusion-available porosity, ε.

	Parameter	Lower limit	Best estimate	Upper limit
Reference buffer	Diffusion-available porosity ε (%) for non-charged and cationic species (same as physical porosity in Table 5-5)	41	43.5	46
	Diffusion-available porosity ε (%) for anions	12.4	17.4	24.1
Reference backfill	Diffusion-available porosity ε (%) for non-charged and cationic species (same as physical porosity in Table 5-6)	44	46	48
	Diffusion-available porosity ε (%) for anions	13.1	18.4	25.6

Effective diffusivity

In case of the effective diffusivity, new experimental data have warranted an update of the recommended data. The approach taken for the effective diffusivity is to sort the different elements into three categories: anions; hydrolysable cationic elements existing in the form of different species; and cations with enhanced diffusion due to surface diffusion (Cs), as have been done in SR-Can (Ochs and Talerico 2004).

The derivation of the D_e data in Table 5-19 is described in Section 5.3.7. What can be added is that the uncertainty range for non-charged and hydrolysable elements is based on the standard error shown in Figure 5-6.

Table 5-19. Effective diffusivity, D_e.

	Parameter	Best estimate	Upper limit	Lower limit
Reference buffer	Effective diffusivity D_e (m^2/s) for non-charged and hydrolysable elements (cations except Cs)	1.4×10^{-10}	2.1×10^{-10}	9.3×10^{-11}
	Effective diffusivity D_e (m^2/s) for anions	1.1×10^{-11}	6.0×10^{-11}	6.0×10^{-13}
	Effective diffusivity D_e (m^2/s) for Cs	4.2×10^{-10}	4.2×10^{-10}	9.5×10^{-11}
Reference backfill	Effective diffusivity D_e (m^2/s) for non-charged and hydrolysable elements (cations except Cs)	1.6×10^{-10}	2.4×10^{-10}	1.1×10^{-10}
	Effective diffusivity D_e (m^2/s) for anions	1.2×10^{-11}	7.0×10^{-11}	1.0×10^{-12}
	Effective diffusivity D_e (m^2/s) for Cs	4.8×10^{-10}	4.8×10^{-10}	1.1×10^{-10}

Sorption partition coefficients

For most elements, the K_d for the buffer and backfill is taken directly from Ochs and Talerico (2004). The exceptions are for Cs, Ra, and Sr, which are rescaled to encompass new CEC values of the clay materials, and elements not reported in Ochs and Talerico (2004).

For all species but Cs, Ra, Sr, and S(IV), the same K_d values apply for MX-80, Deponit CA-N, and Milos backfill. These K_d data for the reference pore water, corresponding to saline and non-saline groundwater in a system that is open with respect to CO_2, are shown in Table 5-16. In Table 5-17, the equivalent data for highly saline pore water, corresponding to highly saline groundwater in a system that is open with respect to CO_2, are shown. Both K_d and $\log_{10}K_d$ values are shown. The number of significant digits in the K_d values are taken directly from Ochs and Talerico (2004) and does not reflect the accuracy with which the data are estimated. Two significant digits have been assigned to the $\log_{10}K_d$ values, and this should fairly well reflect on the accuracy with which the data are estimated.

Table 5-20. Recommended K_d values for the reference buffer and backfill (MX-80, and Asha 2012) in reference pore water, corresponding to saline and non-saline groundwaters. CEC sensitive elements are shown in Table 5-22.

Reference pore water (RPW)						
Radionuclide (Redox State)	**K_d (m^3/kg)**		**Upper K_d limit (m^3/kg)**		**Lower K_d limit (m^3/kg)**	
	Value	**Log value**	**Value**	**Log value**	**Value**	**Log value**
Ac(III)	8	0.92	233	2.4	0.3	–0.52
Ag(I)	-	n.a	15	1.2	0	n.a
Am(III)	61	1.8	378	2.6	10	1.0
C, carbonate species	*ie*, 0	n.a.	ie, 0	n.a.	ie, 0	n.a.
C, methane, organic acids	0	n.a	0	n.a	0	n.a
Cd(II)	0.30	–0.52	13.3	1.1	0.007	–2.2
Ce(III)	8	0.92	93	2.0	0.8	–0.12
Cl(–I)	0	n.a	0	n.a	0	n.a
Cm(III)	61	1.8	378	2.6	10	1.0
Eu(III)	8	0.92	93	2.0	0.8	–0.12
Ho(III)	8	0.92	93	2.0	0.8	–0.12
I(–I)	0	n.a	0	n.a	0	n.a
Mo(VI)	0	n.a	0	n.a	0	n.a
Nb(V)	3	0.48	45	1.7	0.2	–0.70
Ni(II)	0.30	–0.52	3.3	0.52	0.03	–1.6
Np(IV)	63	1.8	1 113	3.0	4	0.55
Np(V)	0.02	–1.6	0.2	–0.81	0.004	–2.4
Pa(IV)	3	0.48	45	1.7	0.2	–0.70
Pa(V)	3	0.48	45	1.7	0.2	–0.70
Pb(II)	74	1.9	457	2.7	12	1.1
Pd(II)	5	0.70	75	1.9	0.3	–0.48
Pu(III)	100	2.0	984	3.0	10	1.0
Pu(IV)	63	1.8	1 111	3.0	4	0.55
Pu(V)	0.02	–1.6	0.2	–0.62	0.002	–2.6
Pu(VI)	3	0.45	28	1.4	0.3	–0.54
Rn(–)	0	n.a	0	n.a	0	n.a
S(–II)	0	n.a	0	n.a	0	n.a
Se(–II)	0	n.a	0	n.a	0	n.a
Se(IV)	0.04	–1.4	0.4	–0.39	0.003	–2.5
Se(VI)	0	n.a	0	n.a	0	n.a
Sm(III)	8	0.92	93	2.0	0.8	–0.12
Sn(IV)	63	1.8	1 764	3.2	2.3	0.35
Tc(IV)	63	1.8	1 764	3.2	2.3	0.35
Tc(VII)	0	n.a	0	n.a	0	n.a
Th(IV)	63	1.8	700	2.8	6	0.75
U(IV)	63	1.8	1 113	3.0	3.6	0.55
U(VI)	3	0.45	18	1.2	0.5	–0.34
Zr(IV)	4	0.56	103	2.0	0.1	–0.88

ie = ion exchange.

Table 5-21. Recommended K_d values for the reference buffer and backfill (MX-80, and Asha 2012) in highly saline pore water, corresponding to highly saline groundwaters. CEC sensitive elements are shown in Table 5-23.

Highly saline pore water (HSPW)						
Radionuclide (Redox State)	**K_d (m^3/kg)**		**Upper K_d limit (m^3/kg)**		**Lower K_d limit (m^3/kg)**	
	Value	**Log value**	**Value**	**Log value**	**Value**	**Log value**
Ac(III)	5	0.71	142	2.2	0.2	–0.74
Ag(I)	-	n.a	15	1.2	0	n.a
Am(III)	24	1.4	152	2.2	4	0.59
C, carbonate species	ie, 0	n.a.	ie, 0	n.a.	ie, 0	n.a.
C, methane, organic acids	0	n.a	0	n.a	0	n.a
Cd(II)	0.07	–1.2	3.0	0.48	0.002	–2.8
Ce(III)	5	0.71	57	1.8	0.5	–0.34
Cl(–I)	0	n.a	0	n.a	0	n.a
Cm(III)	24	1.4	152	2.2	4	0.59
Eu(III)	5	0.71	57	1.8	0.5	–0.34
Ho(III)	5	0.71	57	1.8	0.5	–0.34
I(–I)	0	n.a	0	n.a	0	n.a
Mo(VI)	0	n.a	0	n.a	0	n.a
Nb(V)	3	0.48	45	1.7	0.2	–0.70
Ni(II)	0.07	–1.2	0.8	–0.12	0.01	–2.2
Np(IV)	40	1.6	702	2.8	2	0.35
Np(V)	0.02	–1.6	0.1	–0.84	0.004	–2.4
Pa(IV)	3	0.48	45	1.7	0.2	–0.70
Pa(V)	3	0.48	45	1.7	0.2	–0.70
Pb(II)	46	1.7	287	2.5	7	0.87
Pd(II)	5	0.70	75	1.9	0.3	–0.48
Pu(III)	43	1.6	421	2.6	4	0.64
Pu(IV)	40	1.6	700	2.8	2	0.35
Pu(V)	0.02	–1.7	0.2	–0.66	0.002	–2.6
Pu(VI)	3	0.45	28	1.4	0.3	–0.55
Rn(–)	0	n.a	0	n.a	0	n.a
S(–II)	0	n.a	0	n.a	0	n.a
Se(–II)	0	n.a	0	n.a	0	n.a
Se(IV)	0.05	–1.3	0.6	–0.24	0.005	–2.3
Se(VI)	0	n.a	0	n.a	0	n.a
Sm(III)	5	0.71	57	1.8	0.5	–0.34
Sn(IV)	40	1.6	1 113	3.0	1.4	0.15
Tc(IV)	40	1.6	1 113	3.0	1.4	0.15
Tc(VII)	0	n.a	0	n.a	0	n.a
Th(IV)	40	1.6	442	2.6	4	0.55
U(IV)	40	1.6	703	2.8	2.3	0.35
U(VI)	3	0.45	18	1.2	0.5	–0.34
Zr(IV)	5	0.68	134	2.1	0.2	–0.77

ie = ion exchange.

For the elements Cs, Ra, and Sr, as well as for S(IV), the sorption depends on the CEC value of the clay material. Therefore, the supplied K_d values differ slightly between different materials. For these particular materials, the differences in CEC are so small that the difference in K_d is largely dwarfed by the general uncertainty. Data for the reference pore water are shown in Table 5-22 and data for the highly saline pore water are shown in Table 5-23.

For the elements that are included in this section but were not included in Ochs and Talerico (2004), all but one are either suggested to be non-sorbing or analogue to an element handled in Ochs and Talerico (2004).

Table 5-22. Recommended K_d values for the reference buffer and backfill (MX-80 and Asha 2012) in reference pore water, corresponding to saline and non-saline groundwaters. Only CEC sensitive elements.

Reference pore water (RPW)							
Radionuclide (Redox State)	K_d (m^3/kg)		Upper K_d limit (m^3/kg)		Lower K_d limit (m^3/kg)		Clay material
	Value	Log value	Value	Log value	Value	Log value	
Cs(I)	0.093	–1.0	0.56	–0.26	0.015	–1.8	MX-80
Cs(I)	0.090	–1.0	0.54	–0.27	0.015	–1.8	Asha 2012
Ra(II)	0.0045	–2.3	0.027	–1.6	0.00075	–3.1	MX-80
Ra(II)	0.0044	–2.4	0.026	–1.6	0.00073	–3.1	Asha 2012
S(VI)	0.00083	–3.1	0.0066	–2.2	0.00010	–4.0	MX-80
S(VI)	0.00068	–3.2	0.0054	–2.3	8.5×10^{-5}	–4.1	Asha 2012
Sr(II)	0.0045	–2.3	0.027	–1.6	0.00075	–3.1	MX-80
Sr(II)	0.0044	–2.4	0.026	–1.6	0.00073	–3.1	Asha 2012

Table 5-23. Recommended K_d values for the reference buffer and backfill (MX-80 and Asha 2012) in highly saline pore water, corresponding to highly saline groundwaters. Only CEC sensitive elements.

Highly saline pore water (HSPW)							
Radionuclide (Redox State)	K_d (m^3/kg)		Upper K_d limit (m^3/kg)		Lower K_d limit (m^3/kg)		Clay material
	Value	Log value	Value	Log value	Value	Log value	
Cs(I)	0.031	–1.5	0.18	–0.73	0.0051	–2.3	MX-80
Cs(I)	0.030	–1.5	0.18	–0.75	0.0050	–2.3	Asha 2012
Ra(II)	0.0012	–2.9	0.0070	–2.2	0.00020	–3.7	MX-80
Ra(II)	0.0011	–2.9	0.0068	–2.2	0.00019	–3.7	Asha 2012
S(VI)	0.00022	–3.6	0.0018	–2.7	2.8×10^{-5}	–4.6	MX-80
S(VI)	0.00022	–3.7	0.0017	–2.8	2.7×10^{-5}	–4.6	Asha 2012
Sr(II)	0.0012	–2.9	0.0070	–2.2	0.00020	–3.7	MX-80
Sr(II)	0.0011	–2.9	0.0068	–2.2	0.00019	–3.7	Asha 2012

Concerning sulphur, S(II) as sulphide is assumed to be non-sorbing and S(IV) as sulphate is assumed to be slightly sorbing.

5.3.11 Judgement by the assessment team

There are differences in the target dry density for the buffer and backfill in the PSAR compared to SR-Site. The buffer density is lower and the porosity is higher and there is another backfill material. The small differences and the relative unimportance of the parameters still justifies the use of the parameters from the SR-Site assessment as reproduced above.

5.3.12 Data recommended for use in assessment

The following migration data of the buffer and backfill are recommended for use in the PSAR.

Sorption partitioning coefficient

For non-saline and saline groundwaters, the K_d data of Table 5-20 and Table 5-22 are recommended. The data of Table 5-16 are independent of the bentonite material used (MX-80, Deponit CA-N, and Milos Backfill as seved as example materials in SR-Site or MX-80 and Asha BF as serves as example materials in the PSAR). The data of Table 5-16 are dependent on the bentonite material, and it is stated which data correspond to which material.

For highly saline groundwater the K_d data of Table 5-21 and Table 5-23 are recommended. The data of Table 5-21 are independent of the bentonite material used while the data of Table 5-23 are dependent on the bentonite material, and it is stated which data correspond to which material.

All data are given as best estimate, upper limit, and lower limit. In probabilistic modelling $\log_{10}$ values should be used in triangular distributions in the $\log_{10}$-space.

Effective diffusivity

The data in Table 5-19 should be used for the buffer and backfill. The following distribution should be used, based on the best estimate, upper limit and lower limit data.

- Anions: Double triangular distribution in the $\log_{10}$-space.
- Neutral and cations (except Cs): Triangular distribution in the $\log_{10}$-space.
- Caesium: Right triangular distribution in the $\log_{10}$-space.

Diffusion-available porosity

The data in Table 5-18 should be used for the buffer and backfill. The following distribution should be used, based on the best estimate, upper limit, and lower limit data.

- Anions: Double triangular distribution in the normal space.
- Neutral and cations: Triangular distribution in the normal space.

6 Geosphere data

6.1 Groundwater chemical composition

The aim of this section is to describe the groundwater chemical data used as input to models used in the PSAR assessment.

There are two types of modelling activities that deal with groundwater chemical compositions:
(1) models that have as main purpose to *calculate* groundwater chemical compositions; and
(2) models that *use* groundwater chemical compositions as input conditions.

The process of obtaining the groundwater composition data is mainly based on the analysis of present-day groundwater compositions, described in the site-descriptive models, see the **Site description Forsmark** and Site description Laxemar (SKB 2009c), as well as the results from chemical equilibrium calculations including water-rock interactions (using the computer code PhreeqC (Parkhurst and Appelo 1999)), coupled with the results from the hydrogeological modelling described in Section 6.6. Additional model calculations are used for specific groundwater components, for example to evaluate the transport of the reactive gaseous components (such as O_2).

Important modelling activities that use chemical compositions as input data concern buffer evolution and stability, canister corrosion, radionuclide transport, and hydrogeological modelling. From the perspective of assessing the post-closure safety of a KBS-3 repository, the most important parameters are the main chemical components which affect salinity and ionic strength, as well as sulphide, pH, and redox parameters.

The PSAR is based on the same modelling of Groundwater chemical composition as SR-Site. In the following sections, the modelling strategy is described (Section 6.1.1) followed by an account of the experiences from the SR-Site safety assessment (Section 6.1.2). Since the PSAR is based on the same data as SR-Site, the data qualification (Sections 6.1.3 to 6.1.10) is reproduced from the SR-Site Data report. In Section 6.1.11 the formal judgement by the assessment team to use the qualified data is presented followed by Section 6.1.12 where the recommended data is presented.

6.1.1 Modelling

This section describes data which are expected from the supplier, and the modelling activities where the data are used.

Defining the data requested from suppliers

As input to the PhreeqC modelling the data supplier should deliver the compositions of the end-member groundwaters (identified in the Forsmark site), the mass fractions of these end-members (mixing ratios) and thermodynamic data.

As output from the PhreeqC modelling the supplier should deliver statistics of the:

- Sum of the concentrations of main cations, expressed in charge equivalents as $\Sigma q[M^{q+}]$, where q is the cation charge number and $[M^{q+}]$ is the cation concentration (mol/L).
- Concentrations (mol/L) of the major cations (Na^+, K^+, Ca^{2+}, and Mg^{2+}) and anions (Cl^-, SO_4^{2-}, PO_4^{3-}) and total inorganic carbon.
- Ionic strength (mol/L).
- pH.
- Redox potential *Eh* (mV).

Furthermore, references to files containing the complete results from the PhreeqC modelling should be supplied, from which the complete groundwater composition for individual coordinates and times can be extracted. Based on observations, and as conceptually estimated from the hydrological evolution of the site, best estimate data should be delivered for the following components:

- Concentrations (mol/L) of dissolved molecular hydrogen H_2, acetate CH_3COO^-, ammonium NH_4^+, nitrite NO_2^-, dissolved organic carbon DOC, and methane CH_4.
- Concentration (g/L) of natural colloids.
- Concentration (mol/L) of sulphide HS^-.

As input to the modelling of dissolved oxygen ingress for the most unfavourable situations (infiltration of oxygen-rich waters during glaciation) the data suppliers should deliver: the rock properties (density, porosity, effective diffusivity, and amount of biotite and average biotite grain size) and the flow-related transport resistance (F, yr/m) along recharge flow paths to the canister positions.

Based on oxygen ingress modelling the supplier shall deliver:

- The maximum concentration (mol/L) of dissolved molecular oxygen (O_2) at repository depth for the affected canister positions.

All of the above data should to the extent possible reflect on the reference evolution of the assessment, or appropriate variant cases. The data should reflect the relevant rock volume hosting the repository. Data are not requested for the excavation/operation period. Instead Salas et al. (2010) is referred to, wherein such data are reported.

Modelling activities in which data will be used

Modelling activities resulting in chemical composition data

The chemistry data flow is as follows in the assessment model chain. Groundwater chemistry data collected within the site investigation, and analysed in the site-descriptive modelling, are used as input to the hydrogeological models as a calibration tool. The data are also used to establish the chemical compositions of the end-member waters used when calculating the transport of solutes, for example the composition of the infiltrating meteoric waters, seawater, etc. Collected data also include mineral compositions, abundances, and physical properties of the rocks minerals and fracture fillings. The data are used to build up a conceptual model of the past hydrogeochemical evolution of the site and to evaluate the results in SR-Site. Both the conceptual model and the comparison between model results and analytical data provide confidence in the conclusions of the assessment.

Groundwater compositions for different periods of interest are calculated using the PhreeqC code (Parkhurst and Appelo 1999). This modelling, as described in Salas et al. (2010), requires mixing proportions and compositions of end-member groundwater components. The mixing proportions are obtained directly from, or are based on the results of, hydrogeological modelling described in Sections 6.6 and 6.7. The hydrogeological modelling is also described in Joyce et al. (2010), Vidstrand et al. (2010) and Selroos and Follin (2010). In addition a thermodynamic database is needed, as discussed in this section and also in Section 3.1.

The concentrations of reactive components (CH_4, H_2, DOC, etc) and colloids that cannot be reproduced by the models of mixing and reactions have been conceptually evaluated, based on analytical data. In the case of the sulphide concentration, which is affected by bacterial processes, it can be modelled with PhreeqC using different assumptions to mimic biotic and abiotic processes, but the different assumptions result in quite different concentration ranges. Therefore, the results need to be based on measurement data and observations from the site investigation and monitoring programmes. For some components (e.g. H_2) supporting results are compiled from observations reported in the open literature.

In the case of dissolved molecular oxygen, the maximum concentration at repository depth during the most unfavourable event of the glacial cycle (when the ice front is over the repository) is estimated by reactive transport modelling (Sidborn et al. 2010). This modelling uses transport parameters (cf Section 6.7.2) as well as flow related migration properties (cf Section 6.7) for different flow paths, based on recharge particle tracks obtained from the hydrogeological models.

Modelling activities using chemical composition data

The chemical data supplied in this section are used by other SR-Site modelling activities either quantitatively, for example to calculate the extent of copper corrosion, or qualitatively, for example when motivating why a process can be disregarded in safety assessment modelling. In the following, the important modelling activities using chemical composition data are outlined.

Buffer stability and erosion: Data on the main components of the groundwater at repository depth are used to evaluate the stability and erosion of the buffer and backfill, as detailed in Neretnieks et al. (2009). As input data, statistics on the pH, divalent cations Ca^{2+} and Mg^{2+}, as well as the monovalent cations Na^{+} and K^{+}, are needed. In addition, the sum of the concentrations of main cations, expressed in charge equivalents as $\Sigma q[M^{q+}]$, is needed. According to the design premises, the safety function indicator criteria is that $\Sigma q[M^{q+}] > 4$ mM. Other input data needed are the complete groundwater compositions of the water having the lowest Ca^{2+}/Na^{+} ratio, the lowest Ca^{2+} concentration, the lowest Na^{+} concentration, the highest and lowest total chloride concentration, the highest and lowest total bicarbonate concentration, and the highest and the lowest total sulphate concentration. These data are required for the open repository conditions at 100 years of operation (for which Salas et al. (2010) is referred to); for the temperate period at 2000, 3000, 5000, and 9000 AD; for permafrost conditions; and for the advancement of an ice cap, a period where the repository is fully covered by an ice cap, and ice cap retreat.

Radionuclide transport modelling: The groundwater composition is used for determining the source term (that is the radioelement concentrations) inside failed canisters, in case they are solubility limited (saturated with respect to a thermodynamically stable solid phase), as described in the **Radionuclide transport report**. The salinity is used when estimating the sorption partitioning coefficient K_d of certain radionuclides, as outlined in Section 6.7.2 and detailed in Crawford (2010), and as used in subsequent radionuclide transport modelling. The best estimate and maximum colloid concentrations are used in radionuclide transport calculations to estimate colloid facilitated transport.

Copper corrosion modelling: For modelling of copper corrosion, as detailed in SKB (2010b), statistics on the sulphide concentration is needed, as well as the maximum concentration of dissolved oxygen. In addition, statistics on concentrations of chloride, and the redox potential and pH are needed.

Hydrogeological modelling: Hydrogeochemical data (compositions and end-members) from the site-descriptive modelling have been used as input in the SR-Site hydrogeological modelling (cf Section 6.6).

6.1.2 Experience from SR-Site

The processes influenced by geochemical data with largest effects on repository safety in SR-Site were bentonite erosion, caused by low-salinity groundwaters, and canister corrosion, caused by either sulfide or dissolved oxygen. In addition, the evaluation of the retention of radionuclides relied on groundwater compositions.

Low-salinity groundwaters

The modelling of the evolution of major groundwater components was performed using numerical methods and equivalent porous medium models (ECPM). It may be shown that such models overestimate dispersion unless the discretisation is very refined, and when modelling large volumes of rock, a fine discretisation might be limited by computational resources. In the case of bentonite erosion, an increased modelled dispersion results in higher groundwater salinities, which would overestimate the stability of bentonite. In order to avoid over-optimistic results in SR-Site, analytical models of fresh water infiltration, coupled with salt diffusion from the rock matrix, were used taking the flow paths estimated by recharge particle tracks. The simulations assumed that the inflowing water had zero salinity, and the only geochemical data in the evaluations is then the salinity of the porewaters in the rock matrix, which is quite difficult to determine, and furthermore, it is associated with high uncertainties given the low porosity of the rock at Forsmark. Because of this, it was assumed that that the matrix porewaters were at equilibrium with the fracture goundwaters at the start of the fresh water infiltration.

Sulfide

The measurement of sulfide in groundwater is associated with relatively large measurement difficulties. Sulfide is very reactive, it is quickly oxidised as soon as the groundwaters emerge from the fractures and come in contact with the oxygen in air. Furthermore, in anoxic environments, sulfate-reducing bacteria (SRB) might quickly generate sulfide using the evolved hydrogen from metallic corrosion, or organic compounds, either natural or leached from the sampling equipment. Because of this, sampling artefacts are common when taking groundwater samples for sulfide analyses. A careful evaluation of the groundwater samples with sulfide data was performed in order to obtain a reliable statistical distribution of data. The few groundwater samples with the highest sulfide concentrations had a disproportionate effect on the canister corrosion calculations, which might be a result of the scarcity of the data, and of the inability to model satisfactorily the distribution of sulfide over large spans of space and time.

Oxygen

From the SR-Site assessment it was clear that dissolved oxygen in groundwaters is only expected under a glacial period, because under such conditions organic matter production is negligible below the glacier, where in addition, meltwater infiltration is enhanced by the hydrostatic conditions. The assessment considered recharge paths obtained through particle tracking and it used a set of analytic expressions to model diffusion of dissolved oxygen into the rock matrix where it reacted with dissolved iron(II) in the porewater. Dissolution of biotite in the rock matrix was considered when iron(II) was oxidised and its concentration decreased below a steady state value. Although sensitivity analyses were not performed, the parameters used in the evaluation were pessimistically chosen, and in addition, several processes that could help to remove oxygen were not considered, for example reactions with fracture-filling minerals and microbial processes in the fractures. The conclusion from the assessment was that the influence of oxygen infiltration on canister corrosion will only be minor.

Radionuclide retention

The uncertainty in projected groundwater compositions over safety assessment timescales are expected to have a considerable impact on the uncertainty of geosphere Kd values. For radioelements that sorb by way of surface complexation, small changes in composition (pH and redox potential, in particular) alter Kd values by several orders of magnitude over short spatial distances. Furthermore, in the recommendation of Kd values for SR Site it was recognised that there was a limited possibility to quantify the impact of groundwater chemistry variability on Kd values since the evolution of groundwater chemistry was not resolved on the level of individual migration paths leading from failing canisters to the biosphere. Consequently, relatively cautious assumptions were made in the selection of best estimate Kd values and credible ranges of uncertainty as documented in Crawford (2010). These uncertainties, however, were expected to have a relatively minor impact on the SR-Site results given that the far-field dose rates were largely dominated by radionuclides which are not strongly attenuated by sorptive retention in the geosphere. For the sorbing radionuclides whose Kd uncertainty has a non negligible impact on far-field dose rates (predominantly Se-79 and Ni-59 for short and intermediate timescales, and Ra-226 at very long timescales), the recommended Kd values were considered to be cautious and well-bounded. In the case of Ra-226, very cautious assumptions were also made in the estimation of the near-field source term by assuming vanishingly low solubility of Th in the spent fuel canister and different scenarios of U redox speciation in separate sensitivity case studies. It can also be noted in this context that the predicted locations of canister failure in SR-Site were largely associated with migration paths featuring relatively poor transport retardation potential (low hydrodynamic transport resistance) which also reduced the impact of Kd uncertainty on modelled far-field dose rates.

6.1.3 Supplier input on the use of data (text reproduced from SR-Site Data report)

The supplier notes that the main groundwater chemical components and the provided variabilities of compositions are highly conditioned by the results of the hydrogeological models. However, they qualitatively reflect the conceptual models of the Forsmark site.

The team supplying groundwater compositions have only limited expertise in the fields covered by the "non-chemical" safety assessment models that use these data. Nevertheless, the supplier does not have any reservations concerning the use of the data in SR-Can or SR-Site.

6.1.4 Sources of information and documentation of data qualification (text reproduced from SR-Site Data report)

Sources of information

The main sources of information are: Salas et al. (2010), reporting the hydrogeochemical modelling in Forsmark using PhreeqC; Tullborg et al. (2010), presenting the selection of representative sulphide data from the site investigation and monitoring programme; Sidborn et al. (2010), reporting the oxygen ingress modelling at Forsmark. The full references to these reports are given in Table 6-1.

Table 6-1. Main sources of groundwater chemical information used in data qualification.

Salas J, Gimeno M J, Auqué L, Molinero J, Gómez J, Juárez I, 2010. SR-Site – hydrogeochemical evolution of the Forsmark site. SKB TR-10-58, Svensk Kärnbränslehantering AB.
Sidborn M, Sandström B, Tullborg E-L, Salas J, Maia F, Delos A, Molinero J, Hallbeck L, Pedersen K, 2010. SR-Site: Oxygen ingress in the rock at Forsmark during a glacial cycle. SKB TR-10-57, Svensk Kärnbränslehantering AB.
Tullborg E-L, Smellie J, Nilsson A-C, Gimeno M J, Auqué L F, Brüchert V, Molinero J, 2010. SR-Site – sulphide content in the groundwater at Forsmark. SKB TR-10-39, Svensk Kärnbränslehantering AB.

Categorising data sets as qualified or supporting

Most data are taken from Salas et al. (2010) wherein two categories of data are reported. In the first category data are derived by PhreeqC modelling, providing concentrations of the major cations Na^+, K^+, Ca^{2+}, Mg^{2+} and anions Cl^-, the total inorganic carbon, sulphide, sulphate, and phosphate. In addition the pH, *Eh*, ionic strength, and cation charge equivalents $\Sigma q[M^{q+}]$ are given. Also other data not specifically requested in this Data report are provided in Salas et al. (2010). The data in the second category are not derived by PhreeqC modelling, but are based on observations from the site investigations, as well as on data in the open literature. These data includes the concentrations of DOC, acetate, CH_4, H_2, NO_2^-, NH_4^+, and colloids.

The sulphide concentrations are affected by bacterial processes. Although sulphide is modelled with PhreeqC, different conceptual assumptions provide different ranges of results. The analytical data and the observations from the site investigation and monitoring programmes are considered more reliable. Such sulphide data are compiled in Tullborg et al. (2010).

The ingress of oxygen is modelled in Sidborn et al. (2010) based on the flow pattern and properties provided in Vidstrand et al. (2010) and Joyce et al. (2010) when the ice front is at its worst position, which is directly above the candidate repository volume, as well as on recharge particle tracks (Joyce et al. 2010).

Excluded data previously considered as important

The categorisation of all samples from the monitoring programmes has been revised (Tullborg et al. 2010) with emphasis on the sulphide and Fe(II) data. In some cases, data previously labelled as representative when considering only major groundwater components have been deemed as less representative data for trace elements such as Fe(II), sulphide, Mn(II), dissolved organic carbon, etc.

No other data have been excluded that previously had a significant impact on the perception of the appropriate choice of data values or of modelling approaches.

Table 6-2. Qualified and supporting data sets.

Qualified data sets	Supporting data sets
1. Salas et al. (2010, Table 4-2): Equilibrated end-members compositions, calculated with the coupled and uncoupled database used for the geochemical simulations.	11. Sicada delivery: all groundwater data from Forsmark containing sulphide analyses (delivery note Sicada-09-185).
2. Salas et al. (2010, Appendix 4, Table A4-1): Statistical results for the Base case for the temperate (including submerged) period for pH, *Eh*, ionic strength and concentrations of Na, K, Ca, Mg, total inorganic carbon, Cl, S(VI), S(-II), phosphate, and $\Sigma q[M^{q+}]$.	12. Sicada delivery: monitoring data from Forsmark containing sulphide analyses (delivery note Sicada-10-126).
3. Salas et al. (2010, Appendix 4, Table A4-2): Statistical results for the hydrogeological variant case for the temperate period for the same data as in item 2.	13. The ChemNet data, based on the Extended data freeze 2.3 (December 2007) at the SIMON database (mirror of Modelldatabasen), folder "Forsmark/2.3/ Hydrogeochemistry/Approved", file "Forsmark_2_3.xls".
4. Salas et al. (2010, Appendix 4, Table A4-3): Statistical results for the Base case for the glacial cycle for the same data as in item 2.	
5. Salas et al. (2010, Appendix 4, Table A4-4): Statistical results for the hydrogeological variant case for the glacial cycle for N–S glacier advance for the same data as in item 2.	
6. Salas et al. (2010, Appendix 4, Table A4-5): Statistical results for the case of glacier advance over a frozen soil (permafrost) and periglacial period for the same data as in item 2.	
7. Salas et al. (2010, Table 8-1): Recommended values of DOC, acetate, CH_4, H_2, NO_2^-, NH_4^+ and colloids.	
8. The complete results from the PhreeqC modelling in Salas et al. (2010) are stored in SKBdoc 1262945.	
9. Tullborg et al. (2010), set of sulphide concentrations selected as representative of the present-day groundwater compositions at Forsmark. Numerical values are also stored in SKBdoc 1261474.	
10. Sidborn et al. (2010, Chapter 8): Data on maximum oxygen concentration and affected canister position for ice location II and III.	

Items 1–10. Salas et al. (2010), Tullborg et al. (2010) and Sidborn et al. (2010) are SKB reports produced for SR-Site and concerning the Forsmark site. The reports are produced and reviewed in accordance with the SKB's quality assurance system, and these data are judged as qualified. Detailed references to the literature survey conducted to estimate parameters for item 7 is given in Chapter 8 of Salas et al. (2010).

Items 11–12 are the complete data sets on which the selection of representative sulphide data in Tullborg et al. (2010) is based. These data sets are quality assured but all data points are not necessarily representative for the in situ conditions (for example as result of disturbance from the measurements). Accordingly the data sets are sorted as supporting. The data set used for calculating the sulphide distribution in Forsmark was extracted from Sicada (delivery note Sicada-09-185) and includes all data from the percussion and cored boreholes sections that were analysed for sulphide. Two sources of sulphide data are available: 1) Complete Chemical Characterisation (CCC) data from cored boreholes of the site characterisation programme (Laaksoharju et al. 2008) that include the earlier established (Smellie et al. 2008) categorisation of the samples and 2) data from the monitoring of selected borehole sections in percussion and cored boreholes initiated at different times during and following the site characterisation programme up to November 2009. An additional data set from the monitoring campaign during the spring of 2010 (delivery note Sicada-10-126) is used as support for the motivation of the selection of representative samples.

Item 13 is the complete hydrogeochemical data set delivered from Forsmark site investigation. The same considerations apply as for items 11–12. The data used for the hydrogeochemical modelling and explorative analysis during the site investigations programme were extracted from Sicada as data freezes 2.2 (October, 2006) and 2.3 (April, 2007) and included data from earlier data freezes and newer data stored up to April 2007. Additional data from the monitoring programme and three deep boreholes were included in the Extended 2.3 data freeze (October, 2007).

6.1.5 Conditions for which data are supplied (text reproduced from SR-Site Data report)

Conditions for hydrogeochemical modelling

Concerning the main geochemical parameters, estimated through PhreeqC modelling, the data are highly conditioned by the hydrogeological modelling providing mixing proportions (Joyce et al. 2010) or salinities (Vidstrand et al. 2010). Conditions for the hydrogeological modelling are outlined

in Sections 6.6 and 6.7. The hydrogeological modelling dictates the coordinates for the PhreeqC modelling. However, only subsets of all the coordinates are used in the PhreeqC modelling, representing three different rock volumes (Salas el at. 2010, Section 3.4.3):

- Complete horizontal slice at the repository depth (440–500 m), with 111 900 and 67 795 points for the temperate and the glacial modelling, respectively.
- Data points within the candidate repository volume, included inside the following coordinates: (1630.62, 6701.17); (1633.37, 6701.17); (1633.37, 6698.9); (1630.62, 6698.9) with 65 237 and 24 425 points for the temperate and the glacial modelling, respectively.
- A vertical slice approximately parallel to the shoreline (NW: 1628519 m/6702421; SE: 1636272 m/6694615), with 25 349 and 20 671 points for the temperate and the glacial modelling, respectively.

These subsets of coordinates are used to create input files for PhreeqC to obtain the detailed chemical composition at each coordinate (see Salas et al. 2010, Appendix 1).

The data are also conditioned by the used end-member compositions. For Forsmark the following five end-members are used (Salas el at. 2010, Section 4.4):

- Deep saline.
- Old meteoric.
- Glacial.
- Littorina.
- Altered meteoric.

A basis for defining the end-member compositions are the assumptions of with which minerals are in equilibrium with these waters. Examples of such minerals are calcite, hematite, and quartz. Conditions for each end-member are discussed in Salas et al. (2010, Section 4.4).

The hydrogeochemical modelling results depend on the thermodynamic database (TDB) used. The thermodynamic database used in the simulations, TDB_SKB-2009_Amphos21.dat (stored in SKBdoc 1261302), was developed by Hummel et al. (2002) with some modifications reported in Duro et al. (2006b)[13]. Some specific phases have been considered in order to establish mineral equilibria with the groundwaters or with the reactive mixing (cf Table 6-3). When these species are not included in the SKB-TDB, they are included as phases in the PhreeqC input file (Salas et al. 2010, Section 4.3). The reasons for the selection of these phases and their equilibrium constants are described in Auqué et al. (2006) and Gimeno et al. (2009).

Table 6-3. Additional equilibrium reactions and constants used in PhreeqC modelling. Information taken from Salas et al. (2010, Section 4.3).

Equilibrium reaction	Log *k*
Albite: $NaAlSi_3O_8 + 8H_2O = Al(OH)_4^- + 3Si(OH)_4 + Na^+$	–19.98
K-Feldspar: $KAlSi_3O_8 + 8H_2O = Al(OH)_4^- + 3Si(OH)_4 + K^+$	–22.62
$Fe(OH)_3$(hematite_grenthe): $Fe(OH)_3 + 3H^+ = Fe^{3+} + 3H_2O$	–1.10
FeS(ppt): $FeS + H^+ = Fe^{2+} + HS^-$	–3.00
Kaolinite_G: $Al_2Si_2O_5(OH)_4 + 7H_2O = 2Al(OH)_4^- + 2H^+ + 2Si(OH)_4$	–37.3
Hydroxyapatite: $Ca_5(PO_4)_3OH + 4H^+ = 5Ca^{2+} + 3HPO_4^{2-} + H_2O$	–3.421
Rhodochrosite: $MnCO_3 = Mn^{2+} + CO_3^{2-}$	–11.13

[13] The thermodynamic database TDB_SKB-2009_Amphos21.dat has recently been modified by M. Grivé, D. Arcos and co-workers at Amphos21, Barcelona, Spain in reference to thermodynamic data and to specific aqueous species of iron and sulphur. These updates are documented in SKBdoc 1261302.

The redox potential, Fe, sulphide, and pH are sensitive to the mineral assumed to be controlling the equilibrium and, also, to the presence of absence of sulphate-reducing bacteria. Microbial sulphate-reducing processes are detailed in Tullborg et al. (2010, Chapter 2). The use of Fe(III) oxyhydroxides or amorphous Fe(II) sulphides as equilibrating minerals represents two alternative assumptions defining geochemical behaviour of groundwaters. Equilibrium with Fe(III) oxyhydroxides implies a situation where the redox state is not affected by sulphate-reducing bacteria, while equilibrium with amorphous Fe(II) sulphides characterises a situation with significant activity of sulphate-reducing bacteria. Calculations include alternatively equilibrium with respect to Salas et al. (2010, Section 1.3.2):

- Crystalline Fe(III) oxyhydroxide (Grenthe et al. 1992b) (and redox equilibrium with Fe(II) aqueous species), $Fe(OH)_3(s) + 3H^+ + e^- \leftrightarrow Fe^{2+} + 3H_2O$, where the resulting redox potential is strongly correlated to pH, and/or
- Amorphous Fe(II) monosulphide, $FeS(am) + H^+ \leftrightarrow Fe^{2+} + HS^-$.

The fracture mineralogy at the Forsmark site is described in Sandström and Tullborg (2006) and Sandström et al. (2008). Based on these descriptions the presence of both mineral phases is deemed possible. Thus, when evaluating *Eh* (and iron concentrations) both geochemical cases are included in the so-called "Base Case" and the results from the two cases are pooled when obtaining *Eh* statistics. For the other parameters, equilibrium with respect to Fe(III) oxyhydroxides is only assumed in the Base case. In a third geochemical variant case, a database that uncouples equilibrium reactions between the species including S(-II)/S(VI) is used, in order to evaluate the influence of the kinetics of the redox reaction between the pairs. However, data from this third variant are not propagated to SR-Site.

The different variant cases are outlined in Figure 6-1 (green boxes). The grey shading indicates which variant cases are included in the Base case for the different parameters.

The impacts from the thermal load of the spent fuel, and from the temperature decrease during cold periods within the glacial cycle, on calculated groundwater compositions are not evaluated, but the induced uncertainty is estimated to be small compared to other uncertainties. Other conditions of important for the hydrogeochemical modelling are discussed in Salas et al. (2010) and Gimeno et al. (2010).

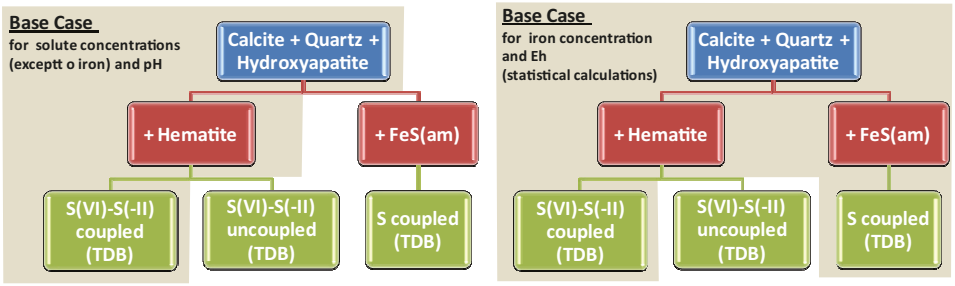

Figure 6-1. *Scheme of the mineral equilibriums assumed in the calculations as geochemical variant cases, and constrains applied in the so-called Base case for the statistical approach (grey area). Reproduced from Figure 4-5 of Salas et al. (2010).*

Conditions for non-modelled components

For a number of requested solutes, the estimated concentrations are based on analytical data. This applies for dissolved molecular hydrogen, acetate, ammonium, nitrite, dissolved organic carbon, methane, colloids, and sulphide. Observed data are predominantly taken from the Forsmark and Laxemar site investigations, but also from Olkiluoto in Finland and, to a minor degree, from other sites such as the Whiteshell Underground Research Laboratory site in Canada. Data from the site investigation and monitoring programmes are obtained at present-day conditions at different depths and rock volumes at the sites. As the groundwater at different depths and rock volumes comprises different proportions of end-members, conclusions can be drawn for other time periods than for the initial temperate. In doing this, governing processes and reactions have been taken into account. In Chapter 8 of Salas et al. (2010) a few conditions are outlined and references to detailed accounts on the conditions are given for H_2, CH_3COO^-, NH_4^+, NO_2^-, DOC, CH_4, and colloids.

Concerning sulphide, the complete data set from the Forsmark site has been revised in Tullborg et al. (2010) and data deemed to be representative for undisturbed conditions have been selected (while disturbed data have been discarded). The sampling procedures and associated sampling conditions, as well as the selection criteria, are outlined in Sections 3.1 and 4.5 of Tullborg et al. (2010).

Conditions for oxygen ingress modelling

The oxygen ingress modelling is conditioned by the following parameters and processes:

- The transport processes, including advection and diffusion into the rock matrix, and rates of kinetically controlled reactions (Sidborn et al. 2010, Sections 2.1 and 2.4). Concerning the advective transport, properties of the flow paths are taken from Joyce et al. (2010) and Vidstrand et al. (2010). The most important period of the glacial cycle for the maximum oxygen concentration is when the ice front is directly above the repository, resulting in increased hydraulic gradients generating the highest groundwater flow through the candidate repository volume (cf Sections 6.6 and 6.7). Therefore, the ice front location strongly affects the possibility of oxygen ingress to the repository depth. The main results in Sidborn et al. (2010) are given for ice locations II and III.
- Abiotic oxidation reactions of the fracture filling minerals and minerals of the rock matrix, chlorite, biotite, and pyrite, and oxidation of dissolved Fe(II) (Sidborn et al. 2010, Section 2.2). These minerals and solutes govern the reducing capacity of the rock matrix. In the so-called Base case a pH of 8 of the intruding glacial melt waters is assumed.
- Numerous biotic reactions that can scavenge oxygen are described in Section 2.3 of Sidborn et al. (2010). In fractured rock, such reactions are predominantly assumed to occur in, or adjacent to, the flow paths. Conditions for the reactions, for example the supply of reductants, are also described. Biotic reactions are not included in the modelling. However, they are important for the argument that the ingress modelling is pessimistic (several biotic reactions are likely to add to the oxygen scavenging). Therefore, the ingress of oxygen is conditioned by the biotic reactions, but the applied oxygen ingress modelling is not.
- The oxygen concentration of the intruding glacial melt water (recharge concentration). For the Base case, the oxygen concentration is assumed to be 1.5 mM O_2 (Sidborn et al. 2010, Sections 5.7 and 7.6). However, a sensitivity analysis has been performed in order to evaluate the role of these values.

6.1.6 Conceptual uncertainty (text reproduced from SR-Site Data report)

General considerations

The chemical processes controlling the compositions of groundwaters are well known. These include equilibrium reactions between aqueous species, such as acid-base and complexation, dissolution and precipitation of minerals, sorption and ion-exchange. This does not mean that the chemical composition of groundwaters can be provided with a high level of confidence. Several reactions, especially those involving minerals, have slow rates and their influence on groundwater compositions is dependent on factors such as reactive surface area, solid to solution ratio, groundwater flow velocity, and turnover time, among others. As a consequence, the composition of groundwaters is influenced by climatic conditions at the surface, by submerged conditions, etc.

A large degree of the uncertainty in the groundwater compositions is due to uncertainties in hydrogeological models and to the intrinsic exclusion of future climatic conditions and unforeseen conditions.

Some aspects of groundwater compositions need a special discussion, such as redox conditions and parameters affected by microbial process, for example sulphide and dissolved organic carbon.

Redox conditions

It is widely accepted that different redox couples in a groundwater system (for example sulphide-sulphate) are not necessarily in equilibrium. Despite of this, PhreeqC is based on overall redox equilibrium and, consequently, the handling of redox components has an intrinsic uncertainty. In addition, several assumptions can be made when modelling the reactions governing the overall redox conditions. In SR-Site two possibilities have been deemed equally probable:

- Equilibrium between aqueous species and Fe(III)-oxyhydroxides.
- Equilibrium between aqueous species and amorphous Fe(II)-sulphide.

To deal with this conceptual uncertainty, results from calculations using both assumptions have been supplied to SR-Site.

The results obtained for the flow conditions when an ice sheet advances and retreats over unfrozen ground (which is one of the cases in hydrogeological modelling) show that glacial melt waters can reach the Forsmark candidate repository, and this could affect the stability of redox sensitive components during the first stages of the glacier advance. The redox conditions are highly conditioned by the hydrogeological modelling, which in turn is conditioned by the estimated properties of the ice front and its movement. As the modelling to such an extent is dependent on assumptions in earlier modelling steps, this is considered as a conceptual uncertainty.

Sulphide

The problem with identifying reliable sulphide values was recognised at an early stage, when the discrepancy between CCC (the initial Complete Chemical Characterisation immediately after drilling) and monitoring samples was found, and also the large variation within the monitoring time series. The parameters that will have largest influence on the sulphide production are SO_4^{2-}, DOC, H_2, and CH_4. The possibility of an increase or decrease in concentrations of these solutes is outlined in Table 6-1 of Tullborg et al. (2010) for the different time periods. It must be assumed that microbial processes will continue during permafrost and glacial conditions. However, it is difficult to know which microbial processes will be quantitatively effective. Although many chemical processes are slowed down by decreased temperatures, it may not necessarily be so for all microbial processes.

Gaseous components

The sources, production rate, and transport mechanisms of geogas are, together with the in situ sulphide concentrations and redox front variations, aspects of the hydrogeochemical modelling associated with the lowest confidence, see **Site description Forsmark**. Gases are natural components in groundwater, but they may also be formed in the repository, mainly as a result of corrosion processes and radiolysis of water in contact with the spent fuel. Some gases are involved in microbiological reactions, e.g. methane, hydrogen, and carbon dioxide (Hallbeck and Pedersen 2008), and they are therefore affected by the uncertainties associated with microbial processes.

Oxygen ingress

There some conceptual uncertainty in the way oxygen scavenging is conceptualised. This is discussed in Chapter 4 of Sidborn et al. (2010). In SR-Site, this conceptual uncertainty is handled by taking a pessimistic approach in limiting the effect of, or totally disregarding, processes that are not well quantified. As the maximum oxygen concentration is estimated for the time period when the ice front margin is located right above the candidate repository volume, uncertainty in previous modelling steps (ice front and hydrogeological modelling) propagates to the oxygen ingress modelling.

6.1.7 Data uncertainty due to precision, bias, and representativity (text reproduced from SR-Site Data report)

Uncertainty in hydrogeochemical modelling with PhreeqC

Four main sources of uncertainties can be identified in the predictive geochemical modelling performed for SR-Site:

1. The number and composition of the end-members used for the mixing calculations.
2. Uncertainties arising from the coupling between hydrological modelling (providing mixing proportions or salinities) and geochemical modelling.
3. The heterogeneous reactions considered to participate in the control of the composition of the mixed waters through equilibrium assumptions.
4. The thermodynamic data used for these equilibrium reactions.

Uncertainty in the compositions of end-member groundwaters

Uncertainties in the composition of end-members directly influence the uncertainty of the simulated groundwater compositions. The chemical compositions of the end-members have been updated in Gimeno et al. (2010) using those estimated for SR-Can and reported in Auqué et al. (2006) as the starting point. Estimation of the number of end-member waters involved in the palaeohydrological evolution of the sites and their chemical compositions are key parameters in the performed simulations. The effects of the associated uncertainties have been widely discussed in the context of the Swedish and Finnish site characterisation programmes (e.g. Gómez et al. 2009, Gimeno et al. 2008, 2009 and references therein).

In particular, for SR-Site the original compositions of the end-member waters used in the geochemical simulations have been carefully reviewed in the site-descriptive modelling (Gimeno et al. 2008, 2009). Some of these waters are represented by real samples from the natural systems and others waters (for the old end-members) are inferred from geological and geochemical information. Thus, compositional uncertainties in these old end-members are greater. Moreover, in some cases, there are some unknown fundamental geochemical parameters (pH, *Eh*, and dissolved Fe(II) and S(-II) concentrations) that have been obtained assuming a series of mineral equilibrium reactions thought to be controlling these variables (e.g. equilibrium with calcite, quartz, Fe(III) oxyhydroxides, and/or amorphous Fe(II) mono-sulphides). Thus, although the selected end-members are able to simulate the overall geochemical character of the present groundwaters, some degree of uncertainty remains.

The number of end-members used in simulations depends on the knowledge of the natural system under study. Thus, it has changed as more information and knowledge has become available from the sites. In the SR-Site exercise, a fifth end-member (Old meteoric end-member), not used in SR-Can calculations, has been included based on the works by Smellie et al. (2008) and Laaksoharju et al. (2009). Uncertainties associated with the end-member compositions are discussed in Salas et al. (2010, Section 9.5).

Uncertainty in the mineral/groundwater reactions

The mineral reactions chosen to be in equilibrium with the groundwater mixtures are reasonable, as they include those with a fast kinetics compared to the simulated time intervals (like calcite) or those identified in apparent equilibrium situations in the present groundwaters (like quartz). However, they represent only a limited subset of those minerals present in the fractures and, thus, other minerals

such as chlorite and illite could participate through dissolution-precipitation reactions. Other solid phases, such as aluminosilicates, could be stipulated as equilibrium constraints, but their selection would be difficult to justify because their thermodynamic constants show important uncertainties (as they depend on the particular mineral composition, degree of order/disorder, etc). Moreover, previous scoping calculations performed for SR-Can (Auqué et al. 2006) show that including chlorite and illite equilibrium in the calculations had a negligible effect on the concentrations of Mg and K.

Other processes different from dissolution-precipitation reactions, like cation exchange, could participate in the hydrochemical evolution of the groundwaters. Cation exchange reactions are kinetically fast and can exert an important control on the major cationic composition of the groundwaters (cf Appelo and Postma 2005, Andersson et al. 2005 and references therein). These reactions may be specially activated during the mixing processes as the salinity of the groundwaters exerts a major control on the intensity and selectivity of the exchangers for the different cations (e.g. Appelo and Postma 2005).

Despite their potential importance, cation exchange processes have not been included in the present modelling due to two main reasons: a) the available cation exchange capacity (CEC) values for fracture filling minerals, a necessary parameter to include cation exchange processes in the predictive modelling, are very scarce and uncertain (Selnert et al. 2008) and b) the thermodynamic database selected by SKB do not have the possibility to deal with cation exchange processes (see below).

Finally, whereas most equilibrium assumptions are generalised in the present groundwaters over the whole studied rock volume, it is not the case of the heterogeneous redox equilibria. The work done for the site-descriptive modelling in Laxemar indicates that in some localised zones of the system, equilibrium with hematite is observed whereas in others, waters seem to be in equilibrium with amorphous Fe(II) sulphides. The approach used for the geochemical calculations simplifies the behaviour of the system imposing, alternatively, the equilibrium conditions in the whole volume of rock. This uncertainty has been dealt with by pooling the results obtained from both equilibrium assumptions in the Base case, giving a wider range of variation for redox parameters but being able to explain the two possible situations present in the real system.

The uncertainties related to redox disequilibrium situations have also been taken into account. A modified version of the thermodynamic database is implemented in Salas et al. (2010) in order to account for the groundwater *Eh* values controlled by the iron system and the Fe(III) oxyhydroxide/Fe(II) redox pair. Although it has been chosen not to propagate results from this variant case to the Base case, modelling results that may be used for assessing the uncertainty are discussed in Salas et al. (2010).

Coupling between hydrological and geochemical data

Hydrogeological model results have been provided by the hydrogeological team of SKB through the standard QA procedures specified for SR-Site. However, two types of hydrological model results have been provided: mixing proportions of the considered end-members for the temperate period and also the submerged under marine water period (Joyce et al. 2010), and salinities for the periglacial, glacial and submerged under fresh water periods (Vidstrand et al. 2010). Transformation of salinities (without any other data available) into mixing proportions gives rise different uncertainties and several simplified assumptions are made (cf Salas et al. 2010, Appendix A1.3).

With the applied approach, the groundwater composition at the end of the temperate period, as calculated from the mixing proportions provided by Joyce et al. (2010), does not deviate drastically from the initial composition of the glacial period, as estimated from the salinities given by Vidstrand et al. (2010). This indicates that there is a certain degree of coherence in the link between the two different hydrogeological models used.

Uncertainties in the thermodynamic database

The thermodynamic data for the mineral phases included in the simulations have been reviewed in Auqué(2006) and Gimeno et al. (2009). Moreover, these data have been applied, verified, and refined in the WATEQ4F database during the study of the present groundwaters in the site-characterisation programmes both in Laxemar and Forsmark.

Consistency between hydrogeochemical modelling and other SR-Site geochemical models using thermodynamic data is an important issue. This is the reason why, instead of using the same WATEQ4F database as in previous geochemical calculations for SR-Can (Auqué et al. 2006) and for the site-descriptive modelling (Gimeno et al. 2008, 2009 and references therein), SKB decided to use a new thermodynamic database known as TDB_SKB-2009_Amphos21.dat. This database was developed by Hummel et al. (2002) and was partially modified by Duro et al. (2006b), in reference to the radionuclides thermodynamic data. The use of this database has limited the capacity of simulating processes such as cation exchange. The same problem has been encountered with some specific solubility data already included and verified in the WATEQ4F database (Auqué et al. 2006, Gimeno et al. 2009)[14] for some important phases in the groundwater systems under study (Gimeno et al. 2009). Knowing the importance of cation exchange, the University of Zaragoza group has developed the methodology and software needed to deal with cation exchange. Some scoping calculations have been performed suggesting that cation exchange would not introduce drastic changes in the results. However, more work is required to verify the results.

As input to the PhreeqC modelling, solubility data for mineral phases of interest have been provided (cf Table 6-3). However, the consistency of this inclusion has not been extensively verified, as was done with the previous database used in SR-Can.

Uncertainty for non-modelled components

The estimated concentrations of colloids, dissolved inorganic and total organic carbon, nitrite, ammonia, acetate, methane and molecular hydrogen are based on observations. Most of these parameters are intimately related to the microbial activity or are being conditioned by different redox processes. This fact makes their evaluation a difficult task due to the complexity and lack of knowledge of microbial processes in the groundwaters of crystalline systems, as well as in the bentonite. Thus, all proposed values have uncertainties and, in some cases, they are especially large (Salas et al. 2010, Chapter 8). This is the case for DOC, acetate, CH_4, H_2, NO_2^-, and NH_4^+ for the excavation/operation period (not requested in this Data report), of CH_4 and H_2 for the glacial period, and of DOC for the submerged period.

The values proposed for CH_4 and H_2 during the glacial period are extrapolated from the highest contents in present groundwaters. The estimation of CH_4 and H_2 concentrations in this period is complicated by the existence of additional processes and different boundary conditions to those present and/or expected in the other periods. The concentration of these gases will be controlled by their production and flow from the deep bedrock and by the active microbial metabolisms (acting as sources and sinks), but also by the impervious frozen layers at the top of the site and by the formation/dissociation of clathrates during permafrost advance and decay. From the preliminary estimations on the fluxes and maximum productions of methane and hydrogen for the Forsmark and Laxemar sites (Delos et al. 2010), low contents of these components are expected (e.g. increased sulphide production under ice sheets is not expected). However, more data and studies are necessary and, also, the microbiological CH_4 production and consumption rates must be assessed.

DOC values during the submerged period have been extrapolated from the highest DOC values in present-day Forsmark groundwaters with an important marine contribution. The use of present-day groundwaters with a clear Littorina contribution as an expected analogue situation for this period would be reasonable. However, the measured DOC values (up to 2.92 mM) are still subjected to different uncertainties (e.g. contamination during drilling/sampling) and, therefore, they remain uncertain. Table 6-4 shows statistics on observed data as taken from the Forsmark and Laxemar site investigations. This indicates the spread at present-day conditions due to both data uncertainty and natural variability. Details on the uncertainty of the individual components are given in Chapter 8 of Salas et al. (2010).

[14] Appendix A in Auqué et al. (2006) contains a detailed discussion of the main difficulties encountered when working with these type of phases, the range of solubility values found in the literature, and the values selected for the SR-Can modelling. See also Appendix C in Gimeno et al. (2009).

Uncertainty in oxygen ingress modelling

There is major data uncertainty in the oxygen ingress modelling relating to the results from the hydrogeological models and, to a minor extent, to the migration properties of the rock matrix. There are also uncertainties related to the rates of abiotic and, in particular, biotic oxygen scavenging. Uncertainties in biotic scavenging rates are handled by pessimistically neglecting biotic scavenging in the modelling. The input data used in the modelling are described in detail in Chapter 5 of Sidborn et al. (2010). Lack of data or knowledge on data variability, and incomplete process understanding, have been handled by pessimistic assumptions.

Table 6-4. Main statistics for the values of the analysed parameters, as measured in the present-day groundwaters at Forsmark, and at Laxemar in the case of acetate and DOC. Data reproduced from Tables 8-2 and 8-3 of Salas et al. (2010).

	Forsmark						Laxemar	
	TOC (mg/L)	DOC (mg/L)	NO_2^- (mol/L)	NH_4^+ (mol/L)	CH_4 g (mol/L)	H_2 g (mol/L)	Acetate (mol/L)	DOC (mol/L)
N total	56	62	16	60	16	12	16	20
Minimum	bdl	bdl	1.43×10^{-8}	0	1.07×10^{-6}	bdl	0	1.66×10^{-4}
Median	2.55	1.95	2.50×10^{-8}	3.22×10^{-5}	2.46×10^{-6}	6.03×10^{-8}	1.49×10^{-5}	4.79×10^{-4}
Mean	4.85	3.5	3.08×10^{-8}	5.42×10^{-5}	1.55×10^{-5}	3.37×10^{-6}	7.55×10^{-5}	2.92×10^{-3}
Standard deviation	6.21	5.51	2.44×10^{-8}	5.62×10^{-5}	5.07×10^{-5}	6.09×10^{-6}	1.73×10^{-4}	7.04×10^{-3}
Maximum	40.3	35.7	1.07×10^{-7}	1.86×10^{-4}	2.05×10^{-4}	1.92×10^{-5}	6.87×10^{-4}	3.06×10^{-2}
P0.1	bdl	bdl	1.43×10^{-8}	0	1.07×10^{-6}	bdl	0	1.66×10^{-4}
P5	bdl	bdl	1.43×10^{-8}	2.13×10^{-6}	1.07×10^{-6}	bdl	0	1.83×10^{-4}
P95	13	13	1.07×10^{-7}	1.70×10^{-4}	2.05×10^{-4}	1.92×10^{-5}	6.87×10^{-4}	0.02136
P99.5	40.3	35.7	1.07×10^{-7}	1.86×10^{-4}	2.05×10^{-4}	1.92×10^{-5}	6.87×10^{-4}	0.03056

bdl: Below detection limit.

Uncertainty in site investigation data

Available data concerning groundwater chemical composition from the site investigations are used to calibrate the hydrogeological models, as well as for estimating the composition of the groundwater end-members, which are in turn used to assess the distribution of the present-day groundwaters and the future groundwater compositions. Therefore, such uncertainty is propagated to the output of PhreeqC modelling. These data are also used for estimating the concentration of components that cannot be modelled.

There is a bias introduced in the data set since *s*ampling has been performed on fractures with high enough transmissivity, meaning that there practically exists no chemistry data for hydraulically very low and non-conductive rock volumes. Exclusion of samples due to technical difficulties may also result in a bias. See Nilsson (2008) for a detailed description of precision in the analyses.

The relative charge balance gives an indication of the quality and uncertainty of the analyses of the major ions. Together with the chloride/electrical conductivity correlation, the charge balance was used to verify that the analytical concentrations of the most dominating ions are consistent. The errors, as calculated for each one of the 1 790 samples in SKB database SIMON, very seldom exceed the acceptable limits ± 5 % (8 samples) and ± 10 % (11 samples) for groundwater and dilute surface waters.

The sulphide data set is based on selected sulphide concentrations obtained during the site investigations, which means that they should represent present-day conditions. There is a representativity issue concerning whether they may be used for entire safety assessment period, which is further discussed in Tullborg et al. (2010). In the process of selection, some data points have been discarded, as they are judged to be contaminated or, otherwise, non-representative. As some of these discarded data points show higher sulphide concentrations than those finally selected, a detailed discussion on the selection procedure is given in Tullborg et al. (2010, Section 4.5). It is judged that this selection procedure should constrain the degree of bias in the data, and assure that they accurately represent the in situ groundwater.

The reliability and quality of the analytical data derived from the monitoring boreholes may be influenced negatively by lack of time series measurements, and uncertainties whether the sample has achieved hydrogeochemical stability and therefore is representative. This became obvious when analysing the sulphide concentration in all five section volumes that normally are discarded before a sample is taken. In many borehole sections, many more than five section volumes are needed to be pumped away in order to achieve a stable chemistry. This has been evaluated in detail in Tullborg et al. (2010), wherein sampling uncertainties are discussed in Chapter 3.

6.1.8 Spatial and temporal variability of data (text reproduced from SR-Site Data report)

Spatial variability

The spatial variability of the concentrations of main components is handled by modelling groundwater compositions for tens of thousands of coordinates in the rock volume surrounding the repository (Salas et al. 2010). This modelling is performed by using PhreeqC and the mixing proportions, the compositions of end-member groundwater components, and the selection of the mineral phases chosen to be in thermodynamic equilibrium with the mixed solutions as input data. The grid providing the coordinates is determined by the hydrogeological modelling (Joyce et al. 2010, Vidstrand et al. 2010). Table 6-5 shows an excerpt of the result file of a PhreeqC simulation, where selected data for seven, out of the tens of thousands, modelled coordinates are displayed. The upper left field shows the coordinates and the upper right field the mixing proportions supplied from the hydrogeological modelling. The lower field shows concentrations of the some of the requested main component (in this example Ca^{2+}, Cl^{-}, Na^{+}, HS^{-} and total inorganic carbon are shown), as well as the pH, *Eh* and ionic strength. The complete result file includes many more columns than shown in Table 6-5 (cf Salas et al. 2010).

Table 6-5. Example of results from PhreeqC calculations, showing groundwater data for seven out of tens of thousands of coordinates. The complete results include more columns with other data not specifically requested in this report.

Row	X(km)	Y(km)	Z(km)	Brine	Littorina	DGW	Glacial	PoreWater
1	1630.62	6698.9	–0.46	6.34×10^{-2}	2.15×10^{-4}	0.9065	7.23×10^{-4}	2.92×10^{-2}
2	1630.64	6698.9	–0.46	6.96×10^{-2}	2.60×10^{-4}	0.8972	8.46×10^{-4}	3.22×10^{-2}
3	1630.66	6698.9	–0.46	7.35×10^{-2}	2.97×10^{-4}	0.8911	9.45×10^{-4}	3.42×10^{-2}
4	1630.68	6698.9	–0.46	7.58×10^{-2}	3.25×10^{-4}	0.8875	1.02×10^{-3}	3.54×10^{-2}
5	1630.7	6698.9	–0.46	7.75×10^{-2}	3.51×10^{-4}	0.8846	1.10×10^{-3}	3.65×10^{-2}
6	1630.72	6698.9	–0.46	7.90×10^{-2}	3.96×10^{-4}	0.8819	1.21×10^{-3}	3.75×10^{-2}
7	1630.74	6698.9	–0.46	7.95×10^{-2}	6.15×10^{-4}	0.8798	1.53×10^{-3}	3.86×10^{-2}
	mCa	**mCl**	**mNa**	**mHS–**	**mC**	**pH**	**Eh**	**IonicStr**
1	3.07×10^{-2}	9.15×10^{-2}	3.53×10^{-2}	4.80×10^{-20}	5.46×10^{-3}	6.56	–196.825	0.127
2	3.37×10^{-2}	9.98×10^{-2}	3.76×10^{-2}	2.24×10^{-20}	5.38×10^{-3}	6.54	–196.825	0.139
3	3.56×10^{-2}	0.1051	3.90×10^{-2}	1.44×10^{-20}	5.34×10^{-3}	6.53	–196.882	0.146
4	3.68×10^{-2}	0.1083	3.99×10^{-2}	1.13×10^{-20}	5.31×10^{-3}	6.53	–197.054	0.150
5	3.76×10^{-2}	0.1106	4.05×10^{-2}	9.44×10^{-21}	5.29×10^{-3}	6.52	–197.34	0.153
6	3.84×10^{-2}	0.1127	4.11×10^{-2}	8.19×10^{-21}	5.28×10^{-3}	6.52	–197.74	0.156
7	3.86×10^{-2}	0.1134	4.13×10^{-2}	8.50×10^{-21}	5.26×10^{-3}	6.52	–198.541	0.157

X (km), Y (km), Z (km) are the coordinates for simulated groundwater composition in Forsmark at 9000 AD.

Brine, Littorina, DGW (altered meteoric), Glacial, PoreWater (old meteoric) are the mixing proportions of the end-member groundwaters.

mCa, mCl, mNa, and mHS- are the concentrations (mol/L) of the solutes. mC is the concentration of total inorganic carbon (HCO_3^{-}+CO_3^{2-}).

pH, Eh, and IonicStr are the pH, redox potential (mV), and ionic strength (mol/L).

The chemical compositions of groundwaters in fractured rock may show a strong spatial variability over short distances. However, over larger distances overall patterns may appear, for example the general salinity increase with depth. Figure 6-2 shows the distribution of total dissolved solids (TDS) at the Forsmark site for different time periods. The repository is indicated in black enlarged squares. As shown, the variation in TDS is quite large within the candidate repository volume, with a trend of more saline waters at the repository location. Numerous of similar images of pH, *Eh*, total inorganic carbon, among others are found in Salas et al. (2010).

The sulphide concentrations being selected as representative in Tullborg et al. (2010) indicate a significant variability, over three orders of magnitude. Figure 6-3 shows the selected measured sulphide concentration versus elevation for percussion and core drilled boreholes. No correlation has been deduced, reflecting that the processes controlling the sulphide concentrations in the groundwaters are widely distributed.

Temporal variability of data

Hydrogeochemical modelling has been performed for the time periods 2000, 3000, 5000, and 9000 AD, as well as for periglacial and glacial periods. During the glacial cycle, there are events of dilution and saline upconing, affecting the concentration of the main components within the candidate repository volume. This is illustrated by the distribution of TDS, in Figure 6-2 for the temperate period, and in Figure 6-4 for the glacial cycle (showing the TDS calculated at glaciation at different ice front locations). Similar images for other parameters are provided in Salas et al. (2010).

The temporal variability of estimated components (but not modelled) is discussed in Salas et al. (2010, Chapter 8). Concerning the sulphide concentration, modelling results indicates that the concentration becomes more diluted with time, wherefore using data measured at present-day conditions is justified.

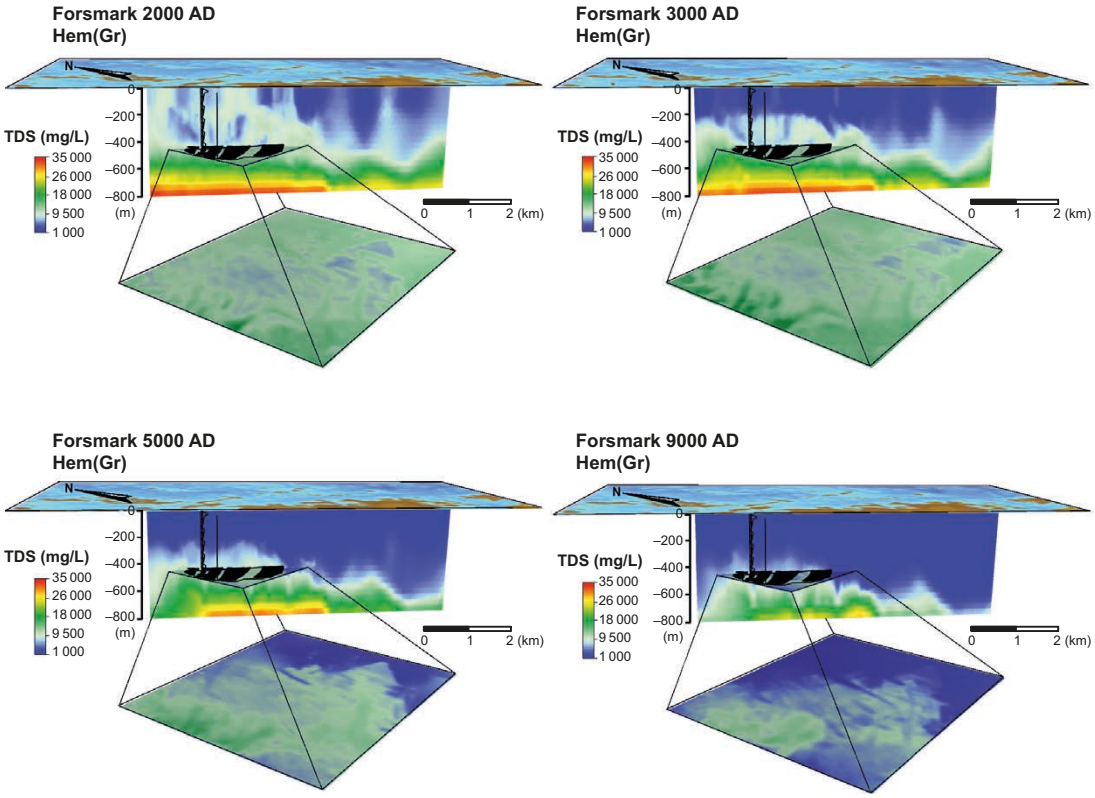

Figure 6-2. *Distribution of the modelled salinity (TDS in mg/L) for Forsmark in vertical slices at times equal to 2000 AD, 3000 AD, 5000 AD, and 9000 AD. Reproduced from Figure 6-1 of Salas et al. (2010).*

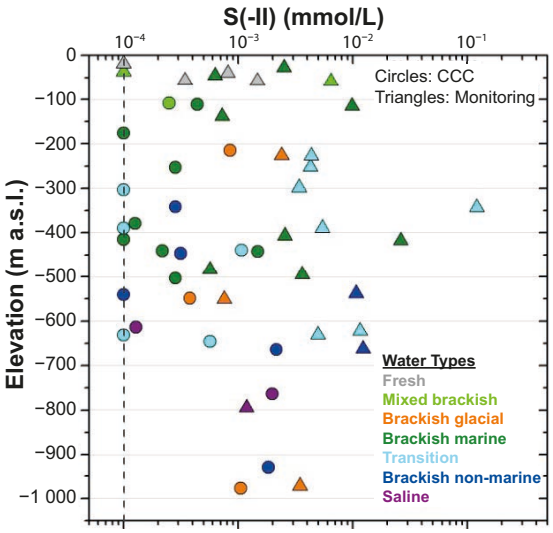

Figure 6-3. *Dissolved S(−II) in groundwaters from percussion and core drilled boreholes from CCC and monitoring sampling versus elevation. The dotted line indicates the detection limit. Image reproduced from Figure 5-5a of Tullborg et al. (2010).*

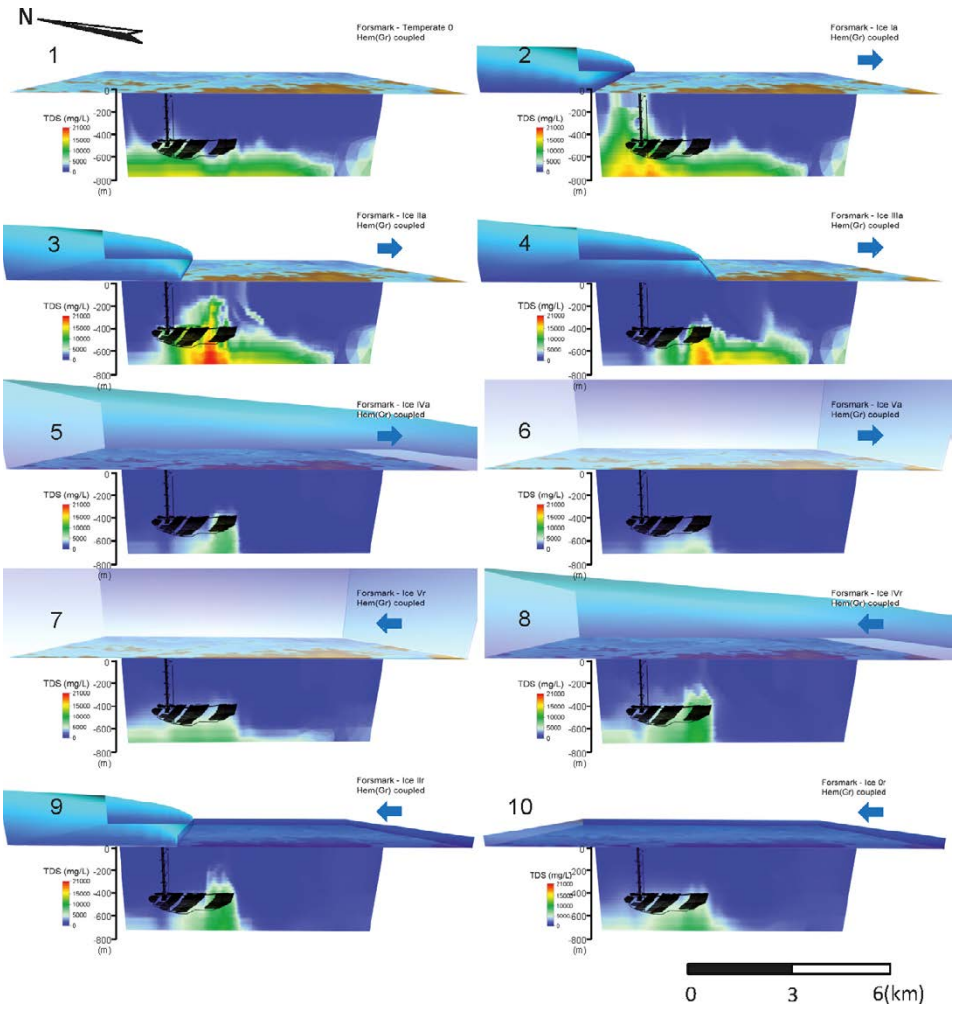

Figure 6-4. *Changes in the distribution of TDS (total dissolved solids, mg/L) shown in vertical slices when an ice sheet advances and retreats over the unfrozen Forsmark area. The figure shows results during the glacial sheet advance (1 to 6) and the glacial retreat (7 to 10) calculated using the model described in Salas et al. (2010, Chapter 3). When the ice sheet retreats the area is covered by a 100 m deep glacial melt water lake. Reproduced from Salas et al. (2010, Figure 7-5).*

6.1.9 Correlations (text reproduced from SR-Site Data report)

The concentrations of chemical components are correlated through the mixing proportion and the stoichiometric coefficient of the equilibrium reactions, as described in Section 6.1.2. Such reactions and the reaction constants are compiled in the thermodynamic database used in the PhreeqC modelling (TDB_SKB-2009_Amphos21.dat). In subsequent modelling (cf the SR-Site Radionuclide transport report (SKB 2010c)) solubility limited concentrations of radioelements in the canister is calculated using a similar approach. It is important that there is consistency in the thermodynamic data used in the two modelling steps. Except for this, there is no correlation that needs to be propagated to subsequent copper corrosion or radionuclide transport modelling.

6.1.10 Result of supplier's data qualification (text reproduced from SR-Site Data report)

End-members

The end-member compositions used for the Forsmark site are justified in Salas et al. (2010) and shown in Table 6-6. The data are reproduced from Table 4-2 of Salas et al. (2010), wherein also end-member compositions for the uncoupled database are found.

Table 6-6. Equilibrated end-members, calculated with the coupled database used for the geochemical simulations. Units in molal (mol/kg) except for pH, temperature, and pe. Data are reproduced from Salas et al. (2010, Table 4-2).

	DeepSaline	Old Meteoric	Glacial	Littorina	Altered Meteoric
T (°C)	15	15	15	15	15
pH	8.000	8.500	9.300	7.951	7.314
pe	–4.449	–4.925	–5.260	–4.422	0.554
Al	7.371×10^{-9}	9.141×10^{-7}	5.205×10^{-6}	3.247×10^{-7}	7.719×10^{-8}
Br	4.156×10^{-3}	7.163×10^{-6}	-	2.812×10^{-4}	7.166×10^{-6}
C_{tot}	3.678×10^{-5}	5.222×10^{-4}	8.515×10^{-5}	1.627×10^{-3}	7.230×10^{-3}
Ca	4.940×10^{-1}	1.184×10^{-3}	7.180×10^{-5}	3.865×10^{-3}	4.702×10^{-4}
Cl	1.366×10^{0}	5.109×10^{-3}	1.410×10^{-5}	1.856×10^{-1}	5.111×10^{-3}
F	8.644×10^{-5}	8.427×10^{-5}	-	2.610×10^{-5}	8.431×10^{-5}
Fe_{tot}	2.525×10^{-7}	8.744×10^{-9}	8.002×10^{-7}	8.262×10^{-6}	1.793×10^{-6}
K	8.222×10^{-4}	1.433×10^{-4}	1.023×10^{-5}	3.469×10^{-3}	1.434×10^{-4}
Li	6.861×10^{-4}	2.018×10^{-6}	-	1.021×10^{-5}	2.019×10^{-6}
Mg	8.952×10^{-5}	3.088×10^{-4}	4.114×10^{-6}	1.865×10^{-2}	3.089×10^{-4}
Mn	2.615×10^{-6}	-	-	-	-
Na	3.801×10^{-1}	1.193×10^{-2}	7.395×10^{-6}	1.617×10^{-1}	1.193×10^{-2}
S_{tot}	1.067×10^{-4}	8.854×10^{-4}	5.305×10^{-6}	9.391×10^{-3}	8.858×10^{-4}
Si	8.808×10^{-5}	1.396×10^{-4}	1.665×10^{-4}	1.282×10^{-4}	1.342×10^{-4}
Sr	3.947×10^{-3}	4.340×10^{-6}	-	3.096×10^{-5}	4.341×10^{-6}

Main chemical components

The PhreeqC results from the numerous modelling cases presented in Salas et al. (2010) are stored as tabulated data in files in SKBdoc 1262945. Table 6-5 shows an excerpt of a resulting file from PhreeqC modelling. Statistical results for the thousands of coordinates for different cases are tabulated in Appendix 4 in Salas et al. (2010). Based on the statistical results, box-and-whisker plots can be made. Figure 6-5 shows the sum of concentrations of the main cations expressed as charge equivalents $\Sigma q[M^{q+}]$ for different time periods and events of the glacial cycle. The indicated 4 mM line[15] corresponds to the criterion for the safety function indicator for SR-Site ($\Sigma q[M^{q+}] > 4$ mM). As shown, only for the glacial cases this criterion fails, and only for the 5th percentile and lower.

[15] The safety function indicator criterion $\Sigma q[M^{q+}] > 4$ mM used in SR-Site has been updated to $\Sigma q[M^{q+}] > 8$ mM in the PSAR.

The underlying data to Figure 6-5 are given in Table 6-7 to Table 6-9, which are reproduced from Appendix 4 of Salas et al. (2010). Table 6-7 shows the statistics for the total concentrations of the major cations Na, K, Ca, and Mg and chloride, ionic strength, pH, *Eh*, and for sulphate, sulphide, phosphate, and total inorganic carbon. The data are for the temperate and submerged period. Statistics for the same parameters are shown for the glacial period for different ice front locations in Table 6-8 and Table 6-9. In Appendix 4 of Salas et al. (2010), statistics are also given for hydrogeological variant cases and for the case where the ice advances over frozen grounds/permafrost. Furthermore, in Salas et al. (2010) numerous of box-and-whisker plots illustrating the data in Table 6-7 to Table 6-9 are found.

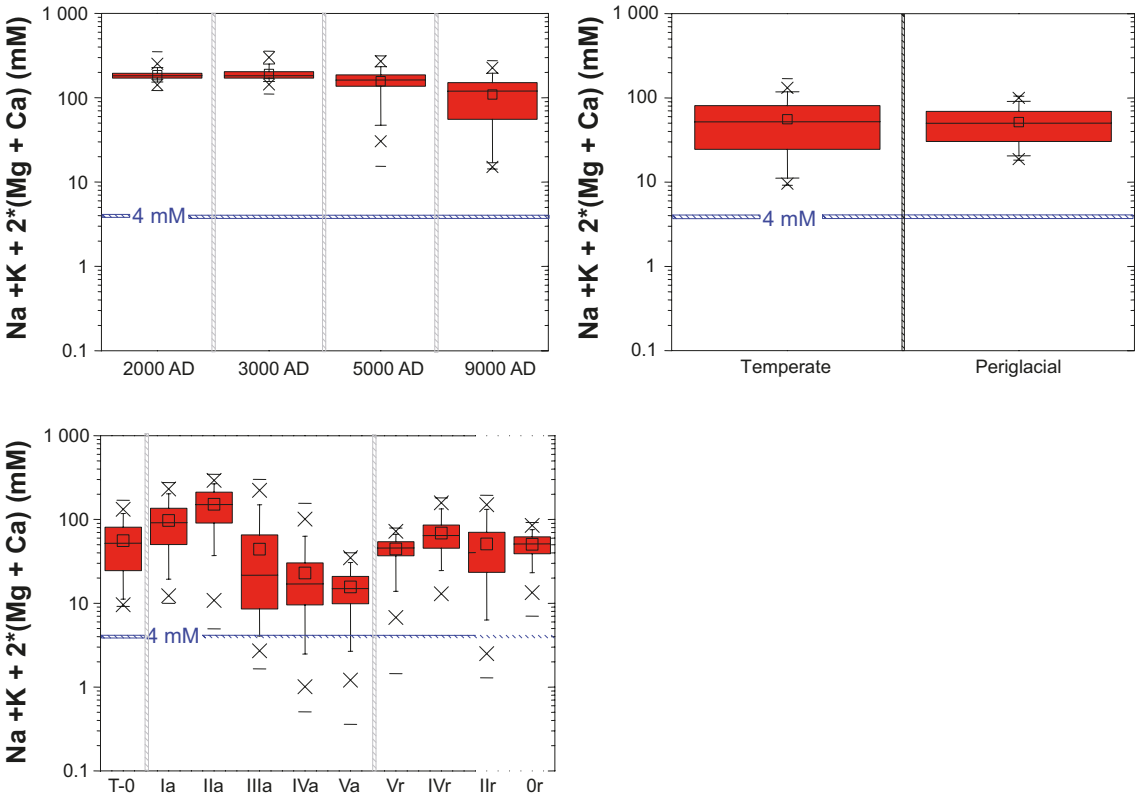

Figure 6-5. *Box-and-whisker plots showing the statistical distribution of the calculated safety function factor $\sum q[M^{q+}]$ for the coordinates located within the candidate repository volume at Forsmark. Upper left figure shows statistics for the temperate period, upper right a comparison between temperate and periglacial period, and lower figure different ice front locations. The statistical measures are the median, the 25th and 75th percentile (box), the mean (square), the 5th and 95th percentile (whiskers), the 1st and 99th percentile (crosses) and the maximum and the minimum values (bars). Excerpts of Figures 6-3, 7-1, and 7-7 of Salas et al. (2010).*

Table 6-7. Statistics for temperate and submerged seawater period for the hydrogeochemical Base case. Reproduced from Salas et al. (2010, Appendix A4-1).

Temperate period	2000 AD																
	pH	Eh	TDS (g/L)	Ionic Str	Na	K	Ca	Mg	Fe	Alk	C	Cl	S(VI)	S(-II)	Si	P	ΣqM^{q+}
Min=	7.07	-260	6.88	0.1507	4.09E-02	1.57E-04	2.86E-03	1.29E-04	1.34E-07	2.15E-04	2.02E-04	1.14E-01	3.37E-04	5.05E-09	1.19E-04	1.43E-08	121.92
0.1%	7.09	-250	7.40	0.1638	4.45E-02	1.65E-04	3.69E-03	1.40E-04	3.10E-07	2.18E-04	2.06E-04	1.23E-01	3.50E-04	1.07E-08	1.21E-04	1.47E-08	130.94
5%	7.21	-242	8.67	0.1897	5.14E-02	1.86E-04	5.73E-03	1.80E-04	7.94E-07	2.67E-04	2.60E-04	1.44E-01	4.69E-04	3.36E-08	1.25E-04	2.09E-08	153.75
Median=	7.44	-221	10.40	0.2249	7.21E-02	7.39E-04	4.92E-02	3.34E-03	8.75E-06	5.08E-04	5.25E-04	1.69E-01	2.00E-03	1.41E-06	1.28E-04	6.29E-08	183.24
95%	7.74	-208	12.89	0.2946	1.42E-01	2.98E-03	7.42E-02	1.60E-02	1.88E-05	1.70E-03	1.70E-03	2.18E-01	8.10E-03	7.88E-06	1.29E-04	6.19E-07	227.91
99.9%	7.89	-198	17.66	0.4183	1.52E-01	3.25E-03	1.06E-01	1.75E-02	2.55E-05	2.14E-03	2.16E-03	3.05E-01	8.82E-03	8.65E-06	1.30E-04	9.04E-07	312.73
Max=	8.05	-196	19.88	0.4730	1.56E-01	3.34E-03	1.21E-01	1.79E-02	2.68E-05	2.43E-03	2.46E-03	3.45E-01	9.05E-03	8.89E-06	1.31E-04	1.11E-06	351.94

Temperate period	3000 AD																
	pH	Eh	TDS (g/L)	Ionic Str	Na	K	Ca	Mg	Fe	Alk	C	Cl	S(VI)	S(-II)	Si	P	ΣqM^{q+}
Min=	6.73	-256	6.49	0.1220	4.30E-02	1.64E-04	2.86E-03	1.34E-04	1.77E-07	2.16E-04	2.04E-04	9.49E-02	3.44E-04	4.02E-11	1.19E-04	1.45E-08	111.20
0.1%	6.91	-250	7.51	0.1548	4.68E-02	1.73E-04	3.48E-03	1.54E-04	3.44E-07	2.23E-04	2.11E-04	1.21E-01	3.68E-04	2.72E-09	1.20E-04	1.52E-08	132.83
5%	7.14	-241	8.81	0.1863	5.42E-02	1.98E-04	5.42E-03	1.96E-04	7.53E-07	2.72E-04	2.66E-04	1.44E-01	4.86E-04	2.90E-08	1.24E-04	2.13E-08	155.60
Median=	7.42	-220	10.43	0.2234	8.26E-02	9.87E-04	4.69E-02	4.74E-03	9.76E-06	6.15E-04	6.43E-04	1.70E-01	2.66E-03	1.94E-06	1.28E-04	8.74E-08	183.46
95%	7.73	-202	14.21	0.3352	1.41E-01	2.97E-03	8.54E-02	1.59E-02	2.00E-05	1.80E-03	1.81E-03	2.44E-01	8.06E-03	7.85E-06	1.29E-04	6.89E-07	251.82
99.9%	7.89	-184	18.96	0.4506	1.51E-01	3.22E-03	1.16E-01	1.73E-02	3.33E-05	2.94E-03	3.05E-03	3.29E-01	8.72E-03	8.55E-06	1.30E-04	1.42E-06	335.57
Max=	8.00	-141	20.18	0.4747	1.54E-01	3.30E-03	1.21E-01	1.77E-02	4.74E-05	3.97E-03	4.12E-03	3.48E-01	8.95E-03	8.77E-06	1.31E-04	2.30E-06	356.77

Temperate period	5000 AD																
	pH	Eh	TDS (g/L)	Ionic Str	Na	K	Ca	Mg	Fe	Alk	C	Cl	S(VI)	S(-II)	Si	P	ΣqM^{q+}
Min=	6.54	-243	1.12	0.0171	1.28E-02	1.64E-04	7.92E-04	1.60E-04	5.99E-07	2.31E-04	2.20E-04	6.21E-03	4.05E-04	1.52E-17	1.21E-04	1.62E-08	15.43
0.1%	6.61	-241	1.29	0.0205	1.50E-02	1.92E-04	9.89E-04	1.99E-04	8.55E-07	2.46E-04	2.36E-04	9.25E-03	4.50E-04	2.32E-14	1.22E-04	1.81E-08	18.52
5%	6.77	-231	2.90	0.0524	3.61E-02	2.51E-04	1.85E-03	4.81E-04	1.32E-06	3.00E-04	2.97E-04	3.61E-02	6.27E-04	4.86E-09	1.25E-04	2.53E-08	47.31
Median=	7.33	-214	9.29	0.1988	7.52E-02	9.37E-04	3.49E-02	4.51E-03	1.35E-05	1.09E-03	1.18E-03	1.51E-01	2.65E-03	1.57E-06	1.28E-04	2.39E-07	163.34
95%	7.52	-179	13.18	0.3096	1.09E-01	2.13E-03	7.74E-02	1.13E-02	3.30E-05	5.82E-03	6.23E-03	2.26E-01	5.85E-03	5.31E-06	1.33E-04	3.93E-06	233.60
99.9%	7.63	-119	17.03	0.4055	1.24E-01	2.55E-03	1.05E-01	1.36E-02	5.38E-05	6.87E-03	7.31E-03	2.95E-01	6.96E-03	6.68E-06	1.34E-04	4.87E-06	301.75
Max=	7.72	-83	17.80	0.4260	1.28E-01	2.64E-03	1.11E-01	1.41E-02	6.57E-05	7.09E-03	7.48E-03	3.10E-01	7.22E-03	6.93E-06	1.34E-04	5.12E-06	315.47

Temperate period	9000 AD																
	pH	Eh	TDS (g/L)	Ionic Str	Na	K	Ca	Mg	Fe	Alk	C	Cl	S(VI)	S(-II)	Si	P	ΣqM^{q+}
Min=	6.48	-238	1.06	0.0158	1.20E-02	1.44E-04	7.72E-04	2.96E-04	6.98E-07	2.66E-04	2.58E-04	5.16E-03	6.05E-04	1.01E-20	1.22E-04	2.06E-08	14.29
0.1%	6.49	-234	1.07	0.0160	1.21E-02	1.47E-04	7.93E-04	3.00E-04	7.31E-07	2.95E-04	2.89E-04	5.36E-03	7.11E-04	2.22E-20	1.23E-04	2.45E-08	14.49
5%	6.57	-226	1.21	0.0189	1.38E-02	1.66E-04	9.61E-04	3.69E-04	1.31E-06	7.03E-04	7.55E-04	7.87E-03	8.90E-04	3.17E-17	1.26E-04	1.07E-07	17.02
Median=	7.07	-198	6.94	0.1470	6.00E-02	7.09E-04	2.23E-02	3.24E-03	1.36E-05	2.67E-03	3.24E-03	1.10E-01	2.08E-03	6.53E-07	1.30E-04	1.12E-06	120.38
95%	7.51	-119	11.13	0.2571	8.36E-02	1.40E-03	6.12E-02	7.17E-03	5.14E-05	6.89E-03	7.33E-03	1.89E-01	3.92E-03	2.81E-06	1.34E-04	4.87E-06	196.27
99.9%	7.56	-62	14.31	0.3339	1.01E-01	1.96E-03	8.15E-02	1.03E-02	7.15E-05	7.10E-03	7.51E-03	2.45E-01	5.39E-03	4.78E-06	1.35E-04	5.10E-06	252.98
Max=	7.57	-57	15.54	0.3620	1.08E-01	2.19E-03	8.70E-02	1.16E-02	7.59E-05	7.13E-03	7.52E-03	2.66E-01	6.00E-03	5.58E-06	1.35E-04	5.13E-06	274.70

Submerged seawater	3000 BC																
	pH	Eh	TDS (g/L)	Ionic Str	Na	K	Ca	Mg	Fe	Alk	C	Cl	S(VI)	S(-II)	Si	P	ΣqM^{q+}
Min=	7.22	-259	5.33	0.1078	3.37E-02	1.22E-04	3.04E-03	1.14E-04	3.16E-07	2.04E-04	1.90E-04	8.50E-02	3.06E-04	5.14E-09	1.23E-04	2.65E-08	94.53
0.1%	7.24	-253	5.78	0.1270	3.66E-02	1.39E-04	3.80E-03	1.17E-04	4.50E-07	2.05E-04	1.91E-04	9.53E-02	3.12E-04	1.36E-08	1.24E-04	2.69E-08	102.17
5%	7.34	-247	7.34	0.1626	4.31E-02	1.54E-04	5.64E-03	1.35E-04	6.04E-07	2.27E-04	2.15E-04	1.22E-01	3.59E-04	4.24E-08	1.26E-04	3.23E-08	130.06
Median=	7.57	-229	9.69	0.2180	5.67E-02	2.05E-04	5.39E-02	2.79E-04	8.67E-06	2.81E-04	2.75E-04	1.63E-01	5.37E-04	1.02E-05	1.28E-04	4.67E-08	171.53
95%	7.77	-215	11.99	0.2865	1.40E-01	2.95E-03	7.45E-02	1.58E-02	2.12E-05	1.62E-03	1.62E-03	2.08E-01	8.00E-03	1.59E-05	1.30E-04	1.16E-06	212.98
99.9%	7.93	-208	14.78	0.3535	1.57E-01	3.37E-03	9.21E-02	1.81E-02	2.51E-05	1.79E-03	1.77E-03	2.56E-01	9.13E-03	2.01E-05	1.32E-04	1.46E-06	262.19
Max=	8.03	-206	15.89	0.3803	1.59E-01	3.40E-03	9.91E-02	1.83E-02	2.60E-05	1.81E-03	1.79E-03	2.76E-01	9.22E-03	2.09E-05	1.33E-04	1.51E-06	281.81

Table 6-8. Statistics for glacial period (ice location 0–IVa) for the hydrogeochemical Base case. Reproduced from Salas et al. (2010, Appendix A4-3).

Temperate	0																
	pH	Eh	TDS (g/L)	Ionic Str	Na	K	Ca	Mg	Fe	Alk	C	Cl	S(VI)	S(-II)	Si	P	ΣqM^{q+}
Min=	6.44	-231	0.76	0.0107	6.85E-03	1.44E-04	7.98E-04	2.83E-04	7.79E-07	3.37E-03	5.17E-03	1.76E-04	7.91E-04	4.27E-22	1.26E-04	3.95E-06	9.20
0.1%	6.46	-231	0.76	0.0107	6.85E-03	1.44E-04	7.98E-04	2.85E-04	7.79E-07	3.43E-03	5.25E-03	1.76E-04	8.00E-04	1.31E-21	1.27E-04	4.08E-06	9.20
5%	6.50	-211	0.87	0.0132	7.52E-03	1.45E-04	1.44E-03	2.91E-04	1.67E-06	3.60E-03	5.44E-03	2.64E-03	8.21E-04	2.86E-20	1.29E-04	4.44E-06	11.17
Median=	6.67	-172	3.20	0.0676	1.93E-02	1.66E-04	1.60E-02	3.02E-04	7.24E-06	4.24E-03	5.95E-03	4.58E-02	8.60E-04	5.48E-06	1.32E-04	5.52E-06	52.07
95%	7.32	-62	6.94	0.1575	3.76E-02	1.99E-04	3.99E-02	3.09E-04	6.69E-05	6.54E-03	7.22E-03	1.13E-01	8.84E-04	6.43E-05	1.34E-04	8.71E-06	118.21
99.9%	7.53	-49	9.00	0.2071	4.75E-02	2.18E-04	5.31E-02	3.09E-04	7.78E-05	7.03E-03	7.48E-03	1.49E-01	8.86E-04	7.52E-05	1.35E-04	9.80E-06	154.56
Max=	7.53	-44	9.85	0.2275	5.16E-02	2.25E-04	5.86E-02	3.09E-04	8.21E-05	7.03E-03	7.48E-03	1.64E-01	8.86E-04	7.93E-05	1.35E-04	9.80E-06	169.54

Glacial (advance)	Ia																
	pH	Eh	TDS (g/L)	Ionic Str	Na	K	Ca	Mg	Fe	Alk	C	Cl	S(VI)	S(-II)	Si	P	ΣqM^{q+}
Min=	6.37	-224	0.81	0.0118	7.14E-03	1.28E-04	1.07E-03	2.51E-04	1.10E-06	3.06E-03	4.71E-03	1.23E-03	7.16E-04	6.02E-24	1.22E-04	3.20E-06	10.03
0.1%	6.38	-220	0.83	0.0123	7.28E-03	1.31E-04	1.21E-03	2.55E-04	1.35E-06	3.09E-03	4.77E-03	1.76E-03	7.26E-04	1.27E-23	1.22E-04	3.29E-06	10.45
5%	6.41	-192	1.35	0.0239	1.00E-02	1.48E-04	4.35E-03	2.76E-04	1.60E-06	3.26E-03	5.02E-03	1.21E-02	7.68E-04	2.75E-22	1.25E-04	3.69E-06	19.41
Median=	6.55	-166	5.44	0.1212	3.02E-02	1.86E-04	3.03E-02	2.94E-04	1.78E-06	3.77E-03	5.58E-03	8.58E-02	8.33E-04	8.32E-08	1.30E-04	4.75E-06	91.60
95%	6.98	-42	11.71	0.2725	6.07E-02	2.41E-04	7.05E-02	3.07E-04	8.37E-05	5.44E-03	6.65E-03	1.97E-01	8.79E-04	8.10E-05	1.34E-04	7.11E-06	202.51
99.9%	7.38	-30	15.02	0.3523	7.67E-02	2.70E-04	9.17E-02	3.09E-04	9.55E-05	6.70E-03	7.31E-03	2.56E-01	8.85E-04	9.28E-05	1.34E-04	9.01E-06	260.93
Max=	7.43	-27	15.87	0.3729	8.08E-02	2.78E-04	9.72E-02	3.09E-04	9.84E-05	6.81E-03	7.36E-03	2.71E-01	8.85E-04	9.56E-05	1.35E-04	9.23E-06	276.00

Glacial (advance)	IIa																
	pH	Eh	TDS (g/L)	Ionic Str	Na	K	Ca	Mg	Fe	Alk	C	Cl	S(VI)	S(-II)	Si	P	ΣqM^{q+}
Min=	6.34	-302	0.30	0.0067	1.47E-03	1.66E-05	1.73E-03	1.25E-05	8.14E-09	3.01E-04	2.65E-04	4.59E-03	2.91E-05	8.23E-25	1.18E-04	6.01E-08	4.96
0.1%	6.35	-293	0.33	0.0074	1.61E-03	1.72E-05	1.92E-03	1.37E-05	1.39E-08	3.27E-04	2.93E-04	5.11E-03	3.23E-05	1.36E-24	1.19E-04	6.83E-08	5.49
5%	6.38	-205	2.26	0.0482	1.30E-02	6.39E-05	1.15E-02	6.86E-05	1.17E-06	1.32E-03	1.46E-03	3.24E-02	1.87E-04	1.44E-23	1.22E-04	6.13E-07	37.05
Median=	6.46	-165	8.79	0.2024	4.65E-02	2.15E-04	5.19E-02	2.77E-04	2.30E-06	3.27E-03	5.03E-03	1.46E-01	7.71E-04	1.05E-06	1.27E-04	3.73E-06	151.09
95%	7.16	-30	15.31	0.3595	7.81E-02	2.73E-04	9.36E-02	2.99E-04	9.51E-05	4.07E-03	5.80E-03	2.61E-01	8.50E-04	9.23E-05	1.34E-04	5.21E-06	266.17
99.9%	8.49	-21	19.30	0.4559	9.74E-02	3.08E-04	1.19E-01	3.05E-04	1.04E-04	4.75E-03	6.27E-03	3.32E-01	8.71E-04	1.01E-04	1.41E-04	6.22E-06	336.62
Max=	8.54	-19	19.91	0.4705	1.00E-01	3.13E-04	1.23E-01	3.05E-04	1.05E-04	4.87E-03	6.33E-03	3.42E-01	8.73E-04	1.03E-04	1.42E-04	6.38E-06	347.32

Glacial (advance)	IIIa																
	pH	Eh	TDS (g/L)	Ionic Str	Na	K	Ca	Mg	Fe	Alk	C	Cl	S(VI)	S(-II)	Si	P	ΣqM^{q+}
Min=	6.36	-348	0.11	0.0023	4.37E-04	1.18E-05	5.95E-04	5.92E-06	5.03E-10	2.00E-04	1.37E-04	1.42E-03	1.04E-05	2.81E-24	1.20E-04	2.72E-08	1.65
0.1%	6.37	-342	0.12	0.0025	4.92E-04	1.20E-05	6.55E-04	6.20E-06	7.06E-10	2.03E-04	1.40E-04	1.60E-03	1.12E-05	1.06E-23	1.21E-04	2.78E-08	1.83
5%	6.48	-311	0.25	0.0055	1.19E-03	1.49E-05	1.41E-03	9.62E-06	7.86E-09	2.39E-04	1.97E-04	3.71E-03	2.07E-05	3.74E-20	1.27E-04	4.06E-08	4.08
Median=	7.57	-233	1.26	0.0291	6.50E-03	3.80E-05	7.45E-03	3.98E-05	1.73E-06	8.58E-04	8.82E-04	2.04E-02	1.06E-04	4.52E-07	1.36E-04	2.92E-07	21.58
95%	8.74	-65	8.68	0.2004	4.56E-02	2.08E-04	5.15E-02	2.86E-04	6.32E-05	3.56E-03	5.32E-03	1.44E-01	8.04E-04	6.08E-05	1.45E-04	4.29E-06	149.49
99.9%	9.21	-29	16.02	0.3766	8.13E-02	2.77E-04	9.82E-02	3.02E-04	9.61E-05	4.29E-03	5.97E-03	2.73E-01	8.60E-04	9.33E-05	1.62E-04	5.57E-06	278.69
Max=	9.27	-24	17.30	0.4074	8.77E-02	2.91E-04	1.06E-01	3.04E-04	1.01E-04	4.63E-03	6.15E-03	2.96E-01	8.68E-04	9.83E-05	1.65E-04	5.96E-06	301.30

Glacial (advance)	IVa																
	pH	Eh	TDS (g/L)	Ionic Str	Na	K	Ca	Mg	Fe	Alk	C	Cl	S(VI)	S(-II)	Si	P	ΣqM^{q+}
Min=	6.67	-372	0.05	0.0007	6.71E-05	1.06E-05	2.07E-04	4.61E-06	3.04E-10	1.87E-04	1.31E-04	1.90E-04	6.71E-06	8.93E-20	1.27E-04	2.47E-08	0.51
0.1%	6.70	-366	0.05	0.0007	7.91E-05	1.07E-05	2.09E-04	4.85E-06	3.61E-10	1.98E-04	1.33E-04	1.90E-04	7.39E-06	6.65E-19	1.28E-04	2.56E-08	0.51
5%	6.93	-327	0.16	0.0033	7.21E-04	1.33E-05	8.39E-04	7.77E-06	5.06E-09	2.23E-04	1.69E-04	2.12E-03	1.56E-05	5.63E-13	1.32E-04	3.44E-08	2.48
Median=	7.87	-254	0.99	0.0229	4.98E-03	2.87E-05	5.92E-03	2.33E-05	4.66E-06	5.22E-04	5.05E-04	1.62E-02	5.88E-05	3.66E-07	1.37E-04	1.36E-07	16.95
95%	8.99	-156	3.66	0.0852	1.90E-02	9.01E-05	2.20E-02	1.11E-04	2.70E-05	1.91E-03	2.30E-03	6.08E-02	3.06E-04	1.96E-05	1.52E-04	1.22E-06	63.19
99.9%	9.60	-88	7.66	0.1811	3.86E-02	1.40E-04	4.73E-02	1.82E-04	5.11E-05	2.84E-03	3.69E-03	1.31E-01	5.12E-04	4.34E-05	1.97E-04	2.60E-06	133.50
Max=	9.63	-80	8.96	0.2120	4.51E-02	1.52E-04	5.55E-02	2.50E-04	5.55E-05	3.78E-03	5.05E-03	1.54E-01	7.10E-04	4.74E-05	2.01E-04	4.30E-06	156.34

Table 6-9. Statistics for glacial period (ice location Va–0r) for the hydrogeochemical Base case. Reproduced from Salas et al. (2010, Appendix A4-3).

Glacial (advance)	Va																
	pH	Eh	TDS (g/L)	Ionic Str	Na	K	Ca	Mg	Fe	Alk	C	Cl	S(VI)	S(-II)	Si	P	ΣqM^{q+}
Min=	7.15	-377	0.04	0.0006	7.40E-06	1.02E-05	1.67E-04	4.11E-06	2.60E-10	1.54E-04	1.01E-04	1.41E-05	5.31E-06	8.61E-12	1.34E-04	1.54E-08	0.36
0.1%	7.21	-365	0.06	0.0009	1.20E-04	1.09E-05	2.52E-04	4.80E-06	4.21E-10	1.58E-04	1.10E-04	3.66E-04	7.20E-06	1.09E-10	1.34E-04	1.71E-08	0.66
5%	7.40	-327	0.17	0.0036	7.81E-04	1.36E-05	9.08E-04	7.59E-06	5.19E-09	1.97E-04	1.48E-04	2.30E-03	1.47E-05	2.48E-08	1.35E-04	2.64E-08	2.68
Median=	7.98	-262	0.88	0.0204	4.38E-03	2.58E-05	5.28E-03	1.94E-05	4.41E-06	4.33E-04	4.11E-04	1.44E-02	4.76E-05	3.57E-07	1.37E-04	1.01E-07	15.01
95%	8.99	-215	1.78	0.0415	8.97E-03	4.56E-05	1.08E-02	5.11E-05	1.72E-05	1.09E-03	1.15E-03	2.96E-02	1.38E-04	9.94E-06	1.52E-04	4.34E-07	30.65
99.9%	9.56	-182	2.28	0.0535	1.15E-02	5.86E-05	1.39E-02	8.01E-05	2.22E-05	1.67E-03	1.80E-03	3.82E-02	2.22E-04	1.48E-05	1.92E-04	8.73E-07	39.43
Max=	9.71	-168	2.32	0.0543	1.18E-02	6.51E-05	1.41E-02	1.03E-04	2.46E-05	2.10E-03	2.33E-03	3.88E-02	2.88E-04	1.71E-05	2.14E-04	1.31E-06	40.13

Glacial (retreat)	Vr																
	pH	Eh	TDS (g/L)	Ionic Str	Na	K	Ca	Mg	Fe	Alk	C	Cl	S(VI)	S(-II)	Si	P	ΣqM^{q+}
Min=	6.97	-359	0.10	0.0020	3.50E-04	1.10E-05	5.42E-04	4.19E-06	4.96E-10	1.22E-04	8.28E-05	1.25E-03	5.39E-06	4.98E-15	1.32E-04	9.94E-09	1.45
0.1%	7.04	-343	0.16	0.0034	6.66E-04	1.20E-05	9.03E-04	4.96E-06	1.23E-09	1.24E-04	8.64E-05	2.30E-03	7.39E-06	7.40E-14	1.32E-04	1.03E-08	2.49
5%	7.22	-293	0.81	0.0189	3.93E-03	2.12E-05	4.95E-03	8.83E-06	4.55E-08	1.64E-04	1.30E-04	1.36E-02	1.61E-05	3.16E-11	1.33E-04	1.83E-08	13.89
Median=	7.69	-244	2.62	0.0622	1.29E-02	4.42E-05	1.63E-02	2.10E-05	4.43E-06	4.06E-04	3.93E-04	4.49E-02	4.88E-05	3.80E-07	1.35E-04	8.55E-08	45.69
95%	8.42	-183	3.82	0.0905	1.90E-02	6.56E-05	2.37E-02	5.19E-05	2.22E-05	1.01E-03	1.09E-03	6.54E-02	1.37E-04	1.50E-05	1.40E-04	3.88E-07	66.58
99.9%	9.20	-148	4.42	0.1050	2.19E-02	7.88E-05	2.75E-02	8.03E-05	2.86E-05	1.51E-03	1.70E-03	7.59E-02	2.20E-04	2.12E-05	1.61E-04	7.75E-07	77.14
Max=	9.42	-133	4.53	0.1081	2.24E-02	8.48E-05	2.84E-02	1.02E-04	3.28E-05	1.85E-03	2.17E-03	7.83E-02	2.84E-04	2.53E-05	1.77E-04	1.13E-06	79.31

Glacial (retreat)	IVr																
	pH	Eh	TDS (g/L)	Ionic Str	Na	K	Ca	Mg	Fe	Alk	C	Cl	S(VI)	S(-II)	Si	P	ΣqM^{q+}
Min=	6.82	-327	0.59	0.0139	2.81E-03	1.64E-05	3.68E-03	5.04E-06	3.08E-09	1.07E-04	6.24E-05	1.00E-02	6.33E-06	5.79E-18	1.27E-04	6.34E-09	0.04
0.1%	6.94	-321	0.62	0.0146	2.96E-03	1.68E-05	3.87E-03	5.44E-06	4.17E-09	1.19E-04	7.83E-05	1.06E-02	7.92E-06	1.67E-16	1.28E-04	9.12E-09	10.72
5%	7.11	-288	1.41	0.0336	6.90E-03	2.69E-05	8.84E-03	8.98E-06	6.71E-08	1.50E-04	1.19E-04	2.43E-02	1.57E-05	1.25E-13	1.30E-04	1.54E-08	24.59
Median=	7.64	-241	3.68	0.0876	1.81E-02	5.54E-05	2.30E-02	2.13E-05	4.73E-06	3.81E-04	3.70E-04	6.35E-02	4.76E-05	7.11E-07	1.34E-04	7.61E-08	64.28
95%	8.32	-159	7.65	0.1831	3.77E-02	1.03E-04	4.82E-02	5.31E-05	2.67E-05	9.52E-04	1.04E-03	1.33E-01	1.36E-04	1.95E-05	1.39E-04	3.54E-07	134.24
99.9%	8.82	-124	9.76	0.2337	4.79E-02	1.26E-04	6.16E-02	8.06E-05	3.56E-05	1.40E-03	1.63E-03	1.70E-01	2.16E-04	2.82E-05	1.47E-04	7.06E-07	171.38
Max=	8.88	-103	10.31	0.2472	5.06E-02	1.28E-04	6.52E-02	1.02E-04	4.35E-05	1.61E-03	1.98E-03	1.80E-01	2.74E-04	3.59E-05	1.48E-04	9.32E-07	181.15

Glacial (retreat)	IIr																
	pH	Eh	TDS (g/L)	Ionic Str	Na	K	Ca	Mg	Fe	Alk	C	Cl	S(VI)	S(-II)	Si	P	ΣqM^{q+}
Min=	6.92	-360	0.09	0.0018	3.06E-04	1.10E-05	4.82E-04	4.19E-06	4.78E-10	1.16E-04	7.56E-05	1.07E-03	5.39E-06	1.00E-16	1.27E-04	8.63E-09	1.29
0.1%	7.02	-354	0.11	0.0022	4.09E-04	1.12E-05	6.00E-04	4.40E-06	6.05E-10	1.17E-04	7.86E-05	1.42E-03	5.90E-06	1.43E-15	1.28E-04	8.89E-09	1.63
5%	7.18	-325	0.37	0.0086	1.74E-03	1.44E-05	2.28E-03	5.60E-06	7.37E-09	1.37E-04	9.29E-05	6.17E-03	8.83E-06	2.69E-12	1.30E-04	1.22E-08	6.33
Median=	7.91	-260	2.30	0.0548	1.13E-02	3.84E-05	1.44E-02	1.53E-05	4.39E-06	2.76E-04	2.53E-04	3.96E-02	3.24E-05	3.81E-07	1.36E-04	4.51E-08	40.15
95%	8.92	-175	7.54	0.1803	3.71E-02	9.92E-05	4.75E-02	4.53E-05	2.37E-05	8.18E-04	8.76E-04	1.31E-01	1.13E-04	1.66E-05	1.50E-04	2.72E-07	132.29
99.9%	9.36	-137	10.08	0.2419	4.95E-02	1.25E-04	6.38E-02	6.50E-05	3.18E-05	1.14E-03	1.30E-03	1.76E-01	1.71E-04	2.46E-05	1.72E-04	4.92E-07	177.18
Max=	9.43	-120	11.11	0.2665	5.45E-02	1.35E-04	7.03E-02	8.51E-05	3.69E-05	1.43E-03	1.69E-03	1.94E-01	2.28E-04	2.94E-05	1.78E-04	7.38E-07	195.23

Submerged glacial lake	0r																
	pH	Eh	TDS (g/L)	Ionic Str	Na	K	Ca	Mg	Fe	Alk	C	Cl	S(VI)	S(-II)	Si	P	ΣqM^{q+}
Min=	7.01	-334	0.41	0.0096	1.93E-03	1.45E-05	2.54E-03	4.69E-06	1.97E-09	1.03E-04	6.25E-05	6.87E-03	5.94E-06	3.99E-15	1.32E-04	6.19E-09	7.02
0.1%	7.11	-329	0.51	0.0120	2.41E-03	1.56E-05	3.17E-03	4.97E-06	2.74E-09	1.05E-04	6.55E-05	8.63E-03	6.58E-06	2.38E-13	1.32E-04	6.64E-09	8.78
5%	7.36	-304	1.33	0.0316	6.45E-03	2.48E-05	8.33E-03	6.74E-06	2.51E-08	1.16E-04	7.95E-05	2.29E-02	1.00E-05	1.85E-09	1.33E-04	8.73E-09	23.17
Median=	7.91	-260	2.93	0.0699	1.43E-02	4.42E-05	1.84E-02	1.45E-05	4.59E-06	2.48E-04	2.25E-04	5.08E-02	2.93E-05	6.02E-07	1.35E-04	3.75E-08	51.21
95%	8.57	-207	4.32	0.1031	2.13E-02	6.44E-05	2.71E-02	3.67E-05	1.91E-05	7.09E-04	7.37E-04	7.48E-02	9.26E-05	1.20E-05	1.42E-04	2.13E-07	75.60
99.9%	8.93	-159	5.16	0.1232	2.54E-02	7.97E-05	3.24E-02	5.75E-05	2.64E-05	1.05E-03	1.16E-03	8.95E-02	1.51E-04	1.91E-05	1.50E-04	4.17E-07	90.37
Max=	8.99	-136	5.26	0.1256	2.59E-02	8.75E-05	3.31E-02	7.32E-05	3.19E-05	1.29E-03	1.48E-03	9.13E-02	1.96E-04	2.45E-05	1.52E-04	6.09E-07	92.12

The maximum and minimum Ca/Na ratios are compiled in Table 6-10 for different climatic periods, together with the maximum and minimum values of a few other parameters of interest for the buffer stability. Many of the data are the same as in Table 6-7 to Table 6-9.

Table 6-10. Minimum and maximum values of a few main geochemical buffer parameters obtained for the Base case over the complete Glacial Cycle in Forsmark. Data reproduced from Table 9-1 of Salas et al. (2010).

Modelling case	Max Cl (mol/L)	Max Ca/Na	Min Ca/Na	Max pH	Min pH	Max[1] carbonate (mol/L)	Min[1] carbonate (mol/L)	Max Ionic strength (mol/L)
Temperate (2000 AD)	3.45×10^{-1}	1.22	0.0240	8.05	7.07	2.46×10^{-3}	2.02×10^{-4}	0.473
Temperate (9000 AD)	2.66×10^{-1}	1.13	0.0496	7.57	6.48	7.52×10^{-3}	2.58×10^{-4}	0.362
Glacial (stage IIa)	3.42×10^{-1}	1.23	0.600	8.54	6.34	6.33×10^{-3}	2.65×10^{-4}	0.471
Glacial (stage Vr)	7.83×10^{-2}	1.55	1.02	9.42	6.97	2.17×10^{-3}	8.28×10^{-5}	0.108
Permafrost (before onset of glaciation)	9.94×10^{-2}	1.04	0.398	7.01	6.52	6.71×10^{-3}	5.52×10^{-3}	0.140
Submerged glacial lake	9.13×10^{-2}	1.32	1.20	8.99	7.01	1.48×10^{-3}	6.25×10^{-5}	0.126
Submerged seawater	2.76×10^{-1}	1.23	0.0241	8.03	7.22	1.79×10^{-3}	1.90×10^{-4}	0.380

[1] Max and min carbonate, also called total inorganic carbon, includes HCO_3^-+CO_3^{2-}.

Best estimate data for non-modelled components

In Chapter 8 of Salas et al. (2010) the concentration of solutes than cannot be modelled using PhreeqC are discussed. Based on analytical data and observations, best estimate data are suggested, as shown in Table 6-11. The data are reproduced from Table 8-1 of Salas et al. (2010), where also data for the excavation/operation period can be found.

Table 6-11. Recommended values of DOC, acetate, CH_4, H_2, NO_2^-, NH_4^+, and colloids for the different periods during the evolution of the Forsmark site. Data reproduced from Table 8-1 of Salas et al. (2010).

Time periods	DOC (mol/L)	Acetate (mol/L)	CH_4 (mol/L)	H_2 (mol/L)	NO_2^- (mol/L)	NH_4^+ (mol/L)	Colloids (µg/L)
Temperate	1.25×10^{-3}	µM range	2×10^{-4}	1.92×10^{-5}	1.07×10^{-7}	4.0×10^{-5}	< 180
Glacial	4.2×10^{-5}	µM range	2×10^{-4}	1.92×10^{-5}	< 1.07×10^{-7}	< 4.0×10^{-5}	20 000
Submerged (marine)	2.9×10^{-3}	µM range	2×10^{-4}	1.92×10^{-5}	1.07×10^{-7}	1.9×10^{-4}	< 180

Best estimate data for sulphide

Hydrogeological modelling indicate that present-day sulphide concentrations at depth are relatively high compared to those of the remaining glacial period (cf columns with S(-II) in Table 6-7 to Table 6-9). As PhreeqC modelling is unable to fully reproduce the microbial influence on the sulphide concentration, the values of the measured sulphide concentrations selected in Tullborg et al. (2010) are recommended for use in SR-Site modelling. Figure 6-6 shows the cumulative distribution function of these selected sulphide concentrations. Practically all sulphide concentrations at the Forsmark site are below $10^{-4.9}$ mol/L (~1.3×10^{-5} mol/L or 0.4 mg/L). It is, however, possible that a few percents of the deposition location in the repository are surrounded by groundwaters that have sulphide concentrations as high as $10^{-3.9}$ mol/L (~1.3×10^{-4} mol/L or 4 mg/L). The numerical data of the CDF are stored in SKBdoc 1261474.

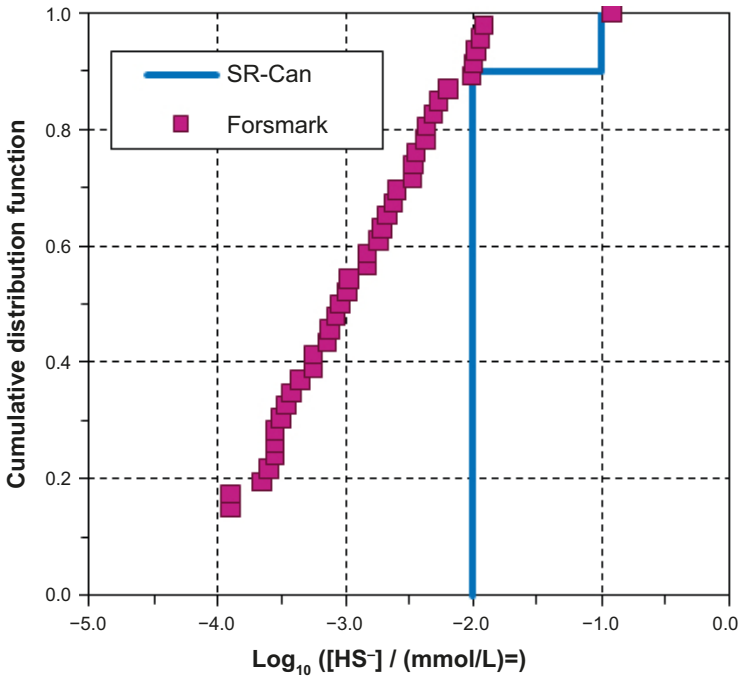

Figure 6-6. *Cumulative distribution function showing the selected sulphide values for groundwaters, recommended for use in SR-Site. The blue curve shows the values used in SR-Can. Reproduced from Figure 7-1 of Tullborg et al. (2010).*

Maximum dissolved oxygen concentration

The oxygen concentration at the repository depth depends on the oxygen concentration of the recharge waters and on the flow related transport resistance, the *F-factor* (yr/m), for the entire recharge flow path, among other things. Figure 6-7 shows the oxygen concentration reaching the deposition holes as a function of the *F-factor*, for the two worst ice locations (II and III). If the *F-factor* is 1 000 yr/m, the oxygen concentration (blue curve) reaching the canister position is ~10^{-3} mol/L. However, as shown by the red CDF for the *F-factor*, no canister position has such a low F-factor for ice location II. Approximately 99 % of the canister positions are reached by flow paths with *F-factors* larger than 50 000 yr/m. However, for such a large *F-factor* all oxygen has been scavenged. For ice location III one can see that at CDF = 0.001 (about 6 canister positions), the oxygen concentration in the range 10^{-4} to 10^{-3} mol/L.

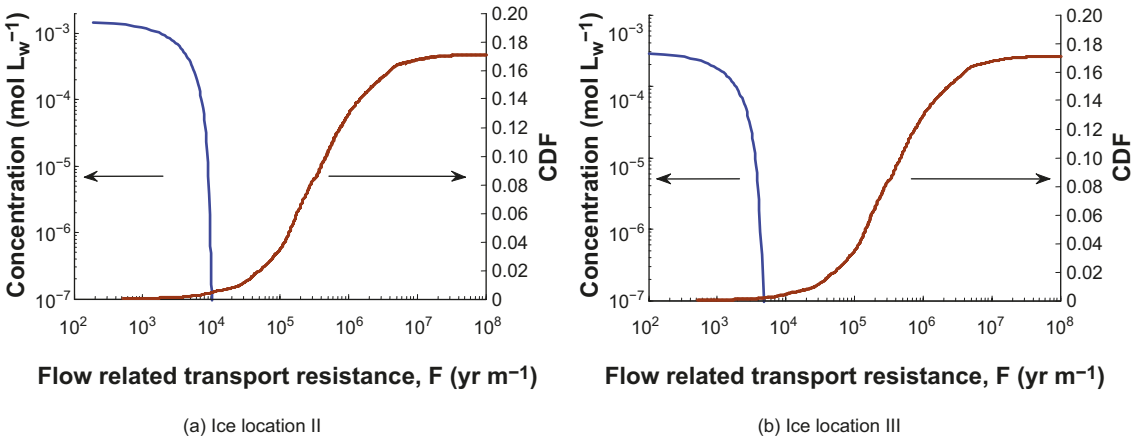

Figure 6-7. *Superpositioned plots of the oxygen concentration profile (blue curve) along flow paths for the oxygen ingress Base case with a 1.5 mM O_2 recharge concentration and CDF (dashed red curves) of flowpaths obtained from hydrogeological modelling for (a) ice location II and (b) ice location III. Reproduced from Figure 8-7 of Sidborn et al. (2010).*

The following is concluded in Sidborn et al. (2010, Section 8.2).

- At a flow path distance corresponding to an *F-factor* of ~5 400 yr/m the oxygen concentration has decreased to 0.3 mM under these conditions. Applying the hydrogeological model results for the worst-case ice location III, 14 canister positions in the repository would be exposed to this concentration or higher. For ice location II none of the canister positions would be exposed to this concentration. At a flow path distance corresponding to an *F-factor* of ~9 400 yr/m the concentration has decreased to 3 μM. This concentration or higher would affect 25 canister positions for ice location III. For ice location II only 6 canister positions would be exposed to this concentration or higher.

It should be noted that these results are valid for a recharging melt water oxygen concentration of 1.5 mM, which is deemed to be a pessimistic value. Also, the results are valid provided that the ice front remains stationary at the most unfavourable position over some time so that steady state hydraulic conditions are established. It is pointed out in Sidborn et al. (2010) that for canisters surrounded by the buffer, much lower concentrations will reach the canister, as result of the transport resistance of the buffer.

6.1.11 Judgement by the assessment team

Input to the PhreeqC modelling

Based on the analysis of uncertainties concerning both the chemical reactions considered and the end-member compositions, the judgement is to use the same data as in SR-Site.

Output from the PhreeqC modelling

Because neither the results from Joyce et al. (2015) nor those from Sidborn et al. (2014) have been further used as input data to other modelling activities (e.g. canister corrosion or radionuclide transport), the judgement is to keep the same data as in SR-Site. The additional results from the coupled hydrogeological-hydrogeochemical modelling of the future evolution during an extended temperate period at Forsmark Joyce et al. (2015) are used to evaluate the effects of the groundwater chemical compositions during this period.

Best estimations for non-modelled chemical components

Since no new information or data has been obtained, the judgement is to use the same data as in SR-Site.

Oxygen ingress

Although numerical experiments show that the effect of different types of heterogeneity should be considered when evaluating the ingress of oxygen, Trinchero et al. (2019) state “the homogeneous analytical solution underestimates the average oxygen interfacial flux”, and thus, the judgement is to use the same data for oxygen ingress as in SR-Site, as the data obtained using the analytical expression are deemed pessimistically chosen.

6.1.12 Data recommended for use in assessment

For the Forsmark end-member groundwaters, the data given in Table 6-6 are recommended. For modelled components, the data given in Table 6-7 to Table 6-10 are recommended. The complete data set from the PhreeqC modelling is stored in SKBdoc 1262945.

For non-modelled data the best estimate values of Table 6-11 are recommended. For sulphide concentrations the CDF in Figure 6-6 is recommended. The underlying sulphide data set is stored in SKBdoc 1261474.

Concerning oxygen ingress, on the order of 10 canister positions may be affected by elevated levels of oxygen, up to concentrations of 1.5 mM O_2, during time periods on the order of a few hundred years per ice front passage.

6.2 Bedrock thermal properties

In the present section, thermal properties of the rock, that is rock thermal conductivity, rock heat capacity, thermal diffusivity, and thermal expansion coefficient, as well as the temperature at repository depth, are presented. These data are mainly needed for evaluating the impact of the thermal load from the spent fuel, which has bearing on the spacing between canister positions in the repository. The bentonite buffer temperature should not exceed 100 °C for any canister deposited. A temperature margin including uncertainties is therefore also presented; see further description in Section 6.2.1.

The thermal properties of the rock are also needed when assessing the long-term thermal evolution of the repository, caused by climate changes. Modelling of the long-term thermal evolution is further discussed in Section 7.1 However, in this present section, data on thermal rock properties, involving geothermal gradient, geothermal surface heat flow, and internal heat generation, will be also discussed in this context.

Furthermore, thermo-hydro-mechanical (THM) analyses of the THM evolution of the repository require thermo-mechanical parameters, where the coefficient of thermal expansion is given in this section but where other mechanical input data are discussed in Section 6.4.

The PSAR is based on the same modelling of Bedrock thermal properties as SR-Site. In the following sections, the modelling strategy is described (Section 6.2.1) followed by an account of the experiences from the SR-Site safety assessment (Section 6.2.2). Since the PSAR is based on the same data as SR-Site, the data qualification (Sections 6.2.3 to 6.2.10) is reproduced from the SR-Site Data report. In Section 6.2.11 the formal judgement by the assessment team to use the qualified data is presented followed by Section 6.2.12 where the recommended data is presented.

6.2.1 Modelling in SR-Site (text reproduced from SR-Site Data report)

This section describes what data are expected from the supplier, and in what SR-Site modelling activities the data are to be used.

Modelling the thermal evolution of the repository is in SR-Site focused on assessing the impact of the heat generated by the spent nuclear fuel. Of particular concern is to assess the peak temperature of the buffer, since it must not exceed 100 °C. There are uncertainties associated with calculation of the peak buffer temperature, meaning that a margin to the design threshold (100 °C) must be established. Establishing a safe, yet not overly pessimistic, margin is an important issue.

The thermal properties are also used to assess the overall thermal evolution of the repository that is used as input to thermo-hydro-mechanical analyses. Furthermore, the thermal properties are also used to assess the large-scale long-term thermal evolution caused by climate changes. Note that thermal data for the latter are required for a much larger area and at a larger scale compared to modelling of the peak buffer temperature in the repository. The demands, e.g. on describing the spatial distribution, are on the other hand much lower. Only mean and uncertainty estimates are required.

Defining the data requested from the supplier

The following data should be delivered for the repository area by the supplier:

- Spatial distribution of the thermal conductivity λ (W/(m·K)) and its potential anisotropy, with correction for temperature and with uncertainty estimates. Different data sets may have to be given for different rock volumes. Especially the lower tail of the distribution is of concern since this is of central importance for canister spacing with respect to the temperature criterion. The temperature field around a canister is dependent on the rock thermal conductivity. Rock having low thermal conductivity will require larger distances between canisters than high conductivity rock.
- Spatial distribution of heat capacity C (J/(m³·K)), with correction for temperature and with uncertainty estimates. Different data sets may have to be given for different rock volumes.
- *In situ* temperature T (°C) at repository depth, with uncertainty estimates.
- Thermal expansion coefficients α (m/(m·K)) for significant rock types, with uncertainty estimates.

- Site-specific temperature margin (°C) data (margin up to 100 °C) in the thermal dimensioning of the repository. The margin constitutes of both general and site-specific uncertainties. Different data sets may have to be given for different rock volumes. The value given constitutes the uncertainty.

In addition, the following data should be delivered for the long-term evaluation caused by climate changes by the supplier:

- Mean value of the thermal conductivity λ (W/(m·K)) and its potential anisotropy, with correction for temperature and with uncertainty estimates. Different data sets may have to be given for different rock volumes, inside and outside the target area.
- Mean value of the heat capacity C (J/(m³·K)) with correction for temperature and with uncertainty estimates. Different data sets may have to be given for different rock volumes, inside and outside the target area.
- Mean value of the thermal diffusivity κ (m^2/s). Different mean values may have to be given for different rock volumes.
- Mean value of the internal heat generation ($\mu W/m^3$) with uncertainty estimates. Different data sets may have to be given for different rock types.
- Mean value of the geothermal gradient (°C/m).
- Mean value of the geothermal surface heat flow (mW/m^2) with uncertainty estimates.

The data should originate from the site investigations and from the assessment of the site investigation data presented in Chapter 6 of the **Site description Forsmark** and its lower level references. Note that pessimistic considerations taken when assessing the peak temperature of the buffer are not necessarily pessimistic when assessing the in situ temperature as impacted by climate change.

SR-Site modelling activities in which data will be used

The SR-Site modelling of the thermal evolution of the near-field is based on a combination of analytical and numerical approaches as further described by Hökmark et al. (2009). The peak buffer temperature is calculated as function of the canister spacing, the tunnel spacing, and the rock thermal properties, whereas a set of fixed assumptions are made for the conditions in the interior of the deposition holes. These assumptions are relevant for dry deposition holes in which the temperatures will tend to be particularly high. This modelling approach has been used for dimensioning the repository, as further described in the SR-Site Underground openings construction report (SKB 2010f) and in the Site engineering report Forsmark (SKB 2009d). However, in SR-Site the objective is to assess the thermal evolution for this selected design. The modelling tools will be the same, whereas the application of the tools may differ somewhat.

The internal solution, i.e. the heat transport in the interior of a dry deposition hole, is practically, but not completely, independent of the host rock properties and the repository layout. In other words the heat transport from the canister through the buffer is for practical purposes independent of the deposition hole rock wall temperature. The solution gives the difference between the rock wall temperature and the maximum bentonite temperature (Hökmark et al. 2009). To find the peak buffer temperature, that temperature difference must be added to the rock wall temperature. This can be done in two ways:

- Adding the temperature difference to analytically calculated rock wall temperatures.
- Adding the temperature difference to numerically calculated rock wall temperatures.

The analytical way (cf Claesson and Probert 1996a, Hökmark and Fälth 2003, Hökmark and Claesson 2005) is fast but based on idealised assumptions of the rock heat transport properties. The analytical solution cannot account explicitly for the spatial variability of the rock heat transport properties. However, by knowing the distribution of the rock thermal conductivity, reasonable values of the dimensioning rock thermal conductivity selected from the low-conductivity tail of the distribution (which represent rock having the least favourable thermal properties) are used in the dimensioning to estimate trial values of the canister spacing required to ensure that the 100 °C criterion will be met for all canisters. For SR-Site, the results of the calculations will be combined with supplementary calculations using the numerical as well as the analytical model, for the actually selected canister spacing in the design.

The numerical way is used to account directly for the spatial variability of thermal conductivity and heat capacity in the rock mass. First a number of realisations of the spatial distribution of thermal conductivity in the 1–2 m scale are selected. This is a scale that corresponds to the lower limit of spatial influence on the canister/buffer temperature according to Chapter 3 in Sundberg et al. (2005b). The selected realisations are the ones with the lowest thermal conductivity in the influence volume to the potential canister positions. Subsequently the peak buffer temperature is calculated with the numerical simulation model for each canister in the selected realisations. This should ensure that the buffer peak temperature is safely bounded. In reality, the majority of the canisters will be placed in much more favourable positions, i.e. in rock portions with higher thermal conductivity resulting in lower buffer temperatures. The numerical simulation of the thermal process in the repository is performed using the explicit finite difference method (FDM) (Eftring 1990). The repository and a certain part of the surrounding rock are described by dividing the region into a grid of sub volumes with different thermal properties from the thermal realisations. The subdivision is made with smaller cells around the canister in order to describe details of the near-field and to obtain a better resolution of large temperature gradients. The cell size is increased the further away the cells are located from the canister. The simulated region consists of a segment including one tunnel with nine deposition boreholes in a row. This region is bounded by symmetry planes in the horizontal directions. In the vertical direction it extends to a sufficient distance, beyond which the thermal properties of the rock have an insignificant effect on the maximum buffer temperature. Only the five central canisters are used in the evaluation of the peak buffer temperature to avoid boundary effects.

There are uncertainties in input data as well as systematic over and underestimates associated with both the local canister/buffer solution and the calculation of the rock wall temperature. Therefore, the dimensioning of the repository, i.e. establishing canister spacing for the different rock domains at a given site, must be made with a margin to the 100 °C threshold. In Hökmark et al. (2009) the different parts that constitutes the margin are described. The margins are optimised for the numerical method.

The overall thermal evolution is in the THM-analyses assessed by the 3DEC code, as further described by Hökmark et al. (2010). The thermal property input needs to this modelling is covered by the input needs of the buffer peak temperature modelling.

The thermal evolution of plugs, the central area, shafts, ramps, top seals and borehole seals are assessed by the analytical solution, using mean values of the site-specific thermal properties given in the **Site description Forsmark**.

Thermo-mechanical models used in SR-Site are described in Section 6.4 and models used for assessing the thermal evolution of the repository, as impacted by climate changes, are discussed in Section 7.1.

6.2.2 Experience from SR-Site

Modelling in SR-Site

See previous section.

Condidions for which data were used in SR-Site

See previous section.

Sensitivity to assessment results

The analyses performed during SR-Site demonstrate that the suggested layouts would conform to the thermal design premises by a substantial margin, even considering remaining uncertainties in the thermal data. In fact, most deposition holes will have a temperature much below the allowed maximum. From a strictly safety point of view, further detailed investigations and modelling of thermal properties is only needed if SKB decides to aim for a more compact design, with adaptation of deposition hole distances and/or residual power in the canisters to the local thermal conditions in the tunnel.

There are at present no new bedrock thermal property values that can be used quantitatively in PSAR; however, it is noteworthy to mention that supplementary parametric calculations performed in SKBdoc 1700389 to assess the effect of differently sized and located rock volumes with low thermal conductivity indicate that the planned spacing between canister positions in SR-Site (SKB 2010a) is conservative with respect to the maximum allowed bentonite buffer temperature.

No additional new insights or results have been obtained on bedrock thermal properties during SR-Site or during the ensuing work addressing review comments on SR-Site.

6.2.3 Supplier input on the use of data (text reproduced from SR-Site Data report)

The supplier broadly agrees with the use of data in SR-Can as described in Section 6.2.2, with the limitations noted above which have lead to modifications in the strategy of SR-Site thermal modelling. Furthermore, the supplier broadly agrees with the use of data in SR-Site, as described in Section 6.2.1.

6.2.4 Sources of information and documentation of data qualification (text reproduced from SR-Site Data report)

Sources of information

Main sources of information on thermal properties used in data qualification are described in Table 6-12. In the thermal site-descriptive modelling, a large number of realisations of thermal properties are produced from stochastic modelling. These realisations are the basis for the description of thermal properties on domain level in the site-descriptive modelling reports, see Table 6-12. However, the thermal property realisations (see Table 6-19) are directly used in the thermal dimensioning, as described in Section 6.2.1.

Within the publications listed in Table 6-12, references to relevant lower level documents can be found.

Table 6-12. Main sources of thermal property information used in data qualification.

Site description Forsmark, 2008. Site description of Forsmark at completion of the site investigation phase. SDM-Site Forsmark. SKB TR-08-05, Svensk Kärnbränslehantering AB.
Sundberg J, Wrafter J, Back P E, Ländell M, Rosén L, 2008a. Thermal properties Forsmark. Modelling stage 2.3. Complementary analysis and verification of the thermal bedrock model, stage 2.2. SKB R-08-65, Svensk Kärnbränslehantering AB.
Back P E, Wrafter J, Sundberg J, Rosén L, 2007. Thermal properties. Site descriptive modelling Forsmark – stage 2.2. SKB R-07-47, Svensk Kärnbränslehantering AB.
Sundberg J, Back P-E, Ländell M, Sundberg A, 2009a. Modelling of temperature in deep boreholes and evaluation of geothermal heat flow at Forsmark and Laxemar. SKB TR-09-14, Svensk Kärnbränslehantering AB.
SKB, 2009d. Site engineering report Forsmark. Guidelines for underground design, step D2. SKB R-08-83, Svensk Kärnbränslehantering AB.

Categorising data sets as qualified or supporting

Qualified and supporting thermal data sets are displayed in Table 6-13 and numbered from item 1 to 15. Detailed justifications to the sorting of the data sets are given in Table 6-14 and Table 6-15. Where different data sets are required for different rock volumes, these are described for the rock domains RFM029 and RFM045. Data outside the target area are described for a number of different rock domains.

Most data sets have a priori been considered to be qualified. They have thereafter been judged to be qualified based on the criteria in the instruction for supplying data to this Data report (see Section 2.3). The exception is the supporting data set accounted for in item 15.

Excluded data previously considered as important

No important data have been excluded from the analysis. Non-used thermal data are described in Section 2.2.3 in SKB (2008).

Table 6-13. Qualified and supporting data sets.

Qualified data sets	Supporting data sets
1. Thermal conductivity: RFM029: Table 6-3 in Back et al. (2007). RFM045: Table 7-1 in Sundberg et al. (2008a). 2. Heat capacity: RFM029, RFM045: Table 7-2 in Sundberg et al. (2008a). 3. Spatial distribution of thermal conductivity and heat capacity in each rock domain and thermal subdomain. Up to 1 000 realisations for each rock domain (SKBdoc 1271438). 4. Thermal conductivity and heat capacity for rock domains outside target area: Properties based on modelling results and data for different rock types in the thermal site-descriptive model version Site (Back et al. 2007, Sundberg et al. 2008a) and version 1.2 (Sundberg et al. 2005a) and geology from site-descriptive model version 1.2 (SKB 2005) and 2.1 (SKB 2006d). 5. Thermal diffusivity: Calculated from thermal conductivity and heat capacity above. 6. Anisotropy in thermal conductivity: Section 6.3.1 in Back et al. (2007). Orientation in Chapter 6 in the **Site description Forsmark**. 7. Temperature dependence in thermal conductivity and heat capacity: Table 2-3 and 2-4 respectively in Sundberg et al. (2008a). 8. Pressure dependency in thermal conductivity: Section 2.5 in Sundberg et al. (2008a). 9. Thermal expansion coefficient: Table 3-19 in Back et al. (2007). 10. Temperature at repository level: Table 2-6 in Sundberg et al. (2008a). 11. Geothermal gradient: Figure 2-4 in Sundberg et al. (2008a). 12. Heat generation: 6.1.3 in Sundberg et al. (2009a). 13. Heat flow: Mean in Section 6.2.2 with uncertainty estimates in Section 8.1 in Sundberg et al. (2009a). 14. Temperature margins are based on the principals in (Hökmark et al. 2009) and site-specific data in Back et al. (2007) and Sundberg et al. (2008a).	15. Temperature dependences for some rock types is taken from the literature, see Table 2-3 and 2-4 respectively in Sundberg et al. (2008a).

Table 6-14. Justification to the sorting of items 1–10 in Table 6-13.

1. The relevant thermal conductivity data as reported in Back et al. (2007) and Sundberg et al. (2008a) are based on data acquired and refined within the Forsmark site description and site investigation phases. These phases have been conducted in conformance with relevant quality assurance routines. Lower level references are carefully listed, thus facilitating traceability (see e.g. Chapter 3 in Back et al. 2007). Through lower level references the traceability is ensured down to relevant quality assurance documents such as method descriptions, task descriptions, etc. In Back et al. (2007) and Sundberg et al. (2008a) issues such as data quality, variability, and representativity are discussed. Nonconformities and uncertainties are also discussed. Much of the thermal data delivered are derived from modelling. In Back and Sundberg (2007), Back et al. (2007) and Sundberg et al. (2008a), the modelling strategy, the modelling tools, and validity of the modelling are described. It is judged that the modelling approach is adequate.

2. The relevant heat capacity data reported in Back et al. (2007) and Sundberg et al. (2008a) are based on data acquired and refined within the Forsmark site description and site investigation phases. The same considerations as for item 1 apply.

3. The spatial distribution of thermal conductivity and heat capacity are described in a large number of realisations for each rock domain, and based on data acquired and refined within the Forsmark site description and site investigation phases. Item 1 and 2 above are based on these realisations. The same considerations as for item 1 apply.

4. The thermal conductivity and heat capacity data for rock domains outside target area are based on thermal properties of different rock types in the site-descriptive model (Back et al. 2007, Sundberg et al. 2008a). Similar considerations as for item 1 apply on the data for different rock types/TRCs (Thermal Rock Classes). However, the requirements are much lower compared to those on data from the target volume. The mean thermal conductivity and heat capacity may be calculated from the proportions of different rock types or based on the dominant rock type (SKB 2005, 2006d).

5. The thermal diffusivity data are calculated, in this present section, based on the data set for thermal conductivity (item 1) and heat capacity (item 2 and 4). As a consequence, the same considerations as for item 1 and 4 apply.

6. The anisotropy in thermal conductivity reported in Back et al. (2007) are based on data acquired within the Forsmark site investigation phases. The same considerations as for item 1 apply. However, no advanced data refinement has been made. Focus has been on providing a relevant mean value for areas where the anisotropy is pronounced. The orientation and strength of anisotropy is further described in Chapter 5 in the Site description Forsmark.

7. The temperature dependences of thermal conductivity and heat capacity reported in Sundberg et al. (2008a) are mainly based on data acquired within the Forsmark and Laxemar site investigation phases. The same considerations as for item 6 apply. The description has focused on mean value for the dominant granite. Data for subordinate rocks have been obtained from similar rock types in Laxemar (Sundberg et al. 2008b) and from literature data given in Sundberg et al. (2008a). This approach has been judged to be adequate since the temperature dependence is moderate and has only minor influence on the maximum bentonite temperature.

8. The pressure dependence in thermal conductivity is described in Sundberg et al. (2008a). The pressure dependence is small and has been neglected in the thermal conductivity modelling. Neglecting the pressure dependence has a slightly pessimistic effect on the results of the thermal conductivity modelling.

9. The thermal expansion coefficient reported in Back et al. (2007) are based on data acquired within the Forsmark site investigation phases. The same considerations as for item 6 apply. Focus has been on providing a relevant mean value.

10. The temperature at repository level reported in Sundberg et al. (2008a) is based on data acquired within the Forsmark site investigation phases. Similar considerations as for item 1 apply. In the thermal modelling, the reliability of temperature logging data has been evaluated in relation to calibration errors and disturbances from drilling. Only approved data has been used in the site-descriptive model. Focus has been on providing both a relevant mean value for repository depth and a measure of variability.

Table 6-15. Justification to the sorting of items 11–15 in Table 6-13.

11. The geothermal gradient data reported in Sundberg et al. (2008a) are based on the temperature logging data described in item 10. As a consequence, the same considerations as for item 10 apply.

12. The internal heat generation data are reported in Sundberg et al. (2009a). It is based on data acquired within the Forsmark site investigation phases. Similar considerations as for item 1 apply. However, no advanced data refinement has been made. Focus has been on providing a relevant mean value.

13. The site-specific geothermal surface heat flow is reported in Sundberg et al. (2009a). The heat flow is based on data acquired within the Forsmark site investigation phases together with data on the past climate evolution (Sundberg et al. 2009a). The heat flow is determined indirectly from geothermal gradient (item 11), thermal conductivity (item 1), thermal diffusivity (item 5), internal heat generation (item 12) and past climate evolution. The uncertainty estimates have been evaluated from uncertainties in the above mentioned parameters together with the influence from e.g. temperature dependences (item 7) and anisotropy (item 6). Similar considerations as for the mentioned items apply (climate evolution and permafrost modelling is further discussed in Section 7.1. Focus has been on providing both a relevant mean for the site and an uncertainty estimate.

14. The temperature margin data are based on the principles and general data in Hökmark et al. (2009) and site-specific data in Back et al. (2007) and Sundberg et al. (2008a). The temperature margin consists of both uncertainties and under- and overestimates in the calculation of the peak buffer temperature. The uncertainties are carefully discussed in Hökmark et al. (2009) and quantified in general terms with example values that can be relevant for the different rock domains. In the Site engineering report (SKB 2009d), site-specific data are used to define a margin for each rock domain.

15. The supporting data on the temperature dependence (item 7) for subordinate rock types is provided by articles in reputable scientific journals, which have been subjected to the customary peer-review process before publication.

6.2.5 Conditions for which data are supplied (text reproduced from SR-Site Data report)

The thermal conductivity and heat capacity in the thermal properties realisations are provided at 20–25 °C and at water saturated conditions. The natural temperature at repository depth is slightly lower. After deposition of the canisters the temperature is going to increase, as a consequence of the heat generation in the canisters. However, the temperature dependence for the thermal conductivity and heat capacity is described in the thermal site-descriptive models in the **Site description Forsmark**.

The thermal conductivity measurements are made on stress released samples. However, the pressure dependence is low when the samples are water saturated.

Further, the thermal transport is assumed to be conductive only. This is a relevant assumption since the thermal transport in the rock mass surrounding the canisters should have an insignificant contribution from convective heat transport.

The thermal expansion coefficients for different rock types are provided at 20–25 °C.

The temperature loggings in water filled boreholes are assumed to correctly describe the temperature in the rock mass.

6.2.6 Conceptual uncertainty (text reproduced from SR-Site Data report)

The major conceptual uncertainty of the thermal rock properties concerns correlations with density. Different correlations with density have been used in the thermal site-descriptive modelling in order to: 1) define the spatial correlation structure for thermal conductivity, 2) subdivide certain TRCs (Thermal rock classes (Back et al. 2007)), and 3) strengthen the thermal conductivity /heat capacity relationship. Both the density and the thermal conductivity of rock is related to the mineralogical composition (Sundberg et al. 2009b). The thermal modelling mentioned in this section refer to the thermal site-descriptive model (**Site description Forsmark**), based on modelling in Back et al. (2007) and Sundberg et al. (2008a).

It has been assumed that thermal conductivity exhibits a similar correlation structure to density. The variogram models, used to describe the spatial correlations structure of the thermal conductivity in the thermal modelling, are primarily based on density loggings (approximately 0.1 m scale) in boreholes, supported by TPS (Transient Plane Source) data if a sufficient amount of data were available. A relationship between thermal conductivity and density has been established (see Section 6.2.2 in the **Site description Forsmark**). Even for rock types where such a relationship is not evident, density logging data are used as input to the variogram modelling. It is reasonable to assume that any spatial dependence in density, as indicated by a variogram, also reflects spatial dependence in thermal conductivity (Back et al. 2007). However, the associated uncertainty is not known. This uncertainty is handled by using slightly pessimistic variogram models in the stochastic modelling.

The relationship between thermal conductivity and density has also been used in order to subdivide different TRCs when necessary.

Referring to the thermal conductivity/density relationship, it is reasonable to assume a corresponding relationship between density and heat capacity. Such a relationship has been found previously (Sundberg et al. 2003), although weaker than that for thermal conductivity versus density. In Sundberg et al. (2008a) a relationship between heat capacity from direct measurements and thermal conductivity is described. The relationship has been used to calculate heat capacity from the modelling results on thermal conductivity in order to complete the thermal conductivity realisations with heat capacity. Uncertainties associated with the thermal conductivity modelling are also present in the modelled heat capacity distribution. In addition, uncertainties related to the relationship between thermal conductivity and heat capacity are added. However, these uncertainties in heat capacity are judged to have only minor results on the calculated maximum buffer temperature (see Section 6.2.1).

The conceptual uncertainty in other parameters is judged to be low.

6.2.7 Data uncertainty due to precision, bias, and representativity (text reproduced from SR-Site Data report)

The data uncertainty can be subdivided into precision, bias, and representativity. The data uncertainty can also be subdivided into uncertainties in primary data and model uncertainties. The discussion is focused on uncertainties in thermal properties inside the target area but is partly also applicable to properties outside the target area (mainly used for the thermal evolution of the repository due to climate changes). Uncertainties specifically related to data outside the target area are explicitly described. The demands on data inside the target area are much higher compared to those on data for permafrost modelling, see Section 6.2.1.

Data uncertainty due to precision and bias

Primary data in the site investigations

Data uncertainty due to precision is believed to have only minor influences for thermal conductivity determinations made by the TPS method. Heat capacity values calculated from simultaneously determined thermal conductivity and thermal diffusivity have a rather wide spread due to the combination of spatial distribution and data precision. Partly the variability is also caused by anisotropy in the samples, which to some degree is normally the case in the Forsmark area. However, in the thermal modelling only heat capacity data from calorimetric determinations have been used. These data show a variability that is believed to be mainly caused by spatial variability.

The temperature loggings in boreholes are disturbed by water movements and the drilling of the borehole. In the SDM-Site model, the reliability of temperature loggings due to disturbance from drilling has been evaluated. As a result of this only "approved" boreholes have been used in the description. However, uncertainties related to water movements are still present, especially at certain parts of the boreholes. However, the mean temperature at repository depth in different boreholes shows a rather small variability between different boreholes. Uncertainties in the temperature loggings are transferred into the determination of geothermal gradient and of heat flow.

The reliability of temperature loggings due to calibration error have been evaluated (Back et al. 2007, Sundberg et al. 2008a). Earlier rather large calibration errors could occur. In the SDM-Site version of the thermal site-descriptive model, only temperature logging data that fulfil certain requirements regarding calibration have been used to describe the *in situ* temperature conditions (Sundberg et al. 2008a). The variability between the temperature at the same relevant elevation in different boreholes is ± 0.4 °C about the mean (Table 2-6 in Sundberg et al. 2008a). For individual boreholes, the uncertainty is ± 0.25 °C (related to equipment).

The heat generation in the rock mass is calculated from the proportions of U, Th, and K (Sundberg et al. 2009a). Uncertainties in the proportions in combination with sparse data for some rock types are transferred to uncertainties in the heat generation. These uncertainties can be rather large. However, the internal heat generation down to repository depth has only minor influence on the calculated surface heat flow and the permafrost modelling.

Potential bias in the determination of the thermal expansion coefficient has been discussed in the thermal site-descriptive model version 1.2 (Sundberg et al. 2005a). The reason for potential bias was that stress dependence had not been assessed and the measurements are made on stress released samples. However, through a literature survey the question could be eliminated.

The uncertainties in the orientation of the boreholes and in the orientation of geological objects in the boreholes, documented by Munier and Stigsson (2007), are judged to have little or no effect on the results of thermal modelling.

Model uncertainties

There are several model uncertainties to consider in the thermal modelling of the spatial distribution of thermal conductivity and heat capacity. The five most important uncertainties identified in site-descriptive model stage 2.2 (Back et al. 2007) were associated with 1) the simulation scale, 2) the simulation volume, 3) the spatial statistical structure of TRCs (lithology), 4) the spatial statistical

thermal models, and 5) the simulation technique. In the complementary site description in model stage 2.3, rock domain RFM045 was remodelled, and special attention was given to the uncertainties in the spatial statistical structure of TRCs (lithology) and the simulation volume (Sundberg et al. 2008a).

A detailed discussion of the above mentioned uncertainties is performed in Back et al. (2007) and Sundberg et al. (2008a) and a summary is provided in the **Site description Forsmark**. Uncertainties associated with the simulation volume and the simulation scale are not believed to have had any major impact on the thermal modelling results. Geological heterogeneities were dealt with by dividing the domains into subdomains. This is believed to have reduced the uncertainty significantly. The remaining uncertainty concerning the variability in proportions is believed to be small. Based on confidence intervals for TRC proportions at borehole scale (see Section 6.1 in Sundberg et al. 2008a), this uncertainty has only a minor effect on the lower thermal conductivity tail (the 1-percentile may vary by about 1 %). This is also discussed under "representativity".

Limited amounts of data for some TRCs result in uncertain spatial statistical thermal conductivity models. The variograms require even more data. It has been assumed that thermal conductivity exhibits a similar correlation structure to density, see discussion above. The spatial statistical thermal conductivity models are believed to be more reliable than in previous versions. Uncertainties in the simulation technique are believed to have only a minor influence on the results.

Uncertainties are also associated in the thermal anisotropic properties of the dominant granite (lineation/foliation), mainly due to few determinations. The mean values of the thermal anisotropic factor at the investigated site may be quite reliable but the spatial distribution has large uncertainties.

There are a number of uncertainties related to the determination of the site-specific heat flow. These uncertainties are related to uncertainties in geothermal gradient, thermal conductivity, thermal diffusivity, internal heat generation, and past climate evolution. A detailed discussion of the above mentioned uncertainties is performed in Section 8.1 in Sundberg et al. (2009a).

The temperature margin to the design criteria (100 °C) consists of uncertainties as well as under- and overestimates in the calculation of the peak buffer temperature. The temperature margin data are based on the principles and general data carefully elaborated in Hökmark et al. (2009) and site-specific data in Back et al. (2007) and Sundberg et al. (2008a). The margins are optimised for the numerical method. Thus, the margin constitutes of both general and site-specific uncertainties.

The uncertainties are discussed in detail in Hökmark et al. (2009). A short summary is presented here and the temperature margin for different rock domains is justified from site-specific data. Non-site specific uncertainties are not described here. Instead the reader is referred to Hökmark et al. (2009). In Table 6-16 and Table 6-17 the different uncertainties in the local solution and the numerically calculated rock wall temperature are summarised. The uncertainties and biases given in these tables represent realistic judgements for the individual parameters. In Table 6-18 the total temperature margin is presented.

Uncertainty U1 in Table 6-16 is site-specific and can be interpolated for different conductivities from Hökmark et al. (2009). The thermal conductivity at low percentiles of the thermal conductivity distribution are approximately 3 W/(m·K) for rock domain RFM029 and 2.5 W/(m·K) for rock domain RFM045. Uncertainties U2–U5 are not site-specific and are discussed in detail in Hökmark et al. (2009).

Table 6-16. Uncertainties in local solution. Modified from Hökmark et al. (2009) with site-specific data from Back et al. (2007) and Sundberg et al. (2008a).

ΔT_{tot}, difference between rock wall temperature and maximum bentonite temperature		Margin, °C, RFM029	Margin, °C, RFM045
Uncertainties related to:			
U1	Geometry of air-filled canister/bentonite gap and variations in barrier conductivity	3.3	3
U2	Moisture redistribution in barrier	0.2	0.2
U3	Spalling	0.1	0.1
U4	Vertical variation of rock conductivity along deposition hole	0.25	0.25
U5	Vertical distribution of heat generation in the canisters	0.2	0.2
Sum ΔT_{tot}		**4.05**	**3.75**

Table 6-17. Uncertainties in numerically calculated rock wall temperature, T_{wall}. Modified from Hökmark et al. (2009) with site-specific data from Back et al. (2007) and Sundberg et al. (2008a).

T_{wall} , Rock wall temperature at canister mid-height at the time of buffer temperature peak		Margin, °C, RFM029	Margin, °C, RFM045
Uncertainties related to:			
U6	Anisotropy within rock type	0.7	0.5
U7	Bias in thermal properties	0.5	0.8
U8	Heterogeneity, site models (in the lower tail)	0.1	0.1
U9	Initial temperature	0.65	0.65
U10	Temperature dependence	0	0
U11	Pressure dependence	–0.2	–0.2
U12	Tunnel backfill	0	0
U13	Strategy uncertainties	-	-
Sum (uncertainties)		1.75	1.85
Over/underestimate because of numerical model simplifications			
S1	Representation of canister	–0.7	–0.7
S2	Numerical precision	–0.8	–0.8
S3	Boundary conditions	0.2	0.4
Sum (under/overestimates)		–1.3	–1.1
Total uncertainties in T_{wall}		**0.45**	**0.75**

Table 6-18. Total temperature margin in numerical solution to establish a definitive spacing.

Uncertainties related to:	Domain RFM029	Domain RFM045
Local solution (Table 6-16)	4.05 °C	3.75 °C
Total T_{wall}. Numerical solution (Table 6-17)	0.45 °C	0.75 °C
Total Margin	4.5 °C	4.5 °C

Uncertainties U6–U10 in Table 6-17 are site-specific. Item U6 is related to the anisotropy in rock. It includes the effect of a foliated rock oriented in an unfavourable orientation compared with repository layout. The anisotropy factor is assumed to be 15 %. In rock domain RFM029 the tunnel orientation is parallel to the subvertical foliation which coincides with the maximum temperature contribution in Hökmark et al. (2009). The temperature contribution is slightly decreased for rock domain RFM045 compared to Hökmark et al. (2009), since the tunnel orientation is not entirely parallel to the foliation in combination with lower dip. The uncertainty due to potential bias in the thermal properties is discussed in uncertainty U7. The temperature effect of the potential bias is interpolated from Hökmark et al. (2009) using site-specific data (1 % percentile). The uncertainty U8, related to the uncertainty in the lower tail of the thermal conductivity distribution (SDM-Site) due to uncertainties in rock type proportions. The temperature effect related to U8 is small.

Uncertainty U9 is related to uncertainties in the *in situ* temperature. The lowest and highest temperatures measured in different boreholes at 400 m depth vary by ± 0.4 °C about the mean (Sundberg et al. 2008a). In addition there is possible bias in the measurements which is estimated to be on the order of 0.25 °C. The initial temperature relevant for the dimensioning problem may differ from the present-day rock temperature because of heat generated during tunnel excavation, ventilation, etc. At the time of writing this text it is not possible to estimate these effects or even to establish if the net effect will be a decreased or an increased effective background temperature (Hökmark et al. 2009).

U10 is related to uncertainties due to the increased rock temperature and the temperature dependence in thermal properties. The uncertainty is very low and not site dependent when temperature dependent properties is included in the numerical approach for thermal dimensioning of the repository (Hökmark et al. 2009). Data on temperature dependent properties are taken from Sundberg et al. (2008a).

Uncertainties U11–U13 are not site-specific. Over- and underestimations due to the representation of the canister and numerical precision in the numerical model are not site-specific (S1–S2). S3 includes the effect of boundary conditions in the numerical model. Since the dimensioning is made on the canister surrounded with rock with very low thermal conductivity it is reasonable to believe that the thermal conductivity in the neighbouring tunnels is higher. 10 % higher thermal conductivity in two neighbouring tunnels gives 0.4 °C in temperature contribution (Hökmark et al. 2009). The difference between the mean thermal conductivity and conductivity around a canister in low conductive rock is typically < 5 % and 10 % for rock domain RFM029 and RFM045 respectively.

Data uncertainty due to representativity

Uncertainties in the proportions of rock types in Boremap (the drill core mapping) have influence on the overall distribution of thermal conductivities for each domain. In Sundberg et al. (2008a) confidence intervals for TRC proportions has been calculated on the basis of the differences between different boreholes. The uncertainties are relatively small for rock domain RFM029 (Sundberg et al. 2008a, Table 6-3) but larger for domain RFM045 (Sundberg et al. 2008a, Table 6-4) because of its lesser degree of homogeneity in geology and thermal properties. However, this uncertainty has only a minor effect on the lower thermal conductivity tail (the 1-percentile may vary by about 1 %).

The samples used for determinations of thermal conductivity and heat capacity for the main rock types are from different sections in different boreholes and are judged to be representative for the different rock types. The representativity can be questioned for subordinate rock types with only few determinations. However, the effect on the domain modelling results from subordinate rock types is small.

The representativity of samples selected for thermal expansion measurements can be questioned. The samples are few and focused to certain parts of the rock volume. However, the variability seems to be quite low.

Also the representativity of the thermal anisotropy can be questioned. The investigations have been focused at one site but the strength of the foliation varies in different parts of the Forsmark area (Chapter 5 in the **Site description Forsmark**).

The thermal data for permafrost modelling include rock domain data outside the target area (cf Section 7.1). The uncertainties in the mean and uncertainty estimates for the thermal conductivity, heat capacity, and heat production are mainly related to the estimates in rock type proportions, if any, and if thermal data are available for the different rock types. For some rock domains data are based on the dominant rock type. The uncertainties can be rather large compared to the rock domain data inside the target area. However, the uncertainties are not believed to have major influence on the permafrost modelling result since other uncertainties are judged to be larger.

The temperature loggings come from several boreholes and are judged to be representative for the site. The temperature data and geothermal gradient data are mainly available for the target area but are judged to meet the needs for the large-scale permafrost modelling, including areas outside the target area.

The heat flow data are judged to be representative for the whole site, including areas outside the target area used in permafrost modelling.

6.2.8 Spatial and temporal variability of data (text reproduced from SR-Site Data report)

Spatial variability of data

The description of the spatial distribution of thermal conductivity and heat capacity has been the main objective in the thermal site-descriptive modelling. Particular emphasis have been made on describing the lower tail of the thermal conductivity distribution since small uncertainties in the lower tail of the thermal conductivity distributions will have a significant impact on canister spacing in repository layout D2, in order to fulfil the maximum temperature criteria on the buffer. Also the uncertainty description in Back et al. (2007) and Sundberg et al. (2008a) is focusing on the lower tail of the thermal conductivity distributions for the different rock domains. The models presented in the site-descriptive modelling, SDM Site, are judged to represent the modelled rock domains and their variability in an appropriate way (**Site description Forsmark**). Confidence in the lower tails of the thermal conductivity distributions is higher for domain RFM029 than domain RFM045. For the latter, this uncertainty is related to the spatial and size distribution of amphibolite.

As an important part of the thermal modelling, data are upscaled from measurement scale to simulations scale (1 m in Forsmark). The temperature development around a canister is influenced by a number of different scales, approximately 2–20 m (Sundberg et al. 2005b). When using the data to calculate large enough spacing between canisters, the simulation scale is used (1 m) (Hökmark et al. 2009). This means that an automatic upscaling is provided in the numerical modelling when calculating the maximum temperature from the data provided in the thermal realisations (see Section 6.2.1). However, in the site-descriptive modelling reports (Back et al. 2007, Sundberg et al. 2008a) there is a need to illustrate the upscaling effect. Upscaling is made to 5 m, a scale that approximately is relevant for the temperature development around the canister, The result for this upscaling is provided in the thermal site-descriptive modelling reports and used for trial values on canister spacing (Hökmark et al. 2009) and uncertainty estimates.

The appropriate scale for the long-term thermal evolution, caused by climate changes, is much larger compared to the scale appropriate for thermal evolution modelling of the near-field of individual canisters. Therefore the mean of thermal conductivity, heat capacity, heat generation, anisotropy etc is relevant for this long-term thermal evolution.

The description of the anisotropy in thermal conductivity has been focused on determining a relevant mean anisotropy factor for foliated parts the dominant granite. Consequently, there are uncertainties in the spatial distribution of the anisotropy.

Temporal variability of data

Except for the in situ temperature, none of the data have temporal variability. The temperature loggings show a significant influence from drilling that is time dependent. If the loggings have been made to close to the drilling the result can be questioned. However, such temperature logging data have been excluded from the evaluation during an approval process, see Section 2.7 in Sundberg et al. (2008a). The natural temperature at repository depth has long-term variability in data. However, this is a very slow process and the natural undisturbed variability is thus insignificant. The long-term thermal evolution of the repository is discussed in Section 7.1. However, the construction of the repository may influence the temperature at repository depth. This is discussed above in Section 6.2.7 in connection to the uncertainty discussion of the temperature margin.

6.2.9 Correlations (text reproduced from SR-Site Data report)

As described in Section 6.2.6, the spatial correlation structure for the thermal conductivity has been based on density logging data. Measurements have been used to support the correlation structure when possible.

A relationship between thermal conductivity and heat capacity is reasonable and have been found and described in Sundberg et al. (2008a), see Figure 6-8. The relationship has been used to calculate the heat capacity C from the thermal conductivity for each cell in the produced realisations from the thermal stochastic modelling. A random error component ε_c has been added to C (see Sundberg et al. 2008a, Section 2.6). This means that the correlations structure for the thermal conductivity has also been used for the heat capacity.

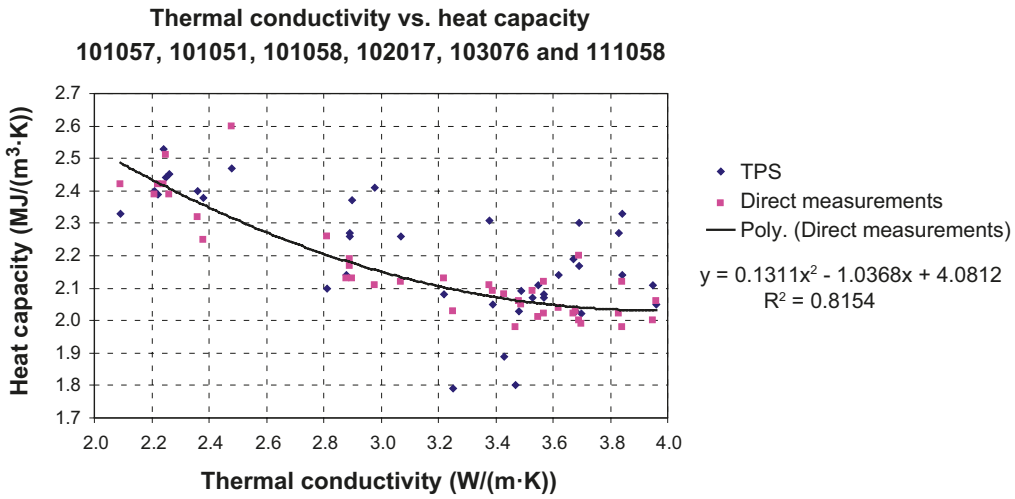

Figure 6-8. *Heat capacity versus thermal conductivity. The second order relationship is based on calorimetric measurements only. Reproduced from Sundberg et al. (2008a, Figure 2-3).*

6.2.10 Result of supplier's data qualification (text reproduced from SR-Site Data report)

The data are presented in the site-descriptive modelling reports (Back et al. 2007, Sundberg et al. 2008a). Here a summary is made.

Thermal conductivity

The thermal conductivity is mainly measured in laboratory with the TPS-method. Thermal conductivity versus elevation for different rock types is illustrated in Figure 6-9. From Figure 6-9 it can be seen that the thermal conductivity for the dominant granite (101057) is high, but lower for some subordinate rock types.

The rock type distribution in boreholes together with the distribution of thermal conductivity data and the correlation structure are used as bases for stochastic modelling of both geology and thermal conductivity. The main result of the thermal modelling for domain RFM029 and RFM045 is the set of 1 000 realisations (500 for domain RFM045) of thermal conductivity from the simulations in the 1 m scale. These realisations have been used in the design of the repository (SKB 2009d) and are input to the SR-Site numerical thermal calculations (see Section 6.2.1). Histograms of the realisations upscaled to 5 m are shown in Figure 6-10 for domain RFM029 and RFM045. The 5 m scaled data are judged to be more relevant for the temperature development around the canister and the peak temperature in the buffer. Summary statistics of the upscaled realisations to 5 m are presented in Table 6-19. These values are valid at 20 °C.

Table 6-19. Thermal conductivity (W/(m·K)) at 20 °C for domains RFM029 and RFM045 based on simulations at the 1 m scale and upscaled to 5 m (data reproduced from Table 6-3 in Back et al. (2007) and Table 7-1 in Sundberg et al. (2008a) respectively). The 0.1–1.0-pecentiles are used as first guess value for the canister spacing in the numerical modelling in SR-Site.

Statistical parameter	RFM029 5 m scale	RFM045 5 m scale
Mean	3.57	3.56
Standard deviation	0.13	0.28
0.1-percentile	2.87	2.36
1-percentile	3.12	2.56
2.5-percentile	3.23	2.73

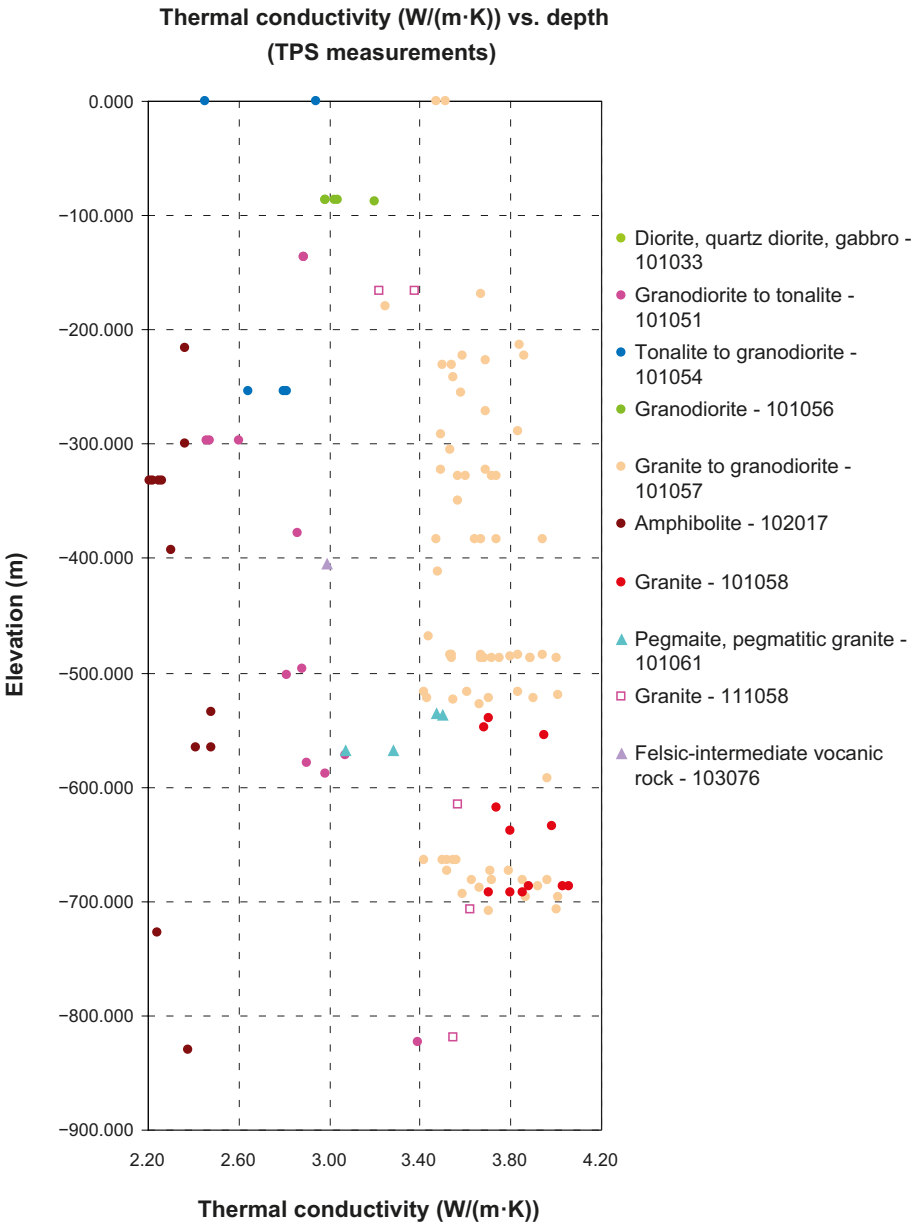

Figure 6-9. *Thermal conductivity versus elevation for different rock types. Samples measured using the TPS method. Reproduced from Back et al. (2007, Figure 3-1).*

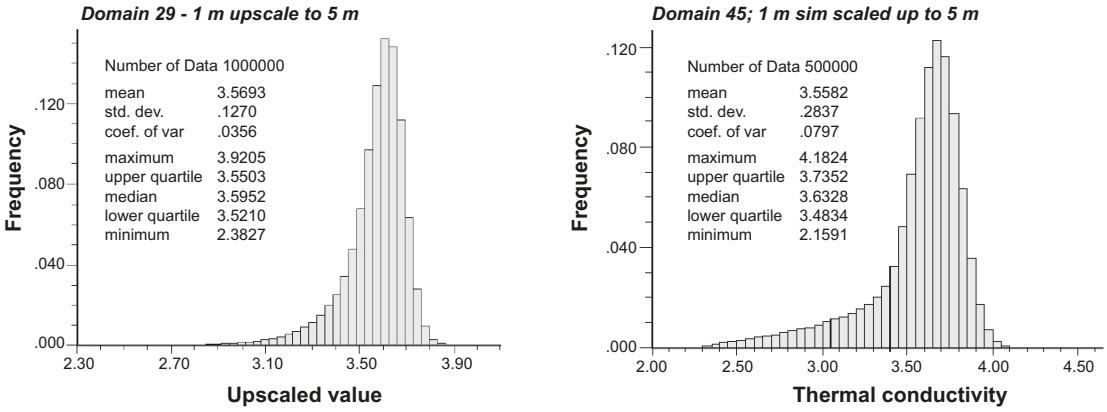

Figure 6-10. *Histogram of thermal conductivity of domain RFM029 (left) and RFM045 (right) simulated at the 1 m scale followed by upscaling to 5 m. Reproduced from Figure 6-3 in Back et al. (2007) and Figure 5-3 in Sundberg et al. (2008a).*

The uncertainties in the lower tail of the modelled thermal conductivity distributions due to uncertainties in rock type proportion is estimated to be 1 % (Sundberg et al. 2008a, Section 8.2).

The thermal conductivity is influenced by the temperature, see Figure 6-11. Thermal conductivity at elevated temperature can be determined from Equation 6-1.

$$\lambda_1 = \lambda_0(1+\alpha_\lambda(T_1-T_0)) \qquad 6\text{-}1$$

where, λ_0 (W/(m·K)) is the thermal conductivity at $T_0 = 20$ °C, λ_1 is the thermal conductivity at the temperature T_1, and α_λ (1/°C) is the temperature coefficient for thermal conductivity.

Estimated mean temperature coefficients for thermal conductivity in different rock types are presented in Table 6-20 and the variability is indicated in Figure 6-12. For some rock types the temperature coefficient is based on similar rock types from the Laxemar site (Sundberg et al. 2008b). For example, the mean temperature coefficient for granite to granodiorite is –10 % per 100 °C. This means that the thermal conductivity at 20 °C is going to be reduced with 5 % if the temperature in the rock mass is raised to 70 °C.

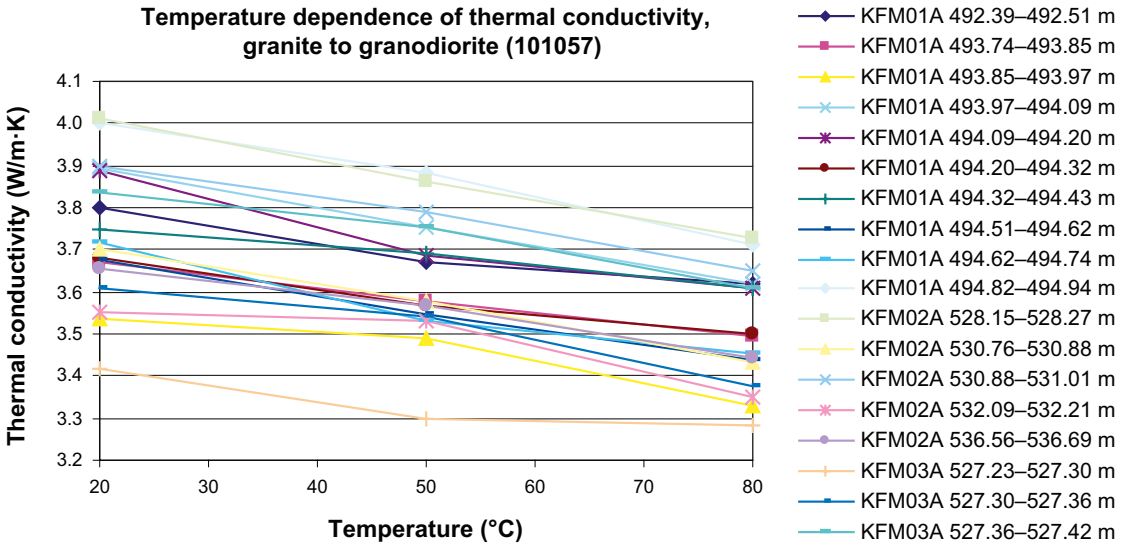

Figure 6-11. *Example of temperature dependence of thermal conductivity for the rock type granite to granodiorite (101057).Reproduced from Back et al. (2007, Figure 3-12).*

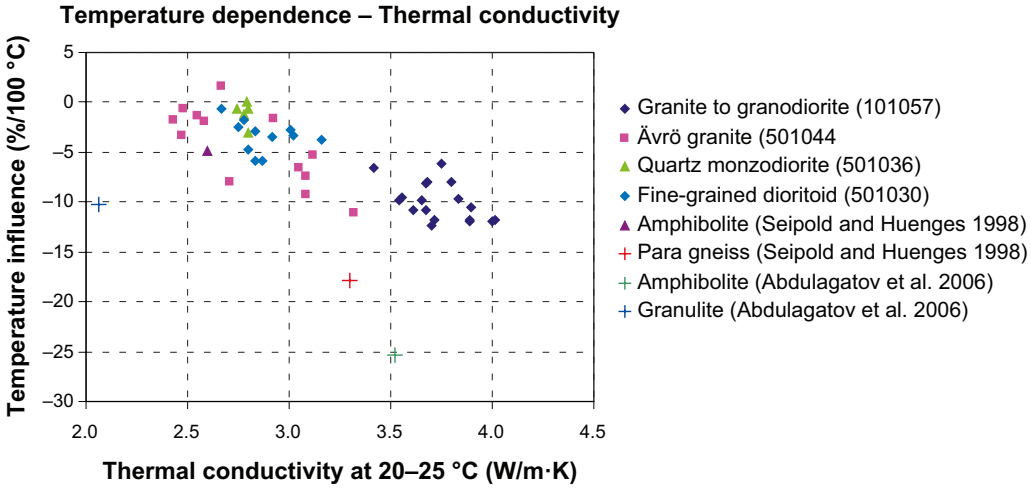

Figure 6-12. *Thermal conductivity (W/(m·K)) at 20–25 °C versus the temperature coefficient (%/100 °C) for the thermal conductivity in different rock types. Rock types with codes beginning with "50" are found in the Laxemar/Simpevarp area. Reproduced from Figure 2-1 in Sundberg et al. (2008a).*

Table 6-20. Estimated mean temperature coefficients for thermal conductivity in different rock types inside target area. The thermal rock class (TRC) to which the rock type has been assigned is also given. Data reproduced from Table 2-3 in Sundberg et al. (2008a).

Rock code	Rock name	TRC	Mean thermal conductivity at approximately 20 °C W/(m·K)	Mean temperature dependence % per 100 °C	Temperature coefficient, α_λ 1/°C	Comments
101057	Granite to granodiorite	57	3.68	–10	-1×10^{-3}	Measured
101051	Granite, granodiorite and tonalite	51	2.85	–5	-5×10^{-4}	Estimated from Figure 6-12
101058	Granite, aplitic	58	3.85	–11	-1.1×10^{-3}	Estimated from Figure 6-12
101061	Pegmatite	61	3.33	–8	-8×10^{-4}	Estimated from Figure 6-12
	Amphibolite	17	2.33	–5	-5×10^{-4}	Literature data (Seipold and Huenges 1998).

Anisotropy in thermal conductivity means that the conductivity (and the thermal diffusivity) is different in different directions. In a foliated rock the thermal conductivity is commonly higher parallel to the foliation plane compared to a direction perpendicular to the foliation. In a lineated rock the thermal conductivity is consequently assumed to be higher in the direction of the lineation. Anisotropy in thermal conductivity due to foliation/lineation in the dominant granite to granodiorite has been measured *in situ* at one location with different methods. Field measurements indicate that thermal conductivity parallel to the foliation plane is higher, by a factor of approximately 1.15, than conductivity perpendicular to the foliation (Back et al. 2007, Sundberg et al. 2008c).

It is logical to assume a pressure dependence on the thermal conductivity. However, the pressure influence is low if the samples are water saturated, approximately 1–2 % (Walsh and Decker 1966), since any increased micro-cracks porosity as a result of pressure release is water filled. All determinations of thermal conductivity in the site investigation programme have been made on water-saturated samples. The pressure dependence has therefore been neglected in the evaluation of thermal conductivity (Sundberg et al. 2008a).

For the large-scale thermal evolution due to climate changes, thermal data are needed for a larger area, outside the target area. Data on mean thermal conductivity, and the associated standard deviation, are supplied in Table 6-21.

Table 6-21. Thermal conductivity (W/(m·K)) and temperature dependence (%/100 °C) for a number of rock domains outside the target area, as well as domain RFM029.

Rock domain	Rock code (dominant)	Dominant rock type (SKB 2005, 2006d)	Thermal conductivity (W/(m·K))		Temperature dependence (%/100 °C)
			mean	Std	mean
RFM003[1, 7]	103076	felsic to intermediate volcanic rock, metamorphic	3.02	0.42	–5
RFM005[1, 7]	101033	diorite, quartz diorite and gabbro, metamorphic	2.51	0.21	–1
RFM007[1, 7]	101033	diorite, quartz diorite and gabbro, metamorphic	2.51	0.21	–1
RFM012[2, 5]	101057	granite to granodiorite, metamorphic	3.45	0.28	–8
RFM018[1, 7]	101054	tonalite to granodiorite, metamorphic	2.73	0.19	–3
RFM020[1, 7]	101058	granite, metamorphic, aplitic	3.83	0.22	–11
RFM021[1, 7]	103076	felsic to intermediate volcanic rock, metamorphic	3.02	0.42	–5
RFM022[1, 7]	111058	granite, fine- to medium grained	3.49	0.27	–9
RFM023[1, 7]	101054	tonalite to granodiorite, metamorphic	2.73	0.19	–3
RFM024[1, 7]	101054	tonalite to granodiorite, metamorphic	2.73	0.19	–3
RFM025[1, 7]	101033	diorite, quartz diorite and gabbro, metamorphic	2.51	0.21	–1
RFM026[1, 6]	101057	granite to granodiorite, metamorphic	3.68	0.17	–10

Table 6-21. Continued.

Rock domain	Rock code (dominant)	Dominant rock type (SKB 2005, 2006d)	Thermal conductivity (W/(m·K))		Temperature dependence (%/100 °C)
			mean	Std	mean
RFM029[3, 5]	101057	granite to granodiorite, metamorphic	3.58	0.29	–9
RFM030[1, 7]	101054	tonalite to granodiorite, metamorphic	2.73	0.19	–3
RFM031[1, 7]	103076	felsic to intermediate volcanic rock, metamorphic	3.02	0.42	–5
RFM032[1, 7]	101058	granite, metamorphic, aplitic	3.83	0.22	–11
RFM033[1, 6]	101057	granite to granodiorite, metamorphic	3.68	0.17	–10
RFM040[1, 6]	111057[8]	granite to granodiorite, metamorphic, veined to migmatitic	3.68	0.17	–10
RFM042[1, 6]	111051[9]	granitoid, metamorphic	3.12	0.30	–5
RFM043[1, 7]	101058	granite, metamorphic, aplitic	3.83	0.22	–11
RFM044[4, 5]	101057	granite to granodiorite, metamorphic	3.48	-	–9

[1] Rock type proportions not known, thermal conductivity for dominating rock type (Back et al. 2007).

[2] Thermal conductivity has been modelled in Sundberg et al. (2005a).

[3] Thermal conductivity has been modelled in Back et al. (2007). Data from 1 m scale.

[4] Thermal conductivity calculated from rock type proportions based on data for rock types in Back et al. (2007), standard deviation not possible to estimate.

[5] Temperature dependence calculated from rock type proportions.

[6] Temperature dependence for dominating rock type (Back et al. 2007).

[7] Temperature dependence estimated from Figure 6-12.

[8] Not investigated, similar to 101057. (Stephens et al. 2007).

[9] Not investigated, assumed similar to 101051.

Heat capacity

Heat capacity distributions at rock domain level have been integrated in the thermal realisation (see Section 6.2.9), used in SR-Site. The results for the 1 m scale for rock domains RFM029 and RFM045 are presented in Figure 6-13 and Table 6-22.

Table 6-22. Mean heat capacity (MJ/(m^3·K)) at 20 °C for domains RFM029 and RFM045 based on the relationship between heat capacity and thermal conductivity, and simulations of thermal conductivity at the 1 m scale. Data from Table 7-2 in Sundberg et al. (2008a).

Statistical parameter	RFM029 1 m scale	RFM045 1 m scale
Mean	2.06	2.12
Standard deviation	0.10	0.15

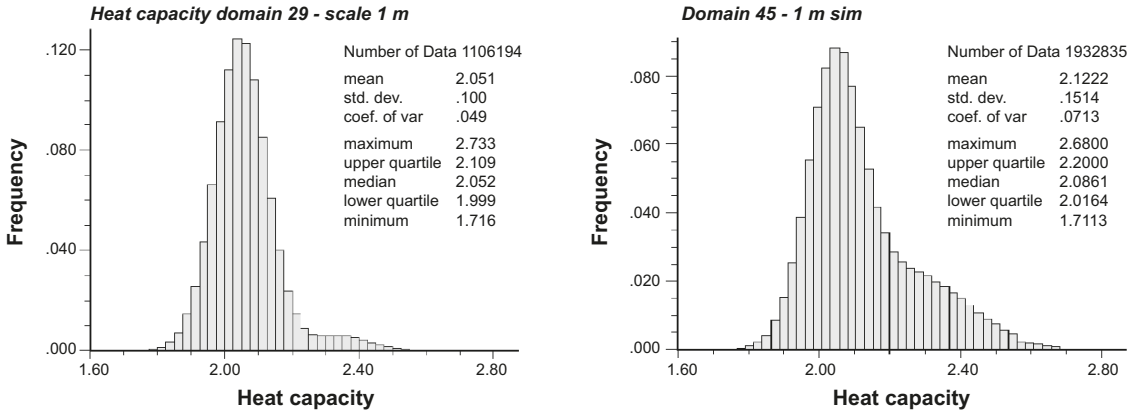

Figure 6-13. *Histogram of heat capacity for domain RFM29 and RFM045 based on the relationship between heat capacity and thermal conductivity and simulations of thermal conductivity at the 1 m scale. Reproduced from Figures 5-7 and 5-8 in Sundberg et al. (2008a).*

The heat capacity is influenced by the temperature. The heat capacity at elevated temperature can be determined from Equation 6-2.

$$C_1 = C_0(1+ \alpha_C(T_1-T_0)) \qquad 6\text{-}2$$

where C_0 and C_1 (MJ/(m^3·K)) is the heat capacity at room temperature T_0 and elevated temperature T_1, respectively, and α_C (1/°C) is the temperature coefficient for heat capacity. Estimated mean temperature coefficients for heat capacity in different rock domains are presented in Table 6-23, and the variability in Figure 6-14.

Table 6-23. Estimated mean temperature coefficients for heat capacity in different rock types inside target area. The thermal rock class (TRC) to which the rock type has been assigned is also given. Data from Table 2-4 in Sundberg et al. (2008a).

Rock code	Rock name	TRC	Mean Heat Capacity at approx 20 °C MJ/(m^3·K)	Mean temperature dependence % per 100 °C	Temperature coefficient, α_c 1/°C	Comments
101057	Granite to granodiorite	57	2.06	29	2.9×10^{-3}	Measured
101051	Granite, granodiorite and tonalite	51	2.15	25	2.5×10^{-3}	Estimated from Figure 6-14
101058	Granite, aplitic	58	2.01	25	2.5×10^{-3}	Estimated from Figure 6-14
101061	Pegmatite	61	1.92[1]	25	2.5×10^{-3}	Estimated from Figure 6-14
	Amphibolite	17	2.41	10	1×10^{-3}	Literature data (Seipold and Huenges 1998)

[1] Based on calculations from TPS data. Other based on calorimetric measurements.

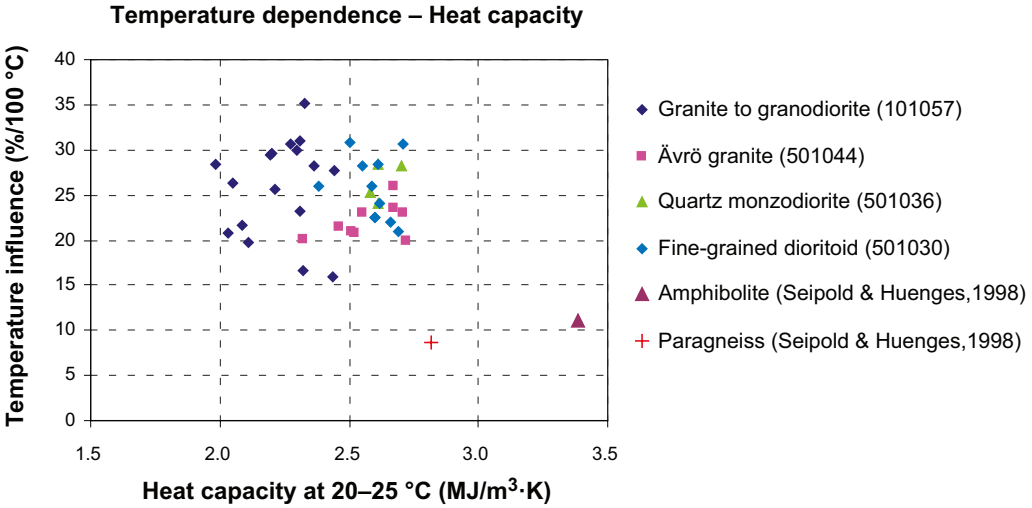

Figure 6-14. *Heat capacity (W/(m·K)) at 20–25 °C versus the temperature coefficient (%/100 °C) for the heat capacity in different rock types. Rock types with codes beginning with "50" are found in the Laxemar/Simpevarp area. Reproduced from Figure 2-2 in Sundberg et al. (2008a).*

For the large-scale thermal evolution due to climate changes, thermal data are needed for a larger area, outside the target area. Data on mean heat capacity are supplied in Table 6-24.

Table 6-24. Heat capacity (MJ/(m³·K)) and temperature dependence (%/100 °C) for a number of rock domains outside the target area, as well as domain RFM029.

Rock domain	Rock code (dominant)	Dominant rock type (SKB 2005, 2006d)	Heat capacity (MJ/(m³·K))		Temperature dependence (%/100 °C)
			mean	Std	mean
RFM003[1, 7]	103076	felsic to intermediate volcanic rock, metamorphic	2.26	-	25
RFM005[1, 8]	101033	diorite, quartz diorite and gabbro, metamorphic	2.33	-	10
RFM007[1, 8]	101033	diorite, quartz diorite and gabbro, metamorphic	2.33	-	10
RFM012[2, 6]	101057	granite to granodiorite, metamorphic	2.17	0.15	28
RFM018[3, 7]	101054	tonalite to granodiorite, metamorphic	2.12	0.20	25
RFM020[3, 7]	101058	granite, metamorphic, aplitic	2.08	0.10	25
RFM021[1, 7]	103076	felsic to intermediate volcanic rock, metamorphic	2.26	-	25
RFM022[4, 7]	111058	granite, fine- to medium grained	2.06	0.05	25
RFM023[3, 7]	101054	tonalite to granodiorite, metamorphic	2.12	0.20	25
RFM024[3, 7]	101054	tonalite to granodiorite, metamorphic	2.12	0.20	25
RFM025[1, 8]	101033	diorite, quartz diorite and gabbro, metamorphic	2.33	-	10
RFM026[4, 6]	101057	granite to granodiorite, metamorphic	2.06	0.06	28
RFM029[5, 6]	101057	granite to granodiorite, metamorphic	2.06	0.10	28
RFM030[3, 7]	101054	tonalite to granodiorite, metamorphic	2.12	0.20	25
RFM031[1, 7]	103076	felsic to intermediate volcanic rock, metamorphic	2.26	-	25
RFM032[3, 7]	101058	granite, metamorphic, aplitic	2.08	0.10	25
RFM033[4, 6]	101057	granite to granodiorite, metamorphic	2.06	0.06	28
RFM040[4, 6]	111057[9]	granite to granodiorite, metamorphic, veined to migmatitic	2.06	0.06	28
RFM042[4, 7]	111051[10]	granitoid, metamorphic	2.15	0.05	25
RFM043[3, 7]	101058	granite, metamorphic, aplitic	2.08	0.10	25
RFM044[11, 6]	101057	granite to granodiorite, metamorphic	2.07	-	28

[1] Rock type proportions not known, heat capacity (TPS measurements) for dominating rock type (Back et al. 2007), too few values to calculate standard deviation.

[2] Heat capacity has been modelled in Sundberg et al. (2005a).

[3] Rock type proportions not known, heat capacity (TPS measurements) for dominating rock type (Back et al. 2007).

[4] Rock type proportions not known, heat capacity (calorimetric measurements) for dominating rock type (Sundberg et al. 2008a).

[5] Heat capacity has been modelled in Sundberg et al. (2008a).

[6] Temperature dependence calculated from measurements (Sundberg et al. 2008a).

[7] Temperature dependence calculated from measurements from corresponding rock types at the Laxemar site (Sundberg et al. 2008a).

[8] Temperature dependence calculated from literature data, too few values to calculate standard deviation (Sundberg et al. 2008a).

[9] Not investigated, similar to 101057 (Stephens et al. 2007).

[10] Not investigated, assumed to be similar to 101051.

[11] Heat capacity calculated from rock type proportions and data for rock types in Back et al. (2007) and Sundberg et al. (2008a). Standard deviation not possible to estimate.

Thermal diffusivity

Thermal diffusivity (m^2/s) is a measure of a material's ability to level out temperature differences. The thermal diffusivity κ for each domain can be calculated from the thermal conductivity λ and heat capacity C for each domain by the following equation:

$$\kappa = \lambda / C \qquad 6\text{-}3$$

In Table 6-25 the calculated mean thermal diffusivity for each domain is given.

Table 6-25. Mean thermal diffusivity (m^2/s) at 20 °C of a number of rock domains based on the heat capacity and thermal conductivity in Table 6-21 and Table 6-24 respectively.

Rock domain	Thermal diffusivity (m^2/s)	Rock domain	Thermal diffusivity (m^2/s)
RFM003	1.34×10^{-6}	RFM026	1.79×10^{-6}
RFM005	1.08×10^{-6}	RFM029	1.74×10^{-6}
RFM007	1.08×10^{-6}	RFM030	1.29×10^{-6}
RFM012	1.59×10^{-6}	RFM031	1.34×10^{-6}
RFM018	1.29×10^{-6}	RFM032	1.84×10^{-6}
RFM020	1.84×10^{-6}	RFM033	1.79×10^{-6}
RFM021	1.34×10^{-6}	RFM040	1.79×10^{-6}
RFM022	1.69×10^{-6}	RFM042	1.45×10^{-6}
RFM023	1.29×10^{-6}	RFM043	1.84×10^{-6}
RFM024	1.29×10^{-6}	RFM044	1.68×10^{-6}
RFM025	1.08×10^{-6}		

Temperature and geothermal gradient

The mean *in situ* temperature measured at 400 m, 500 m and 600 m depth, based on eight boreholes, is estimated to 10.5 °C, 11.6 °C, and 12.8 °C respectively, see Table 6-26 (Sundberg et al. 2008a). The gradient is approximately 11–13 °C/km at repository depth. The temperature and the geothermal gradient versus elevation are displayed in Figure 6-15.

Table 6-26. Temperature (°C) for the "approved" boreholes at the Forsmark site, at different levels. Borehole inclinations are also included for the boreholes, given as lowest and highest angle (modified from Table 2-6 in Sundberg et al. (2008a)).

	Temperature (°C) at depth		
	400 m	500 m	600 m
Arithmetic mean	10.5	11.6	12.8
Uncertainty	± 0.4	± 0.4	± 0.3

Heat generation

The heat generation based on mean proportions of different rock types in the rock and the content of U, Th and K is calculated to 3.16 and 3.11 $\mu W/m^3$ for domain RFM029 and RFM045, respectively (Section 6.1.3 in Sundberg et al. (2009a)). The reason for the slightly higher values for domain level is the significantly higher proportions of pegmatite. The uncertainty is judged to be within ± 30 % based on ± 1 std for the dominant rock types (Sundberg et al. 2009a).

Heat flow

The palaeoclimatically corrected surface mean heat flow at Forsmark is suggested to be 61 mW/m^2 respectively (Section 8.1 in Sundberg et al. 2009a). The heat flow determination is judged to be within +12 % to –14 %.

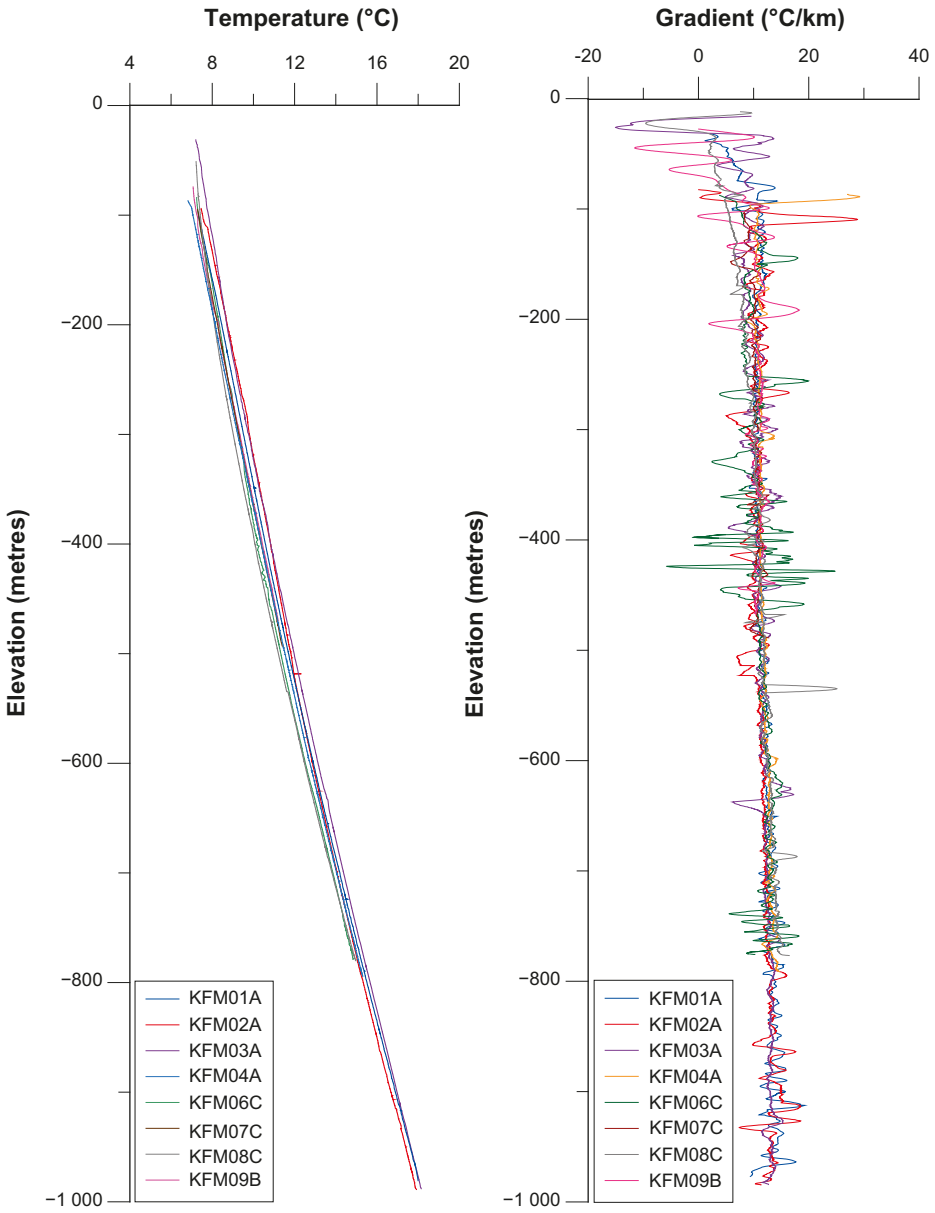

Figure 6-15. *Temperature (a) and vertical geothermal temperature gradients calculated for nine metre intervals (b) for the eight "approved" boreholes at Forsmark. Results from fluid temperature loggings from Figure 2-4 in Sundberg et al. (2008a).*

Thermal expansion coefficient

The mean thermal expansion coefficient for the main granitoid rock types within the target volume varies between 7.5×10^{-6} and 7.8×10^{-6} m/(m·K), see Table 6-27. The mean values of measured thermal expansion for the different rock types are rather similar. Samples of amphibolite (102017) have not been investigated.

Temperature margin

There are uncertainties in input data as well as systematic over- and underestimates associated with the calculation of the peak buffer temperature in the thermal dimensioning of the repository. This is described in Section 6.2.7. The temperature margin up to the criteria is summarised in Table 6-28. The temperature margin is 4.5 °C for both rock domains.

Table 6-27. Measured thermal expansion (m/(m·K)) on samples with different rock types within the temperature interval 20–80 °C. Data from Table 3-19 in Back et al. (2007).

Rock code	Rock name	Arithmetric mean	St. dev.	Min	Max	No. of samples
101057	Granite to granodiorite	7.7×10^{-6}	2.2×10^{-6}	2.1×10^{-6}	1.5×10^{-5}	56
101056	Granodiorite	8.1×10^{-6}	3.4×10^{-6}	5.2×10^{-6}	1.4×10^{-5}	6
101054	Tonalite to granodiorite	7.2×10^{-6}	1.6×10^{-6}	5.3×10^{-6}	8.2×10^{-6}	3
101051	Granite, granodiorite and tonalite	7.8×10^{-6}	1.2×10^{-6}	6.5×10^{-6}	1.0×10^{-5}	6
101058	Granite, aplitic	7.5×10^{-6}	5.4×10^{-7}	6.9×10^{-6}	8.0×10^{-6}	3

Table 6-28. Total temperature margin in numerical solution to establish a definitive spacing.

	Domain 29	Domain 45
Total Margin	4.5 °C	4.5 °C

6.2.11 Judgement by the assessment team

Based on experiences from SR-Site, as presented in Section 6.2.2, which indicates that the SR-Site approach for determining the spacing between canister positions in relation to the uncertainty in bedrock thermal properties is conservative, the judgement is to use the same data as in SR-Site.

6.2.12 Data recommended for use in assessment

All data presented in Section 6.2.10 together with the realisation of thermal properties are recommended to be used in PSAR modelling. Note that data are found both as tabulated and in the text in Section 6.2.10.

6.3 Discrete-Fracture Network (DFN) models

The identification, mapping, modelling, and understanding of bedrock fractures at Forsmark are key components of the site description, which feeds directly into the repository safety assessment. Information of bedrock fractures are important to both the design (available deposition volume, tunnelling, and excavation stability) and the long-term performance (groundwater and heat flow, radionuclide transport in the event that a canister is compromised, and the question of post-glacial seismic safety) of a spent nuclear fuel repository.

The handling of fracture data from the site investigation can be divided into two general classes:

1. Description of the geometry, geology, morphology, genesis, and deformation history of brittle structures in the bedrock at Forsmark.
2. Conceptual and mathematical representation of the fracture system in a format amenable to use in site characterisation, engineering design, and safety assessment efforts.

The description of the geometry and morphology of bedrock fractures includes the assessment of patterns of orientation, geometry and spatial arrangement, intensity, and size as functions of depth, spatial location, and geologic volumes (fracture and rock domains). In addition, properties of importance to mechanical modelling, groundwater flow, and contaminant transport have also been assessed. These properties include aperture, mineral infilling, and fracture surface roughness.

In PSAR the discrete-fracture network (DFN) methodology for the conceptual and mathematical representation of bedrock fractures according to Munier (2004) has been adopted for repository design and numerical simulation. In a discrete-fracture network model, bedrock fractures are generally simplified to circular disks in 3D-space or as n-sided planar polygonal structures. The geometric properties of the fractures can be considered either fixed (deterministic) or variable (stochastic) in space and/or time as probability functions (NRC 1996). This is in contrast to the stochastic continuum approach, frequently

used in numerical modelling of groundwater and heat flow, where the fracture system is treated as bulk volumetric properties (conductivity, storage) of the rock mass and the geometries of individual features are largely ignored. The DFN methodology is well-suited to groundwater flow, contaminant transport, and mechanical modelling in rocks where the fractures dominate the bedrock structure and flow system (such as the massive igneous and metamorphic rocks that make up the bedrock at Forsmark).

The PSAR is based on the same modelling of Discrete fracture network properties as SR-Site. In the following sections, the modelling strategy is described (Section 6.3.1) followed by an account of the experiences from the SR-Site safety assessment (Section 6.3.2). Since the PSAR is based on the same data as SR-Site, the data qualification (Sections 6.3.3 to 6.3.10) is reproduced from the SR-Site Data report. In Section 6.3.11 the formal judgement by the assessment team to use the qualified data is presented followed by Section 6.3.12 where the recommended data is presented.

6.3.1 Modelling (text reproduced from SR-Site Data report)

Elements of Discrete Fracture Network models

As many readers are not likely to be familiar with discrete-fracture network terminology, we have included a brief discussion of terminology relevant to DFN modelling. In a stochastic geological DFN model, the geometries of fractures in space are described using probability distributions calculated from data recorded during the site investigation. To fully describe the geometries and properties of fractures in space, the following parameters must be known:

- Fracture orientation.
- Fracture size (how large the fractures are).
- Fracture intensity (how many fractures there are, and how the number changes spatially).
- Fracture locations (i.e. spatial model).
- Fracture mineralogy (mineral infillings, host-rock alteration).
- Fracture hydraulic properties (transmissivity, hydraulic aperture).
- Fracture mechanical properties (shear stiffness, normal stiffness).

Fractures represent brittle deformation at points of weakness or stress concentrations in the bedrock; the direction (orientation) of the fractures is generally a function of the *in situ* stress state at the time of rock breakage, which in turn can be a function of spatial location. Fractures are rarely randomly oriented; they generally occur as members of sets, which are generally described as a clustering of fracture orientations around a common mean direction. Fractures can also be classified into sets based on other properties, such as fracture mineralogy, structural position (e.g. related to folding), host lithology, or morphology. However, at the Forsmark site, these other properties are at best a third-order effect; sets are primarily a function of fracture orientation.

The orientation of a fracture in space is described in terms of the trend and plunge, in degrees, of the fracture pole (see Figure 6-16), which is perpendicular to the plane of the fracture and is always oriented “down”. The trend and plunge of each fracture pole is then plotted on a stereonet drawn with a lower-hemisphere projection. Fractures with similar orientations will tend to form discrete clusters on the pole plot. The average (mean) fracture orientation, cluster shape and degree of clustering (dispersion) of these sets of fracture poles can be quantified using a hemispherical probability distribution, which allows fracture orientations to be represented in numerical models stochastically.

The most commonly used hemispherical probability distribution is the univariate Fisher distribution (Fisher 1953, Fisher et al. 1993), which, as the spherical equivalent of the normal distribution, will produce poles that are symmetrically distributed around the mean pole in space. The univariate Fisher distribution takes the following form:

$$f(\theta) = \frac{\kappa \cdot \sin\theta \cdot e^{\kappa \cos\theta}}{e^{\kappa} - e^{-\kappa}}, \qquad 0 \le \theta \le \pi \qquad \text{6-4}$$

in which θ (°) is the conjugate angle between the resultant vector r_n (–) and a given pole vector, while κ (–) is the concentration parameter (a measure of the concentration around the central axis) and N (–) the total number of pole vectors. As the value of κ increases, the degree of clustering around the mean

direction increases. Other hemispherical probability distributions, such as the Bingham or Bivariate Normal, can also be used to describe more complex patterns of fracture poles. However, the geological DFN models produced during stage 2.2 site-descriptive modelling at Forsmark utilise only univariate Fisher distributions; please refer to the geological DFN summary report (Fox et al. 2007) for a further discussion on the effects and rationale behind this decision.

Fracture intensity can be described in several different ways; however, SKB and the DFN modelling teams have adopted the terminology of Dershowitz (1985) to describe fracture intensity:

- P_{10}: A measure of lineal fracture intensity in units of (1/m), expressed as the number of fractures within a given measurement length. P_{10} is usually recorded on scanlines along outcrops and tunnel walls, or along the centreline of a cored borehole.
- P_{21}: A measure of areal fracture density in units of (m/m^2), expressed as the sum of the length of all fracture traces within a specified area, divided by that area. P_{21} is generally recorded through two-dimensional surface outcrop or tunnel mapping.
- P_{32}: Volumetric fracture intensity in units of (m^2/m^3), expressed as the sum of the one-sided surface area of all fractures in a specified region divided by the volume of that region. It is generally not possible to measure P_{32} directly; it is usually inferred through empirical relationships to P_{10} and P_{21} or calculated through stochastic simulation.

Fracture size is quantified in terms of one-sided surface area, which is in turn defined by a single variable; the equivalent radius, r (m) of a circular disk fracture. A probability distribution is used to characterise the distribution of fracture radii, generally as a function of fracture set and fracture domain. Note that the specification of fracture size as a radius does not mandate that fractures must be modelled as circular disks; any n-sided polygon is acceptable, so long as the resulting polygon has the same one-sided surface area as the 'equivalent' circular disk fracture using the same value of r. Past site characterisation efforts (Darcel 2003, Darcel et al. 2003, 2006a, b, Hermanson et al. 2005, Fox et al. 2007) have shown that, at least at the two investigated sites of Forsmark and Laxemar in Sweden, the Pareto distribution, which represents a power-law behaviour of fracture size, has been suggested to be the best-fit to observed data.

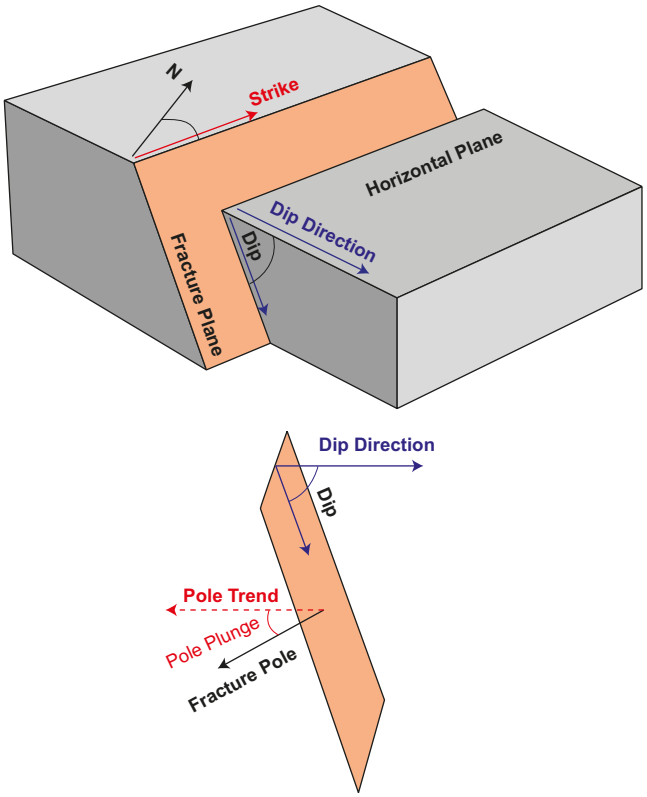

Figure 6-16. *Illustration of terms used to describe the orientation of fractures in space.*

The power-law distribution after Evans et al. (1993), modified to describe fractures in terms of equivalent radius r, takes the form of:

$$f(r) = \frac{k_r \cdot r_0^{k_r}}{r_0^{k_r+1}} \quad r_0 \le r < \infty \qquad 6\text{-}5$$

where r_0 (m) represents the mathematical minimum radius (the smallest fracture described by the power-law), and k_r (–) the shape parameter. In practice, however, the size distribution is often truncated at a maximum size (r_{max}) that is driven either by the limits of available data or the requirements of the project. At Forsmark, a decision has been made to truncate stochastic fracture modelling (that is the geological DFN) at the size of structures with a 1 km^2 one-sided surface area. This is equivalent to a square fracture 1 000 m long on a side, with an area equivalent to that of a circular disc fracture with a radius (r_{max}) of 564.2 m. Structures larger than this are described by the deterministic deformation zone model (cf Chapter 5 of Stephens et al. 2007).

The geological DFN presents two alternative models for estimating the fracture size distribution parameters:

1. r_0-fixed models: In this suite of model alternatives, fracture intensity (P_{32}) and the minimum fracture size are fixed (constrained) so that the radius scaling exponent k_r can be estimated from observed borehole data.
2. k_r-fixed models: In this suite of model alternatives, fracture intensity P_{32} is fixed, while values of k_r are estimated from area-normalised cumulative number plots of outcrop and minor deformation zone (MDZ) trace data from the ground surface. Once k_r and P_{32} are known, r_0 is calculated so as to simultaneously match borehole and outcrop intensities.

The relationship between fracture size and fracture intensity is quite complex; readers are strongly encouraged to consult the geological DFN summary report (Fox et al. 2007) before using any of the geological DFN tables in downstream modelling.

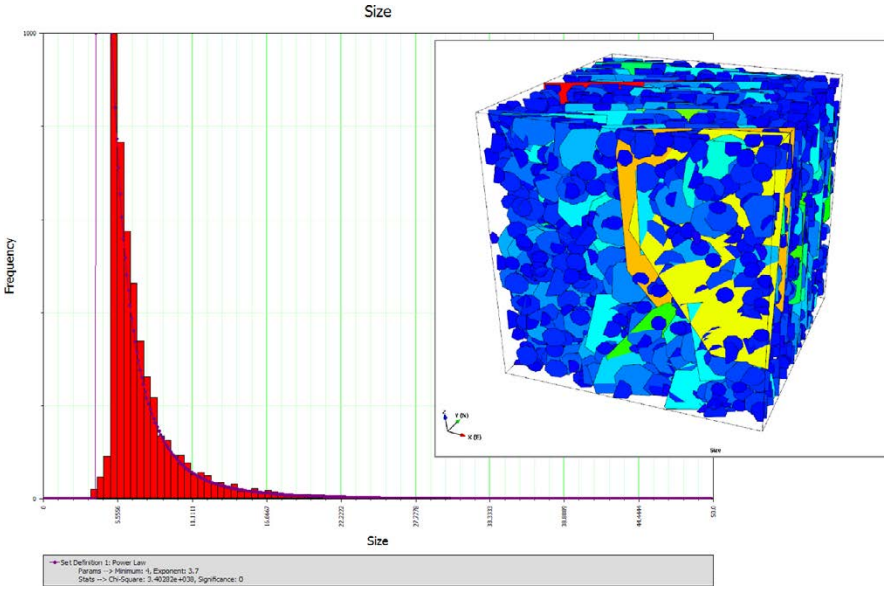

Figure 6-17. *Example of trace length distribution (red histogram) of fractures whose sizes follow a power-law distribution (inset DFN model). Note that due to truncation effects and minimum fracture sizes, the trace length histogram does not show a 'true' power law, in which y (frequency) would asymptotically approach infinity as x (trace length) approached zero.*

Spatial modelling in the geological DFN encompasses a wide variety of aspects of the spacing and locations of the fractures themselves, including:

- Termination relationships between fracture orientation sets.
- Spatial variability of fracture intensity. In the latest version of the geological DFN model, spatial variability is a function of a generalised Gamma distribution (Evans et al. 1993), with correction for variable lithology and fractal intensity scaling.
- Fracture intensity scaling, which describes whether the intensity of fracturing changes as a function of model scale (that is do big fractures have a different P_{32} than small fractures).
- Location of fracture centres in three-dimensional space, including relevant geological or structural controls.

For further readings on the DFN concept and the vocabulary associated with DFN modelling at Forsmark, readers are encouraged to consult SKB's DFN methodology document (Munier 2004).

Defining the data requested from the supplier

The stochastic DFN modelling concerns the modelling of fractures and minor deformation zones outside of deformation zones and inside of fracture domains at Forsmark. These parameters should be based on observed data from each of the fracture domains. The parameters needed to be able to create the geological DFN model in PSAR are specified below:

- Domain: Expressed as the volume for which the DFN parameters are valid, e.g. fracture domains, rock domains, hydraulic domains, and other relevant volumes as required.
- Set ID: Expressed as the fracture set to which the parameters of the fracture sets are valid. It is common practice to use the mean orientations of the planes, such as "ENE", "SubH", etc as the identifiers of the sets.
- Orientation: Expressed as the mean pole of the fractures in the fracture set together with the spreading around this mean pole. Assuming univariate Fisher distribution the orientation model is fully constrained by the mean trend (°) and plunge (°) of the fracture set together with the Fisher concentration parameter κ (–).
- Size: Expressed as the type of size distribution with its location and shape parameter together with the size span of the fractures regarded in the DFN model. Assuming powerlaw (pareto) size distribution, the shape parameter k_r (-) is the negative slope of the complementary cumulative distribution function, CCDF of the equivalent radius distribution, while the location parameter r_0 (m) is the equivalent radius where the CCDF starts to decrease.
- Intensity: Expressed as P_{32} (m^2/m^3), the idealized one-sided fracture surface area per volume of rockmass, within the size span r_{min} (m), minimum regarded equivalent radius, to r_{max} (m), maximum regarded equivalent radius.
- Spatial distribution: Expressed as intensity trends, clustering and termination. The intensity may be expressed as trends in different domains or lithologies. The clustering is expressed as the fractal dimension D (-). The termination is expressed as termination matrices.

Modelling activities in which data will be used

DFN models will be used in SR-Site to:

- Estimate the intersection probabilities of fractures with canisters, deposition holes, and excavation structures. The fracture intersection probabilities control the degree of utilisation of the repository, which influences the rock volume required for a particular design (Munier 2006, 2007).
- Understand the risks of buffer degradation, canister failure, and the compromise of repository integrity during a seismic event. The Forsmark site is set deep within the Fennoscandian Shield, a large area of Archean to Precambrian crystalline igneous and moderate- to high-grade metamorphic rocks that are extremely tectonically stable; the principal seismic risk is estimated to be from faults reactivated through crustal unloading and isostatic rebound after the next glacial cycle (Munier and Hökmark 2004). The risk is quantified by the computation of the number of canisters that are intersected by critically-large fractures (Munier and Hökmark 2004, Fälth and Hökmark 2006, Fälth et al. 2007, 2008, Hedin 2008).

- Describe the saturated bedrock flow system at site and local scales. The groundwater flow model is a fundamental input to hydrochemical and transport models, which themselves are integral parts of the repository safety assessment and post-closure safety calculations. Note that the hydrogeological DFN is a separate entity (cf Section 6.6) from the geological DFN and is not discussed further within this section; nevertheless, both conceptualisations are based on similar fracture data.

6.3.2 Experience from SR-Site

The data gathered during the site investigations and DFN-models developed for the Forsmark site were used during the SR-site modelling. The data used for development of the DFN models came from geological interpretation of borehole and outcrop mapping. Hence, no areal data were gathered from the depth. Due to this lack of data there is no possibility to constrain the size distribution of the fractures seated deep in the bedrock, i.e. FFM01 and FFM06. Instead different assumptions to extrapolate outcrop data from the surface to the depth were used. This led to three different models, labelled TCM (Tectonic Continuum Model), OSM+TFM (Outcrop Scale Model + Tectonic Fault Model) and r0-fixed model. This uncertainty in conceptual extrapolation have a huge large effect on the connectivity of the DFN which can not be constrained until areal data are gathered from depth.

In SR-Site, as previously mentioned, DFN-Data was used to:

- Estimate the intersection probabilities of fractures with canisters, deposition holes, and excavation structures.
- Understand the risks of buffer degradation, canister failure, and the compromise of repository integrity during a seismic event.
- Describe the saturated bedrock flow system at site and local scales.

As the data, gathered from the surface investigations, can not discard any of the three developed DFN models they were all propagated and used for the calculations of fracture displacement under a seismic event. The difference in number of deposition position hosting a fracture that may shear > 5 cm is roughly a factor 2 between the three models, where the TCM model gives the highest number and the OSM+TFM the lowest As discussed in the SR-Site main report (SKB 2011, Section 10.4.4), the TCM model is the model that yields the maximum number of potentially failed canisters by shear load.

The properties of the DFN are crucial for the possibility for water to flow into deposition holes or deposition tunnels. Depending on the spatial distribution of the flow, the risk of piping and erosion of the buffer material will vary. However, despite some remaining uncertainties, the conclusion from SR-site is that the buffer will remain its integrity, given the hydrogeological DFN used and that only deposition holes that meet inflow measurement criteria are utilized.

During SR-Site only one geometric hydrogeological DFN was used, but with 3 different parameter set-ups for transmissivity distribution, hence no conclusions regarding uncertainty due to different conceptual DFN's could be made. However, SR-site conclude that the hydro DFN should benefit from a better constrained Geological DFN. Since SR-Site SKB has put large efforts to the develop methods to have one single DFN concepts that can serve all different disciplines with needed geometry data.

The overall experience from SR-site on the DFN model is that it needs to be more constrained to decrease the probability space, both for conceptual uncertainty and parameter uncertainty. This may be done when new data, especially areal data, from the depth is obtained. Since SR-site SKB has also gained new knowledge regarding DFN generation and constraining DFN to semi-determinism close to tunnels and deposition holes.

6.3.3 Supplier input on the use of data (text reproduced from SR-Site Data report)

Supplier input to the SR-Can Data report (SKB 2006b) consisted of the recommendations and usage presented in the geological DFN summary reports (La Pointe et al. 2005, Hermanson et al. 2005) completed during stage 1.2 of the site-descriptive modelling efforts. Additional review and feedback on model processes and inclusion/exclusion of data was performed by the SR-Can team at SKB.

For SR-Can calculations based on the Forsmark site, the supplier to SR-Can recommended:

- Five fracture orientation sets (four subvertical and one subhorizontal) described using a combination of bivariate Bingham (Bingham 1964), bivariate Fisher (Dershowitz 1979) and univariate Fisher (Fisher 1953) hemispherical probability distributions.
- No consistent variation of fracture intensity with depth was noted; therefore, fracture intensity should be represented as a function of rock domain or model region.
- Poissonian spatial arrangement of fracture centres.
- Euclidean fracture intensity scaling.
- A power-law (Pareto) distribution of fracture radii, with the radius scaling exponent k_r for lineament-related sets calculated using the tracelength-scaling method (La Pointe et al. 2005) with fracture traces from outcrops and combined topographic and geophysical lineaments.
- That Local fracture sets were a mix of exponential and power-law distributions.

Supplier input to SR-Site consists of the detailed DFN parameterisations presented in the stage 2.2 Forsmark geological DFN summary report (Fox et al. 2007), tempered by the additional guidance towards model selection suggested in the **Site description Forsmark**. For SR-Site calculations at the Forsmark site, the supplier recommends the following:

- Fracture orientation should be simulated as a function of fracture domain, using the average parameters for each Global and Local set. Fracture set orientation is specified in terms of the trend and plunge of the univariate Fisher distribution mean pole, as well as the average Fisher concentration parameter κ_{mp}.
- We recommend that, if at all possible, Local orientation sets be simulated using a geocellular-style approach with the conditional probabilities presented on worksheet "Spatial Model". If that is not an option, the adjusted bulk domain intensity values (Local set P_{32} multiplied by the probability of occurrence) should be used.
- Due to the large conceptual uncertainties inherent in the coupled fracture size-intensity models, the TCM (Tectonic Continuum model), OSM+TFM (Outcrop Scale + Tectonic Fault models), and r_0-fixed models should be carried through all SR-Site modelling activities. Both fracture intensity and fracture size should be simulated on a fracture domain basis. The differences between TCM and TCMF (Tectonic Continuum model assuming fractal intensity scaling) are judged to be minimal.
- Fracture intensity P_{32} should be modelled on a domain-by-domain basis using the values for each size-intensity model alternative. We recommend the use of the average P_{32} value to which the size-intensity distribution is coupled, rather than using a Gamma distribution; this is conceptually a simpler method to implement, and the conceptual uncertainty in the size model dwarfs the parameter variability of intensity in space within a single domain. In addition, it was not possible to fit a Gamma distribution to two of the Global sets in both domain FFM01 and FFM02.
- Within a given fracture domain, fracture centres should be distributed in space according to a 3D Poisson point process. In addition, fracture intensity scaling should be treated as Euclidean for all fracture domains.
- We recommend the use of termination matrices from fracture domain FFM02 (worksheet "Termination Matrices" at SKB's model database Modelldatabasen[16]) to describe fracture termination relationships in domains not exposed at the ground surface (FFM01, FFM06).

[16] Modelldatabasen 2007. Model: PFM DFN 2.2.xls. Version 0.6. Approved 2007-11-29, Modified 2009-05-18. Modeller: A. Fox. Simon ID: GEO_WTAGLLAA. https://service.projectplace.com/pp/pp.cgi/r232241793 (access might be given on request).

6.3.4 Sources of information and documentation of data qualification (text reproduced from SR-Site Data report)

Sources of information

The geologic discrete-fracture network models derived as a component of the Forsmark site investigation are presented as stand-alone project reports for each modelling stage. The last geological DFN model was completed during Forsmark stage 2.2 site-descriptive modelling (Fox et al. 2007). Summary tables of relevant geologic DFN parameters, including fracture orientation, size, and intensity statistical distributions, are archived as Microsoft Excel workbooks in SKB's model database Modelldatabasen. A brief summary of the geological DFN, along with descriptions of fracture geometric properties, is presented in the Forsmark stage 2.2 site-descriptive modelling Geology report (Stephens et al. 2007). A list of the main sources of information used in data qualification is presented as Table 6-29. With respect to the development of the stage 2.2 geological DFN parameterisation, references to delivery dates and source tables for primary data (SICADA, SDE, SIMON, and external data sources) are described in detail in Section 2.1 of Fox et al. (2007).

Table 6-29. Main sources of information used in data qualification.

Site description Forsmark, 2008. Site description of Forsmark at completion of the site investigation phase. SDM-Site Forsmark. SKB TR-08-05, Svensk Kärnbränslehantering AB.
Olofsson I, Simeonov A, Stephens M, Follin S, Nilsson A-C, Röshoff K, Lindberg U, Lanaro F, Fredriksson A, Persson L, 2007. Site descriptive modelling Forsmark, stage 2.2. A fracture domain concept as a basis for the statistical modelling of fractures and minor deformation zones, and interdisciplinary coordination. SKB R-07-15, Svensk Kärnbränslehantering AB.
Fox A, La Pointe P, Hermanson J, Öhman J, 2007. Statistical geological discrete fracture network model. Forsmark modelling stage 2.2. SKB R-07-46, Svensk Kärnbränslehantering AB.
Stephens M, Fox A, La Pointe P, Simeonov A, Isaksson H, Hermanson J, Öhman J, 2007. Geology Forsmark. Site descriptive modelling Forsmark stage 2.2. SKB R-07-45, Svensk Kärnbränslehantering AB.
Fox A, Hermanson J, 2006. Identification of additional, possible minor deformation zones at Forsmark through a review of data from cored boreholes. SKB P-06-293, Svensk Kärnbränslehantering AB.

Categorising data sets as qualified or supporting

Geological discrete-fracture network models at Forsmark were constructed exclusively from qualified data extracted from SKB quality-assured databases (SICADA and SDE). Both the geological DFN summary report and the fracture domain identification report (Olofsson et al. 2007) present detailed lists of SICADA, SDE, and qualified SKB data delivery references (Section 2.1 and Chapters 3 and 4, respectively). However, as noted in the method-specific summary report (Fox et al. 2007), early data deliveries of GIS shapefiles did not possess sufficient metadata to refer back to layers within SDE. Qualification of these deliveries is ensured through a reference to the data delivery number, which internally at SKB refers back to a stored SQL query.

With respect to official SKB sources for geological DFN parameters, the Microsoft Excel tables contained in the database SIMON (a mirror of Modelldatabasen) from Forsmark stage 2.2 modelling are considered authoritative. In terms of published references, the tables presented for fracture domains FFM01 and FFM06 in the **Site description Forsmark** are considered the latest qualified geological DFN parameterisation. For all other fracture domains and alternative model cases that are not recommended for use in SR-Site (e.g. intensity in domains labelled 'Affected by DZ'), the geological DFN summary report (Fox et al. 2007) is considered the authoritative source.

The deformation zone (DZ) model at Forsmark was undergoing constant evolution while the geological DFN model was built during stage 2.2 modelling. As such, the DZ geometries used in the geological DFN models represent interim versions rather than final, fully-qualified data. The DZ model was primarily used to exclude data from cored borehole sections inside deformation zones; the borehole/deformation zone intersections were well-established and controlled before the start of DFN modelling. The differences between the interim DZ and final DZ models presented in Stephens et al. (2007) were in the geometries of zones away from borehole control and, as such, have no effect on the geological DFN parameterisation.

In Table 6-30 qualified data sets of special importance are listed. No data set was considered as supporting.

Table 6-30. Qualified and supporting data sets.

Qualified data sets	Supporting data sets
1. All data sets, including related SICADA and SDE tables, referenced in Section 2.2 of stage 2.2 site-descriptive modelling report (Fox et al. 2007).	None.
2. All data sets, including related SICADA and SDE tables, referenced in Sections 3.1, 3.2, 4.1, 6.1, 7.1, 8.1, and Appendix 1 of stage 2.2 site-descriptive modelling report (Olofsson et al. 2007).	
3. PFM DFN 2.2.xls, version 0.6, SIMON database, folder (Forsmark/2.2/Geology/Approved/DFN Models/.	
4. Section 5.6 of the **Site Description Forsmark**.	
5. Tables 5-5 through 5-8 of the **Site Description Forsmark**.	
6. Tables 5-3 and 5-4, published in the Erratum to Fox et al. (2007).	
7. Geological DFN Model implementation: Tables 7-1 through 7-10 in Fox et al. (2007).	
8. Sections 3.6, 3.12, and Chapter 6 of Forsmark stage 2.2 Geology summary report (Stephens et al. 2007).	
9. All data sets referred to in Chapter 2 of Fox et al. (2007).	
10. WellCAD summary plots and BIPS image logs described in Section 3.1 of Fox and Hermanson (2006).	
11. Figures 5-34 and 5-36 of the **Site Description Forsmark**.	
12. Interim DZ geometries (.dxf export), stage 2.2 Forsmark site-descriptive modelling. See Section 2.1.4 of Fox et al. (2007) for further discussion.	

All data sets in this table are considered as qualified with the justification that they are published as part of the site investigation and site characterisation, in conformance with relevant quality assurance routines.

Excluded data previously considered as important

The paradigm for geological DFN modelling changed during stage 2.2 of the site description process at both Forsmark and Laxemar. In particular, the introduction of the fracture domain concept (Olofsson et al. 2007) limited the spatial extent of DFN validity. The geological DFN is parameterised only for domains in which sufficient three-dimensional information was available: FFM01, FFM02, FFM03, and FFM06 (cf (Fox et al. 2007, Figure 1.2)). The previous geological DFN at Forsmark (stage 1.2 modelling) presented DFN properties as a function of rock domains RFM029, RFM018, RFM017, and RFM012 (cf La Pointe et al. 2005, Figure 6-1). In addition, the size of the Forsmark local model domain changed significantly between stage 1.2 and stage 2.2 (see Figure 6-18).

The end result is that stage 2.2 geological DFN models use only minimal data from rock domains RFM017 and RFM012, and exclude data from rock domain RFM018 entirely (cf Figure 6-19). Fracture domain FFM06 is defined based on the contact at depth between rock domains RFM028 and RFM045, the latter of which was not included in stage 1.2 geological DFN modelling.

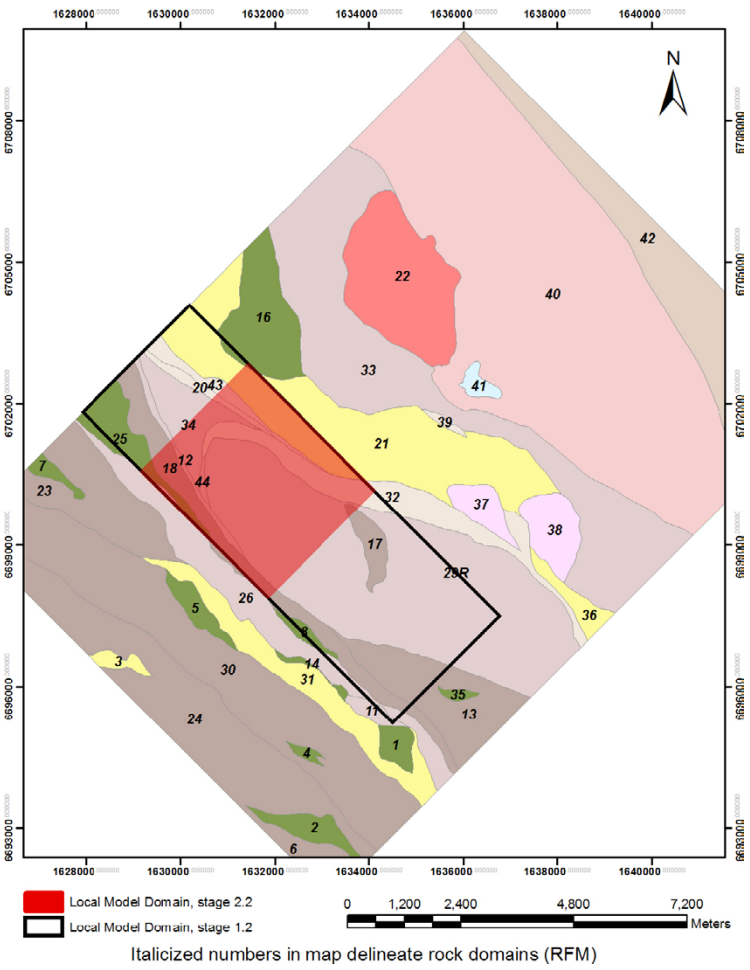

Figure 6-18. *Map of the Forsmark site, with references to stage 1.2 and stage 2.2 model boundaries and the stage 2.2 rock domains, which did not change appreciably from stage 1.2.*

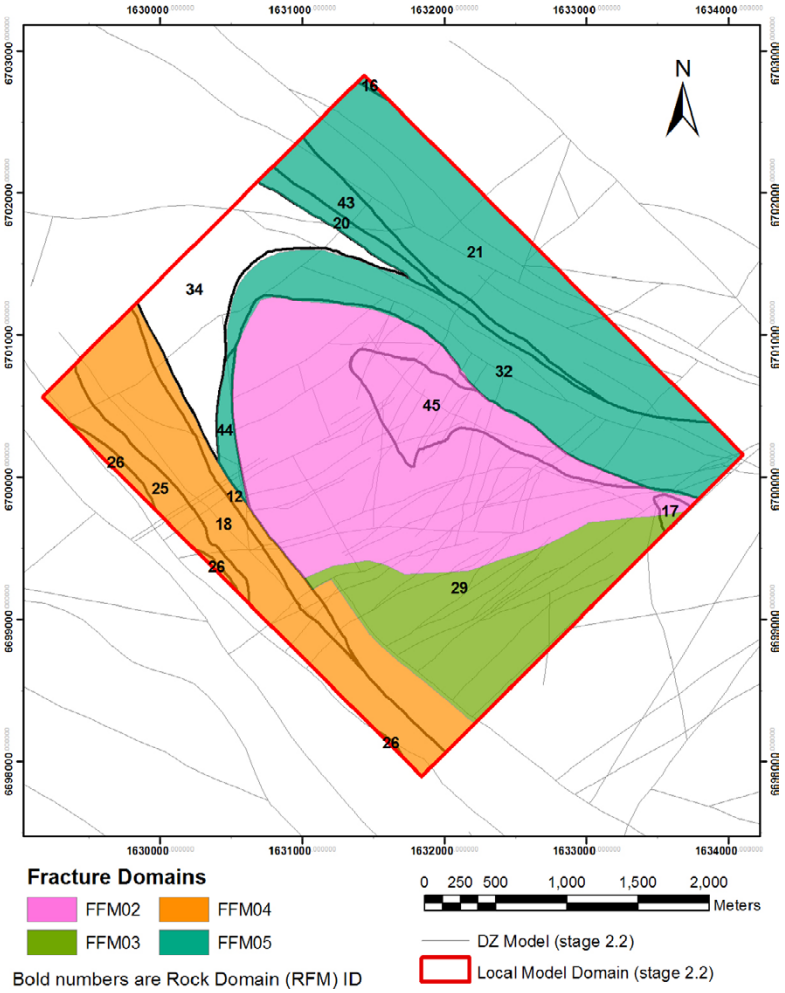

Figure 6-19. *Fracture domains and deterministic deformation zone traces at Forsmark. Note that the DZ traces represent the mid-plane of the zone, which are implemented as complex volumes in RVS. Rock domains are included as numbered polygons. Note that FFM04 and FFM05 are not part of the stage 2.2 geological DFN parameterisation.*

6.3.5 Conditions for which data are supplied (text reproduced from SR-Site Data report)

Geological DFN parameters are supplied for rock volumes within fracture domains FFM01, FFM02, FFM03, and FFM06 inside the Forsmark local model volume (Fox et al. 2007). In addition, the geological DFN describes fractures and minor deformation zones outside the mapped limits of deterministically-modelled deformation zones (Stephens et al. 2007). The geological DFN parameterisation is valid for fractures and minor deformation zones within a size range of r_0 m and 564.2 m; the latter is the equivalent radius of a square fracture with an area of 1 km^2, and represents the transition from stochastic fracture modelling to deterministic deformation zone modelling (Stephens et al. 2007). The geological DFN is defined for all fractures; no distinction is made between open, sealed, or hydraulically-significant fractures.

Changes in fracture properties as functions of future processes (underground construction, de-watering, thermal loading, climate change, or additional mechanical loading from future glacial cycles) were not assessed by the geological DFN team, and are assumed to represent scenario cases in SR-Site.

It is extremely important to note that the stage 2.2 geological DFN report (Fox et al. 2007) presented not one but three alternative models to describe the coupled distributions of fracture size and fracture intensity at Forsmark. All three of the model alternatives fall into the category of 'k_r-fixed' models (cf Section 6.3.1).

1. The Tectonic Continuum (TCM) concept, in which fractures at the outcrop and borehole scale (which are thought to largely consist of joints) are part of a larger population of brittle deformation features that also include the faults and minor deformation zones identified as geophysical and topographic lineaments. Fundamental tenets of the tectonic continuum hypothesis are that fracture size and fracture intensity are coupled (one cannot change without affecting the other), that fracture size is scale-invariant, and that it is consistent with the understanding of brittle deformation zones as intense clusters of connected smaller fractures. The TCM assumes Euclidean intensity scaling.
2. The Tectonic Continuum model assuming fractal intensity scaling (TCMF). This alternative is conceptually the same as the TCM, but utilises pseudo-areas (cf Equation 3-10 in Section 3.2.3 of Fox et al. (2007)) and the fractal mass dimension (Feder 1988) instead of outcrop and model region areas to account for scale-dependent fracture intensity.
3. The Outcrop Scale (OSM) and Tectonic Fault (TFM) concept, in which it is assumed that outcrop and borehole fractures are not part of the same population as minor deformation zones, and that both populations exhibit different size distribution characteristics. Outcrop-scale fractures are assumed to consist predominantly of joints, while minor deformation zones and large fractures are assumed to be predominantly faults. Both models (OSM and TFM) are required to produce a complete description of fracturing in the required scale range (0.5–564.2 m).

During the review of the geological models for the preparation of the **Site description Forsmark**, an uncertainty case from the stage 2.2 DFN summary report was promoted to a full alternative model based on feedback from the Forsmark hydrogeology team and SKB internal reviewers. The fourth alternative model is:

4. The r_0-fixed concept, in which instead of calculating the radius scaling exponent k_r from fracture trace data (which exists for only two of the four fracture domains at Forsmark), the size distribution is inferred from fracture intensity data recorded in cored boreholes. In this alternative model, fracture size is assumed to follow a power law, and the minimum fracture size r_0 is fixed at the radius of the cored boreholes (generally double- or triple-tube NQ/NX core drills, which cut a hole approximately 76 mm in diameter). The ratio of borehole fracture intensity (P_{32BH}) to deformation zone intensity (P_{32DZ}) is inverted to solve for the radius scaling exponent, using Equation 3-11 of Fox et al. (2007).

The Tectonic Continuum model (TCM) was submitted as the recommended size-intensity model alternative for use by the geological DFN team (cf Fox et al. 2007, Section 7.2).

6.3.6 Conceptual uncertainty (text reproduced from SR-Site Data report)

A formal uncertainty analysis performed as a component of the stage 2.2 geological modelling (cf Fox et al. 2007, Chapter 5) identified the following conceptual uncertainties in the geological DFN parameterisation:

- Validity of the Tectonic Continuum hypothesis as opposed to the OSM+TFM or r_0-fixed conceptual models.
- What is the cut-off between large fracture and minor deformation zone (affects the OSM+TFM alternative.
- Which is a more appropriate description of fracture traces in outcrop: linked or unlinked (cf Fox et al. 2007, Section 3.2.3).
- Does fracture intensity follow Euclidean or fractal scaling? This uncertainty is discussed in detail in the SR-Can Data report (SKB 2006b) and in the stage 2.2 geological DFN summary report (Fox et al. 2007). The general recommendations has been that since the departure from Euclidean scaling is inside the estimates of error of the mass dimension, that the assumption of Euclidean scaling is a reasonable one (cf Fox et al. 2007, Section 7.4).
- Can the fracture size model, and, in particular, the radius scaling exponent k_r, for fracture domains not exposed at the ground surface (FFM01, FFM06) be assumed identical to the values established from outcrop trace data in domains at the surface (FFM02, FFM03).

In addition, two mathematical uncertainties (Bechtel-SAIC 2001) were identified:

- Uncertainty in the depth correction for fracture intensity.
- Uncertainty in the lithology correction for fracture intensity.

Finally, there are several aspects of fracture geometry and geology that the geological DFN treats as "assumptions" that could also be considered conceptual uncertainties. These assumptions, which are detailed in Section 3.2.1 of Fox et al. (2007) and are again summarised in Section 6.2 of Stephens et al. (2007), include:

- The length of a deformation zone trace, geophysical lineament, or linked/unlinked fracture trace in outcrop is an accurate and appropriate measure of the trace length of a single feature, for the purposes of deriving the distribution of fracture radii.
- Fracture sets can be usefully identified based solely on orientation.
- The lack of clustering (i.e. Poissonian spatial arrangement) observed in outcrop and borehole data carries over to the large fracture and MDZ-size range within the Forsmark local model volume. Note that this assumption was implied, but not explicitly stated, in the geological DFN summary report (Fox et al. 2007) and was raised as a valid conceptual uncertainty during the finalisation of the site-characterisation efforts (cf the **Site description Forsmark**).

The magnitude of the conceptual and mathematical uncertainties were described and quantified in Section 5.1.2 of Fox et al. (2007) as a component of stage 2.2 geological DFN model reporting in terms of the P_{32} ratios between pairs of alternative models within two different size ranges (0.5–564.2 m and 28–564.2 m). No effort was made to analyse or quantify uncertainty with respect to geological DFN assumptions (using only univariate Fisher distributions; ground magnetic lineaments as fractures, etc).

The P_{32} ratios, which are summarised below in Table 6-31, serve to bracket the uncertainty in both the size and intensity models, as all the alternatives utilise coupled size-intensity models. By far the largest conceptual uncertainty in terms of its effect on P_{32} is the method by which the fracture size distribution is parameterised, with the question of the validity of using size data from the ground surface to parameterise rock volumes at depth a lesser but still important concern. The other remaining conceptual uncertainties are of second-order importance.

Table 6-31. Summary of key conceptual uncertainties and their expected impacts on downstream models. Modified after Table 5-7 of Fox et al. (2007).

Uncertainty	Magnitude	Comments
Fracture size conceptual model	0.3–3.0	Varies significantly as a function of fracture set and fracture domain.
Boundary between OSM and TFM	0.6–0.9	Specifying a boundary between OSM and TFM reduces the total fracture intensity by approximately 1/3.
Euclidean versus Fractal intensity scaling	0.82–1.16	Minor impact, especially on subhorizontally-dipping fractures and MDZ.
Use of size data from surface (FFM02) to parameterise domains at depth	0.3–0.7	This uncertainty case promoted to full-fledged model (r_0-fixed); results in significantly lower intensity in the MDZ size range (28–564.2 m).
Fracture intensity as function of rock domain	0.5–2.0	Impact is greatest for minor rock types such as amphibolite and pegmatite.
Fracture intensity as a function of depth	~ 0.9–1.05	Variable as function of fracture set and fracture domain; ignoring depth-dependency 'slightly' increases mean fracture intensity.

6.3.7 Data uncertainty due to precision, bias, and representativity (text reproduced from SR-Site Data report)

Past modelling efforts at both Forsmark and Laxemar have suggested that conceptual or mathematical uncertainties dominate the geological DFN uncertainty space. However, additional model uncertainties with respect to geological and fracture data do exist; these uncertainties are largely due to limits of the accuracy and coverage from site characterisation efforts. As with the conceptual uncertainties, the biggest effect of data uncertainty is on the coupled size-intensity model. However, no formal quantification or ranking of data uncertainties exists for the stage 2.2 Forsmark geological DFN.

Data uncertainty due to precision

With respect to uncertainty in fracture orientations in base data, the geological DFN models parameterised during Forsmark site description stage 2.2 are fairly well-constrained. Data analysis followed the recommendations of Munier and Stigsson (2007) in only using orientation data for which BIPS logs were available, and avoiding the use of any fracture data for which the overall uncertainty Ω was greater than 10°. In addition, spatial variability of fracture orientations is encompassed by the use of probability distributions for fracture set mean poles and Fisher concentration parameters (cf "Parameter variability", Section 4.1.3 of Fox et al. (2007)). The principal remaining uncertainty in fracture orientations is due to the precision of the strike and dip measurements made on detail-mapped fracture outcrops at Forsmark (cf Fox et al. 2007, Section 4.1.5); the accuracy of these measurements is estimate to be +/– 10°.

As fracture intensity is largely a derived parameter, the precision of its estimate depends on the confidence of the identification of fractures in outcrop and in core. Presently, no formal estimate of the probability of fractures 'missed' during the core logging exists. The uncertainty in Wang's analytical conversion factor (Wang 2005) for borehole fracture intensity (P_{10}) to volumetric fracture intensity (P_{32}) was indirectly evaluated through Monte Carlo simulation. Though no quantified error estimate exists, the Monte Carlo simulation results (cf Wang 2005, Figure 3.10), suggest that the uncertainty is quite small. However, Wang's conversion engenders an additional conceptual uncertainty; it assumes that fractures follow a univariate Fisher distribution, and is therefore not a valid estimator for fracture intensity for fractures with orientations better described by other hemispherical probability distributions (Bingham, Kent). Neither the model parameterization nor the uncertainty analyses completed in the DFN model during Forsmark site description stage 2.2 made any estimates of the magnitude of the uncertainty in P_{32} should the fractures at Forsmark not follow a univariate Fisher distribution.

For the OSM, TCM, and TCMF size model alternatives, k_r is estimated from the trace length scaling exponent k_t, which is calculated by manually fitting a straight line to trace data on an area-normalised CCN (complementary cumulative number) plot. As there are multiple outcrops in the surficial fracture domains (two outcrops in FFM02 and three outcrops in FFM03) with trace length distributions that do not overlap, it is possible to pick multiple values of k_t depending on which outcrop (see Figure 6-20) is used. This uncertainty was addressed in the SDM-Site Laxemar geological DFN analysis (La Pointe et al. 2008), but has not been accounted for in the stage 2.2 Forsmark modelling.

Though no formal uncertainty quantification exists, similar work done during Laxemar stage 2.2 geological DFN modelling (La Pointe et al. 2008) suggests that the uncertainty in the estimation of the trace length scaling exponent is by far the most important uncertainty due to precision.

Data uncertainty due to bias

Data uncertainty due to bias is caused by truncation effects inherent in sampling fracture properties over a variety of scales. The distribution of trace lengths (from which the radius scaling exponent k_r is estimated in the TCM, TCMF, and OSM models) shows a strong censoring effect at twice the minimum trace length mapped (0.5 m); the censoring effect is visible as a flattening of the area-normalised CCN plots, of which an example is presented in Figure 6-20. There is also a censoring effect on the upper end of the outcrop trace data (cf the **Site description Forsmark**); the largest fracture detectable is limited by the size of the outcrops (~10 m) or the minimum resolution of LIDAR and ground magnetic lineaments (~50–100 m). The result of this censoring is that a scale (10 m–100 m) exists within which very little information on fracture size is available. The availability of LIDAR and high-resolution ground magnetic lineament data only partially ameliorates this uncertainty.

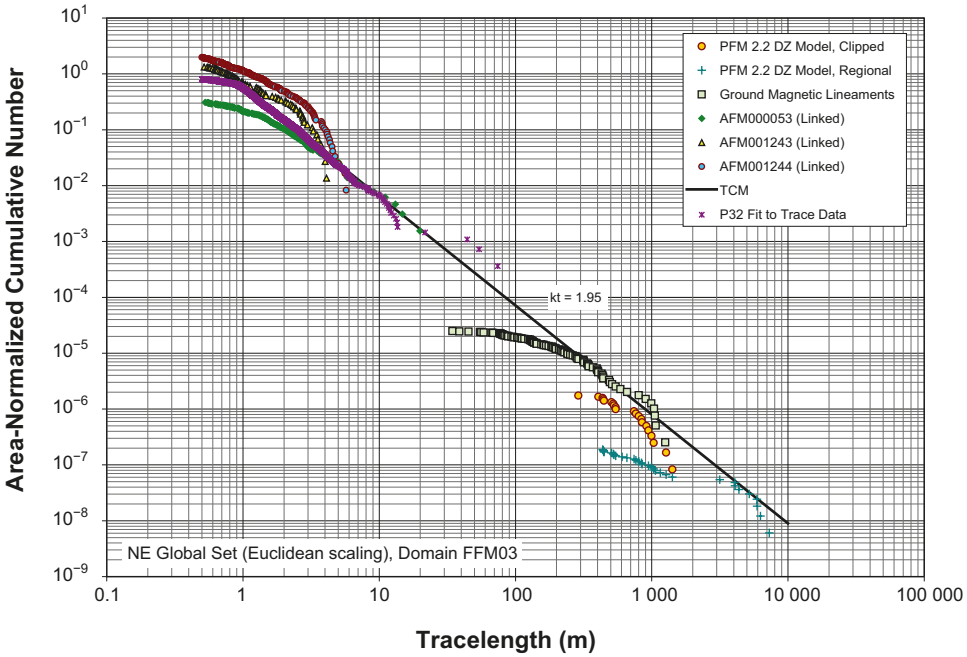

Figure 6-20. *Example area-normalised complementary cumulative number (CCN) plot used to analyse fracture trace length scaling for NE global set in fracture domain FFM03. This style of plot is used to calculate the radius scaling exponent k_r for the TCM, TCMF, and OSM-TFM alternative models. Figure reproduced from Appendix A of Fox et al. (2007).*

Bias due to the orientation of sampling structures (boreholes, outcrops) relative to the orientation of fracture sets has been minimised through the use of the Wang C_{13} (–) conversion factor; this allows for all fracture intensity. Wang's C_{13} does not exist for outcrop data; as such, the detail-mapped fracture outcrops exhibit a bias towards vertically- to subvertically-dipping fractures. The paucity of data on trace lengths of subhorizontally-dipping fractures results in increased uncertainty in the radius distribution for these features. It is difficult to impossible to reduce this uncertainty without additional information, which is not likely to be available until the start of underground construction.

Data uncertainty due to representativity

Between the completion of the fracture domain report for Forsmark (Olofsson et al. 2007) and the completion of geological DFN modelling, a number of additional analyses performed by the deformation zone and geology teams suggested that the breakdown of fractures into "inside DZ" and "outside DZ" was insufficient to characterise the bedrock at Forsmark. An additional category, "Affected by DZ", was adopted by the SKB/SGU geological modelling teams to describe rock volumes in which fracture frequency was increased due to the presence of a nearby deformation zone, but none of the other morphological characteristics of DZ "transition zones" were observed (Stephens et al. 2007).

In the stage 2.2 geological DFN model, there are three alternative models (OSM+TFM, TCM, and TCMF) that rely on the length and intensity of the deterministically-modelled deformation zones and high-resolution lineament maps as a component of the size model. The traces of deformation zones in the Forsmark 2.2 DZ model and the lineaments identified in the high-resolution ground-magnetic surveys were divided into orientation sets, and their trace lengths were plotted on complementary cumulative number (CCN) plots, with lengths normalised by observation area (or pseudo-area, for the fractal scaling case). The clipping of these lineaments against fracture domain or rock domain boundaries would introduce unacceptably large truncation effects and mass defects into the geological model. As such, the parameterisation of the TFM, TCM, and TCMF alternative models uses all structures inside the Forsmark local model area (cf Figure 6-18) and is the same for all fracture domains. Therefore, the uncertainty associated with this question of representativity is constant across all of the size-intensity model alternatives.

This is an appropriate assumption if both the density of lineaments and the relative intensity of each orientation set are roughly uniform over the local model area, and does not differ significantly between fracture domains. However, at Forsmark the relative intensity of NW-striking lineaments is much lower in domain FFM02 (and also presumably in FFM01, which lies directly underneath FFM02 and is 'inside' the tectonic lens) than in the other fracture domains. In other words, there is significant anisotropy in the density of certain lineament sets at Forsmark. Differences in the intensity of MDZ-sized lineaments between fracture domains introduces additional uncertainty into both the fracture intensity and fracture size models, due to the fact that the slope of the power-law exponent (k_r) is partially dependent on the shape of the CCN curve for MDZ-sized lineaments. Uncertainty in the spatial anisotropy of aspect of MDZ-sized lineaments and DZ surface traces was not explored during the Forsmark 2.2 geological DFN modelling, though it is dealt with briefly in an Erratum published to the stage 2.2 geological DFN summary report (Fox et al. 2007). The question of MDZ anisotropy across the Forsmark local model volume is probably the largest representativity uncertainty, though no formal quantification exists.

6.3.8 Spatial and temporal variability of data (text reproduced from SR-Site Data report)

Spatial variability of data

Though the subdivision of the Forsmark local model volume into explicit fracture domains has done much to constrain fracture geometries and properties, significant spatial variability in fracture orientation, the number of fracture sets, and fracture intensity still exists.

During stage 2.2 modelling, the orientations of fractures recorded at outcrops or in borehole data are described in terms of univariate Fisher distributions. Geological DFN model users can choose to describe the fracturing on a domain-by-domain basis using the average mean pole and concentration parameter for all data in that domain (the recommended approach), or by treating both the mean pole orientation and Fisher κ as stochastic parameters following normal distributions (cf Fox et al. 2007, Section 4.1.4). However, no spatial correlation of mean pole orientation or Fisher κ inside an individual fracture domain is used.

Fractures are divided into Global sets, which are seen in nearly all parts of a fracture domain, and Local sets, which are seen in only a subset of outcrops and boreholes. No analysis of spatial correlation within a given fracture domain was performed for the Local sets. The recommendation from the DFN modelling team was to treat the local sets as a conditional probability at a given scale using geocellular-style generation; that is if the conditional probability for a given Local set was 0.2 at 30 m scales, then 20 % of the cells making up a given fracture domain would include fractures from that Local set, generated at full intensity. Alternatively, the local sets can be treated as a bulk property of the fracture domain, with the fracture intensity multiplied by the conditional probability. This approach was not recommended by the DFN teams.

The coupled fracture size-intensity models utilise the mean fracture P_{32} calculated across 6 m long sections of the Forsmark cored borehole array, with adjustments for host lithology and fractal dimension (cf Fox et al. 2007, Section 4.4.4). However, it is also possible to partially capture the spatial variability of fracture intensity within a given fracture domain through the use of a probability distribution for a given scale. Analyses conducted during stage 2.2 modelling (cf Fox et al. 2007, Section 4.4.3) indicate that at scales of 30 m and larger, the spatial variability of all fracture sets can be described using a generalised Gamma distribution (NIST 2007). By describing fracture intensity in this fashion, however, one automatically assumes no spatial or lithological correlation within a fracture domain.

As previously mentioned during the discussion on data uncertainty due to representativity, an issue exists with respect to the spatial variability of large fractures and MDZ. The MDZ size range (28–564.2 m) is described in terms of all structures in the Local model area, and not divided into fracture domains. As such, for some MDZ/lineament sets (in particular, NW-striking MDZ), the existing geological DFN models may not accurately describe spatial variability.

Temporal variability of data

Temporal variability of fracture data has not been taken into account during site-characterisation efforts or reporting.

6.3.9 Correlations (text reproduced from SR-Site Data report)

The following general correlations (most of which have been thoroughly discussed in the previous sections) exist in the geologic DFN models parameterised for use at the Forsmark site:

- Fracture geometric properties (orientation, size, and intensity) are correlated to fracture domain.
- Fracture location, in terms of the fracture centre, is uncorrelated in space, and follows a 3D Poisson point process.
- Modelling results from the stage 2.2 geological DFN analysis indicate a weak correlation between fracture intensity and bedrock lithology (cf Fox et al. 2007, Section 4.4.4). The correlation is strongest for subordinate rock types such as pegmatite and amphibolite. Should lithological correlation be desired during SR-Site modelling, Table 4-99 of Fox et al. (2007) should be used.
- Fracture size and intensity are correlated (coupled) in all recommended models due to the use of power-law relationships. The effects and consequences of this are summarised in previous sections of this document and analysed in detail in Fox et al. (2007), Stephens et al. (2007) and the **Site description Forsmark**.
- No significant (that is predictable in a global or domain-specific fashion) correlation between fracture intensity and true vertical depth exists at Forsmark. This is not to say that there is no variation in fracture intensity with depth; rather, that there is no useful relationship to describe it.

6.3.10 Result of supplier's data qualification (text reproduced from SR-Site Data report)

The authoritative source for all parameters necessary to describe the geological DFN at Forsmark is the quality-assured Microsoft Excel workbook "PFM DFN 2.2.xls", contained within SKB's database Modelldatabasen/SIMON. References to tables in published reports linked in previous sections of this report are provided as a courtesy only; the Modelldatabasen/SIMON database is considered the primary authority. Summary tables of the size-intensity model cases are also presented as Tables 5-5 through 5-8 of the **Site description Forsmark**. Table 6-32 presents an example of the format of the geological DFN model parameterisation tables as contained in SIMON.

Table 6-32. Example of geological DFN parameter table from SIMON database. This table is for the "tectonic continuum" (TCM) conceptual model alternative.

Fracture Domain FFM01, TCM Alternative ('k_r-fixed'), rev 0.6, 2009-05-18.

Frac. Set	Set Type	Orientation Model			Size Model			Intensity model between (r_0–r_{max})		
		Trend	Plunge	κ	r_0	r_{max}	k_r	P_{32}	Cond.* Prob.	Global P_{32}
NE	Global	314.90	1.30	20.94	0.659	564.2	3.020	1.733	1.00	1.733
NS	Global	270.10	5.30	21.34	0.059	564.2	2.780	1.292	1.00	1.292
NW	Global	230.10	4.60	15.70	0.594	564.2	2.850	0.948	1.00	0.948
SH	Global	0.80	87.30	17.42	0.816	564.2	2.850	0.624	1.00	0.624
ENE	Local	157.50	3.10	34.11	0.325	564.2	3.250	2.742	0.09	0.256
EW	Local	0.40	11.90	13.89	0.170	564.2	3.100	1.117	0.15	0.169
NNE	Local	293.80	0.00	21.79	0.039	564.2	3.000	4.395	0.15	0.658
SH2	Local	164.00	52.60	35.43	0.039	564.2	2.610	0.918	0.09	0.082
SH3	Local	337.90	52.90	17.08	0.039	564.2	2.610	0.837	0.08	0.067

* Local fracture sets, i.e. those that do not exist everywhere within the model volume, can either be modelled deterministically through spatial bootstrapping, or stochastically through adjusting the fracture intensity by the conditional probability of their existence in the target volume. See Section 3.2.5 of Fox et al. (2007) for more detail on how to treat local fracture sets in DFN models.

Based on the results of analyses performed during site characterisation, the outcome of discussions with reviewers associated with the site-descriptive modelling, and the professional judgement of the geological DFN team, the following data is recommended for use in the stochastic simulation of fractures and minor deformation zones during SR-Site modelling:

1. Fracture set orientations for Domains FFM01 and FFM06 are provided in the worksheet *"SR_Site_DataReport"* as a function of fracture domain. If orientation parameters are required for other fracture domains, they can be obtained from worksheet "*Orientation*"; the columns "*Trend*", "*Plunge*", and "*Distribution of Fisher K (Mean)*" should be used.
2. The geological DFN is described for all fractures (open, partly open, and sealed) within a size range (equivalent radius) of 0.5 –564.2 m; the DFN parameterisation is not valid outside those limits.
3. Fracture set size distribution models for Domains FFM01 and FFM06 can be obtained from worksheet "*SR_Site_DataReport*" as a function of fracture domain and conceptual model. Note that neither the TCMF alternative nor the other fracture domains at Forsmark are included on this sheet; should parameters for that conceptual model be required, they can be obtained from worksheets "*Size_TectonicContinuum*" or "*Size_OSM+TFM*".
4. Fracture set intensities for Domains FFM01 and FFM06 can be obtained from worksheet "*SR_Site_DataReport*" as a function of fracture domain and conceptual model. If intensity distribution parameters are required for other fracture domains, they can be obtained from worksheet "*Intensity*"; the columns "*Mean P_{32}: OSM, TCM, TCMF* and *TFM*", should be used. Note that this worksheet divides the rock mass into volumes "Affected by DZ" and "Not Affected by DZ"; the geological DFN team recommends only using the values for "Not Affected by DZ".
5. Fracture set terminations for all fracture domains should be taken from worksheet "*Termination Matrices*".

To illustrate the differences between the size-intensity conceptual alternatives at Forsmark, a number of stochastic DFN realisations of each case have been constructed for what is viewed as the most important of the six fracture domains at Forsmark (domain FFM01). This domain was chosen because it represents rock volumes that are most likely to play host to repository deposition holes and access tunnels. Each model was intersected with a 25 m long rectangular tunnel with a square cross section 5 m on a side (as illustrated in Figure 6-21). The traces of all fractures intersecting the simulated tunnel were then recorded. In each tunnel, within a 5 m section, traces for all fractures down to the distribution minimum radii were recorded. Outside of this strip, only traces longer than 0.5 m were recorded, to be consistent with outcrop mapping. The results are presented as Figure 6-22 through Figure 6-24. Note that the TCMF alternative was not simulated; functionally, it is almost identical to the TCM model. Simulations of Local orientation set use domain bulk values (intensity multiplied by probability of occurrence) rather than conditional probability. Though this is inconsistent with the recommendations previously described in Section 6.3.3, the use of bulk domain values is consistent with the likely methodology that the SR-Site modelling team will take to dealing with local fracture sets. As the simulations were designed for use as simple visualizations of the relative differences between conceptual alternatives, and given the relatively low intensity of the Local sets relative to the Global set intensities, this is an acceptable simplification.

6.3.11 Judgement by the assessment team

Since SR-site, no new fracture data from depth deeper than about 100 m have been gathered except for KFM024. This core drilled borehole reaches a length of about 500 m, but these new fracture data are not expected to alter the DFN models developed during the site investigations. However, an effort to infer the uncertainty of the mapped orientations of the fractures in all core drilled boreholes at Forsmark has been carried out. This new information might be used to constrain the orientation models and hence decrease the uncertainty of orientation.

SKB has done extensive efforts to increase knowledge regarding the development and application of DFN models since SR-Site. New conceptual models, including models where fractures grow according to simplified mechanical rules, have been developed, which may decrease the conceptual uncertainty of size distribution at depth. However, this increase in knowledge is so far not fully published and hence, the effects are not quantified yet. The judgement is yet to use the same data in PSAR as in SR-Site. However, this newly gained knowledge will be implemented in coming safety assessments.

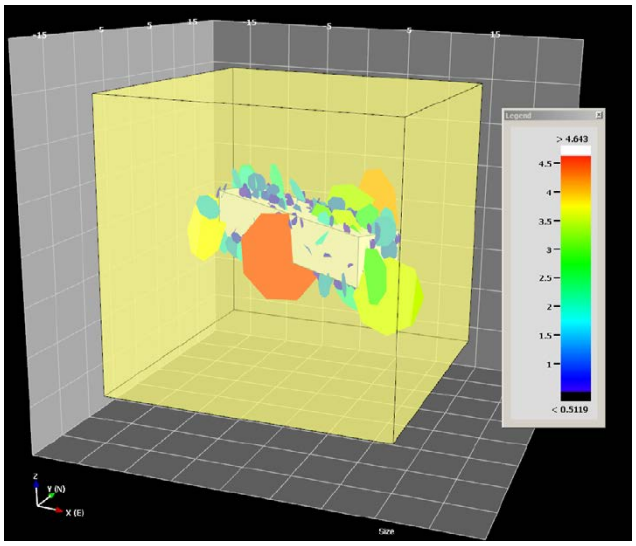

Figure 6-21. *Illustration of the simulation region and sampling tunnel used to produce the DFN trace illustrations in Figure 6-22 to Figure 6-24. The yellow transparent box represents the simulation region, while the white rectangular prism represents the sampling tunnel. This illustration shows fractures from the NW Global Set in domain FFM01, assuming the TCM conceptual alternative. Only fractures intersecting the sampling tunnel that are larger than 0.5 m (equivalent radius) are shown.*

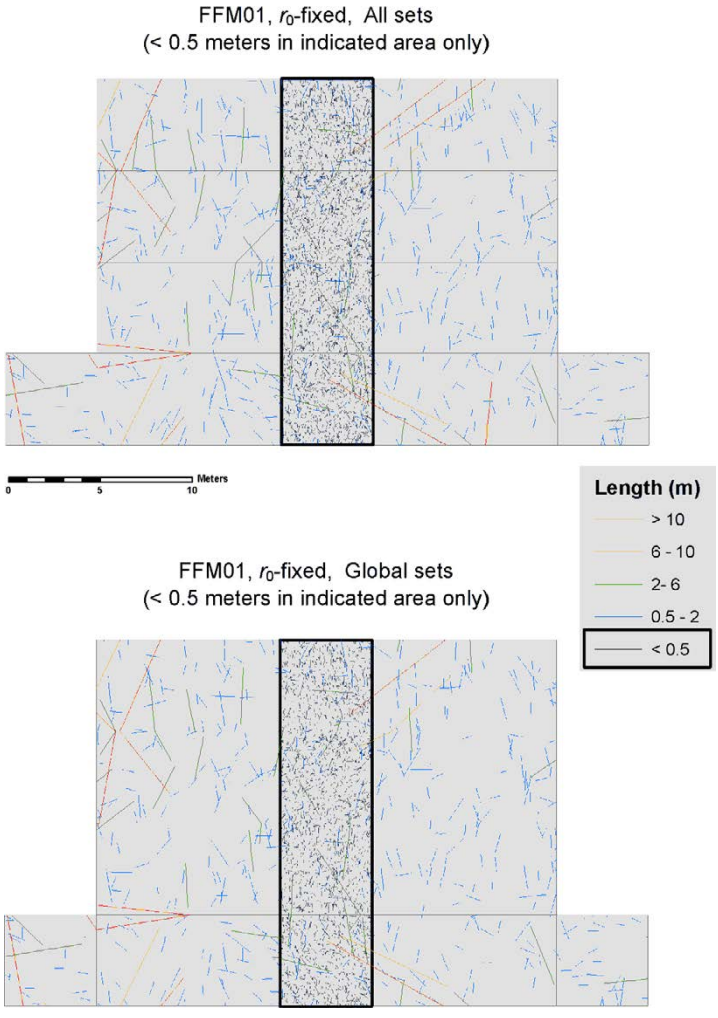

Figure 6-22. *Example tunnel trace map for fracture domain FFM01 using the r_0-fixed fracture size-intensity model alternative. The top figure shows all fractures, while the lower figure includes only fractures from the Global sets.*

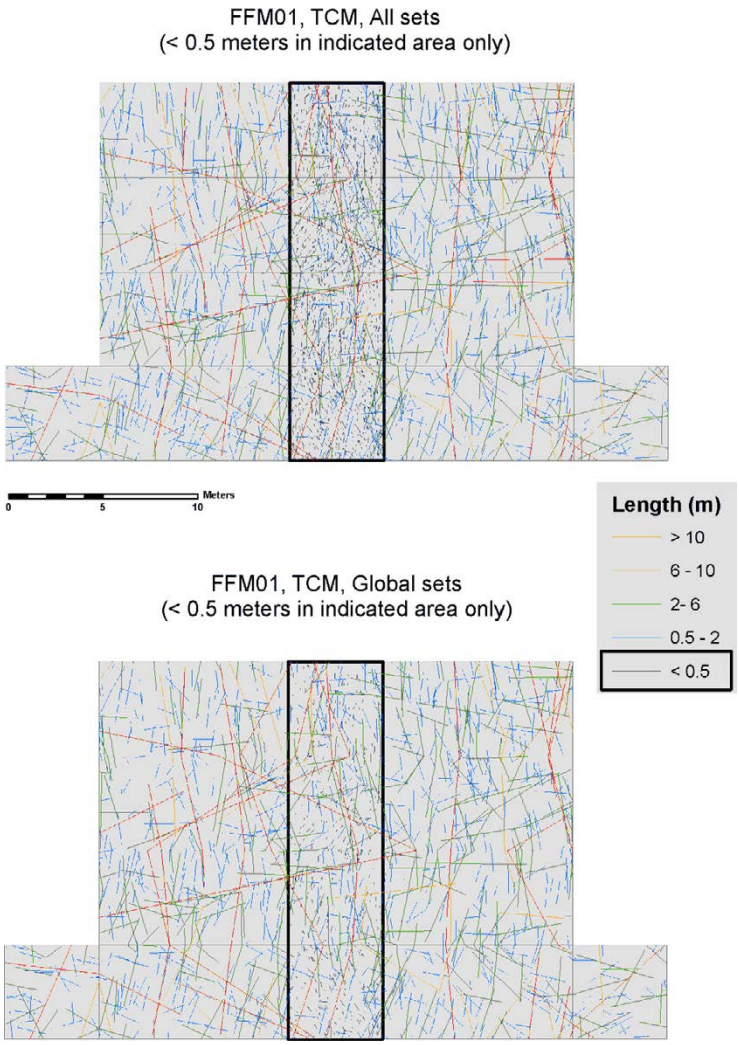

Figure 6-23. *Example tunnel trace map for fracture domain FFM01 using the TCM fracture size-intensity model alternative. The top figure shows all fractures, while the lower figure includes only fractures from the Global sets.*

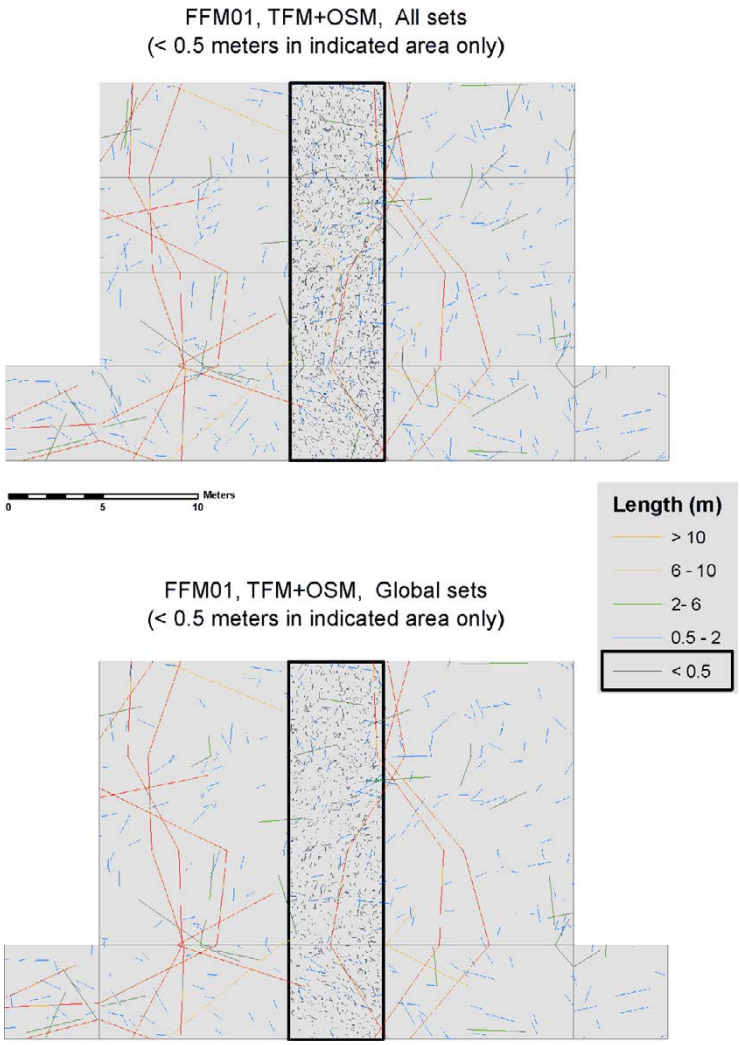

Figure 6-24. *Example tunnel trace map for fracture domain FFM01 using the OSM+TFM fracture size-intensity model alternative. The top figure shows all fractures, while the lower figure includes only fractures from the Global sets.*

6.3.12 Models recommended for use in assessment modelling

The DFN models recommended for use in PSAR modelling are stored in SKB's database for models, Modelldatabasen/SIMON, to ensure adequate QA and version handling. The data in the below tables are reproduced from Modelldatabasen[17].

Table 6-33. DFN model "r0 fixed" for fracture domain FFM01, version 0.6 from Modelldatabasen.

Fracture Domain FFM01, r_0-fixed Alternative								
Set	**Type**	**Trend**	**Plunge**	***K***	r_0 **(m)**	r_{max} **(m)**	k_r	P_{32}
NE	Global	314.90	1.30	20.94	0.039	564.200	2.718	1.733
NS	Global	270.10	5.30	21.34	0.039	564.200	2.745	1.292
NW	Global	230.10	4.60	15.70	0.039	564.200	2.607	0.948
SH	Global	0.80	87.30	17.42	0.039	564.200	2.579	0.624
ENE	Local	157.50	3.10	34.11	0.039	564.200	2.972	0.256
EW	Local	0.40	11.90	13.89	0.039	564.200	2.930	0.169
NNE	Local	293.80	0.00	21.79	0.039	564.200	3.000	0.658
SH2	Local	164.00	52.60	35.43	0.039	564.200	2.610	0.081
SH3	Local	337.90	52.90	17.08	0.039	564.200	2.610	0.067

Table 6-34. DFN model "TCM" for fracture domain FFM01, version 0.6 from Modelldatabasen.

Fracture Domain FFM01, TCM Alternative ('k_r-fixed')								
Set	**Type**	**Trend**	**Plunge**	***K***	r_0 **(m)**	r_{max} **(m)**	k_r	P_{32}
NE	Global	314.90	1.30	20.94	0.659	564.200	3.020	1.733
NS	Global	270.10	5.30	21.34	0.059	564.200	2.780	1.292
NW	Global	230.10	4.60	15.70	0.594	564.200	2.850	0.948
SH	Global	0.80	87.30	17.42	0.816	564.200	2.850	0.624
ENE	Local	157.50	3.10	34.11	0.325	564.200	3.250	0.256
EW	Local	0.40	11.90	13.89	0.170	564.200	3.100	0.169
NNE	Local	293.80	0.00	21.79	0.039	564.200	3.000	0.658
SH2	Local	164.00	52.60	35.43	0.039	564.200	2.610	0.082
SH3	Local	337.90	52.90	17.08	0.039	564.200	2.610	0.067

Table 6-35. DFN model "OSM+TFM" for fracture domain FFM01, version 0.6 from Modelldatabasen.

Fracture Domain FFM01, OSM+TFM Alternative								
Set	**Type**	**Trend**	**Plunge**	***K***	r_0 **(m)**	r_{max} **(m)**	k_r	P_{32}
NE	Global	314.90	1.30	20.94	0.039	28.000	2.640	1.709
NS	Global	270.10	5.30	21.34	0.039	28.000	2.900	1.290
NW	Global	230.10	4.60	15.70	0.039	28.000	2.440	0.898
SH	Global	0.80	87.30	17.42	0.039	28.000	2.610	0.615
ENE	Local	157.50	3.10	34.11	0.039	28.000	2.200	0.188
EW	Local	0.40	11.90	13.89	0.039	28.000	3.060	0.168
NNE	Local	293.80	0.00	21.79	0.039	28.000	3.000	0.657
SH2	Local	164.00	52.60	35.43	0.039	28.000	2.610	0.080
SH3	Local	337.90	52.60	17.08	0.039	28.000	2.610	0.066
NE	Global	315.30	1.80	27.02	28.000	564.200	3.000	0.029
NS	Global	92.70	1.20	30.69	28.000	564.200	2.200	0.0003
NW	Global	47.60	4.40	19.67	28.000	564.200	2.060	0.0003

[17] Modelldatabasen 2007. Model: PFM DFN 2.2.xls. Version 0.6. Approved 2007-11-29, Modified 2009-05-18. Modeller: A. Fox. Simon ID: GEO_WTAGLLAA. https://service.projectplace.com/pp/pp.cgi/r232241793 (access might be given on request).

Table 6-35. Continued.

Fracture Domain FFM01, OSM+TFM Alternative								
Set	**Type**	**Trend**	**Plunge**	***K***	r_0 **(m)**	r_{max} **(m)**	k_r	P_{32}
SH	Global	347.40	85.60	23.25	28.000	564.200	2.830	0.029
ENE	Global	157.90	4.00	53.18	28.000	564.200	3.140	0.087
EW	Global	186.30	4.30	34.23	28.000	564.200	2.850	0.0014

Table 6-36. DFN model "r0 fixed" for fracture domain FFM06, version 0.6 from Modelldatabasen.

Fracture Domain FFM06, r_0-fixed Alternative								
Set	**Type**	**Trend**	**Plunge**	***K***	r_0 **(m)**	r_{max} **(m)**	k_r	P_{32}
NE	Global	125.70	10.10	45.05	0.039	564.200	2.785	3.299
NS	Global	91.00	4.10	19.49	0.039	564.200	2.780	2.150
NW	Global	34.10	0.80	16.13	0.039	564.200	2.662	1.608
SH	Global	84.30	71.30	10.78	0.039	564.200	2.582	0.640
ENE	Local	155.40	8.30	20.83	0.039	564.200	2.865	0.194
SH2	Local	0.00	47.50	12.71	0.039	564.200	2.610	0.429

Table 6-37. DFN model "TCM" for fracture domain FFM06, version 0.6 from Modelldatabasen.

Fracture Domain FFM06, TCM Alternative ('k_r-fixed')								
Set	**Type**	**Trend**	**Plunge**	***K***	r_0 **(m)**	r_{max} **(m)**	k_r	P_{32}
NE	Global	125.70	10.10	45.05	0.351	564.200	3.020	3.299
NS	Global	91.00	4.10	19.49	0.039	564.200	2.780	2.150
NW	Global	34.10	0.80	16.13	0.319	564.200	2.850	1.608
SH	Global	84.30	71.30	10.78	0.793	564.200	2.850	0.640
ENE	Local	155.40	8.30	20.83	0.740	564.200	3.250	0.194
SH2	Local	0.00	47.50	12.71	0.039	564.200	2.610	0.429

Table 6-38. DFN model "OSM+TFM" for fracture domain FFM06, version 0.6 from Modelldatabasen.

Fracture Domain FFM06, OSM+TFM Alternative								
Set	**Type**	**Trend**	**Plunge**	***K***	r_0 **(m)**	r_{max} **(m)**	k_r	P_{32}
NE	Global	125.70	10.10	45.05	0.039	28.000	2.640	3.252
NS	Global	91.00	4.10	19.49	0.039	28.000	2.900	2.146
NW	Global	34.10	0.80	16.13	0.039	28.000	2.440	1.522
SH	Global	84.30	71.30	10.78	0.039	28.000	2.610	0.630
ENE	Local	155.40	8.30	20.83	0.039	28.000	2.200	0.142
SH2	Local	0.00	47.50	12.71	0.039	28.000	2.610	0.423
NE	Global	315.30	1.80	27.02	28.000	564.200	3.000	0.029
NS	Global	92.70	1.20	30.69	28.000	564.200	2.200	0.0003
NW	Global	47.60	4.40	19.67	28.000	564.200	2.060	0.0003
SH	Global	347.40	85.60	23.25	28.000	564.200	2.830	0.029
ENE	Global	157.90	4.00	53.18	28.000	564.200	3.140	0.087
EW	Global	186.30	4.30	34.23	28.000	564.200	2.850	0.0014

6.4 Rock mechanics

This section presents the mechanical properties of the rock and fractures (for fractures also hydro-mechanical properties), as well as the stress conditions needed for the assessment of the thermo-hydro-mechanical (THM) evolution of the rock on different scales. These quantities are assessed from the site-descriptive model reports (SDM-Site) and the version D2 repository layout.

The PSAR is based on the same modelling of Rock mechanics as SR-Site. In the following sections, the modelling strategy is described (Section 6.4.1) followed by an account of the experiences from the SR-Site safety assessment (Section 6.4.2). Since the PSAR is based on the same data as SR-Site, the data qualification (Sections 6.4.3 to 6.4.10) is reproduced from the SR-Site Data report. In Section 6.4.11 the formal judgement by the assessment team to use the qualified data is presented followed by Section 6.4.12 where the recommended data is presented.

6.4.1 Modelling (text reproduced from SR-Site Data report)

This section describes what data are expected from the supplier, and in what assessment modelling activities the data are to be used.

Defining the data requested from the supplier

The modelling requires the following geosphere input data with estimates of spatial and temporal variability, as well as associated uncertainties.

- Rock mass elastic properties for the different scales of importance (Young's modulus E (GPa) and Poisson ratio υ (–)).
- Rock mass density ρ (kg/m^3).
- Uniaxial compressive strength *UCS* (MPa) and spalling strength (% of *UCS*).
- Fracture shear stiffness K_S (GPa/m) and fracture normal stiffness K_N (GPa/m).
- Fracture friction angle φ (°) and fracture cohesion c (MPa).
- Fracture dilation angle ψ (°).
- Principal *in situ* stress magnitudes σ_1, σ_2, and σ_3 (MPa) and orientations of stress components in terms of plunge and trend (°).
- Evolution of stress additions during glacial cycle (glacially induced stresses), principal stress magnitudes σ_1, σ_2, and σ_3 (MPa) and orientations of stress components in terms of plunge and trend (°).
- Stress-transmissivity relations
  - Parameter values for the continuously-yielding joint model (Itasca 2007), that is *JKN* (MPa/mm) and *JEN* (–).
  - Joint roughness coefficient JRC (–).
  - Parameters for exponential expression of hydraulic apertures (Liu et al. 2003), that is er (μm), emax (μm), and α (–).

SR-Site modelling activities in which data will be used

SR-Site assesses the THM-evolution of the rock during the construction and operational phase, during the initial period of temperate climate after closure, and during the remaining part of the reference glacial cycle. The main results of these analyses concern:

1. Estimates of mechanically induced changes of the transmissivity of fractures that intersect the near-field, as well as fractures in the far-field, due to excavation, thermal effects, and effects of ice load.
2. Estimates of the scope and extent (time-frames and location) of fracturing around deposition holes and tunnels (spalling), and based on this, a qualitative assessment of the potential hydraulic impact of this fracturing.
3. Evolution of pore pressures induced by glacial loads and potential for hydraulic jacking at different depths. The modelling work on hydraulic jacking is conducted both by use of closed form solutions and by use of numerical methods.

The mechanical and thermo-mechanical modelling explicitly conducted for SR-Site, relevant to points 1 and 2 above, is done using version 4.1 of the extensively tested *3DEC* code (Itasca 2007). *3DEC* is a distinct element code, particularly developed to analyse the mechanical and thermo-mechanical behaviour of jointed media such as fractured rock. Furthermore, the large-scale effects of parameter variations, deposition sequences, and optimisation are investigated by use of an analytical thermo-mechanical solution (Claesson and Probert 1996b).

The modelling work on point 3 above, evolution of pore pressures and hydraulic jacking, is conducted both by use of specifically for the purpose derived closed form solutions and by use of numerical methods (*UDEC (*Itasca 2005a), *FLAC (*Itasca 2005b) and Code_Bright (CIMNE 2004) models). Results from the hydraulic jacking assessment are presented in a separate report (Lönnqvist and Hökmark 2010).

The results of the rock mechanics modelling, evolution of the glacially induced pore pressures and a summary of the findings from the study on hydraulic jacking are presented in the THM-report (Hökmark et al. 2010).

In addition to the mechanical properties given in this section, the modelling also needs the following thermal/thermo-mechanical (cf Section 6.1), hydraulic (cf Section 6.6), and non-flow related (cf Section 6.8) properties of the rock mass, as well as fracture orientations (cf Section 6.3): The data needed are listed below.

1. Rock mass thermal conductivity λ (W/(m·K)) and heat capacity C (J/(m^3·K)).
2. Rock mass thermal expansion coefficient α (m/(m·K)).
3. *In situ* temperature at repository depth T (°C).
4. Rock mass hydraulic conductivity K (m/s).
5. Rock mass porosity n (–).
6. Fracture transmissivity T (m^2/s).
7. Fracture orientations.
8. Temperature evolution during permafrost (cf Section 7.1 and Hartikainen et al. (2010)).

Furthermore, the modelling needs:

9. Repository design, that is the geometry and dimensions of deposition tunnels and deposition holes (SKB 2007).
10. Layout, that is the coordinates of individual canister positions (SKB 2009a).
11. Initial canister power and decay-rate of the spent nuclear fuel (Hökmark et al. 2009).

6.4.2 Experience from SR-Site

Modelling in SR-Site

See previous section.

Condidions for which data were used in SR-Site

See previous section.

Sensitivity to assessment results

The analyses performed during the SR-site show that the in situ rock stress and the properties of the intact rock are such that thermally induced spalling is likely to occur. Spalling may increase the equivalent flow rate for the Q1 path by more than an order of magnitude, whereas the other paths are not affected. However, this increase has essentially no impact on risk, since spalling will not affect the local Darcy flux in the case of advective conditions in the deposition hole or if the canister is damaged by a shearing fracture.

According to the Site description Forsmark, there are remaining uncertainties with regard to the stress magnitude at Forsmark. There is also uncertainty in the spalling strength. While resolving these uncertainties is important for the design and layout of the repository, especially since the occurrence and amount of spalling affects the number of usable deposition positions, these uncertainties are of somewhat less importance for safety. Nevertheless, the potential for thermally induced spalling is evident considering the current uncertainty range and, since spalling affects one of the safety functions, although not risk itself, further efforts in finding methods to mitigate the spalling are warranted. This also includes a need for further characterisation of both the rock stress and the spalling strength of the rock.

The assessment of coupled thermo-hydro-mechanical processes performed during SR-Site clearly demonstrates that such processes have limited impact on safety. Continued research on the underlying processes is still warranted, although possibly primarily for input to the rock engineering design of the repository. With respect to long term safety issues, those worth further assessment include revisiting the current assumptions on stress-transmissivity couplings for fractures and deformation zones and revisiting current assumptions on excess porewater pressure during the glacial cycle. Current assumptions are judged to overstate the importance of these effects. Further assessment of the assumptions regarding the evolution of stress additions during a glacial cycle is also warranted.

After SR-Site efforts have been carried out in different areas of rock mechanics to increase our knowledge of the fundamental processes and to reduce the uncertainty in key parameters.

Intact rock

No new insights or results have been obtained on the mechanical properties of the intact rock during SR-Site or during the ensuing work addressing review comments on SR-Site.

Fracture mechanical and hydro-mechanical properties

SKB has, in collaboration with Posiva and NWMO, participated in the POST project (Fracture parameterisation for repository design and post-closure analysis), which aimed to improve the knowledge on fracture shear behaviour. Conclusions and experience from the POST project with respect to fracture shear strength, based on laboratory tests, numerical simulations and shear tests on fractures in situ, are summarised in Siren et al. (2017) and references therein. The results indicate that the fracture shear strength values used in SR-Site are conservative.

Recently, Stigsson and Mas Ivars (2019) presented an improved procedure for estimating JCR (Joint Roughness Coefficient) based on a mapped fracture trace. However, the methodology has not yet been applied in the safety assessment framework for PSAR. It is expected to be applied in coming safety assessments.

Additionally, the effect of large-scale undulation on the shear mechanical behaviour of fractures has been studied (Lönnqvist and Hökmark 2015). The results indicate that the values used in SR-Site are conservative.

It is also noteworthy to mention that further field and laboratory studies related to fracture hydro-mechanical properties are presented in Thörn (2015). In this work, hydromechanically coupled experimental field and laboratory setups and methods were developed and used to improve a conceptual model of hydromechanical (HM) fracture behaviour at low compressive stress. Fracture stiffness calculated from the measurement of mechanical deformations and stiffness from hydraulic aperture changes were found to follow trends linked to the storativity of fractures reported in Fransson (2009), which was used in SR Site as support data.

Rock mass properties

A semi-analytical method for the estimation of rock mass mechanical properties based on effective medium theory is under development (Davy et al. 2018, Darcel et al. 2018). At the moment the method allows for stochastic predictions of rock mass elastic properties at different scales based on DFN realizations and combinations of intact rock and fracture mechanical properties under different stress conditions. The methodology is still under development and it is expected to be applied in coming safety assessments.

Stress conditions

Two projects concerning rock stress measurements have been carried out over the past years. The SLITS project (SLIm borehole Thermal Spalling) has developed a method for determination of the rock stress orientation (Hakami 2011) in boreholes. The method is based on inducing thermal stresses in a borehole until spalling occurs and, assuming correlation between the stress field and the induced fracture orientation, the maximum horizontal stress can be calculated. The second project (Hakala et al. 2013) has developed an LVDT (Linear Variable Differential Transformer) cell for rock stress measurement in existing tunnels and shafts. Verification measurements with an LVDT cell in the Äspö HRL at the 450-metre level, where the stress field is well-characterised, show that the results of the measurements with the LVDT cell agree with results from previous studies, which involved overcoring measurements, and with the previously developed stress model (Christiansson and Janson 2003). The newly developed stress measurement techniques are planned to be used during the construction and characterization of the deep repository for spent nuclear fuel.

Furthermore, an updated three dimensional stress model for estimating the spatial variability of the stress tensor, based on the current structural geology model (Stephens and Simeonov 2015), has been developed (Hakala et al. 2019). The updated three dimensional stress model has not yet been applied in the safety assessment framework for PSAR. It is expected to be applied in coming safety assessments.

It is also noteworthy to mention that Figueiredo et al. (2020) have applied the fully tensorial approach for the characterization of the stress variability newly developed by Gao and Harrison (2018a, b) to stress measurements from Forsmark and to numerical results from the three dimensional stress model reported in Hakala et al. (2019). This approach is being further developed and its application to the safety assessment will be reported in coming safety assessments.

6.4.3 Supplier input on the use of data (text reproduced from SR-Site Data report)

The supplier broadly agrees with the handling of data in SR-Can. However, the following issues are recommended to be addressed in SR-Site.

- The *3DEC* code uses a built-in analytical solution, based on a grid of point sources representing the heat generating nuclear waste, to calculate temperatures and temperature increments at each grid point in the numerical model. Depending on the required level of detail, the point sources in selected parts of the repository region can be substituted for vertical line sources or combinations of line sources to better reflect the temperature distribution around individual canisters (see Fälth and Hökmark 2007, Hökmark et al. 2009). The analytical solution is relatively fast and thus provides the opportunity to simulate the thermal and thermo-mechanical evolution over long times in an efficient way. Based on this it is recommended that *3DEC* is used also in SR-Site for near-field and far-field analyses.
- In the SR-Can modelling, a generic layout, with rectangular deposition areas parallel to each other, was applied. For the different models the layout was made site-specific by adjustment of the canister spacings according to preliminary data from the design project. For SR-Site there are much more elaborated site-specific layouts depending on the expected loss of potential canister positions (SKB 2009a). It is recommended that one of these layouts should be used as basis for the thermal models applied in the SR-Site modelling.

- The near-field modelling conducted for the SR-Can safety assessment concerned only centrally located canister within the repository region. In SR-Site, the influence of different locations within the repository region should be investigated.
- In SR-Can, only the mean value of the thermal conductivity was used. This is appropriate for modelling the thermal and thermo-mechanical evolution on a large scale (e.g. repository-scale). The temperature distribution around an individual canister is, during the first few years, to a large extent determined by its own heat contribution and the local thermal properties (Hökmark et al. 2009). Therefore, the spatial distribution of the thermal conductivity (particularly the lower tail of the distribution) needs to be considered when specifying the minimum canister spacing, cf Section 6.2. However, *3DEC* cannot account for spatial variations in the thermal properties. Given the canister spacing, a global value of the rock mass thermal conductivity can be obtained that reproduces the threshold value of the peak buffer temperature (cf Section 6.2). This value is known as the dimensioning value of the thermal conductivity and is usually within the 0.1–2 percentile of the low tail of the thermal conductivity distribution (Hökmark et al. 2009). Using mean the mean value of the thermal conductivity may therefore underestimate the temperature at early times in the near-field. Methods for obtaining the dimensioning value of the thermal conductivity are described in Hökmark et al. (2009). For the near-field modelling in SR-Site, for example modelling of stresses in the walls of a deposition hole, it is recommended that the dimensioning value of the thermal conductivity is also considered.
- Generally, the influence of uncertainty spans in parameters judged to have impact on safety should be investigated.
- It is recommended that the fracture geometry used in the SR-Site modelling is also generic, that is circular, and that, in addition to generically oriented fractures, site-specific data for the orientation of fractures should also be used (e.g. Fox et al. 2007). Furthermore, near-field models should be made larger, such that larger fractures ($\geq$ 50 m radius) can also be accommodated.
- In SR-Can, the representation of the glacial load was based on preliminary ice/crust/mantle 2D calculations. Since then, the technique for performing this type of analyses has been developed significantly, and now includes 3D representations of the crust/mantle-system and variations of the lithosphere stiffness (Lund et al. 2009). It is likely that a 3D-model is capable of making better estimates of the stress evolution during a glacial cycle than the 2D-model used in the SR-Can safety assessment. Thus, results from such 3D-models should be used as input to the *3DEC* analyses for SR-Site.
- Based on the comments by Rutqvist and Tsang (2008), it is recommended that stress-induced transmissivity changes are addressed by relations based on site-specific fracture normal-stiffness data and hydraulic aperture data.

6.4.4 Sources of information and documentation of data qualification (text reproduced from SR-Site Data report)

Sources of information

The main sources of information used in the data qualification of rock mechanics data are presented in Table 6-39. It should be noted that data delivered in this section are used as input to the "THM report" (Hökmark et al. 2010). Accordingly, this report is not considered to be a main source of information.

Table 6-39. Main sources of information used in data qualification.

Site description Forsmark, 2008. Site description of Forsmark at completion of the site investigation phase. SDM-Site Forsmark. SKB TR-08-05, Svensk Kärnbränslehantering AB.
Andersson J C, 2007. Äspö Hard Rock Laboratory. Äspö Pillar Stability Experiment, Final report. Rock mass response to coupled mechanical thermal loading. SKB TR-07-01, Svensk Kärnbränslehantering AB.
Chryssanthakis P, 2003a. Forsmark site investigation. Borehole: KFM01A. Results of tilt testing. SKB P-03-108, Svensk Kärnbränslehantering AB.
Chryssanthakis P, 2003b. Forsmark site investigation. Boreholes: KFM03A and KFM03B. Tilt testing. SKB P-04-178, Svensk Kärnbränslehantering AB.
Chryssanthakis P, 2004a. Forsmark site investigation. Borehole: KFM02A. Results of tilt testing. SKB P-04-08, Svensk Kärnbränslehantering AB.
Chryssanthakis P, 2004b. Forsmark site investigation. Borehole: KFM04A. Tilt testing. SKB P-04-179, Svensk Kärnbränslehantering AB.
Chryssanthakis P, 2004c. Forsmark site investigation. Borehole: KFM05A. Tilt testing. SKB P-04-205, Svensk Kärnbränslehantering AB.
Chryssanthakis P, 2006. Forsmark site investigation. Borehole: KFM09A. Tilt testing. SKB P-06-25, Svensk Kärnbränslehantering AB.
Follin S, Hartley L, Jackson P, Roberts D, Marsic N, 2008. Hydrogeological conceptual model development and numerical modelling using CONNECTFLOW, Forsmark modelling stage 2.3. SKB R-08-23, Svensk Kärnbränslehantering AB.
Glamheden R, Fredriksson A, Röshoff K, Karlsson J, Hakami H, Christiansson R, 2007. Rock mechanics Forsmark. Site descriptive modelling Forsmark Stage 2.2. SKB R-07-31, Svensk Kärnbränslehantering AB.
Jacobsson L, Flansbjer M, 2005a. Forsmark site investigation. Borehole KFM05A. Normal stress test with direct and indirect deformation measurement together with shear tests on joints. SKB P-05-141, Svensk Kärnbränslehantering AB.
Jacobsson L, Flansbjer M, 2005b. Forsmark site investigation. Borehole KFM06A. Normal loading and shear tests on joints. SKB P-05-122, Svensk Kärnbränslehantering AB.
Jacobsson L, Flansbjer M, 2005c. Forsmark site investigation. Borehole KFM07A. Normal loading and shear tests on joints. SKB P-05-213, Svensk Kärnbränslehantering AB.
Jacobsson L, Flansbjer M, 2005d. Forsmark site investigation. Borehole KFM08A. Normal loading and shear tests on joints. SKB P-05-218, Svensk Kärnbränslehantering AB.
Jacobsson L, Flansbjer M, 2006. Forsmark site investigation. Borehole KFM09A. Normal loading and shear tests on joints. SKB P-06-29, Svensk Kärnbränslehantering AB.
Lund B, Schmidt P, Hieronymus C, 2009. Stress evolution and fault stability during the Weichselian glacial cycle. SKB TR-09-15, Svensk Kärnbränslehantering AB.
Martin D, 2005. Preliminary assessment of potential underground stability (wedge and spalling) at Forsmark, Simpevarp and Laxemar sites. SKB R-05-71, Svensk Kärnbränslehantering AB.
SKB, 2009d. Site engineering report Forsmark. Guidelines for underground design, step D2. SKB R-08-83, Svensk Kärnbränslehantering AB.

Categorising data sets as qualified or supporting

The qualified and supporting data sets are presented in Table 6-40. Comments regarding each item are given in Table 6-41. Data sets taken from the site-descriptive modelling (Glamheden et al. 2007) and the **Site description Forsmark** (i.e. points 1, 2, 4, 6, 7, 8 and 9) can a priori be categorised as qualified data. They have subsequently been judged to be qualified according to the instructions for supplying data to this Data report (see Section 2.3).

For the qualified data sets in Table 6-40, more extensive discussions on the uncertainties, variability, and methodology used in the acquisition of data associated with each set of parameters are provided by the references given in Table 6-39 and Table 6-40; a summary is provided in the following sections. For the supporting data sets (with the exception of rock mass density), discussions regarding uncertainties and variability for each set of parameters are provided in the following sections.

Excluded data previously considered as important

No important data have been excluded from the analyses.

Table 6-40. Qualified and supporting data sets.

Qualified data sets	Supporting data sets
1. Intact rock deformation properties: Sections 3.3.1 and 3.3.2 (Glamheden et al. 2007) and Table 7-3 in the **Site description Forsmark**.	9. Spalling strength: Tables 3-2 and A.1 (Martin 2005); Sections 8.2 and 11 (Andersson 2007).
2. Intact rock uniaxial compressive strength: Section 3.2.1 (Glamheden et al. 2007); Section 7.2.1 in the **Site description Forsmark**.	10. Rock mass density: Table 3-4 (Stephens et al. 2007).
3. Rock mass deformation properties: Table 5-9 (Glamheden et al. 2007).	11. Stress-transmissivity relations: Model parameters JKN and JEN for the continuously-yielding joint model: • Chapter 5 (normal stress-normal displacement curves based on direct measurements) in each of Jacobsson and Flansbjer (2005a, b, c, d, 2006). • Joint roughness coefficient: Table 5-1 and appendix in each of Chryssanthakis (2003a, b, 2004a, b, c, 2006). • Initial (or residual) hydraulic aperture: Table 10-25 (Follin et al. 2007b).
4. Fracture shear and normal stiffness: Table 4-15 (Glamheden et al. 2007).	
5. Fracture friction angle and cohesion: Table 4-14 (Glamheden et al. 2007).	
6. Fracture dilation angle: Table 4-16 (Glamheden et al. 2007).	
7. Initial pre-mining stress magnitudes and orientations: Tables 6-7 and 6-8 (Glamheden et al. 2007); Table 2-11 (SKB 2009d).	
8. Evolution of stress additions during glacial cycle: Figure 7-17 (Lund et al. 2009) and underlying data.	

Table 6-41. Justification to the sorting of items in Table 6-40.

1–2. Primary data for intact rock are obtained by laboratory (small) scale testing, see the **Site description Forsmark**. Lower level references to test methods as well as discussions on uncertainties are provided by Glamheden et al. (2007). The values of Young's modulus presented in Glamheden et al. (2007) is based on the tangent Young's modulus evaluated at 50 % of the compressive strength and determined from uniaxial and triaxial compressive tests (Glamheden et al. 2007). Poisson's ratio is evaluated from these test results. No triaxial tests were performed on samples from rock domain RFM045.

3. The deformation properties of the rock mass are obtained from two different modelling approaches (Glamheden et al. 2007):

- An empirical approach, which is based on classification systems and empirical relationships.
- A theoretical approach, which is based on numerical modelling.

The final estimate of the rock mass deformation properties is made by weighting the results together – a process known as "Harmonisation". More detailed information regarding the process is provided by Glamheden et al. (2007).

4–6. The strength and deformation properties of fractures reported in Glamheden et al. (2007) are based on laboratory results from tilt tests and direct shear tests of discrete fractures. The fracture samples are taken from the target volume in fracture domains RFM029 and RFM045, as well as from adjacent fracture domains RFM012, RFM034, and RFM044. Lower level references to test methods as well as discussions on uncertainties are also provided by Glamheden et al. (2007).

- The fracture normal stiffness, KN, is presented as the secant stiffness evaluated between the unloaded state and full loading of the second load cycle.
- The fracture shear stiffness, KS, is presented at the secant shear stiffness evaluated between 30 % and 50 % of the peak shear stress at each level of normal stress (0.5, 5, and 20 MPa).
- The fracture dilation angle, ψ, is presented as the secant dilation angle at three levels of normal stress. It is evaluated between 0.3 and 1.3 mm of shear deformation at the normal stress level 0.5 MPa, between 0.5 and 1.9 mm of shear deformation at the normal stress level 5 MPa, and between 0.7 and 2.1 mm of shear deformation at the normal stress level 20 MPa.
- The Mohr-Coulomb fracture strength properties (peak cohesion and peak friction angle/residual cohesion and residual friction angle) are determined by a least squares fit to the measured peak/residual shear stresses at the three levels of normal stress (0.5, 5, and 20 MPa).

7. The *in situ* stress model for Forsmark, i.e. initial pre-mining stress magnitudes and orientations, are based on overcoring data from the site investigations as well as results from numerical modelling (Glamheden et al. 2007). Further discussions on the methods of acquisition of data as well as uncertainties are provided by Martin (2007). An upper limit of stress magnitudes at repository depth is provided in Table 2-11 (SKB 2009d). These values should only be used for assessments of the risk of spalling due to elevated stress magnitudes (SKB 2009d).

8. The stress additions during a glacial cycle are based on 3D simulations of the glacial isostatic adjustment (Lund et al. 2009) due to a Fennoscandian ice model by Näslund (SKB 2006c). The numerical model used to calculate glacially induced stresses has been extensively tested and verified against other, independent, codes as well as compared with GPS measurements of glacial isostatic adjustments (GIA) data (Lund et al. 2009). Therefore, this data set can be judged to be qualified according to the instructions for supplying data to this Data report.

9. No field experiments of the spalling strength have been performed on the rock types at Forsmark. However, Andersson (2007) suggested that for sites lacking *in situ* data, lower bound estimates of the crack initiation stress based on the strain gauge method may be used to assess the rock mass spalling strength. The spalling strength is expressed as the range 52–62 % of the uniaxial compressive strength (*UCS*) in each rock domain based on the findings from AECL's Mine-by experiment (e.g. Martin 2005), the Äspö Pillar Stability Experiment (APSE) (Andersson 2007) and the ratio between crack initiation stress and *UCS* at Forsmark, see the **Site description Forsmark**. The spalling strength should therefore be considered a supporting data set.

10. The value of the rock mass density is generic (2,700 kg/m^3) and used to calculate the vertical stress component. It should therefore be considered a supporting data set.

11. No field experiments have been carried out at Forsmark to determine the relationship between stress and transmissivity during loading or unloading of fractures. Instead, stress-induced transmissivity changes are based on the continuously-yielding joint model (CY model) (Itasca 2007), using lab-scale stress-stiffness data and average hydraulic apertures at repository depth, and an exponential relation (Liu et al. 2003) to account for a residual aperture at high normal stress. Therefore, the stress-transmissivity relations should be considered a supporting data set.

6.4.5 Conditions for which data are supplied (text reproduced from SR-Site Data report)

All data supplied are valid at present-day conditions at the site and based on current knowledge of the site conditions. The rock volumes the data concern are clearly indicated throughout this section.

The stress additions during a glacial cycle (cf Section 7.1) provided by Lund et al. (2009) are valid at 500 m depth, corresponding to the repository depth.

6.4.6 Conceptual uncertainty (text reproduced from SR-Site Data report)

The following conceptual uncertainty applies to all rock mechanics parameters. As the available site-specific data are collected from a limited area of the site, the mechanical properties are evaluated on the assumption that the rock volume within each geological domain has similar mechanical characteristics, see the **Site description Forsmark**.

Deformation and strength properties of intact rock

Other than the conceptual uncertainties that apply for all rock mechanics parameters, the conceptual uncertainty of the deformation and strength properties of intact rock are judged to be low.

Factors contributing to the conceptual uncertainty of the spalling strength are:

- *Relative humidity:* Reduced humidity seems to increase the spalling strength (Glamheden et al. 2010).
- *Stress path:* The Äspö Pillar Stability Experiment (APSE) (Andersson 2007) was designed to give high tangential stresses in the floor region and some spalling was observed in the hole walls already after excavation (cf Figure 6-33). In the KBS-3 repository, the deposition tunnels are designed and oriented such that the stresses in the floor region are minimised. For a more gentle stress path than in APSE, that is if the tangential stresses after excavation are well below the nominal spalling strength, and followed by a slow stress increase towards the nominal spalling strength during the subsequent heated phase, the spalling strength may be different.

Deformation properties of rock mass

The main conceptual uncertainties associated with the empirical approach of estimating the deformation properties of rock mass are listed below (Glamheden et al. 2007):

- As well as uncertainty in input data (see Section 6.4.7), the size of sample populations and subjectivity in the characterisation of the rock mass will contribute to the conceptual uncertainty.
- No explicit stress dependence in any of the parameters is assumed. The empirical relationships were developed for conditions at shallow depths and low confining pressure. As the empirical relationships will be used to estimate properties at approximately 500 m depth, this will introduce some uncertainty.
- It is assumed that the rock mass is isotropic.
- The applicability of the empirical relationships for high-quality rock mass at a depth of around 500 m is somewhat uncertain and may result in an overestimated value of Young's modulus.

In addition to the conceptual uncertainties that apply for all rock mechanics parameters, a measure of the conceptual uncertainty can be found by examining the differences in results from the empirical and theoretical approaches. The mean values of Young's modulus obtained from the theoretical and empirical approaches deviate by 2–3 GPa from each other in both fracture domains FFM01 and FFM06 (Glamheden et al. 2007). The corresponding difference in Poisson's ratio is 0.01 in fracture domain FFM01 and 0.07 in fracture domain FFM06 (Glamheden et al. 2007).

Fracture mechanical properties

Other than the conceptual uncertainties that apply for all rock mechanics parameters, the conceptual uncertainty of the mechanical and strength properties of fractures is judged to be low. No samples were taken from fracture domain FFM06, but visual inspection of the fractures in that fracture domain suggests that their properties are similar to those in fracture domain FFM01, see the **Site description Forsmark**.

In situ stresses

The main conceptual uncertainties associated with hydraulic fracturing and hydraulic testing of pre-existing fractures (HTPF) methods, as well as the overcoring method (Martin 2007) are:

- In the small-diameter boreholes (used by SKB), only the orientation of the fracture at the injection-borehole wall can be determined. It is assumed that this orientation is the same as the fracture orientation at the end of the test. Note that results from the hydraulic fracturing and HTPF methods are not used in the stress model, which results in a more cautious estimate of the state of *in situ* stress (see the **Site description Forsmark**), cf Section 6.4.7.
- The overcoring method relies on elastic theory. In the stress regime at Forsmark, microcracking may occur during drilling and induce a non-linear stress-strain response, which makes the results difficult to interpret. There is significant scatter in the measurement data, which can be attributed to both uncertainties in the measurement methods as well as spatial variability (Martin 2007) (see also Section 6.2.8). Martin (2007) further states that this type of scatter is more likely to be related to measurement technique than actual variability. However, it is practically impossible to separate the two sources of scatter (Martin 2007).

Evolution of stress additions during a glacial cycle

The main sources of conceptual uncertainty stem from three assumptions:

- The modelling approach.
- The ice model.
- The Earth model.

The conceptual uncertainty is judged to be large and also the source of the largest uncertainty.

Modelling approach

The main conceptual uncertainties associated with the modelling approach by Lund et al. (2009) of the glacially induced stress additions are listed below. The first two bullets together will amount to at most 1 MPa.

- The influence of tectonic strain is not considered, i.e. the possibility that the stabilising ice cover inhibits incremental strain energy release. A horizontal tectonic strain rate of 1×10^{-11} per year, as suggested by for example Muir Wood (1995), would correspond to a horizontal stress increase by 0.06 MPa during a glacial cycle.
- The shear impact of the ice is not considered. Wu (2009) concluded that the shear impact is less than 1 MPa at the surface and decreases with depth.
- Thermo-mechanical effects during the glacial cycle are not considered, i.e. in particular the reduction of the horizontal stresses due to the temperature reduction of the rock during permafrost conditions. These effects are handled in the THM report (Hökmark et al. 2010) and not quantified here.

Ice models

SKB's reference ice model by Näslund (SKB 2006c) is based on a reconstruction of the Weichselian glaciation, cf Figure 6-25. The thickness (~3 km) of Näslund's ice sheet is generally considered rather large (Lund et al. 2009). The ice thickness at Forsmark using a different ice model by Lambeck (2005) is also presented in Figure 6-25. Lambeck's ice is significantly thinner (maximum thickness of around 2 km) and covers the site for a much longer period in time than Näslund's ice. As seen in the figure, there are significant differences between the two models and the stress evolution due to the two ice models would also be expected to be different. Note that the vertical glacially induced stress component reflects the ice load (e.g. Lund et al. 2009).

Figure 6-26 shows the temporal evolution of the glacially induced stresses at a depth of around 5 km due to the two ice models shown in Figure 6-25. The higher stress magnitudes (up to 40 MPa) obtained from Lambeck's model are likely to be a combination of thinner lithosphere, lower upper mantle viscosity and longer duration of ice coverage (Lund et al. 2009).

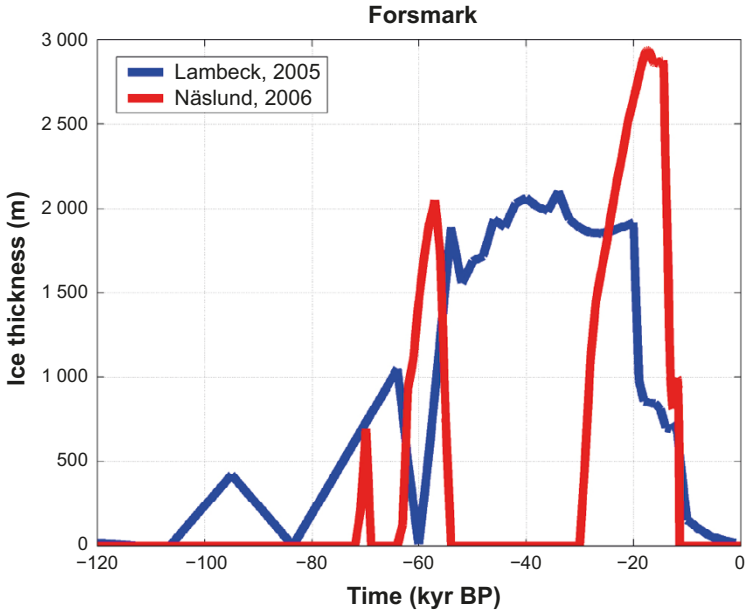

Figure 6-25. *Evolution of ice thickness at Forsmark from two different models. Reproduced from Lund et al. (2009, Figure 4-5 left).*

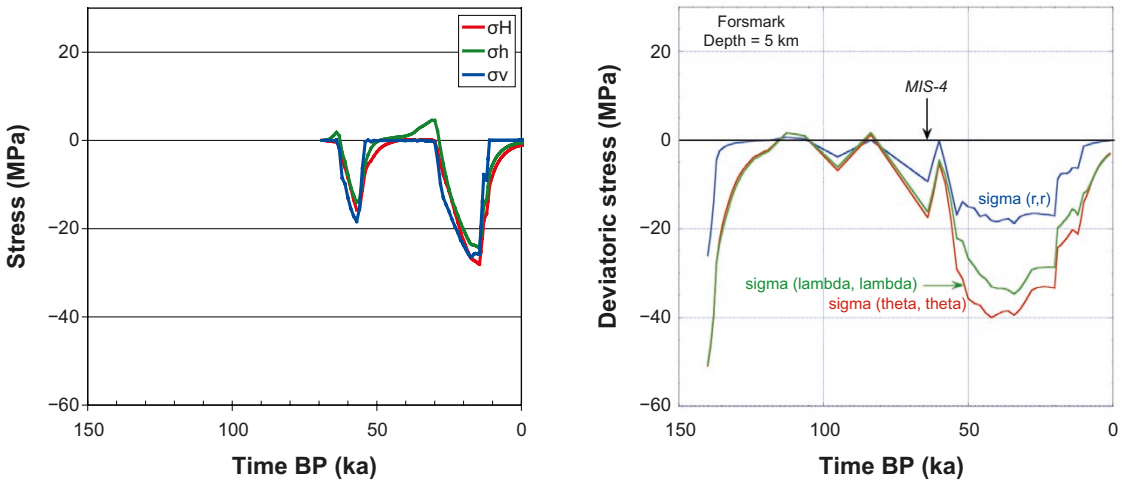

Figure 6-26. *Left: Temporal evolution of the glacially induced stresses (model T9) at 5.5 km depth obtained from ice-crust-mantle analyses performed by Lund et al. (2009) using Näslund's (SKB 2006c) ice model. Right: Modelled stresses at 5 km depth due to Lambeck's ice model, reproduced from Lambeck (2005, Figure 7). Here, compression is negative. The scale of the right figure is the same as in the left figure.*

Earth models

- Three types of Earth models were considered by Lund et al. (2009).
- Models with a 100 km thick uniform compressible elastic plate overlying an incompressible visco-elastic half-space (Model 1).
- Models with a three-layered 100 km thick compressible elastic plate overlying an incompressible visco-elastic half-space (Model T9).
- Models with laterally varying lithosphere (Model T12).

Lund et al. (2009) found that the structure of the lithosphere is less important for the fit to GPS data. Although Model 1 gave the best fit to GPS data (Figure 6-27, left), the deformation modulus is considered too high in the upper parts of the rock. The glacially induced stresses at 500 m depth obtained from this model are 50–90 % larger in magnitude during the second glacial maximum than the corresponding results from the other two models shown in the figure. By inspection of the stress results during the last glacial advance and retreat, the glacially induced stresses from all considered Earth models (except Model 1), appear to be within ± 10 MPa of the results from the Earth model (Model T9) preferred by Lund et al. (2009).

However, horizontal stratification affects results when relative sea level data are considered (Lund et al. 2009). The horizontally stratified models were found to fit GPS data better than the models with lithospheric depth variations, cf Figure 6-27 (middle and right), mainly due to a poor fit to horizontal velocities in the models with depth-varying lithosphere. For relative sea level data the difference between horizontally stratified models and models with lithospheric depth variations were smaller, cf Figure 6-28.

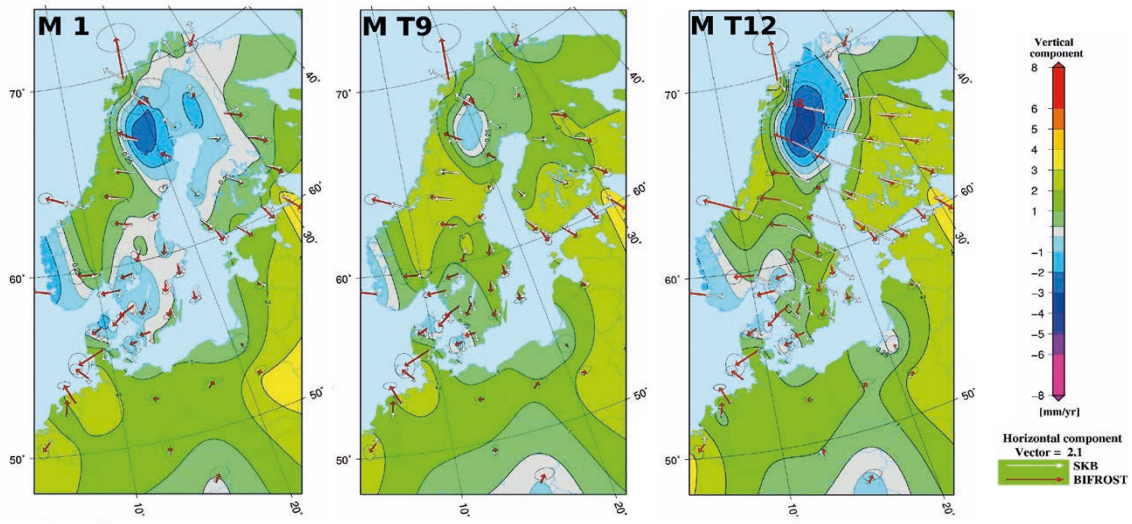

Figure 6-27. *Comparison between data from the Bifrost project (GPS data) and model results. Contours show differences in vertical velocities, whereas arrows show horizontal velocity components from the Bifrost project (red) and model results (white). Reproduced from Lund et al. (2009, Figures 6-2, 6-3, and 6-5).*

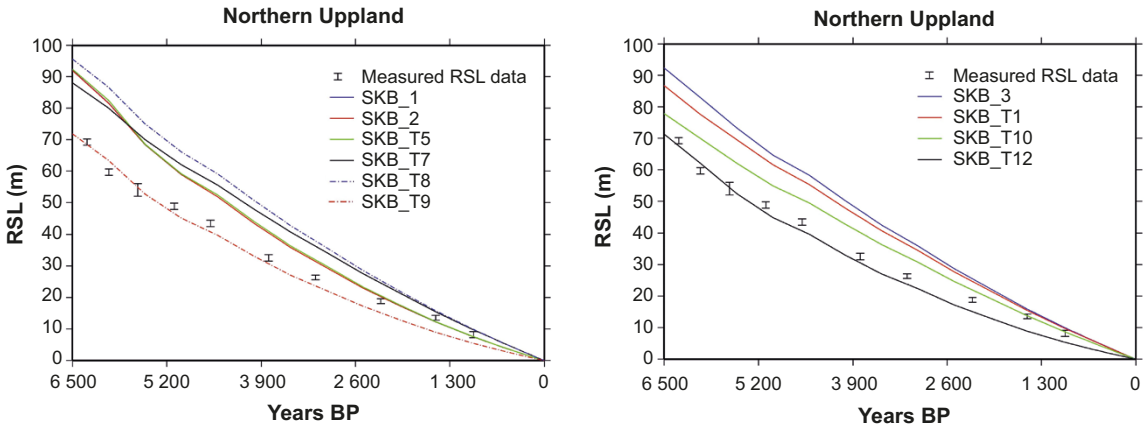

Figure 6-28. *Comparison between measured relative sea level data in northern Uppland and model results from flat layered Earth models (left) and Earth models with variable layer thickness (right). Excerpt from Lund et al. (2009, Figure 6-7).*

Stress-transmissivity relations

The conceptual uncertainty associated with the stress-transmissivity relations is judged to be large and is also, in comparison with uncertainties due to precision, bias, and representativity, the largest uncertainty. The conceptual uncertainty is associated with:

- The nature of stress-stiffness relations of individual fractures.
- Estimates of the variations in mechanical apertures of fractures due to variations in normal stress and, from that, the hydraulic aperture and corresponding fracture transmissivity.
- Fracture data, that is fracture normal stiffness and hydraulic properties of individual fractures.

Considering the uncertainties associated with the stress-transmissivity relations, it is not feasible to derive stress-transmissivity relations for individual fractures. Instead, two stress-transmissivity relations will be given: 1) One based on mean value fracture stiffness data to estimate the average response to variations in normal stress and 2) one based on fracture stiffness data that give an upper bound estimate of the sensitivity to variations in normal stress.

Stress-stiffness relations of individual fractures

For present-day conditions, only weak correlations between transmissivity and normal stress have been observed (Follin et al. 2008), see Figure 6-29. However, these correlations may not adequately describe changes in fracture transmissivity due to the anticipated changes in normal stress during the safety assessment period. There are several models that describe the relation between fracture normal stiffness and normal stress (e.g. Fransson 2009). For the purpose of estimating the sensitivity of fracture transmissivities to variations in normal stress, the stress-dependence of the fracture normal stiffness is approximated by the continuously-yielding (CY) joint model (Itasca 2007), Equation 6-6. Qualitatively, this model is supported by literature data (e.g. Fransson 2009), that is a non-linear increase in fracture normal stiffness with increased compression.

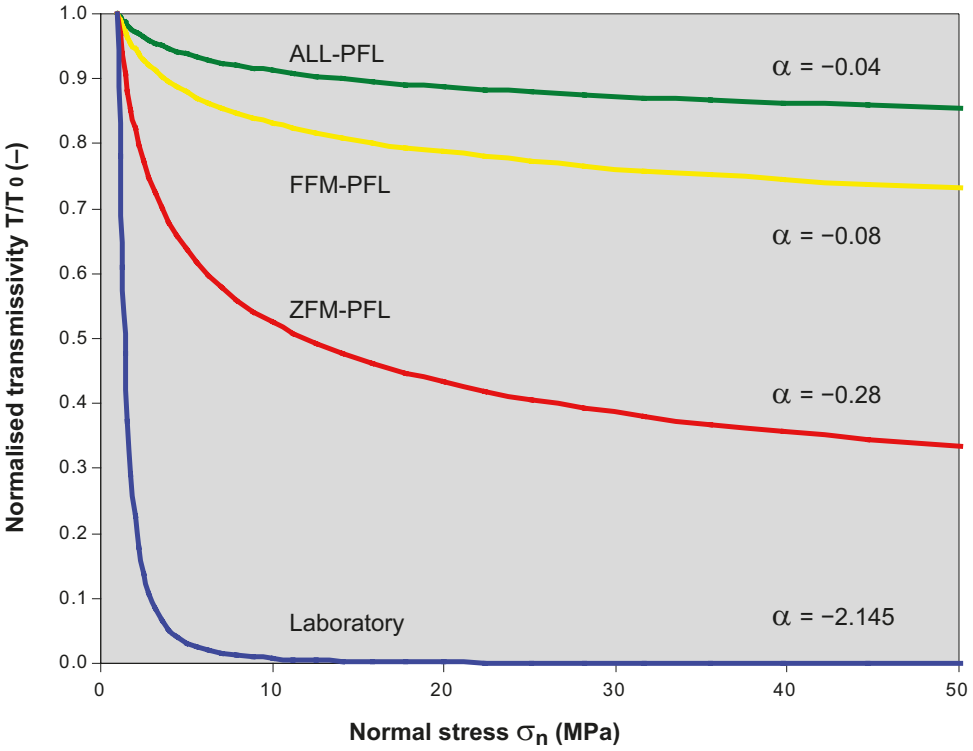

Figure 6-29. *Fit of transmissivity data and estimated normal stress to $T = T_0 \cdot \sigma_n^{\alpha}$ using all transmissivity data in the candidate area (ALL-PFL), transmissivity data from fracture domains FFM01, FFM02 and FFM06 (FFM-PFL) and transmissivity data associated with deterministically modelled deformation zones (ZFM-PFL). Reproduced from Follin et al. (2008, Figure 4-7).*

In the CY model, the relation between fracture normal stiffness and normal stress (σ_N) is defined as:

$$K_N = JKN \cdot \sigma_N^{\,JEN} \qquad 6\text{-}6$$

where *JKN* and *JEN* are a model parameters. *JKN* is defined as the tangent normal stiffness evaluated at 1 MPa, whereas *JEN* is the slope of straight lines fitted to stress-stiffness data in a log-log plot. Values of the parameters *JKN* and *JEN* may be obtained from results of cyclic loading compression tests performed on core samples from the site. Figure 6-30 shows fracture normal stiffnesses at 1, 5, and 10 MPa estimated from stress-deformation plots in Jacobsson and Flansbjer (2005a, b, c, d, 2006) with the CY model (straight lines) fitted to the data points. In the stress-range 1–10 MPa, there is very good agreement between the CY model and the stress-stiffness data obtained from the normal loading tests.

Fracture apertures and transmissivity

The mechanical aperture E at a normal stress of σ is given by Equation 6-7, where the initial aperture is E_0 at a normal stress of σ_0. The hydraulic aperture e is estimated using an empirical relationship (Equation 6-8) (Barton 1982) that relates the mechanical aperture E (μm) and hydraulic aperture e (μm) through the laboratory scale Joint Roughness Coefficient (*JRC*). For naturally loaded joints, the ratio E/e is usually greater than one (Olsson 1998). As a joint is opened, the ratio reduces and approaches one (Olsson 1998).

$$E = E_0 + \Delta E = E_0 - \frac{1}{JKN} \int_{\sigma_0}^{\sigma} \sigma'^{-JEN}\, d\sigma' \qquad 6\text{-}7$$

$$e = \min\left(E, \frac{E^2}{JRC^{2.5}}\right) \qquad 6\text{-}8$$

However, the CY model (Equation 6-7) does not account for a residual aperture, which is important at high normal stress (e.g. Rutqvist and Tsang 2008). This model may therefore overestimate the joint normal closure at high normal stress. To account for this, an exponential expression suggested by Liu et al. (2003) is fitted to the hydraulic apertures calculated from Equations 6-7 and 6-8. The exponential expression is given by Equation 6-9:

$$e = e_r + e_{\max} \exp(-\alpha \cdot \sigma_N) \qquad 6\text{-}9$$

Here, e_r is the residual aperture and σ_N the effective normal stress, whereas e_{max} and α are model parameters. The relative transmissivity, T/T_0, is subsequently calculated from Equation 6-10 assuming the cubic law to hold:

$$T/T_0 = (e/e_0)^3 \qquad 6\text{-}10$$

Here, e_0 is the hydraulic aperture at the reference effective normal stress σ_0.

Fracture data

In order to return a sample to a state that is representative for *in situ* conditions, several load-unload cycles are needed (Martin et al. 1990). Jacobsson and Flansbjer (2005a, b, c, d, 2006) performed two load-unload cycles at normal stress-levels up to 10–20 MPa, cf Figure 6-30 (top row). Here, the parameters *JKN* and *JEN* are evaluated from results obtained after the second load cycle. By visual inspection of the graphs given in Jacobsson and (Flansbjer 2005a, b, c, d, 2006), it appears that the tangent normal stiffness at each of the three considered stress-levels does not vary in any significant way from the first unload cycle through the second load-unload cycle.

The initial mechanical aperture, E_0, is estimated from Equation 6-8 using the mean value of *JRC* (at joint length tested, cf Section 6.4.7) (Chryssanthakis 2003a, b, 2004a, b, c, 2006) and assuming that the corresponding hydraulic aperture is equal to the residual hydraulic aperture, e_r. The residual hydraulic aperture is not a parameter whose value can be estimated from present-day *in situ* transmissivity data presented in the site report, e.g. Follin et al. (2007b). Here, the residual aperture is taken to be the mean present-day hydraulic aperture at large depths (calculated from transmissivity values given by Follin et al. (2007b) through the cubic flow law). Hökmark et al. (2006) concluded that fractures with high

residual, or initial, apertures (i.e. high transmissivity) are less sensitive to variations in normal stress. This is supported by results from hydraulic jacking tests in borehole KLX02 at Laxemar described in e.g. Rutqvist and Tsang (2008) where it was found that pressure sensitivity was strongly dependent on the initial hydraulic permeability. The most conductive fractures were relatively insensitive to injection pressure, whereas the least conductive fractures could be strongly dependent on the injection pressure.

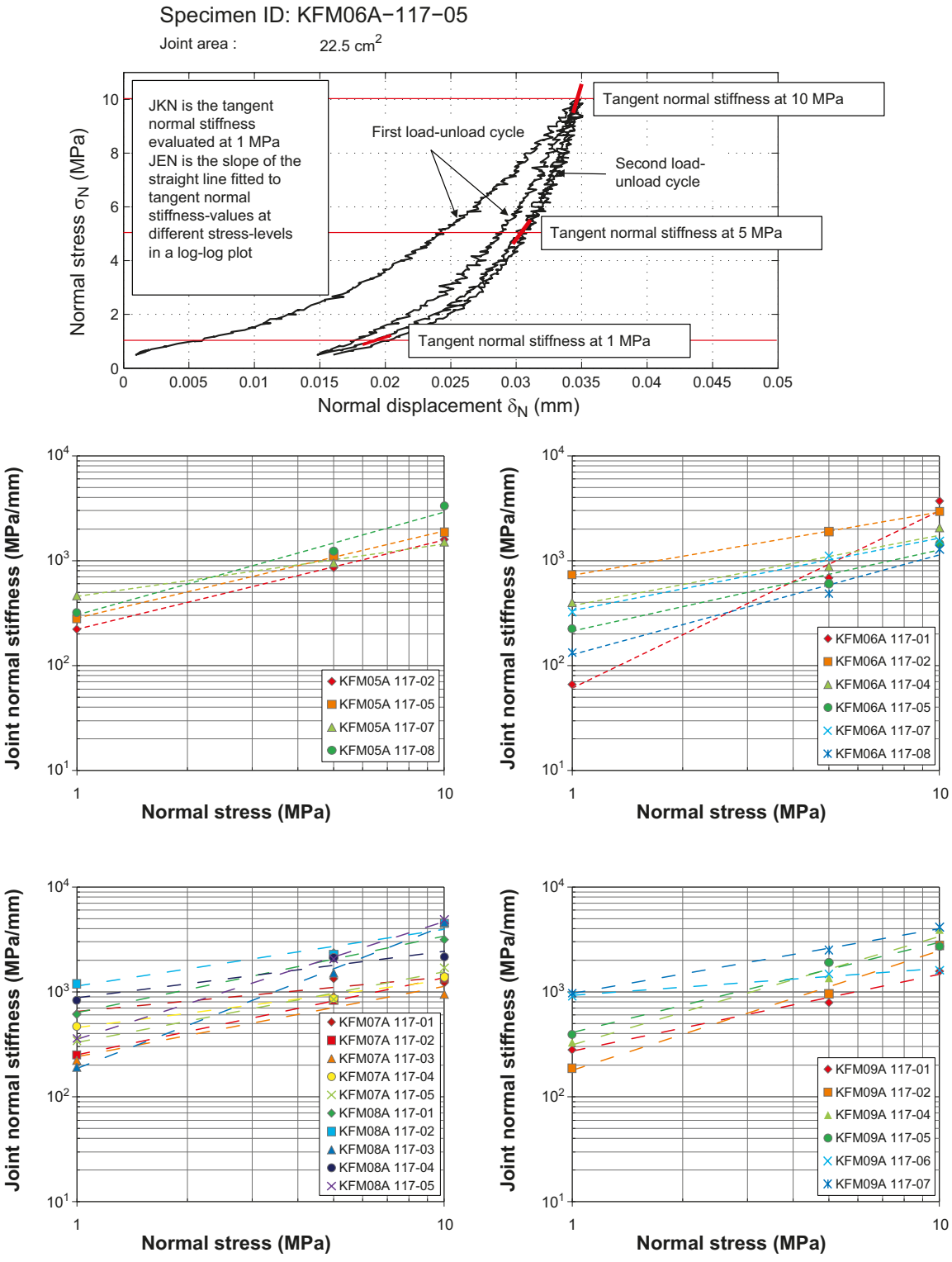

Figure 6-30. *Example of a cyclic loading compression test (top row), modified from Jacobsson and Flansbjer (2005b). CY model (straight lines) fitted to stress-stiffness estimates obtained from stress-deformation curves in Jacobsson and Flansbjer (2005a, b, c, d, 2006). The value of JKN ranges between 67 and 1 193 MPa/mm (mean 436 MPa/mm); JEN ranges between 0.26 and 1.69 (mean 0.78).*

6.4.7 Data uncertainty due to precision, bias, and representativity (text reproduced from SR-Site Data report)

Data uncertainty due to precision and bias

Deformation and strength properties of intact rock

The uncertainties in deformation and strength properties of intact rock due to precision and bias are judged to be low based on the following:

- *Sampling strategy:* In the selection of specimens for mechanical testing, core sections with sealed fractures or imperfections with an acute angle to the axial load were avoided (Glamheden et al. 2007). Furthermore, several specimens were taken close to each other (Glamheden et al. 2007). The spatial variation must therefore be assumed to be greater than that predicted by the laboratory results (Glamheden et al. 2007), cf Section 6.4.8. However, the sampling strategy is not considered to have any significant impact on the uncertainties (SKB 2008).
- *Microcracking:* Coring of granite at depths can induce microcracking, which for moderate microcracking can lead to changes in porosity and in case of excessive microcracking also changes in mechanical properties (Glamheden et al. 2007). Tests on samples of granite to granodiorite (101057) from boreholes KFM01A and KFM02B showed that microcracking is moderate; the microcrack volume corresponds to 5–10 % of measured mean porosity of the given rock type (Glamheden et al. 2007). However, the estimated microcrack volume in the samples is judged to have an only minor or insignificant impact on the mechanical properties.
- *Interlaboratory differences*: As part of the preliminary site description of Forsmark version 1.2, Lanaro and Fredriksson (2005) compared results from laboratory tests performed by the Swedish National Testing and Research Institute (SP) and Helsinki University of Technology (HUT) on samples from boreholes KFM01A, KFM02A, KFM03A, and KFM04A. Lanaro and Fredriksson (2005) found that the mean value uniaxial compressive strength obtained by HUT (samples from KFM01A only) was about 5 % larger than the corresponding mean value obtained by SP. Comparisons of results of Young's modulus obtained from uniaxial testing at the two laboratories were in very good agreement. Corresponding values of Poisson's ratio determined on samples of granite to granodiorite (metagranodiorite) by HUT do not agree with values obtained by SP. Lanaro and Fredriksson (2005) note that the difference in Poisson's ratio could not be explained by natural variations in the rock. It should be noted that the results by HUT were obtained from significantly fewer samples. However, in most rock mechanics calculations, the exact value of Poisson's ratio does not affect the results very much.

No field experiments of the spalling strength of the rock types at Forsmark have been conducted. Therefore the uncertainty due to precision and bias cannot be quantified. However, Andersson (2007) suggests that for sites lacking *in situ* data, lower-bound values of the crack initiation stress from uniaxial laboratory test based on the strain gauge method can be used to assess the spalling strength. In APSE (Andersson 2007), the spalling strength determined for Äspö diorite was 56–62 % of the *UCS*, whereas the onset of crack initiation in uniaxial test based on the strain gauge method was found to occur at 42–48 % of the *UCS*. Figure 6-31 shows the ratio between mean crack initiation stress and mean *UCS* for different rock types in two fracture domains (FFM01 and FFM06) and in deformation zones (DZ and PDZ) at Forsmark. The mean crack initiation stress is about 51–55 % of the mean *UCS*. Therefore, the assumed lower bound spalling strength (52 % of *UCS*,) appears to be adequate.

Deformation properties of rock mass

The rock at Forsmark is dominated by sealed fractures; open fractures are only a small part of the total number (Glamheden et al. 2007). The empirical approach does not consider sealed or partly open fractures as it is based on the occurrence of open fractures (Glamheden et al. 2007). However, the empirical approach relies on information from databases where sealed and partly open fractures are considered, meaning that these types of fractures are implicitly analysed (Glamheden et al. 2007). This implies that the rock mass quality at Forsmark may be overestimated (Glamheden et al. 2007). However, it was found in the theoretical approach that variations in material properties gave a larger spread in evaluated properties of the rock mass than variations in fracture geometry (Glamheden et al. 2007), cf Figure 6-41.

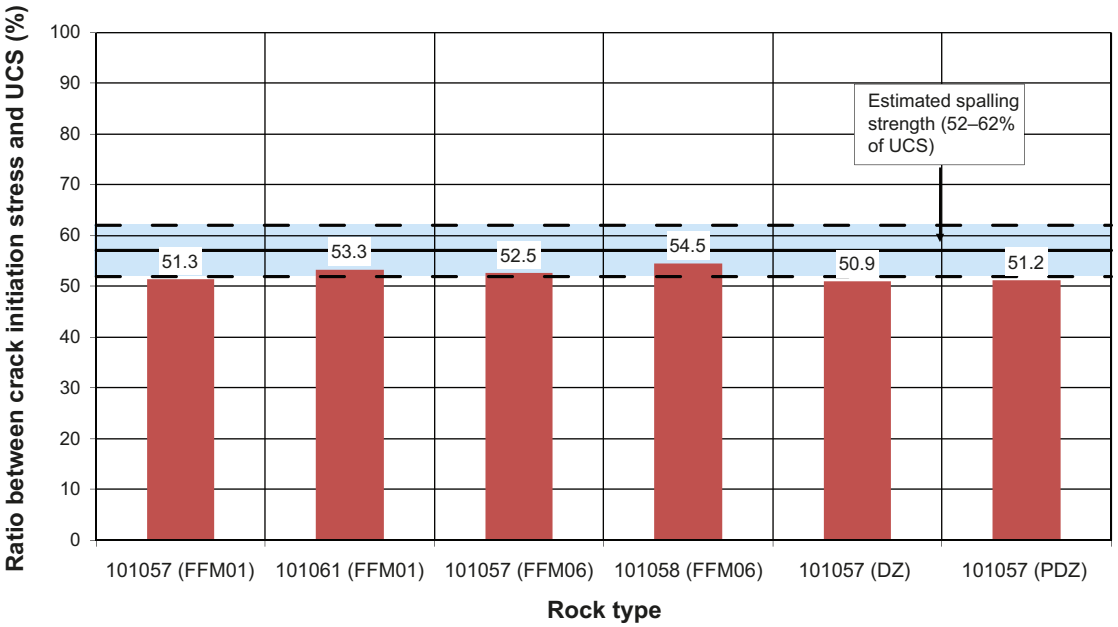

Figure 6-31. *Ratio between the mean crack initiation stress and mean UCS for different rock types in fracture domains FFM01 and FFM06 and in deterministic deformation zones (DZ) and potential deformation zones (PDZ) compared with the estimated spalling strength. Mean value crack initiation stress and UCS compiled from Table 7-3 in the Site description Forsmark.*

Fracture mechanical properties

As part of the preliminary site description of Forsmark version 1.2, Lanaro and Fredriksson (2005) compared results from laboratory tests performed by the Swedish National Testing and Research Institute (SP) and the Norwegian Geological Institute Laboratory (NGI). The fracture stiffness evaluated from normal loading tests was much higher in the tests by NGI. The strength properties evaluated from direct shear tests were also slightly higher in the tests by NGI. Lanaro and Fredriksson (2005) attributed the differences to an indication of slightly different accuracy or testing procedures at the two laboratories. However, the SP results were chosen to represent the properties of fractures at Forsmark as they were more numerous and agreed well with tilt test (Lanaro and Fredriksson 2005).

Since version 1.2 of the preliminary site description, the methodology for shear tests has been modified as it appeared that the deformation of the mould holding the fracture sample affected the deformation of the sample in the normal direction (SKB 2006b). Glamheden et al. (2007) evaluated results from three different test techniques to assess how clamping of the samples in the test apparatus would influence the measurements. Details regarding the different test techniques can also be found in Glamheden et al. (2007). A measurement technique (denoted Type III) that gives a direct measurement of the normal deformation across the fracture was chosen to be the reference test method. Results from the other two techniques were converted to Type III. Glamheden et al. (2007) found that the variations in the fracture normal stiffness was high compared with that of the other fracture parameters.

In situ stresses

There is a considerable amount of scatter in the measured stress magnitudes, which may have been exaggerated due to thermal strains during the overcoring process (Martin 2007). During overcoring it is important that the temperature is kept relatively constant. As a result, the calculated stress magnitudes may also have been influenced by the heat (Martin 2007).

The estimated uncertainty in the horizontal *in situ* stress components is ± 15–25 % (Glamheden et al. 2007). The uncertainty given for the minor horizontal *in situ* stress is correlated to the uncertainty in the major horizontal *in situ* stress; the ratio of σ_H/σ_h is expected to lie in the range 1.4–2.0 (Glamheden et al. 2007). The uncertainty in the trend of the major horizontal *in situ* stress is ± 15° (Glamheden et al. 2007).

The estimated uncertainty in the vertical stress component is ± 2 % in fracture domains FFM01 and FFM06; the corresponding uncertainty in fracture domains FFM02 and FFM03 is ± 10 %. The uncertainty span in the vertical stress component is related to the uncertainty in rock mass density (Martin 2007).

Estimates of small scale spatial variations due to local fractures and material heterogeneities (denoted *local variability* in Glamheden et al. (2007)) are included in the above estimates: 4–12 % (uncertainties in stress magnitudes) and ± 3–6° (orientation of major horizontal *in situ* stress), cf Section 6.4.8.

Evolution of stress additions during glacial cycle

The following factors are found to be contributing the uncertainties due to precision and bias.

- *The numerical code:* The code used in the modelling work has been extensively tested and verified and found to be in good agreement with other independent codes (Lund et al. 2009).
- *The ice model:* SKB's reference ice model (SKB 2006c) used in the modelling by Lund et al. (2009) is based on a reconstruction of the Weichselian glaciation. It is difficult to assess how well it would predict a future glaciation, cf e.g. Figure 6-25. However, there is no reason to believe that future ice sheets will be fundamentally different from previous Late Pleistocene Fennoscandian ice sheets (Lund et al. 2009).
- *The Earth model:* Lund et al. (2009) choose Model T9 (horizontally stratified Earth model) as their preferred model in terms of fit to GPS data and sea level data and as its lithospheric elastic structure is in agreement with the Fennoscandian seismic investigation, cf section on uncertainties due to representativity.

Stress-transmissivity relations

The uncertainties due to precision and bias are assumed to be large and stem from uncertainties in fracture mechanical and hydraulic data as well as uncertainties in the stress-aperture and transmissivity model. In terms of accurately estimating stress-induced transmissivity changes of individual fractures, precision is judged to be poor. However, for providing an upper bound estimate as well as a best estimate of the average sensitivity to stress changes of differently oriented fractures, it is judged that the stress-transmissivity relations provided by Equations 6-9 and 6-10 are adequate.

Equation 6-8 gives an estimate of the hydraulic aperture as a function of the mechanical aperture and the joint roughness coefficient at laboratory scale (l = 100 mm). Chryssanthakis (2003a, b, 2004a, b, c, 2006) remark that due to the small core diameter of the samples (approx. 5 cm), the resulting values of *JRC* are associated with some uncertainty. Figure 6-32 shows a comparison between results obtained at joint length tested (JRC_0) and results extrapolated to 100 mm (JRC_{100}). As seen in the figure, there are only small differences between the measured data and the extrapolated data.

Data uncertainty due to representativity

Deformation and strength properties of intact rock

The variability in the evaluated mean values of strength and deformation properties is small between the different modelling steps, i.e. the increased number of samples since model version 1.2 (SKB 2005) has not influenced the mean values. This suggests that the number of tests is sufficient to describe the deformation and strength properties of intact rock (Glamheden et al. 2007). However, the number of tests in fracture domain FFM01 is much larger than in FFM06, which results in larger uncertainties in the properties in fracture domain FFM06 (Glamheden et al. 2007).

Martin (2005) suggests a spalling strength of 57 ± 2 % of the uniaxial compressive strength (*UCS*) for coarse and medium grained unfoliated crystalline rocks based on the findings from the Äspö Pillar Stability Experiment (APSE) (Andersson 2007) and the Mine-by experiment (Martin 2005), cf Table 6-42. The spalling strength estimated for APSE appears to have been relevant for both the initial (non-heated) phase and the subsequent heated phase, cf Figure 6-33. Therefore, the proposed range in spalling strength (52–62 % of *UCS*, cf Table 6-40) appears to be representative for the excavation and operational phase and the heated phase of the initial temperate period.

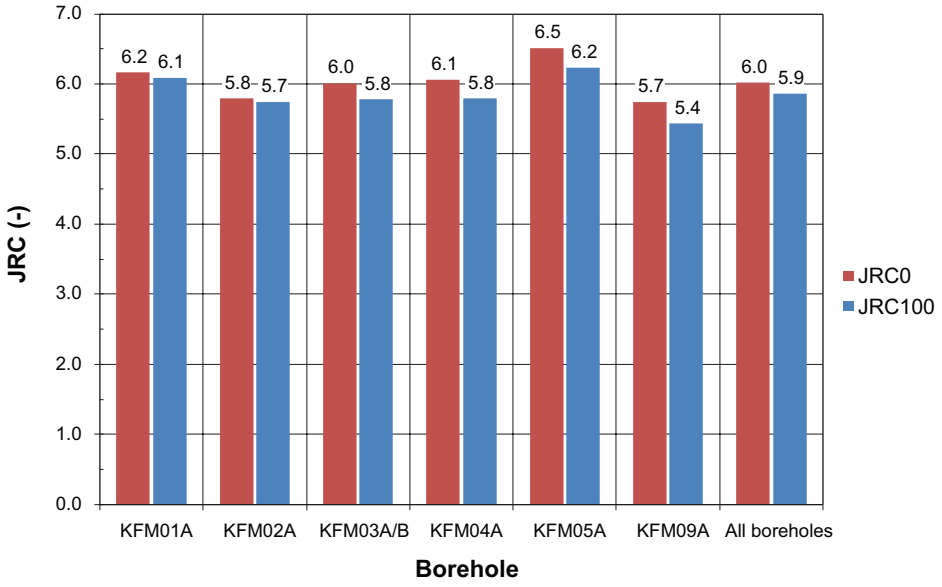

Figure 6-32. *Comparison between the joint roughness coefficient JRC_0 (at joint length tested) and JRC_{100} (measured data extrapolated to 100 mm), compiled from appendices of Chryssanthakis (2003a, b, 2004a, b, c, 2006).*

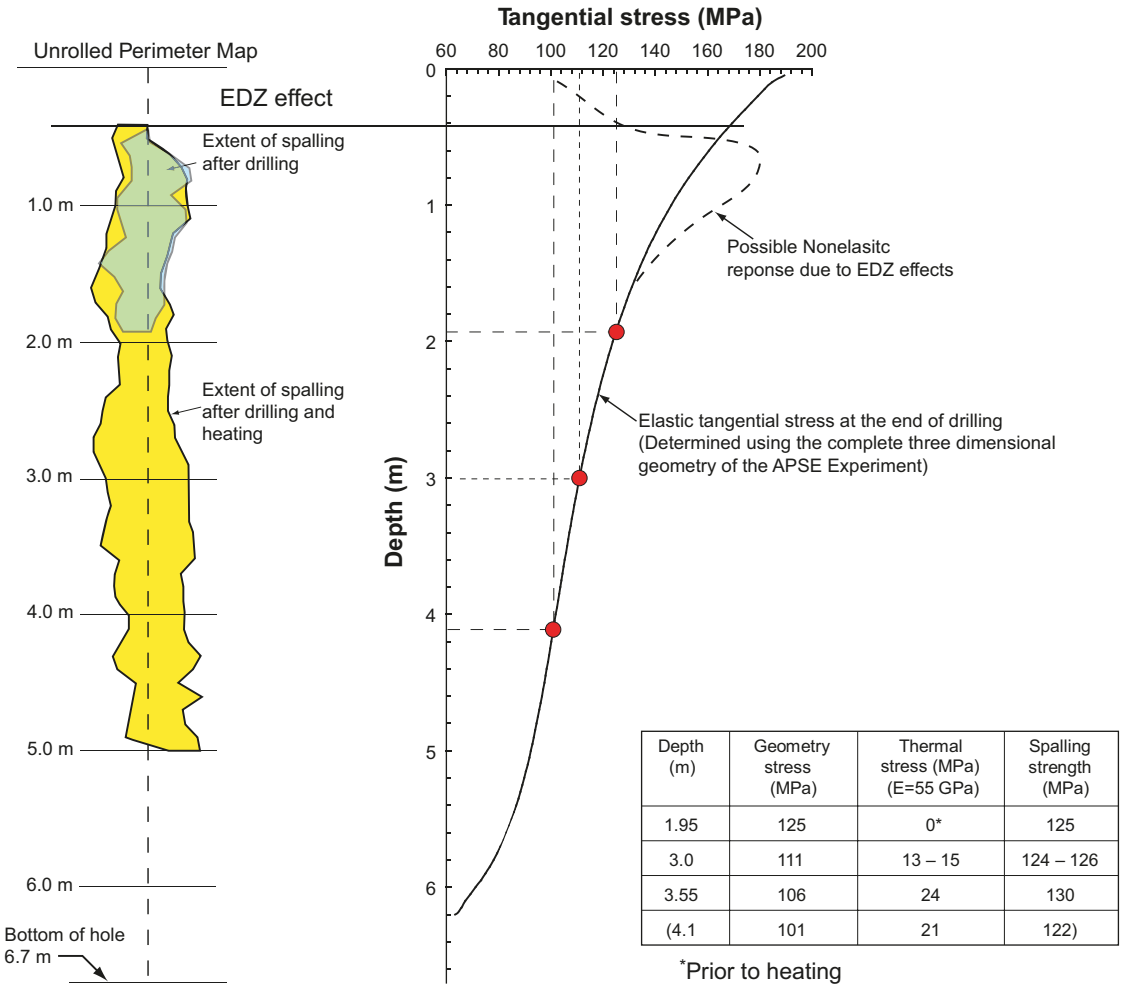

Depth (m)	Geometry stress (MPa)	Thermal stress (MPa) (E=55 GPa)	Spalling strength (MPa)
1.95	125	0*	125
3.0	111	13 – 15	124 – 126
3.55	106	24	130
(4.1	101	21	122)

*Prior to heating

Figure 6-33. *Extent of spalling and estimates of the spalling strength before and during heating. Modified from Martin (2005).*

Table 6-42. Estimates of spalling strength from the Äspö Pillar Stability Experiment (Andersson 2007) and the Mine-by experiment (Martin 2005).

Experiment		Spalling strength (%)	Uncertainty span (%)
APSE		59	± 3
	Äspö Diorite		
Mine-by			
	Lac du Bonnet granite	56	-
	Granodiorite	65	-

Deformation properties of rock mass

In the empirical approach, characterisation of the rock mass quality was performed on borehole sections of 5 m in length (Glamheden et al. 2007). In order to determine the influence of scale, Glamheden et al. (2007) compared results of the rock mass quality characterised at 1 m and 5 m lengths (Bäckström and Lanaro 2007) and found that the difference in scale had an insignificant impact on the results.

The results from the empirical method in site-descriptive modelling stage 2.2 are in good agreement with corresponding results from modelling stage 1.2 (Glamheden et al. 2007). The difference in results between the empirical and theoretical approaches is also small, cf Section 6.4.6.

Fracture mechanical properties

Fracture samples for direct shear tests were meant to be collected at the same depth intervals as intact rock. However, the low fracture frequency at depth limited the possibility to collect appropriate fracture samples for testing (Glamheden et al. 2007).

It is recommended that the values from the direct shear tests, instead of the results from the tilt test, are used as they are based on direct measurements with stress magnitudes comparable to those found at repository depth at Forsmark (Glamheden et al. 2007).

The variability of selected samples is small and the increased number of tests between modelling versions 1.2, 2.1, and 2.2 has not changed the evaluated mean value significantly (Glamheden et al. 2007). Therefore the evaluated mean seems to be representative of the studied fractures and the number of tests seems to be sufficient (Glamheden et al. 2007). The number of tests in fracture domains FFM01 and FFM03 is larger than in the other domains, which implies that the uncertainty in these two fracture domains is smaller. No sample was taken from fracture domain FFM06, but visual inspection of the fractures in that fracture domain suggest that their properties are similar to those in fracture domain FFM01, see the **Site description Forsmark**.

However, it should be noted that the results presented by Glamheden et al. (2007) relate to specimens of 50–60 mm in size. Large-scale properties are likely to deviate from lab-scale properties. It is likely that the shear strength will be reduced in magnitude compared with lab-results (Glamheden et al. 2007). Furthermore, it is possible that the properties of large-scale fractures will differ between fracture sets, although no such differences were seen in the lab-scale tests (Glamheden et al. 2007).

In situ stresses

Estimates of the *in situ* stresses at repository depth have been made by Ask et al. (2007) based on results from hydraulic fracturing and hydraulic tests of pre-existing fractures (HTPF). Estimates have also been made by Martin (2007) based on results from overcoring data and indirect observations. There are large differences in predicted stress magnitudes based on the two methods. In the proposed stress model for the Forsmark site (Glamheden et al. 2007), data from hydraulic fracturing and HTPF measurements have been excluded for two reasons (Martin 2007).

- It is suspected that the hydraulic data does not measure the minimum horizontal stress, but instead the vertical stress component.
- The results do not indicate a thrust regime ($\sigma_H > \sigma_h > \sigma_v$) at Forsmark, which is not in agreement with the evaluated state of stress in the Fennoscandian shield.

The exclusion of hydraulic data from the stress model results in a more cautious estimate of the state of *in situ* stress, cf Table 6-43. The magnitude of the horizontal stress components in the stress model by Glamheden et al. (2007) are approximately twice as large as those of Ask et al. (2007).

The majority of the overcoring stress measurements carried out at depths between 150 m and 250 m were successful, whereas there are very few successful measurements below 250 m (Martin 2007).

No stress measurements have been carried out in fracture domain FFM06. However, the stresses are expected to be similar to those in fracture domain FFM01 (see the **Site description Forsmark**) as:

- The rock mass in both fracture domains have similar stiffness properties.
- Fracture domain FFM06 is located adjacent to fracture domain FFM01 below the gently dipping deformation zone ZFMA2.

Table 6-43. Comparison between stress magnitudes at 400 m and 500 m depth from two stress models based on 1) the overcoring method, indirect observations and numerical modelling (Glamheden et al. 2007) and 2) hydraulic fracturing and HTPF methods (Ask et al. 2007).

Stress model	σH (MPa)	σH, orientation (°)	σh (MPa)	σv (MPa)
Glamheden et al. 2007 (400 m)	38.7 ± 5.8	145 ± 15	20.4 ± 5.1	10.6 ± 0.2
Ask et al. 2007 (400 m)	19.2 ± 0.7	124 ± 6	9.3 ± 1.1	10.4
Glamheden et al. 2007 (500 m)	41.0 ± 6.2	145 ± 15	23.2 ± 4.6	13.3 ± 0.3
Ask et al. 2007 (500 m)	22.7 ± 1.1	124 ± 6	10.2 ± 1.6	13.0

Evolution of stress additions during glacial cycle

Due to practical reasons, the evolution of stress additions during a glacial cycle has been partly based on ice sheet modelling results of SR-Can. The corresponding results for SR-Site are found in Section 7.1.10. There is no reason to believe that future ice sheets will be fundamentally different from previous Late Pleistocene Fennoscandian ice sheets (Lund et al. 2009). In the reference scenario of SR-Can (SKB 2006c), the maximum thickness at Forsmark was around 3 km, cf Figure 6-25. Figure 6-34 shows estimates of the maximum ice sheet thickness for different climate scenarios in SR-Can. Based on modelling of the Saalian ice sheet, the maximum ice sheet thickness at Forsmark (supported by geological observations) was in SR-Can estimated to be 3 200 m; even for more extreme sensitivity cases it is unlikely to exceed 3 700 m (SKB 2006c). This corresponds to an increase in thickness by about 10–30 % compared with the reference case and an increase in vertical stress by about 2.6–8 MPa, as the vertical glacially induced stress reflects the ice load (e.g. Lund et al. 2009). Without explicit modelling work, it is difficult to estimate the impact on the magnitude of the horizontal stress components due to an ice sheet with larger thickness.

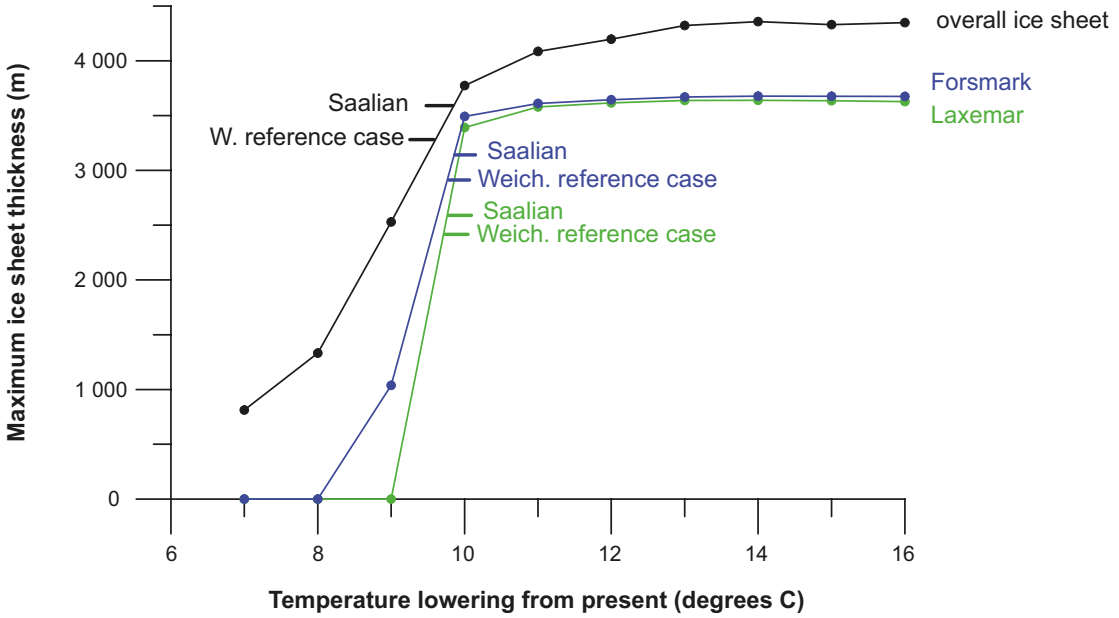

Figure 6-34. *Estimated maximum ice sheet thickness for different climate evolutions in SR-Can. Reproduced from SKB (2006c, Figure 4-32). Note that the corresponding figure for SR-Site is found in Section 7.1.10.*

Although Model 1 gave the best fit to GPS data (Figure 6-27, upper left), the deformation modulus is considered too high in the upper parts of the rock. Lund et al. (2009) choose Model T9 (horizontally stratified Earth model) as their preferred model in terms of fit to GPS data and sea level data and as its lithospheric elastic structure is in agreement with the Fennoscandian seismic investigation, cf Figure 6-35 (middle).

Although there are quantitative differences in resulting stress magnitudes between the Earth models, cf Figure 6-35, the temporal variations largely follow those of the ice model (Figure 6-25). By inspection of the stress results during the last glacial advance and retreat (without considering results from Model 1), the glacially induced stresses from the different Earth models appear to be within ± 10 MPa of those from Model T9. The glacially induced stresses at 500 m depth obtained from Model 1 are 50–90 % larger in magnitude during the second glacial maximum than the corresponding results from the other two models shown in Figure 6-35. The vertical stress is identical in all Earth models and reflects the ice load, that is the thickness of the ice sheet (Lund et al. 2009).

Stress-transmissivity relations

It should be noted that the stress-transmissivity relations become very uncertain as the effective normal stress approaches zero, that is when the transmissivity becomes indefinite. Close to the repository openings, local transmissivity increases could be significant, for example because of shear displacements along fractures in very low compression. However, it is judged that for fractures in compression of a few MPa, the stress-transmissivity relations are relevant as upper bound estimates of the sensitivity to variations in effective normal stress.

It can easily be shown that the sensitivity to variations in normal stress is greatest for a combination of low values of both *JKN* and *JEN*. The distribution of *JKN* values (obtained from Figure 6-30) is shown in Figure 6-36 (left). The values of *JKN* vary between 67 and 1 193 MPa/mm with a seemingly higher proportion of samples with values in the lower part of the range although the sample population is quite small (26 samples). However, the results shown in Figure 6-36 (right) suggest that the value of *JEN* increases with decreasing values of *JKN*.

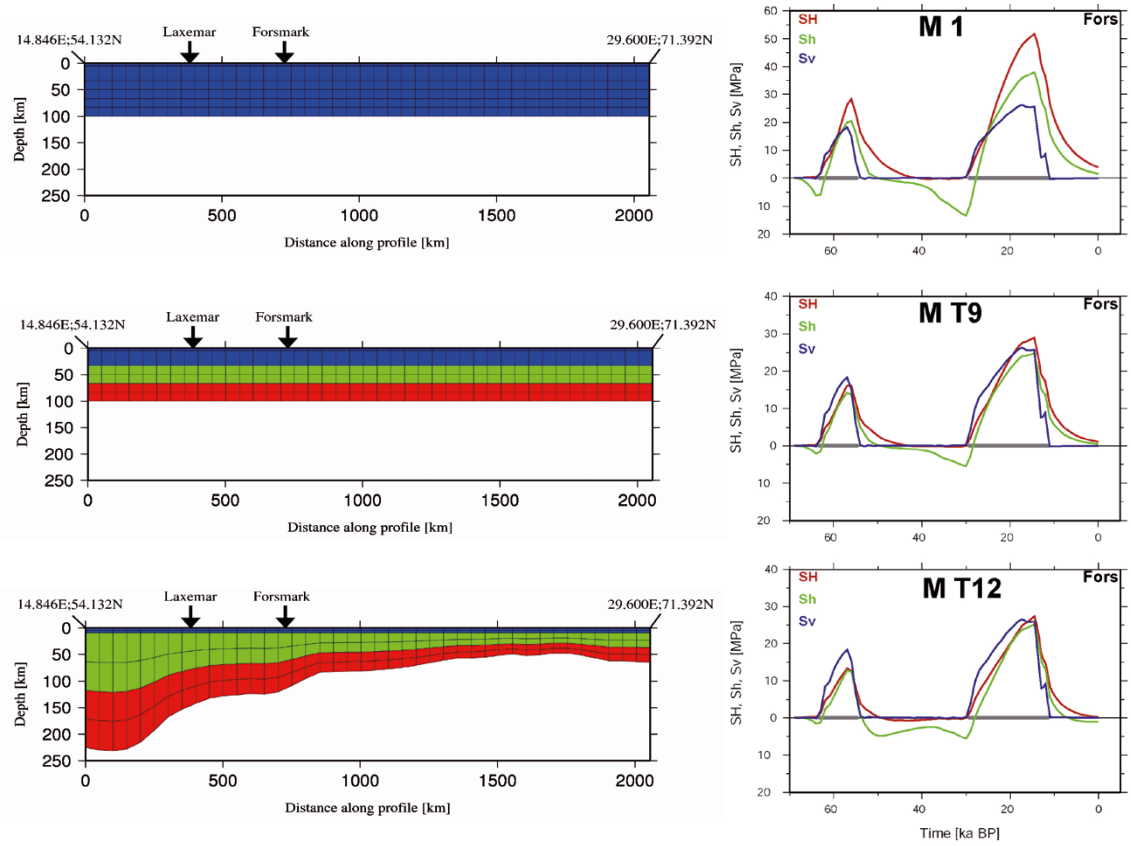

Figure 6-35. *Left: Schematic representation of Earth model. Right: Example of resulting glacially induced stresses at 500 m for each type of Earth model. Reproduced/excerpts from Lund et al. (2009, Figures 5-3 and 7-17).*

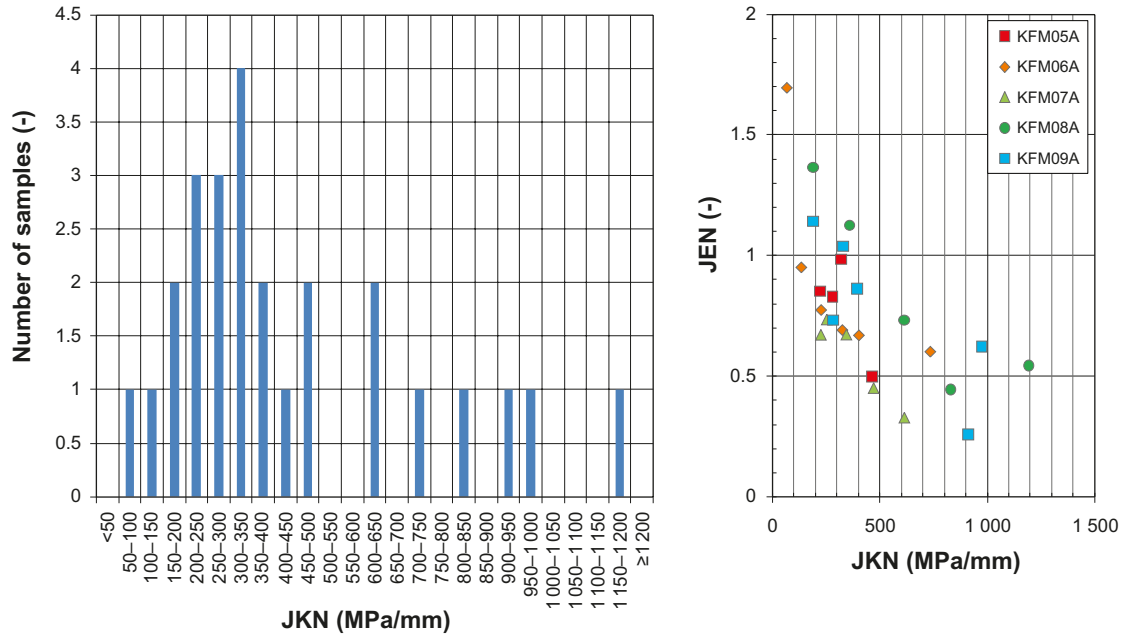

Figure 6-36. *Left: Distribution of JKN values obtained from the stress-stiffness estimates shown in Figure 6-30. Right: JEN as functions of JKN for each borehole in Figure 6-30.*

Figure 6-37 (left) shows examples of stress-transmissivity relations obtained from hydraulic jacking tests in borehole KLX02 at Laxemar. However, the injection tests were carried out near high-flow zones of the borehole (Rutqvist and Tsang 2008). Therefore, these stress-transmissivity relations may be representative of relatively permeable fractures (Rutqvist and Tsang 2008). For comparison, the stress-transmissivity relation used in SR-Can (Hökmark et al. 2006) in Figure 6-37 (right). Rutqvist and Tsang (2008) note that the stress-transmissivity relation used in SR-Can gave a similar response to variations in effective stress, in terms of relative changes from a given stress-level, as the fractures at 266 m and 267 m. A possible explanation for the sensitivity to variations in normal stress of the two fractures at 316 m and 336 m is that mineral filling would tend to clog the fractures at high normal stress (Rutqvist and Tsang 2008).

6.4.8 Spatial and temporal variability of data (text reproduced from SR-Site Data report)

Spatial variability of data

The rock in the candidate area at Forsmark is subdivided into rock domains and fracture domains as shown in Figure 6-38. Rock domain RFM029 is made up of Fracture domains FFM01, FFM02 and FFM03, whereas Rock domain RFM045 coincides with fracture domain FFM06 (Glamheden et al. 2007). The repository is located within fracture domains FFM01 and FFM06, see the **Site description Forsmark**.

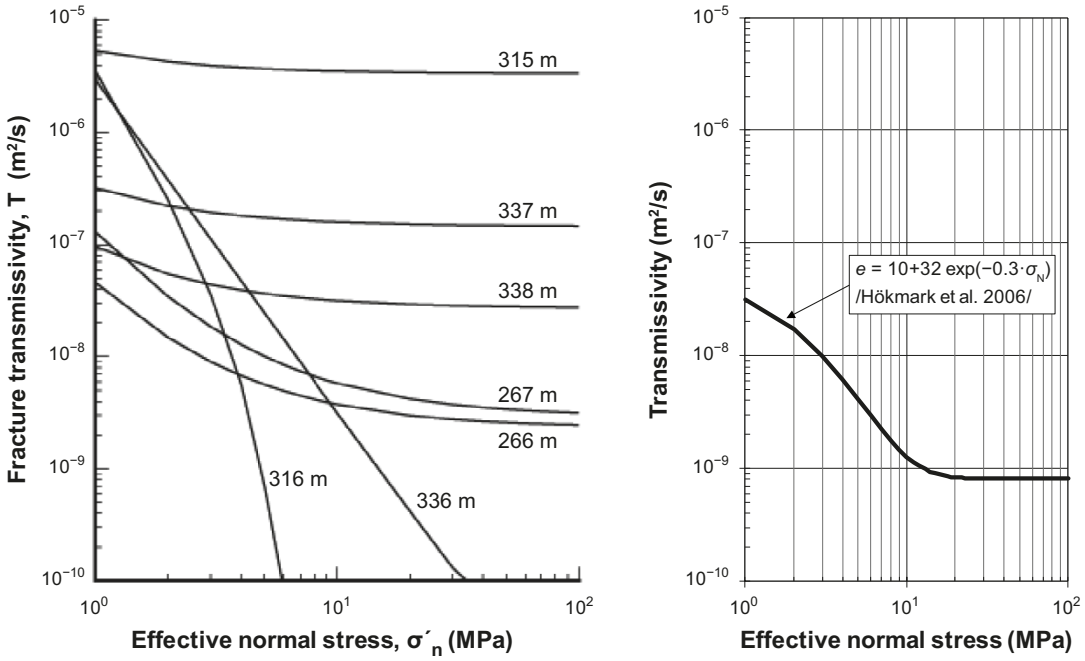

Figure 6-37. *Left: Example of stress-transmissivity relations estimated from hydraulic jacking tests in borehole KLX02 at Laxemar, from Rutqvist and Tsang (2008, Figure 5.1-3). Right: Stress-transmissivity relation based on the exponential expression suggested by Liu et al. (2003) used in SR-Can (Hökmark et al. 2006) (right).*

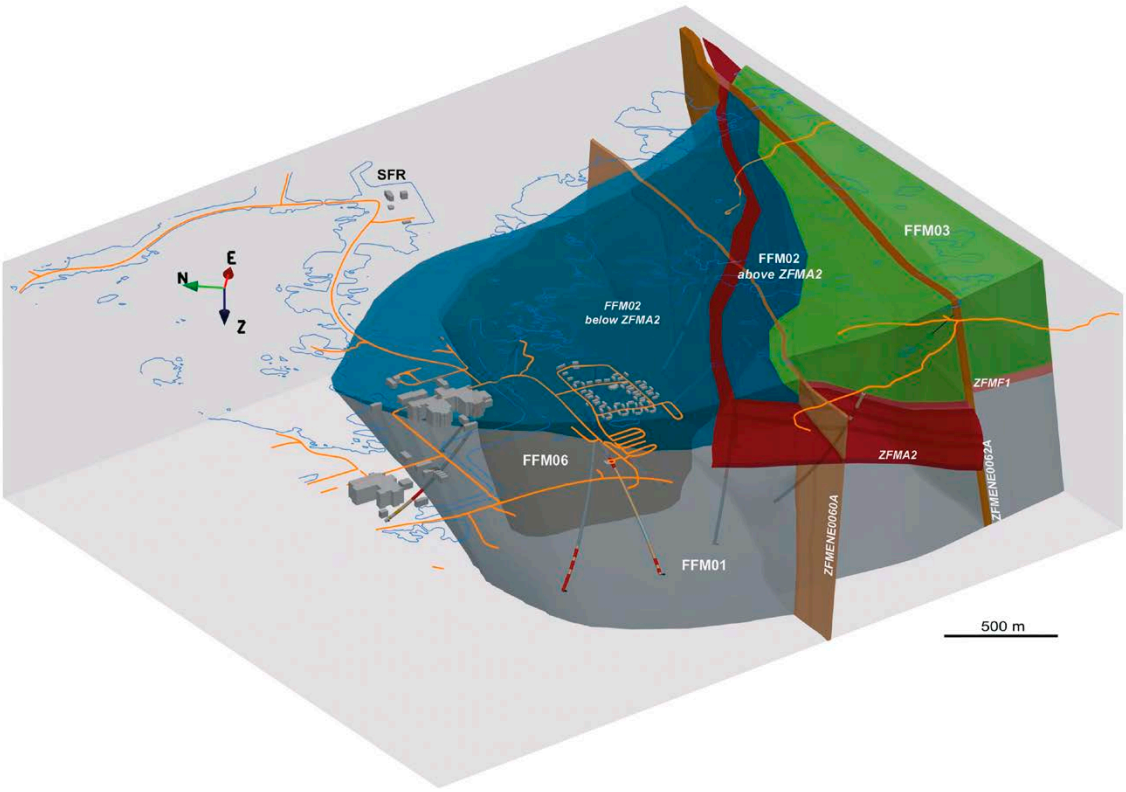

Figure 6-38. *Three-dimensional view to the East–North–East of the candidate area at Forsmark. Reproduced from Figure 5-4 of Olofsson et al. (2007).*

Deformation properties of intact rock

The mean value of Young's modulus (determined from uniaxial compressive tests) in rock domain RFM029 is about 75 GPa irrespective of rock type (Glamheden et al. 2007). For the rock types in rock domain RFM045, the mean value of Young's modulus varies between 80–83 GPa (Glamheden et al. 2007, 2008). A slight reduction in Young's modulus with depth can be observed in granite to metamorphic, medium-grained granodiorite (Glamheden et al. 2007). The reduction is most pronounced to a depth of 300 m. A similar trend was not observed in Poisson's ratio.

Geological features in the area seem to have little influence on the mechanical properties of intact rock (Glamheden et al. 2007). Laboratory results on samples obtained inside or in the near vicinity of deformation zones have property values in a similar range to those obtained outside the deformation zones. This indicates that the mechanical properties in the target area are stable and homogeneous. However, in the selection of specimens for mechanical testing, core sections containing sealed fractures or imperfections that were likely to shear during the test were avoided. Furthermore, several specimens were taken close to each other (Glamheden et al. 2007). The spatial variation must therefore be assumed to be greater than that predicted by the laboratory results (Glamheden et al. 2007).

Strength properties of intact rock

The main rock type (101057) shows a gentle trend of decreasing compressive strength with depth, see the **Site description Forsmark**. The reduction is in the range 10–15 % at depths larger than 500 m (Glamheden et al. 2007). However, this may be due to stress-induced micro-cracking during coring. Similar variations with depth are not found in any other rock types.

Stochastic modelling of the uniaxial compressive strength in rock domains RFM029 and RFM045 at Forsmark (Glamheden et al. 2008), cf Figure 6-39, showed that the spatial distribution of the *UCS* makes up a significant part of the total measured variability. However, the lower percentile estimates of the distribution are rather uncertain (Glamheden et al. 2008). As the spalling strength is expressed as a ratio of the uniaxial compressive strength, the spatial variability is likely to follow the distribution of the uniaxial compressive strength.

Deformation properties of the rock mass

The deformation modulus of the rock mass in rock domain RFM029, as determined by the empirical approach, cf Figure 6-38, varies between 59 GPa (FFM02) and 72 GPa (FFM01) (Glamheden et al. 2007). The rock mass of rock domain RFM045, that is fracture domain FFM06, have a deformation modulus of 70 GPa. Estimates of Poisson's ratio by use of the empirical method gives a value of 0.23 in both fracture domains FFM01 and FFM06. The variations of Young's modulus and Poisson's ratio between fracture domains FFM01, FFM02, FFM03 and FFM06 are shown in Figure 6-40.

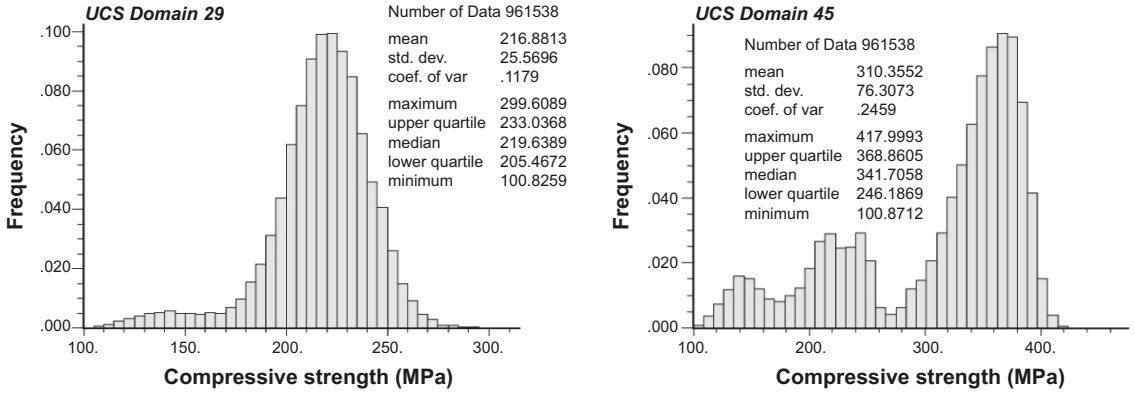

Figure 6-39. *Histograms of the compressive strength simulated at 1 m resolution in Rock Domain RFM029 (left) and RFM045 (right). Reproduced from Figures 3-5 and 3-6 of Glamheden et al. (2008).*

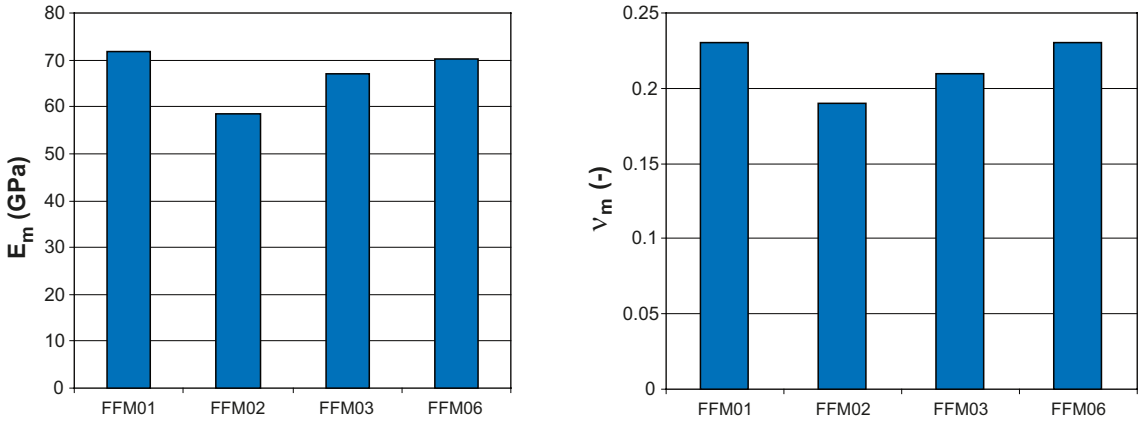

Figure 6-40. *Estimates of the rock mass deformation modulus (left) and Poisson's ratio by use of the empirical method in fracture domains FFM01, FFM02, FFM03, and FFM06, cf Figure 6-38. Reproduced from Figure 5-8 of Glamheden et al. (2007).*

Estimates of the rock mass deformation modulus and Poisson's ratio by use of the theoretical method is provided only for fracture domains FFM01 and FFM06 (Glamheden et al. 2007). The resulting values are 69 GPa and 0.24 (FFM01) and 68 GPa and 0.3 (FFM06), respectively (Glamheden et al. 2007).

Estimates of the spread in the deformation modulus due to variations of the Discrete Fracture Network (DFN) model were in the range 64–73 GPa (Glamheden et al. 2007), cf Figure 6-41 (left). Furthermore, Glamheden et al. (2007) evaluated the rock mass deformation modulus using 40 combinations of material properties randomly taken from the distribution of material data for intact rock and fractures. The influence of variations in material properties was found to be larger than variations due to different realisations of the DFN model. The resulting spread in the deformation modulus was 62–75 GPa, cf Figure 6-41 (right).

The rock mass quality in the target area appears to be of high and uniform quality (Glamheden et al. 2007). There is a slightly higher occurrence of high quality rock in rock domain RFM045 than in RFM029, but the difference is judged to be insignificant from a rock mechanics point of view (Glamheden et al. 2007). Sections with reduced rock mass quality coincide with regions of increased fracture frequency (Glamheden et al. 2007). Analyses of rock from adjacent rock domains show that the rock is of "good competent quality" (Glamheden et al. 2007). Fracture domains FFM01 and FFM06 therefore appear to have very similar mechanical properties, although the fracture density in fracture domain FFM06 is higher than in FFM01 (Glamheden et al. 2007).

Fracture mechanical properties

No clear variation with depth was observed in any of the mechanical properties of fractures (Glamheden et al. 2007).

A measure on the spatial variability was obtained by analysing the size of the statistical spread and comparing results from SDM modelling stage 2.2 with results from previous modelling steps; the small statistical spread and insignificant changes in parameter values between modelling steps indicate that the conditions are homogeneous (Glamheden et al. 2007).

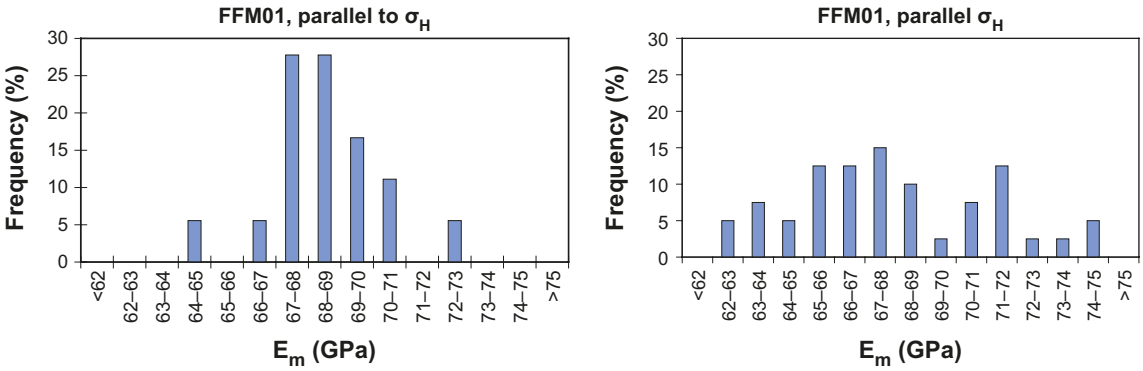

Figure 6-41. *Estimated spread in the evaluated deformation modulus due to the influence of the DFN model (left) and variations in material properties (right). Reproduced from Figure 5-13 of Glamheden et al. (2007).*

In situ stresses

As with the stress magnitudes, there is significant scatter of the orientations of the *in situ* stress tensor (Martin 2007). However, the trend of the major *in situ* stress (σ_1) seems to be consistent at all measured depth-intervals (Martin 2007), cf Figure 6-42.

Numerical modelling of the stress state indicates that the stress field in the target volume is relatively homogeneous (Glamheden et al. 2007). There is very little perturbation of the stress field due to steeply dipping deformation zones. However, the gently dipping deformation zone ZFMA2 perturbs all stresses in the rock mass above it. Results from the numerical modelling show that below ZFMA2 there is very little disturbance of the stress field (see the **Site description Forsmark**), although no successful stress measurements have been performed below ZFMA2 to corroborate this Martin (2007). The changes in horizontal stress with depth is thought to reflect the reduced frequency of open fractures and improved rock mass quality (Martin 2007).

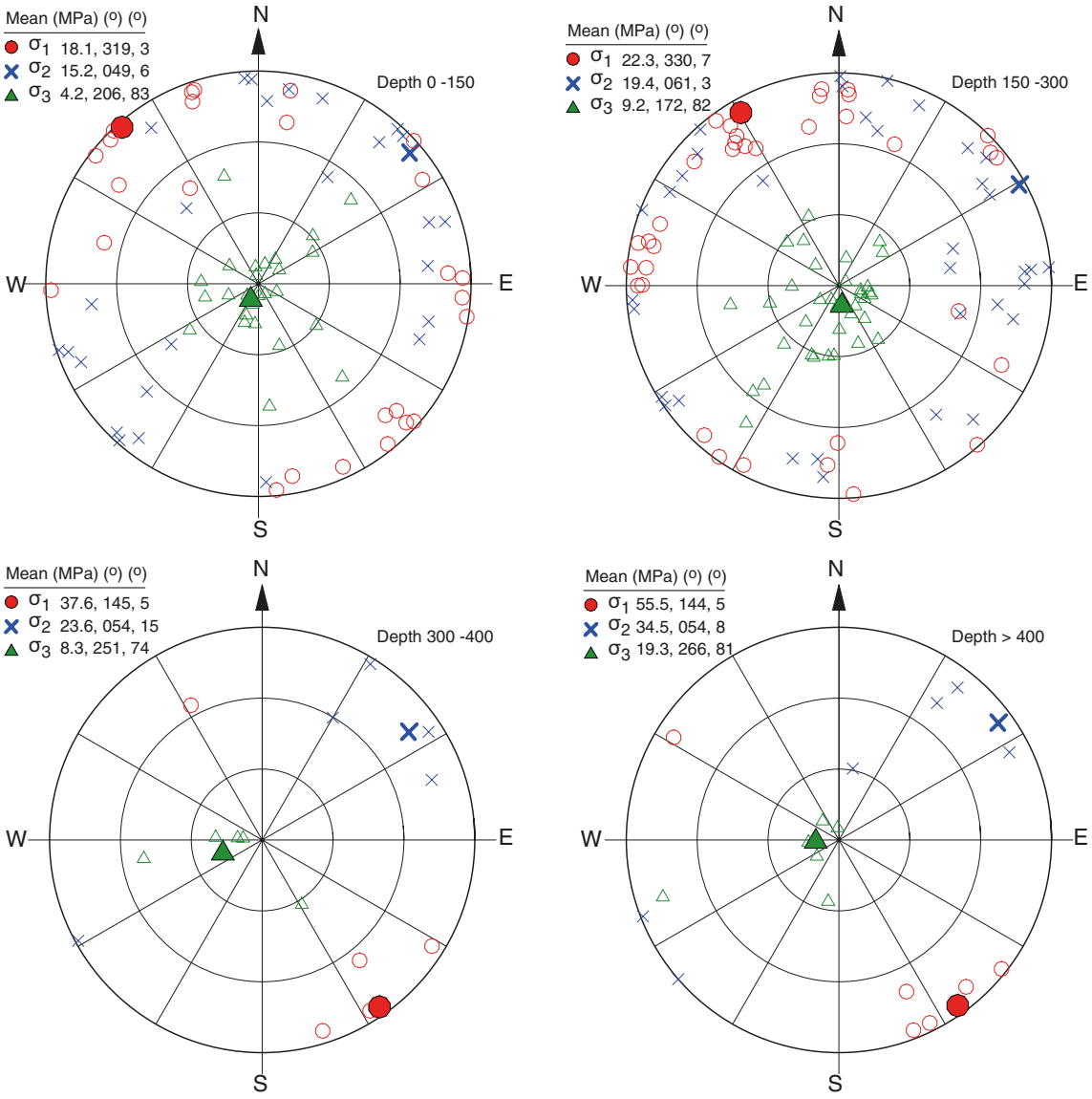

Figure 6-42. *Orientation of the mean stress tensor at four depth intervals based on all overcore measurements in the target area. Reproduced from Martin (2007, Figure 6-14).*

Furthermore, Glamheden et al. (2007) estimate the small scale spatial variations (denoted "local variability") caused by local fractures and material heterogeneities. In fracture domains FFM01 and FFM06 (150–600 m depth) the uncertainty due to local variability is estimated to 4–6 %, whereas in fracture domains FFM02 and FFM03 the corresponding range is 4–12 % (Glamheden et al. 2007). The uncertainty in the orientation of the major horizontal stress due to local variability is ± 3° (fracture domains FFM01 and FFM06) and ± 6° (fracture domains FFM02 and FFM03) (Glamheden et al. 2007). These uncertainties are included in the estimate of the total uncertainty (Glamheden et al. 2007).

Evolution of stress additions during glacial cycle

On a large scale, there are large spatial variations in ice thickness, cf Figure 6-43 (left). The spatial variations also vary with time. However, the ice model has a resolution of 50 times 50 km (Lund et al. 2009). Any lateral spatial variations of the glacially induced stresses at the Forsmark site are unlikely to be of any relevance.

Figure 6-43 (right) shows the temporal evolution (note that the time scale is reversed compared with previous figures) of the glacially induced stresses evaluated at two different depths: 500 m and 1.5 km. In this depth-range the variations with depth are insignificant.

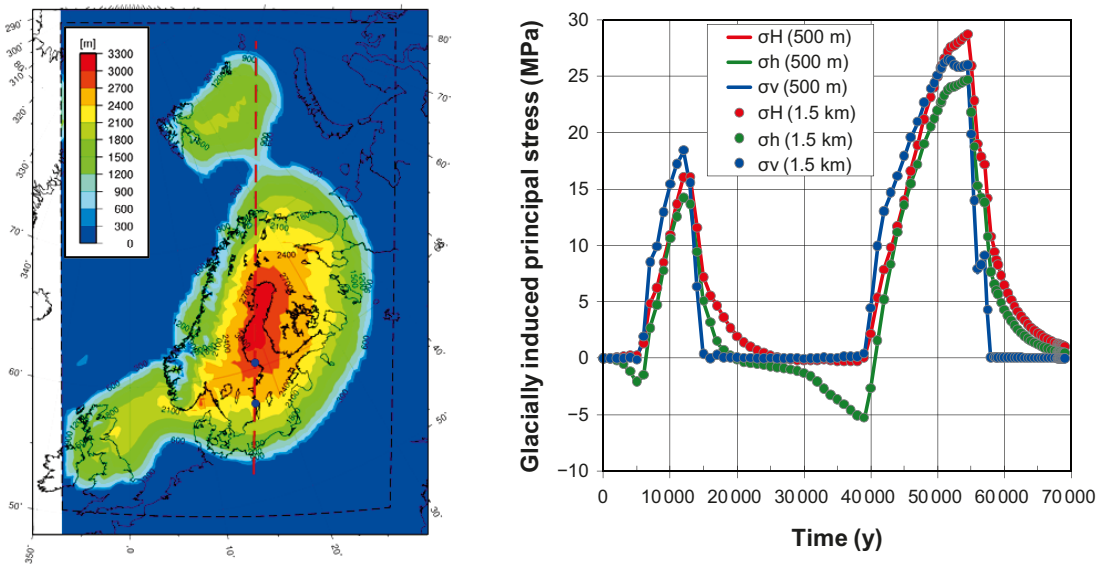

Figure 6-43. *Left: Height of the ice sheet at 18.4 kyr BP when the ice has its largest lateral extent, modified from Lund et al. (2009). Right: Temporal development of the glacially induced principal stresses at 500 m and 1.5 km depth at Forsmark, obtained from ice-crust-mantle analyses (model T9) performed by Lund et al. (2009).*

Stress-transmissivity relations

Figure 6-44 (left) shows values of *JKN* as functions of depth in boreholes KFM05A, -06A, -07A, -08A, and -09A. The depth is estimated from the average value of the upper and lower (Secup and Seclow) sampling depths (Jacobsson and Flansbjer 2005a, b, c, d, 2006). The right part of the figure shows the corresponding values of *JEN* as functions of depth. No clear trend with depth or between boreholes can be observed in the two parameters.

Chryssanthakis (2003a, b, 2004a, b, c, 2006) classified the samples in boreholes KFM01A, -02A, -03A/B, -04A, -05A, and -09A into three joint sets depending on the angle of intersection with the drill core.

- Steeply dipping fractures (set 1).
- Fractures dipping approximately 45° (set 2).
- Sub-horizontal fractures (set 3).

Figure 6-45 (left) shows measured values of *JRC* subdivided into the three joint sets for each borehole, whereas in the right part of the figure all measured *JRC* values are plotted as functions of depth. No clear trend with joint set, depth, or between boreholes can be observed.

Temporal variability of data

Deformation properties of the rock

Within the temperature range 0–150° the temperature dependence of elastic properties are negligible (Lau et al. 1991).

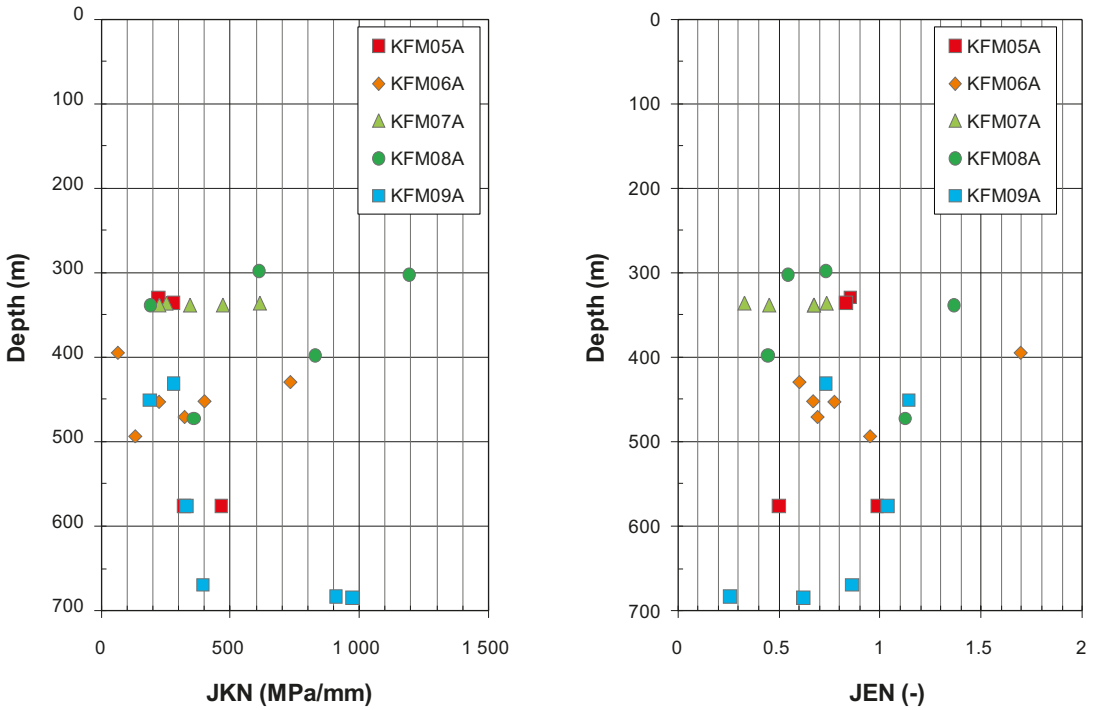

Figure 6-44. *Estimated values of JKN (left) and JEN (right) as functions of depth. Stress-stiffness data obtained from normal stress/normal deformation plots in Jacobsson and Flansbjer (2005a, b, c, d, 2006).*

The elastic properties are determined from uniaxial compressive tests at 50 % of the compressive strength (Glamheden et al. 2007). Examples of typical results from tests performed on granitic rocks are shown in Figure 6-46. Within the stress-range corresponding to 25–75 % of the compressive strength, the secant Young's modulus, and Poisson's ratio do not vary. This indicates that the elastic properties vary insignificantly with pressure for the stress variations (order of 30 MPa at maximum, cf Figure 6-43, right) projected to occur during the glacial cycle. Furthermore, the differences between deformation properties of intact rock and the rock mass are sufficiently small that any pressure dependence can be ignored. As the load is increased, the fractures will be compressed and the elastic properties of the rock mass properties will tend to resemble those of intact rock.

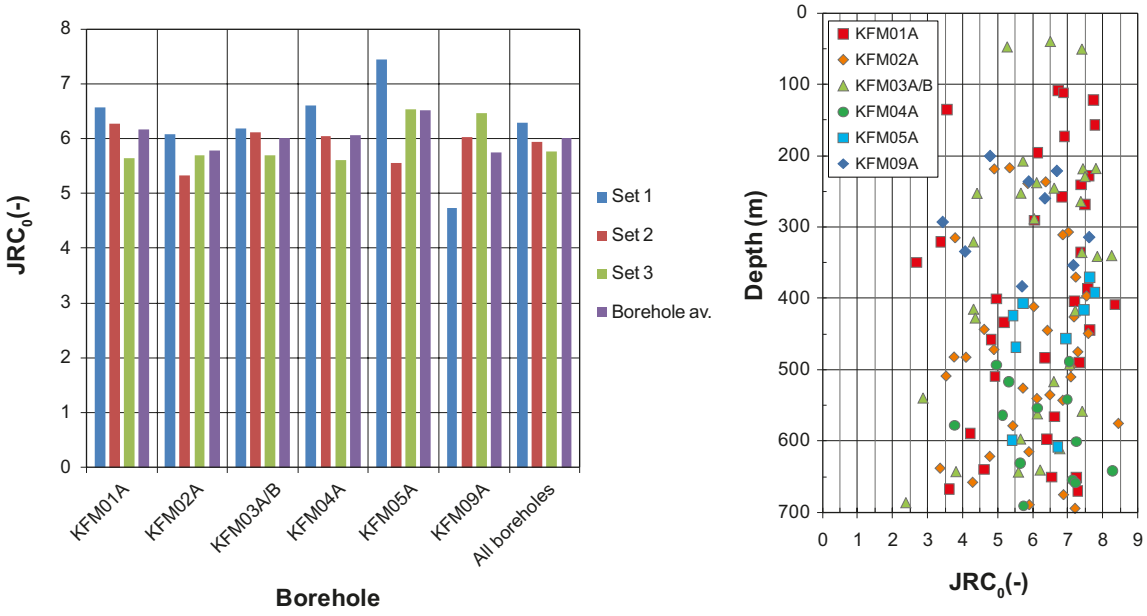

Figure 6-45. *Left: Mean value JRC subdivided into fracture sets for each borehole: Set 1 (steeply dipping fractures), set 2 (fractures dipping approx. 45°), set 3 (sub-horizontal fractures). Right: Joint roughness coefficient (at joint length tested) as functions of depth. Data for both figures compiled from appendices to Chryssanthakis (2003a, b, 2004a, b, c, 2006).*

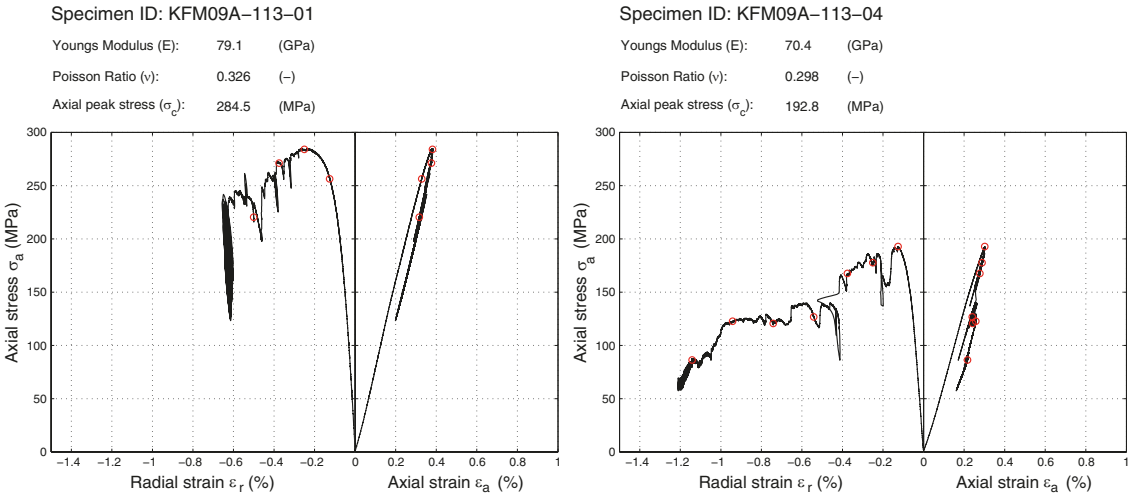

Figure 6-46. *Examples of stress-strain curves obtained from uniaxial compression tests on intact rock samples from borehole KFM09A at Forsmark. Reproduced from images in Jacobsson (2006, Section 5-1).*

Spalling strength

Damjanac and Fairhurst (2010) found that the long-term strength of intact rock without any pre-existing fractures should be equal to or greater than the crack initiation strength (40–60 % of the compressive strength).

Fractures

The fracture normal stiffness, K_N, is obtained from cyclic loading compression tests in which the joints are loaded and unloaded twice up to a normal stress of 10 MPa (or 20 MPa for samples from borehole KFM05A) (Glamheden et al. 2007). The results are presented as the secant normal stiffness evaluated between the unloaded state and full loading of the second load cycle. This quantity does not vary with time or load. However, in general the fracture normal stiffness varies with normal stress, for example as in Equation 6-6.

Direct shear tests were performed at three levels of normal stress, 0.5, 5, and 20 MPa (Glamheden et al. 2007).

- The fracture shear stiffness, K_S, is presented as the secant shear stiffness evaluated between 30 % and 50 % of the peak shear stress at each level of normal stress.
- The fracture dilation, ψ, angle is presented as the secant dilation angle at each level of normal stress.
- The shear strength of a fracture depends on the normal stress. The Mohr-Coulomb fracture strength properties (peak cohesion and peak friction angle/residual cohesion and residual friction angle) are determined by a least squares fit to the measured peak/residual shear stresses at the three levels of normal stress. The fracture cohesion and fracture friction angle do not vary with time or load.

In situ stresses

The present-day *in situ* stresses are taken to be representative of the long-term state of background stress in the Forsmark area. The changes in stress due to the still ongoing post-glacial rebound and the tectonic strain induced by the Mid-Atlantic ridge push (Muir Wood 1995) are significantly smaller in magnitude than the thermal stresses induced by the deposited spent fuel and stresses generated by the ice load during the subsequent glacial phase. Therefore any temporal variations in the *in situ* stresses are ignored.

Evolution of stress additions during glacial cycle

The temporal variations of the glacially induced stress additions 500 m below the ground surface at Forsmark are presented in Figure 6-43 (right). Although quantitatively the stress magnitudes depend on the Earth model, the temporal variations largely follow those of the ice model (Lund et al. 2009), cf Figure 6-25.

Stress-transmissivity relations

The stress-transmissivity relations give estimates of changes in transmissivity due to the loading and unloading of fractures that take place during the time-frame of the safety assessment. As there are no data to suggest otherwise, the stress-transmissivity relations are taken to be relevant for all repository phases, *i.e.* the excavation and operational phase, the initial temperate phase, the glacial phase and the permafrost phase.

6.4.9 Correlations (text reproduced from SR-Site Data report)

In situ stresses

A methodology for estimating the stress that depends on trends in the data has been developed by Martin (2007). It is based on the:

- Principal stress ratio (R): $\sigma_1/\sigma_2 = R$.
- Mean principal stress (M): $(\sigma_1 + \sigma_2 + \sigma_3)/3 = M$.
- Initiation for spalling expressed as a function of the Spalling Ratio (SR) and uniaxial compressive strength (UCS): $(3\ \sigma_1 - \sigma_2)/UCS \geq SR$.

As the vertical stress component can be calculated from the weight of the overburden (Martin 2007), the expressions for R and M (above) are sufficient to determine the horizontal stress components. The horizontal stress magnitudes in fracture domains FFM02 (0–150 m) and FFM01 (below 150 m) are estimated using R = 1.7, cf Figure 6-47 (lower right), and M = 12 MPa (150 m), 17.5 MPa (300 m) and 24 MPa (400 m), Figure 6-47 (lower left) (Martin 2007). The uncertainty in σ_h is correlated to the uncertainty in σ_H, such that the ratio σ_H/σ_h at repository depth is in the range 1.4–2.0 (Glamheden et al. 2007).

Hydraulic diffusivity

The hydraulic diffusivity (Itasca 2005b) is expressed in terms of the hydraulic conductivity (K) and the specific storage coefficient (S_S)

$$\kappa = \frac{K}{S_S} \qquad 6\text{-}11$$

where the specific storage coefficient is given by:

$$S_S = \rho \cdot g\left(\frac{n}{K_w} + \frac{(1-2\nu)(1+\nu)}{E(1-\nu)}\right) \qquad 6\text{-}12$$

Parameters and non site-specific parameter values are explained below. Site-specific parameter values are provided in Sections 6.4.10, 6.4.12 and 6.8.12.

- ρ is the density of water (1 000 kg/m^3), which is assumed to be pressure-independent.
- g is the acceleration due to gravity (9.81 m/s^2).
- n is porosity (–).
- K_w is the bulk modulus of water (2.2 GPa).
- E and ν are Young's modulus and Poisson's ratio of the rock mass, respectively.

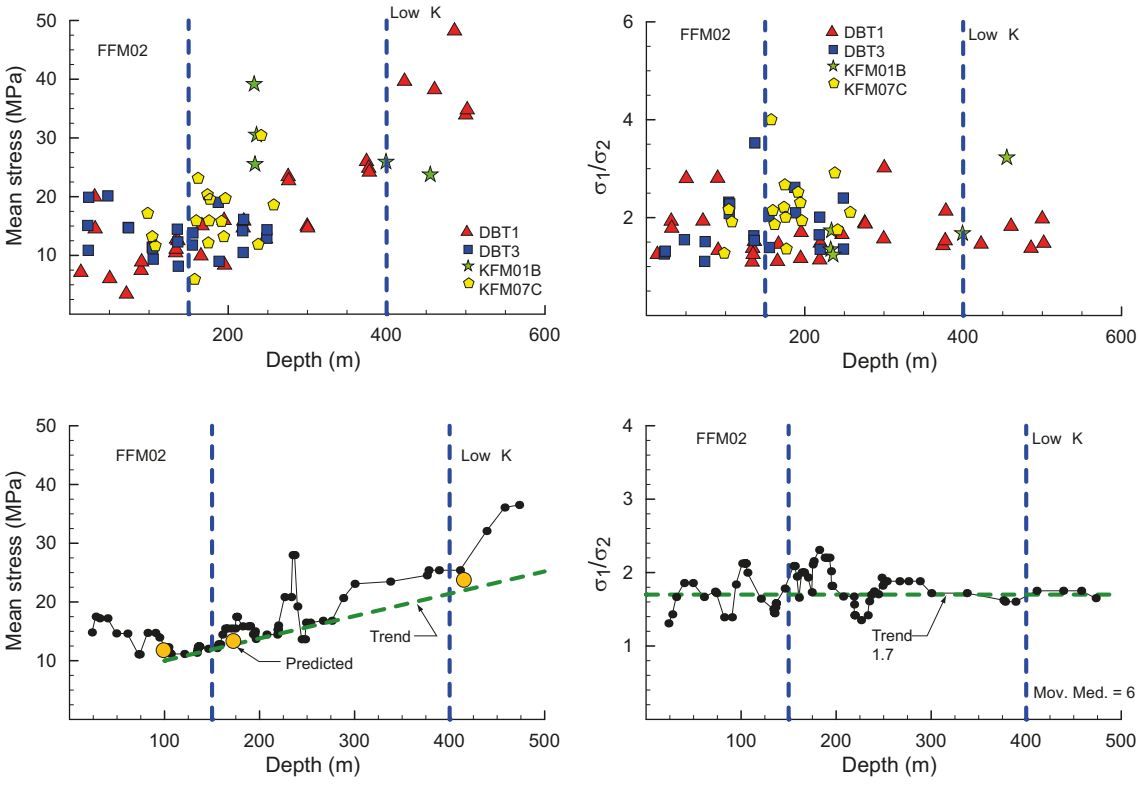

Figure 6-47. *Left column: Mean stress data (top) and mean stress using a data smoothing technique (bottom) as functions of depth. Right column: Principal stress ratio (top) and trend in principal stress ratio (bottom) as functions of depth. Reproduced from Martin (2007, Figures 6-4 and 6-6).*

6.4.10 Result of supplier's data qualification (text reproduced from SR-Site Data report)

The uncertainties associated with the mechanical properties of intact rock, rock mass, and fractures are expressed statistically as a range of variation in the evaluated mean values and quantified for a 95 % confidence interval according to the "Central Limit Theorem" (Glamheden et al. 2007). Minimum and maximum values are based on observed minimum/maximum values of the tested samples (Glamheden et al. 2007).

Deformation and strength properties of intact rock

Deformation and strength properties of intact rock within fracture domain FFM01 and FFM06 are given in Table 6-44. Young's modulus is given by the tangent modulus evaluated at 50 % of the compressive strength (Glamheden et al. 2007). Results are presented for the dominant and subordinate rock types in each fracture domain (see the **Site description Forsmark**), respectively.

- Granite to granodiorite, metamorphic, mediumgrained (101057) and pegmatite, pegmatitic granite (101061) in FFM01.
- More altered (albitized) variants of granite to granodiorite, metamorphic, mediumgrained (101057) and granite, metamorphic, aplitic (101058) in FFM06.

Table 6-44. Deformation and strength properties of intact rock in FFM01 and FFM06. Data from the Site description Forsmark.

Parameter	Unit	FFM01 101057	FFM01 101061	FFM06 101057	FFM06 101058
		Mean/std dev Min–max *Uncert. of mean*	Mean/std dev Min–max *Uncert. of mean*	Mean/std dev Min–max *Uncert. of mean*	Mean/std dev Min–max *Uncert. of mean*
Young's modulus (*E*)	GPa	76/3 69–83 *± 1 %*	74/4 69–80 *± 3 %*	80/1 78–82 *± 1 %*	83/3 80–86 *± 3 %*
Poisson's ratio (*v*)	-	0.23/0.04 0.14–0.30 *± 4 %*	0.30/0.03 0.26–0.35 *± 5 %*	0.29/0.02 0.26–0.31 *± 4 %*	0.27/0.03 0.25–0.31 *± 8 %*
Uniaxial compressive strength (*UCS*)	MPa	226/29 157–289 *± 4 %*	214/32.8 158–266 *± 8 %*	373/20 338–391 *± 3 %*	310/58 229–371 *± 16 %*

Spalling strength

Spalling is assumed to occur when the tangential stresses around an opening reach a certain fraction of the uniaxial compressive strength (*UCS*). Martin (2005) suggested a spalling strength of 57 ± 2 % of the *UCS* for coarse and medium grained crystalline rocks. Based on the estimates by Martin (2005) and values of the crack initiation stress presented in Figure 6-31, the spalling strength is assumed to be 57 ± 5 % of the *UCS*. Spalling strength of the dominating rock types in fracture domains FFM01 and FFM06 (cf Table 6-44) are presented in Table 6-45.

Table 6-45. Estimated spalling strength (57 ± 5 % of mean UCS) of the dominating rock types in fracture domains FFM01 and FFM06, cf Table 6-44.

Rock domain	Rock type	Spalling strength (MPa)
FFM01	101057	129 ± 11
FFM01	101061	122 ± 11
FFM06	101057	213 ± 19
FFM06	101058	177 ± 16

Deformation properties of the rock mass

Deformation properties of the rock mass in fracture domain FFM01 and FFM06 are presented in Table 6-46. The presented values are results from the 'Harmonisation' process of results from the empirical and theoretical approaches (Glamheden et al. 2007).

Table 6-46. Rock mass properties in fracture domains FFM01 and FFM06. Data from Glamheden et al. (2007).

Parameters	Unit	FFM01	FFM06
		Mean/std dev **Min–max** ***Uncertainty of mean***	**Mean/std dev** **Min–max** ***Uncertainty of mean***
Young's modulus (*E*)	GPa	70/8 39–79 *± 2 %*	69/12 40–81 *± 3 %*
Poisson's ratio (*v*)	-	0.24/0.03 0.12–0.33 *± 5 %*	0.27/0.04 0.12–0.37 *± 4 %*

Fracture mechanical properties

Note that no sample was taken from fracture domain FFM06, but visual inspection of the fractures in this fracture domain suggest that their properties are similar to those in fracture domain FFM01, see the **Site description Forsmark**.

Values of fracture peak and residual friction angles and fracture peak and residual cohesion based on results from direct shear tests in fracture domains FFM01, FFM02, FFM03, FFM04, and FFM05 (Glamheden et al. 2007) are presented in Table 6-47.

Values of the secant fracture normal stiffness and secant fracture shear stiffness evaluated at normal stress levels of 0.5 MPa, 5 MPa, and 20 MPa based on direct shear tests of fractures in fracture domains FFM01, FFM02, FFM03, FFM04, and FFM05 (Glamheden et al. 2007) are presented in Table 6-48.

Values of the secant fracture dilation angle evaluated at normal stress levels of 0.5 MPa, 5 MPa, and 20 MPa based on direct shear tests of fractures in fracture domains FFM01, FFM02, FFM03, FFM04, and FFM05 (Glamheden et al. 2007) are presented in Table 6-49.

Table 6-47. Fracture peak friction, fracture peak cohesion, fracture residual friction, and fracture residual cohesion based on results from direct shear tests of fractures in fracture domains FFM01, FFM02, FFM03, FFM04, and FFM05. Data from Glamheden et al. (2007).

Fracture domain	Peak friction, φ_p (°)	Peak cohesion, c_p (MPa)	Residual friction, φ_r (°)	Residual cohesion, c_r (MPa)
	Mean/std dev **Min–max** ***Uncertainty of mean***	**Mean/std dev** **Min–max** ***Uncertainty of mean***	**Mean/std dev** **Min–max** ***Uncertainty of mean***	**Mean/std dev** **Min–max** ***Uncertainty of mean***
FFM01	36.6/2.9 29.3–42.0 *± 2.9 %*	0.8/0.3 0.2–1.3 *± 13.7 %*	34.9/3.4 27.9–41.9 *± 3.6 %*	0.3/0.2 0.1–0.8 *± 24.3 %*
FFM02	36.4/2.5 34.4–40.0 *± 6.7 %*	0.5/0.4 0.2–1.0 *± 78.4 %*	34.8/7.3 24.1–40.3 *± 20.6 %*	0.4/0.6 0.1–1.3 *± 147.0 %*
FFM03	37.0/1.7 34.2–39.0 *± 3.0 %*	0.6/0.2 0.3–0.9 *± 21.8 %*	34.2/6.2 25.7–41.5 *± 11.8 %*	0.5/0.4 0.2–1.1 *± 52.3 %*
FFM04	32.0/3.3 28.5–35.0 *± 11.7 %*	0.9/0.4 0.6–1.4 *± 50.3 %*	32.2/2.5 29.6–34.6 *± 8.8 %*	0.3/0.1 0.2–0.4 *± 37.7 %*
FFM05	37.0/1.8 35.7–38.2 *± 6.7 %*	0.8/0.2 0.7–0.9 *± 34.7 %*	34.3/3.0 32.2–36.4 *± 12.1 %*	0.4/0.1 0.4–0.5 *± 34.7 %*

Table 6-48. Fracture normal stiffness and fracture shear stiffness evaluated at normal stress levels of 0.5 MPa, 5 MPa, and 20 MPa based on results from direct shear tests of fractures in fracture domains FFM01, FFM02, FFM03, FFM04, and FFM05. Data from Glamheden et al. (2007).

Fracture domain	Normal stiffness K_N (GPa/m)	Shear stiffness $K_{S0.5}$ (GPa/m)	Shear stiffness $K_{S5.0}$ (GPa/m)	Shear stiffness $K_{S20.0}$ (GPa/m)
	Mean/std dev Min–max *Uncertainty of mean*	Mean/std dev Min–max *Uncertainty. of mean*	Mean/std dev Min–max *Uncertainty of mean*	Mean/std dev Min–max *Uncertainty of mean*
FFM01	656/396 159–1 833 *± 22.0 %*	10/6 1–23 *± 21.8 %*	26/9 7–46 *± 12.6 %*	34/10 18–52 *± 10.7 %*
FFM02	248/165 115–483 *± 65.2 %*	8/4 4–12 *± 49.0 %*	26/4 21–31 *± 15.1 %*	33/8 25–41 *± 23.8 %*
FFM03	293/193 152–734 *± 43.0 %*	8/4 4–15 *± 32.7 %*	31/7 23–43 *± 14.8 %*	35/10 20–49 *± 18.7 %*
FFM04	1 385/283 1 072–1 624 *± 23.1 %*	8/6 1–12 *± 84.9 %*	16/5 12–22 *± 35.4 %*	23/5 18–29 *± 24.6 %*
FFM05	599/57 559–639 *± 13.2 %*	6/3 4–8 *± 69.3 %*	20/7 14–25 *± 48.5 %*	25/2 23–26 *± 11.2 %*

Table 6-49. Fracture dilation angle evaluated at normal stress levels of 0.5 MPa, 5 MPa, and 20 MPa based on results from direct shear tests of fractures in fracture domains FFM01, FFM02, FFM03, FFM04, and FFM05. Data from Glamheden et al. (2007).

Fracture domain	Dilation angle, $\psi_{0.5}$ (°)	Dilation angle, ψ_5 (°)	Dilation angle, ψ_{20} (°)
	Mean/std dev Min–max *Uncertainty of mean*	Mean/std dev Min–max *Uncertainty of mean*	Mean/std dev Min–max *Uncertainty of mean*
FFM01	14.6/4.1 7.8–27.1 *± 10.2 %*	7.7/2.7 2.5–13.7 *± 12.8 %*	3.2/2.1 0.2–9.6 *± 23.9 %*
FFM02	15.2/2.9 11.5–17.6 *± 18.7 %*	2.2/0.5 1.6–2.6 *± 22.3 %*	2.1/2.2 0.2–4.3 *± 102.7 %*
FFM03	16.4/2.2 14.0–20.2 *± 8.8 %*	3.1/2.1 0.5–6.3 *± 44.3 %*	2.3/1.7 0.2–6.1 *± 48.3 %*
FFM04	10.1/0.7 9.5–10.9 *± 7.8 %*	6.6/1.3 5.4–7.9 *± 22.3 %*	1.3/1.0 0.3–2.2 *± 87.1 %*
FFM05	14.7/0.4 14.4–15.0 *± 3.8 %*	8.8/0.1 8.7–8.8 *± 1.6 %*	2.3/0.5 1.9–2.6 *± 30.1 %*

In situ stresses

The stress model for Forsmark in fracture domains FFM01, FFM02, FFM03, and FFM06 is presented in Table 6-51 cf Figure 6-48. The major principal *in situ* stress (σ_1) appears to have only a very small plunge (approximately 5° (Martin 2007)), cf Figure 6-42. It is therefore judged that the stress components σ_H (major horizontal stress), σ_h (minor horizontal stress) and σ_v (vertical stress) can be approximated to be principal stresses, *i.e.* $\sigma_H = \sigma_1$, $\sigma_h = \sigma_2$ and $\sigma_v = \sigma_3$.

The uncertainty spans for the horizontal *in situ* stresses provided in Table 6-51 include uncertainties due to spatial variability (Glamheden et al. 2007). Note that the uncertainty in σ_h is correlated to the uncertainty in σ_H. The ratio σ_H/σ_h, at repository depth, is expected to lie between 1.4 and 2.0 (Glamheden et al. 2007).

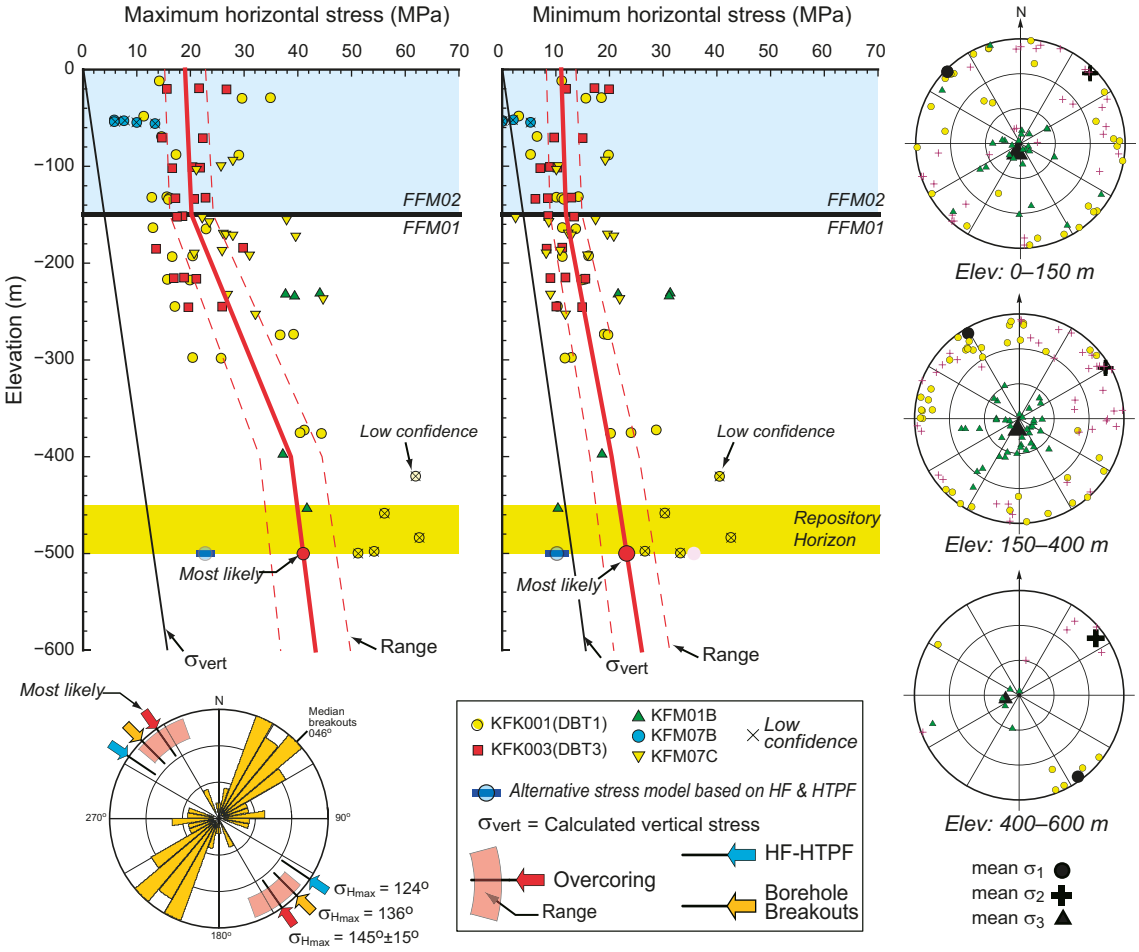

Figure 6-48. *In situ stress model for fracture domains FFM01 and FFM02, cf Table 6-51, with measurement data. Reproduced from Figure 7-18 of Site description Forsmark.*

The vertical stress is assumed to be equal to the weight of the overburden and is calculated using a generic value of the rock mass density, cf Table 6-50. The uncertainty span for the vertical stress given in Table 6-51 reflects the variability associated with the rock mass density (Martin 2007).

In the stress calculations the generic rock mass density shown in Table 6-50 has been used. This density is consistent with site-specific values given in Stephens et al. (2007, Table 3-4).

A 'Proposed Maximum Stress Model'(SKB 2009d), valid at repository depth, is provided in Table 6-52. Note that the stress magnitudes provided in the table should only be used to assess the risk of spalling due to elevated stress magnitudes at repository level (SKB 2009d).

Table 6-50. Generic rock mass density used to estimate the vertical stress gradient. This value is consistent with the densities of the most common rock types in rock domains RFM029 and RFM045 given in Stephens et al. (2007).

Parameter	Unit	Value
Density (ρ)	kg/m^3	2 700

Table 6-51. Stress models for domains FFM01, FFM02, FFM03, and FFM06 at Forsmark (Glamheden et al. 2007).

Domain	*σH* (MPa)	*σH*, orientation (°)	*σh* (MPa)	*σv* (MPa)
FFM01 and FFM06 (150–400 m)	9.1 + 0.074z ± 15 %	145 ± 15	6.8 + 0.034z ± 25 %	0.0265z ± 2 %
FFM01 and FFM06 (400–600 m)	29.5 + 0.023z ± 15 %	145 ± 15	9.2 + 0.028z ± 20 %	0.0265z ± 2 %
FFM02 (0–150 m)	19 + 0.008z ± 20 %	145 ± 15	11 + 0.006z ± 25 %	0.0265z ± 10 %
FFM03	5 + 0.075z ± 20 %	145 ± 15	2.5 + 0.0375z ± 25 %	0.0265z ± 10 %

Table 6-52. Proposed Maximum Stress Model for the repository elevation –450 to –475 m (SKB 2009d).

Depth range (m)	*σH* (MPa)	*σH*, orientation (°)	*σh* (MPa)	*σh*, orientation (°)	*σv* (MPa)
450–475	56 ± 6	145 ± 15	35 ± 8	55	0.0265z ± 0.0005z

Evolution of stress additions during glacial cycle

Model T9, see for example Figure 6-35 (middle right), is the preferred model in terms of fit to GPS data, sea level data and as the lithospheric elastic structure is in agreement with Fennoscandian seismic investigations (Lund et al. 2009). The shear stresses in the vertical plane at 500 m depth can be shown to be negligible. Therefore, the glacially induced stress components (σ_H, σ_h and σ_v) presented at repository depth (here 500 m) in Figure 6-49 are principal stresses. Furthermore, the variations with depth in the upper 1.5 km of the rock are negligible, cf Figure 6-43 (right), this means that the stress additions can be approximated to be constant with depth in the upper 1.5 km of the rock.

Stress-transmissivity relations

For the modelling work in SR-Site, it is recommended that in addition to a stress-transmissivity model based on mean values of fracture normal stiffness data, a model with low values of *JKN* and *JEN* should also be considered. Mean values (and range in parameter values) for the CY model are presented in Table 6-53. By inspection of Figure 6-36 (right), the parameter combination *JKN* = 150 MPa/mm and *JEN* = 0.78 is judged to be sufficiently low. There are only small variations in the mean value of *JRC* between fractures sets (see Figure 6-45). It is therefore recommended that the mean value of *JRC* (6.0, cf Table 6-53) be used in the models.

The residual hydraulic aperture is taken to be the average hydraulic aperture at large depth. It is here set to 20 μm based on reported fracture transmissivities below 400 m depth in fracture domain FFM01 (Follin et al. 2007b), cf Figure 6-50.

Table 6-53. Model parameters for CY model (JKN and JEN) are derived from cyclic loading compression tests by Jacobsson and Flansbjer (2005a, b, c, d, 2006). Estimates of the joint roughness coefficient (JRC) at joint length tested are based on results from tilt testing by Chryssanthakis (2003a, b, 2004a, b, c, 2006).

Parameter	Mean	Min	Max
JKN (MPa/mm)	436	67	1 193
JEN (–)	0.78	0.26	1.69
JRC (–)	6.0	2.2	8.5

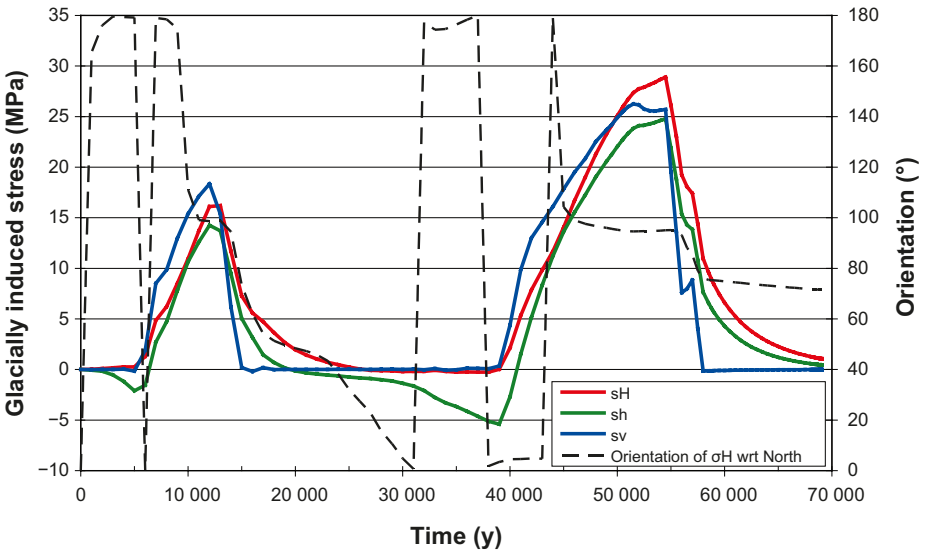

Figure 6-49. *Stress additions and orientation of the major horizontal stress at 500 m depth during the Weichselian glacial cycle obtained from of ice-crust-mantle analyses (Model T9) by Lund et al. (2009). Here, 0° represents North and 180° South.*

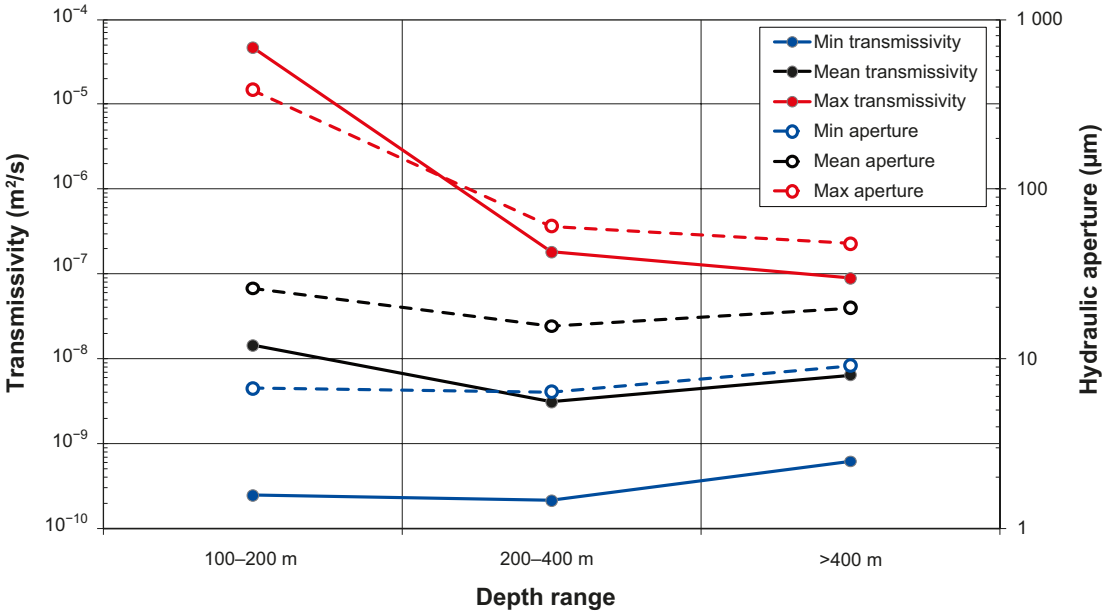

Figure 6-50. *Summary of fracture transmissivities at different depth intervals in fracture domain FFM01 (Follin et al. 2007b, Table 10-25). The corresponding hydraulic apertures are calculated from the transmissivity values through the cubic flow law.*

Figure 6-51 (left) shows the hydraulic aperture obtained by the CY model (Equations 6-7 and 6-8) using the two sets of fracture stiffness data described in the text above evaluated for the initial normal stress σ_0 set to the mean effective stress at repository depth (460 m), $\sigma_0 = (\sigma_H + \sigma_h + \sigma_v)/3 - p$, where σ_H, σ_h and σ_v are the three principal stress components and p is the hydrostatic pore pressure. The initial effective normal stress is here approximated to be 20 MPa based on the stress model by Glamheden et al. (2007), cf Table 6-51 (FFM01). For both sets of fracture stiffness data, an exponential fit (also shown in Figure 6-51, left) to the hydraulic apertures (Equation 6-9) has been made. In the right part of the figure, a comparison is made with the *in situ* stress-transmissivity correlation for Forsmark (Follin et al. 2008) and the stress-transmissivity relation used in the safety assessment SR-Can (Hökmark et al. 2006). The two models based on fracture stiffness data are more sensitive to normal stress variations than the most cautious *in situ* correlation (ZFM-PFL) reported for Forsmark. Parameter values for the two sets of data for the CY model and corresponding values for the exponential expression are presented in Table 6-54.

Table 6-54. Recommended parameter values for the CY model (Equations 6-7 and 6-8) based on 1) average fracture stiffness data, cf Table 6-53 and 2) based on lower bound fracture stiffness data (alternative data set described in the text) with corresponding parameter values for the exponential expression (Equation 6-9).

Model	Parameter	Average	Alternative
CY-model	*JKN* (MPa/mm)	436	150
	JEN (–)	0.78	0.78
	JRC (–)	6.0	6.0
	E_0 (µm)	42	42
Exponential expression	e_r (µm)	20	20
	e_{max} (µm)	13	42
	α (–)	0.13	0.15

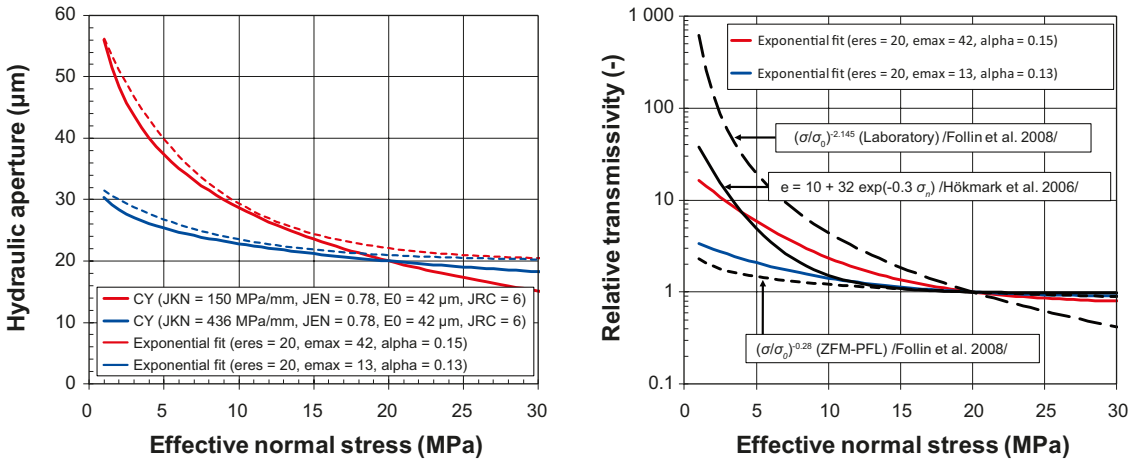

Figure 6-51. *Left: Hydraulic apertures calculated using the CY model (Equations 6-7 and 6-8) compared with exponential fits to the apertures (Equation 6-9), cf Table 6-54. Right: Comparison between in situ stress-transmissivity correlations given by Follin et al. (2008), stress-transmissivity relation used in the safety assessment SR-Can (Hökmark et al. 2006), and the exponential fits suggested in the left figure.*

6.4.11 Judgement by the assessment team

After SR-Site efforts have been carried out in different areas of rock mechanics to increase our knowledge of the fundamental processes and to reduce the uncertainty in key parameters.

Intact rock

No new insights or results have been obtained on the mechanical properties of the intact rock during SR-Site or during the ensuing work addressing review comments on SR-Site.

Fracture mechanical and hydro-mechanical properties

SKB has, in collaboration with Posiva and NWMO, participated in the POST project (Fracture parameterisation for repository design and post-closure analysis), which aimed to improve the knowledge on fracture shear behaviour. Conclusions and experience from the POST project with respect to fracture shear strength, based on laboratory tests, numerical simulations and shear tests on fractures in situ, are summarised in Siren et al. (2017) and references therein. The results indicate that the fracture shear strength values used in SR-Site are conservative.

Roughness Recently, Stigsson and Mas Ivars (2019) presented an improved procedure for estimating JCR (Joint Coefficient) based on a mapped fracture trace. However, the methodology has not yet been applied in the safety assessment framework for PSAR. It is expected to be applied in coming safety assessments.

Additionally, the effect of large-scale undulation on the shear mechanical behaviour of fractures has been studied (Lönnqvist and Hökmark 2015). The results indicate that the values used in SR-Site are conservative.

It is also noteworthy to mention that further field and laboratory studies related to fracture hydro-mechanical properties are presented in Thörn (2015). In this work, hydromechanically coupled experimental field and laboratory setups and methods were developed and used to improve a conceptual model of hydromechanical (HM) fracture behaviour at low compressive stress. Fracture stiffness calculated from the measurement of mechanical deformations and stiffness from hydraulic aperture changes were found to follow trends linked to the storativity of fractures reported in Fransson (2009), which was used in SR Site as support data.

Rock mass properties

A semi-analytical method for the estimation of rock mass mechanical properties based on effective medium theory is under development (Davy et al. 2018, Darcel et al. 2018). At the moment the method allows for stochastic predictions of rock mass elastic properties at different scales based on DFN realizations and combinations of intact rock and fracture mechanical properties under different stress conditions. The methodology is still under development and it is expected to be applied in coming safety assessments.

Stress conditions

Two projects concerning rock stress measurements have been carried out over the past years. The SLITS project (SLIm borehole Thermal Spalling) has developed a method for determination of the rock stress orientation (Hakami 2011) in boreholes. The method is based on inducing thermal stresses in a borehole until spalling occurs and, assuming correlation between the stress field and the induced fracture orientation, the maximum horizontal stress can be calculated. The second project (Hakala et al. 2013) has developed an LVDT (Linear Variable Differential Transformer) cell for rock stress measurement in existing tunnels and shafts. Verification measurements with an LVDT cell in the Äspö HRL at the 450-metre level, where the stress field is well-characterised, show that the results of the measurements with the LVDT cell agree with results from previous studies, which involved overcoring measurements, and with the previously developed stress model (Christiansson and Janson 2003). The newly developed stress measurement techniques are planned to be used during the construction and characterization of the deep repository for spent nuclear fuel.

Furthermore, an updated three dimensional stress model for estimating the spatial variability of the stress tensor, based on the current structural geology model (Stephens and Simeonov 2015), has been developed (Hakala et al. 2019). The updated three dimensional stress model has not yet been applied in the safety assessment framework for PSAR. It is expected to be applied in coming safety assessments.

It is also noteworthy to mention that Figueiredo et al. (2020) have applied the fully tensorial approach for the characterization of the stress variability newly developed by Gao and Harrison (2018a, b) to stress measurements from Forsmark and to numerical results from the three dimensional stress model reported in Hakala et al. (2019). This approach is being further developed and its application to the safety assessment will be reported in coming safety assessments.

Overall judgement

The increase in knowledge summarized above. is so far not fully implemented in relevant safety assessment calculation chains, and hence, the overall effects are not quantified in PSAR. The judgement is thus to use the same data in PSAR as in SR-Site. However, the newly gained knowledge will be implemented in coming safety assessments.

6.4.12 Data recommended for use in assessment

All data provided in Section 6.4.10 are recommended for use in assessment modelling. Reference parameter values for all models are given by the mean value of each parameter. To assess the influence of uncertainties, a small number of parameter values judged to represent the variability are selected and used in the modelling work. Note that the thermal and thermo-mechanical properties of the rock (i.e. thermal conductivity, Table 6-19, heat capacity, Table 6-22, and thermal expansion coefficient, Table 6-27) are described in Section 6.2. For the thermo-mechanical *3DEC* models, the value of the heat capacity is based on the dominating rock type in rock domain RFM029 obtained from stage 2.2 of the site-descriptive modelling for Forsmark (Back et al. 2007).

Mechanical properties of the rock mass

The mechanical properties of the rock mass at all three scales are provided in Table 6-55. It should be noted that here a generic rock mass density is given, which is consistent with site-specific densities. Parameter variations considered in the modelling work are listed in Table 6-56.

Table 6-55. Mechanical properties of the rock mass, cf Table 6-46.

Parameters	Large-scale	Medium-scale (FFM01)	Small-scale (FFM01/FFM06)
Generic density, ρ (kg/m^3)	2700	2700	2700/2700
Young's modulus, E (GPa)	70	70	70/69
Poisson's ratio, ν (–)	0.24	0.24	0.24/0.27

Table 6-56. Uncertainty spans for the mechanical properties of the rock mass, cf Table 6-46.

Parameters	Large-scale	Medium-scale	Small-scale (FFM01/FFM06)
Density, ρ (kg/m^3)	-	-	-/-
Young's modulus, E (GPa)	62–78	-	62–78/57–81
Poisson's ratio, ν (–)	0.21–0.27	-	-/-

Spalling strength

In the near-field spalling assessments, the spalling strength is assumed to be in the range 52–62 % of the uniaxial strength of the dominant rock type in each fracture domain, cf Table 6-57.

Table 6-57. Strength properties of intact rock, cf Table 6-44 and Table 6-45.

Parameter	Unit	FFM01	FFM06
Uniaxial compressive strength (*UCS*)	MPa	226	373
Spalling strength	MPa	118–140	194–231

In situ stresses

In situ stresses as function of depth for the large-scale modelling are provided in Table 6-58.

The most likely *in situ* stresses at repository depth (here 460 m) for the small- and medium-scale near-field modelling are provided in Table 6-59. Five additional stress states (labelled I–V) are also provided in the table to investigate the influence of uncertainties on the potential for spalling.

Table 6-58. In situ stresses as functions of depth for large-scale modelling. The orientation of the major horizontal in situ stress is given with respect to North, cf Table 6-51.

Depth range	σH (MPa)	σH, orientation (°)	σh (MPa)	σv (MPa)
0–150 m	19 + 0.008z	145	11 + 0.006z	0.0265z
150–400 m	9.1 + 0.074z	145	6.8 + 0.034z	0.0265z
400–1 000 m	29.5 + 0.023z	145	9.2 + 0.028z	0.0265z

Table 6-59. Most likely in situ stresses at repository depth (460 m) for small and medium-scale near-field modelling. Alternative in situ stresses (I–V) for small-scale near-field modelling. Stress states I–III are based on the uncertainty spans of the most likely stress model for Forsmark, cf Table 6-51. Stress states IV–V are based on the 'Proposed Maximum Stress Model', cf Table 6-52.

Description	σH (MPa)	σH, orientation with respect to north(°)	σh (MPa)	σv (MPa)
Most likely	40.08	145	22.08	12.19
I	40.08	130–160, largest possible deviation from tunnel axis	22.08	12.19
II	34.07	130–160, smallest possible deviation from tunnel axis	17.66	11.96
III	46.09	130–160, largest possible deviation from tunnel axis	26.50	12.42
IV	56.00	130–160, largest possible deviation from tunnel axis	35.00	12.42
V	62.00	130–160, largest possible deviation from tunnel axis	43.00	12.42

Fractures

The mechanical and Mohr-Coulomb strength properties of fractures are provided in Table 6-60. The fracture cohesion and fracture friction angle are obtained by taking the average value of their mean laboratory-determined peak and residual values. The fracture normal stiffness, fracture shear stiffness, and fracture dilation angle are represented by their mean laboratory determined values. The latter two values are obtained at a normal stress of 20 MPa.

Table 6-60. Fracture mechanical and Mohr-Coulomb strength properties, cf Table 6-47, Table 6-48 and Table 6-49.

Parameters	Large-scale	Medium-scale
Fracture cohesion, c (MPa)	0.5	0.5
Fracture friction angle, φ (°)	35.8	35.8
Fracture normal stiffness, K_n (GPa/m)	-	656
Fracture shear stiffness, $K_{s20.0}$ (GPa/m)	-	34
Fracture dilation angle, ψ_{20} (°)	-	3.2

Glacially induced stresses

The glacially induced stresses (in excess of the present-day *in situ* stresses) at five selected points in time during the glacial cycle are presented in Table 6-61. The stress magnitudes and orientations given in the table do not vary with depth in the upper 1 km of the rock.

Table 6-61. Glacially induced stresses (orientation is given with respect to North), cf Figure 6-49.

Time	σH (MPa)	σH, orientation (°)	σh (MPa)	σv (MPa)
First glacial maximum (12 kyr)	16.11	99	14.26	18.35
First retreat (15 kyr)	7.27	73	5.04	0.20
Forebulge (39 kyr)	0.02	3	–5.40	0.34
Second glacial maximum (54.5 kyr)	28.90	95	24.76	25.71
Second retreat (58 kyr)	10.95	76	7.64	–0.15

Stress-transmissivity relations

Two stress-transmissivity models (Models A and B) are chosen to estimate stress induced transmissivity changes based on the exponential relation suggested by Liu et al. (2003) (Equation 6-9) and the cubic flow law (Equation 6-10). The parameter values for each stress-transmissivity model are given in Table 6-62.

Table 6-62. Parameter values for the exponential expression, Equation 6-9, cf Table 6-54.

Parameter	Model A	Model B
e_r (μm)	20	20
e_{max} (μm)	42	13
α (–)	0.15	0.13

6.5 Spalling and the excavation damaged zone

Repository induced damages to the rock mass affect the groundwater flow and, as a consequence, the solute transport in the fractured rock. Assessments of these rock damages, in terms of spalling and excavation damaged zone (EDZ), are therefore needed as input for the assessment of radiological risk associated with radionuclide transport from the repository. The input data considered in SR-Site are the resulting properties from these damages and alterations. These properties, in turn, are assessed from various sources and assessments, including detailed process modelling, as further described in this section.

The data presented in this section are used as input to Sections 6.6 and 6.7, and associated activities, discussing hydraulic properties of the rock and flow related migration parameters.

The PSAR is based on the same modelling of Spalling and excavation damage zone as SR-Site. In the following sections, the modelling strategy is described (Section 6.5.1) followed by an account of the experiences from the SR-Site safety assessment (Section 6.5.2). Since the PSAR is based on the same data as SR-Site, the data qualification (Sections 6.5.3 to 6.5.10) is reproduced from the SR-Site Data report. In Section 6.5.11 the formal judgement by the assessment team to use the qualified data is presented followed by Section 6.5.12 where the recommended data is presented.

6.5.1 Modelling (text reproduced from SR-Site Data report)

The excavation damaged zone is here defined as "the part of the rock mass closest to the underground opening that has suffered irreversible deformation where shearing of existing fractures as well as propagation and/or development of new fractures has occurred" (Bäckblom et al. 2004). In the SR-Site safety assessment, the concern is on the remaining impact from the tunnelling, that is after re-saturation, on the hydraulic properties. The EDZ basically originates from:

- Excavation damage (i.e. from the blasting or from a Tunnel Boring Machine, TBM, if this is used).
- The changes of the stress field and associated fracturing (spalling) and fracture dilation effects resulting from the changed stress boundary conditions compared to the undisturbed situation.

It should be noted that other definitions of the EDZ exist, but the one adopted here pragmatically focuses on the resulting impact on the rock – and not on the various causes for these impacts.

Defining the data requested from the supplier

Depending on the nature of the excavation damaged zone, the data which need to be supplied differ. If the excavation damaged zone is generally not connected on the tunnel scale:

- The absence of a connected EDZ should be justified based on experimental observations and data.

If the excavation damaged zone is connected on the tunnel scale, giving rise to altered hydraulic properties compared to the properties of the rock prior to construction, the following should be supplied:

- The axial transmissivity T (m^2/s) of the EDZ along the deposition tunnel, as averaged across the tunnel floor.
- The axial transmissivity T (m^2/s) of the EDZ along other tunnels and shafts, as averaged across the tunnel floor (and corresponding for shafts).

Concerning any volume around the deposition holes with altered hydraulic properties compared to the properties of the rock prior to construction (referred to as the spalled zone), the following should be supplied:

- The potential for spalling, with focus on the potential for thermally induced spalling.

If spalling occurs:

- The length L_{zone} (m) and location of the spalled zone along the deposition hole.
- The width W_{zone} (m), and thickness d_{zone} (m) of the spalled zone around the deposition hole.
- The tortuosity τ_y (–) and porosity ε_{zone} (–) of the spalled zone.
- The hydraulic conductivity K (m/s) of the spalled zones. If this conductivity cannot be shown to be small in relation to the transmissivity of the fracture intersecting the deposition hole, or if there is no fracture intersecting the deposition hole, it is sufficient to note that the hydraulic conductivity of the spalled zone is "high".

If no spalling occurs:

- The connected effective transmissivity T (m^2/s) of the deposition hole EDZ, integrated along the full length of the deposition hole wall, and as averaged around the hole. If no such fully connected zone would develop, arguments are needed to state this.

Modelling activities in which data will be used

The data will be incorporated in the groundwater flow models as well as in the migration models used in SR-Site. These models are further described in Section 6.6 regarding hydraulic properties of the rock, and in Section 6.7 regarding flow related migration parameters. The potentials for an EDZ and for spalling are implemented in the following manner:

- The groundwater flow simulations, using ConnectFlow (Serco Assurance 2005), implement the EDZ as a continuous fracture, with a prescribed transmissivity as input, under the floor of all deposition tunnels.
- The source term model, COMP23 (Cliffe and Kelly 2006) considers the possibility of an EDZ with enhanced transmissivity intersecting the upper part of the deposition hole and uses an equivalent flow rate Q2, see Section 6.7, to handle the release from the buffer into the EDZ.
- The far-field radionuclide transport model FARF31 (Norman and Kjellbert 1990, Elert et al. 2004) pessimistically neglects retention in the EDZ.
- For handling spalling in deposition hole walls, a special model was developed for use in SR-Can (Neretnieks 2006), with an additional equivalent flow rate due to the damaged zone caused by spalling. This model has been updated for use in SR-Site (Neretnieks et al. 2010). This model is used for solute transport both towards and from the canister.

6.5.2 Experience from SR-Site

Modelling in SR-Site

See previous section.

Condidions for which data were used in SR-Site

See previous section.

Sensitivity to assessment results

Spalling

The empirical evidence obtained from large scale field tests conducted before SR-Site and the analyses performed during SR-Site conclude that thermally induced spalling is likely to occur, but the counter pressure exerted by bentonite pellets in the slot between buffer and rock wall, may suppress the spalling, or at least keep the spalled slabs in place and minimise the hydraulic transmissivity of the spalled damage zone. The assessment of the impact of spalling demonstrates that spalling may increase the equivalent flow rate for the Q1 path by more than an order of magnitude and that this increase has essentially no impact on risk, since spalling will not affect the local Darcy flux in the case of advective conditions in the deposition hole or if the canister is damaged by a shearing fracture. Other exit paths than Q1 are not affected by spalling. Consequently, further progress in the actions to assess spalling is not critical to safety, but efforts to handle and mitigate thermally induced spalling should continue as this affects one of the safety functions.

New efforts in terms of theoretical, numerical and laboratory studies have been initiated since SR-Site to increase our fundamental knowledge about the spalling process and our capability to predict it.

A new type of laboratory test method to reproduce the spalling process in large core samples in a situation resembling the conditions in a deposition hole in hard rock has been demonstrated (Jacobsson et al. 2018). The crack initiation, crack coalescence and crack damage stresses representing various fracture stages were identified by using acoustic emission monitoring with source localization. The results showed that spalling chips were formed similar to those found in the field which indicates that the test is producing a realistic behaviour. This is valuable since there is a need for a method to determine the crack initiation and damage stress in rock in a controlled repeatable way as an alternative to difficult in situ experiments. The insight and results from this project are part of an ongoing PhD program and have not been used in PSAR. It is expected that they will be used in coming safety assessments.

An effort is being made to increase our theoretical understanding about the spalling process and to refine our capability to numerically simulate it. The latest advances are presented in Potyondy and Mas Ivars (2020) and Saceanu et al. (2020). This research effort is still ongoing and has not yet been used in the safety assessment framework for PSAR. It is expected to be used in coming safety assessments.

Excavation damaged zone

During SR-Site it was concluded that the current design premise requiring that excavation induced damage should be limited and not result in a connected effective transmissivity higher than 10–8 m^2/s along a significant part (i.e. at least 20–30 m) of the disposal tunnel and averaged across the tunnel floor, is adequate. It was also concluded that a more transmissive EDZ starts to affect risk, even though the impact is moderate.

There is ample evidence that a potential EDZ formed during excavation will be kept below the maximum allowed transmissivity as set out by the design premises, and data suggest that a continuous EDZ would not develop at all. It is also clear that further development of the methods to control the EDZ as well as demonstration of the reliability of these methods is needed.

After SR-Site, new insight and results related to excavation damage zone are presented in Ericsson et al. (2015). This project has developed equipment for hydraulic testing and outlined testing and analysis procedures that have provided data permitting the successful characterization of the hydraulic properties of the rock mass in the tunnel floor. Fracture transmissivity is high in the upper 0.1–0.4 m of the tunnel floor, especially in the inner part of each blast round due to the heavier charge weight in the bottom charge. The connectivity of the most transmissive fractures is short and is normally connected to the tunnel floor. The longest connectivity observed in this project was approximately 7 metres, and it is usually less than 3 m. The extensive investigations along 20 m of the TAS04 tunnel floor confirm the studies reported in Olsson et al. (2009) in another tunnel at the Äspö HRL, which has been used in SR-Site.

6.5.3 Supplier input on the use of data (text reproduced from SR-Site Data report)

The supplier broadly agrees with the handling of data in SR-Can. However, the following issues are recommended to be addressed in SR-Site:

- Further enhancing the experimental support for the possibility of excavating the tunnels such as no continuous EDZ develops.
- Reassessing the potential for thermally induced spalling based on the current understanding of the Forsmark site and assessing means of suppressing the spalling by the counter pressure from the bentonite pellets in the buffer.
- Using experimental data in support for the parameter values suggested for characterising the spalled zone.

It is noted that all these issues have been addressed.

6.5.4 Sources of information and documentation of data qualification (text reproduced from SR-Site Data report)

Sources of information

The main sources of information used in the data qualification of data on the EDZ and spalling are presented in Table 6-63.

Categorising data sets as qualified or supporting data

The qualified and supporting data sets are presented in Table 6-64. Comments regarding each item are given in Table 6-65. The following principles have been applied in this assessment:

- For obvious reasons there are no data from actually constructed tunnels at depth at the Forsmark site. However, it is judged that the phenomena of forming EDZ and spalling depends on general rock mechanics processes, which means that data obtained from other sites, such as Äspö HRL, are applicable.
- Data obtained from SKB reports being reviewed and approved in accordance with the SKB QA Plan, can a priori be regarded as qualified data. However, since the report by Bäckblom (2008) is a compilation of data from various sources of varying quality, data regarding EDZ in tunnels presented by Bäckblom may partly be considered to be supporting.
- The assessment on the EDZ in the SR-Site Underground opening construction report (SKB 2010f), is based on the findings by Ericsson et al. (2009), Glamheden et al. (2010). The conclusions reached have been reviewed and accepted by SKB's internal and external experts, and it is thus qualified from that respect.

Excluded data previously considered as important

No important data have been excluded from the analyses.

Table 6-63. Main sources of information used in data qualification for EDZ and spalling.

Underground openings construction report, 2010. Design, construction and initial state of the underground openings. SKB TR-10-18, Svensk Kärnbränslehantering AB.
Andersson J C, 2007. Äspö Hard Rock Laboratory. Äspö Pillar Stability Experiment, Final report. Rock mass response to coupled mechanical thermal loading. SKB TR-07-01, Svensk Kärnbränslehantering AB.
Bäckblom G, 2008. Excavation damage and disturbance in crystalline rock – results from experiments and analyses. SKB TR-08-08, Svensk Kärnbränslehantering AB.
Ericsson L O, Brinkhoff P, Gustafson G, Kvartsberg S, 2009. Hydraulic Features of the Excavation Disturbed Zone – Laboratory investigations of samples taken from the Q- and S-tunnels at Äspö HRL. SKB R-09-45, Svensk Kärnbränslehantering AB.
Glamheden R, Fälth B, Jacobsson L, Harrström J, Berglund J, Bergkvist L, 2010. Counterforce applied to prevent spalling. SKB TR-10-37, Svensk Kärnbränslehantering AB.
Hökmark H, Fälth B, Wallroth T, 2006. T-H-M couplings in rock. Overview of results of importance to the SR-Can safety assessment. SKB R-06-88, Svensk Kärnbränslehantering AB.
Hökmark H, Lönnqvist M, Fälth B, 2010. THM-issues in repository rock. Thermal, mechanical, thermo-mechanical and hydro-mechanical evolution of the rock at the Forsmark and Laxemar sites. SKB TR-10-23, Svensk Kärnbränslehantering AB.
Neretnieks I, Andersson J C, 2009. Characterisation of spalling fragments to obtain data for flow and transport in damaged zones. In Proceedings of the ISRM-Sponsored international symposium on rock mechanics: "Rock characterisation, modelling and engineering design methods" (SINOROCK 2009) held at the University of Hong Kong, China, 19–22 May 2009.
Olsson R, 1998. Mechanical and hydromechanical behaviour of hard rock joints. A laboratory study. PhD thesis. Department of Geotechnical Engineering, Chalmers University of Technology, Sweden.
Olsson M, Niklasson B, Wilson L, Andersson C, Christiansson R, 2004. Äspö HRL. Experiences of blasting of the TASQ tunnel. SKB R-04-73, Svensk Kärnbränslehantering AB.
Olsson M, Markström I, Pettersson A, Sträng M, 2009. Examination of the Excavation Damaged Zone in the TASS tunnel, Äspö HRL. SKB R-09-39, Svensk Kärnbränslehantering AB.

Table 6-64. Qualified and supporting data sets.

Qualified data sets	Supporting data sets
1. Occurrence, location, and extent of any volume around the deposition tunnels, and other tunnels, with altered hydraulic properties compared to the properties of the rock prior to construction: (Olsson et al. 2009, Figures 7-9 and 7-10), (Olsson et al. 2004), SR-Site Underground opening construction report (SKB 2010f).	6. Published data on characterisation of the EDZ in drilled and blasted tunnels (Bäckblom 2008, Table 3-3).
2. Connected effective transmissivity (m^2/s) along the deposition tunnel, or other tunnels, and averaged across the tunnel floor: (Olsson et al. 2009, Figures 7-9 and 7-10), (Ericsson et al. 2009, Chapter 4), SR-Site Underground opening construction report (SKB 2010f).	
3. Occurrence, location, and extent of any volume around the deposition holes, with altered hydraulic properties compared to the properties of the rock prior to construction: Chapters 8 and 9 in Hökmark et al. (2010), Glamheden et al. (2010), Andersson (2007).	
4. The connected effective transmissivity (m^2/s) integrated along the full length of the deposition hole wall and as averaged around the hole: (Bäckblom 2008, Table 3-3). SR-Site Underground opening construction report (SKB 2010f).	
5. Local hydraulic conductivity, tortuosity, porosity, and thickness of the spalled zones, if a spalled zone occurs: (Neretnieks and Andersson 2009, Glamheden et al. 2010).	

Table 6-65. Justifications to the sorting of items in Table 6-64.

1. **Olsson et al. (2009)** characterised natural and excavation induced fractures in rock blocks removed from a section of a tunnel wall at the Äspö HRL. Olsson et al. (2004) concerns assessment of excavation induced fractures at the TASQ-tunnel at Äspö HRL. Generally, the Underground opening construction report concludes that it is possible to control the excavation of a drilled end blasted tunnel such that excavation induced fractures would not form a continuous network. These reports, apart from Olsson et al. (2004), are reviewed and accepted according to the SKB QA-plan. Furthermore, it is judged that the work of Olsson et al. (2004) was carried with a similar quality as their later report. Thus data presented in these reports are judged to be qualified.

2. The excavation induced fractures in the rock side-walls characterised by **Olsson et al. (2009)** are dominantly radial and does not form a continuous network along the axial direction of the tunnel over any significant distance. Ericsson et al. (2009) performed laboratory permeability tests of the fractures in the rock blocks characterised by Olsson et al. (2009). By numerical analyses and analytical expressions, Hökmark et al. (2010) assess the change in fracture transmissivity due to the impact of changing mechanical loads. Generally, the Underground opening construction report concludes that it is possible to control the excavation of a drilled end blasted tunnel such that the excavation induced fractures would not form a continuous network. These reports are reviewed and accepted according to the SR-Site QA-plan and the presented data are thus judged to be qualified.

3. **Hökmark et al. (2010)** performed numerical analyses of the potential for, and the geometrical extension of, thermally induced spalling in deposition holes. Andersson (2007) presents the Äspö Pillar Stability Experiment (APSE) carried out to examine the failure process in a heterogeneous and slightly fractured rock mass when subjected to coupled excavation-induced and thermal-induced stresses. Glamheden et al. (2010) present a field experiment at Äspö HRL, where 0.5 m diameter boreholes are exposed to a thermal load, with and without a confining pressure. These reports, apart from Andersson (2007), are reviewed and accepted according to the SR-Site QA-plan. However, the work of Andersson (2007) was part of a doctoral dissertation and has been subject to an extensive scientific review. Thus data presented in these reports are judged to be qualified.

4. **Bäckblom (2008)**, Table 3-3 compiles published data on characterisation of the EDZ in mechanically excavated tunnels and boreholes. These data are judged to be of more controllable quality and are thus judged to be qualified.

5. **Neretnieks and Andersson (2009)** assessed the tortuosity of the spalled rock fragments obtained from spalling tests at the Äspö Pillar Stability Experiment (APSE) (Andersson 2007). Glamheden et al. (2010) performed hydraulic tests of the thermally spalled zones in one of their tests. These reports are reviewed and accepted according to the SR-Site QA-plan and the presented data are thus judged to be qualified.

6. **Bäckblom (2008)**, Table 3-3 compiles published data on characterisation of the EDZ in drilled and blasted tunnels. The data are of various origin and quality, and it is not evident that there is a clear separation between natural and induced fractures and are thus judged to be supporting.

6.5.5 Conditions for which data are supplied (text reproduced from SR-Site Data report)

The field data on the excavation induced fracturing (Olsson et al. 2009, Ericsson et al. 2009, Bäckblom 2008), concern conditions resulting after rock excavation. The field data on thermally induced spalling (Neretnieks and Andersson 2009, Glamheden et al. 2010) concern conditions after heating, with and without a small counter pressure on the rock wall.

The numerical results by Hökmark et al. (2010) relate to different conditions, ranging from the situation after excavation, assessing impact of the thermal load and assessing the impacts of the glacial loading cycle (with accompanying pore pressure variations and temperature reductions in combination with proglacial permafrost).

6.5.6 Conceptual uncertainty (text reproduced from SR-Site Data report)

Hökmark et al. (2010) base their spalling estimates on results from linear elastic models without considering the possibility that the counter pressure provided by the swelling buffer or pellet slot may be sufficient to prevent or limit the spalling process. Spalling is said to have occurred when the modelled tangential stresses in the walls of a deposition hole or deposition tunnel exceed the nominal spalling strength (52–62 % of the laboratory-determined uniaxial compressive strength, cf Section 6.4). In reality, the spalling strength will be "reached" rather than "exceeded" and thereafter, when the failure is in progress, the linear elastic models are not strictly valid (cf Hökmark et al. 2010). Therefore, the results can only be used to predict in which parts of the deposition holes or tunnel walls spalling may occur. The following sources of conceptual uncertainty have been identified:

- Exceeding the nominal spalling strength does not necessarily mean that spalling will occur. Hökmark et al. (2010) suggest that if the bentonite buffer has had time to take up water and begin to close the buffer-rock gap before the thermal stresses have reached levels that may initiate the spalling process, then the bentonite support pressure may be sufficient to prevent spalling or to limit the growth of failed rock regions. Cho et al. (2002) and Andersson and Eng (2005) have concluded that confining stresses in the order of tens of kPa are sufficient to control spalling.
- The shape and the size of the spalled zone cannot be assessed from the calculations performed by Hökmark et al. (2010). However, experience from the Äspö Pillar Stability Experiment (APSE) (Andersson 2007) indicates that the failures will be notch-shaped and that the notch will self-stabilize at some depth that depends on the stress that prevailed at the time of the failure. Once the notch is stable, subsequent increases in stress will not significantly increase the depth of the failure. The notch developed at APSE was typically 0.5 m wide and 0.1 m deep (Andersson 2007).

Changes in the hydraulic conditions of fractures intersecting the repository region result from variations in normal stress and shear displacements induced by the various load scenarios during the repository phases. Hökmark et al. (2010) estimate variations in transmissivity by applying stress-transmissivity relations derived for the Forsmark site (see Section 6.4 of this report) and results from laboratory-scale shear-flow tests of fracture samples in granitic rock (Olsson 1998) to the modelled fracture normal stresses and shear displacements. The following sources of conceptual uncertainty relating to the estimates of load-induced variations in fracture transmissivities have been identified:

- As noted in Section 6.4, the stress-transmissivity relations become very uncertain as the effective normal stress approaches zero, i.e. at which the transmissivity becomes indefinite. However, Hökmark et al. (2010) argue that, for fractures in compression of a few MPa, the stress-transmissivity relations are relevant as upper bound estimates of the sensitivity to variations in effective normal stress.
- According to Hökmark et al. (2010), there are no corresponding relations that describe transmissivity changes due to shearing. Hökmark et al. (2010) base their transmissivity estimates on results from coupled shear-flow tests on joint samples of *Ävrö granite* performed by Olsson (1998). Laboratory-scale experiments performed at low normal stress (e.g. Olsson 1998, Koyama 2007) indicate that significant increases in transmissivity occur for shear displacements exceeding a few millimetres. However, this transmissivity increase appears to be sensitive to variations in normal stress (Hökmark et al. 2010). Olsson (1998) demonstrated that raising the initial normal stress from 2 MPa to 4 MPa may suppress the potential transmissivity increase almost completely for shear

displacements of 4–5 mm. Hökmark et al. (2010) estimate that shear displacements exceeding about 4 mm that take place under low normal stress, e.g. close to the repository openings, may result in local transmissivity increases of between one and two orders of magnitude. Furthermore, Hökmark et al. (2010) argue that any transmissivity increase due to shearing that takes place under normal stress-levels greater than 6–7 MPa can be ignored. However, they emphasize that this is uncertain, as there are no field data to corroborate the assumption.

6.5.7 Data uncertainty due to precision, bias, and representativity (text reproduced from SR-Site Data report)

Data uncertainty due to precision

The extent of the EDZ around the tunnels excavated using careful drill-and-blast techniques at Äspö HRL was found to vary from a few cm to a few tens of cm (Ericsson et al. 2009). Ericsson et al. (2009) observed a distribution of discontinuous fractures and microcracks and a slightly increased matrix porosity within this zone. Given the heterogeneous nature of this zone it is difficult to know if the transmissivity values reported by Ericsson et al. (2009) for the fractures in individual cored samples taken from this zone are representative, or represent an upper bound value. In addition the transmissivity values of the very small discontinuous fractures were not measured. The precision of the reported transmissivity values of the individual fractures is judged to be adequate but may overestimate the transmissivity of the EDZ and may hence not be representative.

Hökmark et al. (2010) considers a number of cases regarding magnitudes and orientations of the *in situ* stresses and variations in the thermal properties of the rock (cf Section 6.4 of this report). Results from all models indicate that spalling during the excavation and operational phase would not take place other than by exception. For the heated phase of the initial temperate period, the results predict that there will be thermally induced spalling in the majority of the deposition holes (cf sections on conceptual uncertainty and spatial variability). However, the extent of the spalling along the deposition hole wall depends on the assumed state of *in situ* stress and the thermal, thermo-mechanical, and elastic properties of the rock. In terms of agreement with the results obtained from SR-Can (Hökmark et al. 2006), and the fact that models give similar results regarding the potential for spalling, precision is judged to be adequate.

For the estimates of transmissivity changes in the near-field, precision is judged to be poorer mainly based on the uncertainties relating to the stress-transmissivity relations (cf Section 6.4) and assumptions regarding transmissivity increases due to shearing (cf Section 6.5.6).

Data uncertainty due to bias

There is no known bias in the data characterisation by Olsson et al. (2009). The methodology developed for the fracture characterisation was specifically designed to eliminate the bias created by two-dimensional fracture mapping typically carried out in tunnels. Extracting large blocks and slicing the blocks into 10 cm slabs (see Figure 6-52) to develop a three-dimensional fracture pattern eliminated any mapping bias. The wire saw cutting of the blocks and their removal, and the slab cutting likely allowed closed fractures to open and caused some fractures to extend. Therefore the 3D mapped fractures likely overestimate the fracture pattern *in situ*. It is believed that they have carefully characterised all fractures in the excavated rock blocks and have created a new standard for fracture mapping in the EDZ. Any bias introduced by this new technique is judged to be very small.

Ericsson et al. (2009) used well-established laboratory methods to measure the transmissivity of discrete fractures. The bias associated with such laboratory techniques is not considered significant. The selection of fractures for testing can be biased since closed or partially closed fractures are not sampled. Therefore the fracture sampling produces a bias that results in upper bound transmissivity values. This bias is considered acceptable.

Glamheden et al. (2010) concluded that the hole scale used in CAPS project (Counterforce Applied to Prevent Spalling) was too small to be fully representative for the heterogeneous rock conditions encountered at Äspö. The depth of spalling is dependent on hole size, this means that the larger the hole, the greater the depth for given stress conditions, and therefore the conclusions by Glamheden et al. (2010) may be biased by this factor.

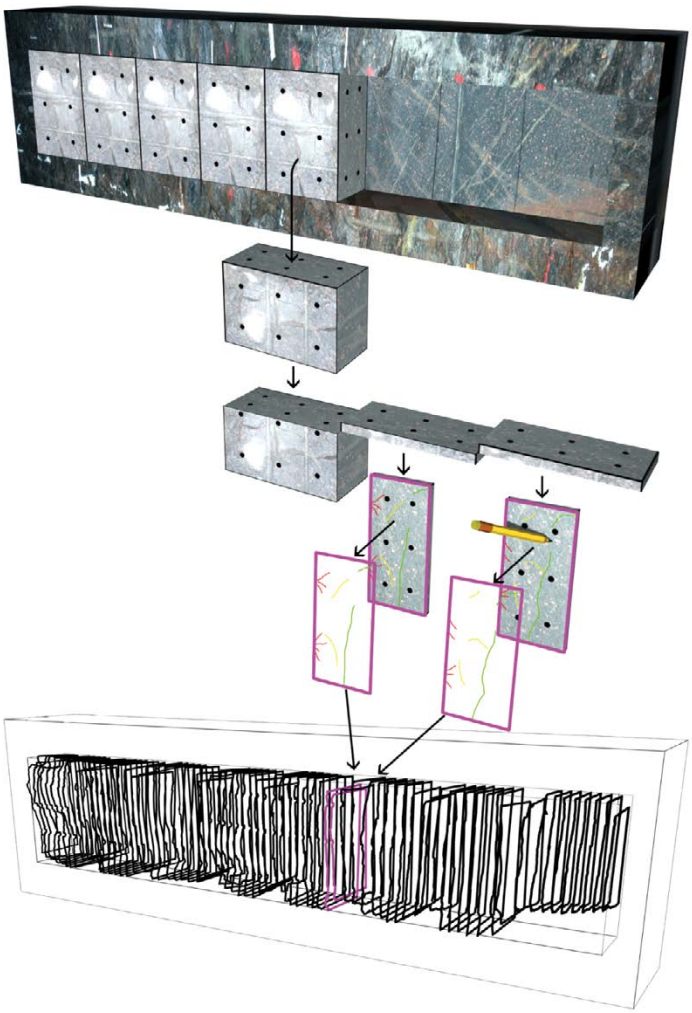

Figure 6-52. *Schematic view of the process of extracting blocks from the tunnel wall, sawing the block into slabs and making a digital 3D model of the tunnel. Reproduced from Olsson et al. (2009, Figure 4-6).*

CAPS hydraulic testing was carried out using standard testing procedures used for borehole testing. Complete saturation during testing could not be ensured. However, it is unlikely these conditions affected the conclusions by Glamheden et al. (2010) regarding the relative transmissivity of the spalled zone. The absolute transmissivity values for the spalled zone may be biased by the test conditions, but the uncertainties due to this bias are judged to be small.

The uncertainties due to bias associated with the numerical models analysed in Hökmark et al. (2010) are judged to be small. However, a potential source of bias relating to the modelling approach has been identified. Hökmark et al. (2010) assess the four repository phases (excavation and operation, heated phase of initial temperate period, permafrost, and glaciation) independently of each other, although in reality they will overlap:

- Hökmark et al. (2010) does not consider any potential thermo-mechanical effects due to already deposited canisters during the construction of the repository, that is the transition from *in situ* conditions to excavated state is assumed to take place in undisturbed rock. For the heated part of the temperate phase, all thermal and thermo-mechanical calculations are performed with the assumption that all canisters are deposited simultaneously. Hökmark et al. (2010) demonstrates that these approximations are valid, unless very specific deposition sequences are used, for example starting and finalising the deposition in neighbouring tunnels or very nearby deposition areas. In particular, the approach appears to be valid for the deposition sequence (Hansson et al. 2009) projected for the Forsmark repository.

- Hökmark et al. (2010) does not consider thermal stresses during the glacial phase. Hökmark et al. (2010) presents thermally induced rock stresses for the first 10 000 years of the heated period of the temperate phase. The authors show that, after 10 000 years, the stresses are within a few MPa of the present-day *in situ* levels. According to the Climate report for SR-Can (SKB 2006c, Figure 4-4), the next major glacial cycle is not projected to occur until about 50 000 years after repository closure. This is in line with the findings in SR-Site (cf Section 7.1). Therefore, it is judged that that the approach taken in Hökmark et al. (2010) is justified. Furthermore, Hökmark et al. (2010) assumes that the permafrost scenario coincides with the forebulge stress regime associated with the second major glacial advancement, that is the point in time with the greatest reduction in horizontal stresses. For the purpose of providing upper bound estimates of transmissivity increases for the permafrost phase, it is judged that the approach taken by Hökmark et al. (2010) is justified.

Data uncertainty due to representativity

The results documented in Olsson et al. (2009) were obtained from a tunnel excavation in fractured rock that utilised careful-blasting techniques. While the data produced by Olsson et al. (2009) represent conditions of a carefully blasted tunnel wall, it must be recognised that there are few as carefully conducted characterisations from other underground excavations. It has been demonstrated by Kuzyk and Martino (2008) that careful blasting techniques can essentially eliminate the connected fracture characteristics that are frequently associated with an EDZ created using traditional drill and blast techniques. Therefore, while the Olsson et al. (2009) data set is unique, it is believed that their findings are applicable to hard rock masses where careful blasting techniques are applied.

As already stated above, it is difficult to know if the transmissivity values reported in Ericsson et al. (2009) for the fractures in individual cored samples taken from this zone are representative, or represent an upper bound value. In addition the transmissivity values of the very small discontinuous fractures were not measured.

The spalling criteria and EDZ data have been obtained from Äspö HRL. The rock mass at Äspö HRL is considered typical of the rock masses found in Fennoscandia. The EDZ fracturing is composed of natural fracturing and excavation-induced fractures. The excavation-induced fractures are a function of the blast design and are hence controlled. The natural fractures are a characteristic of the rock mass and may locally vary. However, at the repository depth this variability is not judged to be significant. The spalling strength developed by Anderssson (2007) at Äspö HRL has been normalised to the laboratory uniaxial compressive strength, which has been measured for all the major rock types at Laxemar and Forsmark.

The results from the rock mechanics modelling performed by Hökmark et al. (2010) are based on idealised descriptions of the rock mass and fractures. The following issues have been identified to be contributing to the uncertainty due to representativity:

- Estimates of the spalling potential are based on results from linear elastic models (Hökmark et al. 2010) without considering structurally controlled failures. As part of the safety assessment SR-Can, Fälth and Hökmark (2007) found that slipping low strength-fractures intersecting the deposition hole tend to increase the tangential stresses between the intersection and the floor and to reduce them below the intersection. However, Hökmark et al. (2006, 2010) concluded that sporadic local, structurally controlled failures should not be considered important for the overall assessment of the spalling potential. This means that, for sparsely fractured rock, the linear elastic models analysed by Hökmark et al. (2010) are judged to be adequate.
- The parameter values chosen to represent the fracture properties are based on results of laboratory-scale tests (cf Section 6.4) and then applied to perfectly planar fractures with a radius of 50 m. Hökmark et al. (2010) states that the effects of large-scale undulations and in-plane asperities may prevent large shear displacements, which means that the largest shear displacements found in their analyses would potentially be overestimated. However, Hökmark et al. (2010) concludes that, for the purpose of obtaining realistic estimates of transmissivity changes due to shearing, this is not very important. Hökmark et al. (2010) founds that the largest shear displacements took place under normal stresses that are judged to be sufficient to suppress dilation and transmissivity increases, see Section 6.5.6.

6.5.8 Spatial and temporal variability of data (text reproduced from SR-Site Data report)

Spatial variability of data

The spatial variability of spalling and transmissivity changes depends mainly on the spatial variability of the thermal, thermo-mechanical, and mechanical properties of the rock and fractures. These variations are assessed in Sections 6.2 and 6.4 of this report. The following additional factors contribute to the spatial variability of the potential for spalling:

- With the exception of the uniaxial compressive strength of intact rock, no systematic large spatial variation in the rock mechanical or heat transport properties, which could have a significant impact on the modelled results, has been observed (cf Sections 6.2 and 6.4). Hökmark et al. (2010) found that the tangential stresses in the walls of the deposition holes are of a similar magnitude in both fracture domains considered for the location of the repository (FFM01 and FFM06), suggesting that the potential for spalling is significantly reduced in fracture domain FFM06. However, in the layout version considered by Hökmark et al. (2010) the majority of canisters (approximately 80 %) will be deposited in fracture domain FFM01.
- *Repository layout, that is tunnel orientation with respect to the major horizontal in situ stress:* It is well known that the tangential stresses in the walls of a deposition hole are minimised if the deposition tunnel is approximately aligned with the major horizontal *in situ* stress. In the layout version considered by Hökmark et al. (2010), the deposition tunnels deviate by 3–22° from the most likely orientation of the major horizontal *in situ* stress, which has a moderately large impact in terms of increasing the stresses around the tunnel (cf Figures 9-5, 9-6, and 9-9 in Hökmark et al. 2010)).
- *The location within the repository region (applies for the heated part of the temperate period):* Canister positions located near a tunnel end or beginning have lower temperatures than more centrally located canister positions (Hökmark et al. 2009). Consequently, the stresses in the walls of the former deposition holes would also be lower. However, the potential for spalling in the walls of such deposition holes has not been analysed by Hökmark et al. (2010). Furthermore, the thermally induced stresses around deposition holes located close to rejected canister positions will also be lower. For the purpose of providing upper bound estimates of the potential for spalling, Hökmark et al. (2010) assumes that no potential canister positions are rejected.

In addition to the spatial variations of the mechanical and hydraulic properties of the fractures, the spatial variations of transmissivity changes depend on the fracture orientations and proximity to, or intersections with, repository openings.

Temporal variability of data

With the exception of the glacially induced stress (and accompanying increase in pore pressure), the thermal, thermo-mechanical, and mechanical properties of the rock mass and fractures are assumed not vary with time (cf Sections 6.2 and 6.4).

The thermo-hydro-mechanical impact on the rock mass and fractures will vary with the induced loads during the different repository phases (Hökmark et al. 2010):

Excavation and operational phase

- *Transmissivity changes:* The range of the stress-induced hydraulic disturbance generated by the excavation is small and the results are independent of the size of the fractures that intersect the near-field.
- *Spalling potential:* Spalling in the walls of deposition holes during the construction and operational phase will occur only by way of exception.

Heated period of the temperate period

- *Transmissivity changes:* The thermal load, induced by the decaying spent fuel, will increase the compression of fractures of almost all orientations, possibly with exception for portions that are directly affected by the proximity to the repository openings. For horizontal fractures there is,

however, a modest loss of compression between tunnels in the early stages of the heated period. The magnitude of fracture shear displacements is only locally affected by the proximity to the repository openings.

- *Spalling potential:* The nominal spalling strength is likely to be exceeded in a large majority of the deposition holes at some point in time during the heated phase (see also sections on spatial variability). For a discussion on the temporal evolution of the spalled zone, see the Section 6.5.6.

Glacial and periglacial period

- *Transmissivity changes:* With the exception of the time-period leading up to a glaciation, during which the crustal flexure tends to reduce the horizontal stresses (forebulge), the compression of the rock increases during the glacial period (Lund et al. 2009). Therefore, the magnitude of the glacially induced pore pressure is decisive of the potential for increased fracture instability or increased transmissivity. Hökmark et al. (2010) show that there are only moderate increases in relative transmissivity (except for limited areas around the repository openings) caused by variations in normal stress. Any additional increase in transmissivity caused by shearing is also likely to be modest.
- *Spalling potential:* Hökmark et al. (2010) does not consider the potential for spalling in the walls of deposition holes during the glacial phase. By the time of the next glacial period, the state of stress in the repository region will (approximately) be equal to that after excavation, cf section on data uncertainty due to bias. The glacially induced stresses are of similar magnitudes to those occurring during the time of the thermal load, and there is likely to be a significant swelling pressure in all deposition holes apart from those where the buffer is lost due to erosion (Hökmark et al. 2010). Therefore, it is judged that if spalling does not take place during the temperate period it will not happen during the remaining of the glacial cycle. Furthermore, if the buffer is lost, the additional impact spalling may have on repository safety is insignificant.

6.5.9 Correlations (text reproduced from SR-Site Data report)

The potential for spalling depends on the properties of the rock mass (elastic properties, heat transport properties, and the coefficient of thermal expansion), the magnitude and orientations of the *in situ* stresses, as well as the near-field design of deposition tunnels and deposition holes. The potential for spalling is assessed by comparison of the calculated tangential stresses (Hökmark et al. 2010) with the estimated spalling strength. The parameter values used in the modelling work are described in Section 6.4.12 of this report. Similarly to the assessment for SR-Can (Hökmark et al. 2006), the possibility that the swelling pressure from the bentonite buffer may suppress spalling is ignored.

Transmissivity changes due to variations in normal stress are calculated using the stress-transmissivity relations described in Section 6.4. Corresponding estimates of transmissivity changes due to shearing are made based on the work by Olsson (1998), see Section 6.5.6. Hökmark et al. (2010) estimates that shear displacements exceeding about 4 mm under low normal stress may result in a transmissivity increase by 1–2 orders of magnitude. However, the authors assume that increasing levels of normal stress will suppress the transmissivity increase such that any increase due to shearing that takes place under normal stress-levels greater than 6–7 MPa can be ignored.

6.5.10 Result of supplier's data qualification (text reproduced from SR-Site Data report)

Data for the tunnels

In this section, the absence of an EDZ that is connected on the tunnel scale is argued, as motivated based on experimental observations and data. This does not necessarily mean that transmissivity in the EDZ is as low as in the undisturbed rock. Accordingly, the axial transmissivity T (m^2/s) of the EDZ along deposition tunnels, other tunnels, and shafts is given.

As stated in the SR-Site Underground opening construction report (SKB 2010f) it is possible to control the drill and blasting of the tunnels such that a continuous fracturing along the axial direction of the tunnel will not develop. This was stated already in SR-Can, based on experiences from the excavation of the TASQ tunnel at ÄSPÖ HRL (Olsson et al. 2004), and has been further confirmed by the intermediate results from the demonstration trial of smooth blasting techniques at the ÄSPÖ HRL (Olsson

et al. 2009, Ericsson et al. 2009). These indicate that blast induced fractures in the rock side-walls are dominantly radial and that such fractures will not be continuous along the axial direction of the tunnel over any significant distance, see Figure 6-53.

Furthermore, available literature suggests that the hydraulic conductivity in drilled and blasted tunnels is on the order of 10^{-8} m/s (Bäckblom 2008) although these conductivities could possibly be very local and may not necessarily be created by the excavation activities.

Hökmark et al. (2010) assessed the potential for tensile stresses developing in the walls of the deposition tunnel. Figure 6-54 shows contours of the vertical stress component in a vertical cross-section perpendicular to the tunnel axis after excavation, and at two different times during the heated phase. Hökmark et al. (2010) did not confirm the assessment made by Rutqvist and Tsang (2008) that tensile failure would develop along tunnel walls. The differences in results can be attributed to the differences in the estimated *in situ* stress-field at repository depth and modelling approach.

The stress redistribution resulting from the tunnel excavation will reactivate some existing near-field fractures. The process has been modelled in a set of numerical analyses (Hökmark et al. 2010), building on the experiences with a similar approach used for SR-Can (Hökmark et al. 2006, Fälth and Hökmark 2007). In short the *3DEC* code is used to determine stress redistribution effects and shear displacements in fractured near-field rock, and then the results are used to estimate possible permeability changes. The numerical analyses cover a series of events ranging from excavation of tunnel, through the heated period of the initial temperate period, to the effects of a glacial cycle with an accompanying increase in pore pressure. Relevant changes, that is changes that extend more than a couple of metres from the openings, only occur after the thermal load is applied, starting from the initial temperate period.

The analyses made by Hökmark et al. (2010) confirm the results obtained for SR-Can (Hökmark et al. 2006), that is an increase in relative transmissivity by about two orders of magnitude within a distance of 1–2 m from the tunnel openings and only marginal changes elsewhere as shown in Figure 6-55 (cf section on temporal variations).

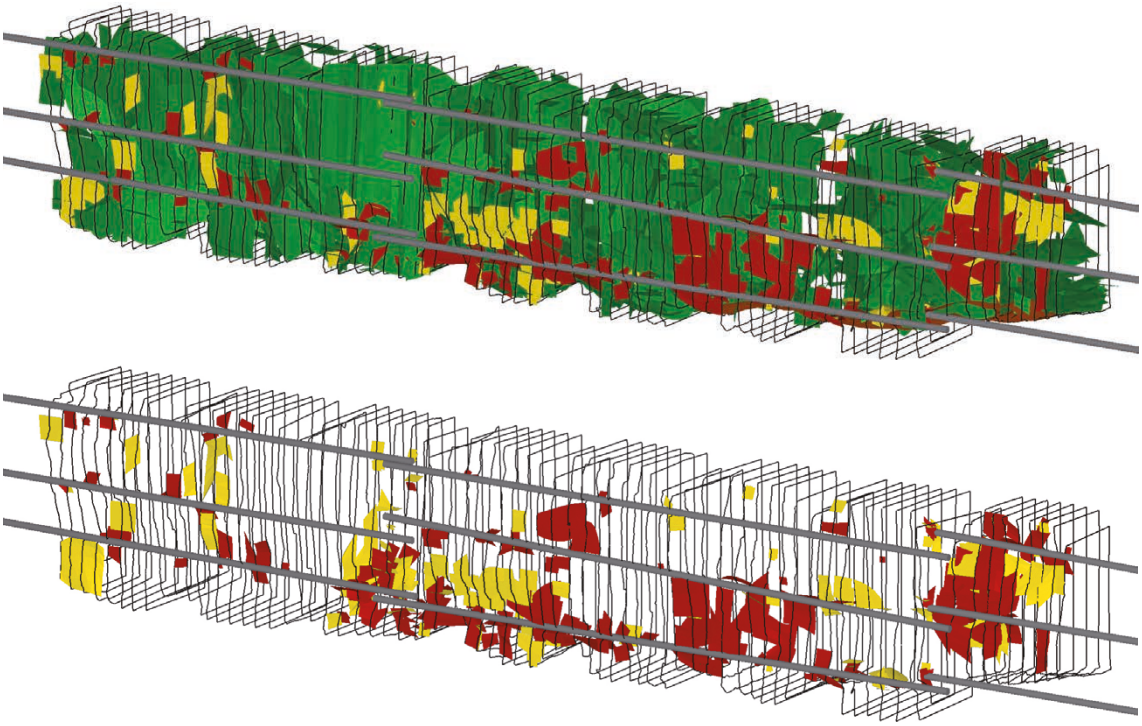

Figure 6-53. *Top: Boreholes, slabs, and all interpreted fractures. Bottom: Ditto but only with blast and blast-induced fractures. The colours indicate different fractures according to: Green = natural, red = blast, and yellow = blast induced. Reproduced from Olsson et al. (2009, Figures 7-9 and 7-10). The length of the test area is 8 m and the height is 1.5 m.*

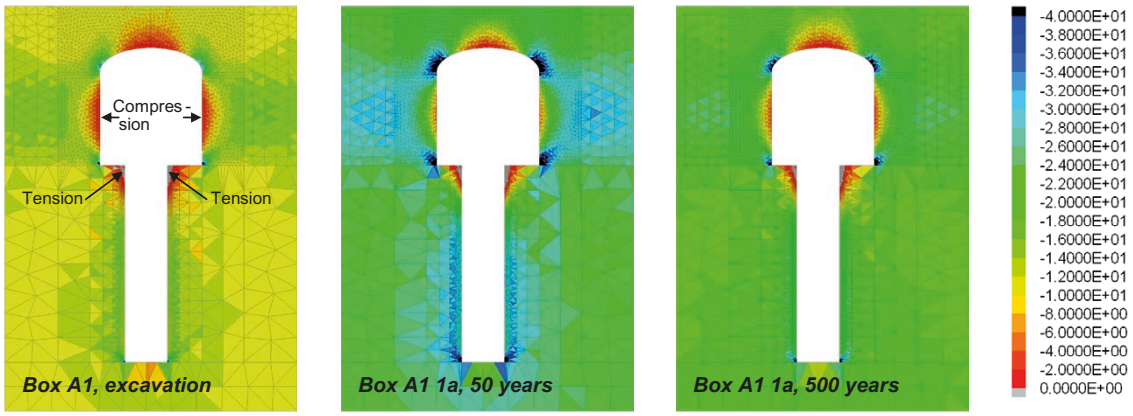

Figure 6-54. *Contours of the vertical stress component after excavation (left), 50 years (middle) and 500 years (right) Stresses are plotted in the range from –40 MPa (compression) to 0 MPa. Note that stress magnitudes that fall outside the range are marked in black for compression and light grey for tension. Modified from Hökmark et al. (2010, Figure H-9).*

Fractures	Nr		Dip range	Strike range
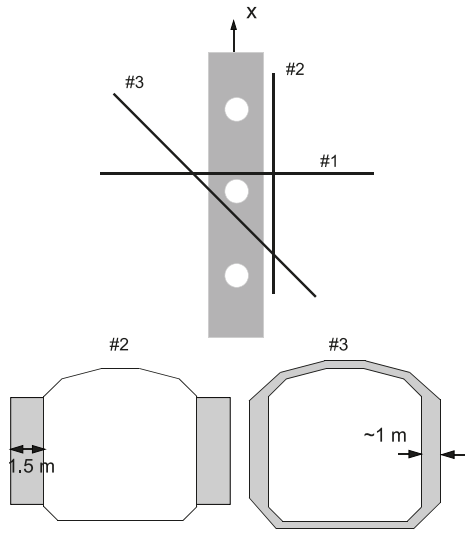	#1	No change in transmissivity	65–90	0±22.5, 180±22.5
	#2	Two orders of magnitude increase at the height section opposing the tunnel, no change elsewhere.	65–90	90±22.5, 270±22.5
	#3	Two orders of magnitude increase at up to 1 m distance from the tunnel periphery	65–90	45±22.5, 270±22.5
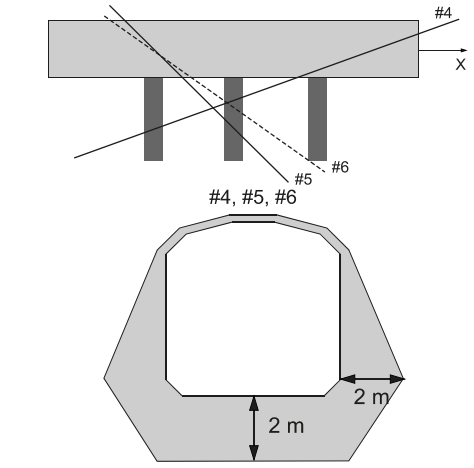	#4	Two orders of magnitude increase in region shown in left figure, no change elsewhere.	0–65	-
	#5	Two orders of magnitude increase in region shown in left figure, no change elsewhere	0–65	-
	#6	Two orders of magnitude increase in region shown in left figure, no change elsewhere	0–65	-

Figure 6-55. *Estimates of transmissivity increases for different fracture orientations based on results from the near-field modelling for the safety assessment SR-Can. Reproduced from Hökmark et al. (2010, Figure 8-3). The grey-shaded areas around the tunnel represent regions with increased transmissivity as given in the right columns.*

An increase of the transmissivity by two orders of magnitude, as compared to the pristine rock with a transmissivity of about 10^{-10} m^2/s, would suggest an axial transmissivity of about 10^{-8} m^2/s in the EDZ.

Very close to the periphery of the tunnel, the normal stress could be low enough that, theoretically, the transmissivity increase could be even larger than that suggested in SR-Can for fractures that are almost parallel to the tunnel axis. However, in reality fractures will not be persistently parallel to the tunnel where there are deposition holes, especially since deposition holes intersected by fractures intersecting more than four deposition holes will be rejected according to the EFPC criterion. This means that this effect can be discarded, or at least captured within the EDZ assumption of $T = 10^{-8}$ m^2/s along the tunnel.

Hökmark et al. (2010) also assess the major principal stress in the centre of the tunnel roof. As opposed to the stresses in the deposition hole walls, the stresses in the centre of the tunnel roof will not exceed the spalling strength during the heated phase. However, stress concentrations in the tunnel roof corners may be high enough to cause spalling.

Data for the deposition holes

The data that should be supplied are listed in Section 6.5.1. This is addressed in the following.

Potential for spalling

The potential occurrence of spalling is site and repository design specific, as it depends on the *in situ* stress, the intact rock mechanical strength, and on the repository layout (*i.e.* orientation of deposition tunnels and near-field design of deposition tunnels and deposition holes). For the heated part of the initial temperate period, additional parameters such as the elastic properties, the heat transport properties, and the thermo-mechanical properties of the rock mass become important. Spalling is the only fracturing mechanism identified as relevant during the initial temperate period.

Hökmark et al. (2010) has revised the assessment of potential for thermally induced spalling presented in SR-Can, using a detailed near-field model geometry that incorporates one tunnel segment with seven canisters, three of which have explicitly modelled deposition holes. The model calculates the tangential stress in the wall of the deposition hole resulting from the excavation, and the subsequent thermal load. The calculated stress is in turn compared with the spalling strength of the rock, which is assumed to be in the range 52–62 % of the uniaxial compressive strength (*UCS*) of intact rock. Hökmark et al. (2010) studied a number of cases with different assumptions regarding the value of the thermal conductivity, and magnitudes and orientations of the *in situ* stress. A summary of these are provided in Table 6-66.

Table 6-66. Summary of stress and thermal conductivity assumptions used in the near-field modelling. Reproduced from Hökmark et al. (2010, Table 9-1). Box A1 and Box B1 relate to different locations within the repository region where the local tunnel orientation deviates the most and the least from the most likely orientation of the major horizontal in situ stress, respectively.

Thermal conductivity	0 Most likely stress magnitudes, most likely stress orientation	I Most likely stress magnitudes, most unfavourable stress orientation	II Lower limit stress magnitudes, most favourable stress orientation	III Upper limit stress magnitudes, most unfavourable stress orientation
Mean	C (Box B1) D (Box A1)	F	A	H
Dimensioning	E (Box B1) G (Box A1)	I	B	J

Table 6-67 shows the depth-intervals along the deposition hole wall in which the mean nominal spalling strength (57 % of *UCS*) is exceeded after excavation, as well as in given time-intervals of the heated phase (time zero represents deposition of the canisters). For the reader who is not familiar with the way of presenting assumptions and results in Table 6-66 and Table 6-67 (Hökmark et al. 2010, Section 9.5) is recommended.

As can be seen from Table 6-67, spalling after excavation will only occur by exception, while thermally induced spalling will generally occur during the heated phase. Therefore, the answer to the question of the potential of thermally induced spalling would be that it is likely to occur in most deposition holes.

Table 6-67. Depth intervals along the deposition hole wall in which the nominal spalling strength (57 % of UCS or about 130 MPa) is exceeded after excavation and during given time-intervals after canister deposition. Reproduced from Hökmark et al. (2010, Table 9-2).

Depth (m)	Excavation									0–1 years									
0–1						F		H	I	J				D		F	G	H	I	J
1–2								H		J				D	E	F	G	H	I	J
2–3								H		J				D	E	F	G	H	I	J
3–4														D	E	F	G	H	I	J
4–5															E	F	G	H	I	J
5–6															E	F	G	H	I	J
6–7																		H	I	J
7–8																				J
Depth (m)	**1–5 years**									**5–50 years**									
0–1				D	E	F	G	H	I	J		B		D	E	F	G	H	I	J
1–2		B	C	D	E	F	G	H	I	J	A	B	C	D	E	F	G	H	I	J
2–3		B	C	D	E	F	G	H	I	J	A	B	C	D	E	F	G	H	I	J
3–4		B	C	D	E	F	G	H	I	J	A	B	C	D	E	F	G	H	I	J
4–5		B	C	D	E	F	G	H	I	J	A	B	C	D	E	F	G	H	I	J
5–6		B	C	D	E	F	G	H	I	J		B	C	D	E	F	G	H	I	J
6–7			C	D	E	F	G	H	I	J		B	C	D	E	F	G	H	I	J
7–8								H	I	J				D	E	F	G	H	I	J

Geometry and location of the spalled zone

An example of the magnitude of the major principal stress and its location on the deposition hole perimeter at stress maximum is provided in Figure 6-56 for cases D and G in Table 6-66.

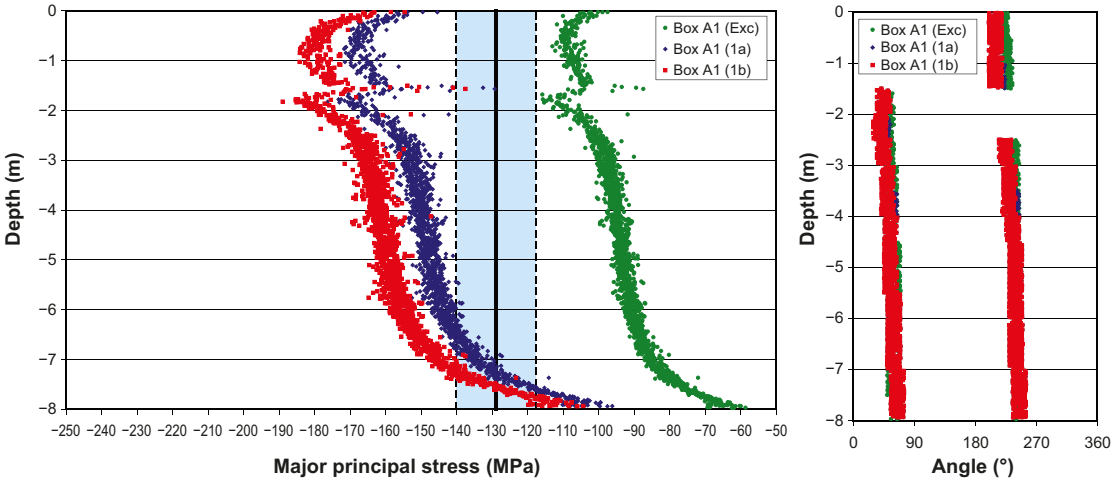

Figure 6-56. *Left: Simulated maximum tangential stress along the deposition hole wall for the most likely in situ stress magnitudes and orientations after excavation (Exc) and after 50 years of heating for two assumptions regarding the thermal conductivity – mean value (1a) and dimensioning value (1b). This example corresponds to cases D and G in Table 6-66 and Table 6-67. Blue area represents spalling strength in fracture domain FFM01 (52–62 % of UCS). Right: Location of maximum stress on deposition hole perimeter. Both figures are obtained from Figure 9-8 in Hökmark et al. (2010).*

As can be deduced from Figure 6-56, for these cases representing the most likely stress magnitudes and orientation (D and G), spalling is likely to occur along the great majority of the deposition hole. Therefore it is reasonable to assume a length of the spalled zone L_{zone} of 8 m, located along the entire length of the deposition hole.

According to Hökmark et al. (2010) there is, at present, no way of directly calculating the actual shape or depth of thermally induced failures. Experience from the APSE (Andersson 2007) indicates that the failures will be notch-shaped and that the notch will self-stabilise at some depth that depends on the stress that prevailed at the time of the failure. Once the notch is stable, subsequent increases in stress will not significantly increase the depth of the failure. The notch developed at APSE was typically 0.5 m wide (Andersson 2007, Figure 6-17) and 0.1 m deep (thick) (Andersson 2007, Figure 6-18). Based on this W_{zone} = 0.5 m and d_{zone} = 0.1 m is suggested.

Tortuosity and porosity of the spalled zone

Neretnieks and Andersson (2009) assessed the tortuosity of the spalled rock fragments obtained from spalling tests at the Äspö Pillar Stability Experiment, carried out to examine the failure process in a heterogeneous and slightly fractured rock mass when subjected to coupled excavation-induced and thermal-induced stresses (Andersson 2007). After the experiment all the rock fragments resulting from the spalling were collected. The rock fragments range in size from less than mm size particles up to large plate like thin irregular sheets. The fragments were photographed and measures of thickness, length, and widths were collected. They typically are 10 times as long as they are thick. This means that in the radial direction the tortuosity, in this case the increase in distance a solute has to travel to move one length unit in the radial direction, is about τ_y = 10. This is because the shape of the rock fragments forces a solute to move in sharp zigzag paths whereas in the tangential-direction, the paths are nearly straight (see Figure 6-57).

According to Neretnieks et al. (2010) there are no data on porosity of the zone, but since the spalling occurs after the deposition hole has been filled with buffer, the expansion cannot be larger than the volume of the gap between the rock wall and the buffer, and a porosity value of ε_{zone} = 0.02 can thus be justified.

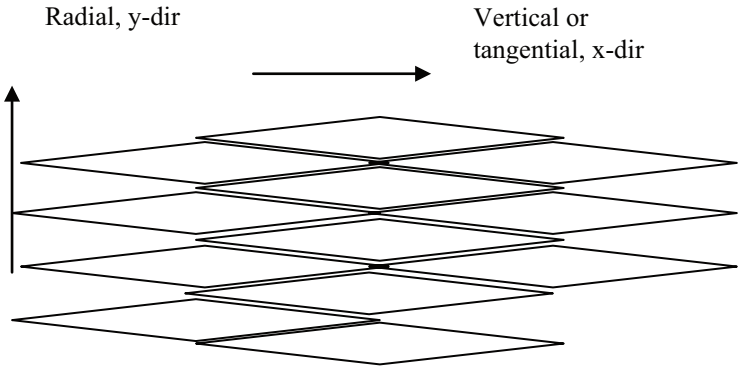

Figure 6-57. *Arrangement of the rock fragments and flow directions. Reproduced from Neretnieks and Andersson (2009).*

Hydraulic conductivity

Neretnieks and Andersson (2009) addressed whether the hydraulic conductivity of the damaged zone could be so small that the water flowing in the intersecting fracture would prefer to flow around the damaged zone instead of flowing through it. Their results suggest that the water would prefer to flow through the zone unless the conductivity could be made one or more orders of magnitude smaller.

SKB has conducted field tests at Äspö HRL (Glamheden et al. 2010) to assess the potential for mitigating spalling by adding small counter pressures. However, while the project supports the possibility that the counter pressure exerted by bentonite pellets in the gap between buffer and rock wall may suppress the spalling, or at least keep the spalled slabs in place and by this minimize the hydraulic conductivity of the spalled damaged zone, current results are inconclusive.

Based on current knowledge and techniques, the hydraulic conductivity of the spalled zone is suggested to be "high".

The connected effective transmissivity T (m^2/s) of the deposition hole EDZ

Findings from the comprehensive literature study (Bäckblom 2008) support that for mechanical excavation techniques in elastic rock conditions, that is full face down-hole drilling, the depth of damaged zone (EDZ) is limited to a few centimetres in the rock surrounding the deposition hole. As a result, connected effective transmissivity will be governed by the natural fractures intersecting the deposition holes, and by the fact that the intersecting fractures have a sufficiently low connected transmissivity.

As stated in the SR-Site Underground opening construction report (SKB 2010f), there is high confidence that elastic rock conditions prevail for the reference design, and consequently that the transmissivity associated with EDZ in deposition holes would be less than 10^{-10} m^2/s. This is under the pre-requisite that no spalling occurs.

6.5.11 Judgement by the assessment team

The increase in knowledge summarized in Section 6.5.2. is so far not fully implemented in relevant safety assessment calculation chains, and hence, the overall effects are not quantified in PSAR. The judgement is thus to use the same data in PSAR as in SR-Site. However, the newly gained knowledge will be implemented in coming safety assessments.

The judgement is therefore to recommend the same data as in SR-Site.

6.5.12 Data recommended for use in assessment

Hydraulic properties along tunnel walls and floor

Table 6-68 lists the recommended axial transmissivity value along tunnel walls. The value is based on the value given as a design premises. However, some variant transmissivity values are also suggested as input for exploring how transmissive an EDZ need to be in order to significantly impact other safety functions, as well as exploring the impact of no axially continuous EDZ at all.

Table 6-68. Recommended axial transmissivity data along deposition tunnels, other tunnels, and shaft.

Parameter	Best estimate value	Variant values
Tunnel and shaft EDZ transmissivity	10^{-8} m^2/s	0, 10^{-7}, 10^{-6} m^2/s

Hydraulic properties in deposition hole wall

Table 6-69 lists recommended hydraulic data along deposition hole walls, and properties of the spalled zone. Two variants are recommended, assuming no spalling or spalling in all deposition holes.

Table 6-69. Recommended data for deposition hole walls.

Parameter	Best estimate value	Variant values
Potential for spalling	High	No spalling
Length of spalled zone, L_{zone}	8 m	No spalling
Thickness of spalled zone, d_{zone}	0.1 m	No spalling
Width of spalled zone, W_{zone}	0.5 m	No spalling
Tortuosity of spalled zone, τ_y	10	No spalling
Spalled zone porosity, ε_{zone}	0.02	No spalling
Hydraulic conductivity of spalled zone, K	High	No spalling
Connected effective transmissivity of deposition hole wall EDZ, in holes where no spalling occurs	10^{-10} m^2/s	-

6.6 Quantities for groundwater flow modelling

The use of hydrogeological models in SR-Site and PSAR allows for simulations of groundwater flow from a deep disposal facility to the biosphere. It also allows for the calculation of performance measures that will provide an input to the safety assessment.

This section provides site-specific data of the quantities associated with the stochastic fracture network realisations for use in the Discrete Fracture Network (DFN) and Equivalent Continuous Porous Medium (ECPM) groundwater flow modelling. It also provides the homogeneous flow and transport properties for use in the Continuous Porous Medium (CPM) groundwater flow modelling. This section only concerns quantities and properties of the rock mass volumes found in between the deterministically modelled deformation zones. The flow and transport properties of the latter, as well as of the regolith found on top of the rockhead, are given in Selroos and Follin (2010). The usage of flow related migration parameters in SR-Site and PSAR is described in Section 6.7.

The PSAR is based on the same modelling of Quantities for groundwater flow modelling as SR-Site. In the following sections, the modelling strategy is described (Section 6.6.1) followed by an account of the experiences from the SR-Site safety assessment (Section 6.6.2). Since the PSAR is based on the same data as SR-Site, the data qualification (Sections 6.6.3 to 6.6.10) is reproduced from the SR-Site Data report. In Section 6.6.11 the formal judgement by the assessment team to use the qualified data is presented followed by Section 6.6.12 where the recommended data is presented.

6.6.1 Modelling (text reproduced from SR-Site Data report)

In SR-Site, groundwater flow in the repository host rock is conceptualised to occur in a discrete fracture network. Hydrogeological DFN models explicitly model the fractures through which the groundwater flows and are characterised by quantities associated with these fractures such as orientation, size, intensity, transmissivity, and aperture. Hydrogeological DFN modelling invokes Monte Carlo simulations (multiple realisations) as the fracture quantities are described statistically.

In order to assess the implications of DFN models on flow and transport on scales larger than that encompassed by the repository host rock, it is often necessary for practical reasons to convert DFN models to models with appropriate continuum flow and transport properties such as hydraulic conductivity, fracture kinematic porosity, and flow wetted fracture surface area per unit volume of rock.

- On a regional model scale, that is in rock mass volumes far away from the repository, the classic continuous porous medium approach with homogeneous flow and transport properties is used.
- On an intermediate model scale, that is on a site scale, the equivalent continuous porous medium approach with heterogeneous flow and transport properties is used in SR-Site. The ECPM properties are derived by means of up-scaling the underlying DFN realisation (Jackson et al. 2000). Since each ECPM model is based on a particular underlying stochastic DFN realisation, the flow and transport properties of the ECPM models are also stochastic. That is, uncertainties relating to the spatial variability are quantified by means of multiple realisations.

In conclusion, in SR-Site, groundwater flow modelling on the repository and site scales is performed using the DFN and ECPM approaches, respectively. On a regional scale, groundwater flow modelling is performed using the CPM approach. The rational for using this mixture of flow concepts in SR-Site is summarised in Selroos and Follin (2010).

Defining the data requested from the supplier

The following quantities associated with the generation of stochastic fracture network realisations for use in the DFN and ECPM groundwater flow modelling are requested from the supplier:

- The fracture orientation model statistics for each suggested fracture set, in terms of the Fisher distribution mean pole trend (°), plunge (°) and concentration κ (–).
- The fracture size model statistics for each suggested fracture set in terms of the Pareto distribution location parameter r_0 (m) and shape parameter k_r (–).
- Statistics for the fracture intensity model, in terms of the open fracture surface intensity per unit volume of rock $P_{32,o}[r_0,564\ \text{m}]$ (m^2/m^3), for each suggested fracture set. The largest fracture radius considered for these data should be 564.2 m (cf Section 6.3).
- The transmissivity model constants a, b, and σ_{logT}, for a semi-correlated transmissivity model, constants a and b for a correlated transmissivity model, and constants μ_{logT} and σ_{logT} for an uncorrelated transmissivity model.
- The aperture model constants a and b for a correlated aperture model.

All these constants should be given for each suggested fracture set. Judged as appropriate by the supplier, different fracture sets should be suggested for different rock mass volumes of the host rock. In addition, the repository system should be taken into account, in case it affects how discrete fractures are connected.

The following quantities for use in the CPM flow modelling are requested from the supplier:

- The hydraulic conductivity K (m/s) of the rock mass volume.
- The kinematic porosity n_e (–) of the rock mass volume.
- The fracture surface area per unit volume a_r (m^2/m^3) of the rock mass volume.

Judged as appropriate by the supplier, different data should be given for different rock mass volumes and may include potential depth trends.

Modelling activities in which data will be used

Groundwater flow modelling in SR-Site is performed with the purpose of:

- Estimating the inflow rate to the repository and the potential for upconing of saline groundwater during open repository conditions.
- Estimating buffer and backfill saturation times after closure of open repository conditions.
- Assessing exit locations of downstream flow paths as well as entrance locations of upstream flow paths starting at different deposition hole positions, and their associated flow-related transport properties such as Darcy fluxes q at repository depth and advective travel times t_w and transport resistances F during saturated temperate, periglacial, or glacial conditions.
- Delivering input data to hydrogeochemical modelling during saturated temperate, periglacial, and glacial conditions. In particular, assessing the potential for increased flow rates in the fractured bedrock at repository depth and upstream transport of dilute and/or oxygenated water from ground surface to repository depth during periglacial and glacial conditions.

The following groundwater flow modelling studies are performed in SR-Site:

- *Excavation and operation phases:* During the excavation and operation phases of the repository, the system is characterised by the tunnels being at atmospheric pressure. Also, the saturation phase of the repository is included in this period, when the backfilled tunnels go from unsaturated to

fully saturated conditions. It should be noted that saturation will also occur after repository closure. Accordingly, this period is somewhat extended in hydrogeological modelling, as compared to what is described as the excavation and operation periods in other disciplines. Simulations of the excavation and operation periods are performed by Svensson and Follin (2010) using the DarcyTools code (Svensson et al. 2010). For the inflow calculations, saturated groundwater flow below the groundwater table, and a simplified description of unsaturated flow above the groundwater table, are used. The DarcyTools code can also handle the saturation process, i.e., two-phase (air-water) flow, in a simplified manner (Enssle and Poppei 2010). Additional simulations of near-surface effects are done using the hydrogeological modelling tool MIKE-SHE (Mårtensson and Gustafsson 2010). The objective of these latter studies is primarily to assess the interaction between the near-surface and deep rock groundwater systems. Also, the near-surface modelling provides information to Environmental Impact Assessment studies conducted outside of the SR-Site modelling.

- *Periods with temperate climate conditions:* The simulations that deal with temperate climate conditions address an approximately 10 000 year long period, extending from repository saturation up till the initiation of the next permafrost-glaciation event. Saturated groundwater flow is modelled including the shoreline displacement as a transient boundary condition. The backfilled tunnels are explicitly included in the models that are based on a nesting of different scales (from regional to site to canister scales) using a mixture of continuum and discrete fracture network representations of the rock mass. Simulations of the temperate period are performed by Joyce et al. (2010) using the ConnectFlow code (Hartley and Holton 2004). The strategy for identifying the most important and/or critical hydrogeological variants to be addressed in the temperate period simulations is to propagate a number of SDM-Site variants to the regional scale simulations. These SR-Site simulations differ from the SDM-Site calculations in that they cover the time period from the end of the last glaciation up till the onset of the next glacial period, whereas the SDM-Site models end at present day conditions. The variants with greatest impact on performance measures are propagated to detailed site and repository scale calculations involving an explicit hydrogeological DFN representation.
- *Periods with periglacial and glacial climate conditions:* The main objective of the periglacial and glacial simulations is to assess the groundwater flow pattern during periods when the upper part of the geosphere may be frozen, thus restricting flow, and/or when a glacial load (glaciation advance and retreat) may imply different recharge and stress conditions. Input is obtained from an ice-sheet model that provides the glacial thickness (cf Section 7.1). A second objective is to study the possible movement of salt due to up-coning during glacial conditions. Simulations of the permafrost and glacial conditions are performed by Vidstrand et al. (2010) using the DarcyTools code. The modelling strategy is to identify important parameter combinations of climatological and rock property conditions, and then implement 3-D models on a large, supra-regional scale. Initial and boundary conditions from these simulations have later been transferred to the site and repository scale ConnectFlow models for detailed analyses of flow and solute transport.

6.6.2 Experience from SR-Site

This section briefly summarises experiences from the SR-Site safety assessment, which may be of direct consequence for the data qualification in this Data report.

The groundwater flow (hydrogeological) modelling performed as part of SR-Site was identical to what is outlined above; i.e., no new simulations have been performed as part of PSAR.

The main sensitivities related to the site-description explored in SR-Site was the uncertainty in the fracture transmissivity-size relationship implying that all three correlation models identified were recommended to be propagated for subsequent analyses of buffer erosion, canister corrosion and radionuclide transport. Here, the semi-correlated model most strongly argued for bu the site-descritptive model performed most favourably, while the fully correlated and uncorrelated models performed worse. Still, all models were propagated through the full assessment.

Other SDM-Site related variants were deemed not to warrant further consideration in the assessment. In addition, some specific safety assessment-motivated variants were addressed; these included e.g. parameterisation of EDZ and crown space, multiple realisations, and adoption of multiple particles at release locations thus addressing fracture network branching.

6.6.3 Supplier input on the use of data (text reproduced from SR-Site Data report)

This section presents data based on site-descriptive modelling activates presented in the **Site description Forsmark** and references therein. However, hydrogeological DFN data taking the repository into account are requested in SR-Site. As the repository layout was not part of the site-descriptive modelling, the fracture size distribution has been modified in the groundwater flow modelling activities being part of SR-Site, in order to account for the repository system impact on how discrete fractures are connected. Therefore, the separation of the supplier and customer is not clear-cut. Even so, we use the supplier/customer terminology requested in the instruction (cf Section 2.3).

The supplier notes that considerable effort has been devoted to correcting the shortcomings of SR-Can. Much of the information originating from the site descriptions have been used as inputs for improving SR-Site models. Thus the input from the supplier has already been implemented. It is also worth mentioning that an improved description of the climatic evolution (cf the SR-Site Climate report SKB 2010g) has been used to improve SR-Site modelling during periods with periglacial and glacial climate conditions.

6.6.4 Sources of information and documentation of data qualification (text reproduced from SR-Site Data report)

Sources of information

The main sources of information are listed in Table 6-70. The publications referred to provide important input to the groundwater flow modelling studies carried out in SR-Site, see Section 6.6.1.

The **Site description Forsmark** summarises the results of a chain of modelling activities in several disciplines. Table 6-71 details the stages and produced documents within the hydrogeology part of this modelling chain. The upper part of the table shows the stages and the cumulative number of cored boreholes providing geometrical and hydraulic information about the fractured bedrock at Forsmark surrounding the future repository (see Section 1.5 for maps that show the locations of the boreholes). Table 6-71 also provides references of the background hydrogeological modelling reports, as well as the reports with geometrical and hydraulic data on the flowing fractures detected with the Posiva Flow Log (PFL). The information is shown in relation to the three model versions and the three modelling stages carried out in preparation of the **Site description Forsmark**.

Follin (2008) is the key reference document on bedrock hydrogeology at Forsmark and summarises the results of a chain of groundwater flow modelling activities carried out on behalf of the **Site description Forsmark**, see Table 6-71.

SKB (2009a) provides the geometry of the repository system that is taken into account in the analyses of how discrete fractures are connected to the repository system. Joyce et al. (2010) provide a detailed description of these analyses.

The SR-Site Climate report (SKB 2010g) provides a description of past and future climate conditions. The understanding of historic data and the suggested reference evolution of the future are used in the groundwater flow modelling study that handles periods with temperate climate conditions (Joyce et al. 2010) and in the study that handles periglacial and glacial climate conditions (Vidstrand et al. 2010).

Selroos and Follin (2010) provides a description of the chosen methodology for groundwater flow modelling in SR-Site; a specification of the setup of the three groundwater flow modelling studies described in Section 6.6.1; and a summary of the simulation results from these studies.

Table 6-70. Main sources of information used in data qualification.

SR-Site Climate report, 2010. Climate and climate-related issues for the safety assessment SR-Site. SKB TR-10-49, Svensk Kärnbränslehantering AB.
Site description Forsmark, 2008. Site description of Forsmark at completion of the site investigation phase. SDM-Site Forsmark. SKB TR-08-05, Svensk Kärnbränslehantering AB.
Follin S, 2008. Bedrock hydrogeology Forsmark. SKB R-08-95, Svensk Kärnbränslehantering AB.
SKB, 2009a. Underground design Forsmark. Layout D2. SKB R-08-116, Svensk Kärnbränslehantering AB.
Selroos J-O, Follin S, 2010. SR-Site groundwater flow modelling methodology, setup and results. SKB R-09-22, Svensk Kärnbränslehantering AB.

Table 6-71. The cumulative number (and percentage) of cored boreholes (KFM) and their cumulative borehole length (km) providing geometrical and hydraulic information about the bedrock at Forsmark at the end of each of the three model versions and three model stages carried out for SDM-Site. Starting with the underlined report numbers, these present correlation analyses of geometrical and hydraulic data of the flowing fractures detected with the Posiva Flow Log method. The report numbers typed in italics describe the hydraulic data gathered and the hydrogeological modelling undertaken. Finally, the report numbers typed in bold summarise the development of the hydrogeological modelling achieved at each stage.

	Initial site investigation (ISI)			**Complete site investigation (CSI)**	
Desk top exercise	**Training exercise**	**Preliminary SDM**	**Feedback and strategy**	**Hydrogeological model**	**Model verification and uncertainty assessment**
Version 0	**Version 1.1**	**Version 1.2**	**Stage 2.1**	**Stage 2.2**	**Stage 2.3**
0 KFM (0 %) Σ length: 0 km	1 KFM (4 %) Σ length: 1 km	5 KFM (21 %) Σ length: 5 km	9 KFM (38 %) Σ length: 7 km	20 KFM (83 %) Σ length: 15.9 km	25 KFM (100 %) Σ length: 19.4 km
R-02-32	R-04-15 R-04-77	R-05-18 *R-05-32* *R-05-60* **R-04-77**	R-06-38 *R-07-20* **P-06-56**	R-07-49 *R-07-48* **P-07-127**	R-08-95 *R-08-23* **P-07-128**

R-02-32: SKB, 2002. Forsmark – site descriptive model version 0. SKB R-02-32, Svensk Kärnbränslehantering AB.

R-04-15: SKB, 2004. Preliminary site description. Forsmark area – version 1.1. SKB R-04-15, Svensk Kärnbränslehantering AB.

R-04-77: Forssman I, Zetterlund M, Rhén I, 2004. Correlation of Posiva flow log anomalies to core mapped features in Forsmark (KFM01A to KFM05A). SKB R-04-77, Svensk Kärnbränslehantering AB.

R-05-18: SKB, 2005. Preliminary site description. Forsmark area – version 1.2. SKB R-05-18, Svensk Kärnbränslehantering AB.

R-05-32: Hartley L J, Cox I, Hunter F, Jackson C P, Joyce S, Swift B, Gylling B, Marsic N, 2005. Regional hydrogeological simulations for Forsmark – numerical modelling using CONNECTFLOW. Preliminary site description. Forsmark area – stage 1.2. SKB R-05-32, Svensk Kärnbränslehantering AB.

R-05-60: Follin S, Stigsson M. Svensson U, 2005. Regional hydrogeological simulations for Forsmark – numerical modelling using DarcyTools. Preliminary site description. Forsmark area – version 1.2. SKB R-05-60, Svensk Kärnbränslehantering AB.

R-06-38: SKB, 2006d. Site descriptive modelling Forsmark stage 2.1. Feedback for completion of the site investigation including from safety assessment and repository engineering. SKB R-06-38, Svensk Kärnbränslehantering AB.

R-07-20: Follin S, Johansson P-O, Levén J, Hartley L, Holton D, McCarthy R, Roberts D, 2007a. Updated strategy and test of new concepts for groundwater flow modelling in Forsmark in preparation of site descriptive modelling stage 2.2. SKB R-07-20, Svensk Kärnbränslehantering AB.

P-06-56: Forssman I, Zetterlund M, Forsmark T, Rhén I, 2006. Forsmark site investigation. Correlation of Posiva Flow Log anomalies to core mapped features in KFM06A and KFM07A. SKB P-06-56, Svensk Kärnbränslehantering AB.

R-07-49: Follin S, Johansson P-O, Hartley L, Jackson P, Roberts D, Marsic N, 2007c. Hydrogeological conceptual model development and numerical modelling using CONNECTFLOW, Forsmark modelling stage 2.2. SKB R-07-49, Svensk Kärnbränslehantering AB.

R-07-48: Follin S, Levén J, Hartley L, Jackson P, Joyce S, Roberts D, Swift B, 2007b. Hydrogeological characterisation and modelling of deformation zones and fracture domains, Forsmark modelling stage 2.2. SKB R-07-48, Svensk Kärnbränslehantering AB.

P-07-127: Teurneau B, Forsmark T, Forssman I, Rhén I, Zinn E, 2008. Forsmark site investigation. Correlation of Posiva Flow Log anomalies to core mapped features in KFM01D, KFM07C, KFM08A, KFM08C and KFM10A. SKB P-07-127, Svensk Kärnbränslehantering AB.

R-08-95: Follin S, 2008. Bedrock hydrogeology Forsmark. Site descriptive modelling, SDM-Site Forsmark. SKB R-08-95, Svensk Kärnbränslehantering AB.

R-08-23: Follin S, Hartley L, Jackson P, Roberts D, Marsic N, 2008. Hydrogeological conceptual model development and numerical modelling using CONNECTFLOW, Forsmark modelling stage 2.3. SKB R-08-23, Svensk Kärnbränslehantering AB.

P-07-128: Forssman I, Forsmark T, Rhén I, 2008. Forsmark site investigation. Correlation of Posiva Flow Log anomalies to core mapped features in KFM02B, KFM08D and KFM11A. SKB P-07-128, Svensk Kärnbränslehantering AB.

Categorising data sets as qualified or supporting data

The data requested in this section were produced during the chain of site-descriptive modelling activities detailed above, but also in SR-Site activities taking into account the repository layout. Most data sets are reproduced from tables or equivalents of background reports, which are referenced in Table 6-72. All data sets that are produced for the Forsmark site within site-descriptive modelling or SR-Site activates are considered as qualified. The sorting of the data sets into qualified or supporting is justified in Table 6-73.

Excluded data previously considered as important

Since SR-Can, no data have been excluded which have had a significant impact on the perception of the appropriate choice of data value, or modelling approach, of the rock mass volumes found in between the deterministically modelled deformation zones.

Table 6-72. Qualified and supporting data sets.

Qualified data sets	Supporting data sets
1. Selroos and Follin (2010, Table 2-2): The fracture orientation, size, and intensity statistics, as well as the fracture transmissivity model constants for the fraction of the repository rock mass volume coinciding with the fracture domains FFM01 and FFM06. 2. Selroos and Follin (2010, Table 2-3): As in 1, but for the fraction of repository rock mass volume coinciding with the fracture domain FFM02. 3. Selroos and Follin (2010, Table 2-4): As in 1, but for the site-scale rock mass volume coinciding with the fracture domains FFM03, FFM04 and FFM05.	4. Selroos and Follin (2010, Figure 5-19): The fracture aperture model constants for the fraction of the repository rock mass volume coinciding with the fracture domains FFM01–06. 5. Selroos and Follin (2010, Table 2-6): The hydraulic conductivity, the kinematic porosity, and the flow wetted fracture surface area per unit volume of rock of the rock mass volumes far away from the repository host rock mass volume (outside FFM01–FFM06).

Table 6-73. Justification of the sorting of items in Table 6-72.

1–3. For the repository host rock mass volume and the site-scale rock mass volume, the fracture orientation model statistics, the fracture size model statistics, the fracture intensity model statistics, and the fracture transmissivity model constants coinciding with fracture domains FFM01 through FFM06 were derived and applied within the site-descriptive modelling through a chain of different modelling activities that were each peer reviewed. These modelling activities comply with the SKB quality assurance system and thus the data are judged as qualified.
4. For the repository host rock mass volume and the site-scale rock mass volume, the fracture aperture model constants coinciding with fracture domains FFM01 through FFM06 were derived at Äspö (Dershowitz et al. 2003) and applied within the site-descriptive modelling through a chain of different modelling activities that were each peer-reviewed. Although these modelling activities comply with the SKB quality assurance system, the model parameters are not based on investigations at Forsmark. These data are therefore sorted as supporting.
5. For the bedrock outside the repository host rock mass volume and the site-scale rock mass volume, approximate CPM values of the hydraulic conductivity were taken from hydraulic single-hole tests in deep boreholes at Finnsjön (Andersson et al. 1991) and applied in the site-descriptive modelling. By the same token, approximate CPM values of the kinematic porosity and the flow-wetted fracture surface area per unit volume of rock are based on an expert judgement and applied in the site-descriptive modelling (Follin et al. 2007c). These data are therefore sorted as supporting.

6.6.5 Conditions for which data are supplied (text reproduced from SR-Site Data report)

Six fracture domains, FFM01–FFM06, are defined in the geological DFN modelling based on spatial differences in the fracture frequency of *all* fractures (Olofsson et al. 2007). The six fracture domains are refined in the hydrogeological DFN modelling based on the differences observed in the frequency of flowing fractures versus depth (see Follin 2008 for details). In summary, three of the six fracture domains were split into two sub-units each (FFM03–FFM05) and two fracture domains were split into three sub-units each (FFM01 and FFM06). One fracture domain was left unchanged (FFM02). Figure 6-58 shows two cartoons of the fracture domains at Forsmark that constitute the rock mass volumes on the repository and site scales.

Structural-hydraulic data from twelve cored boreholes gathered during the site investigations at Forsmark (Follin et al. 2007b) are used in the hydrogeological DFN modelling in SR-Site. The twelve boreholes have been drilled at different locations and in different orientations in the rock mass volumes surrounding the repository as shown in Figure 6-59 and Figure 6-60.

The structural data gathered in the twelve boreholes are analysed for each fracture domain sub-unit based on the analyses of fracture frequency, the spatial arrangement of fractures, fracture orientation, and fracture size described in the geological DFN modelling:

- The Terzaghi corrected frequency $P_{10,o,corr}$ (L–1) and orientation strike, dip (°,°) of open fractures (including fractures mapped as partly open).
- A Poisson process is assumed for the 3-D spatial arrangement of open fractures in each fracture domain sub-unit. This assumption implies a Euclidian scaling of the fracture intensity within each fracture domain sub-unit.
- Five, global, Fisher orientation distributions f(mean pole trend, mean pole plunge, concentration) (°,°,–) are assumed for the open fractures.
- The sizes r (L) of all fractures and open fractures are assumed to be Pareto distributed f(r_0, k_r) (L,–). The value of the location parameter r_0 (L) is fixed to the borehole radius (r_{BH} = 0.038 m), whereas the value of the shape parameter k_r (–) varies between the fracture sets and the fracture domains; for FFM02 one set of k_r values is used, for FFM01 and FFM06 another set of values is used, and for FFM03–FFM05 a third set of values is used.

It is recommended to read Section 6.3 of this Data report, where many issues of relevance for the quantities listed above are detailed. In addition to the analyses of the structural data, the hydraulic data gathered in the twelve boreholes are analysed for each fracture domain sub-unit with regard to:

- The Terzaghi corrected frequency $P_{10,pfl,corr}$ (L^{-1}) and orientation strike, dip (°,°) of flowing fractures detected with the Posiva Flow Log method.
- The specific capacity $Q/\Delta h$ (L^2T^{-1}) of the flowing fractures detected with the PFL method during pumping (Q is the inflow rate (L^3T^{-1}) and Δh is the applied drawdown (L), that is, change in pressure head $\Delta p/(\rho g)$, during the pumping).

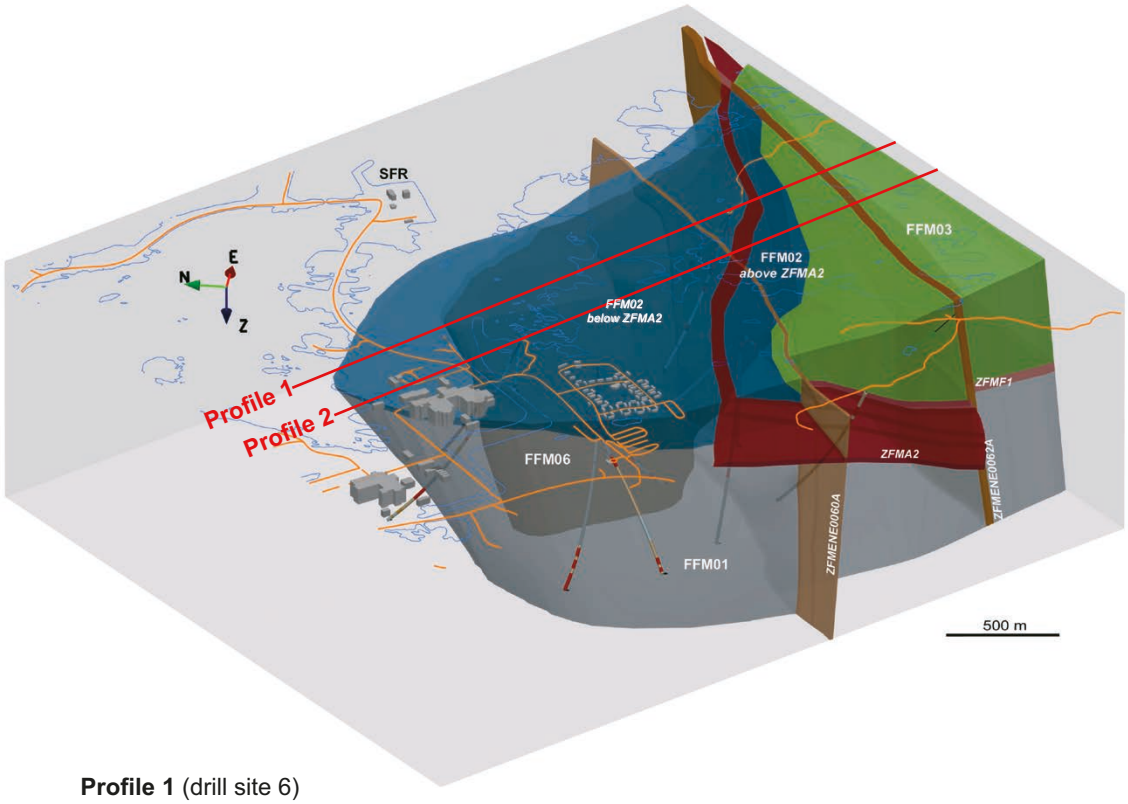

Profile 1 (drill site 6)

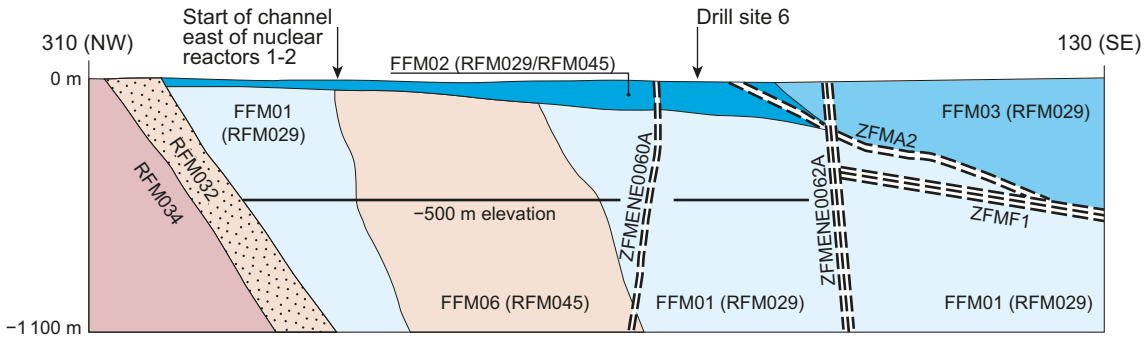

Profile 2 (drill sites 8 and 2)

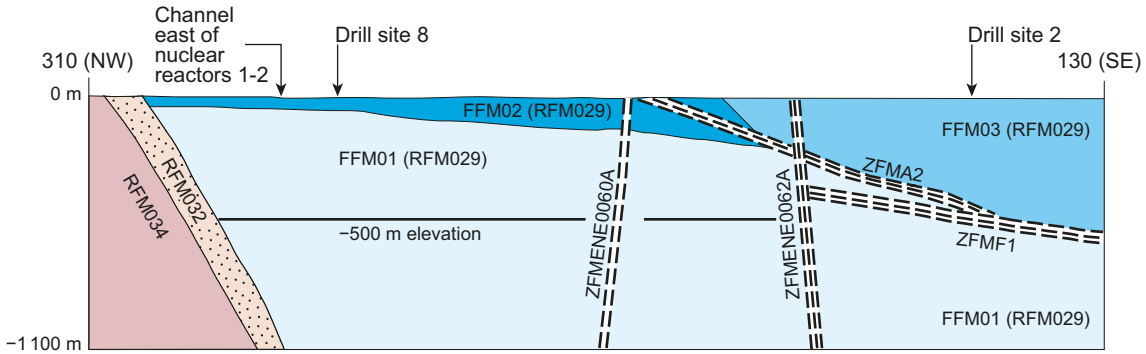

Figure 6-58. *Cartoons showing the fracture domains at Forsmark that constitute the bedrock surrounding the repository. The key fracture domains forming the repository host rock are labelled FFM02, FFM01, and FFM06. Labels beginning with ZFM are names of major deformation zones. Reproduced from Figure 3-11 in Follin (2008) and Figure 5-4 in Olofsson et al. (2007).*

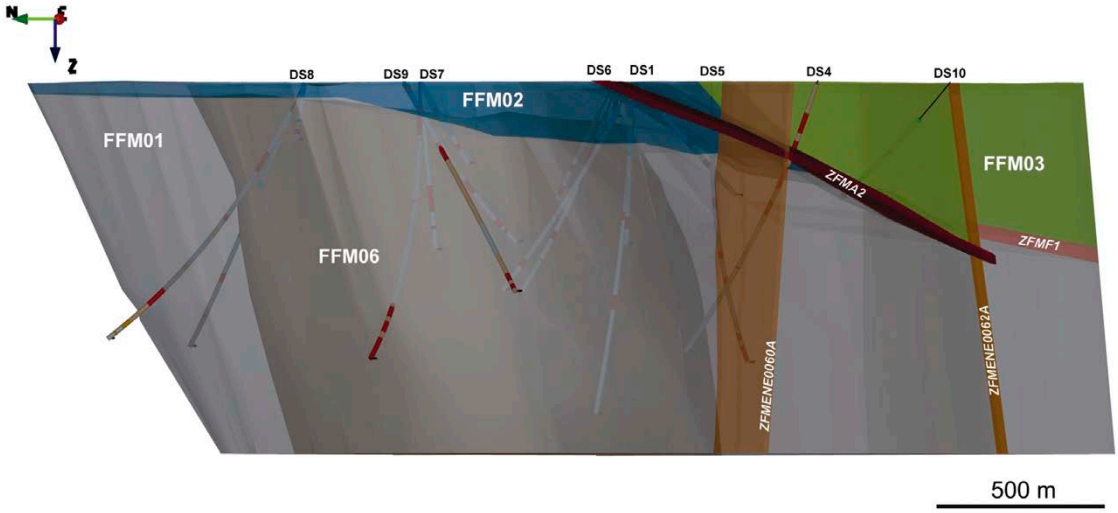

Figure 6-59. *Three-dimensional view towards the east–north–east showing the cored boreholes drilled into the fracture domain model. The key fracture domains are labelled FFM02, FFM01 and FFM06. Labels beginning with ZFM are names of major deformation zones. Reproduced from Figure 5-7 in Olofsson et al. (2007).*

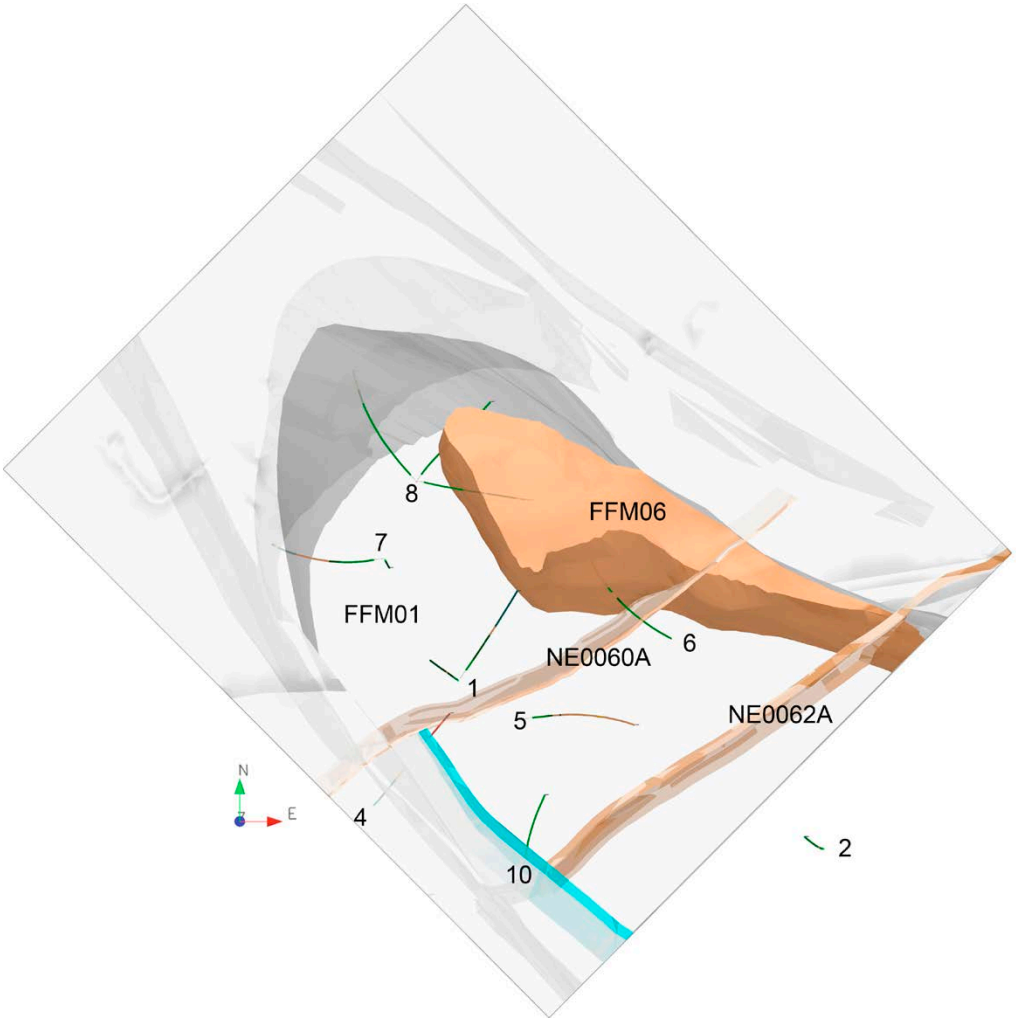

Figure 6-60. *X-ray view through the regolith above the rock mass volumes surrounding the repository. The boreholes shown are all hydraulically investigated with the Posiva Flow Log method. The labels represent drill site numbers (1–10), fracture domains (FFM01 and FFM06) and deformation zones (NE0060A and NE0062A). Here, fracture domain FFM01 is made transparent, whereas FFM06 has a brownish colour. Reproduced from Figure 4-1 in Follin et al. (2008).*

6.6.6 Conceptual uncertainty (text reproduced from SR-Site Data report)

With reference to the geological and hydraulic data analyses presented in Section 6.6.5, several working hypotheses are invoked in the subsequent hydrogeological DFN modelling (see Follin 2008 for details). Three key assumptions in SR-Site are:

1. The fracture surface area per unit volume of rock of *all fractures* greater than the borehole radius $P_{32,a}[r \geq r_{BH}]$ can be estimated from the Terzaghi corrected linear (1-D) borehole fracture frequency of *all fractures*:

   $$P_{32,a}[r \geq r_{BH}] \geq P_{10,a,\,corr} \qquad 6\text{-}13$$

   By the same token, it is assumed that for the *open fractures*, that:

   $$P_{32,o}[r \geq r_{BH}] \geq P_{10,o,corr} \qquad 6\text{-}14$$

2. The fracture surface area per unit volume of rock (fracture intensity) of *all fractures* (*a*) is greater than the fracture intensity of *open fractures* (*o*), which in turn is greater than the fracture intensity of *connected open fractures* (*cof*), which in turn is greater than the measured intensity of *flowing fractures* detected with the PFL method (*pfl*):

   $$P_{32,a} \geq P_{32,o} \geq P_{32,cof} \geq P_{32,pfl} \qquad 6\text{-}15$$

3. The sizes of *all* and *open* fractures, from the smallest fractures to the largest, are power-law distributed (tectonic continuum).

The second and third working hypotheses are illustrated in Figure 6-61. It is noted that it is the intensity of open fractures ($P_{32,o}$) that is used in the hydrogeological DFN modelling to generate the fracture networks.

Another key assumption in SR-Site is the assignment of fracture transmissivity. The quantitative calibration of fracture transmissivity is attempted for three different size-transmissivity correlation models, $T = T(r)$, see Table 6-74. Ten Monte-Carlo realisations are studied for each set of parameter values as a mean to address variability between realisations. For each transmissivity model and hydrogeological DFN realisation a pumping test simulation is carried out.

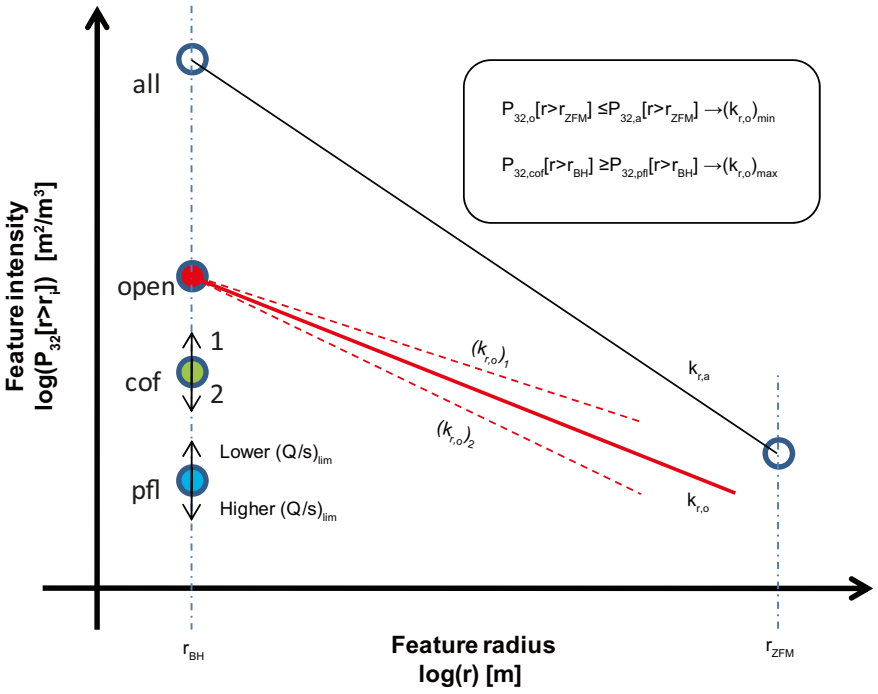

Figure 6-61. *Cartoon showing the working hypothesis of tectonic continua for all fractures and for open fractures, respectively. Given this hypothesis, the possible minimum and maximum limits of the shape parameter for the open fractures, $(k_{r,o})_{min}$ and $(k_{r,o})_{min}$, can be defined as shown. The notation used is explained in the text.*

As a means to assess the 'goodness of fit' for the tested fracture transmissivity models, the following statistics are calculated:

- Average total flow rate to the simulated abstraction borehole over ten realisations.
- Histogram of $\log(Q/\Delta h)$ to the simulated abstraction borehole as an average over ten realisations.
- Bar and whisker plot of minimum, mean minus standard deviation, mean, mean plus standard deviation, maximum of $\log(Q/\Delta h)$ to the simulated abstraction borehole within each fracture set taken over all realisations.
- The average numbers of flowing fractures within each fracture set giving specific capacities to the simulated abstraction borehole above the measurement limit of the PFL method.

Table 6-74. Transmissivity models used for hydrogeological DFN modelling.

Type	Description	Relationship	Parameters
Correlated	Power-law relationship	$\log(T) = \log(a \cdot r^b)$	a, b
Uncorrelated	Log-normal distribution about a specified mean	$\log(T) = \mu_{log(T)} + \sigma_{log(T)}$ N(0,1)	$\mu_{log(T)}$, $\sigma_{log(T)}$
Semi-correlated	Log-normal distribution about a power-law correlated mean	$\log(T) = \log(a \cdot r^b) + \sigma_{log(T)}$ N(0,1)	a, b, $\sigma_{log(T)}$

6.6.7 Data uncertainty due to precision, bias, and representativity (text reproduced from SR-Site Data report)

The heterogeneous nature of the flowing fractures in cored boreholes creates uncertainties in the hydrogeological understanding and modelling. To mitigate these uncertainties, a large number of cored boreholes were drilled at different locations and orientations in the fractured bedrock at Forsmark surrounding the future repository as shown in Figure 6-59 and Figure 6-60. Most of the cored boreholes were hydraulically investigated with two types of test methods, in order to better understand the spatial differences in the near-field and far-field hydraulic properties. The two test methods employed were:

- Difference flow logging with the Posiva Flow Log method during long-term pumping conditions.
- Short-term double-packer injection tests with the Pipe String System (PSS) method.

The shortest length of the borehole interval tested is 0.1 m with the PFL method and 5 m with the PSS method. This difference in spatial resolution affects the interpretation of the measured frequency of flow anomalies, $P_{10,pfl}$, in particular where this frequency is high (small spacing). This is the most important reason why the PFL method was selected as the major single-hole hydraulic test method in SDM-Site.

Data uncertainty due to precision

The cored boreholes have length markers in the borehole wall every 50 m. The maximum uncertainty in position along the borehole of a flow anomaly detected with the PFL method varies with the distance from the length markers. Close to the length markers, the maximum error is c ± 0.2 m. Between the length markers, the maximum possible uncertainty in position is c ± 0.3 m (Forssman et al. 2004, 2006, 2008, Teurneau et al. 2008). The uncertainty in position affects the certainty in the assignment of geometrical properties to the flow anomalies, see below.

The lower detection limit of the specific capacity $Q/\Delta h$ (L^2T^{-1}) is of the order of 1×10^{-9} m^2/s (for both test methods) (Ludvigson et al. 2002, Follin et al. 2007b). The magnitude of the lower detection limit affects the measured frequency of flow anomalies, $P_{10,pfl}$, thus the position of the blue point shown in Figure 6-61.

Data uncertainty due to bias

The uncertainty in determining the exact positions along the borehole of the flow anomalies detected with the PFL method causes uncertainties in the determination of their geometrical properties (strike and dip). The determination reported to SKB's database Sicada honour these uncertainties. That is, the flow anomalies that have several options are assigned a Best Choice orientation and one (or more) Alternative Choice orientations. The hydrogeological DFN modelling presented in the **Site description Forsmark** was based on the Best Choice orientations.

Some examples of reasons that give rise to uncertainties in the geometrical property assignment are:

- Sometimes several *open fractures* with different orientations are within ± 0.3 m of the flow anomaly detected with the PFL method.
- Two or more flow anomalies detected with the PFL can sometimes be correlated to a single geological feature, in particular if this is sub parallel with the borehole trajectory.
- Occasionally, a partly open fracture is closer to the detected flow anomaly than the closest fully open fracture. The orientation of a partly open fracture is considerably much more uncertain, in particular if it is a partly intersecting open fracture.

The methodology used in SDM-Site to determine the geometrical properties of flow anomalies detected with the PFL method in cored boreholes is described in detail for all investigated boreholes (Forssman et al. 2004, 2006, 2008, Teurneau et al. 2008).

Data uncertainty due to representativity

In the general case, the constituent parameters measured during single-hole hydraulic tests in cored boreholes are the flow rate, Q (L^3T^{-1}), and the fluid pressure, p ($ML^{-1}T^{-2}$). Since these are correlated, the parameter measured is the specific capacity, $Q/\Delta p$, which has the same dimension as transmissivity, T (L^2T^{-1}), if pressure is expressed as a hydraulic head, h (L).

The envisaged test conditions of the single-hole hydraulic testing with the PFL and PSS methods are shown in Figure 6-62. The measured specific capacity is dependent on several important aspects, among which the following ones are particularly noted:

- Q_{limit} (L^3T^{-1}); the lower measurement limit of the test method.
- T_{BH} (L^2T^{-1}); the transmissivity of the tested fracture intersecting the borehole. T_{BH} can be affected during the drilling operations. For instance, the fracture can be clogged (positive skin) or stimulated (negative skin).
- C (–); the connectivity of the tested fracture to other fractures away from the borehole. Some fractures are isolated, or are a part of an isolated cluster of fractures. Others are well connected and a part of the overall hydrological system.
- T/S (L^2T^{-1}); the hydraulic diffusivity of the fracture system within the radius of influence.
- t (T); the duration of the hydraulic testing, i.e. the test time.
- ΔL (L); the length of the test interval (test section).

The PFL method uses a short test interval (0.1 m) under approximately steady state flow conditions (the pumping time before testing is 5 000–10 000 minutes). The spatial resolution of the PFL method is suitable to study the frequency and magnitudes of discrete values of the specific capacity. However, the long-term pumping implies that the data obtained from the PFL method can only be used to evaluate the conductive fracture frequency of continuously flowing networks, for example network situations like cases C–F in Figure 6-62. Indeed, the PFL method cannot detect any flow rates for situations such as in cases A and B, which represent single dead-end open fractures or isolated clusters of connected open fractures (compartments). The "hydraulic choke" (or bottleneck) phenomenon shown in case C is important as it affects the magnitude of the specific inflow rate measured at the intercept. If the impact of the "hydraulic choke" is such that the flow rate into the borehole falls below the lower detection limit, the "hydraulic choke" affects the measured number of flow anomalies contributing to the frequency, $P_{10,pfl}$.

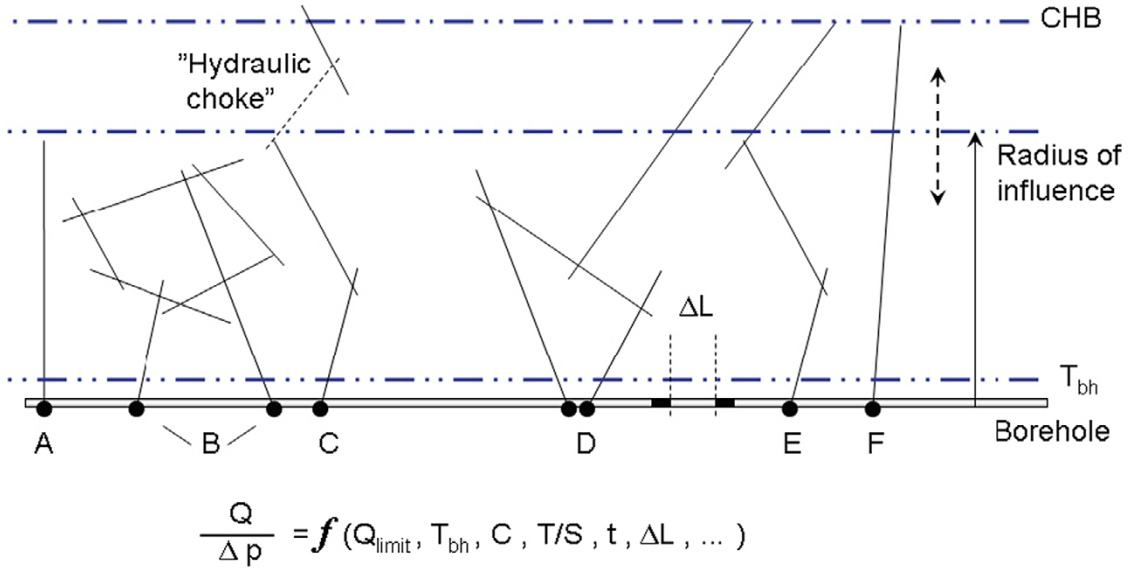

Figure 6-62. *Cartoon showing a borehole with six different symbolic fracture network situations. These are described in the text and referred cases A–F. The specific capacity, Q/Δp, measured in the borehole is dependent on several factors that are also described in the text. For the sake of clarity, the overall hydrogeological system is here indicated by a constant head boundary (CHB) suggesting a pseudo steady state flow regime at long test times. Further, the borehole is rotated 90° to improve the readability. Reproduced from Figure 2-5 in Follin (2008).*

The PSS method uses a longer test interval (> 5 m) and a much shorter pumping time (20 minutes). In effect, the PSS method has greater problems in distinguishing network situations like cases A–B from network situations like cases C–F. This means that using data from the PSS method alone for the hydrogeological DFN modelling could easily result in an over prediction of fracture connectivity in the sparsely fractured bedrock in between the deformation zones.

Due to the differences in spatial resolution and test time, the hydrogeological DFN modelling carried out for SDM-Site was based on data acquired with the PFL method. The results from the PFL measurements reported to Sicada are sometimes called fracture transmissivities. The conceptualisation of the specific capacity of each flow anomaly detected with the PFL method as a fracture transmissivity is based on the short test interval and Thiem's classic formula for steady-state, saturated, radial groundwater flow to a well in a porous medium (Thiem 1906):

$$T = (Q/\Delta h)\,[\ln(r_e/r_{BH}) / (2\pi)] \qquad 6\text{-}16$$

where r_e is the radius of influence of the hydraulic test and r_{BH} is the radius of the cored borehole. The results from the PFL measurements reported to Sicada are based on the assumption that the ratio of r_e/r_{BH} is constant along the borehole. The value of the ratio is chosen such that:

$$T = Q/\Delta h \qquad 6\text{-}17$$

In other words, the values reported to Sicada are not fracture transmissivities of the intersecting fractures, but test section specific capacities, where the intersecting flowing fractures are the last fractures in a network of flowing fractures.

The "hydraulic choke phenomenon" is likely to affect the PFL measurements more than the PSS measurements for the reasons described above. Hence, cross-plots of the specific capacities from the two test methods should allow for a judgment of how common the "hydraulic choke phenomenon" is. Figure 6-63 shows a cross-plot of PSS data versus PFL data from the hydraulic testing of borehole KFM06A (the location of this borehole is shown in Figure 6-60, drill site 6).

The specific capacities shown in Figure 6-63 are in general lower for the PFL method than for PSS method. Noteworthy, the look of the cross-plot shown in Figure 6-63 is repeated for almost every borehole investigated, which implies that the "hydraulic choke phenomenon" is quite common (Follin et al. 2007b).

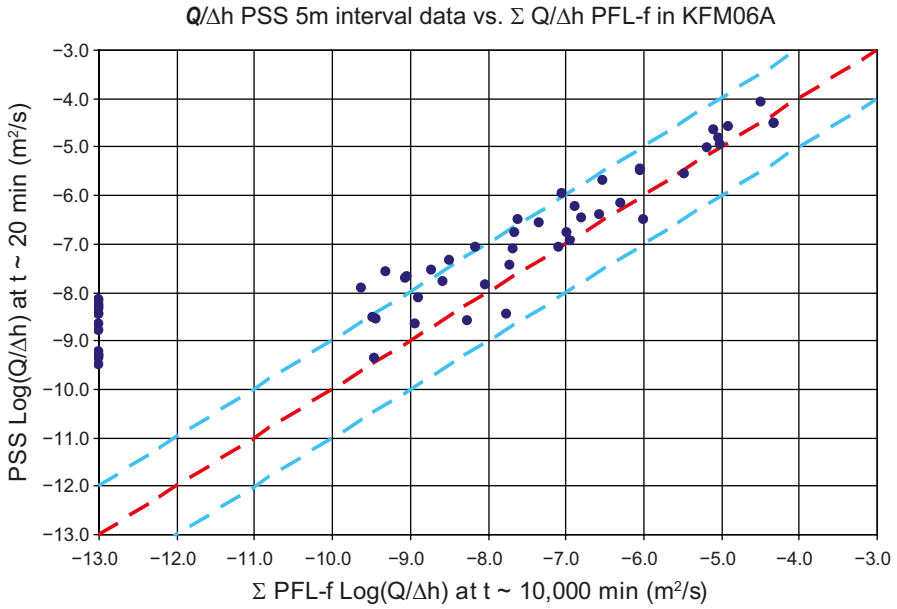

Figure 6-63. *Cross-plot showing specific capacities after 20 min of injection (PSS) versus specific inflow rates after one week of pumping (PFL) in borehole KFM06A. Data from PSS test sections without PFL data are plotted to the left for an arbitrary low value on the abscissa. Reproduced from Figure 4-11 in Follin et al. (2007b).*

In conclusion, the specific capacities of the intersecting features determined with the PFL method are not fracture transmissivities, but specific capacities of "hydraulic chokes" in the connected network of flowing fractures.

This characteristic affects the interpretations of the inferred orientations of the flowing fractures intersecting the borehole detected with the PFL method, since the fractures causing the "hydraulic chokes" may have different "orientations" than the flowing fractures intersecting the boreholes. Although the importance of hydraulic chokes for the distribution of measured specific capacities is not looked at in detail, this important phenomenon is honoured in the methodology used in the hydrogeological DFN modelling, see Section 6.6.5. That is, the measured values of $Q/\Delta h$ are not interpreted as transmissivities of the intersecting fractures, but as test section specific capacities (cf Equation 6-17. A forward modelling approach is used in the calibration process, where T values are generated and assigned to the stochastic network of features according to the three transmissivity models shown in Table 6-74. The different parameters associated with each transmissivity model are then altered until an acceptable match is reached for ten consecutive realisations using four different objective functions, see the four bullets shown at the end of Section 6.6.6.

6.6.8 Spatial and temporal variability of data (text reproduced from SR-Site Data report)

Spatial variability of data

Figure 6-64 shows Terzaghi corrected frequencies of open fractures and of the flowing fractures detected with the PFL method. The data come from the cored drilled boreholes at different locations and orientations in the target volume, that is, FFM02, FFM01, and FFM06, see Figure 6-59 and Figure 6-60. The thicker lines represent average values over all boreholes and the dotted lines represent the spread between individual boreholes, that is, the minimum and maximum values observed in any borehole. Figure 6-65 shows specific capacities of the flowing fractures detected with the PFL method. Again, the thicker line represents the geometric mean over all boreholes and the dotted lines represent the spread between individual boreholes. In conclusion, Figure 6-65 implies that the average Terzaghi corrected frequency of flowing fractures detected with the PFL method is very low at repository depth. Below –400 m elevation, this frequency is approximately 0.036 fractures per metre (36/km). Likewise, Figure 6-65 implies that the average specific capacity at repository depth is low, approximately 6.5×10^{-9} m^3/s per metre of head change.

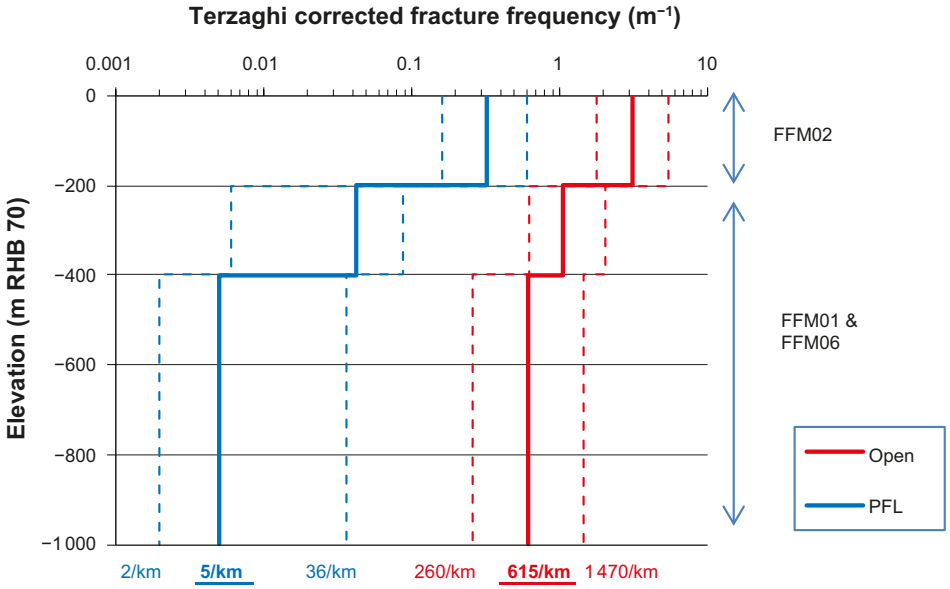

Figure 6-64. *Terzaghi corrected frequencies of open fractures and of the flowing fractures detected with the PFL method. The thicker lines represent average values over all boreholes and the dotted lines represent the spread between individual boreholes, i.e., the minimum and maximum values observed in any borehole (cf Selroos and Follin 2010, Figure 2-9).*

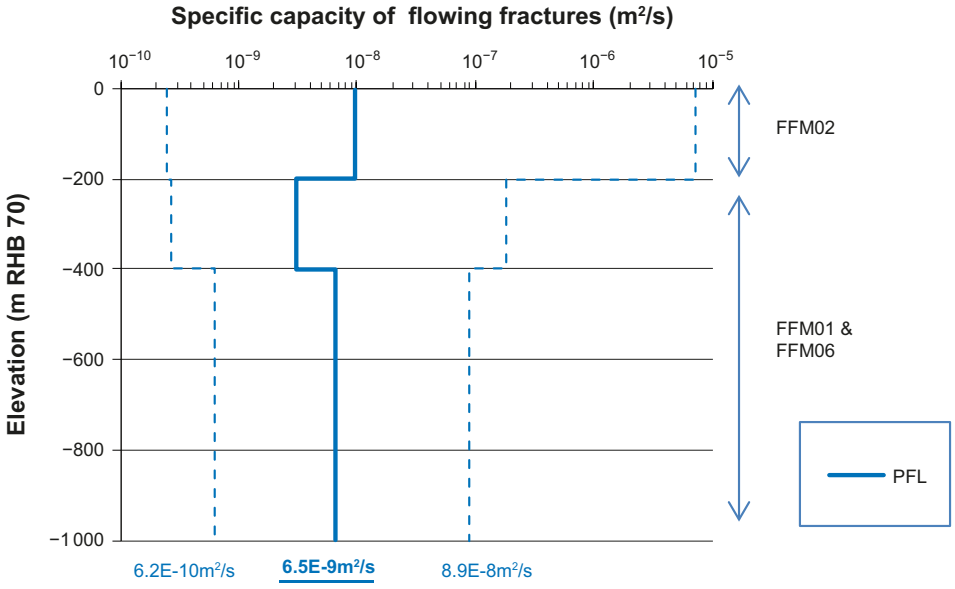

Figure 6-65. *Specific capacities of the flowing fractures detected with PFL method. The thicker line represents the geometric mean over all boreholes and the dotted lines represent the spread between individual boreholes, i.e., the minimum and maximum values observed in any borehole (cf Selroos and Follin 2010, Figure 2-9).*

Temporal variability of data

The geometrical and hydraulic properties reported in the **Site description Forsmark** describe the present-day hydraulic properties. It is advocated that the present-day properties are reasonable for the groundwater modelling of the excavation and operation periods as well as for the temperate period. For the groundwater flow modelling of the periglacial and glacial periods, temporal changes in the hydraulic properties seem more plausible, for example due to the potential impact of freezing and mechanical deformation. The temporal changes in the hydraulic properties to be used for SR-Site are described in Selroos and Follin (2010).

6.6.9 Correlations (text reproduced from SR-Site Data report)

As previously mentioned, the hydrogeological DFN modelling carried out in SDM-Site considers three types of correlation models between fracture transmissivity and fracture size, that is correlated, uncorrelated, and semi-correlated, see Table 6-74. As explained in Section 6.6.7, the use of different correlation models complies with the conclusion that the specific capacities measured at the borehole with the PFL method are not fracture transmissivities of the intersecting fractures but specific capacities of "hydraulic chokes" in the connected network of flowing fractures.

The hydraulic calibration (parameterisation) of the generated DFN realisations reveal that all of the tested transmissivity models give reasonable matches against the four 'goodness of fit' statistics discussed in Section 6.6.6. Hence, none of the tested transmissivity models is discarded in SR-Site. However, the semi-correlated transmissivity model is advocated to be the most realistic of the three models attempted. For SR-Site, it is suggested that the correlated and uncorrelated transmissivity models should be tested as variants.

Particle transport calculations were not carried out in SDM-Site. In SR-Site, particle transport calculations are made in the study dealing with groundwater flow modelling during periods with temperate climate conditions (Joyce et al. 2010) and in the study dealing with groundwater flow modelling during periglacial and glacial climate conditions (Vidstrand et al. 2010). These flow simulations employ a mixture of DFN, ECPM, and CPM representations of the rock mass volumes depending on scale and computer code, see Section 6.6.1 for details.

With respect to the flow related migration parameters discussed in Section 6.7, in particular the flow-related transport resistance (F [TL^{-1}]), the following correlations are noted:

- On a repository scale, a DFN representation will be used in the transport calculations. The flow-related transport resistances along flow paths in a DFN representation is calculated as:

$$F = \sum_f \left(\frac{2\, t_w}{e_t} \right)_f \qquad 6\text{-}18$$

where t_w is the advective travel time [T] in a fracture f along the flow path and e_t is the fracture transport aperture [L]. The fracture transport aperture is assumed to be correlated to the fracture transmissivity T [L^2T^{-1}] as:

$$e_t = a\, T^b \qquad 6\text{-}19$$

with $a = 0.5$ and $b = 0.5$. These values were also used in SDM-Site and originate from the Äspö Task Force (Dershowitz et al. 2003).

Selroos and Follin (2010) presents a range of fracture aperture relationships that could be considered as variants to Equation 6-19. The relationships are discussed in Hjerne et al. (2010), who compare their relative performance with regard to tracer experiments conducted at several Swedish sites.

All but one of the cumulative distribution functions shown in Figure 6-66 represent the different fracture aperture relationships discussed in Hjerne et al. (2010). The cumulative distributions are derived from transmissivity data of fractures that intersect deposition holes. The intersecting fractures belong to a fracture network realisation generated by Joyce et al. (2010) (see Selroos and Follin 2010 for details). Here, the empirical mass balance aperture (δ_m) relationship suggested by Hjerne et al. (2010) with $a = 0.28$ and $b = 0.3$ can be considered to yield an upper fracture aperture estimate for particle tracking calculations. This is due to the fact that in the conducted tracer tests, fractures (flow paths) with preferential properties for tracer transport have been chosen. Hence, the derived mass balance aperture relationship presented by Hjerne et al. (2010) should yield apertures on the larger side and is therefore considered appropriate for use as a bounding variant in SR-Site in particle tracking calculations.

Appendix A of this report discusses the concept of volumetric fracture aperture, e_v and the pink curve in Figure 6-66 shows the cumulative distribution function to be expected based on measurements carried out at Forsmark. The volumetric fracture aperture not only represents the part of the fracture where water flows, but also the part of the fracture holding stagnant water. Accordingly,

it represents the total water filled fracture volume. Therefore, one would expect the cumulative distribution function of the volumetric fracture apertures (violet curve in Figure 6-66) to be shifted towards higher values than the cumulative distribution function of the mass balance aperture (turquoise curve). However, this is not the case, which justifies a questioning of the physical logic of the mass balance aperture relationship for sparsely fractured rock.

The position of the volumetric fracture aperture values also supports discarding the two relations in the lower range (orange and green) as it would otherwise suggest that less than a few percents of the water filled fracture volume are available for water flow. Instead, it is suggested that Figure 6-66 with a and $b = 0.5$, is used as a lower aperture relationship in SR-Site, for example in buffer erosion calculations.

- On a site scale, the continuation of the DFN representation is upscaled to an ECPM finite-element representation provided that the distance from the repository is still within the range of the hydrogeological DFN modelling of the six fracture domains, FFM01–FFM06. Outside the bounds of these fracture domains, there is no hydrogeological DFN and the CPM approach is employed. The flow-related transport resistances along flow paths in the ECPM and CPM finite-element representations is calculated as:

$$F = \sum_{l} \left(\frac{a_r \, \Delta l}{q} \right) \qquad 6\text{-}20$$

where a_r is the fracture surface area per unit volume of rock (L^{-1}), Δl (L) is a step distance along the flow path, e.g., through one finite-element, and q (LT^{-1}) is the Darcy flux in the same finite-element.

Within the range of the ECPM representation, the fracture surface area per unit volume of rock will be calculated as:

$$a_r\,(x, y, z) = 2\, P_{32,element}\,(x, y, z) \qquad 6\text{-}21$$

That is, a_r is treated as a stochastic quantity that varies in space in accordance to a particular realisation of the underlying hydrogeological DFN model. In contrast, a_r is treated as homogeneous, i.e. statistically uniform (deterministic) quantity within the CPM representation.

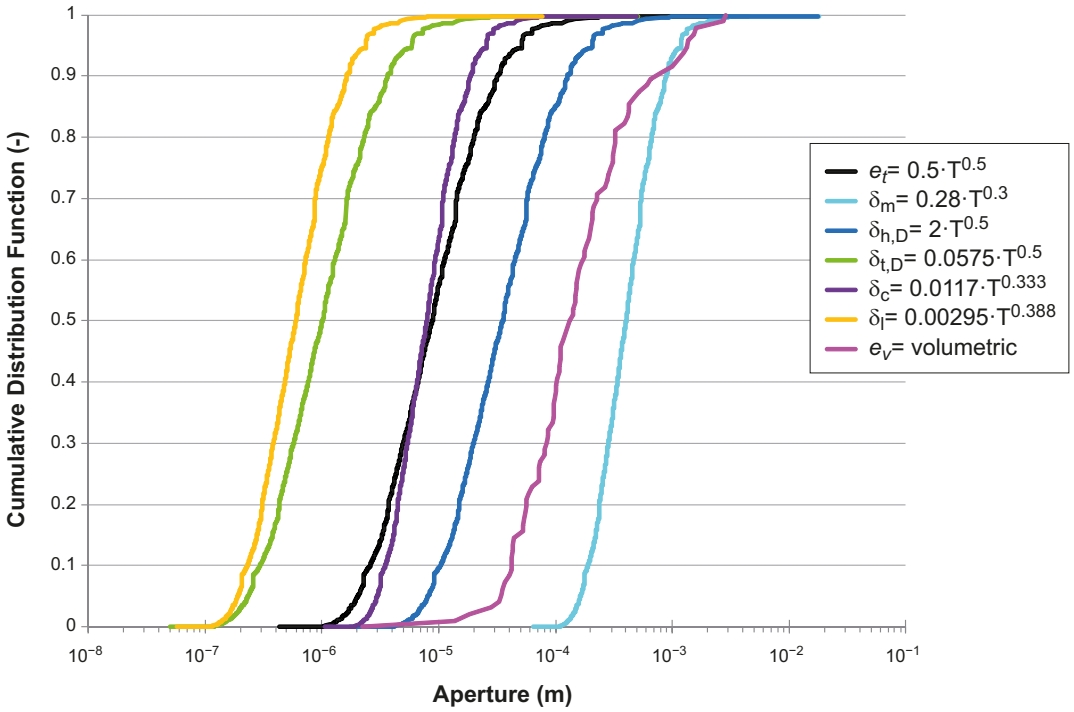

Figure 6-66. *Cumulative distribution functions of different fracture aperture relationships. The black curve represents Equation 6-19, the turquoise curve represents the mass balance fracture aperture relationship presented in Hjerne et al. (2010), and the violet curve represents the volumetric (water filled) fracture aperture data presented in Appendix A. The other curves are discussed in Hjerne et al. (2010).*

6.6.10 Result of supplier's data qualification (text reproduced from SR-Site Data report)

The hydrogeological DFN parameters to be used for FFM01 and FFM06 are tabulated in Table 6-75. Table 6-76 and Table 6-77 show the parameters to be used for FFM02 and FFM03–FFM05, respectively. The values provided for $P_{32,open}$ in these tables represent the Terzaghi corrected linear frequencies of open fractures, $P_{10,open,corr}$.

For the region outside the six fracture domains FFM01–FFM06, that is on a regional scale, there is no site-specific information available in the rock mass volumes between deformation zones from SDM-Site. Therefore, approximate values of homogeneous CPM properties (hydraulic conductivity K, kinematic porosity n_e, and flow-wetted fracture surface area per unit volume of rock mass a_r) are given in Table 6-78. A depth dependency is suggested in accordance with the depth zonations used for fracture domains FFM01 and FFM06. The extended heterogeneity case, described in Selroos and Follin (2010), invokes an ECPM representation on a regional scale and should be considered as a variant to the CPM properties specified in Table 6-78.

Table 6-75. Hydrogeological DFN parameters to be used for fracture domains FFM01 and FFM06.

Elevation	Fracture set name	Orientation set pole: (trend, plunge), conc. κ	Size model, power-law (r_0, k_r)	Intensity ($P_{32,open}$) valid size interval: (r_0, 564 m)	Transmissivity model (Table 6-74)
(m RHB 70)		(°,°, –)	(m, –)	(m^2/m^3)	
> –200	NS	(292, 1) 17.8	(0.038, 2.50)	0.073	Semi-correlated: (a, b, σ_{logT}) = (6.3×10^{-9}, 1.3, 1.0); Correlated: (a, b) = (6.7×10^{-9}, 1.4); Uncorrelated: (μ_{logT}, σ_{logT}) = (–6.7, 1.2)
	NE	(326, 2) 14.3	(0.038, 2.70)	0.319	
	NW	(60, 6) 12.9	(0.038, 3.10)	0.107	
	EW	(15, 2) 14.0	(0.038, 3.10)	0.088	
	HZ	(5, 86) 15.2	(0.038, 2.38)	0.543	
–200 to –400	NS	As above	As above	0.142	Semi-correlated: (a, b, σ_{logT}) = (1.3×10^{-9}, 0.5, 1.0); Correlated: (a, b) = (1.6×10^{-9}, 0.8); Uncorrelated: (μ_{logT}, σ_{logT}) = (–7.5, 0.8)
	NE	As above	As above	0.345	
	NW	As above	As above	0.133	
	EW	As above	As above	0.081	
	HZ	As above	As above	0.316	
< –400	NS	As above	As above	0.094	Semi-correlated: (a, b, σ_{logT}) = (5.3×10^{-11}, 0.5, 1.0); Correlated: (a, b) = (1.8×10^{-10}, 1.0); Uncorrelated: (μ_{logT}, σ_{logT}) = (–8.8, 1.0)
	NE	As above	As above	0.163	
	NW	As above	As above	0.098	
	EW	As above	As above	0.039	
	HZ	As above	As above	0.141	

Table 6-76. Hydrogeological DFN parameters to be used for fracture domain FFM02.

Elevation	Fracture set name	Orientation set pole: (trend, plunge), conc. κ	Size model, power-law (r_0, k_r)	Intensity ($P_{32,open}$) valid size interval: (r_0, 564 m)	Transmissivity model (Table 6-74)
(m RHB 70)		(°,°, –)	(m, –)	(m^2/m^3)	
> –200	NS	(83, 10) 16.9	(0.038, 2.75)	0.342	Semi-correlated: (a, b, σ_{logT}) = (9.0×10^{-9}, 0.7, 1.0); Correlated: (a, b) = (5.0×10^{-9}, 1.2); Uncorrelated: (μ_{logT}, σ_{logT}) = (–7.1, 1.1)
	NE	(143, 9) 11.7	(0.038, 2.62)	0.752	
	NW	(51, 15) 12.1	(0.038, 3.20)	0.335	
	EW	(12, 0) 13.3	(0.038, 3.40)	0.156	
	HZ	(71, 87) 20.4	(0.038, 2.58)	1.582	

Table 6-77. Hydrogeological DFN parameters to be used for fracture domains FFM03–FFM05. Transmissivity is increased by a factor 2 for fracture domain FFM04.

Elevation	Fracture set name	Orientation set pole: (trend, plunge), conc. κ	Size model, power-law (r_0, k_r)	Intensity ($P_{32,open}$) valid size interval: (r_0, 564 m)	Transmissivity model (Table 6-74)
(m RHB 70)		(°,°, –)	(m, –)	(m^2/m^3)	
> –400	NS	(292, 1) 17.8	(0.038, 2.60)	0.091	Semi-correlated: (a, b, σ_{logT}) = (1.3×10^{-8}, 0.4, 0.8); Correlated: (a, b) = (1.4×10^{-8}, 0.6); Uncorrelated: (μ_{logT}, σ_{logT}) = (–7.2, 0.8)
	NE	(326, 2) 14.3	(0.038, 2.50)	0.253	
	NW	(60, 6) 12.9	(0.038, 2.55)	0.258	
	EW	(15, 2) 14.0	(0.038, 2.40)	0.097	
	HZ	(5, 86) 15.2	(0.038, 2.55)	0.397	
< –400 m	NS	As above	As above	0.102	Semi-correlated: (a, b, σ_{logT}) = (1.8×10^{-8}, 0.3, 0.5); Correlated: (a, b) = (7.1×10^{-9}, 0.6); Uncorrelated: (μ_{logT}, σ_{logT}) = (–7.2, 0.8)
	NE	As above	As above	0.247	
	NW	As above	As above	0.103	
	EW	As above	As above	0.068	
	HZ	As above	As above	0.250	

Table 6-78. Homogeneous continuum properties to be used for the rock mass volumes outside the six fracture domains FFM01–FFM06.

Elevation	CPM properties outside FFM01–FFM06		
(m RHB 70)	K (m/s)	n_e (–)	a_r (m^2/m^3)
> –200	1×10^{-7}	1×10^{-5}	0.60
–200 to –400	1×10^{-8}	1×10^{-5}	0.30
< –400	3×10^{-9}	1×10^{-5}	0.30

6.6.11 Judgement by the assessment team

SKB has done extensive efforts to increase knowledge regarding the development and application of DFN models since SR-Site. However, this increase in knowledge is so far neither fully published nor fully implemented in relevant safety assessment calculation chains, and hence, the effects are not quantified yet. The judgement is thus to use the same data in PSAR as in SR-Site. However, this newly gained knowledge will be implemented in coming safety assessments.

6.6.12 Data recommended for use in assessment

The hydrogeological DFN data recommended for use are listed in Table 6-75 for fracture domains FFM01 and FFM06, in Table 6-76 for FFM02, and in Table 6-77 for FFM03–FFM05. The tables include the transmissivity models with their recommended constants. The semi-correlated transmissivity model is advocated to be the most realistic of the three models.

Concerning the aperture/transmissivity correlation (cf Equation 6-19) the following constants are recommended. As best estimate values for hydrogeological modelling and buffer erosion calculations, $a = 0.5$ and $b = 0.5$. As upper bounding values for hydrogeological modelling (particle tracking), $a = 0.28$ and $b = 0.3$.

The hydrogeological CPM data recommended for use are listed in Table 6-78 for rock mass volumes outside fracture domains FFM01–FFM06.

6.7 Flow-related migration properties

Several of the parameters controlling radionuclide transport are related to the amount and distribution of groundwater flow. The values of these flow-related migration parameters are essentially obtained by numerical simulation of groundwater flow using the hydrogeological models described in Section 6.6.

The PSAR is based on the same modelling of flow related migration properties as SR-Site. In the following sections, the modelling strategy is described (Section 6.7.1) followed by an account of the experiences from the SR-Site safety assessment (Section 6.7.2). Since the PSAR is based on the same data as SR-Site, the data qualification (Sections 6.7.3 to 6.7.10) is reproduced from the SR-Site Data report. In Section 6.7.11 the formal judgement by the assessment team to use the qualified data is presented followed by Section 6.7.12 where the recommended data is presented.

6.7.1 Modelling (text reproduced from SR-Site Data report)

This section describes what data are expected from the supplier, and in what SR-Site modelling activities the data are to be used.

Defining the data requested from the supplier

In radionuclide transport modelling, transport from the canister in the near-field is assumed to occur along three release paths. These are the Q1 path, with transport in a fracture intersecting the deposition hole; the Q2 path, with transport in the excavation damaged zone (EDZ); and the Q3 path, with transport in the deposition tunnel to an intersecting fracture. There are thus three release paths from the near-field into the far-field of the geosphere; it is the far-field parameters that are dealt with in this section.

The following flow-related migration parameters are requested for each deposition hole location within the repository:

- Darcy flux q (m/yr) for the Q1, Q2, and Q3 release paths. Also equivalent flow rates Q_{eq} (m^3/year) corresponding to the Q1, Q2, and Q3 release paths (Q_{eq1}, Q_{eq2}, and Q_{eq3}) are needed, which in turn are related to the groundwater flow rates for the Q1, Q2, and Q3 release paths. The Darcy fluxes and flow rates are calculated in fractures intersecting the deposition holes, in the EDZ in the tunnel floor adjacent to the deposition holes, and in fractures intersecting the deposition tunnel for the Q1, Q2, and Q3 release paths, respectively. The relation between flow rate, Darcy flux and equivalent flow rate for the Q1, Q2, and Q3 release paths are detailed in Chapter 3.2.6 and Appendix D of Joyce et al. (2010).
- Recharge and discharge coordinates in the biosphere along flow paths from the Q1, Q2, and Q3 release paths.
- Advective travel time t_w (yr) along flow paths to the recharge and discharge locations for the Q1, Q2, and Q3 release paths.
- Flow-related transport resistance F (yr/m) along flow paths to the recharge and discharge locations for the Q1, Q2, and Q3 release paths.

In addition the following parameters, which are not related to the paths, should be supplied:

- Measures of longitudinal dispersion Pe (–) or a_L (m) along the flow paths.
- Maximum penetration depth for solute diffusion into the rock matrix L_D (m), in case the fracture spacing is limiting (as opposed to the connectivity of the micoporous system discussed in Section 6.8).

Modelling activities in which data will be used

The flow related migration parameters described in this section are used in radionuclide transport calculations and in calculations assessing both the penetration of oxygenated and dilute groundwater from the surface to repository depth.

The radionuclide transport calculations, see the SR-Site Radionuclide transport report (SKB 2010c), are performed using different computer codes for the near-field and far-field, respectively. The near-field code is COMP23/Compulink (Romero et al. 1999, Cliffe and Kelly 2006, Vahlund and Hermansson 2006), and for the far-field either the code FARF31 (Norman and Kjellbert 1990, Elert et al. 2004) or MARFA (Painter and Mancillas 2009) are used. The codes use the following flow related migration parameters:

COMP23:

- Equivalent flow rates Q_{eq1}, Q_{eq2}, and Q_{eq3} for three possible release paths Q1, Q2, and Q3. The equivalent flow rates are obtained based on the calculated flow rates in the groundwater flow models described in Joyce et al. (2010) and briefly summarized in Selroos and Follin (2010).

FARF31 and MARFA:

- Flow related transport resistance F.
- Advective travel time t_w.
- Peclet number Pe in FARF31 or longitudinal dispersivity a_L in MARFA.
- Maximum penetration depth L_D into the matrix if a finite matrix is considered.

Biosphere assessment:

- Coordinates (x, y, z) at the end of each flow path connecting canister positions with exit locations.

The calculations of penetration of oxygenated water (Sidborn et al. 2010) and dilute water are based on analytical solutions using the flow related transport resistance and advective travel time along recharge flow paths.

The flow related transport resistance and advective travel time are integrated parameters along flow paths obtained through particle tracking in the flow models described in Section 6.6. Particles are released at each of the locations corresponding to the Q1, Q2, and Q3 release paths, see above. It is noted that FARF31 reads parameters integrated along the complete flow path, whereas MARFA reads segment wise integrated values; that is, the flow path is divided into a number of segments. This allows for an assignment of different retention models along the flow path; for example, different retention models may be applied to transport in tunnels and in fractured rock.

6.7.2 Experience from SR-Site

Modelling in SR-Site

See previous section.

Condidions for which data were used in SR-Site

See previous section.

Sensitivity to assessment results

This section briefly summarises experiences from the SR-Site safety assessment, which may be of direct consequence for the data qualification in this Data report.

The groundwater flow (hydrogeological) modelling performed as part of SR-Site was identical to what is outlined above; i.e., no new simulations have been performed as part of PSAR. Hence, the flow-related migration properties produced within PSAR are identical to the ones of SR-Site.

The main sensitivities related to the site-description explored in SR-Site was the uncertainty in the fracture transmissivity-size relationship implying that all three correlation models identified were recommended to be propagated for subsequent analyses of buffer erosion, canister corrosion and radionuclide transport. Here, the semi-correlated model provided the most favourable estimates of Darcy flux (equivalent initial flux), while the correlated model gave the highest flux values. For the flow-related transport resistance, the correlated model gave the most pessimistic results, while the other two models were quite comparable, although with more favourable estimates for the semi-correlated model at high values.

Other SDM-Site related variants were deemed not to warrant further consideration in the assessment. In addition, some specific safety assessment-motivated variants were addressed; these included e.g. parameterisation of EDZ and crown space, multiple realisations, and adoption of multiple particles at release locations thus addressing fracture network branching. Here, the assumptions concerning EDZ and crown space parameterisation had the expected impcats on fluxes at the corresponding release locations. Specifically, an increase in EDZ transmissivity resulted in increased fluxes for the Q2 and Q3 release paths, while an introduction of a crown space resulted in increased fluxes for the Q3 release path.

6.7.3 Supplier input on the use of data (text reproduced from SR-Site Data report)

The data supplied in this section have been produced by the SR-Site team; hence no supplier formally exists. None the less, the text is written according to the standard outline of the Data report.

The flow related migration properties are results of the groundwater flow simulations presented in Section 6.6 and in this section. Thus, all data pertinent for defining the groundwater flow simulations are also relevant for the results presented in this section.

6.7.4 Sources of information and documentation of data qualification (text reproduced from SR-Site Data report)

Sources of information

All the data presented in this section result from the groundwater flow simulations. The sources of information and data qualification of the data needed for these simulations are described in detail in Section 6.6 and in the individual modelling reports (Joyce et al. 2010, Vidstrand et al. 2010). A summary of the hydrogeological models and data used is given in Selroos and Follin (2010).

The simulations done are performed as two separate studies, one for the temperate period (Joyce et al. 2010), and one for the periglacial and glacial period (Vidstrand et al. 2010). Full references are given in Table 6-79. These reports summarise the different cases modelled and the justification of these cases.

The Excavation and Operation period is hydrogeologically analysed in Svensson and Follin (2010); this report is not further discussed in the present context since that analysis does not produce flow related migration data for use in subsequent assessment calculations. However, all three reports above are summarised and put in a SR-Site context in Selroos and Follin (2010).

Table 6-79. Main sources of information used in data qualification.

Joyce S, Simpson T, Hartley L, Applegate D, Hoek J, Jackson P, Swan D, Marsic N, Follin S, 2010. Groundwater flow modelling of periods with temperate climate conditions – Forsmark. SKB R-09-20, Svensk Kärnbränslehantering AB.
Vidstrand P, Follin S, Zugec N, 2010. Groundwater flow modelling of periods with periglacial and glacial climate conditions – Forsmark. SKB R-09-21, Svensk Kärnbränslehantering AB.

Categorising data sets as qualified or supporting

In this Data report the hydrogeological subject area is divided on two sections, Section 6.6 and this present section. This present section gives results from the SR-Site hydrogeological modelling, whereas Section 6.6 supplies the most important inputs to such modelling (although other inputs are also needed). Because of this, a deliberate deviation from the instruction given in Section 2.3.4 is made, and no sorting of input data as qualified or supporting is made in this section. What could be said in general concerning input data to hydrogeological modelling is the following:

The data sets used as input to the groundwater flow simulations are detailed in the individual reports referenced in Table 6-79. The main data set is related to the parameterisation of the hydrogeological discrete fracture network model detailed in Section 6.6. Additional data sets needed for the hydrogeological modelling, for example parameterisation of hydraulic conductor domains (deformation zones) and hydrogeological soil domains (regolith), as well as formulation of initial and boundary conditions for both flow and transport of salt and reference waters, are summarised in Selroos and Follin (2010).

Excluded data previously considered as important

No data have been excluded that previously have had a significant impact on the perception of the appropriate choice of data values or modelling approach.

6.7.5 Conditions for which data are supplied (text reproduced from SR-Site Data report)

Data are supplied for temperate period conditions, and for different combinations of periglacial (permafrost) and glacial period conditions, respectively. For the glacial period, also submerged conditions are included (see the SR-Site Climate report (SKB 2010g)for details). The temperate period is modelled as a continuation of today's conditions including the future shoreline displacement process and projected changes in salinity in the Baltic Sea. The present conditions are described in detail in the bedrock hydrogeology report of SDM-Site Forsmark (Follin 2008). The periglacial and glacial periods are more hypothetical; rather than trying to predict the future evolution, the models have been set up to bound the hydrogeological consequences associated with these climatic conditions. The future evolution of the climate is described in the SR-Site Climate report (SKB 2010g).

In the model of temperate conditions (Joyce et al. 2010), the repository is explicitly included in the model. The repository description includes deposition holes, deposition tunnels, transport and main tunnels, as well as the central area including ramp and shafts. Also the excavation damaged zone (EDZ) is included. All tunnels are assumed to be backfilled. Variants are performed on both EDZ and backfill parameterisation.

In the model of periglacial and glacial periods (Vidstrand et al. 2010), the repository is not included. This is justified by the much larger scale (super-regional) considered in these simulations. However, it is noted that boundary conditions are transferred from the super-regional scale model to the smaller scale models of Joyce et al. (2010); by using this approach, detailed flow related migration data incorporating the repository are obtained also for the glacial case.

Conditions in term of geological and other settings governing the hydrogeological data are further described in Section 6.6.5 and in Selroos and Follin (2010).

6.7.6 Conceptual uncertainty (text reproduced from SR-Site Data report)

The conceptual uncertainties associated with the hydrogeological modelling are summarised in Section 6.6 and described in detail in Selroos and Follin (2010).

A few uncertainties with specific relevance for the flow-related transport properties are highlighted here. First, it is noted that the advective travel time and flow related transport resistance are calculated along flow paths in steady-state velocity fields, That is, a snapshot-in-time approach is used. Clearly, different results would be obtained in transient flow fields, but the resulting uncertainty is judged small given that steady-state flow fields bounding the transient evolution are used.

Second, the combination of model scales within the hydrogeological applications as detailed in Selroos and Follin (2010) implies an uncertainty in some cases. Models in ConnectFlow may be combined in two ways: First, models can be embedded in each other in which case they are formally nested such that the whole flow system is solved simultaneously using constraint equations on the model interfaces, resulting in continuity of both pressure and velocity over the interfaces. Second, models may be solved separately using boundary conditions from the larger scale model on the boundaries of the smaller scale model. In this case, velocities are not necessarily continuous, and particles are manually moved from the smaller scale model to the larger scale model at the boundary. This implies an uncertainty in the flow path characteristics. Also, boundary conditions from the super-regional scale periglacial/glacial case model, developed using DarcyTools, are transferred to the smaller-scale temperate case model, developed using ConnectFlow, to calculate performance measures in the detailed repository scale. The transfer of boundary conditions between not only scales but also numerical codes implies an additional uncertainty.

An uncertainty stems also from the fact that individual fractures in the hydrogeological DFN model are modelled as homogeneous, whereas in reality there is some spatial variation of the aperture field within each fracture. In SR-Can, this uncertainty was dealt with by reducing all calculated flow related transport resistance values F by a factor of ten. In SR-Site, the F values are left unmodified based on arguments compiled in the SR-Site Radionuclide transport report (SKB 2010c). First, fracture-to-fracture variability is generally larger than within-fracture variability in aperture. Second, fluid can only enter and leave fractures on a limited area, significantly constraining the meander of flow paths. Third, substantial portions of the non-contacting fracture surface area outside of the dominant flow channels may still be accessible by diffusion within the fracture pore space and thus provide additional surface area for radionuclides to interact with the rock matrix.

Finally, the assumed relationship between fracture transmissivity and aperture will affect the calculated advective travel times. However, the uncertainty is considered small; moreover, the advective travel times do not have a strong influence on subsequently calculated entities within the compliance calculations.

6.7.7 Data uncertainty due to precision, bias, and representativity (text reproduced from SR-Site Data report)

Since the temperate period model resolves fractures at smaller scales and also has an explicit representation of the repository structures relative to the glacial period model, one may argue that a higher degree of precision is present in the former model. There is thus a relative difference in precision between the two models. However, it should be noted that the flow related transport properties data also for the periglacial/glacial conditions are calculated in the more detailed site-scale and repository-scale models developed for the temperate modelling, by transfer of boundary conditions from the super-regional scale glacial model to the site-scale and repository-scale models.

Since the super-regional periglacial/glacial model is set up to bound hydrogeological consequences for periglacial/glacial climate conditions rather than to provide a detailed prediction of the future, the results (performance measures) of these analyses are biased towards pessimism relative to the temperate period results.

There may be judged to be differences between the different performance measures concerning precision (accuracy) and bias in results. The two flow measures Darcy flux q and equivalent flow rate Q_{eq} depend primarily on the permeability and connectivity of the fractures system and applied boundary conditions. The accuracy of these measures is thus as good as the underlying description of the bedrock and knowledge of boundary conditions. When it comes to advective travel time, t_w, additional assumptions need to be made concerning porosity and/or transport aperture, both of which are highly uncertain entities. Hence, the advective travel time is associated with much more uncertainty than the flow measures. The flow related transport resistance F also requires additional assumptions concerning the flow-wetted surface along the flow path. This entity can be estimated with greater certainty than the aperture or porosity, but is still subject to great uncertainty. However, in an explicit discrete fracture network model, the flow-wetted surface is explicitly defined through the network properties, and thus the uncertainty in flow-wetted surface is given by the uncertainty in the discrete fracture network model, see Section 6.6. The resulting uncertainty in F is judged to be greater than the uncertainty in q or Q_{eq}, but smaller than in t_w.

The provided values on Peclet number, longitudinal dispersivity, and maximum penetration depth do not originate from the modelling described above, but are based on judgement and underlying data. The uncertainty can be judged minor for Peclet number and longitudinal dispersivity; also, the chosen values of these parameters generally have a small effect on calculated radionuclide transport characteristics. The uncertainty in maximum penetration depth is related to the uncertainty in fracture frequency, and is thus smaller than other uncertainties discussed here.

It is not possible to provide detailed quantitative measures of the uncertainties listed above (combination of conceptual, precision, bias, and representativity). However, it is judged that the greatest uncertainty is associated with the periglacial/glacial model, followed by the uncertainty discussed in relation to the performance measures of the temperate model, and finally followed by the uncertainties associated with Peclet number, longitudinal dispersivity, and maximum penetration depth. Due to the conceptual uncertainty related to understanding of periglacial/glacial processes, several variants as described in Table 6-84 in Section 6.7.10 are propagated to the assessment calculations. Also for the temperate period calculations, see Table 6-82, uncertainties are handled by propagating several variants. The key uncertainty is related to the assumed fracture size-transmissivity relationship. The uncertainties related to Peclet number, longitudinal dispersivity, and maximum penetration depth are so small that no variants are deemed necessary to propagate.

6.7.8 Spatial and temporal variability of data (text reproduced from SR-Site Data report)

Spatial variability of data

The calculated Darcy fluxes are point values in space; one point (three points, if a distinction is made between release paths Q1, Q2, and Q3) for each canister deposition hole position is considered. Depending on the underlying variability of the hydraulic properties and boundary conditions for assumed flow, the Darcy fluxes will display a variation.

The advective travel time and flow related transport resistance are Lagrangian quantities integrated along flow paths within the FARF31 application. The integration implies an averaging; that is, the order between high and low values along the path does not matter as long as the cumulative result is the same. However, it is noted that the integrated values obtained at the end of each flow path will vary between flow paths even though averaging takes place. Specifically, there tends to be large variability in tw and F values due to the varying nature of the flow path distribution; that is, some flow paths are short and primarily located in high permeability features such as deformation zones, whereas other flow paths are long and characterised by low permeability conditions.

In Table 6-80 and Table 6-81 statistics of the Darcy flux and flow related transport resistance are exemplified in tabulated form for two central cases; the temperate period at 2000 AD, and the glacial case without permafrost for an ice front location right above the repository. In Table 6-81 the flow paths lengths for recharge and discharge are also given. The tables are based on the hydrogeological base case with stochastic fractures but homogeneous deformation zones (including a depth trend). The tables thus reflect a single realisation. There is some variability in the entities in Table 6-81 between realisations (not shown in table), indicating that the spatial variability results in uncertainty. Multiple realisations are considered within the temperate period only; within the periglacial/glacial period, the conceptual uncertainties are judged to dominate over the uncertainty implied by spatial variability.

The advective travel time is generally strongly correlated to the flow related transport resistance. Also, the equivalent flow rate is directly related to the Darcy flux, so the results shown in Table 6-80 and Table 6-81 provide a good overview of the characteristics of the different cases. Furthermore, it is noted that the flow path length provided in Table 6-81 for the glacial case is not a formal performance measure, but is provided in the table in order to illustrate differences between recharge and discharge flow paths. As indicated, recharge flow paths tend to be longer than discharge flow paths for the glacial conditions. Also advective travel time and flow related transport resistance along the recharge and discharge flow paths, respectively, may thus be quite different.

Table 6-80. Resulting statistics of Darcy flux (m/yr) at deposition hole locations, and flow-related transport resistance F (yr/m) for the temperate period at 2000 AD for the three release paths Q1, Q2, and Q3. Fraction of particles in the last row indicates the fraction of released particles discharging at the top surface of the model; the statistics for F in the table are based on this fraction.

Log(*q*), Log(*F*)	*q* (Q1)	*q* (Q2)	*q* Q(3)	*F* (Q1)	*F* (Q2)	*F* (Q3)
Mean	–5.40	–2.39	–5.37	6.60	6.25	6.18
Median	–5.37	–2.42	–5.34	6.60	6.36	6.28
5th percentile	–7.17	–3.15	–6.61	5.39	4.27	4.34
10th percentile	–6.79	–3.02	–6.35	5.67	5.04	5.03
25th percentile	–6.12	–2.78	–5.86	6.15	5.77	5.72
75th percentile	–4.69	–2.02	–4.87	7.06	6.86	6.77
90th percentile	–4.12	–1.75	–4.49	7.56	7.37	7.25
95th percentile	–3.73	–1.57	–4.26	7.92	7.71	7.56
Std deviation	1.07	5.00×10^{-1}	7.24×10^{-1}	7.67×10^{-1}	9.72×10^{-1}	9.30×10^{-1}
Variance	1.15	2.50×10^{-1}	5.24×10^{-1}	5.88×10^{-1}	9.45×10^{-1}	8.66×10^{-1}
Max value	–7.64	-5.13×10^{-1}	–1.98	9.14	9.42	8.84
Min value	–8.61	–4.18	–7.93	3.54	2.95	3.02
Fraction of particles	0.399	1.000	1.000	0.243	0.830	0.682

Table 6-81. Resulting statistics of path length L (m), flow-related transport resistance F (yr/m), and Darcy flux (m/yr) at deposition hole locations for the Glacial case without permafrost for an ice front location right above the repository. Subscripts "re" and "di" represent recharge and discharge flow paths, respectively.

Log(*L*), Log(*q*), Log(*F*)	L_{re}	F_{re}	*q*	L_{di}	F_{di}
Mean	4.447	6.101	–3.517	3.085	4.278
Median	4.447	6.093	–3.526	3.071	4.285
5th percentile	4.435	5.794	–4.724	2.874	3.644
10th percentile	4.437	5.855	–4.604	2.906	3.773
25th percentile	4.441	5.982	–4.071	2.979	4.033
75th percentile	4.454	6.236	–3.190	3.180	4.454
90th percentile	4.458	6.373	–2.338	3.273	4.888
95th percentile	4.461	6.418	–1.745	3.345	4.984
Std deviation	0.008	0.187	0.825	0.145	0.402
Variance	0.000	0.035	0.681	0.021	0.161
Max value	4.475	6.463	–0.747	3.606	5.801
Min value	4.430	5.574	–4.998	2.789	2.919
Fraction of particles	0.390	0.390	1.000	0.895	0.895

Peclet number and longitudinal dispersivity are provided as effective values for the whole model domain; hence judgement concerning spatial variability in these properties is not relevant. Maximum penetration depth depends on average fracture spacing, see Section 6.7.10 for details. Fracture spacing clearly varies in space; specifically fracture frequency tends to decrease with depth. However, for the modelling in SR-Site, a single value of maximum penetration depth representative for the rock at repository depths is chosen.

Temporal variability of data

Temporal variability is handled by using different model set-ups for the different climate domains, that is, temperate and periglacial/glacial, respectively, and also by representing a time evolution within the different climate domains.

In the temperate domain modelling, the triplets (Darcy flux or equivalent flow rate, advective travel time, and flow related transport resistance) are calculated at snapshots-in-time. The chosen snapshots are 2000 AD, 3000 AD, 5000 AD, and 9000 AD. The differences in calculated triplets are due to the fact that the snapshots-in-time are characterised by different shoreline positions. A more distant shoreline position (lower elevation) results in longer flow paths from the repository and generally slightly higher advective travel times and flow related transport resistance values. The Darcy flux at the canister deposition hole positions is not affected as much by the shoreline position.

During the glacial period, both higher and lower flow conditions are experienced. When the ice front is in close proximity to the repository (located right above the repository), Darcy fluxes are high and advective travel times and flow related transport resistance values low. However, these conditions only last for a short time period. Conversely, when the site is completely ice covered, Darcy fluxes are lower and advective travel times and flow related transport resistance values higher, as compared to the temperate period. This time period may last for tens of thousands of years (cf the SR-Site Climate report 2010g). Also the period with submerged conditions, when the ice sheet has retreated, is characterised by lower Darcy fluxes than during the temperate period. The periglacial/glacial simulations are described in detail in Vidstrand et al. (2010) and summarised in Selroos and Follin (2010).

6.7.9 Correlations (text reproduced from SR-Site Data report)

The same correlations as described for SR-Can above are relevant for conditions within SR-Site. However, in SR-Site these correlations are explicitly used in a more rigorous manner than in SR-Can, as explained below.

Detailed models incorporating the repository structures are only available for the temperate period modelling utilising combined site-scale and repository-scale models. Thus, transport issues related to engineered structures such as the EDZ can only be studied in these models. In the super-regional scale model used for periglacial and glacial conditions, the repository is not included. Two alternative approaches to resolve this shortcoming are utilised in SR-Site. In the first approach, triplets from a given climate period and snapshot-in-time are used directly, or alternatively in the case of the periglacial/glacial domain, boundary conditions from the super-regional scale model are transferred to the site-scale and repository-scale models for calculation of performance measures. It is recognised that the snapshots emanating from the site-scale and repository-scale models have higher resolution than snapshots from the super-regional scale model.

In the second approach, the values of the triplets from the temperate period model are re-scaled based on the Darcy flux ratio between temperate period conditions and the other conditions considered (e.g. periglacial, glacial, or submerged). The scaling is argued to be appropriate based on the correlation between the triplets. It is fully recognised that flow path characteristics in terms of length and discharge locations will vary between different climatic states; hence, an assumption is made that these different characteristics are of second order relative to the changes implied by the change in flow magnitude.

6.7.10 Result of supplier's data qualification (text reproduced from SR-Site Data report)

Below, references are made to the resulting triplets for the different cases considered within the temperate, periglacial, and glacial period simulations. Within each period, the importance of the cases for subsequent assessment calculations is discussed.

At the end of the section, the suggested Peclet number, longitudinal dispersivity, and maximum penetration depth are presented.

Temperate period

In Table 6-82 the temperate period cases analysed in Joyce et al. (2010) that result in input for the radionuclide transport models are listed. Furthermore, references are made to where tabulated results can be found for each case. For each modelling case, a data file is delivered for each Q1, Q2, and Q3 release path. Table 6-83 shows an excerpt of such a data file, displaying four out of 6916 rows (one row for each deposition hole).

Table 6-82. Modelling cases and sources of tabulated results.

Hydrogeological modelling case	Sources of tabulated triplets used by FARF31	Sources of segment data used by MARFA
Hydrogeological base case	SKBdoc 1255039	SKBdoc 1256019
Alternative DFN transmissivity-size relationships	SKBdoc 1255039	SKBdoc 1256019
Inclusion of possible deformation zones	SKBdoc 1255039	
Unmodified vertical hydraulic conductivity	SKBdoc 1255039	
Extended spatial heterogeneity	SKBdoc 1255039	
Tunnel variants	SKBdoc 1255039	SKBdoc 1256019

Table 6-83. Excerpt from resulting data file from hydrogeological modelling. Four out of 6916 rows are displayed. The resulting data files also feature other columns than shown in the excerpt, with data not specifically requested in this present section.

POINT	XS	YS	ZS	XE	YE	ZE	OKFLAG
1	1631091.11	6700709	–473.89	1631609	6701245	–0.63	0
2	1631085.04	6700712	–474.01	1631602	6701257	–0.74	0
3	1631081.05	6700715	–474.11	1631559	6701239	–0.73	0
4	1631076.02	6700719	–474.22	1631607	6701256	–0.72	0
POINT	**T0**	**U0**	**QEQ**	**TW**	**F**	**L**	
1	2.00×10^{3}	4.05×10^{-3}	5.32×10^{-4}	3.96×10^{1}	1.53×10^{5}	1.65×10^{3}	
2	2.00×10^{3}	8.37×10^{-3}	7.65×10^{-4}	1.56×10^{1}	9.58×10^{4}	1.26×10^{3}	
3	2.00×10^{3}	4.34×10^{-3}	5.65×10^{-4}	2.78×10^{1}	2.09×10^{5}	1.52×10^{3}	
4	2.00×10^{3}	8.05×10^{-3}	9.90×10^{-4}	2.02×10^{1}	9.49×10^{4}	1.44×10^{3}	

Point indicates path number.
XS, YS and ZS are coordinates for start of flow path.
XE, YE and ZE are coordinates for exit location.
OKFLAG indicates whether or not a particle reached the model boundary.
T0 is release time.
U0 is Darcy flux (m/yr) for Q1 and Q2; UR is used for Q3 (not shown in this excerpt).
QEQ is the equivalent flow rate for Q1 and Q2; QEQR is used for Q3 (not shown in this excerpt).
TW is the advective travel time in the rock, i.e. in the DFN (yr).
F is the flow related transport resistance for the rock, i.e. in the DFN (yr/m).
L is the path length in the rock, i.e. in the DFN (m).

The so-called Hydrogeological base case is a representation of site conditions based on the understanding as expressed in the SDM-Site model (Follin 2008). The justification for the other variants are given in Selroos and Follin (2010) and the implementation is described in Joyce et al. (2010). It is here argued that the Hydrogeological base case is the central case to propagate to assessment and compliance calculations. It is the case that best represents perceived site conditions.

In Figure 6-67, cumulative distribution functions of the Darcy flux, advective travel time, and flow related transport resistance for the different snapshots-in-time are exemplified.

Within the Alternative fracture size-transmissivity relationships, both completely correlated and un-correlated models have been studied. Both the correlated and uncorrelated models yield less favourable results than the semi-correlated model, but are hard to defend from a hydrogeological perspective. Nevertheless, it is argued that these cases need to be propagated. Out of the two, the correlated model exhibits tails of high Darcy fluxes and low *F*-values; hence this case is likely more important to propagate. It is also judged important to analyse multiple realisations of these cases in order to capture the uncertainty implied by spatial variability.

The Tunnel cases representing a gradual decline in the properties of the EDZ result in correspondingly more unfavourable results. The case with a crown-space, that is a consolidation of the backfill material in the tunnel resulting in a gap between backfill and tunnel ceiling, also yields unfavourable results. It is argued that within the tunnel cases, both the crown-space case and the worst EDZ case (EDZ with $T = 1 \times 10^{-6}$ m^2/s) need to be propagated.

The cases based on inclusion of possible deformation zones, an unmodified vertical hydraulic conductivity, and the extended spatial heterogeneity, do not greatly modify the results and are hence not further discussed here.

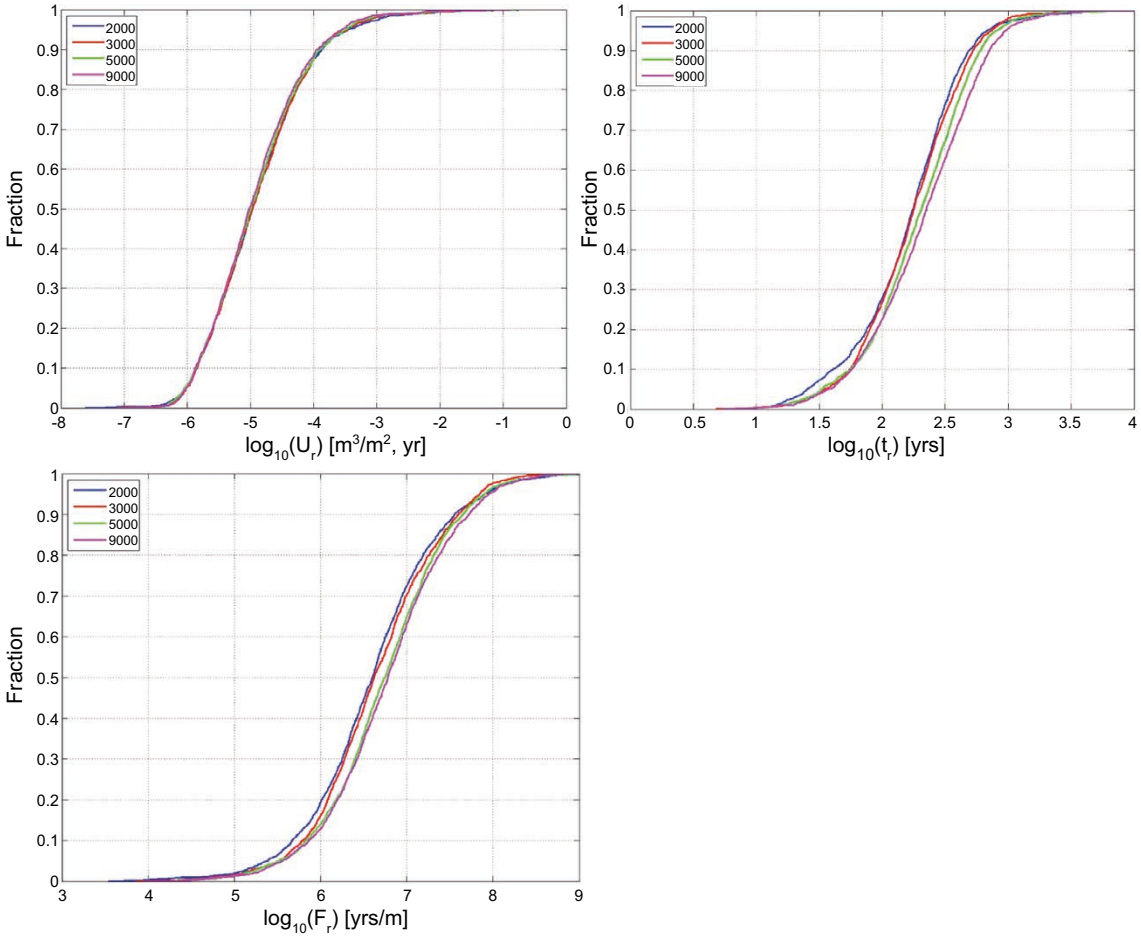

Figure 6-67. *Normalised CDF plots of Darcy flux q (denoted U_r in figure caption,) t_w, and F (denoted t_r, and F_r in figure captions to indicate that t_w and F are calculated in the bedrock described as a DFN only) in the Hydrogeological base case model at 2000 AD, 3000 AD, 5000 AD, and 9000 AD for release path Q1. The t_w and F_r plots are based on particles successfully reaching the model top boundary (cf Selroos and Follin 2010, Figure 5-9).*

Periglacial and glacial period

In Table 6-84 the periglacial and glacial period cases analysed in Vidstrand et al. (2010) are listed. Also, the glacial case based on a transfer of boundary conditions from the super-regional model of Vidstrand et al. (2010) to the smaller scale model of Joyce et al. (2010) is included in the table. Furthermore, references are made to where tabulated results can be found for each case (on the same form as displayed in Table 6-83).

Table 6-84. Modelling cases and sources of tabulated results.

Hydrogeological modelling case	Sources of tabulated triplets
Glacial case without permafrost.	SKBdoc 1255039
Glacial case without permafrost and North–South ice profile.	SKBdoc 1255039
Glacial case without permafrost and Distorted permeability conditions.	SKBdoc 1255039
Glacial case with permafrost – no permafrost tongue. Glacial case with permafrost – 2 km permafrost tongue.	SKBdoc 1255039
Glacial case without permafrost – boundary conditions transferred from super-regional to site-scale and repository-scale models.	SKBdoc 1255039

The variant with a North–South ice profile direction addresses the uncertainty in ice direction, whereas the variant with distorted permeability conditions addresses an uncertainty in permeability (hydraulic conductivity) related to mechanical effects (see Vidstrand et al. 2010 for details).

In addition to the cases listed in Table 6-84, results can be extracted for a case with permafrost but no ice (that is, permafrost has developed but the ice sheet has not yet arrived), and for a submerged case (when the ice sheet has completely retreated and the site is covered by a sea). Results for these two cases are contained within the Glacial case without permafrost for the submerged case, and within results for the Glacial case with permafrost for the permafrost only case. The set-up of these modelling cases is described in more detail in Vidstrand et al. (2010) and summarised in Selroos and Follin (2010). It is noted that the Glacial case without permafrost and glacial cases with permafrost together constitute a base case; that is, during glacial advance permafrost and an ice sheet exist together, while during retreat no permafrost is present and the glacier is warm based, see the SR-Site Climate report (SKB 2010g) for further details.

The glacial case without permafrost, with an ice front location above the repository, yields the most unfavourable results. This is the case for which boundary conditions are transferred to the site-scale and repository-scale models incorporating an explicit representation of the repository. For the other ice front locations, the results are much more favourable. Figure 6-68 shows the normalised Darcy flux calculated in the super-regional model for the glacial case without permafrost in a few observation points at repository depth during a glacial advance and retreat. Values are normalized to the flux value for temperate conditions. It is clearly seen that high groundwater flow conditions are experienced during the two ice front passages, while during ice coverage the Darcy flux in most observation locations are below the corresponding temperate value.

The alternative cases considered, that is the North–South ice profile and Distorted permeability variant (modified transmissivity for some fractures) do not provide substantially different results and are not suggested to be propagated.

In Figure 6-69, the median as well as maximum and minimum Darcy flux values representing the full set of deposition hole locations are shown as obtained in Vidstrand et al. (2010). The results indicate that the situation with permafrost only, that is the period before onset of the glacial advance provides more favourable conditions than the temperate case. The Glacial case without permafrost provides the highest fluxes, while the cases with combined permafrost and ice sheet provide somewhat more favourable conditions than the pure glacial case. The Glacial maximum case, that is, when the site is fully covered by an ice sheet, and the submerged case provide more favourable conditions than the temperate case.

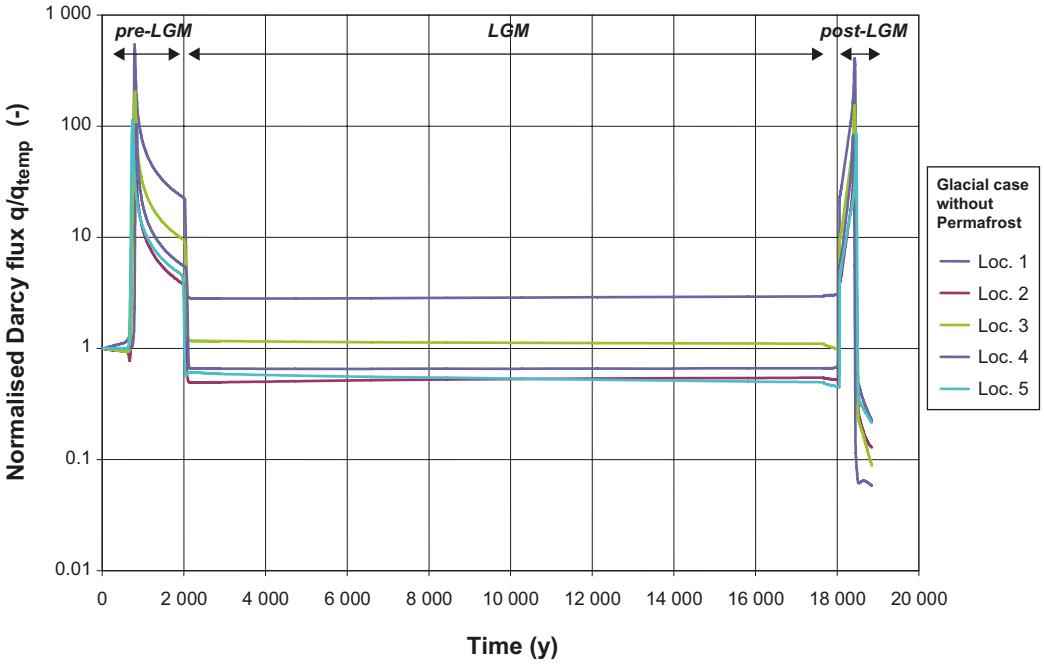

Figure 6-68. *Change in Darcy flux ratio, (q/q_{temp}) during a cycle of approximately 18 ka. Between the two ice front passages, the model domain is completely covered by ice. The time scale represents the model simulation time rather than calendar time. Reproduced from Vidstrand et al. (2010, Figure 6-7).*

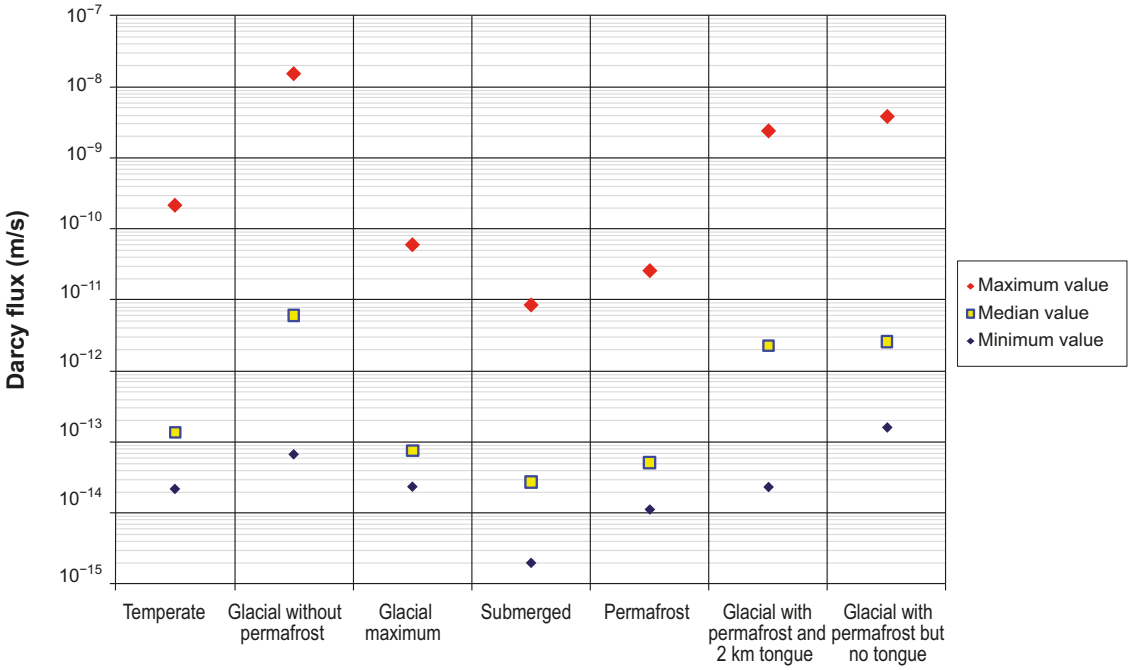

Figure 6-69. *Estimated Darcy fluxes for the main climate situations considered in a full glacial cycle. Minimum, maximum, and median values based on all deposition holes are shown for each situation. Reproduced from Figure 6-17 of Vidstrand et al. (2010).*

It is suggested that the glacial case without permafrost for the ice sheet location with the front right above the repository is propagated to subsequent assessment calculations. This is also the case where results exist from the detailed model with the repository explicitly included.

If a glacial cycle is to be represented, it is suggested that the Only permafrost (for a site with permafrost but no ice sheet), Glacial case with permafrost (for an advancing ice sheet), Glacial maximum (for a site covered by the ice sheet), Glacial case without permafrost (for a retreating ice sheet), and Submerged (for a fully retreated ice sheet) are used.

Peclet number, longitudinal dispersivity, and maximum penetration depth

The Peclet number (Norman and Kjellbert 1990), which relates to the relative importance of advective versus dispersive transport mechanisms along the individual flow paths through a dimensionless ratio, has not been further addressed since the SR-Can safety assessment. The central value recommended in SR-Can, which is 10, is recommended for use as a single point value in SR-Site. The justification is twofold:

- Large scale dispersion is handled through multiple flow paths in the groundwater flow models. Longitudinal dispersion along individual flow paths has a minor effect on breakthrough characteristics. Field evidence from tracer tests suggests that the dispersion length typically is 10 per cent of the distance of a tracer test; this yields a Peclet number of 10.
- Since dispersion is more of a model concept than a strict process, it is hard to justify shapes of distributions.

Given a path length of 500 m, representing a short path in the temperate simulations, a longitudinal dispersivity of 50 m corresponds to the Peclet number used in FARF31. Thus, in MARFA, a single value of the longitudinal dispersion, a_L = 50 m, is used.

Concerning the maximum penetration depth, it is argued in Section 6.8 that the matrix pore space is connected over all distances of interest within the assessment. Thus, the maximum penetration depth is given by the average fracture spacing. This is reported in the site-descriptive model (Follin et al. 2007c, Table 3-4) and is approximately 25 m for the rock in the depth interval –200 m to –400 m in fracture domain FFM01. The maximum penetration depth is half the fracture spacing, i.e., 12.5 m. It is suggested that this value is used as a deterministic value in SR-Site, also for rock at repository depth.

6.7.11 Judgement by the assessment team

SKB has done extensive efforts to increase knowledge regarding the development and application of discrete fracture network (DFN) models since SR-Site. Specifically, studies of flow and solute transport in single fracture and DFN models characterized by internal fracture aperture heterogeneity have been performed (Zou et al. 2017, Stigsson 2019, Frampton et al. 2019). Also, single fracture models (with aperture variability) incorporating rock stress effects have been developed (Stigsson 2019, Zou et al. 2018, Zou and Cvetkovic 2020). These studies indicate that it may not be conservative from a safety assessment perspective to neglect such internal fracture aperture variability when modelling solute and radionuclide transport.

However, this increase in knowledge is so far not fully implemented in relevant safety assessment calculation chains, and hence, the overall effects are not quantified in PSAR. The judgement is thus to use the same data in PSAR as in SR-Site. However, the newly gained knowledge will be implemented in coming safety assessments.

6.7.12 Data recommended for use in assessment

The assessment team recommends that the following cases, out of those tabulated in Table 6-82 and Table 6-84, are propagated.

Temperate period:

- Hydrogeological base case.
- Alternative DFN transmissivity-size relationships (correlated and uncorrelated).
- Tunnel variants including both EDZ and crown space cases.

Periglacial and Glacial period:

- Glacial case without permafrost.
- If a glacial cycle is to be considered, it is suggested to include the following cases: Only permafrost (for a site with permafrost but no ice sheet), Glacial case with permafrost (for an advancing ice sheet), Glacial maximum (for a site covered by the ice sheet), Glacial case without permafrost (for a retreating ice sheet), and Submerged (for a fully retreated ice sheet). It is further noted that for the Glacial case with permafrost, the case with no tongue under the ice sheet is suggested.

References to data files providing Q_{eq}, F, t_w, and q are given in Table 6-82 and Table 6-84. Furthermore, the Peclet number, longitudinal dispersivity, and maximum penetration depth recommended for use in SR-Site are listed in Table 6-85.

Table 6-85. Data recommended for use in SR-Site.

Parameter	Recommended data
Peclet number, *Pe* (–)	10
Longitudinal dispersivity, a_L (m)	50 m
Maximum penetration depth, L_D (m)	12.5 m

6.8 Non-flow related migration properties

Migration of solutes through fractured rock depends on several parameters. The data handled in this section, concerning the effective diffusivity, diffusion available porosity, sorption partitioning coefficient, and the scale on which the porous system is connected are related to the rock matrix properties themselves. These data are site-specific, depending on the geological settings and groundwater composition.

Other parameters of importance for solute transport are closely related to the groundwater flow, that is, they are “flow related”, and are discussed in Section 6.7.

The PSAR is based on the same modelling of Non-flow related migration properties as SR-Site. In the following sections, the modelling strategy is described (Section 6.8.1) followed by an account of the experiences from the SR-Site safety assessment (Section 6.8.2). Since the PSAR is based on the same data as SR-Site, the data qualification (Sections 6.8.3 to 6.8.10) is reproduced from the SR-Site Data report. In Section 6.8.11 the formal judgement by the assessment team to use the qualified data is presented followed by Section 6.8.12 where the recommended data is presented.

6.8.1 Modelling (text reproduced from SR-Site)

This section describes what data are expected from the supplier, and in what SR-Site modelling activities the data are to be used.

Defining the data requested from the supplier

The following data should be delivered by the supplier:

- The diffusion available porosity ε (–), also commonly referred to as the porosity, for the undisturbed rock matrix. Different species may experience different diffusion available porosity. When necessary, different porosities should be delivered for different rock volumes, judged as appropriate by the supplier.
- The effective diffusivity D_e (m^2/s) for the elements of the selected inventory and for dissolved O_2 and Fe^{2+}. The D_e should represent the undisturbed rock matrix. In estimating the effective diffusivity, it may be necessary to discuss the formation factor F_f (–). When necessary, different effective diffusivities should be delivered for different rock volumes, judged as appropriate by the supplier.
- The scale on which the porous system is connected L (m), thus allowing for matrix diffusion.
- The sorption partitioning coefficient K_d (m^3/kg) for the elements of the selected inventory. The uncertainty estimate of K_d data should encompass the underlying uncertainties in groundwater compositions that are likely to be encountered (cf Section 6.1). When possible and necessary, different K_d data should be delivered for different rock volumes, judged as appropriate by the supplier.

The elements of the selected inventory, for which transport parameters are required, are: H (assumed as HTO), C (inorganic and organic compounds), Cl, Ni, Se, Sr, Zr, Nb, Mo, Tc, Pd, Ag, Cd, Sn, I, Cs, Sm, Eu, Ho, Pb, Ra, Ac, Th, Pa, U, Np, Pu, Am, and Cm (see Section 2.2).

Modelling activities in which data will be used

Migration of dissolved radionuclides in the rock matrix occurs predominantly by diffusive transport, which in SR-Site is modelled by using Fick's laws. The diffusive transport will occur in the porewater that saturates the microporous system of rock at depth. Species will also, to different degrees, interact with the mineral surfaces surrounding the microporous system. Sorption of radionuclides in the far-field is in SR-Site modelled using a linear relation (justified by a low radionuclide concentration and equilibrium) between sorbed species and solute concentrations. The proportionality coefficient is the sorption partitioning coefficient K_d.

Radionuclide migration through the far-field is in SR-Site modelled by the transport simulation codes FARF31 (Norman and Kjellbert 1990, Elert et al. 2004) and MARFA (Painter and Mancillas 2009). The general approach taken when modelling radionuclide transport in the far-field is described in the SR-Site Radionuclide transport report (SKB 2010c).

Solute transport modelling of dissolved oxygen in fractured rock is described in Sidborn et al. (2010) and requires matrix diffusion data for dissolved oxygen and Fe^{2+}.

As part of the hydrogeological modelling, summarised in Selroos and Follin (2010), the salinity of the groundwater is estimated based on solute transport calculations that predominantly include matrix diffusion of chloride. However, for this modelling it is not necessarily pessimistic to use the matrix diffusivity of the undisturbed rock matrix, as delivered in this section, and additional considerations may be needed. In Appendix A of this Data report, a dedicated text on matrix diffusivities for use in hydrogeological modelling is given.

6.8.2 Experience from SR-Site

This section briefly summarises experiences from the SR-Site safety assessment, which may be of direct consequence for the data qualification in this Data report.

In the SR-Site Data report (SKB 2010a), it was noted that since SR-Can a number of issues that may give rise to uncertainty in D_e have been studied in detail. These uncertainties were reported in the SR-Site Data report itself, and in background documents. In addition, as mentioned in the up-dated Radionuclide transport report (Section 2.5.2), supplementary calculations performed in Löfgren (2014), Löfgren (2015) and Crawford and Löfgren (2019) indicate that the uncertainties associated with the formation factor and effective diffusivity estimates in SR-Site are shown to be too small to impact radionuclide transport modelling to any significant degree. It is also noted that the effective diffusivities are pessimistically chosen (based on in situ electrical resistivity measurements) relative to other safety assessments, and that the effective diffusivity close to fracture surfaces is likely to be

higher than that of the deep rock matrix. It is clearly demonstrated in Crawford and Löfgren (2019) that it is approximately the first decimeter of the rock matrix that dominates the retention effect for the SR-Site corrosion case (and other canister positions with F-factors of similar order of magnitude).

There are at present no new K_d values that can be used quantitatively in PSAR; however, it is noteworthy to mention that supplementary calculations performed in Crawford (2014) indicates that altered K_d values (due to changing pH conditions) may not have a very significant impact on overall dose rates since they are strongly source-term-determined. The conclusion can be further supported by the fact that since the leaking canister positions exhibit relatively low F-factors, the geosphere provides a very small attenuation effect for the dose-dominant nuclides in the main calculation cases which are greatly source-term dependent. This is also described in the **Radionuclide transport report** (Section 2.2).

6.8.3 Supplier input on the use of data (text reproduced from SR-Site Data report)

Diffusion available porosity

The supplier has no input on the use of the diffusion available porosity in safety assessments. However, there may be a need to clarify the difference between different types of porosities, and also the terminology used. For a more detailed discussion, and for references to the open literature, the SR-Site Geosphere process report (SKB 2010h) is recommended.

The physical porosity n (–), which is also called the total porosity, is comprised of connected and unconnected porosity. The connected porosity is comprised of transport porosity ε_t (–) and storage porosity. In essence, the transport porosity it the part of the porosity in which long range transport of solutes can occur through the rock matrix. In the storage porosity, also called dead-end porosity, no long-range but only short-range transport (typically on the millimetre scale or less) of solutes occurs. In igneous rock, an electrical double layer at the pore walls (mineral surfaces) hinders anions from occupying all pore space. Normally one considers that non-charged species and cations are not excluded from the electrical double layer, and thus can occupy the entire pore space. In this text, the diffusion available porosity, out of the connected porosity, is denoted ε (–).

Effective diffusivity and formation factor

Two approaches have been utilised for obtaining the effective diffusivity D_e of different solutes. The classical approach is to obtain the D_e for one or a few solutes in diffusion tracer tests. From the D_e of one solute, the D_e of another solute can be scaled based on the solute's D_w (m^2/s), which is the diffusivity in unconfined porewater. When performing this scaling, the formation factor F_f (–) is used, which is a factor representing the geometry of the porous system, but is normally defined as independent of the solute (under the prerequisite that there is no exclusion effect or enhancing effect, such as surface diffusion):

$$D_e = D_w \cdot F_f \qquad 6\text{-}22$$

Obtaining D_e has been done in laboratory through-diffusion tracer tests within the site investigation programme. It should be noted that as the laboratory tracer test is performed at different conditions than in situ, corrections of the obtained D_e are needed. The most important deviating condition in laboratory experiments, as compared to in situ, concerns the stress situation. In this text, a comparison of data from electrical resistivity measurements in situ and in the laboratory is used for estimating a transfer factor for differences in the stress situation. In doing this, the analogue between electro-migration and diffusion is used.

A second approach used is to first estimate the formation factor of the rock matrix by use of the in situ electrical resistivity method, and as a second step to obtain D_e by multiplying the formation factor with the solute's D_w. Estimating the formation factor by use of the in situ electrical resistivity method has routinely been done in the site investigation programme.

It has been decided to propagate data from both approaches to SR-Site if necessary, as the approaches are conceptually different. However, as seen later in this section, the data obtained by the two approaches are very similar. Therefore, only one set of data will be finally suggested for SR-Site.

It should be pointed out that since SR-Can, a number of issues that may give rise to uncertainty in D_e have been studied in detail. These uncertainties are reported in this text and in background documents. The reporting may give the impression that new uncertainties has arisen since SR-Can. However, the case is rather that known uncertainties of SR-Can have been better described. We are confident that the overall uncertainty concerning D_e has been reduced since SR-Can, and that it is relatively modest compared with many other uncertainties of the safety assessment.

Sorption partitioning coefficient

K_d data recommended for use in SR-Site are based in part on site-specific data obtained during the Forsmark and Laxemar site investigations, and in part on data contained in the open scientific literature. Site-specific data are available for the non-redox sensitive radionuclides of Cs(I), Sr(II), Ra(II), Am(III)/Eu(III), and Ni(II) in contact with different site-specific rock types and groundwater compositions. The groundwater compositions used in the laboratory investigations can broadly be described as being fresh, saline, marine, and brine in character and represent the approximate range of groundwater compositions encountered in situ at the Forsmark and Laxemar sites at the present day. Site-specific data are also available for the redox sensitive solutes U and Np for the same groundwater types and at mildly oxidising (atmospheric) conditions. K_d values for other trivalent actinide and lanthanide elements are assumed to be identical to that for Am(III) and Eu(III) sorption owing to the strong geochemical analogy existing between these solutes.

K_d data ranges for all other radionuclides and redox states are derived from literature sources for measurements performed using similar geological materials and contact groundwater compositions. For radionuclides where reliable measurement data was unavailable, geochemical analogies have been used to estimate approximate K_d ranges thought to be pessimistic for application within SR-Site.

Being a surface mediated process, sorption is sensitive to both the available surface area of constituent minerals whereon sorption can occur, as well as their geochemical properties. Because sorption partitioning data are obtained by laboratory experiments using crushed and sieved rock samples (frequently from different sites), corrections need to be made to extrapolate the data to be applicable for Forsmark site-specific rock types under in situ conditions. These corrections are referred to as *transfer factors* in SR-Site and are applied in a multiplicative fashion to the laboratory derived K_d data to obtain values appropriate for safety assessment calculations. Differences in surface area between crushed samples and intact rock are accounted for using a mechanical damage transfer factor f_m (–). Mineralogical differences between rock used in sorption experiments and the in situ rock are accounted for using a cation exchange capacity (CEC) transfer factor f_{cec} (–). For solutes that sorb principally by ion-exchange, a groundwater chemistry transfer factor f_{chem} (–) is defined to account for differences in groundwater composition under application conditions, relative to those used in laboratory sorption measurements.

6.8.4 Sources of information and documentation of data qualification (text reproduced from SR-Site Data report)

Sources of information

K_d, D_e, and ε data from the Forsmark laboratory site investigation programme is compiled in Selnert et al. (2008) and summarised in Byegård et al. (2008). Site investigation data on in situ apparent formation factors obtained by electrical methods are reported in various site investigation reports by Löfgren and co-authors (e.g. Löfgren 2007). Laboratory and in situ data are subsequently processed as part of Forsmark SDM-Site in Crawford (2008). A comparative study on formation factors obtained by tracer tests and electrical methods is reported in Löfgren et al. (2009). All these reports are written in accordance with the SKB quality assurance system and data therein can be seen as qualified, unless otherwise stated.

Concerning K_d data, a dedicated SR-Site report has been prepared to support this Data report. In this report (Crawford 2010), a detailed account of the various data sources used and specific details concerning individual radioelements are given. Raw sorption partitioning coefficients and BET surface area data from the Forsmark and Laxemar site investigations were obtained from the SIMON database. These data were used as a basis for the derivation of recommended K_d data ranges for site-specific rock types for the radioelements Cs, Sr, Ra, Ni, Am/Eu, Np(V), and U(VI). It should be noted

that K_d data from the Laxemar site are extrapolated to be applicable to Forsmark metagranite, and are subsequently pooled with the data obtained for actual Forsmark rock samples when estimating ranges of K_d uncertainty.

Recommended K_d ranges for solutes not among those studied in the site investigations were derived from sorption data and other supporting data described in the open literature. These data are also extrapolated to be applicable for Forsmark metagranite. Groundwater compositions during the temperate phase of repository evolution, as presented in Section 6.1, are documented in SKBdoc 1262945. The above mentioned publications, and others, are listed in Table 6-86.

Table 6-86. Main sources of information used in data qualification.

Crawford J, 2008. Bedrock transport properties Forsmark. Site descriptive modelling, SDM-Site Forsmark. SKB R-08-48, Svensk Kärnbränslehantering AB.

Byegård J, Selnert E, Tullborg E-L, 2008. Bedrock transport properties. Data evaluation and retardation model. Site descriptive modelling, SDM-Site Forsmark. SKB R-08-98, Svensk Kärnbränslehantering AB.

Selnert E, Byegård J, Widestrand H, 2008. Forsmark site investigation. Laboratory measurements within the site investigation programme for the transport properties of the rock. Final report. SKB P-07-139, Svensk Kärnbränslehantering AB.

Löfgren, 2007. Forsmark site investigation. Formation factor logging in situ by electrical methods in KFM01D and KFM08C. SKB P-07-138, Svensk Kärnbränslehantering AB.

Löfgren M, Pettersson M, Widén H, Crawford J, 2006. Forsmark site investigation. Formation factor logging *in situ* by electrical methods in KFM05A and KFM06A. SKB P-06-91, Svensk Kärnbränslehantering AB.

Waber H N, Gimmi, T, Smellie J A T, 2009. Porewater in the rock matrix. Site descriptive modelling, SDM-Site Forsmark. SKB R-08-105, Svensk Kärnbränslehantering AB.

Waber H N, Smellie J A T, 2005. Forsmark site investigation. Borehole KFM06A: Characterisation of pore water. Part I: Diffusion experiments. SKB P-05-196, Svensk Kärnbränslehantering AB.

Löfgren M, Vecernik P, Havlova V, 2009. Studying the influence of pore water electrical conductivity on the formation factor, as estimated based on electrical methods. SKB R-09-57, Svensk Kärnbränslehantering AB.

Löfgren M, 2004. Diffusive properties of granitic rock as measured by in situ electrical methods. Ph. D. thesis. Royal Institute of Technology, Stockholm, Sweden.

Crawford J, 2010. Bedrock K_d data and uncertainty assessment for application in SR-Site geosphere transport calculations. SKB R-10-48, Svensk Kärnbränslehantering AB.

Categorising data sets as qualified or supporting

The most important data sets used in qualifying the porosity, effective diffusivity, and formation factor are listed in Table 6-87. The great majority of the data comes from the Forsmark site investigation. It should be noted that the data sets in turn often rely on other measurements, which are references in the listed publications. Comments on the sorting of these data sets are given in Table 6-88.

The K_d data recommended for use in SR-Site represent a mix of data obtained during the site investigations at Forsmark and Laxemar, as well as data obtained from literature sources and deemed of sufficient quality to be appropriate for use in safety assessment calculations. In the compilation of K_d data ranges recommended for use in SR-Site, the focus has been primarily on the use of site-specific data where available. Data obtained from rock samples native to the Laxemar site are pooled with those obtained for Forsmark site-specific materials, but only after making corrections for differences in BET surface area and CEC. For radionuclides where site-specific data are not available, qualified literature sources have been used. In general, the data derived from literature sources are thought to be associated with larger uncertainties owing to differences in methodology, as well as different material properties of rock types and contact water compositions used in sorption experiments. The various sources of information and the data qualification are described fully in Crawford (2010), although some specific comments are given in Table 6-88.

Table 6-87. Qualified and supporting data sets.

Qualified data sets	Supporting data sets
1. Crawford (2008, Table 4-6): Porosities of different rock types. 2. Jacobsson (2007, Appendix B): Micro crack volume induced in excavation and preparation of samples (implying that only 80 % of the porosity seen at the laboratory exist in situ). 3. Selnert et al. (2008, Appendix 2): Effective diffusivities from through diffusion measurements. Data used extracted from Sicada (delivery note Sicada_09_098). 4. Thunehed (2007) and corresponding publications. Apparent formation factors measured by the electrical resistivity method at the laboratory. Data used extracted from Sicada (delivery note Sicada_09_098). 5. Löfgren (2007): Apparent in situ formation factors for KFM01D and KFM08C. Data used extracted from Sicada. 6. Löfgren et al. (2006): Apparent rock matrix resistivities for KFM06A. Data used extracted from Sicada. 7. Waber and Smellie (2005, Table A7): Porewater chloride concentrations of KFM06A. 8. Crawford and Sidborn (2009, Figure D-5) (and underlying data by Ohlsson (2000) and Löfgren (2004)): Surface conductivities versus apparent formation factor at the Oskarshamn site. 9. (Löfgren et al. 2009): Surface conductivities versus apparent formation factor at the Forsmark site. (Table 6-1, κ_s DC average and Table 6-5, F_f^{app} DC average). 10. (Crawford 2010): K_d values for radionuclides studied in Forsmark (Table 6-1) and Laxemar site investigations derived from raw data sets stored in the SIMON database. Qualified K_d data sets derived from open literature sources.	11. (Birgersson and Neretnieks 1988): in situ diffusion experiment at the Stripa mine with iodide showing D_p around 10^{-10} m^2/s (e.g. Figure 8.22) and ε around 0.3 % (e.g. Appendix 5). 12. (André et al. 2009): Specific surface area determinations on intact drill cores used to estimate transfer factors for undisturbed in situ rock at Forsmark. 13. (Sidborn et al. 2010): Fe content of Forsmark and Laxemar rock types used as a proxy to estimate CEC transfer factors for conversion of Laxemar site data to Forsmark rock types. 14. (Vilks et al. 2005), Tables 5 and 6: D_e data for HTO and iodide indicating anion exclusion of about half an order of magnitude.

Table 6-88. Justifications to the sorting of items in Table 6-87.

1–9. These are either site investigation reports of site-descriptive modelling reports written in compliance with the SKB system of quality assurance. All data are judged to be qualified. Unless otherwise stated, data concern relevant rock types of the Forsmark site. Data points non-representative for the undisturbed rock matrix at the site have been excluded in the data interpretation. It should be noted that in item 8, data from the Oskarshamn site have been used. These data are still judged as qualified, as they are obtained on drill core samples of similar geology as the rock at the Forsmark site.

10. This is a dedicated background reference for K_d data qualification used in SR-Site. It contains data obtained from the Forsmark and Laxemar site investigations. These data are judged as qualified. The reference also contains data derived from literature sources for solutes not investigated during the site investigations. These data are also judged to be qualified. All K_d data have been extrapolated to be valid for Forsmark metagranite under in situ conditions using multiplicative transfer factors to account for differences in sorptive surface area and mineralogy.

11. The report of Birgersson and Neretnieks (1988), that is a solid piece of scientific work, is written outside the SKB data qualification framework. As is performed on rock at the Stripa mine site it is judged as supporting.

12/ BET surface areas of intact monoliths of Forsmark metagranite (SKB rock code 101057) (André et al. 2009) were used to derive surface area and mechanical damage transfer factors for undisturbed in situ conditions. Although of central importance for the extrapolation of recommended K_d values these data are judged as supporting.

13. CEC transfer factors for conversion of Laxemar site-specific data to Forsmark appropriate values were estimated using statistical models of Fe content compiled by Sidborn et al. (2010) as a proxy for biotite mineral content. Since the data for both sites are obtained using the same method this is considered to be a reliable means of correcting for the CEC of different rock types. Although of central importance for the extrapolation of recommended K_d values these data are judged as supporting.

14. Vilks et al. (2005) is produced as part of the LTDE-SD programme at Äspö HRL. As the data concern rock that is not site-specific, and as the report is produced by an organisation outside SKB, the data are sorted as supporting (although still considered as adequate).

Excluded data previously considered as important

There are publications suggesting a porous system of crystalline rock which is only connected over a limited scale (millimetres to centimetres) (e.g. Miller et al. 1994). It is recognised that the extent of the pore connectivity has been debated (see e.g. Löfgren and Neretnieks 2006, Benning and Barnes 2009 for a brief summary). However, based on the present knowledge we consider the suggestion of very limited pore connectivity in crystalline rock as obsolete, or at least not applicable for the rock types at the Forsmark and Laxemar site investigation areas.

A correlation often referred to (the so-called Archie's law) is that between the formation factor and connected porosity. However, this correlation is very weak in the porosity region of interest ($\varepsilon \sim 0.1$ to 0.4 %), as shown by Byegård et al. (2008, Figure 3-5), and its usefulness is limited. Therefore, no data that are based on Archie's law are used in the data qualification.

In some cases literature data previously considered in SR-Can have been disregarded in the current recommendations on the grounds of a more restrictive set of selection criteria in SR-Site. The minimum basic requirement for literature data included in the K_d compilation is generally that the contact solution composition (ionic strength), BET surface area, and CEC (or some proxy indicator thereof) should be recorded for the material used in the reported studies. This was to enable quantitative transfer factors to be calculated for extrapolation of data to Forsmark site-specific materials. In a small number of cases this requirement was relaxed when data for the same materials were documented in other references by the same authors, although not in the primary reference. Expert judgment was then used to subjectively assess the quality of the reported data before a final decision was made whether or not to include the data in the compilation. Literature sources were generally not used for assigning K_d data for radioelements where site-specific data were available, although in some cases they are used as an independent check on the recommended ranges proposed.

Recent results not used

Parallel to the SR-Site project, the Long Term Sorption Diffusion Experiment (LTDE-SD) at the Äspö Hard Rock Laboratory is being finalised. Although the data presented in Widestrand et al. (2010a, b) and Nilsson et al. (2010) are interesting, it has not been practically possible to include them in this data qualification, due to the timing[18]. However, data produced earlier in the LTDE-SD programme (Vilks et al. 2005) have been used.

6.8.5 Conditions for which data are supplied (text reproduced from SR-Site Data report)

Part of this text borders on a data uncertainty discussion, and similar issues are also dealt with in Section 6.8.7.

General in situ conditions

- All data delivered should represent in situ conditions, where the most significant conditions are listed below.
- *Rock type and degree of alteration/disturbance:* The rock type is of importance for solute transport. The rock types dominating the target area are metamorphic and medium grained granite to granodiorite (SKB rock code 101057) and pegmatitic granite and pegmatite (rock code 101061). For a description of the rock types present at the Forsmark site, and their mineralogy, Stephens et al. (2007, Section 3.4) and Selnert et al. (2008, Section 4.2) are recommended.

  Rock adjacent to advective flow paths may be altered and disturbed. This may affect solute transport and it is generally assumed that radionuclide retention in altered and disturbed rock is increased, compared to in undisturbed rock. Although solute transport properties for the undisturbed rock matrix are requested, the transport consequences of altered and disturbed rock are included in the uncertainty discussions.

[18] At the time of finalising this Data report, the LTDE-SD reports are still in the factual review process.

- *Groundwater composition:* Interactions between solutes and rock mineral surfaces are influenced strongly by the groundwater composition. The groundwater composition at Forsmark, and its evolution during the glacial cycle, is described in Section 6.1.
- *In situ temperature:* The pore space geometry, interactions between solutes and rock mineral surfaces, and transport rate of solutes in the pores are to different degree affected by the temperature. The in situ temperature is dependent on the depth and also on the climate. Presently, the in situ temperature at 500 m depth is measured to be in the interval 11.2–12.0 °C, see the **Site description Forsmark** Section 6.2.9. However, during permafrost the temperature at repository depth may decrease to just a few degrees above freezing (see Section 7.1).
- *In situ stress:* The pore space geometry is affected by the stress placed upon the rock matrix. In Forsmark, the maximum horizontal and vertical stresses are estimated to be 41.0 ± 6.2 and 13.2 ± 0.3 MPa, respectively, see the **Site description Forsmark** Section 7.2.4. The stress is thought to substantially increase during glaciation (cf Section 6.4.10).

Consequence for ε and D_e

Rock type and degree of alteration/disturbance: The connected porosity, the formation factor, and the effective diffusivity are very much affected by the rock type, with its specific texture and grain size distribution. In the site investigations, the porosity and effective diffusivity have been obtained on hundreds of drill core samples from drill sites DS1 to DS9, ensuring that all important rock types at the site are included in the laboratory campaign (see e.g. Selnert et al. 2008, appendices 1 and 2). A great majority of the drill core samples used for the measurements were characterised as fresh rock, which means that the rock matrix seems to be undisturbed upon visible inspection. Only a few samples were altered or contained visible microfractures. Generally, altered rock display higher porosity and effective diffusivity than undisturbed rock (see e.g. Selnert et al. 2008, Figures 4-6 and 4-14).

Formation factors have been logged by the in situ electrical resistivity method in boreholes on drill sites DS1 to DS8, and tens of thousands of data points have been obtained. The data used in this text are obtained at locations at least a few decimetres away from the nearest open fracture. Therefore, rock matrix alteration/disturbance adjacent to flow paths is not accounted for. In addition, a great number of formation factors have been obtained by the laboratory electrical resistivity method. These measurements were performed on predominantly undisturbed drill core samples from drill sites DS1 to DS6, DS8, and DS9.

Groundwater composition: The porewater composition at depth, which may affect the data delivered in this section, should to a large extent mirror the groundwater composition and its evolution after repository closure, with two exceptions. The first is in the electrical double layer at mineral surfaces, where cations are up-concentrated. The second is in rock volumes many meters away from flow paths, where the pore water may differ from the fracture water as equilibration by means of diffusion takes such long time. However, such distant rock volumes are of little consequence for the safety assessment.

The physical porosity is not affected by the porewater composition. However, for the diffusion available porosity of different solutes, the porewater composition may to a lesser degree be affected by anion exclusion, in turn affecting the diffusion available porosity.

According to Equation 6-23, D_w is affected by the viscosity of the porewater:

$$\boldsymbol{D_{w,T2} = D_{w,T1} \cdot \frac{T_2}{T_1} \cdot \frac{\eta_1}{\eta_2}} \qquad 6\text{-}23$$

where $D_{w,T1}$ and $D_{w,T2}$ are the diffusivities in unconfined porewater at the temperatures T_1 and T_2 (K), and η_1 and η_2 (Ns/m^2) are the porewater viscosity at the two temperatures. Except for being affected by the temperature, the viscosity is also affected by the porewater composition. Often when estimating the effective diffusivity, the effect of the porewater composition on the viscosity is not accounted for. Instead, it is assumed that the D_w in the porewater can be approximated by the D_w at infinite dilution. Anderko and Lencka (1998) studied how D_w is affected by the salinity of different solutions. For salt concentrations typical of groundwater at repository depth, this should lead to a decrease in D_w of only a few percent, compared to D_w at infinite dilution. Even for solutions similar to brine, the diffusivity

would not decrease by more than about 10 %. It is realistic to claim that the uncertainty in viscosity from the groundwater composition is overshadowed by uncertainty introduced by the varying temperature during the glacial cycle.

It is generally thought that the effect of anion exclusion on the effective diffusivity decreases with increasing salinity (e.g. Lehikoinen et al. 1992). A laboratory study on a drill core sample from the Forsmark and Laxemar sites (Löfgren et al. 2009) indicate that the overall effect of anion exclusion on D_e is limited to a factor of few, even at very low salinities. As anion exclusion seems to be limited even at very low salinities, the relation between salinity and anion exclusion is of lesser consequence.

The formation factor is a geometric factor that is unaffected by the porewater composition.

In situ temperature and stress: In the site investigations, the connected porosity, formation factor, and effective diffusivity have been measured in the laboratory at atmospheric pressure and room temperature. The increase in temperature, compared to the in situ temperature, is relatively small and should have an insignificant effect on the porosity but possibly a small effect on the pore space geometry (by way of redistribution of mineral grains due to their thermal expansion).

The substantial decrease in ambient stress in the laboratory may somewhat have increased the pore volume, as compared to in situ. In addition, porosity may have been induced in the excavation and sampling procedure. More importantly, changes in the ambient stress may, together with excavation induced damage, significantly have affected the pore space geometry, resulting in an increased formation factor and effective diffusivity. The effective diffusivity is normally assumed to be the product of D_w and the formation factor (cf Equation 6-22), where the formation factor depends on the pore space geometry:

$$F_f = \varepsilon_t \cdot \frac{\delta}{\tau^2} \qquad 6\text{-}24$$

where ε_t (–) is the transport porosity, and δ (–) and τ^2 (–) are the constrictivity and tortuosity of the porous system, respectively. Especially the constrictivity/tortuosity factor is expected to be affected by changes in ambient stress, as pore throats (also called bottlenecks) may become constricted or even closed off by the increasing stress. Because of the above mentioned issues, data obtained in the laboratory needs to be reduced by a transfer factor.

Changes in the pore space geometry due to changing ambient conditions were certainly a factor in the uplift of the bedrock, more than a billion years ago. The changes of in situ stress during a glacial cycle, mainly induced by the formation and melting of an ice cap, are smaller in comparison but probably not negligible. In Skagius and Neretneiks (1986) granite samples from Finnsjön, a site closely located to Forsmark, were re-stressed in the laboratory with up to 35 MPa overpressure. Even when going from 30 to 35 MPa overpressures there was a slight decrease in the formation factor (Skagius and Neretnieks 1986, Figure 6). If extrapolating the data to encompass an additional 30 MPa overpressure, due to the hydrostatic pressure induced by the thickest ice cap (cf Section 7.1), it is conceivable that the formation factor would be halved, compared to at 35 MPa overpressure. The extrapolation in itself is speculative, and it is unknown if samples that have once been de-stressed can be re-stressed and still represent the in situ rock. The potential effect from the ice cap is intended to be encompassed by the data range suggested in Section 6.8.10.

Consequence for the sorption partitioning coefficient

Rock type and degree of alteration/disturbance: Generally, sorption of solutes on weathered or altered rock is stronger than on unaltered rock, although the extent to which this occurs depends on the nature of the alteration and the properties of individual sorbing solutes. In some cases, however, sorptive properties may not be appreciably changed by alteration processes, or at least not nearly to the same extent as would be predicted on the basis of the typically increased surface area and CEC of the altered rock.

Mechanical damage and CEC transfer factors are used to correct laboratory sorption data obtained from the Forsmark and Laxemar site investigations to K_d values appropriate for Forsmark metagranite (SKB rock code 101057) under in situ conditions. This rock type is assumed as a standard reference material for SR-Site, since its BET surface area data is documented by André et al. (2009) for intact monolithic

samples. The majority of sorption measurements, BET surface areas, and supporting geochemical data (specifically iron content) also concern this material, which makes it an obvious choice for parameterisation of the in situ rock.

The sorptive surface area of the intact rock matrix is not expected to vary greatly amongst the different unaltered rock types. Here, the term "unaltered" is intended to mean with respect to hydrothermal action as distinct from metamorphic alteration. It is noted, however, that the biotite content (Sandström and Stephens 2009) for Forsmark metagranite (1.8–12.4 % vol. based on 49 samples) is somewhat greater than that for pegmatic granite (0.3–5.2 % vol. based on 5 samples) thereby implying a reduced sorptivity for the pegmatic rock type.

Groundwater composition: Key parameters which influence sorption processes are pH and carbonate in the case of surface complexing radionuclides, as well as the presence of solutes that compete for sorption sites. Various dissolved ligands in groundwater can directly compete to bind radionuclides at the expense of sorption. In addition to direct competitive effects for radionuclide binding in solution, carbonate is considered to be particularly important in that it can also form ternary surface complexes with certain radionuclides. The sorption of, for example, ternary carbonate complexes of uranyl and neptunyl (i.e. U(VI) and Np(V)) is well described in the literature and has been directly confirmed by spectroscopy (e.g. Bargar et al. 1999, Arai et al. 2007). For ion-exchanging solutes, direct competition with base cations in the groundwater is expected to have the greatest impact on sorptivity.

A chemistry transfer factor is used to account for differences between contact solution compositions used in laboratory investigations and groundwater compositions under application conditions (based on the temperate climate case). For surface complexing solutes, it was not deemed feasible to estimate chemistry transfer factors and this uncertainty was assumed to be part of the overall level of uncertainty associated with the data.

The sorption of redox sensitive radionuclides is strongly influenced by the redox state (*Eh*) of the groundwater, which is determined by the presence of redox controlling pairs such as $Fe^{2+}/Fe(OH)_3$ or $SO_4^{2-}/FeS_{(am)}$ and is also related to pH and dissolved carbonate concentration. The redox speciation of radioelements places an important control on chemical behaviour. This is particularly true for elements that switch between anionic (usually non-sorbing) and cationic (usually sorbing) forms when they change redox state. Other important instances occur when one of the redox states is much more readily solubilised, or less prone to sorb than the other. In the K_d data compilation, oxidised and reduced states were considered separately.

In situ temperature and stress: With regard to temperature, solutes that have exothermic sorption reactions can, on theoretical grounds, be expected to have slightly reduced sorption at higher temperatures, whereas solutes with endothermic sorption reactions can be expected to have slightly increased sorption. Temperature can also have an indirect impact on sorption by altering the species distribution of the solutes in groundwater. By altering the thermodynamic conditions for solution speciation reactions, competitive effects are therefore subtly altered. The general effect of temperature is, however, expected to be vanishingly small relative to the overall uncertainty of the sorption data and is therefore neglected.

Increased stress conditions may reduce access of solutes to the pore system by compressing the available microporous space and by pinching off diffusive pathways, thereby restricting access to sorption sites. It is possible that available sorptive surface areas under in situ stress conditions might be less than that estimated on the basis of laboratory measurements of BET surface area on intact core samples. The effect of this, however, is also thought to be small relative to the overall sorption data uncertainty and has therefore been neglected in the recommendation of K_d data.

6.8.6 Conceptual uncertainty (text reproduced from SR-Site Data report)

Conceptual uncertainty of ε and D_e

There is no significant conceptual uncertainty associated with the physical porosity, or the connected part of that physical porosity. However, there is still a lack of knowledge on exclusion effects in crystalline rock where the two major exclusion effects are size exclusion and anion exclusion. In the site investigation campaign, the connected porosity has been measured by water saturation or C^{14}-PMMA methods. It is safe to assume that solutes can enter where these fluids have entered. The negatively charged mineral grains of igneous rock, surrounding the pores, induce a positively charged electrical

double layer in the porewater adjacent to the pore wall (e.g. Stumm and Morgan 1996). Generally, the thickness of the electrical double layer is so small that its volume should be insignificant compared to the connected pore volume.

The effective diffusivity and formation factor are discussed at length, from conceptual points of view, in the SR-Site Geosphere process report (SKB 2010h). Here, only the most important conceptual uncertainty issues are presented.

The validity of assuming Fickian diffusion can be questioned as it does not address multi-component mass transfer and interactions between the charged solutes and charged pore walls. The Maxwell-Stephan diffusion model (Krishna and Wesselingh 1997) is better equipped to handle this issue, but has other problems, predominantly associated with a lack of input data for different solutes and systems. In the SR-Site Geosphere process report (SKB 2010h) it is suggested that one should continue to use Fickian diffusion in SR-Site. However, it should be remembered when discussing data uncertainty that the conceptual uncertainty is non-trivial. This is of importance when comparing data obtained by conceptually different methods, as the data are evaluated by equations that do not to 100 % represent the studied system.

There are conceptual uncertainties concerning Equation 6-22. The equation only applies in case there are no exclusion effects, for example anion exclusion and size exclusion, or enhancing effects such as surface diffusion. As such effects are present; there is the issue of how to correct for them. This was in SR-Can dealt with by lowering the effective diffusivity of all anions by a correction factor of 10. No correction factor was implemented for non-charged species or cations (even though it was suspected that there may be a surface diffusion effect for certain cations (Liu et al. 2006)).

When estimating the formation factor or effective diffusivity based on electrical methods, the analogy between ionic mobility and diffusivity is used. With the Einstein relation one can convert ionic mobility μ ($m^2/V \cdot s$) to diffusivity, as shown by Equation 6-25:

$$D = \frac{\mu R T}{z F} \qquad 6\text{-}25$$

where z (–) is the charge number of the ionic solute, and R (J/mol·K), T (K), and F (C/mol) are the gas constant, temperature, and Faraday constant, respectively. There are similar conceptual uncertainties associated with this analogy, and its applicability in the porous system of crystalline rock, as with the usage of Fickian diffusion theory. Perhaps one can say that there may be even more uncertainty associated with this analogy, as relatively few experiments and tracer tests have been carried out using electromigration as the migration mechanism.

When estimating formation factors based on electrical resistivity measurements, it is evident that surface conduction in the electrical double layer introduces uncertainty. Therefore, in this document we chose to refer to all formation factors measured by electrical resistivity methods as apparent formation factors, unless corrections have been performed for surface conduction effects. It should be cautioned that this terminology was not used in site investigation reports (e.g. Selnert et al. 2008) and not consistently in SDM reports (e.g. Crawford 2008). By correcting for surface conduction effects, the formation factor can be estimated from the apparent formation factor (as discussed in Sections 6.8.7 and 6.8.10).

It is conceivable that anion transport in pore throats or bottlenecks may be limited. In such a bottleneck, a significant portion of the pore cross section area may be occupied by the electrical double layer. This is illustrated in Figure 6-70, showing a pore where the bottleneck is almost completely occupied by the positively[19] charged electrical double layer (dashed line). In case the bottle neck is even more constricted due to an increase in ambient stress, anion transport may be completely hindered while cation transport is allowed for. The consequence for the safety assessment of this conceivable “membrane” effect is conceptually uncertain.

[19] For anions it should be noted that the repulsive force from the negatively charged mineral surface outweighs the attractive force from the electrical double layer.

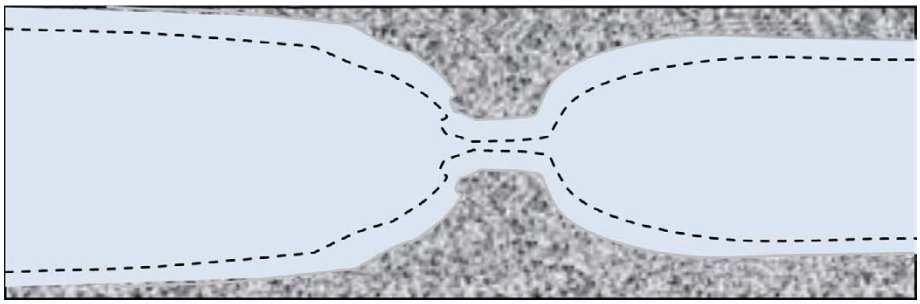

Figure 6-70. *Illustration of a pore bottleneck occupied by the electrical double layer.*

As there in general is significant conceptual uncertainty regarding D_e, and as the models used in the safety assessment only to a certain degree represent the studied system, the uncertainty discussed in this section may overshadow data uncertainty discussed in Section 6.8.7 and natural variability discussed in Section 6.8.8. This needs to be reflected upon in the final data selection. We believe that conceptual uncertainty effects are encompassed by the uncertainty ranges suggested in Section 6.8.10.

Conceptual uncertainty of K_d

The use of a linear model of sorption as implied by the constant K_d concept is a simplification of what in reality is a complex, chemically reactive transport process. Generally speaking, the K_d value is simply a statement of the expected equilibrium ratio of sorbed and dissolved solute for a given set of conditions, and is not necessarily related to considerations of any specific sorption mechanism or retention process. The use of a constant K_d value in safety assessment modelling, however, implies a retention process with particular characteristics that is combined with a model of advective and diffusive mass transfer to give a quantitative measure of solute transport retardation. For this reason it is very important that the magnitude of the K_d value selected to represent the retardation process correctly captures the physics of the postulated retention mechanism. It should be noted that the term "sorption" is a very broad concept that describes the processes by which dissolved solutes are sorbed (adsorbed or absorbed) on, or in another substance (IUPAC 1997), which can also be taken to include processes such as surface precipitation and solid solution formation. In the context of radionuclide transport (and the sense in which the term is used in this report), however, "sorption" is used strictly to refer to adsorptive interaction with mineral surfaces by way of electrostatic and covalent chemical bonding, and specifically excludes other related processes.

The conceptual uncertainty related to the use of a constant K_d, however, extends also to the interpretation of laboratory data used to establish its magnitude. This is a significantly more difficult type of uncertainty to handle owing to that if processes giving rise to retention in laboratory investigations are incorrectly identified as sorption, this can invalidate the subsequent modelling of transport retardation. Although such reaction mechanisms are frequently favourable as additional retardation processes, over and above that provided by purely sorptive interactions, the danger of these confounding processes is that they scale differently with regard to the physics of sorptive retardation modelled in safety assessment transport calculations.

Great care is generally taken in laboratory investigations to avoid situations where confounding factors might skew the interpretation of sorptive retention. This is generally achieved by using extremely low trace concentrations of radionuclides and designing experiments to avoid situations where abrupt changes in solution chemistry might occur. Such processes, however, are very difficult to control and in most cases there is still some residual uncertainty concerning the true nature of the retention process as it is quantified.

The scale on which the porous system is connected

Based on recent research, we suggest that the porous system of the host rock is connected on all scales relevant for a safety assessment. Furthermore, we suggest that there is little conceptual uncertainty associated with this view. However, it should be noted that up until recently the issue of long-range pore connectivity has been debated within the scientific community (see e.g. Löfgren and Neretnieks 2006), and that our view may be challenged.

6.8.7 Data uncertainty due to precision, bias, and representativity (text reproduced from SR-Site Data report)

Diffusion available porosity

There are three general steps that need to be taken when estimating the in situ diffusion available porosity from laboratory measurements, all in which data uncertainty may be induced. The first step includes estimating the connected porosity of the laboratory samples at hand. The second step is estimating how much the laboratory porosity overestimates the in situ porosity, as the laboratory samples are de-stressed. As a third step, one needs to estimate the fraction of the in situ connected porosity that is diffusion available.

Concerning measurements of the connected porosity in the laboratory, such are made using a water saturation technique and a C^{14}-PMMA impregnation technique. If the sample is completely saturated in the water saturation technique, the data uncertainty is small. If the samples are only partly saturated, the porosity will be underestimated, possibly giving rise to a general bias. However, on average this effect is not expected to be large (cf Section 4.3 of Selnert el al. 2008). The C^{14}-PMMA technique is described in Penttinen et al. (2006). The rock sample is saturated by a C-14 labelled monomer which polymerises in the porous system. The connected porosity is calculated by using 2D autoradiographs of sawn rock surfaces. In the site investigations, the method gave similar results as the water saturation technique, although it underestimated the porosity values by 10 to 40 %, relative to the water saturation technique (Selnert et al. 2008).

There are indications from porewater studies (e.g. Waber and Smellie 2008) that the laboratory water (re)-saturation technique may slightly overestimate the in situ porosity, owing to stress release and drill core damage effects. In Waber and Smellie (2009) iodide was added to the drilling fluid while core drilling a section of borehole KFM02B. In case of immediate stress release and creation of additional porosity, this iodide spiked drill fluid would (to some extent) enter the induced porosity. By leaching the samples at the laboratory, the induced porosity could be estimated from the leached iodide. The conclusion was that the additional porosity induced in the drilling was insignificant (only a fraction of 2.4 % of the connected pore volume). However, a recognised limitation to this method is that the constriction of the drillcore by the drill stem will inhibit significant stress release in the borehole. The effect of potential stress release after the drillcore is taken out of the borehole is missed. If comparing the results from this study with those of the study discussed in the below paragraph, one may draw the conclusion that most of the porosity is induced after the drillcore is removed from the drill stem.

In a second study, 16 drillcore samples of rock type 101057 from boreholes KFM01A and KFM02B were subjected to hydrostatic compression tests and subsequent triaxial compression tests (Jacobsson 2007). The volume of micro cracks, originating from stress relaxation and mechanical damage effects from the core drilling, was estimated by analysing the volumetric response during the hydrostatic compression tests. From the measurements the induced micro crack porosity could be singled out. Based on Table 5-3 and 5-5 of Jacobsson (2007), the mean and standard deviation of the estimated micro crack porosity are 0.05 % ± 0.03 %. This should be compared with the recommended stress released porosity of 0.23 % ± 0.11 % for rock type 101057 (Table 4-6, outside deformation zone, no visible fracture (Crawford 2008)). Based on this comparison, it is reasonable to suggest that the stress-released connected porosity should be multiplied by a factor of about 0.8 to represent in situ conditions. This factor is also suggested to be propagated to SR-Site.

Concerning the fraction that is diffusion available, out of the connected porosity, we argue that this fraction is close to unity, even for anions. The thickness of the electrical double layer is very small compared to the average pore aperture. While the pore aperture on average is on the micrometer scale or somewhat less (see Figure 8-20 of Birgersson and Neretnieks (1988) and image in Möri et al. (2003) that is reproduced in Löfgren et al. (2007, Figure 2-6), the electrical double layer is rather on the scale of a few nanometres (e.g. Hiemenz 1986, Chapter 12). However, it is noted that this position may be disputed. For example, in Lehikoinen et al. (1992) it is argued that the electrical double layer plays the role of excluding a significant fraction of the pore space for anions.

All in all, the measured laboratory porosity may be somewhat underestimated in cases where the saturation is incomplete. On the other hand, due to the fact that rock is de-stressed in the laboratory, directly applying laboratory data to in situ conditions may give rise to a slight overestimation. With the accumulated knowledge, it is reasonable to say that the error in the recommended diffusion available porosity should not be more than 50 %.

Effective diffusivity and formation factor

Depending on whether the formation factor and/or effective diffusivity are measured in situ or in the laboratory the conditions and methods differ, which will in turn affect the data uncertainty. In the below text, data obtained during the site investigations or other campaigns of interest are divided into four general categories:

- Through-diffusion measurements in the laboratory.
- Electrical resistivity measurements in the laboratory.
- Electrical resistivity measurements in situ.
- In-diffusion measurements in situ (but not performed at Forsmark).

Through-diffusion measurements in the laboratory: The effective diffusivity has been measured in the laboratory using HTO as the tracer. By evaluating the break-through curves from the experiments based on Fick's second law, the effective diffusivity and capacity factor can be evaluated (see Selnert et al. 2008, Sections 3.4 and 4.4 for details). Figure 6-71 shows an example of breakthrough data and the associated modelled breakthrough curve.

As can be seen in Figure 6-71, the model produces a good fit to the data and very limited data uncertainty is introduced. For more information on through-diffusion measurements (Selnert et al. 2008, Byegård et al. 2008, Crawford 2008) are recommended.

The recommended way of correcting the data for de-stressed laboratory conditions relies on information from in situ and laboratory electrical resistivity measurements, as described below and in Section 6.8.10.

Electrical resistivity measurements in the laboratory: These measurements, described in e.g. Thunehed (2007), may be used for estimating a transfer factor for de-stressed laboratory conditions, applied to D_e data from laboratory through diffusion measurements. By measuring the electrical resistivity ρ_r (ohm·m) of rock samples saturated by an electrolyte of known electrical conductivity κ_w (S/m), the apparent formation factor F_f^{app} (–) can be obtained:

$$F_f^{app} = \frac{1}{\kappa_w \cdot \rho_r} \qquad 6\text{-}26$$

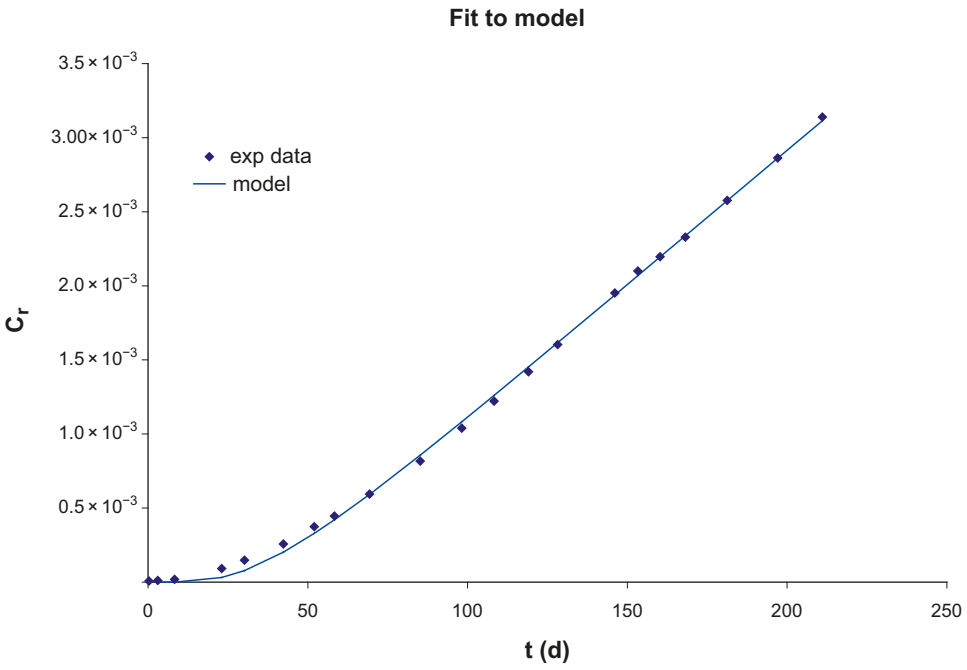

Figure 6-71. *Breakthrough curves in through diffusion test. On the y-axis is the tracer concentration and on the x-axis the time. Diamonds represent experimental data and curve the model results. Reproduced from Figure 4-12 of Selnert et al. (2008).*

When estimating the formation factor based on the apparent formation factor, one needs to make corrections for surface conduction. The influence of surface conduction on the apparent formation factor is discussed in Crawford and Sidborn (2009, Appendix D) and Löfgren et al. (2009). In summary, negatively charged mineral grains surround the pores and induce a positively charged electrical double layer in the porewater, directly adjacent to the pore wall (see Figure 6-70). The cations in this electrical double layer cannot be removed by for example leaching, as electro-neutrality at the mineral grain/porewater interface must be upheld. In this layer, current can be propagated in a process called surface conduction (e.g. Revil and Glover 1997) at an amount that is suggested to be fairly independent on the porewater chemical composition. When measuring the formation factor based on electrical measurements, one wants to study the current propagated in the bulk part of the pore, as this current is directly influenced by the formation factor. Accordingly, one needs to subtract the current propagated in the electrical double layer from the total current running through the porous system. This is done in Equation 6-27, in terms of formation factors and electrical conductivities (see derivation in Crawford and Sidborn (2009):

$$F_f = F_f^{app} - \frac{\kappa_s}{\kappa_w} \qquad 6\text{-}27$$

where κ_s (S/m) is the surface conductivity. In has been shown that there is an empirical relation between the formation factor and surface conductivity, which is estimated to:

$$\kappa_s = 0.0012 \cdot F_f^{0.415} \qquad 6\text{-}28$$

This empirical relation is based on data in Ohlsson (2000), Löfgren (2004) and Löfgren at al. (2009), which are shown in Figure 6-72.

By combining Equations 6-27 and 6-28, Equation 6-29 is obtained:

$$F_f = F_f^{app} - \frac{0.0012 \cdot F_f^{0.415}}{\kappa_w} \qquad 6\text{-}29$$

This is the semi-empirical equation suggested for use in SR-Site when performing corrections for surface conductions, particularly for in situ but also for laboratory apparent formation factors. In the site investigation laboratory programme, samples have been saturated with a highly saline solution (1 M NaCl) prior to the resistivity measurements. This effectively reduces the magnitude of the correction, as the apparent formation factor only overestimates the formation factor by a few percents.

After performing the correction, the obtained formation factors should be similar to those obtained in the through-diffusion experiments on the same drill core samples. Figure 6-73 shows the laboratory apparent formation factors obtained by electrical methods versus the corresponding formation factors obtained in through-diffusion tracer tests, using HTO as the tracer.

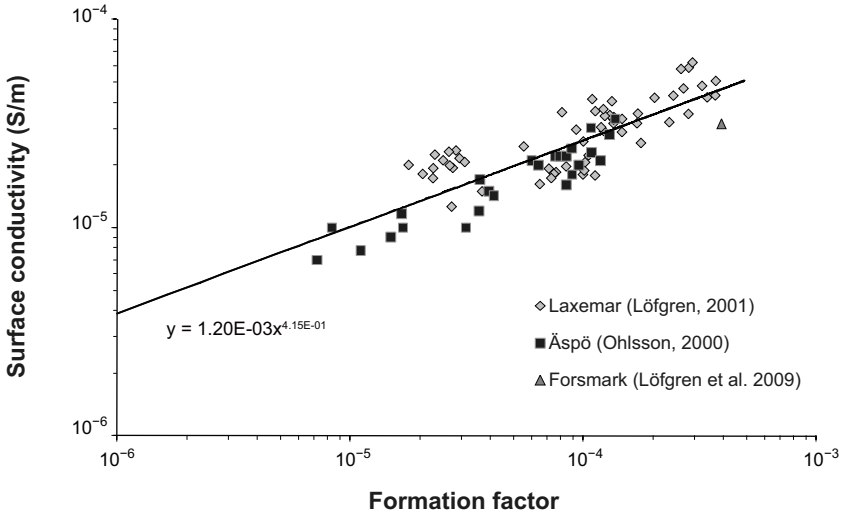

Figure 6-72. *Surface conductivity versus formation factor. Based on measurements on crystalline rock samples from the Oskarshamn and Forsmark sites.*

Although the y-axis shows the apparent formation factor, the appearance of Figure 6-73 would be very similar if instead the formation factor was displayed, due to the very limited effect of surface conduction. The data indicate that the electrical method provides formation factors that, on average, are about two times larger than the through diffusion formation factors. This factor of about two has been observed previously (e.g. Ohlsson 2000), also on sample on the decimetre scale (Löfgren and Neretneisk 2006). A recent study on samples saturated by a solution of a similar electrical conductivity as the in situ porewater confirms this picture (see Figure 7-9 of Löfgren et al. (2009), but note that the discrepancy partly may be due to anion exclusion). An explanation for this may be that there are limitations in the applicability of the analogy between diffusion and electromigration in crystalline rock. Another explanation is that as alternating current is used in the resistivity measurements, capacitance effects may affect the results. If so, capacitance effects can only partly account for the deviation, as comparative resistivity measurements using alternating and direct current give similar results (Löfgren and Nerentieks 2006, Löfgren et al. 2009).

Electrical resistivity measurements in situ: By measuring the in situ electrical resistivity of the rock surrounding a borehole, and by estimating the electrical conductivity of the porewater, the apparent formation factor can be obtained (cf Equation 6-26). The method and measurements are described in e.g. Löfgren and Nerentieks (2002) and Löfgren (2007). The advantage of these measurements is that the apparent formation factors are obtained at the in situ stress. The disadvantage is that they are associated with a number of sources for data uncertainty, where the prominent are listed below:

- The validity of the analogy between ionic mobility and diffusivity, and other unknown sources of uncertainty manifesting in a somewhat overestimated formation factor as compared to through diffusion formation factors.
- Surface conduction, giving rise to an enhanced current running through the sample.
- Water-bearing fractures disturbing the rock resistivity measurements.
- The electrical conductivity of the porewater, which is estimated from the electrical conductivity of freely flowing water and from data obtained by porewater extraction/leaching of drill core samples in the laboratory.

Other sources for minor data uncertainty are discussed at length in Appendix H of Crawford (2008) and Appendix D of Crawford and Sidborn (2008). Concerning the analogy between diffusion and electromigration (as already discussed above) it is likely that this uncertainty is limited to a factor of about two, also in situ.

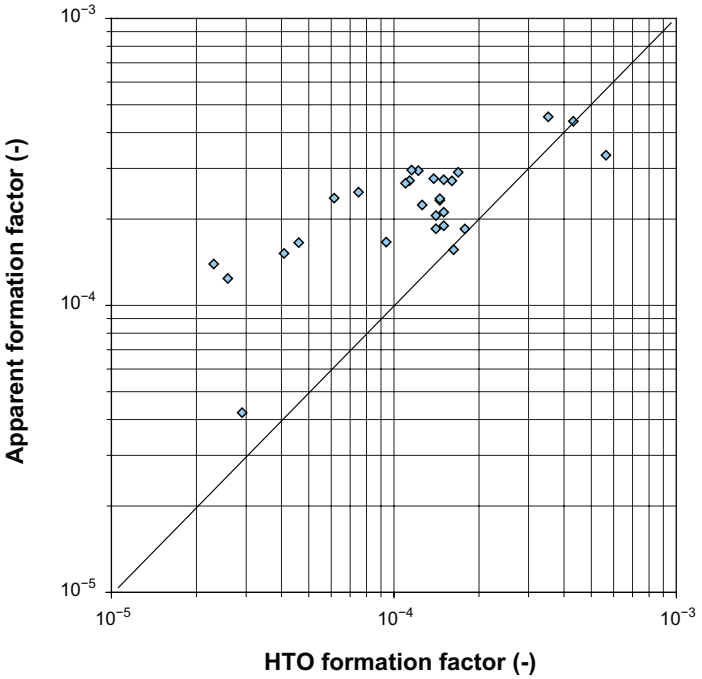

Figure 6-73. *Comparison between laboratory apparent formation factors and through diffusion tracer test (HTO) formation factors. Modified from Figure 3-6 in Byegård et al. (2008). Data from Selnert et al. (2008) and Sicada (delivery note Sicada_09_098). Data also found in and reports by Thunehed (e.g. Thunehed 2007).*

Concerning the effect of surface conduction, this can be handled by use of Equation 6-29. However, it should be noted that the correction is much more significant at the intermediate electrical conductivities of the in situ porewater, as compared to in the laboratory. To avoid unreasonably large corrections, no in situ formation factors are estimated if the porewater electrical conductivity is below 0.5 S/m. For a typical F_f of 10^{-5} and a κ_w of 0.5 S/m, the apparent formation factor overestimates the formation factor by a factor of three, according to Equation 6-29.

Concerning the handling of water-bearing fractures intersecting the borehole and disturbing the measurements, it was decided in the site investigations to propagate two types of formation factors:

- *The rock matrix formation factor:* as valid for the undisturbed and non-fractured rock matrix. These data are obtained at locations at least 0.5 m away from any open fracture.
- *The fractured rock formation factor:* as valid for the fractured rock volume, except for that directly adjacent to detected flow paths. This rock volume is to different degrees intersected by fractures that are open but hydraulically non-conductive (in practice a fracture was assigned as hydraulically non-conductive if no hydraulic response could be detected by using the Posiva flow log). These data are obtained at locations at least 0.5 m away from any detected flow anomaly.

By making this division, most of the data uncertainty introduced by fractures intersecting the borehole is avoided and all in all, the data uncertainty is small. This present text relies on the rock matrix formation factor, as it is requested to supply migration data for the undisturbed rock. Most likely the capacity for matrix diffusion is enhanced in rock volumes directly adjacent to flow paths, as compared to the undisturbed rock. Therefore, the data delivered in this section are pessimistic if used for radionuclide retention calculation. However, in modelling where it is not intuitive that a lower effective diffusivity gives rise to a higher radiological risk, using these data is not necessarily the correct choice. It can for example be argued that when modelling the diffusive transport of salt (as part of hydrogeological modelling) it may be valid to use the effective diffusivity of the fractured rock directly adjacent to flow paths (cf Appendix A of this report).

The electrical conductivity of the in situ porewater has been estimated based on two methods. The first is by measuring the electrical conductivity on freely flowing groundwater at specific fractures, and using this as an estimate for the porewater of the surrounding rock mass. Such measurements have been performed in the hydrogeochemical programme (Laaksoharju et al. 2008) and by the Posiva flow log (e.g. Väisäsvaara et al. 2006). The data uncertainty associated with the actual measurements is relatively small but larger uncertainty may be introduced when extrapolating the results to rock volumes tens or of meters away from freely flowing water.

For a few boreholes there are complementary measurements where the porewater of drill cores is extracted/leached (e.g. Waber and Smellie 2005). From the evaluated porewater chloride concentration, the electrical conductivity at the in situ temperature can be calculated. Figure 6-74 shows the chloride concentration of borehole KFM01D, KFM06A, and KFM08C.

The data uncertainty introduced when estimating the porewater chloride concentration from the extraction/leaching, as well as when assessing the in situ electrical conductivity from the chloride concentration, is relatively small (the total error is estimated to be within 50 %). Part of this uncertainty originates in the stress-release of the samples, giving rise to an additional porosity that may manifest in a somewhat underestimated porewater chloride concentration.

As becomes evident in Section 6.8.10, the recommended in situ formation factors are only based upon measurements in boreholes KFM01D, KFM06A, and KFM08C, as porewater extraction/leaching has been performed in these boreholes. In KFM01D and KFM08C, the measured electrical conductivity of the porewater and freely flowing groundwater are similar. Therefore data from both methods were used as bases for estimating an electrical conductivity profile in the borehole. However, for KFM06A the results deviate. Therefore it was chosen to base the electrical conductivity profile only of data from the porewater extraction/leaching. This result in a recalculation of the apparent formation factors, compared to those delivered in Löfgren et al. (2006), which is further described in Section 6.8.10. For these three boreholes, it is considered that the electrical conductivity profile is not generally overestimated, or underestimated, by more than a factor of two.

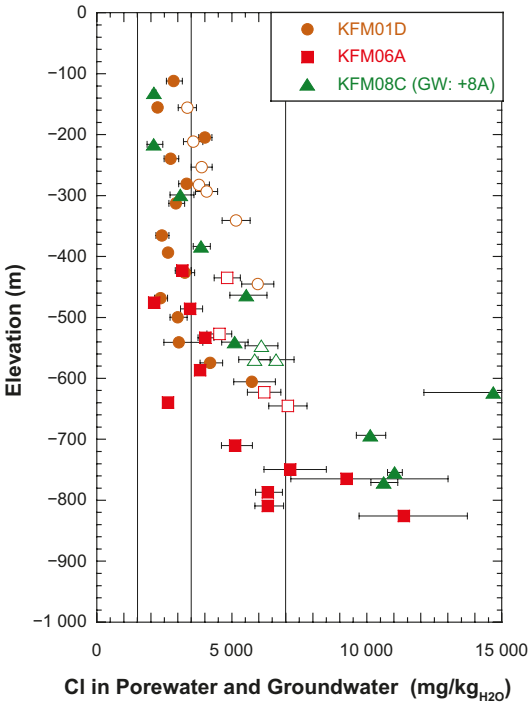

Figure 6-74. *Chloride concentration of porewater and groundwater at Forsmark. Filled legends represent porewater and unfilled legends represent groundwater. Reproduced from Figure 4-27 of Laaksoharju et al. (2008).*

In-diffusion measurements in situ: Results from in situ in-diffusion experiments in the intact rock matrix can more or less be considered to be without artefacts, even though they are associated with data uncertainty. In Sweden, two such long-term experiments have been performed in crystalline rock; one at the Stripa mine (Birgersson and Neretnieks 1988, 1990) and one at the Äspö Hard Rock Laboratory. In the Stripa campaign – part III, in situ pore diffusivities D_p between 2×10^{-11} and 5×10^{-10} m^2/s were obtained for iodide (see Figure 8.22 of Birgersson and Neretnieks (1988)). This converts to effective diffusivities between about 6×10^{-14} and 2×10^{-12} m^2/s (using $\varepsilon = 0.3$ %). This is somewhat higher than suggested for Forsmark, but still close enough to suggest that the Forsmark data are reasonable. *In situ* results from the Äspö Hard Rock Laboratory campaign LTDE-SD, outlined in SKB (2009e), are still being evaluated. Accordingly they are not part of this data qualification.

Anion exclusion

As discussed previously, anion exclusion affects the effective diffusivity by way of lowering it (e.g. Liu et al. 2006). In SR-Can a reduction factor of 10 was applied on D_e for anions, to account for anion exclusion. This is in line with the reduction factor earlier proposed in the Finnish spent fuel management programme (e.g. Rasilainen et al. 2001).

In the Phase I/II laboratory part of the Long Term Sorption Diffusion Experiment (LTDE-SD), performed on rock samples from the Äspö Hard Rock Laboratory, through diffusion tracer tests on a number of drill core samples were performed (Vilks et al. 2005). In these tests, the non-charged tracer HTO and the anionic tracer iodide simultaneously diffused through the rock samples. The results indicate that the anionic tracer on average had about a half an order of magnitude (rather than one order of magnitude) lower effective diffusivity than the non-charged tracer (Vilks et al. 2005, Tables 5 and 6).

Laboratory results from the Finnish program, comparing Cl-36 and H-3 diffusion in the laboratory (Lehikoinen et al. 1992, Table 2), can be used in support of a reduction factor somewhere between half an order and one order of magnitude. However, these tracer tests seem to have been performed on more “tight” rock (lower formation factor) than that at Forsmark.

SKB has recently conducted a laboratory tracer test study using iodide as the tracer in the through electromigration method (TEM). In through electromigration tracer tests, an electrical potential gradient is used as the (main) driving force, as opposed to a concentration gradient in traditional diffusion tracer tests (Löfgren and Neretnieks 2006). These measurements were performed on the same Forsmark drill core samples that had previously been subjected to through diffusion measurements using HTO as the tracer. By comparing the results (cf samples 2 to 5 in Figure 7-13 of Löfgren et al. 2009) only relatively small deviations could be detected. If taking the ratio of the TEM formation factors (data from duplicate sampling tabulated in Chapter 7 of Löfgren et al. 2009) and through diffusion formation factors for the corresponding samples (Löfgren et al. 2009, Table 4-1), this ratio is on average 0.87 with the standard deviation 0.45. Although there are difficulties involved in comparing data from tracer tests based on different transport mechanisms, the results indicate a modest effect of anion exclusion, and that the reduction factor of 10 used in SR-Can is excessive.

It is recognised that there is great uncertainty in this reduction factor, especially as it should be applied to in situ conditions where the porous system to some extent is compressed compared to in the laboratory. However, in view of the results from the in situ diffusion experiments at Stripa (Birgersson and Neretnieks 1988) using anionic tracers, suggesting that anion exclusion decreases the effective diffusivity by half an order of magnitude, as compared to D_e for cations and non-charged solutes, seems reasonable.

In practise, Equation 6-30 is suggested for use in estimating D_e for anions from D_e data for cations and non-charged solutes:

$$\log_{10}(D_e, anions) = \log_{10}(D_e) - 0.5 \qquad 6\text{-}30$$

The scale on which the porous system is connected

We suggest that the porous system is connected on all scales relevant for the safety assessment (at least decametre scale), and that there is little uncertainty or variability.

We base our suggestion on three pieces of evidence:

- Long-range matrix diffusion has been observed in in situ tracer tests, for example in Birgersson and Nerentieks (1988, 1990) where a diffusion profile of at least 40 cm was obtained in intact rock (40 cm was the scale of the overcored rock in the campaign).
- Current can be propagated by solutes in the saturated porous system of the undisturbed rock, on at least the metre scale (e.g. Crawford 2008, Appendix H). By using a focused rock resistivity tool in situ, the current is sent into the rock matrix perpendicular to the borehole axis, at least three meters into the bedrock (but probably also on a larger scale, e.g. Löfgren and Neretnieks 2002).
- By studying the chemical composition of the porewater of intact rock, and by this way studying large-scale diffusion profiles, it is suggested that in situ diffusion occurs over at least several tens of metres (Waber et al. 2009).

Sorption partitioning coefficient

The principal biases and uncertainties which might affect the magnitude of the K_d value have been briefly discussed as conceptual uncertainty in Section 6.8.6. These biases concern both the extrapolation of data from laboratory experiments to in situ application conditions as well as the correct identification of sorptive retention processes in laboratory investigations. Here, the term “bias” is used to describe various epistemic uncertainties relating to a lack of knowledge about the sorption processes as they are quantified and extrapolated from one reference condition to another.

Measurement of sorption

Laboratory sorption measurements are typically carried out on crushed rock samples for different contact times and groundwater compositions. The use of crushed materials is dictated by the need to minimise diffusive disequilibrium effects so that sorption measurements can be made in a realistic time frame. In most cases, the apparent partitioning ratio R_d (m^3/kg) is estimated by way of a radiometric mass balance that relates the initial and final activity of the contacting solution to the amount of solute sorbed. Usually the amount sorbed is not measured directly, so the accuracy with which the initial

and final solution activity can be quantified is of great importance for the overall accuracy of the R_d estimate. If the activity variance of the initial blank solutions (i.e. reference solutions without added geological material) is sufficiently large relative to the final activity of the solution with geological materials added, then it may not be possible to quantify the existence of sorption in a statistical sense. Similarly, if the strength of sorption is sufficiently high that the remaining solute in the contact solution is at or below the limit of detection, then it may not be possible to quantify an upper limit to the R_d value. In a practical sense, this means that it is very difficult to quantify the R_d of solutes much lower than 10^{-4} m^3/kg or larger than ~ 1 m^3/kg.

Extrapolation of data to site-specific conditions, using transfer factors

Given that the sorption of solutes takes place on the surfaces of geological minerals, the sorption properties of the rock are strongly correlated with the available surface area of mineral grains within the micro-porosity of the rock matrix. The crushing of rock materials generally results in the creation of new mineral surfaces that are not representative of the undisturbed rock in situ. This may include both freshly cleaved mineral surfaces as well as surfaces belonging to previously unconnected pore spaces in the rock. This needs to be specifically considered when extrapolating laboratory derived sorption partitioning coefficients to values applicable for the rock matrix under in situ conditions. The surface area of rock is typically assessed using the BET (Brunauer et al. 1938) method. This gives an approximate estimate of the total surface area which can then be used to approximately relate the sorptive properties of different rock types and crushed size fractions.

Sorption of solutes frequently occurs preferentially on one, or more mineral phases of the rock which may not comprise more than a few percent of the total mineralogical composition of the rock. In the cases where preferential sorption does occur, it is typically associated with the so-called dark minerals, biotite (or its alteration product, chlorite) and to a lesser extent hornblende. These minerals also typically dominate the cation exchange capacity (CEC) of the rock. The cation exchange capacities of rocks used in laboratory investigations are not necessarily representative of the site-specific rock types of importance. This is a particular problem for the extrapolation of literature data to data applicable at site-specific conditions. For this reason, the cation exchange capacity of the rock needs to be considered (for certain elements) when extrapolating laboratory measured sorption properties to in situ conditions.

Transfer factors are defined to extrapolate sorption data for a particular rock type, crushed size fraction, and water composition to more accurately represent the sorptive properties of the intact rock matrix in the repository volume. Since the creation of new surface area relates to both the crushing process and microstructural damage incurred during bore core sample retrieval, the transfer factor relating the surface area of crushed rock to in situ conditions is referred to as the mechanical damage transfer factor, f_m. The transfer factor for extrapolation between rock types with different cation exchange capacities is referred to as the CEC transfer factor, f_{cec}. For the site-specific data sets from Forsmark and Laxemar, where measurements were made on a number of particle size fractions, an additional surface area transfer factor, f_A (–) was used to standardise measurements to a given reference particle size. The transfer factors are multiplicative and relate the apparent partitioning ratio R_d to the K_d value recommended for intact site-specific in situ rock for the particular laboratory groundwater composition (here, termed K_d^0):

$$K_d^0 = (R_d \cdot f_A) \cdot f_m \cdot f_{cec} \qquad 6\text{-}31$$

In the background report detailing data selection and extrapolation (Crawford 2010, Section 5.1), these transfer factors have been used to predict ranges of K_d values thought to be pessimistic for the purposes of SR-Site. In certain cases, both surface area and CEC need to be considered, whereas in other cases only surface area effects appear to be important. This is handled on a case by case basis and is informed as far as possible by available supporting information in the scientific literature. Since the values derived for f_m and f_{cec} are typically based on a small number of measurements from a limited set of bore core samples, the standard errors of the measurement data are used to estimate an uncertainty distribution which can be used to expand the range of extrapolated K_d values to account for uncertainty in these transfer factors. Being defined as ratios of variables that either have normal or lognormally distributed errors themselves, the uncertainty distributions for the transfer factors can be assumed to be lognormally distributed (more detailed reasoning for this choice can be found in Crawford (2010)).

Since the K_d can be expected to vary in response to different groundwater compositions, an additional chemistry transfer factor, f_{chem}, is defined to correct for differences between the groundwater compositions used in laboratory investigations and application conditions. Where appropriate for SR-Site, the f_{chem} transfer factor is calculated on the basis of groundwater compositional statistics in a large control volume surrounding the repository. This is done without consideration of individual flow path trajectories or spatial correlations. As a result, the overall groundwater compositional variability is lumped together as an assumed compositional uncertainty for randomly located flow paths within the control volume.

Since the uncertainty distribution of f_{chem} is not necessarily log-normally distributed, this transfer factor must be applied by convolution of the individual probability density functions for K_d^0 and f_{chem}:

$$K_d = K_d^0 \otimes f_{chem} \qquad 6\text{-}32$$

Generally, the status of the site investigation and literature data is such that it is not possible to define quantitative chemistry transfer factors to account for groundwater compositions deviating outside of the ranges which have been investigated in the laboratory. In most cases this means that it must be assumed that the laboratory derived data represent a sufficiently broad range of groundwater compositions that all uncertainty related to groundwater composition is implicitly internalised in the K_d ranges recommended for use in SR-Site.

For radionuclides that sorb by way of a surface complexation mechanism, it is expected that pH and dissolved carbonate concentration have the largest impact on the sorption magnitude, followed by competition from other groundwater solutes for sorption sites. Competition for sorption sites by other groundwater constituents is handled by using groundwater compositions in sorption experiments that broadly approximate those expected under application conditions. The pooling of R_d data, obtained for a range of different contacting solution compositions, thereby internalises the impact of uncertain/variable groundwater composition in the final K_d ranges recommended for use in SR-Site. Although the contact solution compositions used in laboratory investigations do not exactly span the projected application groundwater conditions, this approach is judged reasonable. Owing to the typically small liquid to solid ratios and small liquid volumes used in laboratory experiments, compositional drift of contact solutions occurs, which increases the span of the laboratory compositions. This effect is also internalised in the recommended K_d ranges.

In a small number of cases, the laboratory data are sufficiently detailed that chemistry transfer factors can be defined to account for changing groundwater compositions. Principally, this affects the elements Cs, Sr, Ra, and Ni. In these cases, a combination of empirical and ion-exchange modelling approaches have been used in an attempt to give more accurate predictions of appropriate K_d ranges for application groundwater conditions at different times. Since it is not possible to rigorously account for temporally variable K_d values in safety assessment calculations, in cases where evolving groundwater compositions imply a net change in sorptivity over time, K_d ranges are chosen to represent sorptive properties for the most unfavourable groundwater composition expected to prevail for an extended period of time (during the temperate climate domain). For ion-exchanging solutes this typically implies the selection of K_d ranges for the most saline conditions expected.

Redox state under application conditions

The predominance of various oxidised and reduced species of redox sensitive radionuclides under application conditions has been addressed by thermodynamic modelling using the PhreeqC code in conjunction with the SKB thermodynamic database and the groundwater compositions projected for SR-Site as supplied by the SR-Site hydrogeological modelling team (cf Section 6.1).

Impact of various biases on data suitability for application conditions

With regard to the scaling of laboratory R_d data to K_d values deemed appropriate for in situ conditions, the corrections implied by the mechanical damage and CEC transfer factors (f_m and f_{cec}) are associated with large conceptual and data measurement uncertainties. Since the sorptivity of the rock is assumed to be linearly proportional to total BET surface area and CEC, this can introduce a considerable bias in data extrapolation. It is clear from both the site investigation data, as well as some of the literature

references, e.g. Huitti et al. (1996), that the measured sorptivity of altered and weathered materials do not scale simply relative to their unaltered counterparts with regard to surface area and CEC. In many cases the sorptivity is higher than for unaltered rock types, although not nearly as much as would be expected based on BET surface area and CEC. This is partly due to the fact that not all mineral phases contribute equally to the overall sorptivity and partly due to the alteration of strongly sorbing minerals such as biotite to other less strongly sorbing forms such as chlorite. The extrapolation of sorption data for such materials to make predictions of sorption properties for unaltered rock types can therefore give rise to excessively over-pessimistic transfer factors that are not physically meaningful. The same can also be said for rocks with very different mineralogical compositions, compared to the target rock type (Forsmark metagranite, SKB rock code 101057) of relevance for safety assessment calculations.

Data for altered materials have been avoided as far as possible in the data selection process, although in some cases it has been necessary to use literature data for rocks taken from sites with somewhat different geochemical characteristics to Forsmark or Laxemar site-specific rocks. All rock samples obtained from the Forsmark and Laxemar sites are considered to be sufficiently similar geochemically that the sorption data can be extrapolated using appropriately scaled transfer factors to represent Forsmark metagranite.

When several data sets are combined for different rock types (and groundwater compositions in cases where f_{chem} cannot be estimated), the combined data uncertainty is frequently dominated by differences between data sets rather than internal variations of the underlying individual data sets. This can lead to very broad uncertainty distributions for K_d with 95 % confidence intervals ranging over as much as 2–4 orders of magnitude. Generally speaking, extrapolation of data to site-specific conditions gives uncertainty ranges that appear to increase with the number of data sets used in the assessment.

Although there were close to 950 data points each for Cs, Sr, and Am/Eu sorption at the Forsmark site, these were based on crushed rock samples from 8 different borehole sections featuring three distinct rock types. Sorption data for Ni, Ra, Np(V), and U(VI) (roughly 200 data points each) were based on crushed rock samples from two borehole sections representing a single rock type. The sorption measurements were made using a variety of contact groundwater compositions described as fresh, marine, saline, and brine. Roughly the same numbers of data points exist for Laxemar site-specific rock types. Although the large number of data points gives the impression that there is a very good statistical basis for parameterisation of site-specific materials, it should also be remembered that the total number of data points includes replicates as well as different contact times and particle size fractions of the same crushed core sample.

Most literature data examined, on the other hand, were based on crushed samples taken from a single borehole section at a particular site. These generally take the form of replicate samples for a single particle size and contact time (occasionally different spike concentrations of the element being studied). It is therefore probable that there is some degree of bias in the estimated uncertainty distributions for literature data since these are based on much smaller sample sets representing a restricted range of varied experimental parameters.

To account for the sample size biasing effect of the typically small data sets reported in the literature sources, the uncertainty of the mechanical and CEC transfer factors was propagated in the calculations to give an expanded uncertainty interval in the final data range. This was achieved using a re-sampling technique based on aggregation of the underlying uncertainty distributions for individual data points (essentially assuming a Gaussian mixture model for uncertainty aggregation). Since a large amount of variation was already apparent in the site-specific data sets, this technique was not deemed necessary in those cases.

A particular bias, that has not been previously mentioned, concerns the interpretation of time dependent behaviour in laboratory measurements. The Forsmark and Laxemar site investigation data consisted of R_d values measured on different crushed size fractions and a geometric time schedule for contact times ranging from 1–180 days. However, since the time dependent behaviour in the raw data sets for site data appears to be a minor component of the overall variability/uncertainty, the data sets are considered in their entirety without any filtering with regard to particle size or contact time. Generally it was found that attempts to fit the data to simplified models of time dependent behaviour (i.e. modelling of diffusive disequilibrium) gave rise to highly non-conservative K_d ranges owing to the uncertainty of other model parameters required to make the fit. A pronounced pH drift of up to

1.5 pH units was also documented in a number of (all) control samples at the conclusion of the sorption experiments which confers additional doubt on the assumption of diffusive disequilibrium being the primary mechanism for the observed time dependent behaviour. It was concluded that the most pessimistic assumption with regard to derivation of recommended data for SR-Site was to neglect the time dependent behaviour and assume it as a component of the overall data uncertainty. Full reasoning behind this choice can be found in Crawford (2010).

6.8.8 Spatial and temporal variability of data (text reproduced from SR-Site Data report)

Spatial variability of porosity

In Section 4.4.1 of Crawford (2008), the porosity measured in the site investigation laboratory programme is summarised. By comparing the porosity of different rock types, in deformation zones and non-deformed rock, it can be concluded that the spatial variability is small (cf Table 4-6 of Crawford 2008). For the three dominating rock types of rock domain RMF029, the arithmetic mean ± one standard deviation is 0.23 ± 0.09 % for 101051, 0.4 ± 0.23 % for 101061, and 0.24 ± 0.13 % for 101057 for the non-deformed rock matrix. Subordinate rock types in non-deformed rock show very similar porosities. In deformation zones, the values are somewhat higher. In rock domain RFM045, rock type 101058 is dominating (see Table 4-1 of Crawford 2008). For this rock type, the arithmetic mean ± one standard deviation of the porosity is 0.22 ± 0.06 %.

The porosity should be flow path averaged before use in SR-Site solute transport modelling. This means that all porosities encountered along the flow path should be averaged, by way of taking their arithmetic mean. As the natural variability of local porosities is so small, the flow path averaged porosity can for safety assessment purposes be regarded to feature no significant spatial variability.

Spatial variability of effective diffusivity and formation factor

In Section 4.4.2 of Crawford (2008), the formation factor as measured by through-diffusion measurements in the site investigation laboratory programme is summarised. By comparing the formation factor of different rock types it can be concluded that the spatial variability is small (cf Table 4-9 of Crawford (2008)). For the rock types dominating the samples, the arithmetic mean ± one standard deviation was $(1.0 \pm 0.8) \times 10^{-4}$ for 101051, and $(1.6 \pm 1.5) \times 10^{-4}$ for 101057 for the non-deformed rock matrix. Subordinate rock types in non-deformed rock show very similar data. The results suggest only a small difference between non-deformed rock and rock in deformation zones. It should be remembered that the laboratory data are believed to be substantially affected by mechanical damage and stress-release.

In Appendix H of Crawford (2008) the in situ apparent formation factors, as measured in the site investigation downhole programme, are summarised. Figure 6-75 shows the cumulative distribution functions (CDF) for different rock types.

As can be seen there are relatively small differences between rock types. In Crawford (2008, Appendix H) the correlation length was investigated by means of variograms. It was shown that roughly 20 % of the variance occurs with a correlation length of roughly 1 m or less, while on the order of 80 % is associated with a correlation length of about 5–7 m. As the formation factor and effective diffusivity should be flow path averaged before used in SR-Site solute transport modelling, the spatial variability between flow paths is suggested to be minor.

Spatial variability of sorption partitioning coefficient

The K_d for a particular radionuclide can be generally expected to vary along a flow path depending on the local geochemical composition of the rock, its available sorptive surface area, and local groundwater composition. In the RETROCK project (RETROCK 2004) it was demonstrated formally that, under certain simplifying assumptions, the flow path average product of the bulk rock density, K_d, and D_e is a parameter of central importance for the estimation of solute transport retardation by matrix diffusion and sorption.

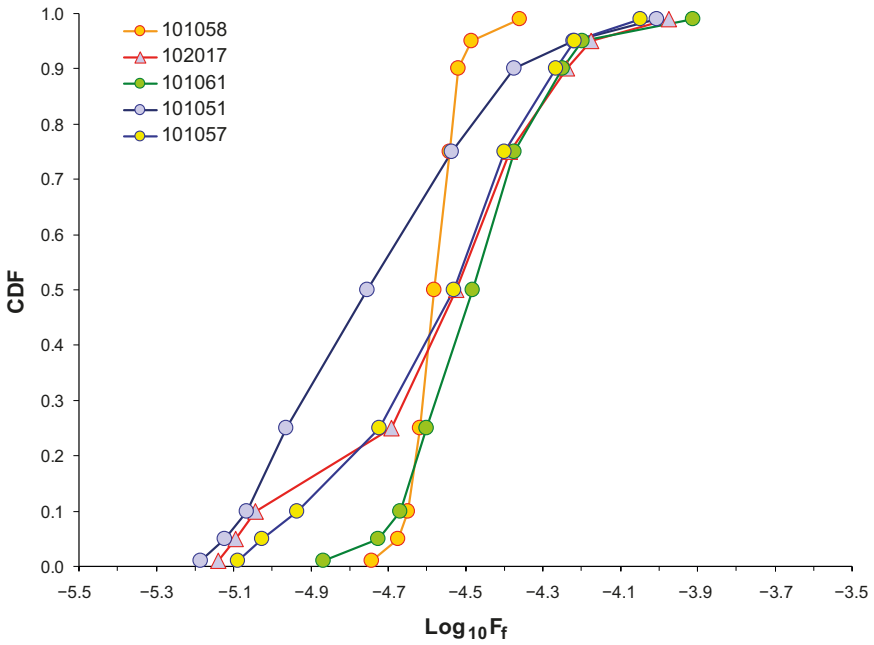

Figure 6-75. *In situ rock matrix apparent formation factors for different rock types in rock domain RFM029. Reproduced from Figure H-10 in Crawford (2008). Note that F_f should be denoted F_f^{app} according to the present terminology. The numbers (101058 etc are SKB rock type codes).*

In cases where one can differentiate between spatial variability in K_d data and uncertainty it is possible, in principal, to define a flow path average. If the spatial distributions of D_e and K_d are assumed to be independent and identically distributed it is relatively straightforward to show that the product of mean D_e and mean K_d is equal to the mean of the product of D_e and K_d. This suggests that the appropriate flow path average measure of K_d along a flow path is the arithmetic mean of the distribution describing the spatial variability of K_d. In the compilation of K_d values recommended for use in SR-Site, however, uncertainty is by far the dominating feature of the empirically derived data. It is therefore not possible to defend the use of a simple arithmetic mean K_d as a flow path average for modelling purposes, and the median of the K_d uncertainty distribution must be assumed as the best estimate of the flow path average.

If the groundwater composition was assumed to be spatially variable although temporally invariant, it would also be possible to estimate flow path specific (average) chemistry transfer factors (f_{chem}) for radionuclide transport from the repository. The spatial distribution of groundwater compositions are, however, supplied without reference to specific flow paths or radionuclide release locations and therefore this is not strictly possible. Since this information is not available, spatial variation in groundwater composition is therefore treated as a sub-component of overall K_d data uncertainty. Calculations made for the elements Cs, Sr, Ra, and Ni, for which it is possible to calculate chemistry transfer factors, indicate that the impact of variable groundwater chemistry is relatively minor in comparison to the overall empirical data uncertainty, and therefore does not need to be considered in detail.

Temporal variability of porosity, effective diffusivity, and formation factor

The porosity, effective diffusivity, and formation factor do not feature significant temporal variability. In the SR-Site Geosphere process report (SKB 2010h) it is noted that during glaciation, the additional pressure from the ice cap may slightly compress the porous system. Additionally, changes in pore water chemistry may slightly modify the effective diffusivity and anion exclusion. However, these effects are judged to be minor and it is recommended not to account for temporal variability in these data. Instead the data ranges given aim to encompass these effects.

Temporal variability of sorption partitioning coefficient

The use of codes that assume a constant K_d value in transport calculations precludes the possibility of including the direct impact of temporally variable K_d values in the safety assessment. For the purposes of safety assessment, however, it is more important to cautiously bound the envelope of radiological risk rather than simulate reactive transport processes exactly as they would occur. To account for temporal changes in groundwater chemistry, which might influence sorption, K_d values are chosen for the most unfavourable hydrochemical conditions expected to prevail for an extended period of time during the repository groundwater evolution. For ion-exchanging solutes, this means a selection of K_d values for the most saline conditions expected. For other, surface-complexing solutes it has not been possible to quantitatively assess the impact of changing groundwater compositions, owing to the large uncertainties inherent in the selected K_d data. During the temperate time period, for example, the gradual freshening of the groundwater due to meteoric intrusion is expected to give a trend towards lower pH and higher carbonate concentrations over time. It is not clear in most cases whether this should be expected to give rise to higher or lower sorptivity, owing to the complexity of the surface complexation mechanisms and the ambiguous nature of the available measurement data. This uncertainty has been handled to the extent possible by combining data sets for all relevant groundwater compositions to provide an overall range of uncertainty that implicitly includes these effects. For redox sensitive solutes it is necessary to also consider the consequences of temporal hydrochemical variability on the particular redox species being transported. The gradual freshening of the groundwater in the repository environment during the temperate climate domain, for example, suggests that it cannot be guaranteed that uranium will always be in reduced form in the rock.

Full details concerning the handling of uncertainties relating to temporal variability can be found in Crawford (2010).

6.8.9 Correlations (text reproduced from SR-Site Data report)

Porosity, effective diffusivity, and formation factor

The important functional relationships between the formation factor, effective diffusivity, rock resistivity, etc are shown in Equations 6-22 to 6-29 (although the latter two are semi-empirical relationships).

If choosing an effective diffusivity from a PDF, the same data should be applied for all cations and neutral species, for all flow paths. This effective diffusivity should be corrected by a reduction factor to account for anion exclusion, and be applied for all anions and flow paths.

For the porosity range of interest for SR-Site, the porosity should not be correlated to the formation factor or effective diffusivity (that is, the so-called Archie's law should not be used).

Sorption partitioning coefficient

The correlations of K_d data are discussed in Section 3.2 of Crawford (2010). Correlations in sorptivity are assumed in the assignment of K_d values for elements where no data is available. The use of "analogue" solutes in place of actual data is based on geochemical similarity and consideration of specific reaction mechanisms. Correlations are also considered in the stochastic selection of K_d values for use in transport calculations. It is expected, for example, that K_d values for ion exchanging solutes will be mutually correlated with ionic strength. Similarly for cations that sorb by way of a surface complexation mechanism, any shift in hydrochemical conditions should give rise to similar impacts on sorption (although not necessarily in equal proportionality) for all solutes that have an analogous reaction chemistry. One exception is made for redox sensitive solutes since the transition from reducing to oxidising forms occurs at different *Eh* levels for different elements. Uranium, for example, could possibly be present in oxidised form while plutonium, neptunium, and technetium remain in reduced form at the redox potentials projected during the SR-Site temperate climate domain.

Together with the tabulated recommended K_d data in Table 6-89 (see Section 6.8.10), each element, or redox speciation, is either assigned a correlation group (1 or 2) or no correlation group (–).

Sorption partitioning coefficient and effective diffusivity

If performing transport modelling where certain solutes that normally sorbs are assumed to be non-sorbing (e.g. what-if modelling), a rational for this may be that the radioelements predominantly exist in anionic form. As an example this may be the case for a number or radioelements if oxidising conditions prevail in the repository. In such a case, it may be prudent to use the effective diffusivity for anions for these radioelements. In other cases, cationic forms may be (pessimistically) assumed to be non-sorbing due to competition of other solutes (for example at high salinities). If this is the grounds for assuming pessimistic K_d values, it may be prudent to use the D_e of cations.

6.8.10 Result of supplier's data qualification (text reproduced from SR-Site Data report)

Diffusion available porosity

As discussed in Section 6.8.8, the porosity obtained in the laboratory for the dominating rock type (101051) of rock domain RDM029 is 0.23 ± 0.09 %. For the dominating rock type (101058) of RFM045, the laboratory porosity is 0.22 ± 0.06 %. As the repository is suggested to be predominantly located in rock domain RFM029 we suggest an averaged laboratory porosity of 0.23 % for the host rock.

For correction of laboratory porosities to in situ porosity it is recommended to multiply the laboratory porosity by a factor of 0.8 (see discussion in Section 6.8.7). From this, we suggest an averaged in situ porosity of 0.18 %. The porosity should be flow path averaged before use in solute transport modelling. As the natural variability of local porosities (obtained on cm-scale samples) is so small, it is considered that there is no significant spatial variability between flow paths. Therefore, the single point value 0.18 % is recommended for the flow path averaged in situ porosity.

Concerning the diffusion available porosity, the fraction of the connected pore space that is available for solutes is close to unity, for anions, cations, and non-charged species. Therefore, the suggested flow path averaged diffusion available in situ porosity is 0.18 % for all solutes. The uncertainty associated with this single point value is so small that no range is suggested.

Formation factor and effective diffusivity

As discussed in Section 6.8.7, directly basing the recommended in situ formation factors and effective diffusivities on laboratory through diffusion data would lead to overestimated data. Corrections are needed to reflect the fact that samples in the laboratory are stress released. On the other hand, directly basing the recommended data on in situ apparent formation factors would also lead to overestimated data, as surface conduction effects need to be corrected for. In addition, there are effects associated with the electrical resistivity method that are not well understood, which introduce minor data uncertainty. To derive the data in a more robust fashion, the formation factor and effective diffusivity are estimated from two conceptually different methods, and data from both of these methods are compared. The two methods are to:

1. Base the recommended data on in situ formation factors, after performing the surface conduction correction according to Equation 6-29. The effective diffusivity is then the product of F_f and D_w in the case of no exclusion effects. For anions, a reduction factor is needed to account for anion exclusion.
2. Base the recommended data on through-diffusion D_e data, but only after correcting for stress release and mechanically induced damage. This is done by multiplying the laboratory D_e by a transfer factor, which is based upon differences in the formation factors obtained by electrical methods in situ and in the laboratory. For anions, a reduction factor is needed to account for anion exclusion.

Method 1: In the Sicada database, apparent in situ formation factors are stored from 10 deep boreholes in Forsmark. However, only for three of these boreholes there is direct information on the porewater chemical composition (cf Figure 6-74). These boreholes are KFM01D and KFM08C (Löfgren 2007) and KFM06A (Löfgren et al. 2006). For boreholes KFM01D and KFM08C, the measured electrical conductivities of the porewater and freely flowing groundwater generally agree. Therefore, the suggested electrical conductivity profiles of Löfgren (2007) are kept. For borehole KFM06A, however, the electrical conductivity profile of the porewater disagrees with that of the freely flowing groundwater. As the

data from the porewater extraction/leaching are considered to be more representative, we chose to base the electrical conductivity profile for the borehole solely on them. This approach disagrees with that of Löfgren et al. (2006), wherein the profile was based on the electrical conductivity of freely flowing groundwater (to comply with the method description at the time). Because of this, the apparent formation factors of KFM06A have been recalculated, as accounted for below.

As a base for the recalculated apparent formation factors in KFM06A, the same rock matrix resistivities are used as in Löfgren et al. (2006). The exception is that no rock matrix resistivity from above the borehole length 305 m is used, due to the reassessed pore water electrical conductivity profile and due to the criterion that $\kappa_w > 0.5$ S/m. The new electrical conductivity profile is based on porewater chloride concentrations given in Table A7 of Waber and Smellie (2005). The conversion between chloride and electrical conductivity is based upon a relation in Löfgren (2007, Equation 4-4) (which in turn is based on linear regression of chloride data and electrical conductivity data in borehole KFM01D). The correction from laboratory temperature to in situ temperature was assumed to match that of borehole KFM08C (extrapolated from Table 4-4 of Löfgren 2007). In other words the temperature versus depth profile in KFM06A was assumed to match that in KFM08C. Figure 6-76 shows the new electrical conductivity profile for KFM06A.

This electrical conductivity profile was used together with rock matrix resistivities of KFM06A and Equation 6-26 to obtain recalculated apparent formation factors. It was also used for correcting the apparent formation factors into the formation factor, by use of Equation 6-29.

Figure 6-77 shows the cumulative distribution functions of the formation factors of KFM01D, KFM08C, and KFM06A, after performing the surface conduction correction according to Equation 6-29. In addition, the CDF of all 10 130 data points from the boreholes are shown by the yellow curve.

All data points from the three boreholes, in the form of $\log_{10}(F_f)$ are shown in a histogram in Figure 6-78, together with the best fit normal distribution with $\mu = -4.71$ and $\sigma = 0.16$.

As flow path averaged migration parameters should be used in solute transport modelling, we have not seen it worthwhile to study the skewness and kurtosis of the dataset. Instead, it is recommended to base the flow path averaged formation factor on the arithmetic mean of all the formation factors. For the 10 130 formation factors, the arithmetic mean is 2.11×10^{-5}.

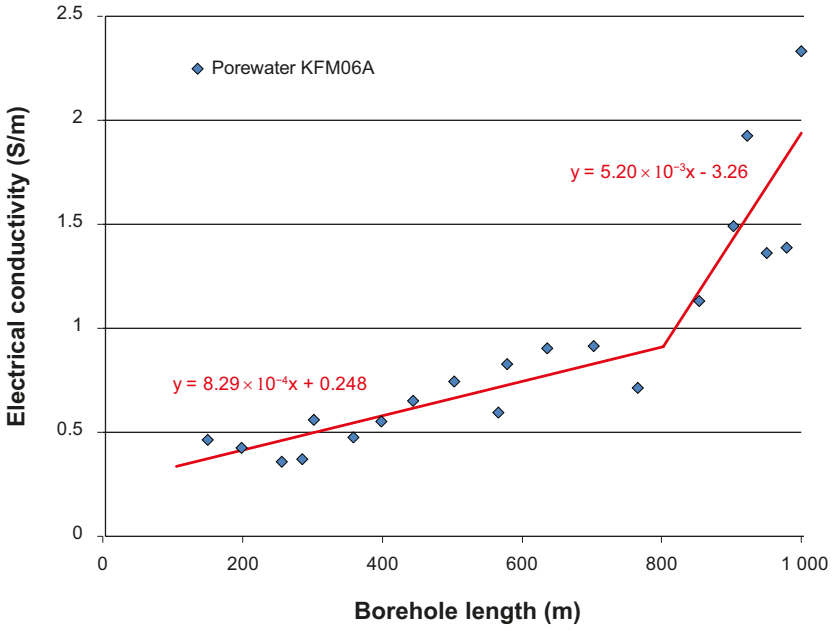

Figure 6-76. *Suggested electrical conductivity profile in borehole KFM06A.*

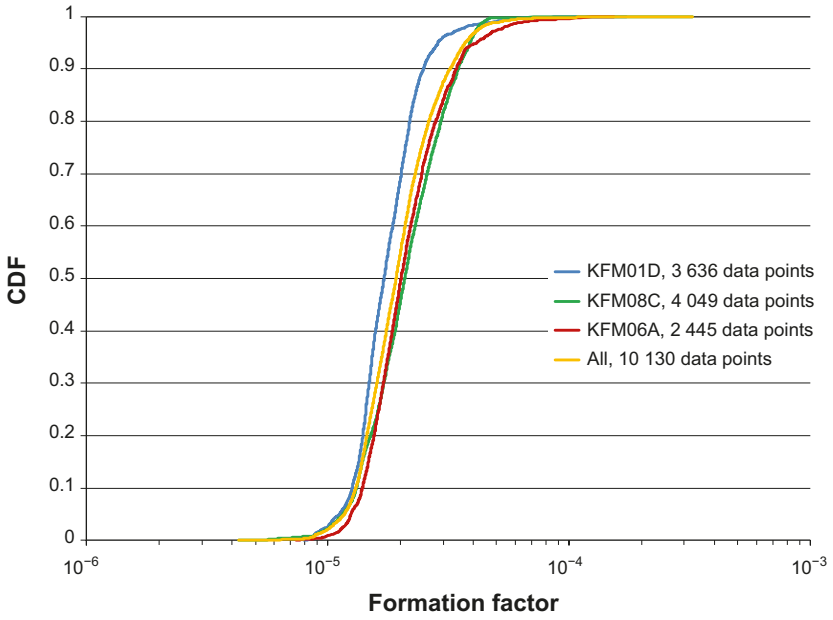

Figure 6-77. *CDFs of formation factors for borehole KFM01D, KFM06A, and KFM08C.*

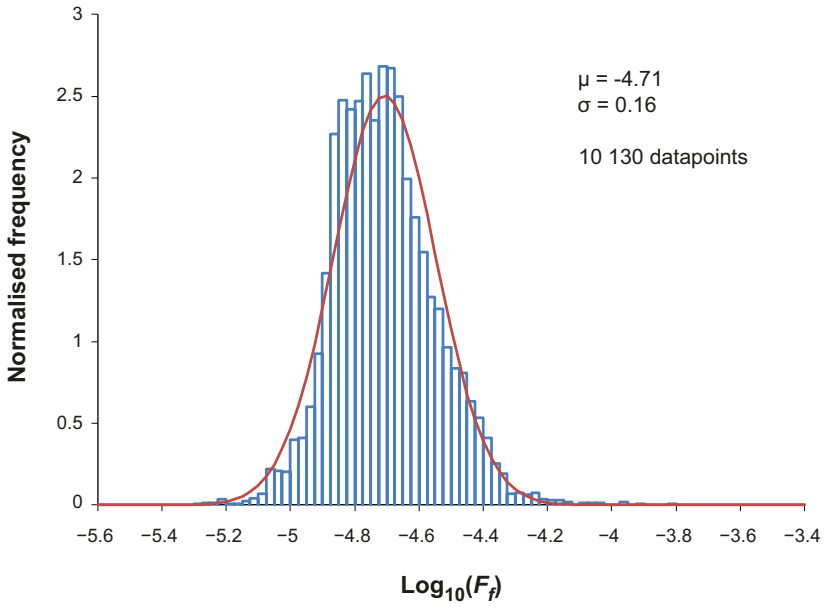

Figure 6-78. *Histogram of all data from boreholes KFM01D, KFM06A, and KFM08C, together with best fit normal distribution.*

Method 2: Effective diffusivities from through diffusion measurements are tabulated in Appendix 2 of Selnert et al. (2008). Most of these data were used as a basis for the recommendations in this text. However, in small volumes of the bedrock at Forsmark, highly porous episyenite was found and sampled. The samples with a porosity above 10 % are considered to be non-representative for the site and when treating the data statistically, such samples were excluded. A histogram of the 58 included data points, in the form of $\log_{10}(D_e)$, are shown in Figure 6-79, together with the best fit normal distribution.

As previously cautioned, these data should not be used without performing corrections for the de-stressed conditions at the laboratory. In performing this correction, we use formation factors obtained by electrical methods in situ and in the laboratory.

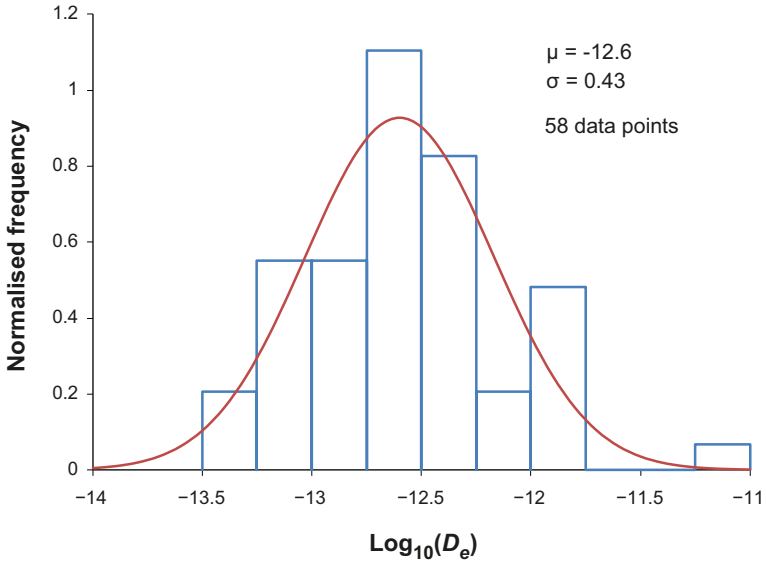

Figure 6-79. *Histogram of all effective diffusivities from laboratory through diffusion measurements, except for those of samples with a porosity over 10 %.*

The blue curves of Figure 6-80 show the CDF of all in situ formation factors obtained in KFM01D, KFM06A, and KFM08C, together with the best fit log-normal distribution (cf yellow curve of Figure 6-77 and Figure 6-78). In addition, in red curves, the corresponding CDF for data from laboratory measurements is shown together with the best fit log-normal distribution. In the laboratory, 163 drill core samples were studied with the electrical resistivity method. Note that all these data have been corrected for surface conduction effects by using Equation 6-29.

As can be seen, the formation factors obtained in the laboratory are about one order of magnitude higher than those obtained in situ. The ratios between the laboratory and in situ formation factors at different CDF values are shown in the figure, where at the CDF value 0.5, the ratio is 11.5. The difference seems to be larger for larger formation factors, and smaller for smaller formation factors. In spite of this fact, we chose to take a simplistic approach and suggest that all laboratory effective diffusivities should be divided by a transfer factor of 11.5. After applying this transfer factor, the in situ effective diffusivity is estimated.

Comparison of method 1 and 2: In Figure 6-81, the CDF of the in situ D_e from method 2 is shown in red. This is based on 58 data points from laboratory through diffusion measurements, which have been reduced by a factor of 11.5. In comparison, the CDF of the in situ effective diffusivities based on the in situ electrical resistivity method is shown (method 1). Here the effective diffusivity is obtained from the product of the formation factors and $D_w = 1 \times 10^{-9}$ m^2/s.

As can be seen, the two methods of obtaining in situ D_e give very similar results, and deviations are within the data uncertainty of the methods. As so many data points have been obtained with the in situ electrical resistivity method, we chose to propagate results from it to SR-Site. Results from the through diffusion measurements are still considered as important and confirmatory.

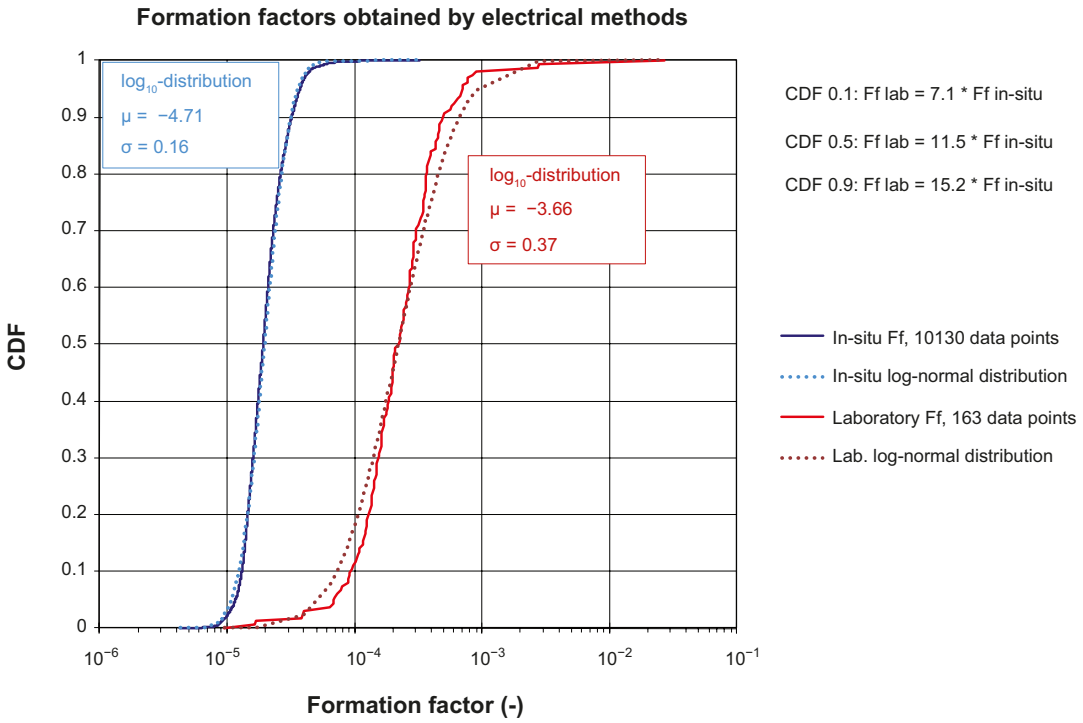

Figure 6-80. *Blue curves: CDF and best fit log-normal distribution of in situ formation factors for borehole KFM01D, KFM06A, and KFM08C. Red curves: CDF and best fit log-normal distribution of laboratory formation factors obtained by the electrical resistivity method.*

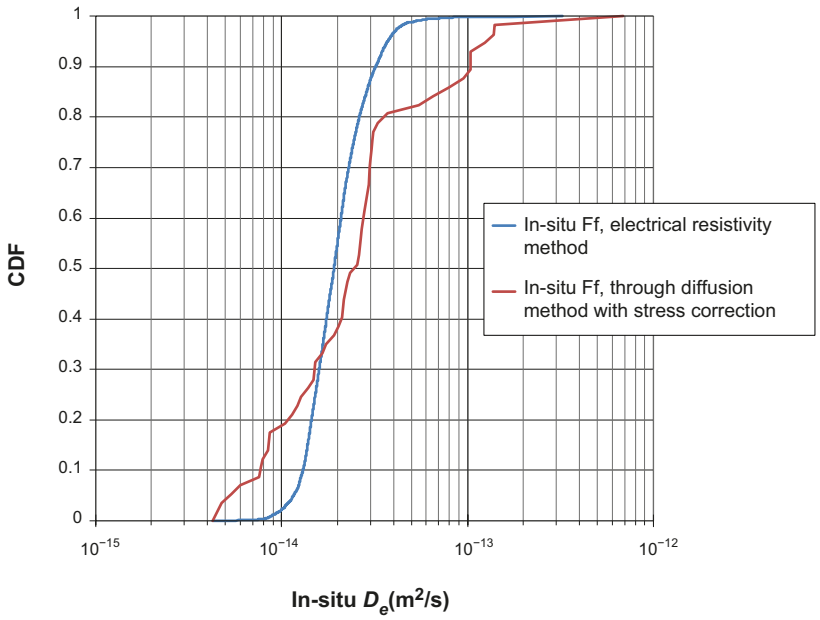

Figure 6-81. *Comparison of CDFs of in situ D_e obtained by the two methods.*

Recommended data: For the flow path averaged in situ formation factor, we recommend using the arithmetic mean value of the 10 130 data points from borehole KFM01D, KFM06A, and KFM08C. This equals 2.11×10^{-5}. If using a D_w of 1×10^{-9} m^2/s, the corresponding D_e becomes 2.11×10^{-14} m^2/s. No uncertainty range based on natural variability of the formation factor is assigned to this value, as the deviations between flow paths are considered to be insignificant for safety assessment calculations. However, as discussed in this text there is significant conceptual and data uncertainty associated with D_e that cannot be corrected for, due to lack of knowledge. Furthermore, there is uncertainty in which D_w should be used for the individual radionuclide, as 1) the temperature and salinity will vary during the glacial cycle, which would give rise to temporal variation in D_w, and as 2) each radionuclide may exist as a number of different species, each having an individual D_w. These uncertainties may give rise to bias that cannot be reduced by flow path averaging (as D_e estimates for all rock volumes along a flow path would potentially suffer from the same bias).

To account for these uncertainties we take on a simplistic approach and suggest that the best estimate flow path averaged D_e has an associated error of half an order of magnitude. It seems to be appropriate to distribute this error symmetrically in the log space. The great majority of flow path averaged D_e values should be found within this one order of magnitude range. Therefore it is suggested that the error corresponds to two standard deviations (i.e. the specified range contains 95.4 % of the data points). The grounds for this approach are the following.

- The D_w for different species of importance generally differ by half and order of magnitude or less.
- Reasonable porewater temperatures and salinities should not affect D_w by more than a factor of two.
- Uncertainty in the analogy between diffusion and electromigration appears to be contained within a factor of two.
- Uncertainty in correction for surface conduction appears to be contained within a factor of two.
- Based on expert judgment it seems fair to assume that the great majority of flow paths encounter an averaged value of D_e varying over one order of magnitude.

Based on this we suggest that the $\log_{10}$-normal distribution with the following parameters should be used for the flow path averaged in situ D_e, where there are no exclusion effects:

- $\mu = -13.7$, $\sigma = 0.25$.

In case there is anion exclusion, we suggest that the entire distribution is shifted downwards by half an order of magnitude (cf Equation 6-30). This gives a $\log_{10}$-normal distribution with the following parameters for anions:

- $\mu = -14.2$, $\sigma = 0.25$.

Here it should be noted that a radioelement may have a speciation allowing for cationic, neutral, and anionic forms. Therefore, in case of a radionuclide transport modelling code that only allows for one D_e per radioelement, one must choose whether the radioelement predominantly is in its cationic, neutral, or anionic form.

It is cautioned that the suggested standard deviation is due to uncertainty, and not due to natural variability. Accordingly this distribution cannot again be averaged.

Sorption partitioning coefficient, K_d

Based on the data extrapolation and qualification procedures described in Crawford (2010), K_d data have been estimated for application conditions in SR-Site. The data are based on the use of Forsmark metagranite (rock code 101057) as a reference rock type and consider the impact of all known sources of uncertainty that can be reasonably quantified. For the impact of temporally variable groundwater compositions, K_d values have been chosen pessimistically to reflect the least favourable conditions for transport retardation. A selection of the recommended data are shown in Figure 6-82 as box and whisker plots along with a comparison with data previously used in SR-Can (SKB 2006b). Similar plots depicting the recommended data for trivalent actinides and lanthanides are given in Figure 6-83.

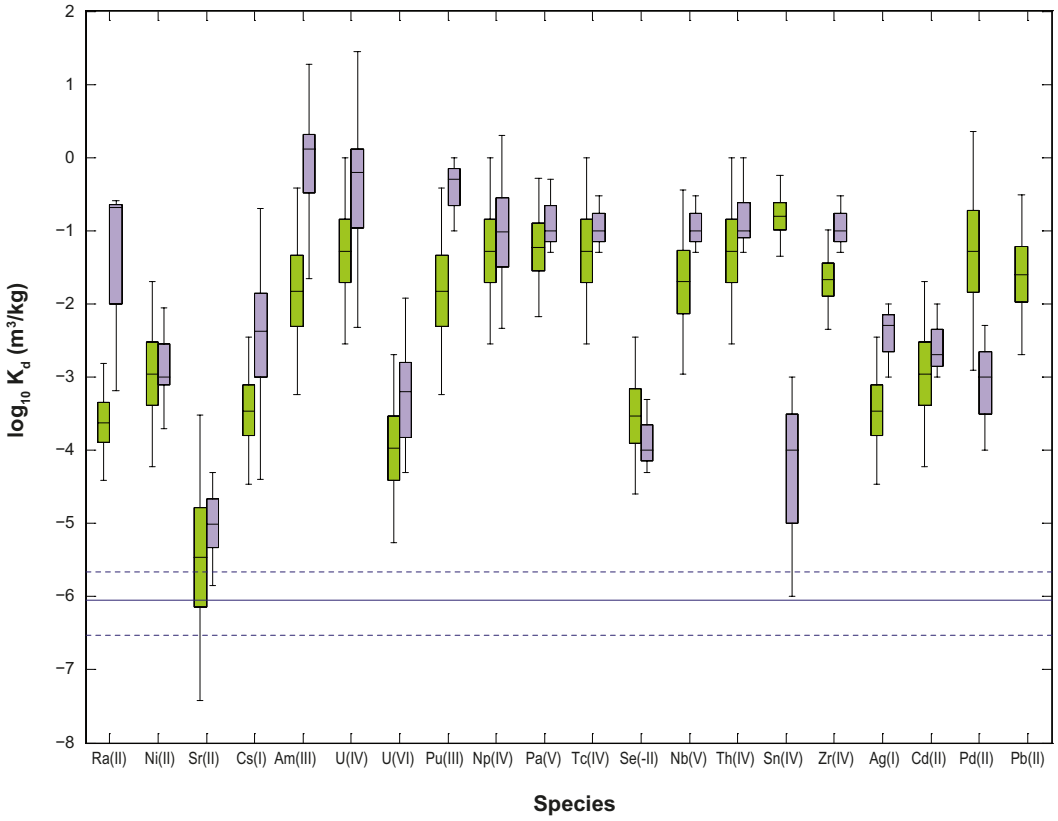

Figure 6-82. *Recommended $log_{10}K_d$ ranges for SR-Site temperate climate case application conditions (green box plots). Data previously recommended for use in SR-Can are shown for comparative purposes (purple box plots). The coloured portion of the box plot represents the 25 %–75 % interquartile range with the median given as the horizontal dividing line. Whiskers of the box plot represent the 95 % confidence interval. A lower effective bound on relevant K_d values is provided by the storage porosity of the rock matrix which is shown as the horizontal unbroken reference line in the figure along with a 95 % confidence interval for this estimate (broken lines).*

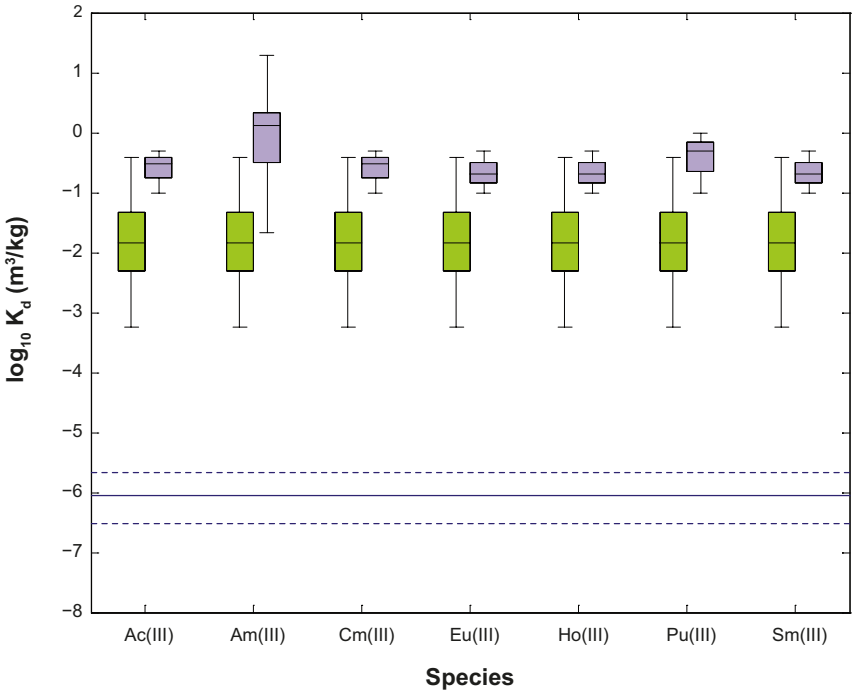

Figure 6-83. *Recommended $log_{10}K_d$ ranges of trivalent actinides and lanthanides for SR-Site temperate climate case application conditions (green box plots). Data previously recommended for use in SR-Can are shown for comparative purposes (purple box plots). Other plot details are the same as in Figure 6-82.*

The data are given in the form of log-normal distributions which implicitly include the combined impact of uncertainty as well as spatial and temporal variability. The median of the log-transformed K_d uncertainty may be taken to be the best estimate value for central case deterministic calculations. Although flow path averaging effects would normally suggest the use of the arithmetic mean K_d value, the use of the median is deemed a more appropriate choice given that uncertainty (rather than variability) is the dominant contribution to the statistical dispersion of the K_d ranges. For stochastic simulations in SR-Site, it is recommended that the log-normal distributions are sampled uniformly between the 2.5 % and 97.5 % percentiles (that is the distribution should be truncated).

The recommended K_d data for the Forsmark site are supplied in Table 6-89. These data are recommended for all rock volumes throughout repository evolution.

Table 6-89. Recommended sorption partitioning coefficient, K_d values for use in SR-Site simulations of the Forsmark site. The predominant species for redox sensitive elements are highlighted in bold text. Values are given for the best estimate (median), parameters for the log-normal distribution (μ and σ), as well as lower and upper limits corresponding to the 2.5 % and 97.5 % percentiles, respectively. For each row a correlation group (1 or 2) or no correlation group (–) is assigned.

Radionuclide (Redox State)	Best estimate K_d (m^3/kg)	$\log_{10}K_d$ – μ	$\log_{10}K_d$ – σ	Lower K_d limit (m^3/kg)	Upper K_d limit (m^3/kg)	Corr. Group
Ac(III)	1.48×10^{-2}	–1.83	0.72	5.74×10^{-4}	3.83×10^{-1}	2
Ag(I)	3.49×10^{-4}	–3.46	0.51	3.46×10^{-5}	3.52×10^{-3}	1
Am(III)	1.48×10^{-2}	–1.83	0.72	5.74×10^{-4}	3.83×10^{-1}	2
C, HCO_3^-	0.0	-	-	0.0	0.0	-
C, CH_4	0.0	-	-	0.0	0.0	-
C, -CO_2H	0.0	-	-	0.0	0.0	-
Cd(II)	1.10×10^{-3}	–2.96	0.65	5.97×10^{-5}	2.04×10^{-2}	1
Cl(-I)	0.0	-	-	0.0	0.0	-
Cm(III)	1.48×10^{-2}	–1.83	0.72	5.74×10^{-4}	3.83×10^{-1}	2
Cs(I)	3.49×10^{-4}	–3.46	0.51	3.46×10^{-5}	3.52×10^{-3}	1
Eu(III)	1.48×10^{-2}	–1.83	0.72	5.74×10^{-4}	3.83×10^{-1}	2
H(I)	0.0	-	-	0.0	0.0	-
Ho(III)	1.48×10^{-2}	–1.83	0.72	5.74×10^{-4}	3.83×10^{-1}	2
I(-I)	0.0	-	-	0.0	0.0	-
Mo(VI)	0.0	-	-	0.0	0.0	-
Nb(V)	1.98×10^{-2}	–1.70	0.64	1.11×10^{-3}	3.53×10^{-1}	2
Ni(II)	1.10×10^{-3}	–2.96	0.65	5.97×10^{-5}	2.04×10^{-2}	1
Np(IV)	$\mathbf{5.29\times10^{-2}}$	**–1.28**	**0.65**	$\mathbf{2.84\times10^{-3}}$	$\mathbf{9.84\times10^{-1}}$	**2**
Np(V)	4.13×10^{-4}	–3.38	0.74	1.48×10^{-5}	1.15×10^{-2}	2
Pa(IV)	5.92×10^{-2}	–1.23	0.48	6.76×10^{-3}	5.18×10^{-1}	2
Pa(V)	$\mathbf{5.92\times10^{-2}}$	**–1.23**	**0.48**	$\mathbf{6.76\times10^{-3}}$	$\mathbf{5.18\times10^{-1}}$	**2**
Pb(II)	2.52×10^{-2}	–1.60	0.56	2.05×10^{-3}	3.10×10^{-1}	2
Pd(II)	5.20×10^{-2}	–1.28	0.83	1.22×10^{-3}	2.21	2
Pu(III)	$\mathbf{1.48\times10^{-2}}$	**–1.83**	**0.72**	$\mathbf{5.74\times10^{-4}}$	$\mathbf{3.83\times10^{-1}}$	**2**
Pu(IV)	5.29×10^{-2}	–1.28	0.65	2.84×10^{-3}	9.84×10^{-1}	2
Pu(V)	9.14×10^{-3}	–2.04	0.60	6.19×10^{-4}	1.35×10^{-1}	2
Pu(VI)	9.14×10^{-3}	–2.04	0.60	6.19×10^{-4}	1.35×10^{-1}	2
Ra(II)	2.42×10^{-4}	–3.62	0.41	3.87×10^{-5}	1.51×10^{-3}	1
S(-II)	0.0	-	-	0.0	0.0	-
Se(-II)	$\mathbf{2.95\times10^{-4}}$	**–3.53**	**0.55**	$\mathbf{2.50\times10^{-5}}$	$\mathbf{3.48\times10^{-3}}$	**-**
Se(IV)	2.95×10^{-4}	–3.53	0.55	2.50×10^{-5}	3.48×10^{-3}	-
Se(VI)	2.95×10^{-4}	–3.53	0.55	2.50×10^{-5}	3.48×10^{-3}	-
Sm(III)	1.48×10^{-2}	–1.83	0.72	5.74×10^{-4}	3.83×10^{-1}	2
Sn(IV)	1.59×10^{-1}	–0.80	0.28	4.51×10^{-2}	5.58×10^{-1}	2
Sr(II)	3.42×10^{-6}	–5.47	0.99	3.84×10^{-8}	3.05×10^{-4}	1
Tc(IV)	$\mathbf{5.29\times10^{-2}}$	**–1.28**	**0.65**	$\mathbf{2.84\times10^{-3}}$	$\mathbf{9.84\times10^{-1}}$	**2**
Tc(VII)	0.0	-	-	0.0	0.0	-
Th(IV)	5.29×10^{-2}	–1.28	0.65	2.84×10^{-3}	9.84×10^{-1}	2
U(IV)	$\mathbf{5.29\times10^{-2}}$	**–1.28**	**0.65**	$\mathbf{2.84\times10^{-3}}$	$\mathbf{9.84\times10^{-1}}$	**2**
U(VI)	$\mathbf{1.06\times10^{-4}}$	**–3.97**	**0.66**	$\mathbf{5.53\times10^{-6}}$	$\mathbf{2.05\times10^{-3}}$	**2**
Zr(IV)	2.13×10^{-2}	–1.67	0.35	4.48×10^{-3}	1.02×10^{-1}	2

6.8.11 Judgement by the assessment team

Diffusion available porosity

Since no new information or data has been obtained, the judgement is to use the same data as in SR-Site.

Effective diffusivity and formation factor

Based on the new information obtained since SR-Site, which indicates that the uncertainties related to the effective diffusion coefficient and formation factor are too small to have a significant impact on transport calculations, and that the effective diffusivity values in SR-Site are pessimistically chosen, the judgement is to use the same data as in SR-Site.

Scale on which the porous system is connected

Since no new information or data has been obtained, the judgement is to use the same data as in SR-Site.

Sorption partitioning coefficient

Based on the new information obtained since SR-Site, which indicates that altered K_d values may not have a very significant impact on overall dose rates, the judgement is to use the same data as in SR-Site.

6.8.12 Data recommended for use in assessment

Porosity data recommended for use in the assessment are summarised in Table 6-90. It should be noted that the suggested values are flow path averaged.

The effective diffusivity data recommended for use in the assessment are summarised in Table 6-91. It should be noted that the probability density function reflects on uncertainty and temporal variability, and not on spatial variability. Spatial variability is already handled by suggesting flow path averaged values. The D_e values for different elements should be correlated (cf Section 6.8.10).

Table 6-90. In situ diffusion available porosity suggested for use in the assessment.

Type of solute	ε (%)
Cations and non-charged solutes	0.18
Anions	0.18

Table 6-91. Flow path averaged in situ effective diffusivity recommended for use in the assessment.

Type of solute	Best estimate D_e (m^2/s)	$Log_{10}D_e$ (m^2/s) – μ	$Log_{10}D_e$ (m^2/s) – σ	Probability density function
Cations and non-charged solutes	2.1×10^{-14}	–13.7	0.25	Log-normal
Anions	6.6×10^{-15}	–14.2	0.25	Log-normal

Concerning the scale on which the porous system is connected *L (m)*, it is suggested to be connected on all scales relevant for the safety assessment (at least on the decametre scale). This means that the maximum penetration depth L_D (m) for matrix diffusion is dependent on half the spacing between hydraulically conductive fractures, as discussed in Section 6.7.

Sorption data recommended for use in SR-Site are summarised in Table 6-89. The K_d data are given in the form of log-normal distributions characterised by a mean (μ) and standard deviation (σ). For stochastic simulations, it is suggested that the distributions are sampled uniformly between the upper and lower limits defined by the 2.5 % and 97.5 % percentiles. The best estimate K_d value for use in deterministic calculations is given as the median of the K_d distribution. K_d data of the same correlation group (1 or 2) should be correlated.

7 Surface system data

7.1 Climate and climate related data

In this section, data on climate- and climate related processes are described, including air and ground-surface temperatures, ice sheet thickness, permafrost depth, relative sea level change, and denudation of bedrock.

Many of the data in this section describe reconstructed data for the past 120 000 years, i.e. for the last glacial cycle. In order to construct a *Reference glacial cycle* for the future, these reconstructed data are in the safety assessment, as a first step, repeated for the coming ~100 000 years. In addition to this Reference glacial cycle, complementary cases of future climate development are constructed, in which climate-related processes are modified to describe possible developments with a potentially larger impact on repository safety than the Reference glacial cycle. The complementary climate cases describe and cover various aspects of the large uncertainties that are related to future variations in climate and climate-related processes on 100 000 and one million year time scales. The data presented in this section are generally justified in the **Climate report**, and supporting lower level references.

7.1.1 Modelling

Defining the data requested from the supplier

The following data should be delivered for the Forsmark area by the supplier:

- Time series of air- and ground-surface temperatures (°C) in the Forsmark region for the past 120 000 years.
- Time series of ice thickness (m) and ice surface gradients (°) over Forsmark for the past 120 000 years.
- Ice thickness for a case with a maximum thick ice sheet over Forsmark.
- Time series of relative sea level change at Forsmark for the Reference glacial cycle for the past 120 000 years.
- Time series of relative sea level changes at Forsmark for the Global warming and Extended global warming climate cases for the coming 120 000 years.
- Time series of depths of permafrost and perennially frozen ground at Forsmark for the past 120 000 years, as well as for complementary case with surface boundary conditions more favourable for permafrost development resulting in maximum glacial cycle permafrost and freezing depths.
- Theoretical illustrative values on permafrost and freezing depths from a full set of sensitivity simulations.
- Data on future denudation of the crystalline bedrock surface at Forsmark over the coming 100 000 and 1 million years.

The reconstructed data for the past 120 000 years should be repeated for the coming 120 000 years to construct the Reference glacial cycle for the PSAR. In this process, the time of 120 000 years before present (BP) should be set as the present day.

Modelling activities in which data will be used

The requested climate- and climate related data are used in a number of PSAR modelling activities. Data on air temperature are needed for simulations of ice sheet and permafrost development, and for the evaluation of thermal gradients and geothermal heat flow. Data on changing ice sheet configurations over time are needed for studies of variations in stress in the Earth's crust, which in thermo-hydro-mechanical (THM) analyses are used for assessing the potential for glacially induced faulting. Ice sheet data are also needed for simulations of groundwater flow under glacial conditions. Data from permafrost simulations are needed in order to make appropriate selections of conditions when

studying surface hydrology and groundwater changes associated with colder climates, as well as for the assessment of potential freezing of the buffer and back-fill at repository depth during future periods of periglacial climate. Data on relative sea level changes are needed for a proper description of the past and future evolution of the landscape as influenced by the isostatic recovery from the last glacial cycle and sea level changes (e.g. rising sea levels associated with global warming), for instance in order to model future lake formation. These data are also used for studying groundwater flow in potential future situations when the isostatic uplift has progressed further. Knowledge on permafrost and glacial evolution are also necessary when investigating various THM processes, and for assessing the potential for freezing of various parts of the repository. The flow of climate- and climate related data is described in the following list:

- Air and ground-surface temperature data are used for:
  - ice sheet modelling,
  - permafrost modelling,
  - groundwater flow and permafrost modelling,
  - calculations of thermal gradients and geothermal heat flow.
- Data on ice sheet thickness and ice surface gradients are used for:
  - modelling of stress evolution and fault stability during glacial conditions,
  - groundwater flow and permafrost modelling,
  - simulation of Glacial Isostatic Adjustment (GIA),
  - analysis of the safety assessment scenario ‘canister failure due to isostatic load’.
- Data on relative sea level changes are used for:
  - modelling of landscape evolution,
  - permafrost simulations,
  - modelling of groundwater flow.
- Data on permafrost, perennially frozen depths, and bedrock temperatures are used in analysis of repository freezing in the PSAR freezing scenario. In addition, the general picture obtained from the permafrost modelling results are used to set up simulations on:
  - surface and groundwater flow, with the modelling code MIKE-SHE,
  - groundwater flow simulations, with the modelling code DarcyTools,
  - calculations of hydraulic jacking.
  - Analysis the safety assessment scenario ‘buffer freezing’.
- Data on bedrock denudation are used for:
  - Analysis of the stability and age of the bedrock surface,
  - Analysis of potential changes in repository depth over the assessment period.

7.1.2 Experience from SR-Site

The experience from SR-Site is that all data described under 7.1.1 were necessary to conduct the safety assessment. Many of the data sets were necessary for other safety assessment activites, such as relative sea level data for the landscape development, ice sheet data for e.g. groundwater flow simulations under glacial conditions, surface air temperature data for permafrost modelling, etc (cf Section 7.1.1). Other data were used directly in relation to the safety functions and had a more direct effect on the outcome of the safety assessment. Specifically, i) the maximum ice sheet thickness was used to derive the maximum hydrostatic pressure at repository depth under glacial conditions within the scenario *Canister failure due to isostatic load*, and ii) the maximum freezing depths, and results from associated sensitivity simulations, were used for assessing the potential for freezing of the buffer clay and back-fill material in the *Buffer freezing* scenario.

During the SR-Site work on maximum ice sheet thicknesses, a need for an in-depth study of this issue was identified, and hence a dedicated study on maximum possible ice sheet thicknesses was performed after SR-Site see Section 7.1.1. In line with this, also a number of other types of climate- and climate related data used in SR-Site needed to be updated for the PSAR(Section 7.1.1).

7.1.3 Supplier input on use of data in PSAR

In this section, the supplier cannot be separated from the customer, as the PSAR team have produced the data (although based on observations from other groups). Hence, no supplier formally exists. None the less, the text is written according to the standard outline of the Data report.

7.1.4 Sources of information and documentation of data qualification

Sources of information

The main source of information for the data sets on air temperature, ice thickness, relative sea level changes, and permafrost depths is the **Climate report**. Within the **Climate report**, references to relevant lower-level documents can be found for each data set. The full reference is given in Table 7-1.

Table 7-1. Main sources of information used in data qualification.

SKB, 2020. Post-closure safety for the final repository for spent nuclear fuel at Forsmark – Climate and climate-related issues, PSAR version. SKB TR-20-12, Svensk Kärnbränslehantering AB.

Categorising data sets as qualified or supporting

All data sets in the **Climate report** have a priori been considered to be qualified, since they are from either SKB technical reports that have undergone required QA handling, or from published peer-reviewed scientific papers. They have thereafter been judged to be qualified based on the criteria in the instruction for supplying data for the Data report (cf Section 2.3). Qualified climate-related data sets are displayed in Table 7-2 and numbered from 1 to 11. Detailed comments on the items are given in Table 7-3.

Excluded data previously considered as important

No data are excluded that previously were considered important.

Table 7-2. Qualified and supporting data sets. All data sets and references to figures are from the Climate report. In the Climate report, many underlying data sets are also illustrated in figures. The data sets are also sumarised in Näslund (2021), with references to the storage locations of the data files.

1. The air temperature data for the last glacial cycle including submerged periods, as reported in the Climate report, are based on data from a peer-reviewed scientific publication, which, within the safety assessment work, have been modified by considering the altitude effects of an ice sheet using an ice sheet model. The method of doing this is described in detail in the Climate report (Appendix A) and in the lower-level references therein. All relevant lower-level references are listed in the Climate report, facilitating traceability. Lower-level references in the form of peer-reviewed scientific papers are all considered qualified. In the Climate report, and in lower-level report references therein, issues such as data quality, variability, representativity, and uncertainties are discussed. Many of the climate data delivered are derived from modelling. In the Climate report, and lower-level references, the modelling strategy, modelling tools, and validity of the modelling are described. It is judged that the modelling approaches are adequate for the purposes of the PSAR.
2. The ground-surface temperature data for the last glacial cycle with and without ice-sheet are based on the air temperature data in item 1 and on numerical permafrost modelling (Section 3.4 in the Climate report). The same considerations as for item 1 apply.
3. The reconstructed ice sheet thickness data for the last glacial cycle are based on a model reconstruction of the Weichselian ice sheet (Section 3.1 in the Climate report) The same considerations as for item 1 apply.
4. The maximum ice sheet thicknesses data for the peak Saalian glaciation are based on climate- and ice sheet model simulations (Section 5.4 in the Climate report). The same considerations as for item 1 apply.
5. The theoretical ice sheet profile data are based on an equation given in a glaciological textbook, referred to in the Climate report (Appendix B, Equation B-2) and a lower-level reference therein. This ice sheet profile has been selected to represent an advancing ice sheet over Forsmark for the PSAR reference glacial cycle.
6. The simulated ice sheet profile data are based on a model reconstruction of the Weichselian ice sheet (Section 3.1 in the Climate report). The same considerations as for item 1 apply. This ice sheet profile (the least steep simulated profile from 14 300 years BP, see Appendix B in the Climate report) has been selected to represent a retreating ice sheet over Forsmark in the PSAR Reference glacial cycle.
7. The ice surface gradient data for the last glacial cycle are calculated from the data in item 6 (Appendix B in the Climate report). The same considerations as for item 6 apply.
9. The relative sea level data for the reference evolution are based on Glacial Isostatic Adjustment simulations (Section 3.3 in the Climate report) and extrapolations of up-to-present Holocene isostatic uplift rates at the Forsmark site (Appendix E in the Climate report). The same considerations as for item 1 apply.
10. The relative sea level data for the Global warming and Extended global warming climate cases are based on Glacial Isostatic Adjustment simulations (Section 5.1 and 3.3 in the Climate report), extrapolations of up-to-present Holocene isostatic uplift rates at the Forsmark site (Appendix E in the Climate report), and peer-reviewed published data on possible future sea level rise under two carbon emission scenarios (Section 5.1 in the Climate report). The same considerations as for item 1 apply.
11. The permafrost development data for the last glacial cycle (including bedrock temperatures, ground-surface temperatures, permafrost depths, and freezing depths) are based on numerical permafrost simulations (Section 3.4 in the Climate report). The same considerations as for item 1 apply.
12. The permafrost development data for the Severe permafrost climate case (including bedrock temperatures, ground-surface temperatures, permafrost depths, and freezing depths) are based on numerical permafrost simulations (Section 5.5 in the Climate report). The same considerations as for item 1 apply.
13. The permafrost development data from sensitivity studies (bedrock thermal conditions, surface conditions, air temperature curve, and presence or absence of heat from the repository) are based on numerical permafrost simulations (Section 3.4 and 5.5 in the Climate report). The same considerations as for item 1 apply.

7.1.5 Conditions for which data are supplied

There is a large range of parameters that influence climate and result in changes in climate on a wide range of time scales. In turn, climate is affected by many of these parameters, resulting in positive or negative feed-back mechanisms. For a description of these processes, see the **Climate report**.

7.1.6 Conceptual uncertainty

For the climate- and climate-related data it is often difficult to distinguish data uncertainty from conceptual uncertainty. Therefore, the combined uncertainty is discussed in this section, and no additional information is given in Section 7.1.7.

The uncertainty in climate evolution over the coming 100 000 years is dealt with by the construction of several alternative climate cases for Forsmark, see below.

Air and ground-surface temperatures

The air temperature data for Forsmark originate from a reconstruction of a palaeotemperature curve for Greenland. In this reconstruction, there are various contributions to uncertainty, such as the transformation of ice core $\delta^{18}O$ values to air temperatures. Other uncertainties are introduced when this proxy palaeotemperature curve is used for the reconstruction of the Weichselian ice sheet and for the estimation of palaeotemperatures for the Forsmark region. Given these steps, it is obvious that large uncertainties exist in the resulting palaeotemperature curve for the Forsmark region (cf Figure 7-1 in Section 7.1.10). In order to estimate these uncertainties, the temperature curve has been compared against other reconstructions of temperature from Greenland ice cores and with existing independent proxy records and modelling results on Fennoscandian palaeotemperatures (**Climate report**, Appendix A).

Based on how the air temperature curve for the last glacial cycle has been produced in detail, and on the comparison with temperature proxy and model data for periods of the last glacial cycle (cf the **Climate report**, Appendix A), it is estimated that the uncertainty in the temperature curve reconstructed for the last glacial cycle is:

- not larger than 6 °C for periods with the largest uncertainties,
- up to c 4–5 °C for the major part of the temperature curve, and
- for some parts of the curve, such as the Holocene, noticeably smaller than 4 °C.

The uncertainty introduced by repeating a Reference glacial cycle, based on reconstructed conditions for the last glacial cycle, for the coming 100 000 years is dealt with by the construction of complementary climate cases describing situations e.g. where a warmer climate than the reference evolution would postpone glacial- and permafrost conditions into the future, or cases where permafrost might develop earlier than in the Reference glacial cycle.

In summary, the construction of complementary climate cases (with thicker and thinner ice sheets, deeper and shallower permafrost, and relative sea level developments other than those in the reference evolution, cf the **Climate report**, Chapter 5) take care of, in an indirect way, the large uncertainties in the temperature curve used to construct the future Reference glacial cycle.

Ice sheet duration, ice thickness, and ice surface gradients

The uncertainty in ice sheet duration is dealt with by the construction of alternative climate cases with e.g. longer (**Climate report**, Section 5.3) and shorter (**Climate report**, Sections 5.1 and 5.2) ice sheet coverage over the Forsmark site than in the Reference glacial cycle.

The uncertainty in ice thickness is taken care of by the analysis of cases with a thicker ice sheet than in the Reference glacial cycle (**Climate report**, Section 5.4).

The uncertainties in ice surface gradients are taken care of by the inclusion of a range of possible ice surface profiles (**Climate report**, Appendix B). These uncertainties are also addressed by ensuring that cases are studied in which the ice margin pauses at the Forsmark site.

Relative sea level changes

The uncertainty in future changes in relative sea level is dealt with by the construction of alternative climate cases with the relative sea level at Forsmark affected by a raise in global sea level for different degrees of global warming (**Climate report,** Sections 5.1 and 5.2).

Permafrost depths

The uncertainty in permafrost depth is dealt with by the construction and analysis of alternative climate cases with surface conditions more favourable for permafrost growth than the Reference glacial cycle (**Climate report,** Section 5.5).

The uncertainty in temperature, as such, in the input air temperature curve used for the permafrost simulations of the last glacial cycle has been estimated to be 6 °C or less (see above). This rather large uncertainty is still considerably smaller than the temperatures range analysed in some of the permafrost sensitivity model simulations (**Climate report**, Sections 3.4 and 5.5). When the results are compared with known levels and variations in temperature for the last glacial cycle, it is concluded that an unrealistically large lowering of the temperature curve is required in order for the −6 °C isotherm (i.e. the temperature at which a frozen buffer clay and backfill material may start having detrimental effects on the canister and surrounding host rock, to reach repository depth (see Section 7.2.11 and **Climate report**, Section 5.5).

7.1.7 Data uncertainty due to precision, bias, and representativity

Generally for these data, one can say that conceptual uncertainty outweighs data uncertainty. However, due to difficulties in distinguishing data uncertainty from conceptual uncertainty, the combined uncertainty is discussed in Section 7.1.6 for the different data sets. In addition, results from sensitivity assessments that can be used to assess the overall uncertainty are presented in Section 7.1.10.

7.1.8 Spatial and temporal variability of data

For the air temperature, ice thickness, ice surface gradients, and relative sea level changes, spatial variability within the site is not captured in the data presented in this section. Data from the models are typically of a regional character (with the exception of the relative sea level data), from which data for the Forsmark region are extracted. However, in the description of the evolution of climate and climate-related conditions for e.g. the Reference glacial cycle, these data are taken to represent the conditions specifically at the location of the spent fuel repository. The spatial representativity of the data described in this section, and the spatial representativity of the resulting development of climate domains (**Climate report**, Section 1.2) in e.g. the Reference glacial cycle, is further described in the **Climate report** (Section 4.5.4, heading *Transitions between climate domains*).

The permafrost and freezing depths are not only related to the regional climate, but also to local properties of the surface system and geosphere. For the permafrost simulations, such surface system and geosphere data have been used from the site investigations. The spatial variability in permafrost growth is described by the 2-D permafrost model, influenced by e.g. altitude, vegetation, locations of water bodies, precipitation and bedrock thermal properties.

This section concerns the climate evolution, where temporal variability is generally handled by giving time series of data. An example is the air temperature curve (Figure 7-1), giving estimated temperatures from 120 000 years BP until present. For other data, data are given for a certain point in time, and in yet other cases even without specifying a specific time. The latter can be exemplified with the value on maximum possible future ice sheet thickness over the repository. For this data, a specific time is not given at which the value is said to be valid over the one million year assessment period.

7.1.9 Correlations

The evolution of climate and climate-related processes sets the conditions for many other safety assessment diciplines and modelling exercises. In PSAR, the uncertainty in future climate development is handled by identifying and analysing a Reference glacial cycle (**Climate report**, Section 4.5) with five complementary climate developments (climate cases) that may occur over the assessment period (**Climate report**, Chapter 5). Data have been estimated for each climate case. No interpolation has been made between climate cases. The identified climate cases are used to bound the uncertainty ranges in future developments of climate and climate-related processes.

As no interpolations are made between climate cases, there is no correlation that needs to be propagated to other SR-Site modelling activities.

7.1.10 Result of supplier's data qualification

The requested data are justified in the **Climate report**. A brief summary is given here.

Air and ground-surface temperatures

The reconstructed air temperature curves for Forsmark for the last glacial cycle are shown in Figure 7-1. The blue curve shows the reconstructed last glacial cycle air temperature for Forsmark, including two periods when the site was overridden by the Weichselian ice sheet, and two subsequent periods when the Forsmark site was submerged by the Baltic sea. For the ice-covered periods, the temperature constitutes the basal ice temperature calculated with the ice sheet model (**Climate report**, Section 3.1), whereas for periods with submerged conditions the temperature is set to +4 °C. Figure 7-1 also shows what the reconstructed temperatures would look like if the site had *not* been covered by an ice sheet or been submerged (red curve, partly hidden by the blue curve). The curves have been used as input to the PSAR permafrost simulations (cf the **Climate report**, Sections 3.4, 5.5 and Hartikainen et al. 2010). The uncertainty of the temperature curves is discussed in Section 7.1.6 and in the **Climate report** (Appendix A).

Figure 7-2 shows the reconstructed ground-surface temperature for Forsmark for the past 120 000 years. These data were produced by the 1-D permafrost modelling performed in SR-Can (SKB 2006c), using the data in Figure 7-1 as input. As in Figure 7-1, reconstructions with and without the presence of the Weichselian ice sheet and submerged conditions are shown. An alternative more detailed way of calculating ground temperatures was applied in the 2-D permafrost simulations performed for SR-Site (cf the **Climate report**, Section 3.1 and Hartikainen et al. 2010). The uncertainty in the temperature curves, and the way it is dealt with, is discussed in Section 7.1.6.

References to locations of numerical data characterising the evolution of air and ground-surface temperatures for different climate cases are given in Table 7-3.

Table 7-3. Sources for numerical temperature data.

Parameter	Document
Air temperature – Reference glacial cycle	SKBdoc1278727
Air temperature – Severe permafrost case	SKBdoc1278727
Ground-surface temperature – Reference glacial cycle	SKBdoc1278728
Ground-surface temperature – Severe permafrost case	SKBdoc1278728

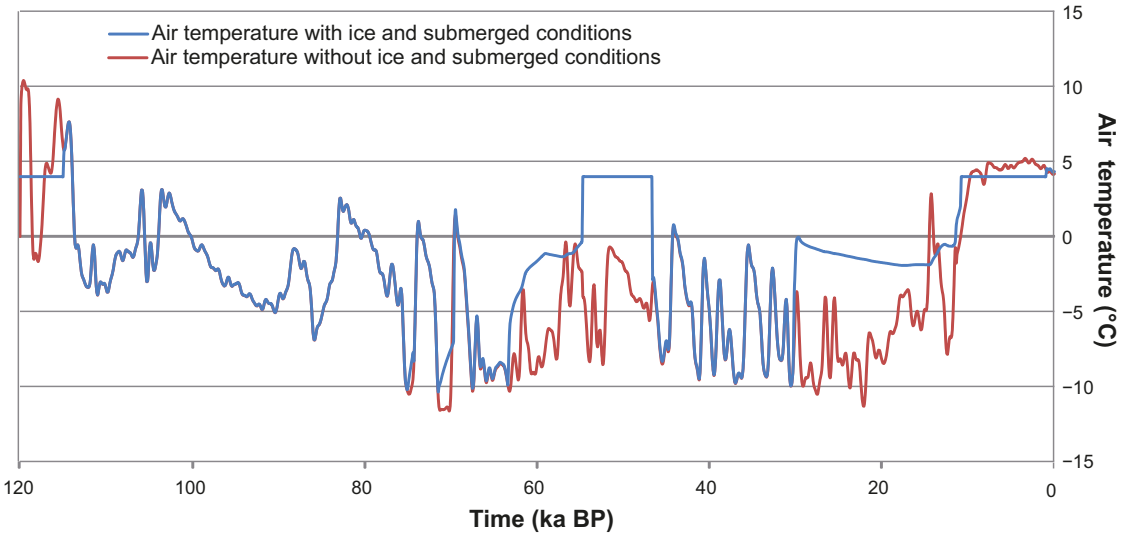

Figure 7-1. *Reconstructed air temperature curve for the Forsmark region for the last glacial cycle. The blue curve includes periods of ice sheet coverage, i.e. it shows simulated basal ice temperatures for glaciated periods, air temperatures for ice-free periods, and also a temperature of +4 °C for submerged periods. The red line shows reconstructed last glacial cycle air temperatures as they would have been without the presence of the Weichselian ice sheet and without submerged periods. The temperature scale shows absolute temperatures. Reproduced from Figure 3-44 of the Climate report.*

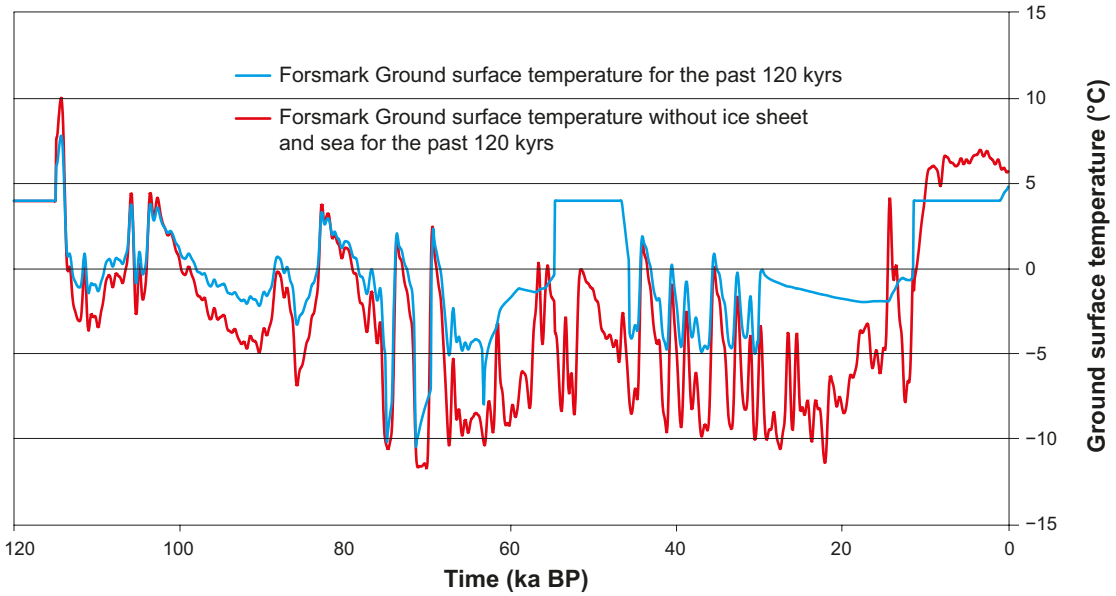

Figure 7-2. *Ground-surface temperature for Forsmark for the past 120 000 years with (blue) without (red) ice sheet and submerged conditions (reproduced from Figure A4 of the Climate report). The temperature scale shows absolute temperatures. The underlying data were used as input data in Sundberg et al. (2009c) and Vidstrand et al. (2010).*

Since SR-Site, new insights have been obtained on the air temperature from independent terrestrial records in Northern Europe, especially during the early (115 000 – 74 000 years ago) and the middle phases (59 000 – 24 000 years ago) of the last glacial cycle (Helmens 2013, 2019), as well as during the deglaciation phase of the Fennoscandian ice sheet from ~ 20 000 to ~ 11 000 years ago (Schenk and Wohlfarth 2019). These new air temperature reconstructions are broadly within the uncertainty range of the air temperature curve for the last 120 000 years used in the PSAR.

Ice thickness and ice surface gradients over Forsmark for the past 120 000 years

The reconstructed ice sheet thickness at Forsmark for the last glacial cycle is shown in Figure 7-3. The site is covered by the Weichselian ice sheet during two phases, centred around 60 000 and 20 000 years BP. About half of the glacial cycle has passed before the ice sheet reaches the Forsmark region. In this reconstruction, Forsmark is free of ice during the major part of the so-called Marine Isotope Stage 3 period (59 000 – 24 000 years BP), i.e. the period preceding the Last Glacial Maximum at around 20 000 years BP. This is in line with several recent studies of the Weichselian glacial history, see discussion and references in the **Climate report** (Sections 4.2 to 4.4).

It is recommended that these data (Figure 7-3) are repeated for the coming 120 000 years to construct the Reference glacial cycle for the PSAR. In this process, the time of 120 000 years BP set as present-day.

The uncertainty of the timing of the first future glacial inception and duration of future glacial phases at Forsmark are taken care of by complementary cases with longer and shorter ice sheet coverage than in the reconstructed last glacial cycle (**Climate report**, Sections 5.1, 5.2 and 5.3).

The maximum ice thickness over Forsmark (~2 900 m) occurred, as expected, during the Last Glacial Maximum, at around 20 000 years BP. The uncertainty in future maximum ice sheet thickness is addressed in a complementary climate case describing larger ice thicknesses (**Climate report**, Section 5.4). The maximum possible ice sheet thicknesses over Fennoscandia and Forsmark, were studied by dedicated simulations of the largest known configuration of Eurasian Quaternary ice sheet (during the Saalian glaciation). Steady-state climate and ice sheet simulations (of the peak Saalian ice sheet at 140 000 ka BP) were performed by Colleoni et al. (2014). In addition, a full range of univariate and multi-variate sensitivity analyses of all parameters affecting the simulated the peak Saalian ice thicknesses were performed (Quiquet et al. 2016). In this way, a thorough treatment of the uncertainties associated with the simulation the peak Saalian ice sheet was obtained. An analysis of the results, methodology and assumptions made in the ice sheet modelling study resulted in a maximum ice sheet thickness of 4 000 m over Forsmark, see **Climate report** Section 5.4.5 and Table 7-9. The 4 000 m value on maximum ice sheet thickness, corresponding to a glacially induced additional hydrostatic pressure of 36 MPa, is propagated to the PSAR safety assessment scenario Canister failure due to isostatic load.

Table 7-4. Ice thickness and associated hydrostatic pressure contribution over Forsmark based on the Reference glacial cycle and the maximum ice-sheet thickness case in the PSAR.

	Ice thickness	Hydrostatic pressure
Reference glacial cycle	2 900 m	26 MPa
Maximum ice-sheet thickness	4 000 m	36 MPa

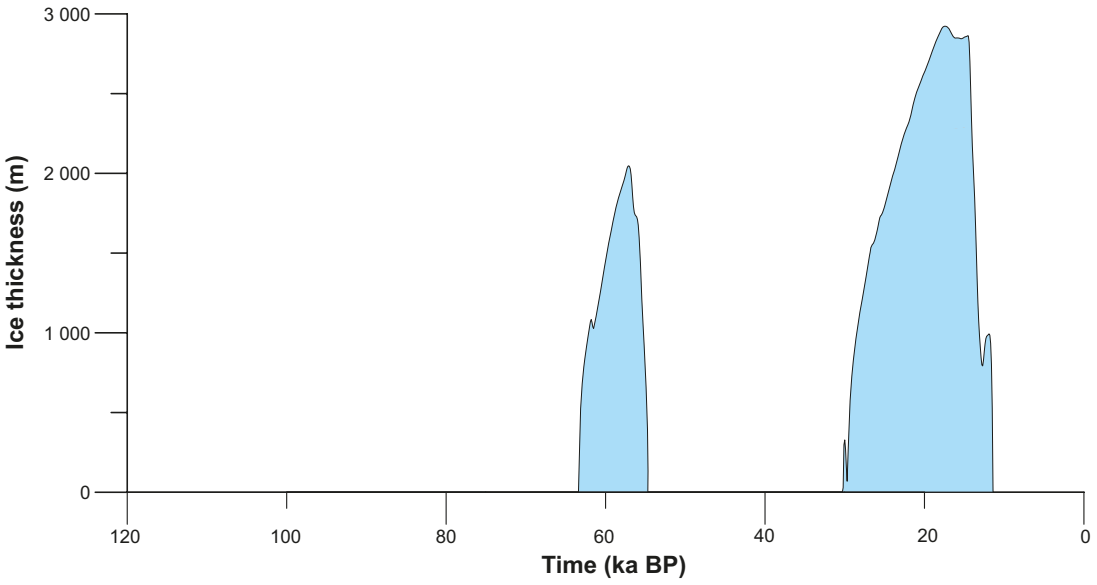

Figure 7-3. Reconstructed Weichselian ice sheet thickness for the Forsmark region for the past 120 000 years. Reproduced from Figure 4-19 of the Climate report.

Ice surface gradients

Figure 7-4 shows the theoretical Reference glacial cycle ice sheet profile (black line) and the simulated Reference glacial cycle ice sheet profile (red line). The profiles are described in the **Climate report (**Appendix B). The theoretical profile is steeper than simple parabolic profiles sometimes used to describe ice sheet profiles. Since this theoretical profile is considered to be more realistic than simple parabolic profiles, and because it is steeper than the steepest of the simulated advancing ice profiles (cf the **Climate report**, Appendix B), this theoretical profile is selected to represent an *advancing ice sheet* over Forsmark for the PSAR Reference glacial cycle.

The red line in Figure 7-4 shows a simulated profile from the deglaciation phase of the Weichselian ice sheet at 14 300 years BP. For the location of this profile, see the **Climate report** (Appendix B). This profile is the least steep retreat profile analysed from the Weichselian ice sheet reconstruction. This profile is selected to represent a *retreating ice sheet* over Forsmark for the PSAR Reference glacial cycle.

The two profiles in Figure 7-4, constitute, in their frontal parts, the steepest, and the least steep profiles of all profiles analysed in the **Climate report** (Appendix B), and they are considered to cover a broad enough span of possible profiles to be employed in other PSAR studies.

Figure 7-7 shows time series data on ice surface gradiens calculated from ice thickness data from the reconstruction of the Weichselian ice sheet. Naturally, ice surface-gradient data are only present for the periods of ice sheet coverage (cf Figure 7-3). In Figure 7-7, the gradient for the most frontal-near, and steepest, part of the ice sheet is not shown.

It is recommended that these data are repeated for the coming 120 000 years to construct the Reference glacial cycle in the PSAR. The time scale should be projected into the future in the same way as for the ice thickness data described above. References to locations of numerical data for the reference ice sheet profiles and surface gradients are given in Table 7-5.

Table 7-5. Sources for numerical ice sheet profiles and surface gradient data.

Parameter	Document
Reference advancing ice sheet profile	SKBdoc 1278733
Reference retreating ice sheet profile	SKBdoc 1278735
Reference ice sheet surface gradients	SKBdoc 1278734

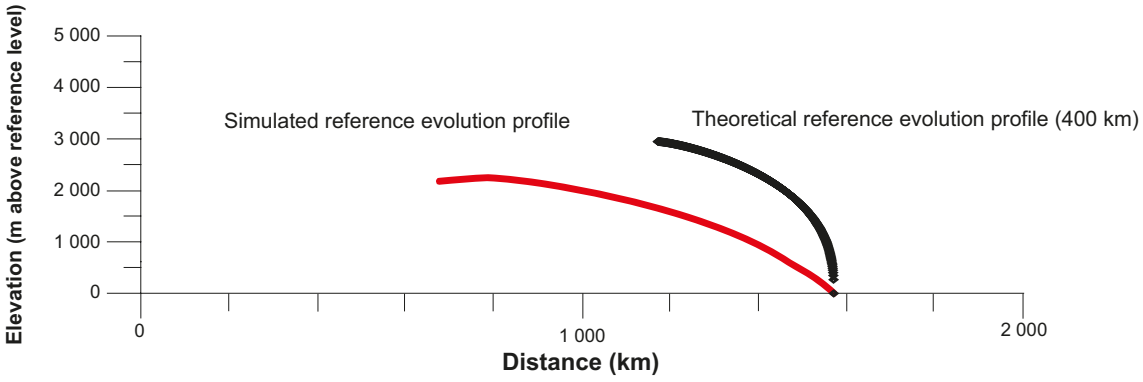

Figure 7-4. *The theoretical reference evolution ice sheet profile data (black) and the simulated last glacial cycle ice sheet profile from the deglaciation (red). For descriptions of the profiles, see the Climate report, Appendix 2. Modified from Figure B-7 of the Climate report.*

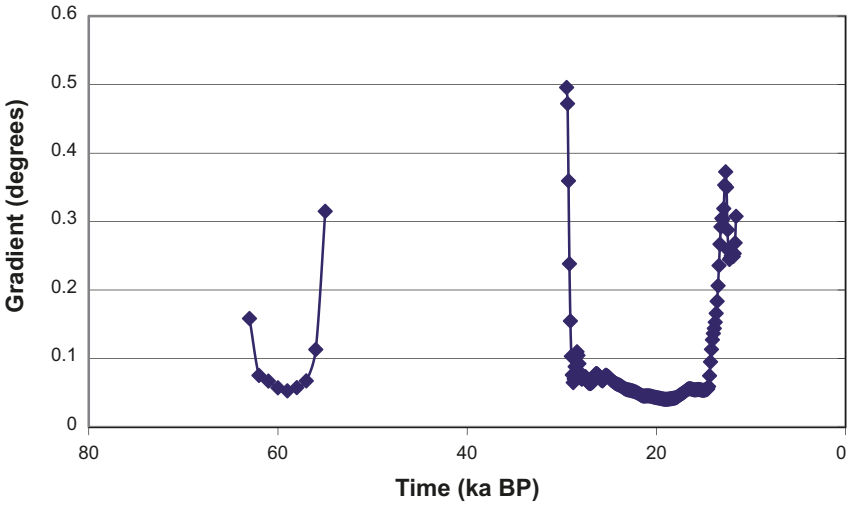

Figure 7-5. *The ice surface-gradient data calculated from ice thickness data from the reconstruction of the Weichselian ice sheet. Reproduced from Figure B-5 of the Climate report.*

Relative sea level changes

The field of future sea level rise is rapidly developing. New data on relative sea level have since SR-Site been obtained for the Global warming and Extended global warming climate cases. The data have been obtained both from recent scientific literature (compiled and analysed in Climate report Sections 5.1 (Global warming climate case) and 5.2 (Extended global warming climate case), as well as from a dedicated sea level study performed for the Forsmark site (Pellikka et al. 2020). The latter study includes the local relative sea level rise at the Forsmark site as well as the additional temporary rise during severe storms (storm surge). Probability distributions were calculated for the two individual contributions, as well as for the combined total sea level rise during storms. In addition, the probability distributions were calculated for 2050, 2080 and 2100 AD, as well as for three different global warming (carbon emission) scenarios. These scenarios included the IPCC RCP4.5 medium emission scenario, on which the Global waming climate case is based, and the IPCC RCP8.5 high emission scenario, on which the Extended global waming climate case is based. In this way, a thorough treatment of the very large uncertainties associated with future sea level rise up to 2100 AD was obtained.

Data on relative sea level changes for the PSAR Reference glacial cycle, Global warming- and Extended Global warming climate cases are illustrated in Figure 7-6. The data are based on Global Isostatic Model simulations, extrapolations of up-to-present Holocene isostatic uplift rates at the Forsmark site, and peer-review published data on future sea level rise given different degrees of global warming (see details in the **Climate report,** Sections 4.5 and 5.1). The figure shows relative sea level changes from the time of the Weichselian deglaciation of Forsmark (at 8 800 BC), through the present time, and into the future. Given the existing large uncertainty in future climate development and sea level rise, the future projections of relative sea level for the Global warming and Extended global warming climate cases both contain a low-end and high-end variant. For detals on this, see the **Climate report**, Sections 5.1 and 5.2.

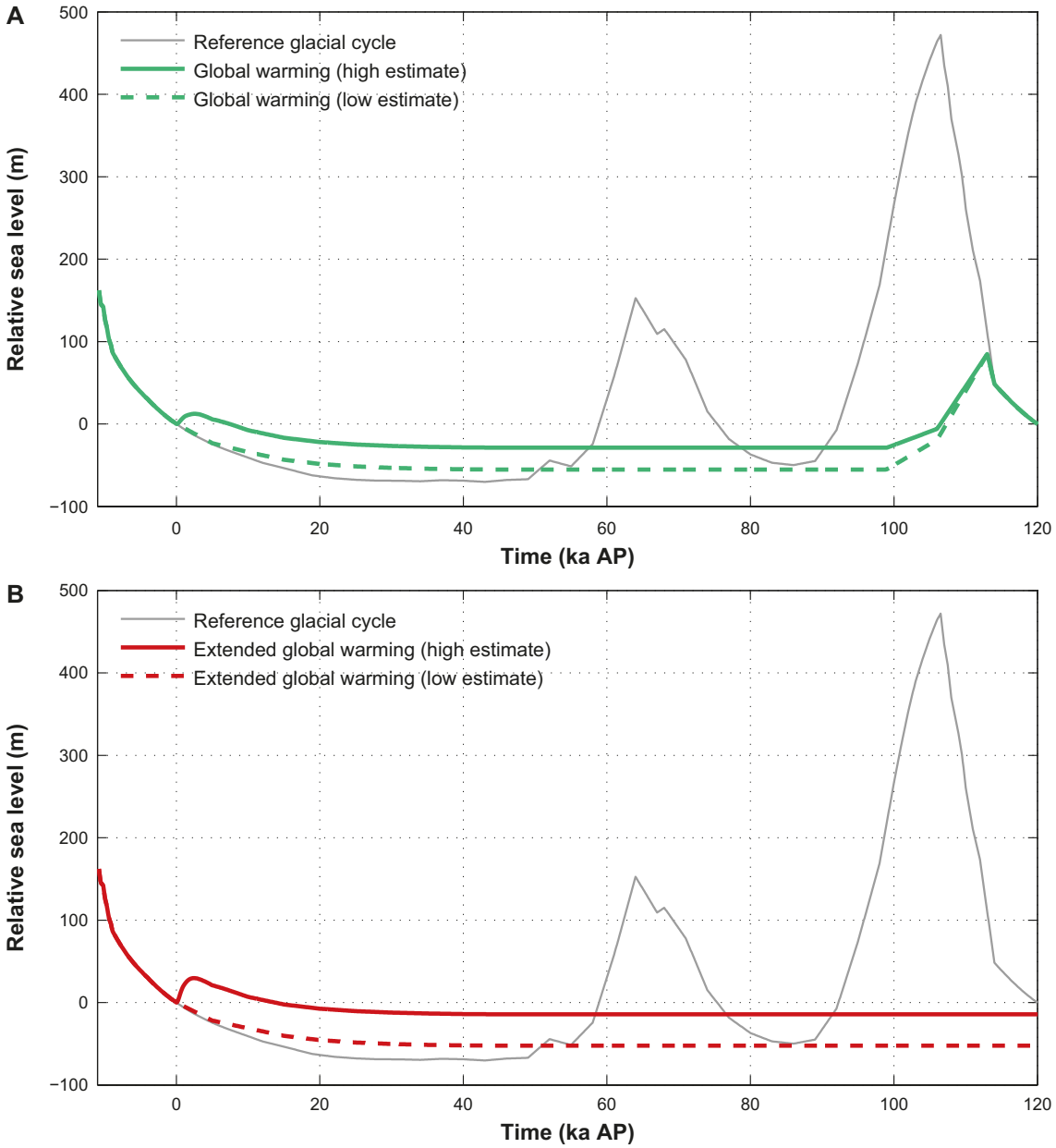

Figure 7-6. *A) Relative sea level changes for the Reference glacial cycle (grey) and the Global warming climate case (green solid and dashed lines). B) Relative sea level changes for the Reference glacial cycle (grey) and the Extended global warming climate case (red solid and dashed lines). Both the Global warming and Extended global warming climate cases include a high-end and low-end projection of potential future change in relative sea level at Forsmark (see the Climate report, Sections 5.1 and 5.2). Reproduced from Figures 5-6 and 5-25 of the Climate report.*

In the Reference glacial cycle, the Forsmark site is submerged by the Baltic Sea following the two periods of ice sheet coverage (cf Figure 7-3). In the Global warming and Extended global warming climate cases, the initial period could either be dominated by a transgression (described by the high-end projections) or by a continued sea regression similar to that of today (for the low-end projections). For the two high-end projections, the trnsgression is more pronounced (higher maximum relative sea level rise and longer period before the relative sea level has returned to present day level) for the Extended global warming climate case (Figure 7-7).

In the Global warming and Extended global warming climte cases, a complete collapse of the Greenland ice sheet is assumed in the GIA simulations. This causes a global mean sea level rise of 7 m. However, the gravitational effects associated with the mass re-distribution that follows from the ice sheet collapse results in a zero net effect in relative sea level change in the Baltic region (see the **Climate report**, Section 5.1), and is therefore not seen in Figure 7-3. However, there are other uncertainties related to global warming, such as the actual amount of temperature increase, the associated response of the West Antarctic and East Antarctic ice sheet to this warming, and the resulting amount of themal expansion of ocean water. These uncertainties results in the high- and low-end projections in relative sea level for the Forsmark site in the Global warming and Extended global warming climate caases. However, after the initial phase with these large uncertainties, the results of the glacial isostatic adjustment modelling suggest that in the long run the Forsmark site will be situated above the Baltic sea level until the end of the 120 000 year period.

In the Global warming and Extended Global warming climate cases, shorter phases of high water stands during storm events are expected at the Forsmark site(cf the **Climate report**, Section 5.2), but these events are judged not to affect post-closure repository safety.

References to locations of numerical data on relative sea level changes for the Reference glacial cycle, Global warming, and Extended Global warming climate cases are given in Table 7-6.

Table 7-6. Sources for numerical data on changes in relative sea level.

Case	Document
Reference glacial cycle	SKBdoc 1939139
Global warming climate case	SKBdoc 1939139
Extended global warming climate case	SKBdoc 1939139

Permafrost depths

The reconstructed permafrost depth at Forsmark for the last glacial cycle is seen in Figure 7-8 (from 1-D modelling) and Figure 7-9 (from 2-D modelling). The deepest permafrost occurs prior to the first ice sheet advance over the site, at 70 000 years BP. The 2-D model in Figure 7-9 only shows the time period up to 70 000 BP, when the Weichselian ice sheet starts to cover the site. As can be seen, the results of the two models agree.

The uncertainty of the timing and duration of future permafrost periods at Forsmark is handled in complementary cases with longer and shorter periods of permafrost coverage than in the reconstructed last glacial cycle (**Climate report**, Sections 5.1, 5.2 and 5.5).

In order to study a case with maximum deep permafrost during a glacial cycle, related to the presence or absence of an ice sheet over the site and other associated changes, a Severe permafrost climate case was investigated (see the **Climate report**, Section 5.5 and Hartikainen et al. 2010).

An assumption of a cold periglacial climate is here combined with an assumption of a very dry climate, without the presence of an ice sheet, vegetation, winter snow cover, and post-glacial submerged conditions, in order to favour permafrost growth. The resulting evolutions of maximum permafrost depth, maximum depth of perennially frozen ground, and maximum depth of the −2 and –4 °C isotherms over the repository are seen in Figure 7-9.

The underlying data in Figure 7-7 and Figure 7-8 are repeated for the coming 120 000 years to construct the Reference glacial cycle for the PSAR. In this process, the time of 120 000 years BP is set as present-day. Furthermore, for the Severe permafrost climate case, the data underlying the results shown in Figure 7-9 should be used. References to the locations of the underlying numerical data are given in Table 7-8.

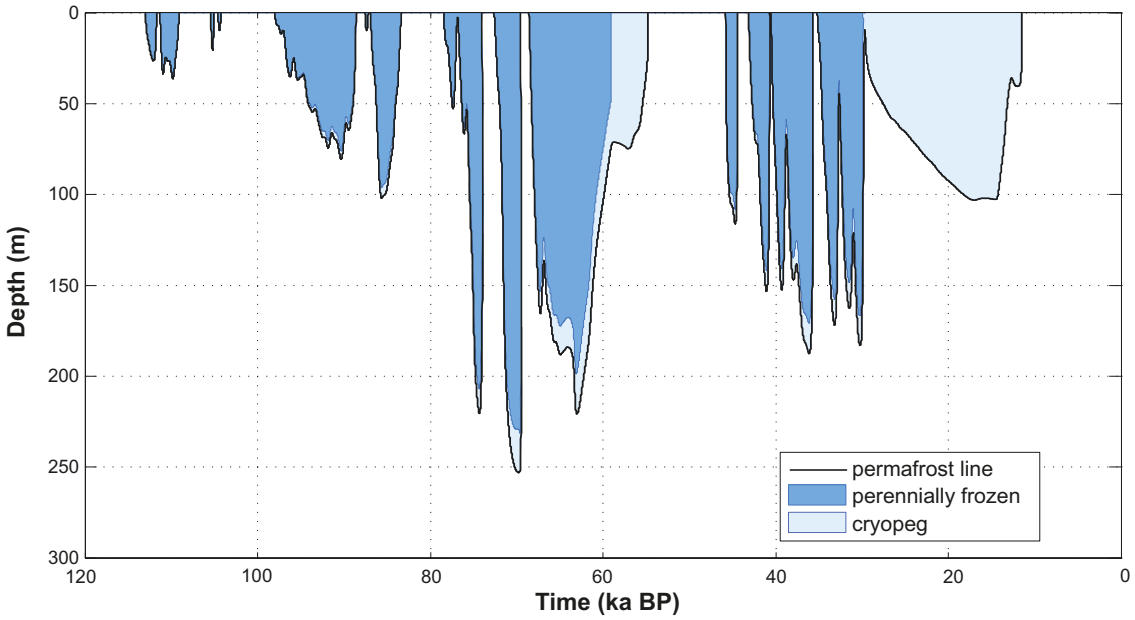

Figure 7-7. *Reconstructed evolution of permafrost and perennially frozen ground at the location of the planned spent nuclear fuel repository for the last glacial cycle for. The results were obtained by a 1-D permafrost model (Climate report, Section 3.4). The permafrost depth is defined by the 0 °C isotherm, whereas the cryopeg comprises unfrozen parts of the permafrost, with negative temperatures, due to e.g. high pressure under glacial conditions. Reproduced from Figure 3-45 of the Climate report.*

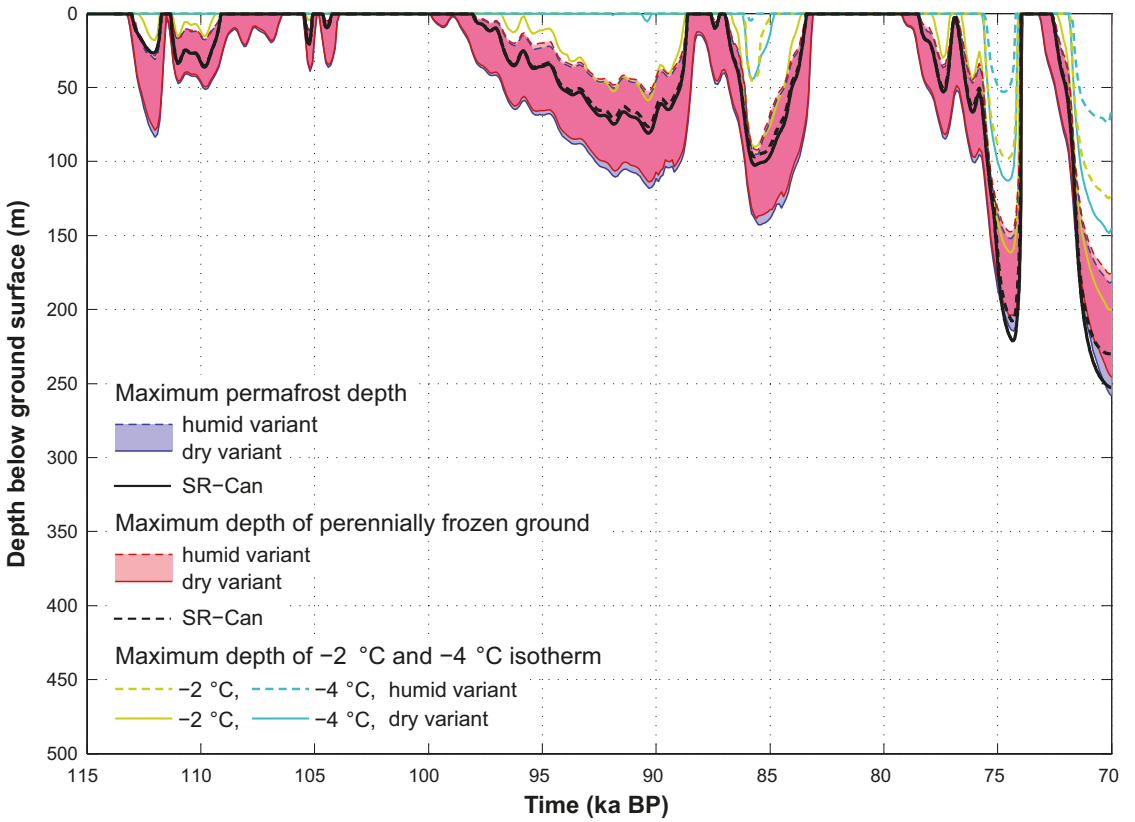

Figure 7-8. *Evolution of permafrost depth, depth of perennially frozen ground and depths of the −2 and –4 °C isotherms over the repository for last glacial cycle climate conditions. The results were obtained by a 2-D permafrost model. The shaded areas in blue and red represent the range when considering dry and humid climate variants (see the Climate report, Section 3.4). The lilac colour indicates that the results for permafrost and perennially frozen ground overlap. Modified from Figures 3-59 and 4-29 of the Climate report.*

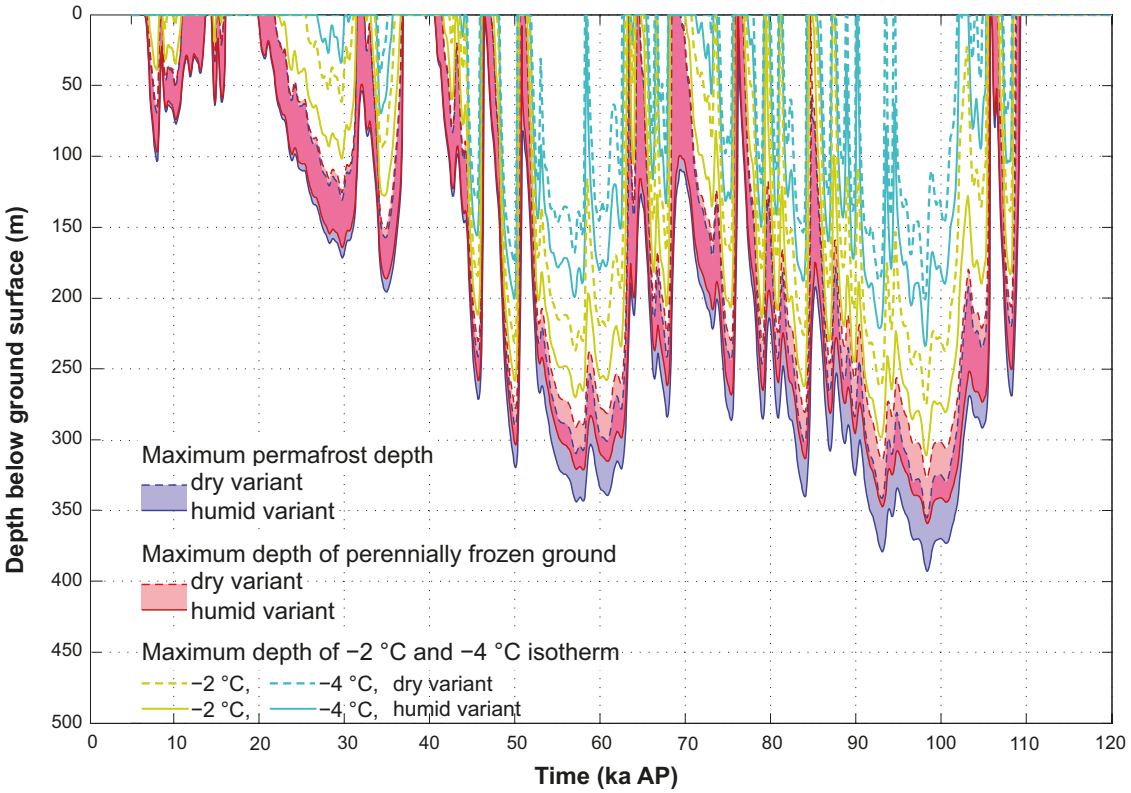

Figure 7-9. *Evolution of maximum permafrost depth, maximum depth of perennially frozen ground and maximum depth of −2 and –4 °C isotherms at the repository location for the Severe permafrost climate case. For a description of the assumations made for producing a case with maximum deep permafrost, see the Climate report, Section 5.5. The shaded areas in blue and red represent the range when considering the dry and humid climate variants of the Severe permafrost case. The darker lilac colour indicates that the results for permafrost and perennially frozen ground overlap. Reproduced from Figure 5-40 of the Climate report.*

The maximum depths of different isotherms and perennially frozen ground for the two climate cases are given in Table 7-7. In the table, the uncertainty range is given based on the sensitivity analyses listed in Table 7-10. The uncertainty intervals are based on the most pessimistic combination of uncertainties relevant for each case. Several of the combinations are considered quite unrealistic, see the **Climate report** Sections 3.4.4. and 5.5. In this context it should also be noted that the range of relevant sensitivity studies are not the same for the Reference glacial cycle and the Severe permafrost case, which is why the uncertainty interval reaches deeper in the Reference glacial cycle than in the Severe permafrost case, see the **Climate report**, Section 5.5.

Table 7-7. Maximum depths of permafrost (0 °C isotherm), perennially frozen ground, and −2 °C and −4 °C isotherms for the Reference glacial cycle and the Severe permafrost climate case. The uncertainty intervals, resulting from the sensitivity experiments in Table 7-10, are discussed in the text.

Case	Maximum permafrost depth (0 °C isotherm) [uncertainty interval]	Maximum depth perennially frozen ground [uncertainty interval]	Maximum depth −2 °C isotherm [uncertainty interval]	Maximum depth −4 °C isotherm [uncertainty interval]
Reference glacial cycle	259 m [down to 463 m]	246 m [down to 422 m]	200 m [down to 388 m]	148 m [down to 316 m]
Severe permafrost case	393 [down to 456]	359 [down to 408]	311 [down to 359]	234 [down to 268]

Table 7-8. Sensitivity analyses made within the permafrost simulations.

Sensitivity experiment	Reference
Constant surface temperatures between –2 and –20 °C	**Climate report**, Figure 3-41
Humid and dry climate variants	**Climate report**, Section 3.4 and 5.5: all simulations of last glacial cycle conditions and Severe permafrost case.
Last glacial cycle: uncertainty in geothermal heat flow	Hartikainen et al. 2010, Figure 5-41
Last glacial cycle: uncertainty in bedrock thermal conductivity	Hartikainen et al. 2010, Figure 5-42
Last glacial cycle: uncertainty in bedrock thermal diffusivity	Hartikainen et al. 2010, Figure 5-43
Last glacial cycle: mixed thermal diffusivities with the highest difference for adjacent rock domains	Hartikainen et al. 2010, Figure 5-44
Last glacial cycle: combination of uncertainties in bedrock thermal properties and geothermal heat flow	**Climate report**, Figure 3-74 Hartikainen et al. 2010, Figure 5-45
Last glacial cycle: combination of uncertainties in surface and bedrock thermal properties	**Climate report**, Figure 3-75 Hartikainen et al. 2010, Figure 5-46
Last glacial cycle: combination of uncertainties in air temperature, surface conditions and bedrock thermal properties	**Climate report**, Figure 3-76 Hartikainen et al. 2010, Figure 5-48
Last glacial cycle: influence of heat from the repository	**Climate report**, Figure 3-77 Hartikainen et al. 2010, Figure 5-49
Last glacial cycle: convective heat transfer and salinity transfer by groundwater flow	**Climate report**, Figure 3-78 Hartikainen et al. 2010, Figure 5-50
Shifting of the entire air temperature curve reconstructed for the last glacial cycle by +6, 0, –4, –6, –8, –10, –12, –14 and –16 °C	**Climate report**, Figures 3-68, 3-70, 3-71, 3-72, 3-73 Hartikainen et al. 2010, Figure 4-1, 5-37, 5-38, 5-39, 5-40
Shifting of the entire air temperature curve reconstructed for the last glacial cycle by +6 and –6 °C combined with uncertainty in climate humidity.	**Climate report**, Figure 3-69 Hartikainen et al. 2010, Figure 5-36
Severe permafrost case: combination of uncertainties in surface and bedrock thermal properties	Hartikainen et al. 2010, Figure 5-47

Based on a complementation request by SSM, theoretical permafrost and freezing depths were calculated for a hypothetical case with a ten times higher glacial erosion (i.e. 20 m of erosion per glacial cycle) than that used in SR-Site (2 m per glacial cycle), see the **Climate report**, Section 5.5.4. In this hypothetical case, the surface denudation reduces the repository depth by 20 m for each future 120 ka long glacial/interglacial cycle, resulting in that permafrost, groundwater freezing, and the isotherm for freezing of backfill and buffer reach closer to the repository over time. Towards the end of the 1 Ma analysis period, the permafrost would, in this hypothetical case, penetrate c 140 m deeper than during the first glacial cycle. However, based on new studies on past and future bedrock denudation at the Forsmark site, this hypothetical case is judged as unrealistic, see the following section (Bedrock denudation over the coming 100 000 and 1 million years).

Bedrock denudation over the past and coming 100 000 and 1 million years

A dedicated study on past and future denudation, including glacial erosion, of the basement rock surface at Forsmark has been performed since SR-Site, using a detailed multi-methodological approach that included geomorphological analyses and cosmogenic nuclide analyses (Hall et al. 2019). The results from the nuclide analyses yield typical total denudation depths (25 % and 75 % percentiles), including glacial erosion, of the basement bedrock surface at Forsmark and neighbouring areas in the Uppland county of 1.6 to 3.5 m for the last glacial cycle (last ~ 100 000 years) and 13–27 m for the last one million years. The total denudation ranges (0 and 100 % percentiles) over the same periods are 0–8.6 and 2–61 m respectively. In addition, the depth of total denudation of basement rock, including glacial erosion, over the coming 100 000 years is preliminarily estimated to less than 1 m. Over the coming one million years, a mid-range (25 % and 75 % percentiles) of total denudation depths is preliminarily estimated to 5–28 m, whereas the corresponding full range (5 and 95 % percentiles) is 2–43 m. The individual ranges obtained mainly reflect a large (expected) variability in denudation between the cosmogenic sample locations. Given the above results on estimated denudation over the coming 1 million years, it is for the PSAR recommended to use a maximum value on bedrock denudation at the Forsmark site of 50 m for this time period.

The typical last glacial cycle denudation rates from the nuclide analyses, 1.6 to 3.5 m (Hall et al. 2019, Chapter 5) are in line with the denudation results of the bedrock geomorphological analysis in Hall et al. (2019, Chapter 4) which typically suggested ~2 m of bedrock denudation per glacial cycle. It was also concluded that in basins and trenches, erosion rates may exceed 3 m per glacial cycle. These typical denudation rates for the Forsmark site show that assuming 20 m of glacial erosion per glacial cycle everywhere over the site, as done in the hypothetical case on permafrost and freezing depths in the section above, is unrealistic (see also the **Climate report**, Sections 3.5, 5.1.6, 5.5.4 and Appendix G). Furthermore, the results from the cosmogenic nuclide analyses and the geomorphological studies show that the denudation/erosion rates used in SR-Site (2 m per glacial cycle) were reasonable.

7.1.11 Judgement by the assessment team

Air and ground-surface temperatures in the Forsmark region for the past 120 000 years

Based on the new information obtained since SR-Site, which broadly conforms to the SR-Site air temperature reconstruction, the judgement is to use the same data as in SR-Site.

Ice sheet thickness and ice surface gradients over Forsmark for the past 120 000 years

Since no new information or data has been obtained on ice thicknesses for the Reference glacial cycle, the judgement is to use the same data as in SR-Site.

Maximum ice sheet thickness over Forsmark

Based on the new data on maximum ice sheet thickness of the largest Quaternary ice sheet over Fennoscandia and Forsmark (including its uncertainty analysis) presented since SR-Site (Colleoni et al. 2014, Quiquet et al. 2016, and the **Climate report**, Section 5.4), the judgement is to use these data in the PSAR.

Relative sea level changes at Forsmark for the Reference glacial cycle

Since no new information or data has been obtained, the judgement is to use the same data as in SR-Site in the PSAR.

Relative sea level changes at Forsmark for the Global warming and Extended global warming climate cases

Based on the new data and information on relative sea level that has been obtained since SR-Site for the *Global warming* and *Extended global warming climate cases* (including their uncertainties) (**Climate report**, Sections 5.1 and 5.2), the judgement is to use these new data in the PSAR.

Permafrost and ground-freezing depths at Forsmark for the past 120 000 years

The hypothetical values on permafrost and freezing depths calculated for the SSM complementation were based on a 10 times higher glacial erosion rate than used in SR-Site. Subsequent studies on past and future bedrock denudation at the Forsmak site showed that this assumption of 20 m of glacial erosion per glacial cycle everywhere over the Forsmark site is unrealistic, and furthermore that the glacial erosion values used in SR-Site (2 m per glacial cycle) were reasonable. The judgement is therefore that the freezing depths used in SR-Site are still adequate to use in the PSAR. In this context, it is also worth noting that the SR-Site freezing criteria for the buffer clay (−4 °C) and backfill material (−2 °C) have been changed. In the PSAR, the temperature for which a frozen buffer clay and backfill material may start having detrimental effects on the canister and surrounding host rock has been changed to −6 °C for both materials. This gives an even larger margin to detrimental freezing temperatures than in SR-Site.

Based on the above, and that no new data has been obtained since SR-Site, the judgement is to use the same data as in SR-Site in the PSAR.

Bedrock denudation over the coming 100 000 and 1 million yearsfrost

New data on potential future denudation of bedrock at the Forsmark site has been obtained since SR-Site. The judgement is to use these new data in the PSAR.

7.1.12 Data recommended for use in assessment

In the following, insights and data that have been updated since SR-Site are described.

Air- and ground-surface temperatures in the Forsmark region for the past 120 000 years

New insights have been obtained on the air temperature from independent terrestrial records in Northern Europe, especially during the early (115 000 – 74 000 years ago) and the middle phases (59 000 – 24 000 years ago) of the last glacial cycle (Helmens 2013, 2019), as well as during the deglaciation phase of the Fennoscandian ice sheet from ~ 20 000 to ~ 11 000 years ago (Schenk and Wohlfarth 2019). These new air temperature reconstructions are broadly within the uncertainty range of the air temperature curve for the last 120 000 years used in the PSAR.

Ice thickness and ice surface gradients over Forsmark for the past 120 000 years

New insights and data have been obtained since SR-Site on the maximum possible ice sheet thicknesses over Fennoscandia and Forsmark, based on dedicated simulations of the largest Quaternary ice sheet (during the Saalian glaciation) over Fennoscandia and Fennoscandia. Steady-state ice sheet simulations of the peak Saalian ice sheet at 140 000 ka BP were performed. In addition, a full range of univariate and multi-variate sensitivity analyses of all parameters affecting the simulated ice thicknesses were performed (see Colleoni et al. 2014 and Quiquet et al. 2016). In this way, a thorough treatment of the uncertainties associated with the simulation the peak Saalian ice sheet was obtained. An analysis of the results, methodology and assumptions made in the ice sheet modelling study resulted in a maximum ice sheet thickness of 4 000 m over Forsmark, see the **Climate report**, Section 5.4.5 and Table 7-9.

Table 7-9. Ice thickness and associated hydrostatic pressure contribution over Forsmark based on the reference glacial cycle and the maximum ice-sheet thickness case in the PSAR.

	Ice thickness	Hydrostatic pressure
Reference glacial cycle	2 900 m	26 MPa
Maximum ice-sheet thickness	4 000 m	36 MPa

Relative sea level changes at Forsmark for the Global warming and Extended global warming climate cases

New data on relative sea level have been obtained for the *Global warming* and *Extended global warming climate cases*. The data have been obtained both from recent scientific literature (compiled and analysed in the **Climate report**, Sections 5.1.3 (*Global warming climate case*) and 5.2.3 (*Extended global warming climate case*) as well as from a dedicated study performed for Forsmark (TR-19-23). The latter study includes the local relative sea level rise at the Forsmark site as well as the additional temporary rise during severe storms (storm surge). Probability distributions were calculated for the two individual contributions as well as for the combined total sea level rise during storms. In addition, the probability distributions were calculated for 2050, 2080 and 2100 AD, as well as for three different global warming (carbon emission) scenarios. These scenarios included the IPCC RCP4.5 medium emission scenario, on which the *Global waming climate case* is based, and the IPCC RCP8.5 high emission scenario, on which the *Extended global waming climate case* is based. In this way, a thorough treatment of the very large uncertainties associated with future sea level rise up to 2100 AD was obtained.

Permafrost and ground-freezing depths at Forsmark for the past 120 000 years

Based on a complementation request by SSM, theoretical permafrost and freezing depths were calculated for a hypothetical case with a ten times higher glacial erosion (i.e. 20 m of erosion per glacial cycle) than that used in SR-Site (2 m per glacial cycle), see the **Climate report**, Section 5.5.4. In this hypothetical case, the surface denudation reduces the repository depth by 20 m for each future glacial cycle, resulting in that permafrost, groundwater freezing, and the isotherm for freezing of backfill and buffer reach closer to the repository over time. Towards the end of the 1 Ma analysis period, the permafrost would, in this hypothetical case, penetrate c 140 m deeper than during the first glacial cycle. However, regarding the realism of this hypothetical denudation case, see the next section.

Bedrock denudation over the coming 100 000 and 1 million years

A dedicated study on past and future denudation (including glacial erosion) of the basement rock surface at Forsmark has been performed since SR-Site, using a detailed multi-methodological approach including geomorphological analyses and cosmogenic nuclide analysis (Hall et al. 2019). The results from the nuclide analysis yielded typical total denudation depths (25 % and 75 % percentiles), including glacial erosion, of the basement bedrock surface at Forsamark and neighbouring areas in the Uppland county of 1.6 to 3.5 m for the last glacial cycle (last ~ 100 000 years) and 13–27 m for the last one million years. The total denudation range (0 and 100 % percentiles) over the same periods are 0–8.6 and 2–61 m respectively. In addition, the depth of total denudation, including glacial erosion, of basement rock over the coming 100 000 years was preliminarily estimated to less than 1 m. Over the coming one million years, a mid-range (25 % and 75 % percentiles) of total denudation depths was preliminarily estimated to 5–28 m, whereas the corresponding full range (5 and 95 % percentiles) were 2–43 m. Given the above results on estimated denudation over the coming 1 million years, it is recommended to use a maximum value on bedrock denudation at the Forsmark site of 50 m for this time period.

The typical glacial cycle denudation rates from the nuclide analysis of 1.6 to 3.5 m for the last glacial cycle were in line with the results of the bedrock geomorphological analysis in Hall et al. (2019) which typically suggested ~ 2 m of bedrock denudation per glacial cycle (while it was concluded that in basins and trenches, erosion rates may exceed 3 m per glacial cycle). These typical denudation rates for the Forsmark site show that the assumption of 20 m of glacial erosion per glacial cycle everywhere over the site, as assumed in the theoretical case on permafrost and freezing depths above, is unrealistic. These results also show that the denudation/erosion values used in SR-Site (2 m per glacial cycle) were reasonable.

7.2 Landscape dose conversion factors

In the PSAR, doses to humans are assessed for a number of scenarios by either multiplying radionuclide activity release rates, or pulse activity releases, to the biosphere by pre-calculated radionuclide-specific landscape dose conversion factors (*LDF*s). The chain of models used to calculate the releases, as well as the application of the *LDF*s in the dose calculations, are described in detail in the **Radionuclide transport report**.

Two different types of landscape dose conversion factors (*LDF*) are discussed in this section. The first is simply denoted *LDF* (or sometimes *basic LDF*), which is applicable to long-term continuous releases. The second is modified landscape dose conversion factors for pulse releases, denoted *LDF pulse* in this report, which are applicable to releases of radionuclides that reach the biosphere during relatively short time periods (years to hundreds of years).

The data set used in the PSAR has not been updated since SR-Site, except for an additional *LDF*-value for Rn-222. Part of the data qualification (Sections 7.2.3 to 7.2.9) has been reproduced from SR-Site.

7.2.1 Modelling

Defining the data requested from the supplier

The *LDF* for each potentially released radionuclide is defined as the mean annual effective dose to a representative individual of the most exposed group, resulting from a constant activity release rate to the biosphere of 1 Bq/year of this radionuclide. The *LDF pulse,* used for pulse activity releases of specific radionuclides, is defined as the mean annual effective dose to a representative individual of the most exposed group, resulting from a one-year pulse release of 1 Bq to the biosphere. For both factors, the exposure is averaged over the lifetime of an individual (taken to be 50 years), and the maximum *LDF* for each radionuclide over all potential discharge areas (biosphere objects) and over time was used. For more details about the *LDF* concept, see the SR-Site **Biosphere synthesis report** and Avila et al. (2010).

The *LDF*s are provided for the below listed radionuclides of the selected inventory, as described in Section 2.2.1. The inclusion and exclusion criteria are described and justified in the SR-Site Radionuclide transport report (SKB 2010c):

- Ac-227, Ag-108m, Am-241, Am-243, C-14, Ca-41, Cl-36, Cm-244, Cm-245, Cm-246, Cs-135, Cs-137, Ho-166m, I-129, Nb-94, Ni-59, Ni-63, Np-237, Pa-231, Pb-210, Pd-107, Po-210, Pu-239, Pu-240, Pu-242, Ra-226, Rn-222[20], Se-79, Sm-151, Sn-126, Sr-90, Tc-99, Th-229, Th-230, Th-232, U-233, U-234, U-235, U-236, U-238, and Zr-93.

The *LDF pulse* are provided only for radionuclides which may be released as a pulse and which are not obviously insignificant for the assessment:

- Ag-108m, Cl-36, Cs-135, I-129, Nb-94, Ni-59, Se-79, Sn-126, and Tc-99.

Radionuclide decay of single radionuclides and in selected decay chains was considered in the SR-Site *LDF* calculations. The decay chains included in the assessment are listed in the SR-Site **Biosphere synthesis report**.

For each radionuclide, (basic) *LDF* and the *LDF pulse* values were pessimistically chosen to be constant at the maximum value calculated for the entire climate domain and for all biosphere objects considered in the biosphere modelling.

7.2.2 Experience from SR-Site

Modelling in SR-Site

The endpoints of the biosphere modelling, the *LDFs*, are built upon a number of underlying data and modelling results associated with different degrees of simplifications, uncertainties and degree of caution. Large amounts of site-specific information have been collected in order to better understand transport and accumulation of elements in the biosphere at the site. This understanding underpins the conceptual and numerical models. Moreover, site data has, as far as possible, been used to parameterise the radionuclide model which is used to calculate environmental concentrations and subsequent human exposure. Uncertainties enter all aspects of the data collection, interpretation, conceptual model formulation and mathematical implementation. Possible effects of different kind of uncertainties in underlying data and models on the *LDFs* are discussed in detail in Avila et al. (2010).

Conditions for which data were used in SR-Site

The *LDF*s are used for calculation of maximum annual effective doses to a representative individual of the most exposed group, resulting from long-term continuous releases of radionuclides to the biosphere. Through a chain of modelling activities within SR-Site, the activity that is assessed to be released to the biosphere for each radionuclide per year is calculated for different scenarios. This activity release rate is multiplied with the *LDF* to obtain a dose rate. In practice, the *LDF* values obtained for temperate climate conditions are used in the majority of the dose calculations, whereas *LDF*s for other climate conditions are used in a few sensitivity cases (see the SR-Site Radionuclide transport report (SKB 2010c) for details).

[20] The LDF for Rn-222 was estimated for exposure from drilled well-water, and is thus valid for conditions were such a well may exist (i.e. temperate and global warming conditions).

For a number of radionuclides, associated with the rapid release fraction discussed in Section 3.2, a short-term pulse release from a canister, that is almost instantaneous on safety assessment time scales is possible. Unless the radionuclides are considerably retarded in the engineered barrier and/or geosphere, short-term pulse releases to the biosphere may occur. In this case, the activity of the entire pulse for each radionuclide is multiplied by the radionuclide-specific *LDF pulse*. The *LDF pulse* is used for calculation of maximum annual effective doses to a representative individual of the most exposed group.

The following data were provided by the supplier and used in the analyses:

- Radionuclide-specific *LDF*s, in units of Sv/y per Bq/y, for temperate climate conditions, i.e. climate conditions similar to those of today.
- Radionuclide-specific *LDF*s (Sv/y per Bq/y) for periglacial climate conditions, which represent a colder climate than today with permafrost at the site.
- Radionuclide-specific *LDF*s (Sv/y per Bq/y) for glacial climate conditions, which represent a period when the considered area is covered by an ice sheet. *LDF*s calculated for postglacial submerged conditions, with temperate climate conditions, were used to represent glacial conditions in the present assessment.
- Radionuclide-specific *LDF*s (Sv/y per Bq/y) for the global warming climate case, representing a case with a prolonged period of temperate conditions and initially increased air temperatures.
- Radionuclide-specific values of the modified *LDF* for pulse releases, the *LDF pulse* (Sv/y per Bq). *LDF pulse* is provided for temperate climate conditions only.

Sensitivity to assessment results in SR-Site.

In Chapter 11 in the SR-Site **Biosphere synthesis report,** a systematic evaluation of the effects of uncertainties on the *LDFs* used in SR-Site demonstrated that the handling of system and model uncertainties was balanced. Site-representative values were used for model parameters, and their uncertainties were not handled in a cautious way, whereas the definition of the most exposed group was clearly cautious. However, the effect of quantified uncertainties was limited and is therefore not expected to have a significant effect on the assessment endpoint. Thus, it was concluded that the maximum LDFs used in SR-Site are robust estimates for the most exposed group, reflecting process understanding and the most precise description of the site available, and that the biosphere modelling performed in SR-Site is still valid for the PSAR assessment.

Alternative modelling in SR-Site

No alternative modelling was performed.

Correlations used in SR-Site modelling

The same correlations that were used in SR-Site is used in the PSAR assessment.

Identified limitations of the data used in SR-Site modelling

In the SR-Site biosphere work it was recognised that there is a potential to reduce uncertainties, in particular with respect to processes describing the partitioning of radionuclides between the solid and liquid phases (i.e. Kd) and biological uptake (i.e. CR). Thus, if the final risk estimates in future safety assessments are close to the regulatory limits, it would be reasonable to try to reduce the uncertainty associated with these processes, at least for dose contributing radionuclides. Accordingly, collection of additional data on Kd and CR for important radionuclides has been initiated in order to reduce parameter uncertainties in the coming SAR safety assessment.

7.2.3 Supplier input on the use of data (text reproduced from SR-Site Data report)

LDF values have been delivered by the SR-Site biosphere modelling team to the SR-Site main project, where the dose assessments are performed. Thus, the SR-Site biosphere modelling team is recognised as the supplier and the SR-Site main project as the customer. Supplier inputs, partly based on the regulatory authorities' comments on SR-Can, were given at an early stage and have already been incorporated in SR-Site.

7.2.4 Sources of information and documentation of data qualification (text reproduced from SR-Site Data report)

The main sources of information on the SR-Site *LDF*s are Avila et al. (2010) and Chapter 10 in the **Biosphere synthesis report**, wherein *LDF* values for the Forsmark site are presented. The scrutinising of supporting data in lower-level references is part of the qualification process of the **Biosphere synthesis report** and Avila et al. (2010), and is not dealt with in this report. Full references to the main sources of information are given in Table 7-10.

Table 7-10. Main sources of information used in the data qualification.

Biosphere synthesis report, 2010. Biosphere assessment of SR-Site Forsmark – synthesis and summary of results. SKB TR-10-09, Svensk Kärnbränslehantering AB.
Avila R, Ekström P-A, Åstrand P-G, 2010. Landscape dose conversion factors used in the safety assessment SR-Site. SKB TR-10-06, Svensk Kärnbränslehantering AB.

Categorising data sets as qualified or supporting

The *LDF* and *LDF pulse* delivery for each radionuclide and climate domain consists of the maximum value for all times and biosphere objects. These maximum values are reported as described in Table 7-12. In a broad sense, the data supporting the *LDF* calculations include a large amount of data from the site investigation, site description, and safety assessment modelling. These supporting data are discussed in Avila et al. (2010) and the **Biosphere synthesis report**, and their lower level references, and are not further discussed here.

The delivered maximum *LDF*s (item 1 in Table 7-12) are considered to be appropriate as the approach to derive the *LDF*s is consistent with recommendations from the ICRP (ICRP 2006) and with the SSMFS 2008:37 guidelines (SSM 2008). In this approach, the dose conversion factors obtained from the biosphere assessment are based on best estimates of input parameter values from deterministic simulations. In addition, probabilistic simulations have been used to quantify the impact of uncertainties on the model results.

The delivered maximum values of *LDF pulse* (item 2 in Table 7-12) are considered to be appropriate as they are derived using the model developed and tested as described above for the *LDF*s. No probabilistic uncertainty analysis specifically focusing on the pulse releases has been performed. However, such an analysis is not considered necessary for the pulse release cases, given their relatively lower importance in the safety assessment.

Table 7-11. Qualified and supporting data sets.

Qualified data sets	Supporting data sets
1. *LDF's* for each radionuclide for the different climate domains presented in Avila et al. (2010) and as illustrated in Figure 10-1 of the **Biosphere synthesis report**.	
2. *LDF pulse* for each radionuclide for the temperate climate domain presented in Avila et al. (2010) and Table 10-2 of the **Biosphere synthesis report**.	
1–2. Avila et al. (2010) and the **Biosphere synthesis report** are reports produced for the Forsmark site within the SR-Site project. The data have been produced in accordance with the present data qualification framework and the SKB quality assurance system.	

Excluded data previously considered as important

With reference to the methodological differences between SR-Can and SR-Site, and to the limitations of the SR-Can *LDF*s (cf Section 7.2.2), it should be noted that *LDF*s calculated for SR-Can should not be used in SR-Site.

7.2.5 Conditions for which data are supplied (text reproduced from SR-Site Data report)

Figure 7-10 shows the Forsmark site under present-day conditions (2000 AD) and the biosphere objects used in the SR-Site biosphere modelling. In total, ten biosphere objects, containing a discharge area during any period of the present interglacial, were identified. Five additional biosphere objects located downstream of the discharge areas were also identified. Finally, to represent discharge directly into a stream or a wetland without an initial lake stage, the basin of one of the original biosphere objects (object 121) was partitioned into three separate objects (denoted 121_1, 121_2 and 121_3).

In the biosphere transport and dose calculations, *LDF*s are calculated over time for each radionuclide and each biosphere object. The *LDF*s are only applicable to continuous, uniform long-term releases. If applied to scenarios where the system has not reached equilibrium, the calculated doses might be substantially overestimated. Therefore, modified conversion factors for pulse releases with durations of years to hundreds of years have also been calculated (*LDF pulse*). *LDF*s have been calculated for the three climate domains of the reference glacial cycle, and also for the global warming climate case. *LDF pulse* values have only been calculated for the temperate climate domain (see Avila et al. 2010 for details).

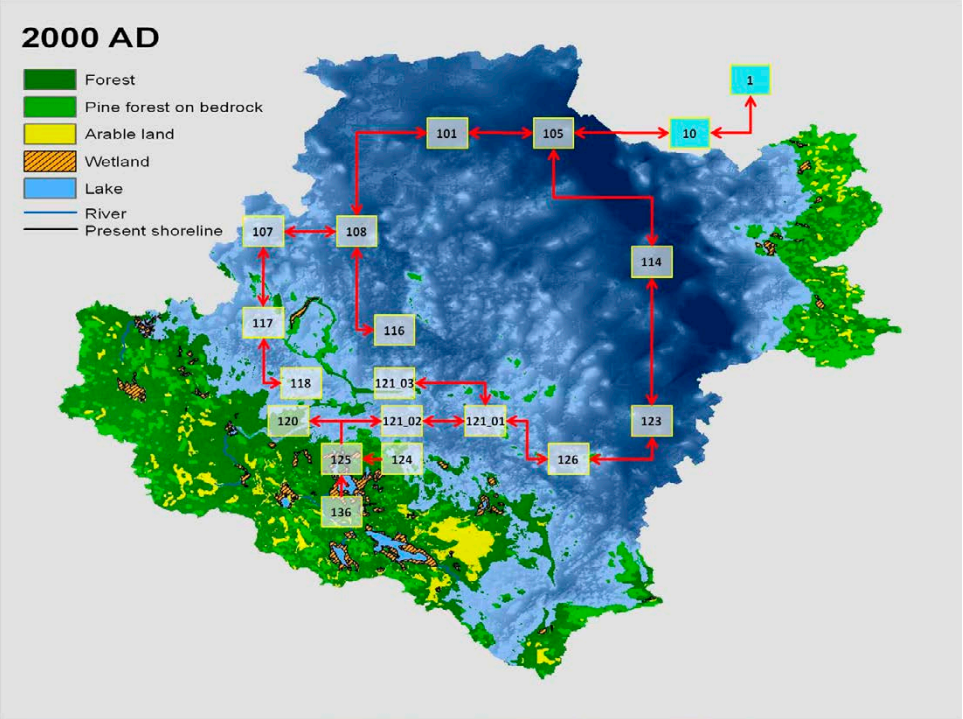

Figure 7-10. *The Forsmark site under present-day conditions (2000 AD) and biosphere objects used in the SR-Site biosphere modelling. Excerpt from Figure 7-11 of the Biosphere synthesis report.*

Temperate climate domain

The interglacial period, i.e. the period from the deglaciation to the onset of periglacial conditions (cf the **Climate report**), is represented by climate conditions similar to those of today and is, in accordance with the reference glacial cycle, assumed to prevail for 18 400 years (i.e. from –9000 to 9400 AD). As land has emerged sufficiently from the sea, wetlands are assumed to be converted to arable land. Drinking water for humans and livestock during the terrestrial stage of this period is assumed to be supplied by equal parts from surface water and from a contaminated well drilled into the bedrock (cf Chapter 8 in the **Biosphere synthesis report**). The calculation period starts at the time for the deglaciation around 9000 BC, when the landscape is covered by the sea (i.e. submerged conditions). The length of the submerged period differs between biosphere objects since it takes almost 10 000 years from the emergence of the first biosphere object from the sea, until the shoreline has passed over the whole model area.

The *LDF*s have been calculated over time for each of the biosphere objects shown in Figure 7-10. Important inputs to assess the succession of the objects are the shore-level changes and climate data provided in Section 7.1. Other conditions and inputs are described in Avila et al. (2010). An example of the variation of *LDF*s, during the successional development of biosphere object 121_03 through time, is shown in Figure 7-13 in Section 7.2.8.

The *LDF pulse* value for a particular radionuclide has been calculated for the biosphere object that had the highest *LDF* for a constant release of that nuclide. Three release times (–9000, 3500, and 9400 AD) and for two release durations (one year and 50 years) have been used in the modelling. It follows that the *LDF pulse* values are applicable only to release scenarios where the releases to the biosphere occur during short time periods (years or hundreds of years).

Periglacial climate domain

The temperate domain is followed by a period of periglacial conditions in the reference glacial cycle. During this period, the climate is colder than today, with episodes of deep permafrost. For the periglacial *LDF* calculation, periglacial conditions are modelled to prevail from the emergence of a biosphere object from the sea, until the onset of the next glaciation around 59 600 AD. When assessing the periglacial *LDF*s, the model disregards the fact that biosphere objects will emerge during temperate conditions and instead assumes that they emerge during periglacial conditions. During this period, it is assumed that agriculture is not possible, and drinking water from a contaminated deep drilled well is not accessible (cf Chapter 8 in the **Biosphere synthesis report**). The modelling approach for calculating *LDF*s for periglacial conditions is discussed in Avila et al. (2010), where also results of supporting simulations are reported.

Glacial climate domain

Exposure of humans under glacial conditions, when the site is covered by an ice sheet, is unlikely. Nevertheless, if releases occur, humans may be exposed to radionuclides through ingestion of sea food when the ice margin is situated above or close to the repository. As a cautious estimate of the exposure from releases during glacial conditions, the *LDF*s from the open sea stage during a temperate climate (i.e. submerged conditions) are used in the assessment. Thus, *LDF* values for submerged conditions are calculated in order to provide estimates of *LDF*s for glacial conditions.

Global warming climate case

In the SR-Site global warming climate case, it is assumed that the temperate climate domain is extended by approximately 50 000 years compared with the reference glacial cycle (i.e. the temperate climate domain prevails until 59 600 AD, see the SR-Site Climate report (SKB 2010g), Section 5.1). The assumptions made in the global warming climate case affect inputs to biosphere modelling in terms of shore-level changes, temperatures, etc (cf Section 7.1). Assumptions concerning human usage of the landscape during this period are the same as for the interglacial period, i.e. wetlands are converted to arable land when possible and drinking water for humans and livestock is supplied by equal parts from surface water and water from a contaminated well drilled into the rock.

7.2.6 Conceptual uncertainty (text reproduced from SR-Site Data report)

The sources of conceptual uncertainty that contribute to uncertainty in *LDF* estimates can be grouped as follows:

- Difficulties to make accurate predictions of the long-term development of the climate, the long-term future landscape configuration, and the future use of the biosphere by humans.
- Simplified mathematical representations of the conceptual models, e.g. discretisation of the lower regolith compartment. Such uncertainties have to be evaluated by the use of alternative approaches and simulation cases, or by discussing the potential implications of simplifying assumptions.

A comprehensive study of conceptual uncertainties affecting the derived *LDF* values has been carried out and is fully described in Avila et al. (2010) and summarised in the **Biosphere synthesis report**. Several cautious assumptions have been adopted in treating conceptual uncertainties.

7.2.7 Data uncertainty due to precision, bias, and representativity (text reproduced from SR-Site Data report)

The supplied *LDF*s are selected maximum values obtained from deterministic simulations, using best estimate values of a large number of supporting parameters as input data. Thus, the *LDF*s are deterministic values obtained from a model, and not measured values, which should be considered in a data uncertainty discussion. The model input parameters are derived using measured and/or modelled data, which are associated with uncertainties that may, or may not, be important for the assessment of the calculated *LDF*s. The overall data uncertainty of the *LDF*s, arising from uncertainties in the underlying input data, is discussed in the following.

Probabilistic analysis of data uncertainty

The supplied *LDF*s values are pessimistically chosen to be constant at the maximum value calculated for the entire climate domain and for all biosphere objects considered in the biosphere modelling. This approach should encompass most of the associated data uncertainty. To substantiate this, a probabilistic uncertainty analysis has been performed, where the impact of variations and uncertainties in underlying data has been examined. The analysis has been made for a number of radionuclides; for the individual biosphere object for which the maximum *LDF* of each radionuclide was obtained. This probabilistic analysis included several steps. First, the uncertainty associated with each parameter was characterised based on available site specific and generic data, as well as by elicitation of expert judgement. Second, probability distributions were assigned to each parameter used as inputs to the deterministic *LDF* model. Third, by a combination of Monte Carlo simulations and systematic studies of the variation of time-dependent parameters as a group (since these are strongly correlated), the uncertainty in the deterministically determined *LDF* could be estimated.

The *LDF* distributions resulting from the probabilistic analysis were shown to be approximately log-normally distributed, with a 90 % confidence interval typically spanning two orders of magnitude (cf Figure 7-11). The deterministic value is generally close to the median of the probabilistic distribution, and the *LDF*s used in the safety assessment thus reflect the central tendency, or the typical outcome, when parameter value uncertainties are considered.

It should be noted that the probabilistic analysis is not fully correlated, which enables combinations of input data that do not coexist exist in the reality. This may give rise to unrealistic extreme values manifesting in the large data ranges seen in Figure 7-11. Such extreme values should to a lesser extent affect the median value than the arithmetic mean. Accordingly, the deterministic value should be compared with the median value. For a few radionuclides, the probabilistic median value is significantly larger than the deterministic value (U-238 and Zr-93). However, by examining these nuclides it can be concluded that they have a very modest contribution to risk. Accordingly, this discrepancy should be of little consequence for the safety assessment. This is discussed in more detail in the **Biosphere synthesis report** and in Avila et al. (2010).

No similar probabilistic analysis has been performed for the *LDF pulse*. However, it should be noted that the *LDF pulse* is derived using the model developed and tested for the *LDF*s.

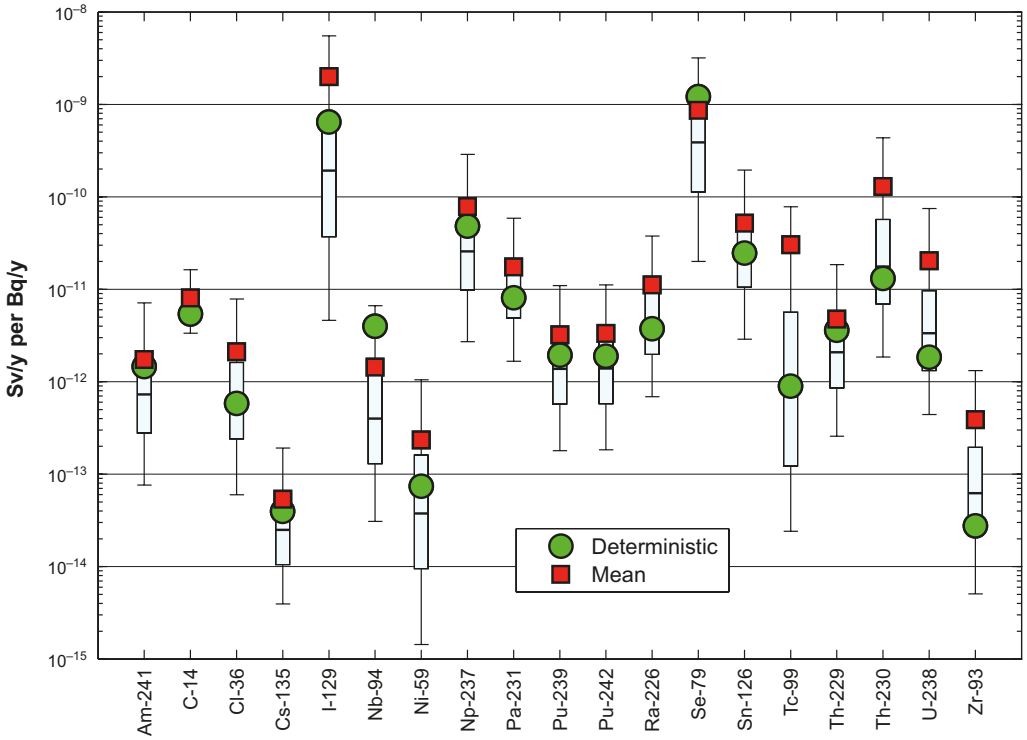

Figure 7-11. *Variation in interglacial LDFs obtained from probabilistic simulations for a subset of the analysed radionuclides. The LDF distributions are taken at the time when the median of the probabilistic output reached its peak. The mean (square) from the simulations are contrasted against the SR-Site LDF (circle). The box represents the 25th percentile, the median and the 75th percentile of the LDF distribution from the simulation, and whiskers represent the 90 percent confidence interval. Reproduced from Figure 12-6 of the Biosphere synthesis report.*

Data uncertainty due to bias

By adopting a methodology of choosing the maximum calculated *LDF* value for each radionuclide as representative for all biosphere objects and times within the climate domain, the creates a bias toward high values. In reality, the releases might be directed to several biosphere objects during a simulation period. Hence, doses obtained with the delivered *LDF* values can be considered as pessimistic estimates.

Data uncertainty due to representativity

For each parameter used in the derivation of *LDF* values, describing a property or flow component in the biosphere objects, a best estimate value has been derived from site and/or generic literature data. The parameter variation has been described by a probability density function (PDF), which has been also used for obtaining the best estimate values. In deriving PDFs for the parameters, as far as possible, only natural variations appropriate to a specific climate domain have been considered. However, for some parameters no site-specific data were available, or the data available were not sufficient to characterise the PDFs. In these cases, literature data, or a combination of literature and site data, have been used for obtaining the characteristics of the PDFs. This was the case for element-specific parameters (distribution coefficients and concentration ratios), for which PDFs were parameterised from a combination of site-specific and generic data using Bayesian methods (Nordén et al. 2010).

Biosphere objects develop in time, but for the purpose of the present assessments the properties within a biosphere object are assumed to be homogeneous and to represent yearly averages. Thus, the parameter values that are used in the simulations for derivation of *LDF* values should give representative descriptions of compartments and flows between compartments within a biosphere object, disregarding spatial variation within compartments and seasonal variations during a year.

LDF pulse was only studied for one biosphere object. Accordingly the representativity of *LDF pulse* is lower than of the *LDF*.

7.2.8 Spatial and temporal variability of data (text reproduced from SR-Site Data report)

The *LDF*s represent the highest values for each radionuclide over all biosphere objects during the whole simulation time period corresponding to different climate conditions. Hence, the delivered *LDF* for a specific climate domain or case is constant in time and space. However, the *LDF* values are derived on the basis of time-dependent doses per unit release rate, obtained from simulations for different biosphere objects with their different properties. These underlying data for different times and objects provide an indication of data uncertainties associated with spatial and temporal variations, and are therefore briefly discussed below. For a detailed description of the study of spatial and temporal variations in calculated *LDF*s, the reader is referred to Avila et al. (2010).

Uncertainty due to spatial variability

The calculated *LDF*s vary between the biosphere objects (cf Figure 7-12), but the degree of variation depends on radionuclide properties. For radionuclides where exposure from food is the dominant exposure pathway (i.e. C-14, Cl-36, I-129, Nb-94, Np-237, Se-79, Sn-126, and Tc-99), the *LDF*s typically vary by two or even three orders of magnitude between objects (excluding object 105). However, for radionuclides where drinking water is an important exposure pathway (e.g. Am-241, Pa-231, Pu-231, Pu-239, Pu-242, Ra-226, and Th-229) the variation between objects is typically below a factor of three. Note that the value at the limit of the upper error bar is used as the deterministically determined *LDF* (cf the green dots in Figure 7-11). Biosphere object 105, which is in the sea stage during the whole temperate period, has consistently lower *LDF*s for all radionuclides, by three orders of magnitude or more, and is therefore shown separately by green squares in Figure 7-12.

In the calculation of the *LDF pulse*, only one biosphere object (121_3) has been used, which is the object that generates the maximum *LDF* in the long-term release simulation. Consequently, the spatial variability of *LDF pulse* has not been evaluated.

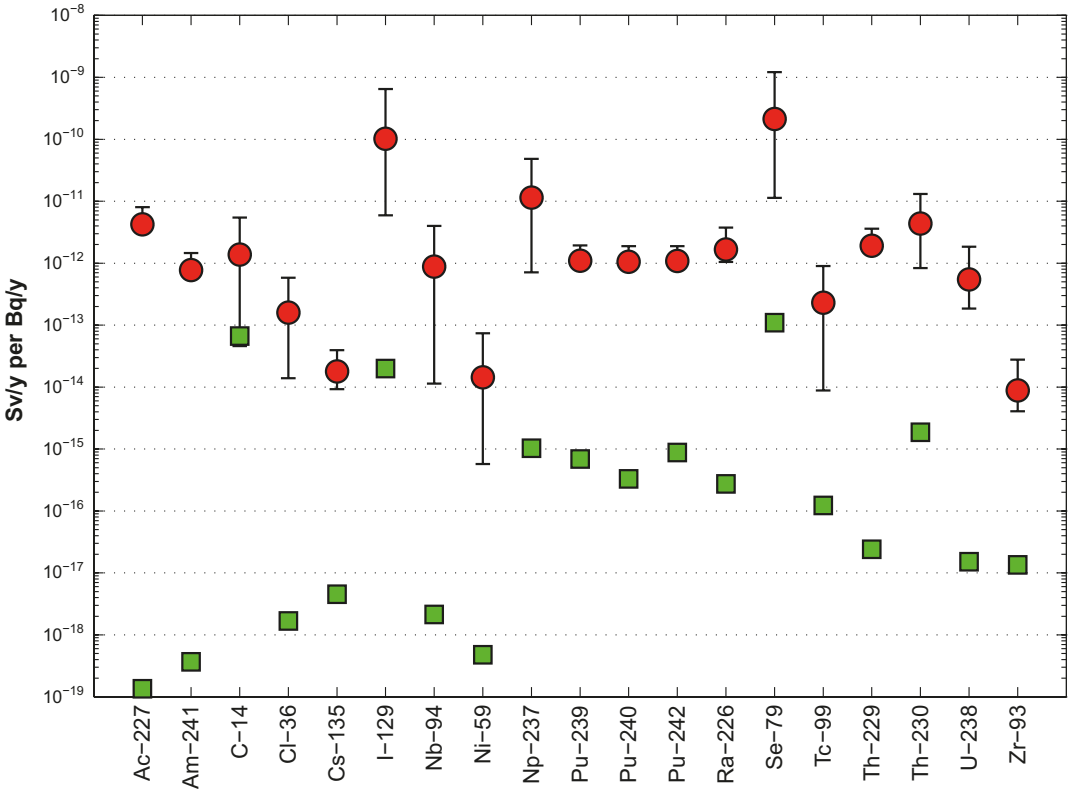

Figure 7-12. *Mean, minimum, and maximum values of LDF's for a selection of radionuclides across biosphere objects (excluding object 105) for temperate climate conditions. The LDF values for object 105 are shown separately (green squares). Reproduced from Figure 10-4 of the Biosphere synthesis report.*

Uncertainty due to temporal variability

The derivation of *LDF* values included finding, for each biosphere object, the maximum value of the time dependent annual dose per unit release rate (Sv/y per Bq/y) for each radionuclide in each climate domain or case considered. The time series for unit release rates were obtained from simulations with the radionuclide model for the biosphere and showed a similar pattern for all radionuclides. Examples of time series of dose rates per unit release rate are presented in Figure 7-13.

The effects of the shoreline regression and the subsequent succession of biosphere objects on *LDF*s are similar for many of the dose contributing radionuclides. During the sea stage (1), *LDF*s increase continuously with time, reflecting a gradually increasing activity concentration in the sea water. The *LDF*s increase further in the transition stage (2). In Figure 7-13 , the selected biosphere object develops directly into a wetland, and the increase in the *LDF* during the transition stage is a function of the gradual accumulation of the radionuclides in wetland peat.

In the terrestrial stage (3) the wetland is fully developed. A steep increase in *LDF*s early in this stage occurs when it is first possible to transform the wetland into arable land. From this point, further wetland accumulation only marginally affects the *LDF*s. For some radionuclides, accumulation results in a slight increase of *LDF*s (e.g. Ni-59), whereas for others (Se-79, I-129) wetland concentrations slightly decrease under long-term stable conditions. A more detailed description of the temporal variability of the *LDF*s, including explanations of the short-term transients displayed in Figure 7-13, is provided in the **Biosphere synthesis report**.

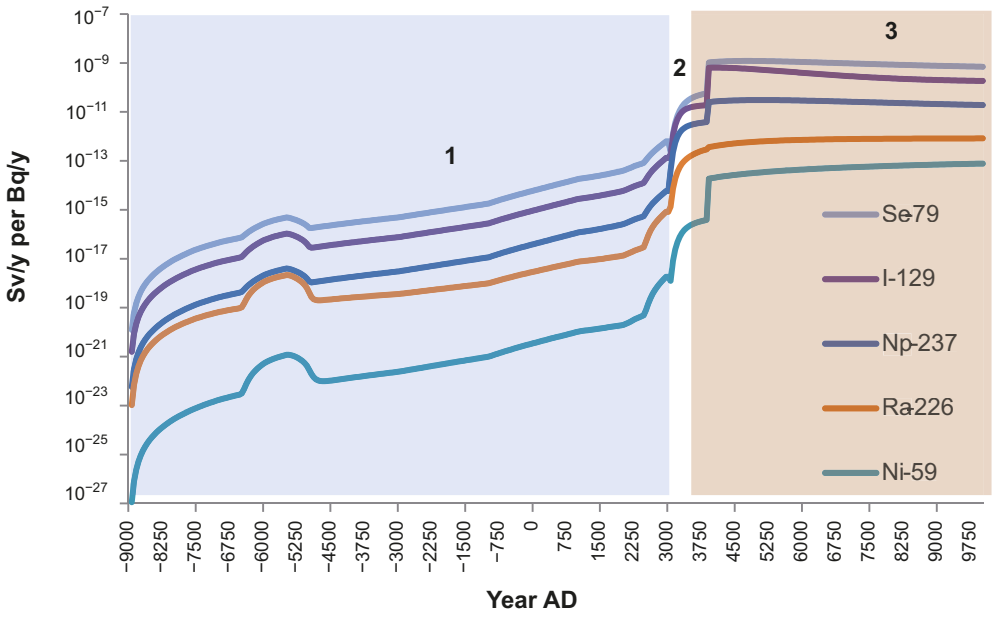

Figure 7-13. *The development of LDF's for a number of dose-contributing radionuclides during an inter-glacial for biosphere object 121_3. Se-79, I-129, Rs-226, and Ni-59 have their maximum LDF's from this biosphere object. The objects goes through three development stages: 1) the sea stage (blue), 2) the transitional stage (white), and 3) the terrestrial stage (brown). Note that object 121_3 does not go through a lake stage, but the sea bay develops directly into a wetland. Reproduced from Figure 10-3 of the Biosphere synthesis report.*

In the case of *LDF pulse*, the duration and the timing of the pulse release might be of importance, as further evaluated in Avila et al. (2010) and the **Biosphere synthesis report**. The *LDF pulse* has been calculated for three release times (–9000, 3500, and 9400 AD) and for two release durations (one and 50 years). The results show that the differences due to changes in pulse duration for radionuclides with high retention in the regolith are insignificant, whereas for radionuclides with low retention (Cl-36 and Tc-99) the *LDF pulse* values decrease by less than one order of magnitude when the duration of the pulse is extended. Furthermore, the results reported in Avila et al. (2010), and summarised in the **Biosphere synthesis report,** show that the effect of the time of the release on the *LDF pulse* values is insignificant for radionuclides with a high retention in the regolith. For radionuclides with low retention, such as Tc-99 and Cl-36, the *LDF pulse* is dependent on the succession stage of the biosphere object and the present human land use.

7.2.9 Correlations (text reproduced from SR-Site Data report)

The model that has been used for derivation of *LDF* values, i.e. the radionuclide model described in Avila et al. (2010), relies on several element- and radionuclide-specific parameters that are correlated with each other. This means that *LDF*s obtained for different radionuclides might also be correlated. However, the delivered *LDF*s have been obtained from independent deterministic simulations for each radionuclide and parameter correlations have not been considered. Furthermore, parameter correlations have not been considered in the probabilistic simulations carried out within the sensitivity and uncertainty analyses discussed above. In summary, no correlation needs to be propagated to the SR-Site main project.

7.2.10 Result of supplier's data qualification

The *LDF*s recommended for use in SR-Site for the temperate, periglacial, and glacial climate domains, and for the global warming case are supplied in Table 7-12.

Table 7-12. LDF's (Sv/y per Bq/y) for assessment of long-term releases under different climate conditions: temperate, permafrost, glacial, and the global warming case. Data reproduced from Avila et al. (2010).

Radionuclide	Temperate *LDF*	Periglacial *LDF*	Glacial *LDF*	Global warming *LDF*
Ag-108m	7.05×10^{-13}	8.75×10^{-15}	4.60×10^{-16}	7.05×10^{-13}
Ac-227	8.0×10^{-12}	8.92×10^{-16}	6.44×10^{-17}	8.0×10^{-12}
Am-241	1.46×10^{-12}	1.10×10^{-14}	1.57×10^{-17}	1.46×10^{-12}
Am-243	1.53×10^{-12}	1.95×10^{-13}	1.41×10^{-15}	1.60×10^{-12}
C-14	5.44×10^{-12}	5.40×10^{-12}	8.51×10^{-13}	5.44×10^{-12}
Ca-41	9.90×10^{-14}	9.25×10^{-15}	1.92×10^{-16}	9.90×10^{-14}
Cl-36	5.84×10^{-13}	4.36×10^{-13}	2.22×10^{-17}	5.84×10^{-13}
Cm-244	8.74×10^{-13}	8.14×10^{-19}	2.18×10^{-20}	8.74×10^{-13}
Cm-245	1.58×10^{-12}	2.20×10^{-14}	3.59×10^{-16}	1.64×10^{-12}
Cm-246	1.55×10^{-12}	1.59×10^{-14}	2.10×10^{-16}	1.57×10^{-12}
Cs-135	3.96×10^{-14}	3.02×10^{-13}	4.33×10^{-17}	2.85×10^{-13}
Cs-137	1.20×10^{-13}	9.47×10^{-18}	3.67×10^{-20}	1.20×10^{-13}
Ho-166m	5.90×10^{-14}	8.42×10^{-16}	1.48×10^{-18}	5.90×10^{-14}
I-129	6.46×10^{-10}	2.61×10^{-11}	1.70×10^{-13}	6.46×10^{-10}
Nb-94	4.00×10^{-12}	1.06×10^{-13}	2.12×10^{-17}	1.15×10^{-11}
Ni-59	7.39×10^{-14}	1.31×10^{-15}	3.99×10^{-18}	1.99×10^{-13}
Ni-63	1.21×10^{-15}	6.30×10^{-18}	1.86×10^{-20}	1.21×10^{-15}
Np-237	4.83×10^{-11}	2.21×10^{-11}	8.67×10^{-15}	4.83×10^{-11}
Pa-231	8.10×10^{-12}	1.71×10^{-13}	2.77×10^{-15}	1.27×10^{-11}
Pb-210	5.07×10^{-12}	2.60×10^{-17}	2.19×10^{-18}	5.07×10^{-12}
Pd-107	6.73×10^{-15}	2.68×10^{-15}	4.63×10^{-18}	9.42×10^{-15}
Po-210	8.86×10^{-12}	3.10×10^{-20}	9.28×10^{-21}	8.86×10^{-12}
Pu-239	1.94×10^{-12}	2.01×10^{-13}	6.35×10^{-15}	2.04×10^{-12}
Pu-240	1.88×10^{-12}	1.25×10^{-13}	4.10×10^{-15}	1.89×10^{-12}

Table 7-12. Continued.

Radionuclide	Temperate *LDF*	Periglacial *LDF*	Glacial *LDF*	Global warming *LDF*
Pu-242	1.89×10^{-12}	2.32×10^{-13}	7.20×10^{-15}	2.17×10^{-12}
Ra-226	3.75×10^{-12}	9.79×10^{-13}	4.46×10^{-15}	3.77×10^{-12}
Se-79	1.21×10^{-9}	5.79×10^{-11}	9.55×10^{-13}	1.21×10^{-9}
Sm-151	7.16×10^{-16}	1.01×10^{-20}	4.58×10^{-22}	7.16×10^{-16}
Sn-126	2.47×10^{-11}	6.14×10^{-13}	1.55×10^{-14}	1.09×10^{-10}
Sr-90	2.19×10^{-13}	7.18×10^{-17}	1.96×10^{-19}	2.19×10^{-13}
Tc-99	8.98×10^{-13}	2.80×10^{-13}	1.58×10^{-15}	8.98×10^{-13}
Th-229	3.61×10^{-12}	6.95×10^{-14}	9.58×10^{-17}	3.68×10^{-12}
Th-230	1.31×10^{-11}	1.50×10^{-11}	1.74×10^{-14}	6.42×10^{-11}
Th-232	1.72×10^{-12}	4.53×10^{-13}	1.18×10^{-16}	2.59×10^{-12}
U-233	2.50×10^{-12}	2.52×10^{-12}	1.96×10^{-15}	1.91×10^{-11}
U-234	3.62×10^{-12}	1.06×10^{-11}	4.46×10^{-15}	7.14×10^{-11}
U-235	2.76×10^{-12}	1.33×10^{-13}	5.64×10^{-16}	1.99×10^{-11}
U-236	1.85×10^{-12}	2.92×10^{-14}	1.93×10^{-17}	1.05×10^{-11}
U-238	1.85×10^{-12}	8.05×10^{-13}	1.03×10^{-16}	1.58×10^{-11}
Zr-93	2.77×10^{-14}	6.50×10^{-16}	8.17×10^{-17}	1.06×10^{-13}

As shown in Table 7-12, the *LDF*s cover a range of several orders of magnitude. Thus, a constant activity release rate of, for example, Se-79 to the biosphere would result in an six orders of magnitude higher exposure than would an equally large release rate of Sm-151, given temperate conditions and similar use of natural resources. As explained in Section 7.2.5, *LDF*s for periods when the biosphere objects are submerged by the sea are used as cautious estimates for the glacial domain.

During the reference evolution, exposure is consistently higher under temperate climate conditions than under the other climate domains. The only radionuclide for which the temperate climate domain has a considerably lower *LDF* is Cs-135, which due to strong retention (high K_d) and long half-life shows the highest *LDF* under periglacial climate conditions. For all radionuclides, *LDF*s during submerged conditions are below those of temperate climate conditions by two orders of magnitude or more.

LDF pulse values derived for radionuclides that may be released as a pulse to the biosphere are presented in Table 7-13 The values correspond to the maximum annual doses obtained in simulations with a pulse release during one year, occurring at different times within the temperate climate domain.

Table 7-13. LDF pulse values recommended for assessment. Data reproduced from Table 10-2 of the Biosphere synthesis report.

Radionuclide	*LDF pulse* Sv/y per Bq
Ag-108m	5.1×10^{-16}
Cl-36	4.3×10^{-15}
Cs-135	1.8×10^{-16}
I-129	5.6×10^{-14}
Nb-94	3.2×10^{-16}
Ni-59	9.7×10^{-18}
Se-79	9.7×10^{-14}
Sn-126	2.3×10^{-15}
Tc-99	2.8×10^{-15}

7.2.11 Judgement by the assessment team

During the SR-Site evaluation process, as responses to requests by SSM, SKB provided supplementary information about the biosphere analysis from which the Landscape Dose Conversion Factors (*LDFs*) were derived. The supplementary information focused primarily on clarifications, e.g. about the definition and handling of biosphere objects and the hydrology, and did not substantially affect the estimated *LDFs*. Some of SSMs questions are still remaining for SKB to handle in coming safety assessments, but SSM's general conclusion from the evaluation process was that the estimated *LDFs* were reasonable. This conclusion was partly based on independent estimates of *LDFs* initiated by SSM, and partly on SKB's approach to pessimistically combine the maximum *LDF* values from different radionuclides, independently of when (time) or where (biosphere objects) the maximum of the individual radionuclides occurred.

In response to a specific request by SSM (SSM2011-2426-103), SKB estimated an additional *LDF* value for radon-222 from using water from a drilled well. This exposure pathway was not originally included in the SR-Site dose estimates and resulted in marginally higher maximum total doses (less than 10 %). Some remaining comments and requests given in the SSM review report (SSM 2018:07) have been handled and/or implemented in the biosphere modelling for SR-PSU (SKB 2014), and/or more recently in SE-SFL (SKB 2019b). For example, new exposure groups were introduced in SR-PSU, the representation of regolith layers in terms of model compartments was improved, object-specific hydrological parameters were derived for separate ecosystem states, and K_d (distribution coefficients) and *CR* (concentration ratio) values were updated using new data and increasing weight was given to site-specific data. The resulting differences between *LDF*s from SR-Site and SR-PSU were analysed in SR-PSU (Section 10.4.2 in SKB 2014). The analysis showed that no *LDF* value was more than one order of magnitude larger in SR-PSU than in SR-Site. Among the radionuclides contributing most to the dose in SR-Site, the SR-PSU *LDF*s were either marginally higher (e.g. 12 % higher for Ra-226), whereas the *LDFs* for other radionuclides were substantially lower in SR-PSU (e.g. Se-79 and I-129).

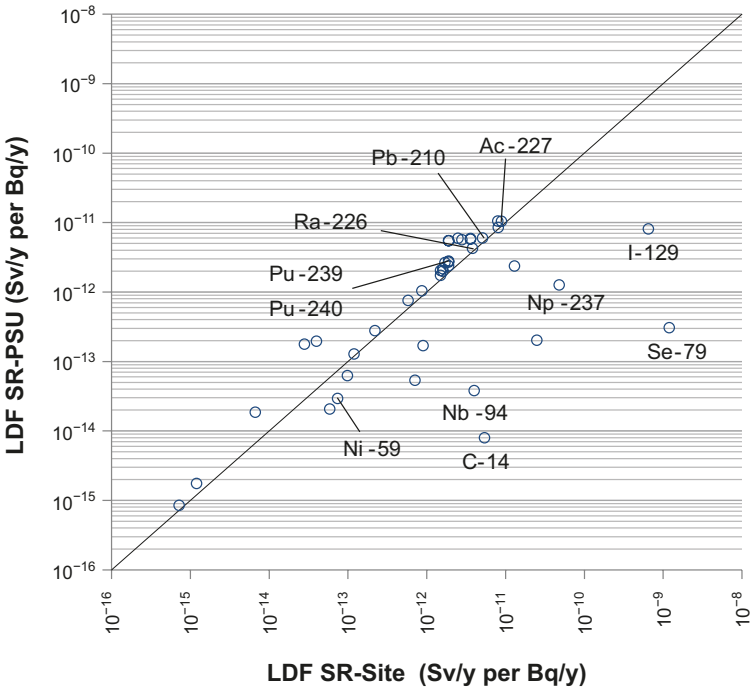

Figure 7-14. *LDF-values from the SR-PSU plotted versus LDF-values from SR-Site (data from Figure 10-1 in SKB 2014). The LDF values for the most dose-contributing radionuclides in the SR-Site compliance scenarios are indicated in the plot and the black line shows the one to one regression relationship between the two LDF datasets.*

In a recent supplementary report to SSM (Kautsky 2015) the updated and more site-specific K_d- and *CR*-values from the SR-PSU were used in time dynamic biosphere modelling of doses for some illustrative calculation cases (i.e. not *LDFs* for the compliance case). The results from this exercise confirmed the conclusions from the comparison of *LDFs* between SR-Site and SR-PSU, that doses would not increase substantially by using updated K_d- and *CR*-values.

In SE-SFL, several additional updates of the biosphere model were introduced and evaluated. These include for example a higher discretisation of deeper regolith layers. The conclusion from SE-SFL was similar to that of the uncertainty analysis presented in SR-Site (Section 5.2.1 in Avila et al. 2010). That is, for most radionuclides an increased vertical discretization has a limited or no effect on the *LDF*-values, and this is partly due to the importance of alternative exposure pathways unaffected by the biosphere discretization (such as the drilled well). However, for a few radionuclides with long residence times relative to the radionuclide half-life, which may expose humans through accumulation in crops, the coarse resolution used in SR-Site was clearly cautious (e.g. Cs-135).

Based on SSM's conclusions that the SR-Site *LDFs* are reasonable, that the *LDFs* from the safety assessment for the extended SFR, SR-PSU, are not substantially larger than the original SR Site *LDF* values, and the limited effects on results by the model development in the latest safety assessment, SE-SFL, the judgement is to use the same data as in SR-Site. In the next assessment step for the spent nuclear fuel repository, SAR, implementation of relevant changes and updates to the radionuclide transport model are planned.

7.2.12 Data recommended for use in assessment

Based on the conclusions above, the recommended *LDF* values for use in the safety assessment can be found in Table 7-12, and the *LDF pulse* values in Table 7-13. In addition, the *LDF* value for Rn-222 ($5.1 \cdot 10^{-14}$ Sv Bq^{-1}) reported in Hedin and Kautsky 2015 (and based on SKBdoc Avila 2013), is recommended for use during conditions when a drilled well may exist (i.e. temperate and global warming climate conditions).

References

SKB's (Svensk Kärnbränslehantering AB) publications can be found at www.skb.com/publications. SKBdoc documents will be submitted upon request to document@skb.se, with the exception of internal documents.

References with abbreviated names

Backfill production report, 2021. Produktionsrapport Återfyllning. SKBdoc 1525864 ver 4.0, Svensk Kärnbränslehantering AB. (In Swedish.) (Internal document.)

Biosphere synthesis report, 2010. Biosphere analyses for the safety assessment SR-Site – synthesis and summary of results. SKB TR-10-09, Svensk Kärnbränslehantering AB.

Buffer, backfill and closure process report, 2022. Post-closure safety for the final repository for spent nuclear fuel at Forsmark – Buffer, backfill and closure process report, PSAR version. SKB TR-21-03, Svensk Kärnbränslehantering AB.

Buffer production report, 2022. Produktionsrapport Buffert. SKBdoc 1392269 ver 5.0, Svensk Kärnbränslehantering AB. (In Swedish.) (Internal document.)

Canister production report, 2022. Produktionsrapport Kapsel. SKBdoc 1407944 ver 2.0, Svensk Kärnbränslehantering AB. (In Swedish.) (Internal document.)

Climate report, 2020. Post-closure safety for the final repository for spent nuclear fuel at Forsmark – Climate and climate-related issues, PSAR version. SKB TR-20-12, Svensk Kärnbränslehantering AB.

Closure production report, 2022. Produktionsrapport Förslutning. SKBdoc 1387771 ver 3.0, Svensk Kärnbränslehantering AB. (In Swedish.) (Internal document.)

Fuel and canister process report, 2022. Post-closure safety for the final repository for spent nuclear fuel at Forsmark – Fuel and canister process report, PSAR version. SKB TR-21-02, Svensk Kärnbränslehantering AB.

Model summary report, 2022. Post-closure safety for the final repository for spent nuclear fuel at Forsmark – Model summary report, PSAR version, SKB TR-21-05, Svensk Kärnbränslehantering AB.

Post-closure safety report, 2022. Post-closure safety for the final repository for spent nuclear fuel at Forsmark – Main report, PSAR version. SKB TR-21-01, Svensk Kärnbränslehantering AB.

Radionuclide transport report, 2022. Post-closure safety for the final repository for spent nuclear fuel at Forsmark – Radionuclide transport report, PSAR version. SKB TR-21-07, Svensk Kärnbränslehantering AB.

Site description Forsmark, 2008. Site description of Forsmark at the completion of the site investigation phase, SDM-Site Forsmark. SKB TR-08-05, Svensk Kärnbränslehantering AB.

Spent fuel report, 2021. Använt kärnbränsle att hantera i KBS-3-systemet. SKBdoc 1380282 ver 3.0, Svensk Kärnbränslehantering AB. (In Swedish.) (Internal document.)

Underground openings construction report. Produktionsrapport Bergutrymmen. Svensk Kärnbränslehantering AB. (In Swedish.) (Internal document.) *In prep*.

Regular references

AACE, 2008. Risk analysis and contingency determination using range estimating. TCM framework: 7.6 – risk management. AACE International recommended practise No. 41R-08.

Agrenius L, 2010. Aktivitetsinnehåll i kapslar för slutförvar. SKBdoc 1221579 ver 2.0, Svensk Kärnbränslehantering AB. (In Swedish.)

Ahmad A, Bond L J (eds), 2018. ASM handbook. Volume 17, Nondestructive evaluation of materials. Materials Park, OH: ASM International.

Alverlind L, 2016. Isostatic pressure load of canister with scaled iron material model. Report 5000484-1, Revision 4, Inspecta Technology AB. SKBdoc 1089758 ver 3.0, Svensk Kärnbränslehantering AB.

Anderko A, Lencka M M, 1998. Modeling self-diffusion in multicomponent aqueous electrolyte systems in wide concentration ranges. Industrial & Engineering Chemistry Research 37, 2878–2888.

Andersson C, Eng A, 2005. Äspö Pillar Stability Experiment. Final experiment design, monitoring results and observations. SKB R-05-02, Svensk Kärnbränslehantering AB.

Andersson C-G, Andersson M, Erixon B, Björkegren L-E, Dillström P, Minnebo P, Nilsson K-F, Nilsson F, 2005. Probabilistic analysis and material characterisation of canister insert for spent nuclear fuel. Summary report. SKB TR-05-17, Svensk Kärnbränslehantering AB.

Andersson J C, 2007. Äspö Hard Rock Laboratory. Äspö Pillar Stability Experiment, Final report. Rock mass response to coupled mechanical thermal loading. SKB TR-07-01, Svensk Kärnbränslehantering AB.

Andersson J-E, Nordqvist R, Nyberg G, Smellie J, Tirén S, 1991. Hydrogeological conditions in the Finnsjön area. Compilation of data and conceptual model. SKB TR 91-24, Svensk Kärnbränslehantering AB.

André M, Malmström M E, Neretnieks I, 2009. Specific surface area determinations on intact drillcores and evaluation of extrapolation methods for rock matrix surfaces. Journal of Contaminant Hydrology 110, 1–8.

Appelo C A J, Postma D, 2005. Geochemistry, groundwater and pollution. 2nd ed. Leiden: Balkema.

Arai Y, Moran P B, Honeyman B D, Davis J A, 2007. In situ spectroscopic evidence for neptunium(V)-carbonate inner-sphere and outer-sphere ternary surface complexes on hematite surfaces. Environmental Science & Technology 41, 3940–3944.

Ask D, Cornet F, Brunet C, Fontbonne F, 2007. Forsmark site investigation. Stress measurements with hydraulic methods in boreholes KFM07A, KFM07C, KFM08A, KFM09A and KFM09B. SKB P-07-206, Svensk Kärnbränslehantering AB.

Askeljung C, Granfors M, Roth O, 2019. Release of ^{108m}Ag from irradiated pwr control rod absorbers under deep repository conditions. SKB R-19-21, Svensk Kärnbränslehantering AB.

Auqué L F, Gimeno M J, Gómez J B, Puigdomenech I, Smellie J, Tullborg E-L, 2006. Groundwater chemistry around a repository for spent nuclear fuel over a glacial cycle. Evaluation for SR-Can. SKB TR-06-31, Svensk Kärnbränslehantering AB.

Avila R, Ekström P-A, Åstrand P-G, 2010. Landscape dose conversion factors used in the safety assessment SR-Site. SKB TR-10-06, Svensk Kärnbränslehantering AB.

Avila R, 2013. Derivation of a dose factor for Rn-222 release to a well. SKBdoc 1418460 ver 1.0, Svensk Kärnbränslehantering AB.

Back P-E, Sundberg J, 2007. Thermal site descriptive model. A strategy for the model development during site investigations – version 2. SKB R-07-42, Svensk Kärnbränslehantering AB.

Back P-E, Wrafter J, Sundberg J, Rosén L, 2007. Thermal properties. Site descriptive modelling Forsmark – stage 2.2. SKB R-07-47, Svensk Kärnbränslehantering AB.

Baes C F, Mesmer R E, 1976. The hydrolysis of cations. Malabar, FL: Krieger.

Bargar J R, Reitmeyer R, Davis J A, 1999. Spectroscopic confirmation of uranium(VI)-carbonato adsorption complexes on hematite. Environmental Science & Technology 33, 2481–2484.

Barton N, 1982. Modelling rock joint behaviour from in situ block tests: Implications for nuclear waste repository design. Technical Report ONWI-308, Office of Nuclear Waste Isolation, Columbus, Ohio.

Bauhn L, Hansson N, Ekberg C, Fors P, Delville R, Spahiu K, 2018a. The interaction of molecular hydrogen with α-radiolytic oxidants on a (U,Pu)O_2 surface. Journal of Nuclear Materials 505, 54–61.

Bauhn L, Hansson N, Ekberg C, Fors P, Spahiu K, 2018b. The fate of hydroxyl radicals produced during H_2O_2 decomposition on a SIMFUEL surface in the presence of dissolved hydrogen. Journal of Nuclear Materials 507, 38–43.

Bazer-Bachi F, Descostes M, Tevissen E, Meier P, Grenut B, Simonnot M-O, Sardin M, 2007. Characterization of sulphate sorption on Callovo-Oxfordian argillites by batch, column and through-diffusion experiments. Physics and Chemistry of the Earth 32, 552–558.

Bechtel-SAIC, 2001. Uncertainty Analyses and Strategy. SA011481M4 REV 00, Bechtel-SAIC Company, Las Vegas, Nevada, USA.

Benning J L, Barnes D L, 2009. The effects of scale and spatial heterogeneities on diffusion in volcanic breccias and basalts: Amchitka Island, Alaska. Journal of Contaminant Hydrology 106, 150–165.

Bingham C, 1964. Distribution on the sphere and on the projective plane. PhD thesis. Yale University, New Haven, Connecticut.

Birgersson L, Neretnieks I, 1988. Diffusion in the matrix of granitic rock. Field test in the Stripa mine. Final report. SKB TR 88-08, Svensk Kärnbränslehantering AB.

Birgersson L, Neretnieks I, 1990. Diffusion in the matrix of granitic rock: Field test in the Stripa mine. Water Resources Research 26, 2833–2842.

Bond A E, Hoch A R, Jones G D, Tomczyk A J, Wiggin R M, Worraker W J, 1997. Assessment of a spent fuel disposal canister. Assessment studies for a copper canister with cast steel inner component. SKB TR 97-19, Svensk Kärnbränslehantering AB.

Bosbach D, Böttle M, Volker M, 2010. Experimental study of Ra^{2+} uptake by barite ($BaSO_4$). Kinetics of solid solution formation via $BaSO_4$ dissolution and $Ra_xBa_{1-x}SO_4$ (re) precipitation. SKB TR-10-43, Svensk Kärnbränslehantering AB.

Bradbury M H, Baeyens B, 1997. A mechanistic description of Ni and Zn sorption on Na-montmorillonite. Part II: modelling. Journal of Contaminant Hydrology 27, 223–248.

Bradbury M H, Baeyens B, 2003. Near-field sorption data bases for compacted MX-80 bentonite for performance assessment of high-level radioactive waste repository in Opalinus Clay host rock. Nagra Technical Report NTB 02-18, Nagra, Switzerland.

Brantley S L, Kubicki J D, White A F (eds), 2008. Kinetics of water-rock interactions. New York: Springer Science+Business Media.

Brendler V, Vahle A, Arnold T, Bernhard G, Fanghänel T, 2003. RES^3T – Rossendorf expert system for surface and sorption thermodynamics. Journal of Contaminant Hydrology 61, 281–291.

Brookins D G, 1988. Eh-pH diagrams for geochemistry. Berlin: Springer.

Brown P, Curti E, Grambow B, Ekberg C, 2005. Chemical thermodynamics. Vol. 8. Chemical thermodynamics of zirconium. Amsterdam: Elsevier.

Brunauer S, Emmet P H, Teller E, 1938. Adsorption of gases in multimolecular layers. Journal of the American Chemical Society 60, 309–319.

Byegård J, Selnert E, Tullborg E-L, 2008. Bedrock transport properties. Data evaluation and retardation model. Site descriptive modelling, SDM-Site Forsmark. SKB R-08-98, Svensk Kärnbränslehantering AB.

Bäckblom G, 2008. Excavation damage and disturbance in crystalline rock – results from experiments and analyses. SKB TR-08-08, Svensk Kärnbränslehantering AB.

Bäckblom G, Christiansson R, Lagerstedt L, 2004. Choice of rock excavation methods for the Swedish deep repository for spent nuclear fuel. SKB R-04-62, Svensk Kärnbränslehantering AB.

Bäckström A, Lanaro L, 2007. Forsmark site investigation. Rock mechanics characterisation of boreholes KFM01B, KFM07C, KFM09A and KFM09B. SKB P-07-115, Svensk Kärnbränslehantering AB.

Börgesson L, Johannesson L-E, Sandén T, Hernelind J, 1995. Modelling of the physical behaviour of water saturated clay barriers. Laboratory tests, material models and finite element application. SKB TR 95-20, Svensk Kärnbränslehantering AB.

Carbol P, Cobos-Sabate J, Glatz J-P, Grambow B, Kienzler B, Loida A, Martínez Esparza Valiente A, Metz V, Quiñones J, Ronchi C, Rondinella V, Spahiu K, Wegen D H, Wiss T, 2005. The effect of dissolved hydrogen on the dissolution of ^{233}U doped UO_2(s), high burn-up spent fuel and MOX fuel. SKB TR-05-09, Svensk Kärnbränslehantering AB.

Cederqvist L, Garpinger O, Nielsen I, 2018. Evaluation of depth controller for friction stir welding of copper canisters. Posiva SKB Report 08, Posiva Oy, Svensk Kärnbränslehantering AB.

Cho J W, Oscarson D W, 1996. Diffusive transport through compacted Na- and Ca-bentonite. Journal of Contaminant Hydrology 22, 189–202.

Cho J W, Jung C H, Chun C H, Park H S, Whang J H, Lee B H, 1993. Diffusion of radionuclides in compacted bentonite. In Proceedings of Conference on High Level Radioactive Waste Management, La Grande Park, IL. American Nuclear Society, 2278–2283.

Cho N, Martin C D, Christiansson R, 2002. Suppressing fracture growth around underground openings. In Hammah, R (ed). NARMS-TAC 2002: mining and tunneling innovation and opportunity: proceedings of the 5th North American Rock Mechanics Symposium and the 17th Tunnelling Association of Canada Conference, Toronto, 7–10 July 2002. University of Toronto, Canada, 130–138.

Christiansson R, Janson T, 2003. A test of different stress measurement methods in two orthogonal bore holes in Äspö Hard Rock Laboratory (HRL), Sweden. International Journal of Rock Mechanics and Mining Sciences 40, 1161–1172.

Chryssanthakis P, 2003a. Forsmark site investigation. Borehole: KFM01A. Results of tilt testing. SKB P-03-108, Svensk Kärnbränslehantering AB.

Chryssanthakis P, 2003b. Forsmark site investigation. Boreholes: KFM03A and KFM03B. Tilt testing. SKB P-04-178, Svensk Kärnbränslehantering AB.

Chryssanthakis P, 2004a. Forsmark site investigation. Borehole: KFM02A. Results of tilt testing. SKB P-04-08, Svensk Kärnbränslehantering AB.

Chryssanthakis P, 2004b. Forsmark site investigation. Borehole: KFM04A. Tilt testing. SKB P-04-179, Svensk Kärnbränslehantering AB.

Chryssanthakis P, 2004c. Forsmark site investigation. Borehole: KFM05A. Tilt testing. SKB P-04-205, Svensk Kärnbränslehantering AB.

Chryssanthakis P, 2006. Forsmark site investigation. Borehole: KFM09A. Tilt testing. SKB P-06-25, Svensk Kärnbränslehantering AB.

CIMNE, 2004. Code_Bright. Version 2.2 users guide. Departemento de Ingenieria del Terreno, Cartográfica y Geofísica, Universidad Politécnica de Cataluña, Spain.

Claesson J, Probert T, 1996a. Temperature field due to time-dependent heat sources in a large rectangular grid. Derivation of analytical solution. SKB TR 96-12, Svensk Kärnbränslehantering AB.

Claesson J, Probert T, 1996b. Thermoelastic stress due to a rectangular heat source in a semi-infinite medium. Derivation of an analytical solution. SKB TR 96-13, Svensk Kärnbränslehantering AB.

Clarens F, Serrano-Purroy D, Martínez-Esparza A, Wegan D, Gonzalez-Robles E, de Pablo J, Casas I, Giménez J, Christiansen B, Glatz J-P, 2008. RN fractional release of high burn-up fuel: effect of HBS and estimation of accessible grain boundary. In Lee W E, Roberts J W, Hyatt N C, Grimes R W (eds). Scientific basis for nuclear waste management XXXI: symposium held in Sheffield, United Kingdom, 16–21 September 2007. Warrendale, PA: Materials Research Society. (Materials Research Society Symposium Proceedings 1107), 439–446.

Cliffe K A, Kelly M, 2006. COMP23 version 1.2.2 user's manual. SKB R-04-64, Svensk Kärnbränslehantering AB.

Colleoni F, Wekerle C, Masina S, 2014. Long-term safety of a planned geological repository for spent nuclear fuel in Forsmark – estimate of maximum ice sheet thicknesses. SKB TR-14-21, Svensk Kärnbränslehantering AB.

Coulson J M, Richardson J F, Backhurst J R, Harker J H, 1990. Chemical engineering. Vol. 1. Fluid flow, heat transfer and mass transfer. 4th ed. Oxford: Pergamon.

Crawford J, 2008. Bedrock transport properties Forsmark. Site descriptive modelling, SDM-Site Forsmark. SKB R-08-48, Svensk Kärnbränslehantering AB.

Crawford J, 2010. Bedrock K_d data and uncertainty assessment for application in SR-Site geosphere transport calculations. SKB R-10-48, Svensk Kärnbränslehantering AB.

Crawford J, 2014. Memorandum: Retardation of radionuclide transport in cement affected groundwater – response to the request by SSM for supplementary information on retention of radionuclides (SSM2011-2426-110), item 1. SKBdoc 1421672 ver 1.0, Svensk Kärnbränslehantering AB.

Crawford J, Löfgren M, 2019. Modelling of radionuclide retention by matrix diffusion in a layered rock model. SKB R-17-22, Svensk Kärnbränslehantering AB.

Crawford J, Sidborn M, 2009. Bedrock transport properties Laxemar. Site descriptive modelling, SDM-Site Laxemar. SKB R-08-94, Svensk Kärnbränslehantering AB.

CRC, 2008. CRC Handbook of chemistry and physics: a ready-reference book of chemical and physical data. 88th ed. Boca Raton, FL: CRC Press/Taylor & Francis Group.

Cubicciotti D, Sanecki J E, 1978. Characterization of deposites on inside of LWR cladding. Journal of Nuclear Materials 78, 96–111.

Cui D, Low J, Sjöstedt C J, Spahiu K, 2004. On Mo-Ru-Tc-Pd-Rh-Te alloy particles extracted from spent fuel and their leaching behaviour under Ar and H_2 atmospheres. Radiochimica Acta 92, 551–555.

Cui D, Ekeroth E, Fors P, Spahiu K, 2008. Surface mediated processes in the interaction of spent fuel or α-doped UO_2 with H_2. In Shuh D K, Chung B W, Albrecht-Schmitt T, Gouder T, Thompson J D (eds). Actinides 2008: basic science, applications and technology. Warrendale, PA: Materials Research Society. (Materials Research Society Symposium Proceedings 1104), 87–99.

Curie P, Curie Mme P, Bémont G, 1898. On a new, strongly radioactive substance, contained in pitchblende. Comptes Rendus 127, 1215–1217.

Curti E, Puranen A, Grolimund D, Jädernas D, Sheptyakov D, Mesbah A, 2015. Characterization of selenium in UO_2 spent nuclear fuel by micro X-ray absorption spectroscopy and its thermodynamic stability. Environmental Science: Processes & Impacts 17, 1760–1768.

Damjanac B, Fairhurst C, 2010. Evidence for a long-term strength threshold in crystalline rock. Rock Mechanics and Rock Engineering 43. doi:10.1007/s00603-00010-00090-00609

Darcel C, 2003. Äspö Hard Rock Laboratory. True Block Scale Continuation project. Assessment of the feasibility of tracer tests with injection in "background fractures" using a model based on a power-law fracture length distribution. SKB IPR-03-41, Svensk Kärnbränslehantering AB.

Darcel C, Bour O, Davy P, 2003. Stereological analysis of fractal fracture networks. Journal of Geophysical Research 108, 2451. doi:10.1029/2002JB002091

Darcel C, Davy P, Bour O, de Dreuzy J-R, 2006a. Discrete fracture network for the Forsmark site. SKB R-06-79, Svensk Kärnbränslehantering AB.

Darcel C, Davy P, Bour O, de Dreuzy J-R, 2006b. Reconstructing the 3D fracture distribution model from core (10 cm) to outcrop (10 m) and lineament (10 km) scales. EOS: Transactions of the American Geophysical Union 87, Fall Meeting Supplement.

Darcel C, P Davy, Le Goc R, Mas Ivars D, 2018. Rock mass effective properties from a DFN approach. Second International Discrete Fracture Network Engineering Conference, Seattle, WA, 20–22 June 2018.

Davis J A, Kent D B, 1990. Surface complexation modeling in aqueous geochemistry. In Hochella M F, White A F (eds). Mineral-water interface geochemistry. Washington, DC: Mineralogical Society of America. (Reviews in mineralogy), 177–260.

Davy P, C Darcel, Le Goc R, Mas Ivars D , 2018. Elastic properties of fractured rock masses with frictional properties and power-law fracture size distributions. Journal of Geophysical Research: Solid Earth 123, 6521–6539.

Delos A, Trinchero P, Richard L, Molinero J, Dentz M, Pitkänen P, 2010. Quantitative assessment of deep gas migration in Fennoscandian sites. SKB R-10-61, Svensk Kärnbränslehantering AB.

Dershowitz W, 1979. A probabilistic model for the deformability of jointed rock masses. MSc thesis. Massachusetts Institute of Technology, Cambridge, Massachusetts.

Dershowitz W S, 1985. Rock joint systems. PhD thesis. Massachusetts Institute of Technology, Cambridge, Massachusetts.

Dershowitz W, Winberg A, Hermanson J, Byegård J, Tullborg E-L, Andersson P, Mazurek M, 2003. Äspö Hard Rock Laboratory. Äspö Task Force on modelling of groundwater flow and transport of solutes. Task 6c. A semi-synthetic model of block scale conductive structures at the Äspö HRL. SKB IPR-03-13, Svensk Kärnbränslehantering AB.

Descostes M, Blin V, Bazer-Bachi F, Meier P, Grenut B, Radwan J, Schlegel M L, Buschaert S, Coelho D, Tevissen E, 2008. Diffusion of anionic species in Callovo-Oxfordian argillites and Oxfordian limestones (Meuse/Haute-Marne, France), Applied Geochemistry 23, 655–677.

Dillström P, 2014. Probabilistic analysis of BWR canister inserts for spent nuclear fuel in the case of an earthquake induced rock shear load. Report 50014130-1, Revision 5, Inspecta Technology AB. SKBdoc 1412158 ver 1.0, Svensk Kärnbränslehantering AB.

Dillström P, 2015. Damage tolerance analysis of BWR-canister inserts for spent nuclear fuel in the case of an earthquake induced rock shear load – Influence of using more detailed models. Report 5000264-1, Revision 2, Inspecta Technology AB. SKBdoc 1450913 ver 1.0, Svensk Kärnbränslehantering AB.

Dillström P, Bolinder T, 2010. Damage tolerance analysis of canister inserts for spent nuclear fuel in the case of an earthquake induced rock shear load. SKB TR-10-29, Svensk Kärnbränslehantering AB.

Duro L, Grivé M, Cera E, Gaona X, Domènech C, Bruno J, 2006a. Determination and assessment of the concentration limits to be used in SR-can. SKB TR-06-32, Svensk Kärnbränslehantering AB.

Duro L, Grivé M, Cera E, Domènech C, Bruno J, 2006b. Update of a thermodynamic database for radionuclides to assist solubility limits calculation for performance assessment. SKB TR-06-17, Svensk Kärnbränslehantering AB.

Dverstorp B, Strömberg B, 2008. SKI's and SSI's review of SKB's safety report SR-Can. SKI Report 2008:23, Swedish Nuclear Power Inspectorate, SSI Report 2008:04 E, Swedish Radiation Protection Authority.

Döse C, Samuelsson E, 2006. Forsmark site investigation. Boremap mapping of telescopic drilled borehole KFM10A. SKB P-06-204, Svensk Kärnbränslehantering AB.

Eftring B, 1990. Numerisk beräkning av temperaturförlopp: ett fysikaliskt betraktelsesätt (Numerical calculation of thermal processes: a physical approach). PhD thesis. Lund University, Sweden. (In Swedish.)

Ekeroth E, Low J, Zwicky H-U, Spahiu K, 2009. Corrosion studies with high burnup LWR fuel in simulated groundwater. In Hyatt N C, Pickett D A, Rebak R B (eds). Scientific basis for nuclear waste management XXXII. Warrendale, PA: Materials Research Society. (Materials Research Society Symposium Proceedings 1124), paper Q02-07.

Ekeroth E, Granfors M, Schild D, Spahiu K, 2020. The effect of temperature and fuel surface area on spent nuclear fuel dissolution kinetics under H_2 atmosphere. Journal of Nuclear Materials 151981. doi:10.1016/j.jnucmat.2019.151981

Elert M, Gylling B, Lindgren M, 2004. Assessment model validity document FARF31. SKB R-04-51, Svensk Kärnbränslehantering AB.

Enssle C P, Poppei J, 2010. Implementation and testing of an improved methodology to simulate resaturation processes with DarcyTools. SKB R-09-54, Svensk Kärnbränslehantering AB.

Ericsson L O, Brinkhoff P, Gustafson G, Kvartsberg S, 2009. Hydraulic Features of the Excavation Disturbed Zone – Laboratory investigations of samples taken from the Q- and S-tunnels at Äspö HRL. SKB R-09-45, Svensk Kärnbränslehantering AB.

Ericsson L O, Thörn J, Christiansson, R, Lehtimäki T, Ittner H, Hansson K, Butron C, Sigurdsson O, Kinnbom P, 2015. A demonstration project on controlling and verifying the excavation-damaged zone. Experience from the Äspö Hard Rock Laboratory. SKB R-14-30 , Svensk Kärnbränslehantering AB.

Eriksen T E, Jacobsson A, 1981. Ion diffusion in compacted Na and Ca bentonites. KBS TR 81-12, Svensk Kärnbränslehantering AB.

Eriksen, T E, Jansson M, 1996. Diffusion of I^-, Cs^+ and Sr^+ in compacted bentonite. Anion exclusion and surface diffusion. SKB TR 96-16, Svensk Kärnbränslehantering AB.

Eriksson T, 2009. SKB – Referensrapport till SAR allmän del kapitel 6 – Källtermer. SKBdoc 1179234 ver 1.0, Svensk Kärnbränslehantering AB. (In Swedish.)

Evans M, Hastings N, Peacock B, 1993. Statistical distributions. 2nd ed. New York: Wiley.

Evins L Z, 2013. Treatment of silver in solubility calculations. SKBdoc 1396561 ver 1.0, Svensk Kärnbränslehantering AB.

Evins L Z, Hedin A, 2013. Uppskattning av riskbidrag från bränslerester. SKBdoc 1395834 ver 1.0, Svensk Kärnbränslehantering AB. (In Swedish.)

Evins L Z, Hedin A, 2020. Failed fuel in special containers: potential contribution to risk calculated in the post-closure safety for the spent nuclear fuel repository. SKBdoc 1872793 ver 1.0, Svensk Kärnbränslehantering AB.

Evins L Z, Juhola P, Vähänen M, 2014. REDUPP Final report. Posiva Working Report 2014-12, Posiva Oy, Finland.

Feder J, 1988. Fractals. New York: Plenum Press.

Ferry C, Piron J-P, Poutesquen A, Poinssot C, 2008. Radionuclides release from the spent fuel under disposal conditions: re-evaluation of the Instant Release Fraction. In Lee W E, Roberts J W, Hyatt N C, Grimes R W (eds). Scientific basis for nuclear waste management XXXI: symposium held in Sheffield, United Kingdom, 16–21 September 2007. Warrendale: Materials Research Society. (Materials Research Society Symposium Proceedings 1107), 447–454.

Fidalgo A B, Roth O, Puranen A, Evins L Z, Spahiu K, 2020. Aqueous leaching of ADOPT and standard UO_2 spent nuclear fuel under H_2 atmosphere. MRS Advances 5, 167–175.

Figueiredo B, Sjöberg J, Mas Ivars D, 2020. Use of a fully tensorial approach to characterize the stress variability at Forsmark. In Billaux D, Hazzard J, Nelson M, Schöpfer M (eds.) Proceedings of the 5th International Itasca Symposium, Vienna, 17–20 February 2020. Minneapolis: Itasca International, Inc., Paper 12-08.

Fisher N I, Lewis T, Embleton B J J, 1993. Statistical analysis of spherical data. Cambridge: Cambridge University Press.

Fisher R, 1953. Dispersion on a sphere. Proceedings of the Royal Society of London – Series A 217, 295–305.

Follin S, 2008. Bedrock hydrogeology Forsmark. Site descriptive modelling, SDM-Site Forsmark. SKB R-08-95, Svensk Kärnbränslehantering AB.

Follin S (ed), 2019. Multidisciplinary description of the access area of the planned spent nuclear fuel repository in Forsmark prior to construction. SKB R-17-13, Svensk Kärnbränslehantering AB.

Follin S, Stigsson M, Svensson U, 2005. Regional hydrogeological simulations for Forsmark – numerical modelling using DarcyTools. Preliminary site description. Forsmark area – version 1.2. SKB R-05-60, Svensk Kärnbränslehantering AB.

Follin S, Johansson P-O, Levén J, Hartley L, Holton D, McCarthy R, Roberts D, 2007a. Updated strategy and test of new concepts for groundwater flow modelling in Forsmark in preparation of site descriptive modelling stage 2.2. SKB R-07-20, Svensk Kärnbränslehantering AB.

Follin S, Levén J, Hartley L, Jackson P, Joyce S, Roberts D, Swift B, 2007b. Hydrogeological characterisation and modelling of deformation zones and fracture domains, Forsmark modelling stage 2.2. SKB R-07-48, Svensk Kärnbränslehantering AB.

Follin S, Johansson P-O, Hartley L, Jackson P, Roberts D, Marsic N, 2007c. Hydrogeological conceptual model development and numerical modelling using CONNECTFLOW, Forsmark modelling stage 2.2. SKB R-07-49, Svensk Kärnbränslehantering AB.

Follin S, Hartley L, Jackson P, Roberts D, Marsic N, 2008. Hydrogeological conceptual model development and numerical modelling using CONNECTFLOW, Forsmark modelling stage 2.3. SKB R-08-23, Svensk Kärnbränslehantering AB.

Forssman I, Zetterlund M, Rhén I, 2004. Correlation of Posiva flow log anomalies to core mapped features in Forsmark (KFM01A to KFM05A). SKB R-04-77, Svensk Kärnbränslehantering AB.

Forssman I, Zetterlund M, Forsmark T, Rhén I, 2006. Forsmark site investigation. Correlation of Posiva Flow Log anomalies to core mapped features in KFM06A and KFM07A. SKB P-06-56, Svensk Kärnbränslehantering AB.

Forssman I, Forsmark T, Rhén I, 2008. Forsmark site investigation. Correlation of Posiva Flow Log anomalies to core mapped features in KFM02B, KFM08D and KFM11A. SKB P-07-128, Svensk Kärnbränslehantering AB.

Fox A, Hermanson J, 2006. Identification of additional, possible minor deformation zones at Forsmark through a review of data from cored boreholes. SKB P-06-293, Svensk Kärnbränslehantering AB.

Fox A, La Pointe P, Hermanson J, Öhman J, 2007. Statistical geological discrete fracture network model. Forsmark modelling stage 2.2. SKB R-07-46, Svensk Kärnbränslehantering AB.

Frampton A, Hyman J D, Zou L, 2019. Advective transport in discrete fracture networks with connected and disconnected textures representing internal aperture variability. Water Resources Research 55, 5487–5501.

Fransson Å, 2009. Literature survey: Relations between stress change, deformation and transmissivity for fractures and deformation zones based on in situ investigatons. SKB R-09-13, Svensk Kärnbränslehantering AB.

Fritzell A, 2017. KBP1012 Verifiering av återfyllningens utformning avseende funktion i KBS-3-förvaret. SKBdoc 1531424 ver 1.0, Svensk Kärnbränslehantering AB. (In Swedish.) (Internal document.)

Fälth B, Hökmark H, 2006. Seismically induced slip on rock fractures. Results from dynamic discrete fracture modeling. SKB R-06-48, Svensk Kärnbränslehantering AB.

Fälth B, Hökmark H, 2007. Mechanical and thermo-mechanical discrete fracture near-field analyses based on preliminary data from the Forsmark, Simpevarp and Laxemar sites. SKB R-06-89, Svensk Kärnbränslehantering AB.

Fälth B, Hökmark H, Munier R, 2007. Seismically induced shear displacements in repository host rock fractures. In Proceedings of the 9th Canadian Conference on Earthquake Engineering, Ottawa, Ontario, 26–29 June 2007.

Fälth B, Hökmark H, Munier R, 2008. Seismically induced slip on rock fractures – expanded study with particular account of large earthquakes. In 42nd U.S. Rock Mechanics Symposium and 2nd U.S.-Canada Rock Mechanics Symposium, San Francisco, 29 July – 2 June 2008. Madison, WI: Omnipress.

Fälth B, Hökmark H, Munier R, 2010. Effects of large earthquakes on a KBS-3 repository. Evaluation of modelling results and their implications for layout and design. SKB TR-08-11, Svensk Kärnbränslehantering AB.

Gamsjäger H, Bugajski J, Gajda T, Lemire R J, Preis W, 2005. Chemical thermodynamics. Vol. 6. Chemical thermodynamics of nickel. Amsterdam: Elsevier.

Gao K, Harrison J P, 2018a. Multivariate distribution model for stress variability characterization. International Journal of Rock Mechanics and Mining Sciences 102, 144–154.

Gao K, Harrison J P, 2018b. Scalar-valued measures on stress dispersion. International Journal of Rock Mechanics and Mining Sciences 106, 234–242.

García-Gutiérrez M, Cormenzana J L, Missana T, Mingarro M, 2004. Diffusion coefficients and accessible porosity for HTO and ^{36}Cl in compacted FEBEX bentonite. Applied Clay Science 26, 65–73.

Gimeno M J, Auqué L F, Gómez J B, Acero P, 2008. Water-rock interaction modelling and uncertainties of mixing modelling. SDM-Site Forsmark. SKB R-08-86, Svensk Kärnbränslehantering AB.

Gimeno M J, Auqué L F, Gómez J B, Acero P, 2009. Water-rock interaction modelling and uncertainties of mixing modelling. Site descriptive modelling, SDM-Site Laxemar. SKB R-08-110, Svensk Kärnbränslehantering AB.

Gimeno M J, Auqué L F, Gómez J B, Salas J, Molinero J, 2010. Hydrogeochemical evolution of the Laxemar site. SKB R-10-60, Svensk Kärnbränslehantering AB.

Glamheden R, Fredriksson A, Röshoff K, Karlsson J, Hakami H, Christiansson R, 2007. Rock mechanics Forsmark. Site descriptive modelling Forsmark Stage 2.2. SKB R-07-31, Svensk Kärnbränslehantering AB.

Glamheden R, Lanaro F, Karlsson J, Lindberg U, Wrafter J, Hakami H, Johansson M, 2008. Rock mechanics Forsmark. Modelling stage 2.3. Complementary analysis and verification of the rock mechanics model. SKB R-08-66, Svensk Kärnbränslehantering AB.

Glamheden R, Fälth B, Jacobsson L, Harrström J, Berglund J, Bergkvist L, 2010. Counterforce applied to prevent spalling. SKB TR-10-37, Svensk Kärnbränslehantering AB.

Goldstein T P, Aizenshtat Z, 1994. Thermochemical sulfate reduction. A review. Journal of Thermal Analysis and Calorimetry 42, 241–290.

Gómez J B, Laaksoharju M, Skårman E, Gurban I, 2009. M3 version 3.0: Verification and validation. SKB TR-09-05, Svensk Kärnbränslehantering AB.

Grandia F, 2013. Reply to comments and questions from SSM concerning Ba-Ra sulphate co-precipitation in canister. SKBdoc 1416537 ver 1.0, Svensk Kärnbränslehantering AB.

Grandia F, Merino J, Bruno J, 2008. Assessment of the radium-barium co-precipitation and its potential influence on the solubility of Ra in the near-field. SKB TR-08-07, Svensk Kärnbränslehantering AB.

Grenthe I, Fuger J, Konings R J M, Lemire R J, Muller A B, Nguyen-Trung C, Wanner H, 1992a. Chemical thermodynamics. Vol 1. Chemical thermodynamics of uranium. Amsterdam: North-Holland.

Grenthe I, Stumm W, Laaksoharju M, Nilsson A C, Wikberg P, 1992b. Redox potentials and redox reactions in deep groundwaters systems. Chemical Geology 98, 131–150.

Grivé M, Domènech C, Montoya V, García D, Duro L, 2010a. Simple Functions Spreadsheet tool presentation. SKB TR-10-61, Svensk Kärnbränslehantering AB.

Grivé M, Domènech C, Montoya V, García D, Duro L, 2010b. Determination and assessment of the concentration limits to be used in SR-Can. Supplement to TR-06-32. SKB R-10-50, Svensk Kärnbränslehantering AB.

Grivé M, Idiart A, Colàs E, Duro L, 2013a. Handling of uncertainty in thermodynamic data. Amphos21 Final report. SKBdoc 1396560 ver 1.0, Svensk Kärnbränslehantering AB.

Grivé M, García D, Campos I, Idiart A, Duro L, 2013b. Simple Functions Spreadsheet tool: Phosphates update and Temperature assessment. Amphos21 Final report. SKBdoc 1415884 ver 1.0, Svensk Kärnbränslehantering AB

Guillaumont R, Fanghänel J, Neck V, Fuger J, Palmer D A, Grenthe I, Rand M H, 2003. Chemical thermodynamics. Vol 5. Update on the chemical thermodynamics of uranium, neptunium, plutonium, americium and technetium. Amsterdam: Elsevier.

Hakala M, Siren T, Kemppainen K, Christiansson R, Martin D, 2013. In-situ stress measurements with the new LVDT-cell – method description and verification. Posiva 2012-43, Posiva Oy, Finland.

Hakala M, Ström J, Valli J, Juvani J, 2019. Structural control on stress variability at Forsmark. SKB R-19-23, Svensk Kärnbränslehantering AB.

Hakami E, 2011. Rock stress orientation measurements using induced thermal spalling in slim boreholes. SKB R-11-12, Svensk Kärnbränslehantering AB.

Hall A M, Ebert K, Goodfellow B W, Hättestrand C, Heyman J, Krabbendam M, Moon S, Stroeven A P, 2019. Past and future impact of glacial erosion in Forsmark and Uppland. Final report. SKB TR-19-07, Svensk Kärnbränslehantering AB.

Hallbeck L, Pedersen K, 2008. Explorative analysis of microbies, colloids and gases. SDM-Site Forsmark. SKB R-08-85, Svensk Kärnbränslehantering AB.

Hanson B, 2008. Examining the conservatisms in dissolution rates of commercial spent nuclear fuel. In Proceedings of the 12th International High-Level Waste Management Conference. Las Vegas, Nevada, 7–11 September 2008. New York: American Nuclear Society, 404–411.

Hansson B, Magnusson J, Söderlund P, 2009. Underground design Forsmark, Layout D2. Layout and construction plan. SKB R-08-113, Svensk Kärnbränslehantering AB.

Hartikainen J, Kouhia R, Wallroth T, 2010. Permafrost simulations at Forsmark using a numerical 2D thermo-hydro-chemical model. SKB TR-09-17, Svensk Kärnbränslehantering AB.

Hartley L J, Holton D, 2004. CONNECTFLOW Release 8.0 Technical Summary Document. SA/ERRA C/TSD02V1, Serco Assurance, UK.

Hartley L J, Cox I, Hunter F, Jackson C P, Joyce S, Swift B, Gylling B, Marsic N, 2005. Regional hydrogeological simulations for Forsmark – numerical modelling using CONNECTFLOW. Preliminary site description. Forsmark area – stage 1.2. SKB R-05-32, Svensk Kärnbränslehantering AB.

Hedin A, 2008. Semi-analytic stereological analysis of waste package/fracture intersections in a granitic rock nuclear waste repository. Mathematical Geosciences 40. doi:10.1007/s11004-008-9175-3

Hedin A, Kautsky U, 2015 Svar till SSM på begäran daterad 2013-02-11 om komplettering rörande radionuklidtransport och dos. SKBdoc 1418468 ver 2.0, Svensk Kärnbränslehantering AB. (In Swedish.)

Helmens K, 2013. The last interglacial-glacial cycle (MIS 5-2) re-examined based on long proxy records from central and northern Europe. SKB TR-13-02, Svensk Kärnbränslehantering AB.

Helmens K F, 2019. The last 130 000 years in Fennoscandia reconstructed based on a long and fossil-rich sediment sequence preserved at Sokli, northern Finland. New evidence for highly dynamic environmental and climate conditions. SKB TR-18-04, Svensk Kärnbränslehantering AB.

Hermanson J, Forssberg O, Fox A, La Pointe P, 2005. Statistical model of fractures and deformation zones. Preliminary site description, Laxemar subarea, version 1.2. SKB R-05-45, Svensk Kärnbränslehantering AB.

Hernelind J, 2010. Modelling and analysis of canister and buffer for earthquake induced rock shear and glacial load. SKB TR-10-34, Svensk Kärnbränslehantering AB.

Hiemenz P C, 1986. Principles of colloid and surface chemistry. 2nd ed. New York: Dekker.

Hjerne C, Nordqvist R, Harrström J, 2010. Compilation and analyses of results from cross-hole tracer tests with conservative tracers. SKB R-09-28, Svensk Kärnbränslehantering AB.

Huitti T, Hakanen M, Lindberg A, 1996. Sorption of cesium, radium, protactinium, uranium, neptunium, and plutonium on rapakivi granite. Posiva 96-23, Posiva Oy, Finland.

Hummel W, Berner U, 2002. Application of the Nagra/PSI TDB 01/01: solubility of Th, U, Np and Pu. Nagra Technical Report NTB 02-12, Nagra, Switzerland.

Hummel W, Berner U, Curti E, Pearson F J, Thoenen T, 2002. Nagra/PSI chemical thermodynamic data base 01/01. Boca Raton: Universal Publishers.

Hökmark H, Claesson J, 2005. Use of an analytical solution for calculating temperatures in repository host rock. Engineering Geology 81, 353–364.

Hökmark H, Fälth B, 2003. Thermal dimensioning of the deep repository. Influence of canister spacing, canister power, rock thermal properties and nearfield design on the maximum canister surface temperature. SKB TR-03-09, Svensk Kärnbränslehantering AB.

Hökmark H, Fälth B, Wallroth T, 2006. T-H-M couplings in rock. Overview of results of importance to the SR-Can safety assessment. SKB TR-06-88, Svensk Kärnbränslehantering AB.

Hökmark H, Lönnqvist M, Kristensson O, Sundberg J, Hellström G, 2009. Strategy for thermal dimensioning of the final repository for spent nuclear fuel. SKB R-09-04, Svensk Kärnbränslehantering AB.

Hökmark H, Lönnqvist M, Fälth B, 2010. THM-issues in repository rock. Thermal, mechanical, thermo-mechanical and hydro-mechanical evolution of the rock at the Forsmark and Laxemar sites. SKB TR-10-23, Svensk Kärnbränslehantering AB.

ICRP, 2006. Assessing dose of the representative person for the purpose of radiation protection of the public, and the optimisation of radiological protection: broadening the process. Oxford: Pergamon. (ICRP Publication 101; Annals of the ICRP 36)

Ishidera T, Miyamoto S, Sato H, 2008. Effect of sodium nitrate on the diffusion of Cl^- and I^- in compacted bentonite. Journal of Nuclear Science and Technology 45, 610–616.

Itasca, 2005a. UDEC – universal distinct element code, user's guide. Minneapolis, MN: Itasca Consulting Group, Inc.

Itasca, 2005b. FLAC – Fast lagrangian analysis of continua, user's guide. Minneapolis, MN: Itasca Consulting Group, Inc.

Itasca, 2007. 3DEC – 3-dimensional distinct element code, version 4.1, user's guide. Minneapolis, MN: Itasca Consulting Group, Inc.

IUPAC, 1997. Compendium of chemical terminology: IUPAC recommendations. 2nd ed. Oxford: Blackwell Science.

Jackson C P, Hoch A R, Todman S, 2000. Self-consistency of a heterogeneous continuum porous medium representation of a fractured medium. Water Resources Research 36, 189–202.

Jacobsson L, 2006. Forsmark site investigation. Borehole KFM09A. Uniaxial compression test of intact rock. SKB P-06-27, Svensk Kärnbränslehantering AB.

Jacobsson L, 2007. Forsmark site investigation. Boreholes KFM01A and KFM02B. Micro crack volume measurements and triaxial compression tests on intact rock. SKB P-07-93, Svensk Kärnbränslehantering AB.

Jacobsson L, Flansbjer M, 2005a. Forsmark site investigation. Borehole KFM05A. Normal stress test with direct and indirect deformation measurement together with shear tests on joints. SKB P-05-141, Svensk Kärnbränslehantering AB.

Jacobsson L, Flansbjer M, 2005b. Forsmark site investigation. Borehole KFM06A. Normal loading and shear tests on joints. SKB P-05-122, Svensk Kärnbränslehantering AB.

Jacobsson L, Flansbjer M, 2005c. Forsmark site investigation. Borehole KFM07A. Normal loading and shear tests on joints. SKB P-05-213, Svensk Kärnbränslehantering AB.

Jacobsson L, Flansbjer M, 2005d. Forsmark site investigation. Borehole KFM08A. Normal loading and shear tests on joints. SKB P-05-218, Svensk Kärnbränslehantering AB.

Jacobsson L, Flansbjer M, 2006. Forsmark site investigation. Borehole KFM09A. Normal loading and shear tests on joints. SKB P-06-29, Svensk Kärnbränslehantering AB.

Jacobsson L, Appelquist K, Lindqvist J-E, Åkesson U, 2018. Spalling initiation experiments on large hard rock cores. SKB R-14-12, Svensk Kärnbränslehantering AB.

Jégou C, Peuget S, Broudic V, Roudil D, Deschanels X, Bart J M, 2004. Identification of the mechanism limiting the alteration of clad spent fuel segments in aerated carbonated groundwater. Journal of Nuclear Materials 326, 144–155.

Johannesson L-E, Sandén T, Dueck A, Ohlsson L, 2010. Characterization of a backfill candidate material, IBECO-RWC-BF. Baclo Project – Phase 3. SKB R-10-44, Svensk Kärnbränslehantering AB.

Johansson F, Evins L Z, 2013. Svar till SSM på begäran om redovisning av bränslerester från Studsvikanläggningen. SKBdoc 1396040 ver 1.0, Svensk Kärnbränslehantering AB.

Johnson L H, Tait J C, 1997. Release of segregated nuclides from spent fuel. SKB TR 97-18, Svensk Kärnbränslehantering AB.

Johnson L H, Poinssot C, Ferry C, Lovera P, 2004. Estimates of the instant release fraction of UO_2 and MOX fuel at t = 0. Nagra NTB 04-08, Nagra, Switzerland.

Johnson L, Ferry C, Poinssot C, Lovera P, 2005. Spent fuel radionuclide source-term model for assessing spent fuel performance in geological disposal. Part I: Assessment of the instant release fraction. Journal of Nuclear Materials 346, 56–65.

Johnson L Günther-Leopold I, Kobler Waldis J, Linder H P, Low J, Cui D, Ekeroth E, Spahiu K, Evins L Z, 2012. Rapid aqueous release of fission products from high burn-up LWR fuel: Experimental results and correlations with fission gas release. Journal of Nuclear Materials 420, 54–62.

Jonsson M, Emilsson G, Emilsson L, 2018. Mechanical design analysis for the canister. Posiva SKB Report 04, Posiva Oy, Svensk Kärnbränslehantering AB.

Joyce S, Simpson T, Hartley L, Applegate D, Hoek J, Jackson P, Swan D, Marsic N, Follin S, 2010. Groundwater flow modelling of periods with temperate climate conditions – Forsmark. SKB R-09-20, Svensk Kärnbränslehantering AB.

Joyce S, Woollard H, Marsic N, Sidborn M, 2015. Future evolution of groundwater composition at Forsmark during an extended temperate period. SKB R-14-26, Svensk Kärnbränslehantering AB.

Karnland O, Sandén T, Johannesson L-E, Eriksen T E, Jansson M, Wold S, Pedersen K, Motamedi M, Rosborg B, 2000. Long term test of buffer material. Final report on the pilot parcels. SKB TR-00-22, Svensk Kärnbränslehantering AB.

Karnland O, Olsson S, Nilsson U, 2006. Mineralogy and sealing properties of various bentonites and smectite-rich clay materials. SKB TR-06-30, Svensk Kärnbränslehantering AB.

Karnland O, Olsson S, Dueck A, Birgersson M, Nilsson U, Hernan-Håkansson T, Pedersed K, Nilsson S, Eriksen T E, Rosborg B, 2009. Long term test of buffer material at the Äspö Hard Rock Laboratory, LOT project. Final report on the A2 test parcel. SKB TR-09-29, Svensk Kärnbränslehantering AB.

Kautsky U, 2015. Svar till SSM på begäran om komplettering rörande radionuklidtransport och dosberäkning med koppling till ythydrologi. SKBdoc 1440564 ver 2.0, Svensk Kärnbränslehantering AB. (In Swedish.)

Kienzler B, Duro L, Lemmens K, Metz V, De Pablo J, Valls A, Wegen D H, Johnson L, Spahiu K, 2017. Summary of the Euratom Collaborative Project FIRST – Nuclides and conclusions for the safety case. Nuclear Technology 198, 260–276.

Koyama T, 2007. Stress, flow and particle transport in rock fractures. PhD thesis. Royal Institute of Technology (KTH), Stockholm, Sweden.

Krishna R, Wesselingh J A, 1997. The Maxwell-Stephan approach to mass transfer. Chemical Engineering Science 52, 861–911.

Kudo K, Komatsu K, 1999. Reduction of alkali metal carbonate to methane with water in the presence of Raney alloy. Journal of Molecular Catalysis A: Chemical 145, 159–167.

Kuzyk G W, Martino J B, 2008. Development of excavation technologies at the Canadian Underground Research Laboratory. In Bäckblom G (ed). Proceedings of the International Conference Underground Disposal Unit Design & Emplacement Processes for a Deep Geological Repository, Prague, 16–18 June 2008.

Laaksoharju M, Gurban I, Skårman C, 1998. Summary of hydrochemical conditions at Aberg, Beberg and Ceberg. SKB TR 98-03, Svensk Kärnbränslehantering AB.

Laaksoharju M, Smellie J, Tullborg E-L, Gimeno M, Hallbeck L, Molinero J, Waber N, 2008. Bedrock hydrogeochemistry Forsmark. Site descriptive modelling, SDM-Site Forsmark. SKB R-08-47, Svensk Kärnbränslehantering AB.

Laaksoharju M, Smellie J, Tullborg E-L, Wallin B, Drake H, Gascoyne M, Gimeno M, Gurban I, Hallbeck L, Molinero J, Nilsson A-C, Waber N, 2009. Bedrock hydrogeochemistry Laxemar. Site descriptive modelling, SDM-Site Laxemar. SKB R-08-93, Svensk Kärnbränslehantering AB.

Lambeck K, 2005. Glacial load stresses: Can existing faults or other zones of crustal weakness be reactivated during glacial cycles? In Hora S, Jensen M (eds). Expert panel elicitation of seismicity following glaciation in Sweden. SSI Report 2005:20, Swedish Radiation Protection Authority.

Lanaro F, Fredriksson A, 2005. Rock Mechanics Model – Summary of the primary data. Preliminary site description Forsmark area – version 1.2. SKB R-05-83, Svensk Kärnbränslehantering AB.

La Pointe P R, Olofsson I, Hermanson J, 2005. Statistical model of fractures and deformation zones for Forsmark. Preliminary site description Forsmark area – version 1.2. SKB R-05-26, Svensk Kärnbränslehantering AB.

La Pointe P, Fox A, Hermanson J, Öhman J, 2008. Geological discrete fracture network model for the Laxemar site. Site descriptive modelling, SDM-Site Laxemar. SKB R-08-55, Svensk Kärnbränslehantering AB.

Lau J O S, Jackson R, Gorski B, 1991. The effects of temperature and pressure on the mechanical properties of Lac du Bonnet grey granite. In Roegiers J-C (ed). Rock mechanics as a multidisciplinary science: proceedings of the 32nd US Symposium on Rock Mechanics, University of Oklahoma, Norman, 10–12 July 1991. Rotterdam: Balkema.

Lehikoinen J, Muurinen A, Olin M, Uusheimo K, Valkiainen M, 1992. Diffusivity and porosity studies in rock matrix. The effect of salinity. Espoo: Technical Research Centre of Finland. (VTT Research Notes 1394)

Lemire R J, Fuger J, Nitsche H, Potter P, Rand M H, Rydberg J, Spahiu K, Sullivan J C, Ullman W J, Vitorge P, Wanner H, 2001. Chemical thermodynamics. Vol. 4. Chemical thermodynamics of neptunium and plutonium. Amsterdam: Elsevier.

Lemmens K, González-Robles E, Kienzler B, Curti E, Serrano-Purroy D, Sureda R, Martínez-Torrents A, Roth O, Slonszki E , Mennecart T, Günther-Leopold I, Z. Hozer H, 2017. Instant release of fission products in leaching experiments with high burnup nuclear fuels in the framework of the Euratom project FIRST-Nuclides. Journal of Nuclear Materials 484, 307–323.

Lilja C, 2012. Inre övertryck i kapseln. SKBdoc 1333208 ver 2.0, Svensk Kärnbränslehantering AB.

Lindborg T (ed), 2008. Surface system Forsmark. Site descriptive modelling, SDM-Site Forsmark. SKB R-08-11, Svensk Kärnbränslehantering AB.

Liu H-H, Rutqvist J, Zhou Q, Bodvarsson G S, 2003. Upscaling of normal stress-permeability relationships for fracture networks obeying fractional Levy motion. In GeoProc 2003: proceedings of the International Conference on Coupled T-H-M-C processes in Geo-systems: Fundamentals, Modelling, Experiments & Applications, Stockholm, Sweden, 13–15 October 2003. Royal Institute of Technology, Sweden.

Liu J, Löfgren M, Neretnieks I, 2006. SR-Can. Data and uncertainty assessment. Matrix diffusivity and porosity in situ. SKB R-06-111, Svensk Kärnbränslehantering AB.

Liu N, Qin Z, Noël J J, Shoesmith D W, 2017. Modelling the radiolytic corrosion of α-doped UO_2 and spent nuclear fuel. Journal of Nuclear Materials 494, 87–94.

Ludvigson J-E, Hansson K, Rouhiainen P, 2002. Methodology study of Posiva difference flow meter in borehole KLX02 at Laxemar. SKB R-01-52, Svensk Kärnbränslehantering AB.

Lund B, Schmidt P, Hieronymus C, 2009. Stress evolution and fault stability during the Weichselian glacial cycle. SKB TR-09-15, Svensk Kärnbränslehantering AB.

Löfgren M, 2004. Diffusive properties of granitic rock as measured by in situ electrical methods. PhD thesis. Royal Institute of Technology, Stockholm, Sweden.

Löfgren M, 2007. Forsmark site investigation. Formation factor logging in situ by electrical methods in KFM01D and KFM08C. SKB P-07-138, Svensk Kärnbränslehantering AB.

Löfgren M. 2014. Artefacts associated with electrical measurements of the rock matrix formation factor Artefacts associated with electrical measurements of the rock matrix formation factor. SKBdoc 1417017 ver 1.0 , Svensk Kärnbränslehantering AB.

Löfgren M, 2015. Artefacts associated with electrical measurements of the rock matrix formation factor With comments on handling in, and potential consequences for, the safety assessment SR-Site. SKB R-14-20, Svensk Kärnbränslehantering AB.

Löfgren M, Neretnieks I, 2002. Formation factor logging in situ by electrical methods. Background and methodology. SKB TR-02-27, Svensk Kärnbränslehantering AB.

Löfgren M, Neretnieks I, 2006. Through-electromigration: A new method of investigating pore connectivity and obtaining formation factors. Journal of Contaminant Hydrology 87, 273–252.

Löfgren M, Pettersson M, Widén H, Crawford J, 2006. Forsmark site investigation. Formation factor logging in situ by electrical methods in KFM05A and KFM06A. SKB P-06-91, Svensk Kärnbränslehantering AB.

Löfgren M, Crawford J, Elert M, 2007. Tracer tests – possibilities and limitations. Experience from SKB fieldwork: 1977–2007. SKB R-07-39, Svensk Kärnbränslehantering AB.

Löfgren M, Večernik P, Havlova V, 2009. Studying the influence of pore water electrical conductivity on the formation factor, as estimated based on electrical methods. SKB R-09-57, Svensk Kärnbränslehantering AB.

Lönnqvist M, Hökmark H, 2010. Assessment of potential for glacially induced hydraulic jacking at different depths. SKB R-09-35, Svensk Kärnbränslehantering AB.

Martin C D, 2005. Preliminary assessment of potential underground stability (wedge and spalling) at Forsmark, Simpevarp and Laxemar sites. SKB R-05-71, Svensk Kärnbränslehantering AB.

Martin C D, 2007. Quantifying in situ stress magnitudes and orientations for Forsmark. Forsmark stage 2.2. SKB R-07-26, Svensk Kärnbränslehantering AB.

Martin C D, Davison C C, Kozak E T, 1990. Characterizing normal stiffness and hydraulic conductivity of a major shear zone in granite. In: Barton N, Stephansson O (eds). Rock joints: proceedings of the International Symposium on Rock Joints, Loen, Norway, 4–6 June 1990. Rotterdam: Balkema.

Mihara M, 2000. The comparison concerned with hydraulic conductivities and effective diffusion coefficients for nuclides between Na and Ca bentonite. JNC Technical Note 1340, Japan Nuclear Cycle Development Institute, Ibarabi, Japan, 61–68.

Miller W, Alexander R, Chapman N, McKinley I, Smellie J, 1994. Natural analogue studies in the geological disposal of radioactive waste. Amsterdam: Elsevier. (Studies in Environmental Science 57)

Muir Wood R, 1995. Reconstructing the tectonic history of Fennoscandia from its margins: The past 100 million years. SKB TR 95-36, Svensk Kärnbränslehantering AB.

Munier R, 2004. Statistical analysis of fracture data, adapted for modelling Discrete Fracture Networks-Version 2. SKB R-04-66, Svensk Kärnbränslehantering AB.

Munier R, 2006. Using observations in deposition tunnels to avoid intersections with critical fractures in deposition holes. SKB R-06-54, Svensk Kärnbränslehantering AB.

Munier R, 2007. Demonstrating the efficiency of the EFPC criterion by means of Sensitivity analyses. SKB R-06-115, Svensk Kärnbränslehantering AB.

Munier R, 2010. Full perimeter intersection criteria. Definitions and implementations in SR-Site. SKB TR-10-21, Svensk Kärnbränslehantering AB.

Munier R, Hökmark H, 2004. Respect distances. Rationale and means of computation. SKB R-04-17, Svensk Kärnbränslehantering AB.

Munier R, Stigsson M, 2007. Implementation of uncertainties in borehole geometries and geological orientation data in Sicada. SKB R-07-19, Svensk Kärnbränslehantering AB.

Muurinen A, Penttilä-Hiltunen P, Uusheimo K, 1989. Diffusion of chloride and uranium in compacted sodium bentonite. In: Lutze W, Ewing, R C (eds). Scientific basis for nuclear waste management XII: symposium held in Berlin, Germany, 10–13 October 1988. Pittsburgh, PA: Materials Research Society. (Materials Research Society Symposium Proceedings 127), 743–748.

Muzeau B, Jégou C, Delaunay F, Broudic V, Brevet A, Catalette H, Simoni E, Corbel C, 2009. Radiolytic oxidation of UO_2 pellets doped with alpha emitters ($^{238/239}Pu$). Journal of Alloys and Compounds 467, 578–589.

Mårtensson E, Gustafsson L-G, 2010. Hydrological and hydrogeological effects of an open repository in Forsmark. Final MIKE SHE flow modelling results for the Environmental Impact Assessment. SKB R-10-18, Svensk Kärnbränslehantering AB.

Möri A, Mazurek M, Adler M, Schild M, Siegesmund S, Vollbrecht A, Ota K, Ando T, Alexander W R, Smith P A, Haag P, Bühler C, 2003. The Nagra-JNC in situ study of safety relevant radionuclide retardation in fractured crystalline rock. IV: The in situ study of matrix porosity in the vicinity of a water conducting fracture. Nagra Technical Report 00-08, National Cooperative for the Disposal of Radioactive Waste, Switzerland.

NEA, 2005. NEA Sorption Project, phase II: interpretation and prediction of radionuclide sorption onto substrates relevant for radioactive waste disposal using thermodynamic sorption models. Paris: Nuclear Energy Agency, OECD.

Neretnieks I, 2006. Flow and solute transport in a zone damaged due to spalling. SKB R-06-91, Svensk Kärnbränslehantering AB.

Neretnieks I, Andersson J C, 2009. Characterisation of spalling fragments to obtain data for flow and transport in damaged zones. In Proceedings of the ISRM-Sponsored international symposium on rock mechanics: ”Rock characterisation, modelling and engineering design methods” (SINOROCK 2009) held at the University of Hong Kong, China, 19–22 May 2009.

Neretnieks I, Liu L, Moreno L, 2009. Mechanisms and models for bentonite erosion. SKB TR-09-35, Svensk Kärnbränslehantering AB.

Neretnieks I, Liu L, Moreno L, 2010. Mass transfer between waste canister and water seeping in rock fractures. Revisiting the Q-equivalent model. SKB TR-10-42, Svensk Kärnbränslehantering AB.

Nilsson A-C, 2008. Analytical uncertainties. In Kalinowski B E (ed). Background complementary hydrogeochemical studies. SDM-Site Forsmark. SKB R-08-87, Svensk Kärnbränslehantering AB, 139–154.

Nilsson K, Byegård J, Selnert E, Widestrand H, Höglund S, Gustafsson E, 2010. Äspö Hard Rock Laboratory. Long Term Sorption Diffusion Experiment (LTDE-SD). Results from rock sample analyses and modelling. SKB R-10-68, Svensk Kärnbränslehantering AB.

NIST, 2007. Gamma distribution, Chapter 1.3.6.11, NIST/SEMATECH e-handbook of statistical methods, National Institute of Standards and Technology, United States Department of Commerce, Washington DC. Available at: http://www.itl.nist.gov/div898/handbook/eda/section3/eda366b.htm

Nordén S, Avila R, de la Cruz I, Stenberg K, Grolander S, 2010. Element-specific and constant parameters used for dose calculations in SR-Site. SKB TR-10-07, Svensk Kärnbränslehantering AB.

Nordström E, 2009. Fission gas release data for Ringhals PWRs. SKB TR-09-26, Svensk Kärnbränslehantering AB.

Norman S, Kjellbert N, 1990. FARF31 – A far field radionuclide migration code for use with the PROPER package. SKB TR 90-01, Svensk Kärnbränslehantering AB.

NRC, 1996. Rock fractures and fluid flow: contemporary understanding and applications. Washington DC: National Academy Press.

Näslund J-O, 2021. Climate data used in the PSAR for the Spent nuclear fuel repository. SKBdoc 1927730 ver 1.0, Svensk Kärnbränslehantering AB. (Internal document.)

Ochs M, Lothenbach B, Wanner H, Sato H, Yui M, 2001. An integrated sorption-diffusion model for the calculation of consistent distribution and diffusion coefficients in compacted bentonite. Journal of Contaminant Hydrology 47, 283–296.

Ochs M, Talerico C, 2004. SR-Can. Data and uncertainty assessment. Migration parameters for the bentonite buffer in the KBS-3 concept. SKB TR-04-18, Svensk Kärnbränslehantering AB.

Odorowski M, Jégou C, de Windt L, Broudic V, Jouan G, Peuget S, Martin C, 2017. Effect of metallic iron on the oxidative dissolution of UO_2 doped with a radioactive alpha emitter in synthetic Callovo-Oxfordian water. Geochimica et Cosmochimica Acta 219, 1–21.

Ohlsson Y, 2000. Studies of ionic diffusion in crystalline rock. PhD thesis. Royal Institute of Technology, Stockholm, Sweden.

Oldberg K, 2009. Distribution of fission gas release in 10 × 10 fuel. SKB TR-09-25, Svensk Kärnbränslehantering AB.

Olin Å, Noläng B, Osadchii E G, Öhman L O, Rosén E, 2005. Chemical thermodynamics. Vol 7. Chemical thermodynamics of selenium. Amsterdam: Elsevier.

Ollila K, Myllykylä E, Tanhua-Tyrkkö M, LavonenT, 2013. Dissolution rate of alpha-doped UO_2 in natural groundwater. Journal of Nuclear Materials 442, 320–325.

Olofsson I, Simeonov A, Stephens M, Follin S, Nilsson A-C, Röshoff K, Lindberg U, Lanaro F, Fredriksson A, Persson L, 2007. Site descriptive modelling Forsmark, stage 2.2. A fracture domain concept as a basis for the statistical modelling of fractures and minor deformation zones, and interdisciplinary coordination. SKB R-07-15, Svensk Kärnbränslehantering AB.

Olsson M, Niklasson B, Wilson L, Andersson C, Christiansson R, 2004. Äspö HRL. Experiences of blasting of the TASQ tunnel. SKB R-04-73, Svensk Kärnbränslehantering AB.

Olsson M, Markström I, Pettersson A, Sträng M, 2009. Examination of the Excavation Damage Zone in the TASS tunnel, Äspö HRL. SKB R-09-39, Svensk Kärnbränslehantering AB.

Olsson R, 1998. Mechanical and hydromechanical behaviour of hard rock joints: a laboratory study. PhD thesis. Chalmers University of Technology, Sweden.

Oscarson D W, Hume H B, Sawatsky N G, Cheung S C H, 1992. Diffusion of iodide in compacted bentonite. Soil Science Society of American Journal 56, 1400–1406.

Painter S, Mancillas J, 2009. MARFA version 3.2.2 user's manual: migration analysis of radionuclides in the far field. SKB R-09-56, Svensk Kärnbränslehantering AB.

Parkhurst D L, Appelo C A J, 1999. User's guide to PHREEQC (version 2): a computer program for speciation, batch-reaction, one-dimensional transport, and inverse geochemical calculations. Denver, CO: U.S. Geological Survey. (Water-resources investigations report 99-4259.)

Parkhurst D L, Appelo C A J, 2001. User's guide to PHREEQC (Version 2.4.6): a computer program for speciation, batch-reaction, one-dimensional transport and inverse geochemical calculations. Denver, CO: U.S. Geological Survey.

Pellikka H, Särkää J, Johansson M, Pettersson H, 2020. Probability distributions for mean sea level and storm contribution up to 2100 AD at Forsmark. SKB TR-19-23, Svensk Kärnbränslehantering AB.

Penttinen L, Siitari-Kauppi M, Ikonen J, 2006. Forsmark site investigation. Determination of porosity and micro fracturing using the ^{14}C-PMMA technique in samples taken from Forsmark area. SKB P-06-60, Svensk Kärnbränslehantering AB.

Pipon Y, Toulhoat N, Moncoffre N, Bererd N, Jaffrezic H, Barthe M F, Desgardin P, Raimbault L, Scheidegger A M, Carlot G, 2007. Chlorine diffusion in uranium dioxide: thermal effects versus radiation enhanced effects. In Dunn D, Poinssot C, Begg B (eds). Scientific basis for nuclear waste management XXX. Warrendale, PA: Materials Research Society. (Materials Research Society Symposium Proceedings 985), NN05-03.

PNL, 1991. Characterization of spent fuel approved testing material – ATM-104. Report PNL-5109-104/UC-802, Pacific Northwest Laboratory.

Posiva SKB, 2017. Safety functions, performance targets and technical design requirements for a KBS-3V repository. Conclusions and recommendations from a joint SKB and Posiva working group. Posiva SKB Report 01, Posiva Oy, Svensk Kärnbränslehantering AB.

Potyondy D O, Mas Ivars D, 2020. Simulating spalling with a flat-jointed material. In Billaux D, Hazzard J, Nelson M, Schöpfer M (eds.) Proceedings of the 5th International Itasca Symposium, Vienna, 17–20 February 2020. Minneapolis: Itasca International, Inc., Paper: 03-01.

Puigdomenech I, 2002. MEDUSA (Make Equilibrium Diagrams Using Sophisticated Algorithms) Windows interface to the MS-DOS versions of INPUT, SED and PREDOM (FORTRAN programs drawing chemical equilibrium diagrams) Vers. 31 July. 2002. Royal Institute of Technology (KTH), Stockholm.

Puranen A, Barreiro A, Evins L Z, Spahiu K, 2017. Spent fuel leaching in the presence of corroding iron. MRS Advances 2, 681–686.

Puranen A, Roth O, Evins L Z, Spahiu K, 2018. Aqueous leaching of high burnup UO_2 fuel under hydrogen conditions. MRS Advances 3, 1013–1018.

Quiquet A, Colleoni F, Masina S, 2016. Long-term safety of a planned geological repository for spent nuclear fuel in Forsmark, Sweden and Olkiluoto, Finland. Phase 2: impact of ice sheet dynamics, climate forcing and multi-variate sensitivity analysis on maximum ice sheet thickness. SKB TR-16-02, Svensk Kärnbränslehantering AB.

Raiko H, Sandström R, Rydén H, Johansson M, 2010. Design analysis report for the canister. SKB TR-10-28, Svensk Kärnbränslehantering AB.

Ramebäck H, Albinsson A, Skålberg M, Eklund U B, Kjellberg L, Werme L, 2000. Transport and leaching of technetium and uranium from spent UO_2 fuel in compacted bentonite clay. Journal of Nuclear Materials 277, 288–294.

Ramebäck H, Albinsson A, Skålberg M, Eklund U B, Kjellberg L, Werme L, 2000. Transport and leaching of technetium and uranium from spent UO_2 fuel in compacted bentonite clay. Journal of Nuclear Materials 277, 288–294.

Rand M, Fuger J, Grenthe I, Neck V, Rai D, 2009. Chemical thermodynamics. Vol 11. Chemical thermodynamics of thorium. Paris: Nuclear Energy Agency, OECD.

Rard J A, Rand M H, Anderegg G, Wanner H, 1999. Chemical thermodynamics. Vol 3. Chemical thermodynamics of technetium. Amsterdam: Elsevier.

Rasilainen K, Hölttä P, Siitari-Kauppi M, Suksi J, Lehikoinen J, Valkiainen M, Timonen J, Lindberg A, Marcos N, 2001. Retardation mechanism studies for performance assessments. Espoo: Technical Research Centre of Finland. (VTT Research notes 2096.)

RETROCK, 2004. RETROCK Project. Treatment of geosphere retention phenomena in safety assessments. Scientific basis of retention processes and their implementation in safety assessment models (WP2). SKB R-04-48, Svensk Kärnbränslehantering AB.

Revil A, Glover P W J, 1997. Theory of ionic-surface electrical conduction in porous media. Physical Review B 55, 1757–1773.

Romero L, Thompson A, Moreno L, Neretnieks I, Widén H, Boghammar A, 1999. Comp23/ Nuctran user's guide. Proper version 1.1.6. SKB R-99-64, Svensk Kärnbränslehantering AB.

Rutqvist J, Tsang C-F, 2008. Review of SKB's work on coupled THM processes within SR-Can. External review contribution in support of SKI's and SSI's review of SR-Can. SKI Report 2008:08, Swedish Nuclear Power Inspectorate.

Saceanu M C, Paluszny A, Zimmerman R W, Mas Ivars D, 2020. Numerical modelling of spalling around a nuclear waste storage deposition borehole using a fracture mechanics approach. Published at 54TH US Rock Mechanics / Geomechanics Symposium – ARMA2020 (ARMA 20–1396), Colorado School of Mines, Golden, Colorado, 28 June – 1 July 2020.

Salas J, Gimeno M J, Auqué L, Molinero J, Gómez J, Juárez I, 2010. SR-Site – hydrogeochemical evolution of the Forsmark site. SKB TR-10-58, Svensk Kärnbränslehantering AB.

Sandström B, Stephens M, 2009. Mineralogy, geochemistry, porosity and redox properties of rocks from Forsmark. Compilation of data from the regional model volume for SR-Site. SKB R-09-51, Svensk Kärnbränslehantering AB.

Sandström B, Tullborg E-L, 2006. Forsmark site invetigation. Mineralogy, geochemistry, protosity and redox capacity of altered rock adjacent to fractures. SKB P-06-209, Svensk Kärnbränslehantering AB.

Sandström B, Tullborg E-L, Smellie J, MacKenzie A B, Suksi J, 2008. Fracture mineralogy of the Forsmark site. SDM-Site Forsmark. SKB R-08-102, Svensk Kärnbränslehantering AB.

Santos B G, Noël J J, Shoesmith D W, 2006. The influence of Ca ions on the development of acidity in corrosion product deposits on SIMFUEL, UO_2. Journal of Nuclear Materials 350, 320–331.

Sato H, 1998. Data setting for effective diffusion coefficients (D_e) of nuclides in the buffer for reference case in performance assessments of the geological disposal of high-level radioactive waste (I). PNC Technical Report TN8410 98–097, Power Reactor and Nuclear Fuel Development Corporation, Japan.

Sato H, Ashida T, Kohara Y, Yui M, Sasaki N, 1992. Effect of dry density on diffusion of some radionuclides in compacted sodium bentonite. Journal of Nuclear Science and Technology 29, 873–882.

Sato H, Ashida T, Kohara Y, Yui M, 1993. Study on retardation mechanism of ^{3}H, ^{99}Tc, ^{137}Cs, ^{237}Np, and ^{241}Am in compacted sodium bentonite. In Interrante C G, Pabalan R T (eds). Scientific Basis for Nuclear Waste Management XVI. Pittsburgh, PA: Materials Research Society. (Materials Research Society Symposium Proceedings 294), 403–408.

Schenk F, Wohlfarth B, 2019. The imprint of hemispheric-scale climate transitions on the European climate during the last deglaciation (15.5 ka to 9 ka BP). SKB TR-18-05, Svensk Kärnbränslehantering AB.

Seipold U, Huenges E, 1998. Thermal properties of gneisses and amphibolites – high pressure and high temperature investigations of KTB-rock samples. Tectonophysics 291, 173–178.

Selnert E, Byegård J, Widestrand H, 2008. Forsmark site investigation. Laboratory measurements within the site investigation programme for the transport properties of the rock. Final report. SKB P-07-139, Svensk Kärnbränslehantering AB.

Selroos J-O, Follin S, 2010. SR-Site groundwater flow modelling methodology, setup and results. SKB R-09-22, Svensk Kärnbränslehantering AB.

Serco Assurance, 2005. ConnectFlow Release 9.0 Technical Summary Document. SA/ ENV/ CONNECTFLOW/15, Serco Assurance, UK.

Sidborn M, Sandström B, Tullborg E-L, Salas J, Maia F, Delos A, Molinero J, Hallbeck L, Pedersen K, 2010. SR-Site: Oxygen ingress in the rock at Forsmark during a glacial cycle. SKB TR-10-57, Svensk Kärnbränslehantering AB.

Sidborn M, Marsic N, Crawford J, Joyce S, Hartley L, Idiart A, de Vries L M , Maia F, Molinero J, Svensson U, Vidstrand P, Alexander R, 2014. Potential alkaline conditions for deposition holes of a repository in Forsmark as a consequence of OPC grouting. Revised final report after review. SKB R-12-17, Svensk Kärnbränslehantering AB.

Silva R J, Bidoglio G, Rand M H, Robouch P B, Wanner H, Puigdomenech I, 1995. Chemical thermodynamics. Vol. 2. Chemical thermodynamics of americium. Amsterdam: Elsevier.

Singh B, 2016. Nuclear data sheets for A = 79. Nuclear Data Sheets 135, 193–382.

Singh S, Jain A K, Tuli J K, 2011. Nuclear data sheets for A = 222. Nuclear Data Sheets 112, 2851–2886.

Siren T, Hakala M, Valli J, Christiansson R, Mas Ivars D, Lam T, Mattila J, Suikkanen J, 2017. Parametrisation of fractures – Final report. Posiva 2017-01, Posiva Oy, Finland.

Skagius K, Neretnieks I, 1986. Diffusion in crystalline rocks of some sorbing and nonsorbing species. In Skagius K. Diffusion of dissolved species in the matrix of some Swedish crystalline rocks. PhD thesis. Royal Institute of Technology, Stockholm, Sweden.

SKB, 1999a. Deep repository for spent nuclear fuel. SR 97 – Post-closure safety. Main report – Vol I, Vol II and Summary. SKB TR-99-06, Svensk Kärnbränslehantering AB.

SKB, 1999b. SR 97 – Processes in the repository evolution. Background report to SR 97. SKB TR-99-07, Svensk Kärnbränslehantering AB.

SKB, 2002. Forsmark – site descriptive model version 0. SKB R-02-32, Svensk Kärnbränslehantering AB.

SKB, 2004. Preliminary site description. Forsmark area – version 1.1. SKB R-04-15, Svensk Kärnbränslehantering AB.

SKB, 2005. Preliminary site description. Forsmark area – version 1.2. SKB R-05-18, Svensk Kärnbränslehantering AB.

SKB, 2006a. Long-term safety for KBS-3 repositories at Forsmark and Laxemar – a first evaluation. Main report of the SR-Can project. SKB TR-06-09, Svensk Kärnbränslehantering AB.

SKB, 2006b. Data report for the safety assessment SR-Can. SKB TR-06-25, Svensk Kärnbränslehantering AB.

SKB, 2006c. Climate and climate-related issues for the safety assessment SR-Can. SKB TR-06-23, Svensk Kärnbränslehantering AB.

SKB, 2006d. Site descriptive modelling Forsmark stage 2.1. Feedback for completion of the site investigation including input from safety assessment and repository engineering. SKB R-06-38, Svensk Kärnbränslehantering AB.

SKB, 2007. Final repository facility. Underground design premises/D2. SKB R-07-33, Svensk Kärnbränslehantering AB.

SKB, 2008. Confidence assessment. Site descriptive modelling, SDM-Site Forsmark. SKB R-08-82, Svensk Kärnbränslehantering AB.

SKB, 2009a. Underground design Forsmark. Layout D2. SKB R-08-116, Svensk Kärnbränslehantering AB.

SKB, 2009b. Design premises for a KBS-3V repository based on results from the safety assessment SR-Can and some subsequent analyses. SKB TR-09-22, Svensk Kärnbränslehantering AB.

SKB, 2009c. Site description of Laxemar at completion of the site investigation phase SDM-Site Laxemar. SKB TR-09-01, Svensk Kärnbränslehantering AB.

SKB, 2009d. Site engineering report Forsmark. Guidelines for underground design. Step D2. SKB R-08-83, Svensk Kärnbränslehantering AB.

SKB, 2009e. Äspö Hard Rock Laboratory. Annual report 2008. SKB TR-09-10, Svensk Kärnbränslehantering AB.

SKB, 2010a. Data report for the safety assessment SR-Site. SKB TR-10-52, Svensk Kärnbränslehantering AB.

SKB, 2010b. Spent nuclear fuel for disposal in the KBS-3 repository. SKB TR-10-13, Svensk Kärnbränslehantering AB.

SKB, 2010c. Radionuclide transport report for the safety assessment SR-Site. SKB TR-10-50, Svensk Kärnbränslehantering AB.

SKB, 2010d. Corrosion calculations report for the safety assessment SR-Site. SKB TR-10-66, Svensk Kärnbränslehantering AB.

SKB, 2010e. Fuel and canister process report for the safety assessment SR-Site. SKB TR-10-46, Svensk Kärnbränslehantering AB.

SKB, 2010f. Design, construction and initial state of the underground openings. SKB TR-10-18, Svensk Kärnbränslehantering AB.

SKB, 2010g. Climate and climate related issues for the safety assessment SR-Site. SKB TR-10-49, Svensk Kärnbränslehantering AB.

SKB, 2010h. Geosphere process report for the safety assessment SR-Site. SKB TR-10-48, Svensk Kärnbränslehantering AB.

SKB, 2011. Long-term safety for the final repository for spent nuclear fuel at Forsmark. Main report of the SR-Site project. SKB TR-11-01, Svensk Kärnbränslehantering AB.

SKB, 2014. Biosphere synthesis report for the safety assessment SR-PSU. SKB TR-14-06, Svensk Kärnbränslehantering AB.

SKB, 2019a. Supplementary information on canister integrity issues. SKB TR-19-15, Svensk Kärnbränslehantering AB.

SKB, 2019b. Biosphere synthesis for the safety evaluation SE-SFL. SKB TR-19-05, Svensk Kärnbränslehantering AB.

Slagle O D, Davis N C, Parchen L J, 1994. AVLIS modified direct denitration: UO_3 powder evaluation. PNL-8481, Pacific Northwest Laboratory, Richland, WA.

Smart N R, Blackwood D J, Werme L, 2002a. Anaerobic corrosion of carbon steel and cast iron in artificial groundwaters: Part 1 – Electrochemical aspects. Corrosion 58, 547–559.

Smart N R, Blackwood D J, Werme L, 2002b. Anaerobic corrosion of carbon steel and cast iron in artificial groundwaters: Part 2 – Gas generation. Corrosion 58, 627–637.

Smellie J, Tullborg E-L, Nilsson A-C, Sandström B, Waber N, Gimeno M, Gascoyne M, 2008. Explorative analysis of major components and isotopes. SDM-Site Forsmark. SKB R-08-84, Svensk Kärnbränslehantering AB.

Sokolnicki M, Pöllänen J, Pekkanen J, 2006. Forsmark site investigation. Difference flow logging in borehole KFM10A. SKB P-06-190, Svensk Kärnbränslehantering AB.

Spahiu K, 2012. Svar till SSM på begäran om komplettering om inverkan av vätgas på bränsleupplösning.. SKBdoc 1372969 ver 1.0. Svensk Kärnbränslehantering AB. (In Swedish.)

Spahiu K, Evins L Z, 2014. Svar till SSM på begäran om förtydligande angående bränsleupplösning. SKBdoc 1452302 ver 1.0 Svensk Kärnbränslehantering AB. (In Swedish.)

Spahiu K, Werme L, Eklund U-B, 2000. The influence of near field hydrogen on actinide solubilities and spent fuel leaching. Radiochimica Acta 88, 507–511.

Spahiu K, Cui D, Lundström M, 2004. The fate of radiolytic oxidants during spent fuel leaching in the presence of dissolved near field hydrogen. Radiochimica Acta 92, 625–629.

SSM, 2008. Strålsäkerhetsmyndighetens föreskrifter och allmänna råd om skydd av människors hälsa och miljön vid slutligt omhändertagande av använt kärnbränsle och kärnavfall (The Swedish Radiation Safety Authority's Regulations on the Protection of Human Health and the Environment in connection with the Final Management of Spent Nuclear Fuel and Nuclear Waste) (in Swedish). Stockholm: Swedish Radiation Safety Authority. (SSMFS 2008:37)

SSM, 2018. Strålsäkerhet efter slutförvarets förslutning. SSM Report 2018:07, Swedish Radiation Safety Authority. (In Swedish.)

Stenhouse M, Jégou C, Brown P, Meinrath G, Nitsche H, Ekberg C, 2008. Review of SR-Can: Evaluation of SKB's handling of spent fuel performance, radionuclide chemistry and geosphere transport parameters. External review contribution in support of SKI's and SSI's review of SR-Can. SKI Report 2008:17, Swedish Nuclear Power Inspectorate.

Stephens M B, Simeonov A, 2015. Description of deformation zone model version 2.3, Forsmark. SKB R-14-18, Svensk Kärnbränslehantering AB.

Stephens M B, Fox A, La Pointe P R, Simeonov A, Isaksson H, Hermanson J, Öhman J, 2007. Geology Forsmark. Site descriptive modelling Forsmark stage 2.2. SKB R-07-45, Svensk Kärnbränslehantering AB.

Stigsson M, 2019. Structural uncertainties of rock fractures and their effect on flow and tracer transport. PhD thesis. KTH Royal Institute of Technology, Stockholm, Sweden.

Stigsson M, Mas Ivars D, 2019. A novel conceptual approach to objectively determine JRC using fractal dimension and asperity distribution of mapped fracture traces. Rock Mechanics and Rock Engineering 52, 1041–1054.

Stumm W, Morgan J J, 1996. Aquatic chemistry: chemical equilibria and rates in natural waters. 3rd ed. New York: Wiley.

Sundberg J, Back P-E, Bengtsson A, Ländell M, 2005a. Thermal modelling. Preliminary site description Forsmark area – version 1.2. SKB R-05-31, Svensk Kärnbränslehantering AB.

Sundberg J, Back P-E, Hellström G, 2005b. Scale dependence and estimation of rock thermal conductivity. Analysis of upscaling, inverse thermal modelling and value of information with the Äspö HRL prototype repository as an example. SKB R-05-82, Svensk Kärnbränslehantering AB.

Sundberg J, Wrafter J, Ländell M, Back P E, Rosén L, 2008a. Thermal properties Forsmark. Modelling stage 2.3. Complementary analysis and verification of the thermal bedrock model, stage 2.2. SKB R-08-65, Svensk Kärnbränslehantering AB.

Sundberg J, Wrafter J, Back P-E, Rosén L, 2008b. Thermal properties Laxemar. Site descriptive modelling, SDM-Site Laxemar. SKB R-08-61, Svensk Kärnbränslehantering AB.

Sundberg J, Wrafter J, Mossmark F, Sundberg A, 2008c. Forsmark site investigation. Anisotropy of thermal properties in granite at Forsmark. Large-scale field measurements and comparison with small-scale field measurements and laboratory measurements. SKB P-07-194, Svensk Kärnbränslehantering AB.

Sundberg J, Back P-E, Ländell M, Sundberg A, 2009a. Modelling of temperature in deep boreholes and evaluation of geothermal heat flow at Forsmark and Laxemar. SKB TR-09-14, Svensk Kärnbränslehantering AB.

Sundberg J, Back P-E, Ericsson L O, Wrafter J, 2009b. Estimation of thermal conductivity and its spatial variability in igneous rocks from in situ density logging. International Journal of Rock Mechanics and Mining Sciences 46, 1023–1028.

Sundberg J, Back P-E, Ländell M, Sundberg A, 2009c. Modelling of temperature in deep boreholes and evaluation of geothermal heat flow at Forsmark and Laxemar. SKB TR-09-14, Svensk Kärnbränslehantering AB.

Svensson D, Lundgren C, Johannesson L-E, Norrfors K, 2017. Developing strategies for acquisition and control of bentonite for a high level radioactive waste repository. SKB TR-16-14, Svensk Kärnbränslehantering AB.

Svensson D, Eriksson P, Johannesson L-E, Lundgren C, Bladström T, 2019. Development and testing of methods suitable for quality control of bentonites as KBS-3 buffer and backfill. SKB TR-19-25, Svensk Kärnbränslehantering AB.

Svensson U, Follin S, 2010. Groundwater flow modelling of the excavation and operation phases – Forsmark. SKB R-09-19, Svensk Kärnbränslehantering AB.

Svensson U, Ferry M, Kuylenstierna H-O, 2010. DarcyTools, Version 3.4. Concepts, methods and equations. SKB R-07-38, Svensk Kärnbränslehantering AB.

Tait J C, Cornett R J J, Chant L A, Jirovec J, McConnell J, Wilkin D L, 1997. Determination of Cl impurities and ^{36}Cl instant release from used Candu fuel. In Gray W J, Triay I R (eds). Scientific basis for nuclear waste management XX. Warrendale, PA: Materials Research Society. (Materials Research Society Symposium Proceedings 465), 503–510.

Takase H, Benbow S, Grindrod P, 1999. Mechanical failure of SKB spent fuel disposal canisters. Mathematical modelling and scoping calculations. SKB TR-99-34, Svensk Kärnbränslehantering AB.

Teurneau B, Forsmark T, Forssman I, Rhén I, Zinn E, 2008. Forsmark site investigation. Correlation of Posiva Flow Log anomalies to core mapped features in KFM01D, KFM07C, KFM08A, KFM08C and KFM10A. SKB P-07-127, Svensk Kärnbränslehantering AB.

Thiem G, 1906. Hydrologische methoden. Leipzig: Gebhardt.

Thunehed H, 2007. Forsmark site investigation. Resistivity measurements on samples from KFM01A, KFM01B, KFM02A, KFM05A and KFM06A. SKB P-07-51, Svensk Kärnbränslehantering AB.

Thörn J, 2015. The impact of fracture geometry on the hydromechanical behaviour of crystalline rock. PhD thesis. Department of Civil and Environmental Engineering, Chalmers University of Technology, Sweden.

Trinchero P, Sidborn M, Puigdomenech I, Svensson U, Ebrahimi H, Molinero J, Gylling B, Bosbach D, Deissmann G, 2019. Transport of oxygen into granitic rocks: role of physical and mineralogical heterogeneity. Journal of Contaminant Hydrology 220, 108–118.

Tullborg E-L, Smellie J, Nilsson A-C, Gimeno M J, Auqué L F, Brüchert V, Molinero J, 2010. SR-Site – sulphide contents in the groundwater at Forsmark. SKB TR-10-39, Svensk Kärnbränslehantering AB.

Unosson, M, 2016. Numerical simulation of earthquake induced rock shear through a deposition hole – Crack initiation and propagation in an insert with pre-existing intertubular and edge crack planes. SKBdoc 1474363 ver 1.0, Svensk Kärnbränslehantering AB.

Vahlund F, Hermansson H, 2006. Compulink. Implementing the COMP23 model in Simulink. SKB R-06-86, Svensk Kärnbränslehantering AB.

van den Bos B, 2018. Pre study of eddy current testing to detect forging laps on copper lids. SKBdoc 1531045 ver 1.0, Svensk Kärnbränslehantering AB.

van Loon L R, Glaus M A, Müller W, 2007. Anion exclusion effects in compacted bentonites: towards a better understanding of anion diffusion. Applied Geochemistry 22, 2536–2552.

van Loon L R, Soler J M, Jakob A, Bradbury M H, 2003a. Effect of confining pressure on the diffusion of HTO, $^{36}Cl^{-}$ and $^{125}I^{-}$ in layered argillaceous rock (Opalinus Clay): diffusion perpendicular to the fabric. Applied Geochemistry 18, 1653–1662.

van Loon L R, Soler J M, Bradbury M H, 2003b. Diffusion of HTO, $^{36}Cl^{-}$ and $^{125}I^{-}$ in Opalinus Clay samples from Mont Terri: effect of confining pressure. Journal of Contaminant Hydrology 61, 73–83.

Večerník P, Jedináková-Křížová V, 2006. Diffusion of 99-Technetium in compacted bentonite under aerobic and anaerobic conditions. Czechoslovak Journal of Physics 56, 665–672.

Vidstrand P, Follin S, Zugec N, 2010. Groundwater flow modelling of periods with periglacial and glacial climate conditions – Forsmark. SKB R-09-21, Svensk Kärnbränslehantering AB.

Vilks P, Miller N H, Stanchell F W, 2005. Phase II in situ diffusion experiment. Report 06819-REP-01200-10128-R00, Ontario Power Generation, Nuclear Waste Management Division, Canada.

Väisäsvaara J, Leppänen H, Pekkanen J, Pöllänen J, 2006. Forsmark site investigation. Difference flow logging in borehole KFM08C. SKB P-06-189, Svensk Kärnbränslehantering AB.

Waber H N, Smellie J A T, 2005. Forsmark site investigation. Borehole KFM06A: Characterisation of pore water. Part I: Diffusion experiments. SKB P-05-196, Svensk Kärnbränslehantering AB.

Waber H N, Smellie J A T, 2008. Characterisation of porewater in crystalline rocks. Applied Geochemistry 23, 1834–1861.

Waber H N, Smellie J A T, 2009. Forsmark site investigation. Borehole KFM02B: Characterisation of pore water. Part I: Diffusion experiments and pore water data. SKB P-09-14, Svensk Kärnbränslehantering AB.

Waber H N, Gimmi, T, Smellie J A T, 2009. Porewater in the rock matrix. Site descriptive modelling, SDM-Site Forsmark. SKB R-08-105, Svensk Kärnbränslehantering AB.

Walsh J B, Decker E R, 1966. Effect of pressure and saturating fluid on the thermal conductivity of compact rock. Journal of Geophysical Research 71, 3053–3061.

Wang X, 2005. Stereological interpretation of rock fracture traces on borehole walls and other cylindrical surfaces. PhD thesis. Virginia Polytechnic Institute and State University, Blacksburg, Virginia.

Weber J, Barthel J, Klinkenberg M, Bosbach D, Kruth M, Brandt F, 2017. Retention of ^{226}Ra by barite: The role of internal porosity. Chemical Geology 466, 722–732.

Werme L O, Johnson L H, Oversby V M, King F, Spahiu K, Grambow B, Shoesmith D W, 2004. Spent fuel performance under repository conditions: A model for use in SR-Can. SKB TR-04-19, Svensk Kärnbränslehantering AB.

Widestrand H, Byegård J, Selnert E, Skålberg M, Höglund S, Gustafsson E, 2010a. Äspö Hard Rock Laboratory. Long Term Sorption Diffusion Experiment (LTDE-SD). Supporting laboratory program – Sorption diffusion experiments and rock material characterisation. With supplement of adsorption studies on intact rock samples from the Forsmark and Laxemar site investigations. SKB R-10-66, Svensk Kärnbränslehantering AB.

Widestrand H, Byegård J, Kronberg M, Nilsson K, Höglund S, Gustafsson E, 2010b. Äspö Hard Rock Laboratory. Long Term Sorption Diffusion Experiment (LTDE-SD). Performance of main in situ experiment and results from water phase measurements. SKB R-10-67, Svensk Kärnbränslehantering AB.

Wikramaratna R S, Goodfield M, Rodwell W R, Nash P J, Agg P J, 1993. A preliminary assessment of gas migration from the copper/steel canister. SKB TR 93-31, Svensk Kärnbränslehantering AB.

Wilson C N, 1990a. Results from NNWSI series 2 bare fuel dissolution tests. Report PNL-7169, Pacific Northwest Laboratories.

Wilson C N, 1990b. Results from NNWSI series 3 spent fuel dissolution tests. Report PNL-7170, Pacific Northwest Laboratories.

Wilson C N, Gray W J, 1990. Measurement of soluble nuclide dissolution rates from spent fuel. In Oversby V M, Brown P W (eds). Scientific basis for nuclear waste management XIII Warrendale, PA: Materials Research Society. (Materials Research Society Symposium Proceedings 176), 489–498.

Wu P, 2009. State-of-the-science review of the stress field during a glacial cycle and glacially induced faulting. NWMO TR-2009-09, Nuclear Waste Management Organization, Canada.

Yu J-W, Neretnieks I, 1997. Diffusion and sorption properties of radionuclides in compacted bentonite. SKB TR 97-12, Svensk Kärnbränslehantering AB.

Zou L, Cvetkovic V, 2020. Impact of normal stress-induced closure on laboratory-scale solute transport in a natural rock fracture. Journal of Rock Mechanics and Geotechnical Engineering 12, 732–741.

Zou L, Jing L, Cvetkovic V, 2017. Modeling of solute transport in a 3D rough-walled fracture–matrix system. Transport in Porous Media 116, 1005–1029.

Zou L, Cvetkovic V, Jing L, Man Ivars D, 2018. Impact of normal stress caused closure on fluid flow and solute retention in rock fractures. In Proceeding of CouFrac2018, Wuhan, China, 12–14 November 2018.

Åkesson M, Börgesson L, Kristensson O, 2010a. SR-Site Data report. THM modelling of buffer, backfill and other system components. SKB TR-10-44, Svensk Kärnbränslehantering AB.

Åkesson M, Kristensson O, Börgesson L, Dueck A, Hernelind J, 2010b. THM modelling of buffer, backfill and other system components. Critical processes and scenarios. SKB-10-11, Svensk Kärnbränslehantering AB.

Appendix A

Using results from in situ electrical resistivity loggings in support of data needed in hydrogeological modelling (reproduced from SR-Site Data report)

A1 Introduction

Within the site investigations, in situ electrical resistivity loggings have been performed as part of the standard geophysical downhole programme. Results from these measurements can be used in support of two sets of data used in SR-Site hydrogeological modelling:

- The fracture transport aperture e_t (m), which is discussed in Section 6.6.
- The effective diffusivity D_e (m^2/s) of salt diffusing to or from the fractured rock surrounding a flow path.

The data presented in this appendix support other data used in SR-Site, and are not themself intended to be qualified. Therefore, the standard outline for data qualification used in this Data report is not followed. The data presented here are not presented elsewhere.

This appendix will begin with outlining the downhole rock resistivity methods, used in the site investigations. It will continue by outlining the methodology used for estimating the volumetric fracture apertures, and supply some results. Finally the effective diffusivity for use in salt transport modelling is discussed. For the reader who has no background knowledge on these subjects, it may be worthwhile studying Sections 6.6 and 6.8, where a multitude of references for further reading are given.

A2 Downhole rock resistivity loggings

In downhole rock resistivity loggings, a geophysical tool that emits an alternating electrical current is wired up or down a borehole. In this way the electrical resistance of the surroundings of the borehole is measured. The measurements are performed each decimetre along the borehole and data are presented as the rock resistivity ρ (ohm · m). The current is propagated both in the water filled microporosity of the non-fractured rock matrix (cf Section 6.8), and in the stagnant or flowing groundwater of open fractures. Basically no current is propagated in the rock minerals, due to their high electrical resistivity.

Figure A-1 illustrates the tool as lowered down a borehole. The red square represents the current electrode sending out the current normal to the borehole axis into the surrounding rock. What is not shown in the figure is that other electrodes are needed to focus the electric field, so that the current does not spread out radially but cylindrically from the current electrode (cf Löfgren and Neretnieks 2002).

The orange curve in Figure A-1 illustrates the resulting rock resistivity log. As the current electrode is surrounded by non-fractured rock, the emitted current is propagated in the microporous network of the rock matrix. Heterogeneity in the microporous network manifests in a somewhat varying rock resistivity, which is illustrated by the moderately fluctuating curve. As the current electrode is in front of the open fracture, current can also be propagated in the fracture water. If the fracture aperture is large enough, the current propagated in the fracture water will outweigh the current propagated in the surrounding rock matrix. It should be noted that the amount of electrical current that is propagated in the fracture water is independent of the fracture water flow rate.

In Figure A-2, a rock resistivity log from borehole KFM10A in Forsmark is shown, from the borehole length interval 330–340 m.

On the x-axis, red diamonds represent locations where open fractures have been identified in the drill core mapping (cf Löfgren 2007). Blue triangles represent locations where groundwater flow has been detected in the hydrogeological loggings, using the Posiva flow log (PFL). As can be seen, open fractures corresponding to flow anomalies, as well as open fracture giving rise to no hydraulic response, clearly affect the measured rock resistivity.

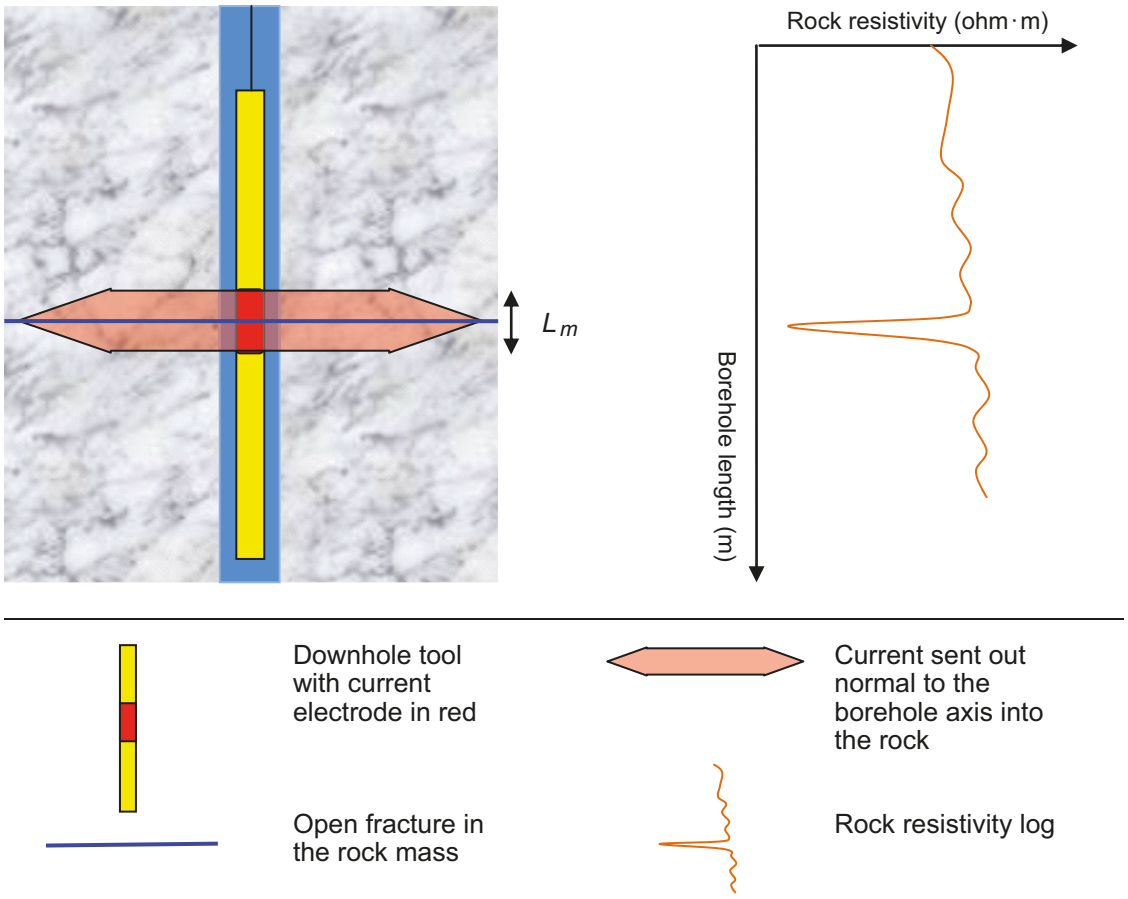

Figure A-1. *Illustration of the downhole tool, emitting an electrical current into the bedrock, and of the resulting rock resistivity log.*

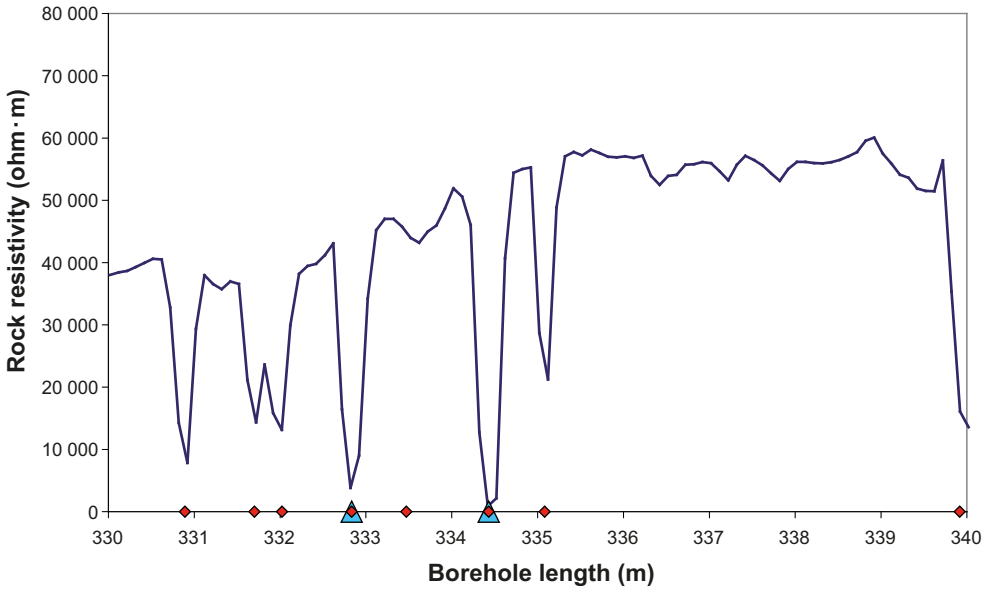

Figure A-2. *Rock resistivity log of KFM10A and locations of open fractures and PFL anomalies.*

The rock resistivity does not only depend on the properties of the rock matrix and of the open fracture, but also on the electrical resistivity of the porewater and groundwater, respectively. As outlined in Section 6.8 of this report, the electrical resistivity of the porewater and groundwater has been studied in the site investigations. Typical values of the electrical resistivity are between 1–2 ohm·m at repository depth (cf Section 6.8.10).

A3 Estimating volumetric fracture apertures from rock resistivity loggings

A3.1 Basic theory

Figure A-1 shows a situation where the borehole is generally surrounded by non-fractured rock, but where an open fracture intersects the borehole at a 90° angle. In the figure, the thickness of the investigated section (i.e., the thickness of the current field sent out into the rock) is denoted by L_m (m). The resistance R (ohm) of the investigated section in can be calculated by:

$$\frac{1}{R} = \frac{1}{R_r} + \frac{1}{R_f} \qquad \text{A-1}$$

Where R_r (ohm) and R_f (ohm) is the resistance of the rock and fracture, respectively. If the current is assumed to leave the tool in a perfect dish, 1-D equations can be used when comparing the resistances. This is done in Equation A-2.

$$\frac{L_p}{\rho \cdot L_m} = \frac{L_p}{\rho_w \cdot e_v} + \frac{L_p}{\rho_r \cdot (L_m - e_v)} \qquad \text{A-2}$$

where L_p (m) is the penetration depth of the current into the fracture and rock matrix, ρ (ohm·m) is the measured rock resistivity, ρ_w (ohm·m) is the resistivity of the groundwater in the fracture, e_v (m) is the volumetric fracture aperture, and ρ_r (ohm·m) is the resistivity of the non-fractured rock matrix.

If assuming that the penetration depths in the fracture and rock matrix are equal, the term L_p can be cancelled. As e_v is insignificant in comparison to L_m it can be calculated by:

$$e_v = \rho_w L_m \cdot \left(\frac{1}{\rho} - \frac{1}{\rho_r} \right) \qquad \text{A-3}$$

In case the fracture plane is not normal to the borehole axis, this must be corrected for. The case is illustrated in Figure A-3.

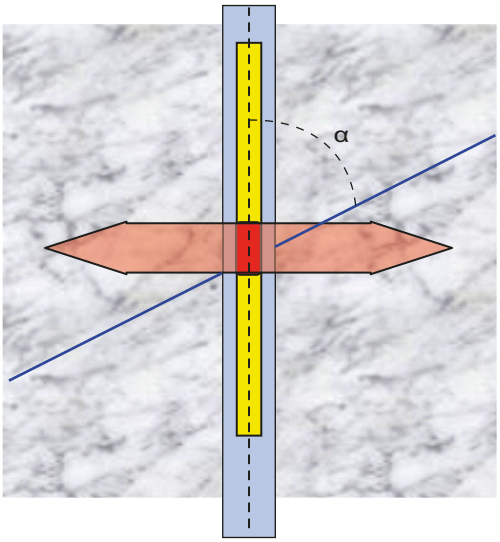

Figure A-3. *Illustration of the downhole tool, emitting current into the rock matrix, and an open fracture intersecting the borehole at an angle α.*

A somewhat simplified way of correcting for this is by multiply Equation A-3 by $\sin(\alpha)^{-1}$, where α is the angle shown in Figure A-3:

$$e_v = \rho_w L_m \cdot \left(\frac{1}{\rho} - \frac{1}{\rho_r} \right) \cdot \frac{1}{\sin(\alpha)} \qquad \text{A-4}$$

Equation A-4 requires that the shape of the current field is not affected by the fracture intersecting the borehole at an angle. This may not be entirely true and therefore the results should be seen as approximate. To not induce too large errors, it is recommended that the angle should be should be at least 45° (and not exceed 135° in Figure A-3), otherwise the data point should be discarded.

A3.2 Example of how to estimate the volumetric fracture aperture

This section shows an example of how to practically go ahead when estimating the volumetric fracture aperture. This is exemplified by the fracture at borehole length 335.1 in borehole KFM10A (see Figure A-2). In the following it is shown how all parameters of Equation A-4 can be estimated from site investigation data.

The length of the investigated section, L_m

The length of the investigated section L_m depends to a large extent on the configuration of the downhole tool used, but also to a minor extent on the local borehole fluid resistivity, rock resistivity, and rock resistivity heterogeneity. For this study, L_m has been obtained empirically, based on observations. This has been done by assuming that L_m equals half the thickness of a well-defined resistivity dip. The rationale is that the tool needs to be moved the distance of two investigation sections to capture the entire decrease and subsequent increase of the rock resistivity, constituting the dip.

In Figure A-2 the thickness of a resistivity dip is between 0.4 m (cf borehole length 335.1 m) and 0.5 m (cf borehole length 330.9 m). Based on the experience from the site investigations (see numerous of site investigation reports, e.g. Löfgren 2007) it is judged that these values are representative, and that a typical thickness of a well-defined resistivity dip is 0.45 m. Based on this, the single point value for L_m of 0.225 m is assigned.

It is noted that this value is uncertain and can be overestimated or underestimated by a factor judged to be less than two. It is also noted that estimated volumetric fracture apertures scale linearly with the assumed value of L_m (cf Equation A-4). If again examining Figure A-2, one can see that between the open fractures at 334.43 and 335.08 m, three rock resistivity values, one value for each decimetre, match that of the undisturbed rock matrix. This indicates that when the tool is about 18 cm from the fracture, the resistivity is unaffected by it[21]. On the other hand, if examining the resistivity between the fractures at 331.70 and 332.02 m, it seems to be affected by the fractures. This indicates that when the tool about 16 cm from a fracture, the fracture affects the resistivity. For the individual case, circumstances such as the angles of the fractures influence the above discussed distance. In the light of these two and other observations, an assumed value of L_m of 0.225 m seems reasonable.

The measured rock resistivity at the fracture, ρ

When estimating the volumetric fracture aperture, ρ is the measured resistivity at the open fracture, which is taken as the minimum rock resistivity value of the corresponding dip. At borehole length 335.1 in borehole KFM10A, this value is about 21 200 ohm·m.

The resistivity of the rock matrix, ρ_r

This is the resistivity of the non-fractured rock matrix. It is assumed that the resistivity of the rock matrix directly adjacent to the fracture is the same as that at a small distance from the fracture. In Figure A-2, the rock resistivity between the borehole lengths 336 and 339 m appears to be unaffected by open fractures and should therefore represent the non-fractured rock matrix. On average, the rock

[21] 0.18 m = (335.08 − 334.43 − 0.3) / 2.

resistivity of this interval is about 55 900 ohm·m. From the drill core mapping, one can notice that the rock type of the studied borehole section in Figure A-2 is the same (cf Table A-1 or page 25 of Döse and Samuelsson 2006). In general in this study, care has been taken to estimate the rock matrix resistivity from data on the same rock type as that surrounding the fracture. When estimating ρ_r in this work, a few criteria have been used:

- The mean value of ten rock resistivity data points has been taken.
- The distance from the data points and any open fracture should be at least 0.5 m.
- The data points should be located within 5 m of the studied fracture, and the rock type of the studied section should be the same.

The electrical resistivity of the ground water, ρ_w

The electrical resistivity of the groundwater has been measured by the Posiva difference flow log, as well as in the hydrogeological programme. In site investigation reports, the data are often presented as the electrical conductivity κ_w (S/m), which is the reciprocal to the resistivity. For example, at the borehole length 315.3 m in KFM10A, the electrical resistivity has been measured to 0.80 S/m at 25 °C (Sokolnicki et al. 2006, Table 6-2), which corresponds to a ρ_w of about 1.8 ohm·m at the in situ temperature.

Generally in this study, interpolations and extrapolations based on the few data points available in the boreholes have been used to obtain ρ_w values at different borehole lengths (cf Section 6.8.10). At the borehole length 335 m, the interpolation suggests a ρ_w of 2.0 ohm·m.

The fracture angle, α

The α-value of a fracture is noted in the drill core mapping. Table A-1 is an excerpt from the multitude of data obtained in the drill core mapping.

Table A-1. Excerpt of drill core mapping data taken from SICADA.

ACTIVITY TYPE	IDCODE	ADJUSTED SECUP	FRACT INTERPRET	CONFIDENCE	ALPHA	BEST ROCK CODE	FEATURE ID
GE041	KFM10A	330.891	Open	Probable	61.3	101057	3CD046D98A150D25
GE041	KFM10A	331.701	Open	Possible	55.3	101057	E25046D98A15104C
GE041	KFM10A	332.023	Open	Possible	35.4	101057	FBD046D98A15118D
GE041	KFM10A	332.834	Open	Certain	37.2	101057	F21046D98A1514B5
GE041	KFM10A	333.471	Open	Possible	57.8	101057	8A5046D98A151730
GE041	KFM10A	334.430	Open	Certain	44.0	101057	BAD046D98A151AEC
GE041	KFM10A	335.082	Open	Probable	75.3	101057	A09046D98A151D76
GE041	KFM10A	337.200	Sealed	Certain	51.1	101057	CF1046D98A1525B5
GE041	KFM10A	339.916	Open	Possible	57.9	101057	945046D98A153048
GE041	KFM10A	340.033	Open	Possible	63.2	102017	F75046D98A1530BC

In Table A-1 “ADJUSTED SECUP” is the borehole length; “FRACT INTERPRET” shows whether the fracture is judged to be open, partly open, or sealed in situ; “CONFIDENCE” indicates with what confidence this judgment was made, where certain is the highest degree of confidence, followed by probable and possible; “ALPHA” is the α-value; and “BEST ROCK CODE” indicates the rock type of the section. In our example, the open fracture at 335.082 m has the α-value 75.3°. It should be noted that sealed fractures have little effect on the rock resistivity.

The resulting volumetric fracture aperture, e_v

If inserting the above data into Equation 4, the following volumetric fracture aperture can be calculated for the open fracture at 335.1 m:

$$e_v = 2.0 \cdot 0.225 \cdot \left(\frac{1}{21\,200} - \frac{1}{55\,900} \right) \cdot \frac{1}{\sin(73.5°)} = 14\ \mu m \qquad \text{A-5}$$

As can be seen in Figure A-2, no hydraulic response was detected at the studied fracture. If instead performing the same operations for the nearby fracture at 334.4 m (ρ = 894 ohm · m), which is identified as hydraulically conductive, the obtained volumetric fracture aperture is 710 µm. However, for this fracture the value is more uncertain, as α = 44°. As a result the data point was discarded from the study.

A3.3 The study and the results

In the study, 160 fractures were investigated, each corresponding to an interpreted PFL-anomaly. Selected PFL-anomalies from all drill sites at the Forsmark site investigation area, except from DS9 and DS12, were investigated. Fractures from the shallow bedrock were avoiding by only examining PFL-anomalies from boreholes lengths of 250 m and larger. In addition, sections with many closely located PFL anomalies were avoided, as they often occur in highly fractured rock making it difficult to match an anomaly to an individual rock resistivity dip. Except for this, the selection of the PFL-anomalies followed no thought-through pattern, which is a weakness of the study. In future work with this method it would be interesting to assess, if not actual apertures of individual fractures in zones, then at least the combined effect of them as water volumes in zones.

It should be noted that the coordinates of the different logs sometimes mismatch by a few centimetres or even a few decimetres. Therefore, there is a degree of uncertainty induced when assigning an open fracture to a (nearby) rock resistivity dip. Uncertainty is also induced when assigning a resistivity dip to an identified PFL anomaly. In this study, which has been a desktop study, only limited certainty can be achieved when matching the logs. The matching would benefit from making careful judgments in each case, for example by simultaneously examining the drill core and the anomalies of the logs. For this study, it is judged that the matching described above only induce minor errors. However, would one want to take the study one step further, and investigate the relation between the volumetric fracture aperture and the transmissivity assigned to each PFL anomaly, a more careful methodology would be required.

The positions of the PFL-anomalies, the rock resistivity data, and the drill core mapping data were taken from SICADA[22]. The raw data needed as input to Equation A-4 are given in Table A-2 for the studied fractures, at the end of this section.

Out of the 160 studied fractures, 97 had an α value at 45° or above. All other data points were discarded. Figure A-4 shows the CDF (cumulative distribution function) of the estimated volumetric fracture aperture for the remaining 97 fractures.

The median volumetric fracture aperture is 0.13 mm, while its arithmetic mean is 0.30 mm, for the data shown in the figure. Figure A-4 also shows the CDF of the best fitted log-normal distribution, for comparison. The distribution parameters are:

- $\text{Log}_{10}(e_v(\text{m}))$: $\mu = -3.83$, $\sigma = 0.51$

It should be noted that numerous of data points in Figure A-4 are obtained in rock volumes that may not represent the sparsely fractured host rock intended for the repository. Therefore, a special study was made only including data from boreholes at drill sites DS1, DS5, DS6, and DS8, which are located at the intended location for the repository (cf Chapter 1 for a map of the drill sites). The resulting CDF for the remaining 27 data points is shown in Figure A-5.

[22] Locations of PFL-anomalies: Data delivery note Sicada_09_169. Rock resistivity data: Data delivery note Sicada_09_167. Drill core mapping data: Data delivery note Sicada_09_062

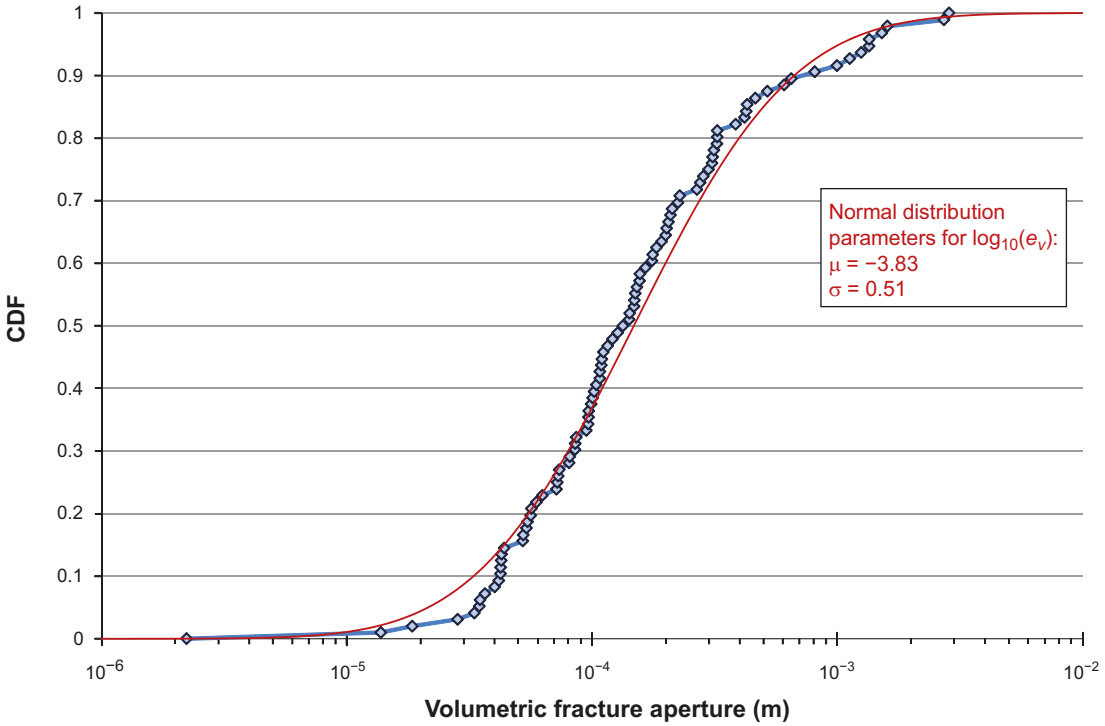

Figure A-4. *CDF of volumetric fracture apertures associated with 97 PFL anomalies at Forsmark (blue diamonds), and CDF of best fitted log-normal distribution (red curve).*

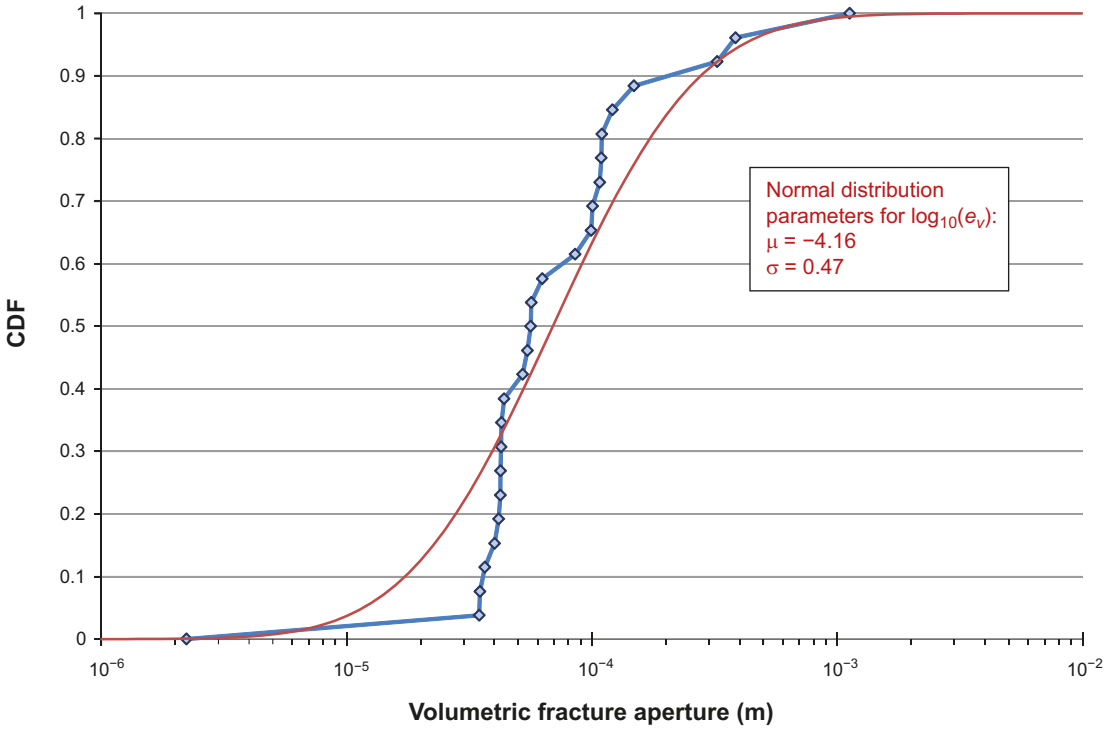

Figure A-5. *CDF of volumetric fracture apertures associated with 27 PFL anomalies at the Forsmark target area (blue diamonds), and CDF of best fitted log-normal distribution (red curve).*

As can be seen, discarding boreholes outside the target area does not have a major impact on the resulting CDF, even though the median value is decreased by about a factor of two, to 56 µm, and the arithmetic mean is decreased to 130 µm.

A3.4 Using e_v to support e_t

It is judged that the entire data set shown in Figure A-4 represents the study, and may be propagated as supporting data when estimating the fracture transport aperture. Here a caution is warranted. The volumetric fracture aperture e_v is not easily used for estimating the actual value of the fracture transport aperture e_t, but should rather be used for estimating its upper limit. As described in the SR-Site Geosphere process report (SKB 2010h), channelling is expected in fractures. This means that part of the fracture plane holds flowing water while part holds stagnant water. While the fracture transport aperture should represent the part holding flowing water (as averaged over the fracture plane), the volumetric fracture aperture should represent all water in the fracture. This gives Equation A-6:

$$e_v > e_t \qquad \text{A-6}$$

Another common situation giving rise to $e_v > e_t$ is when fractures are constricted, and where the constrictions control the water flow. Such a constriction can be located many metres away from the borehole. If so, it does not affect the electrical resistivity measurement, which is only affected by the local fracture around the borehole (say within one or two meters). Only in the case of parallel fracture surfaces, with no constriction and no channelling effects, e_v would equal e_t.

Table A-2. Raw data for use in Equation A-4, for the studied 160 fractures.

Borehole	Borehole length (m)	ρ (ohm·m)	ρ_w (ohm·m)	ρ_r (ohm·m)	Open/Sealed	α (°)	e_v (μm)
KFM01D	264.3	5025	1.27	36099	Open	62.4	56
KFM01D	307.4	1048	1.25	32890	Open	54.1	324
KFM01D	316.9	3122	1.25	37270	Sealed	50.3	110
KFM01D	353.2	3556	1.24	27141	Open	35.6	124
KFM01D	355.2	5752	1.24	33659	Open	53.3	52
KFM01D	369.5	7044	1.23	46530	Open	54.7	42
KFM01D	377.9	2686	1.23	37832	Open	53.3	121
KFM01D	382	3618	1.23	46831	Open	56.8	85
KFM01D	431.5	5938	1.21	44738	Sealed	74.3	42
KFM01D	571.2	1124	1.17	28728	Sealed	35.1	398
KFM02A	266.6	81	0.48	1736	Open	54	1599
KFM02A	273	365	0.47	1596	Sealed	13.5	1166
KFM02A	894	6263	0.46	11092	Open	40.4	16
KFM02B	271	4760	1.24	29295	Open	17.8	183
KFM02B	330.7	5911	1.20	38618	Open	39.7	64
KFM02B	399.4	14699	1.15	42612	Open	62.5	14
KFM02B	410.8	2970	1.14	30056	Open	74.9	81
KFM02B	412.2	6060	1.14	23260	Open	73.8	33
KFM02B	414.5	291	1.14	7920	Open	42	1284
KFM02B	419.4	3634	1.14	13677	Open	75.4	54
KFM02B	420.5	871	1.14	16639	Open	59.9	324
KFM02B	422.3	1465	1.14	8998	Open	58.8	175
KFM02B	423.3	227	1.13	12459	Open	41.8	1663
KFM02B	426.1	619	1.13	31629	Open	70.7	429
KFM02B	426.9	1008	1.13	18089	Open	57.8	285
KFM02B	428.4	6169	1.13	18089	Open	76.8	28
KFM02B	429.6	974	1.13	20806	Open	69.1	267
KFM02B	436.4	5043	1.13	18951	Open	42.3	61
KFM02B	497.1	2703	1.09	17647	Open	66.2	85
KFM02B	502	1896	1.09	8803	Open	18.2	385
KFM03A	314.4	2139	0.61	45262	Sealed	59.4	72
KFM03A	358.5	446	0.60	14253	Sealed	66.1	323
KFM03A	359.6	837	0.60	12570	Open	75.7	156
KFM03A	362.6	1307	0.60	11980	Open	73.7	97
KFM03A	368.6	711	0.60	9494	Open	58.2	209
KFM03A	369.4	429	0.60	9494	Sealed	75.9	310

Table A-2. Continued.

Borehole	Borehole length (m)	ρ (ohm·m)	ρ_w (ohm·m)	ρ_r (ohm·m)	Open/Sealed	α (°)	e_v (µm)
KFM03A	372.6	183	0.60	5397	Open	41	1099
KFM03A	375.1	1648	0.60	31084	Open	45	111
KFM03A	380.8	1815	0.60	35028	Open	9.5	445
KFM03A	381.6	934	0.60	17797	Open	56.5	165
KFM03A	388.6	92	0.60	23922	Open	72.4	1519
KFM03A	451.3	243	0.58	25680	Open	55.9	649
KFM03A	454.6	977	0.58	24617	Open	47.6	177
KFM03A	462.4	973	0.58	38168	Open	61.3	150
KFM03A	500.5	1213	0.58	47555	Open	64.3	116
KFM03A	515.9	1772	0.57	43853	Open	74.1	73
KFM03A	517.7	1883	0.57	52862	Open	64.2	74
KFM03A	533.7	1681	0.57	41330	Open	65.8	81
KFM03A	642.2	2587	0.55	32777	Open	26.8	103
KFM03A	643.9	125	0.55	21738	Open	52.5	1250
KFM03A	803.8	364	0.43	11513	Open	56.1	314
KFM03A	813.7	212	0.43	34897	Open	76.6	463
KFM03A	944.2	299	0.36	35673	Open	74.8	276
KFM03A	986.2	796	0.34	22902	Open	18.7	296
KFM03A	992.9	731	0.34	12443	Open	16.1	368
KFM04A	257.6	2370	0.72	9783	Open	13.1	285
KFM04A	273.9	1235	0.72	13507	Open	39.4	194
KFM04A	297.1	922	0.71	3037	Open	31	284
KFM04A	313	3587	0.71	11953	Open	38.7	58
KFM04A	338.8	1681	0.70	2807	Open	6.4	786
KFM04A	343.4	1380	0.70	8111	Open	67.5	104
KFM04A	346	2086	0.70	5590	Open	69.4	52
KFM04A	355.5	811	0.70	4599	Open	48.5	224
KFM04A	358.2	1450	0.70	4384	Open	54.6	97
KFM04A	359.8	64	0.70	3194	Open	56.9	2855
KFM04A	419	570	0.68	5251	Open	40.4	387
KFM04A	421.9	753	0.68	3782	Open	28	394
KFM04A	521.5	7418	0.66	36185	Open	62.6	19
KFM04A	954.8	2544	0.41	15497	Open	44.6	45
KFM05A	702.7	1370	0.99	24920	Open	13	714
KFM05A	720	21800	0.99	22760	Sealed	58.3	2
KFM06A	303	6301	1.05	41280	Sealed	55.1	40
KFM06A	306.2	6068	1.05	44135	Open	54.8	42
KFM06A	308.4	7054	1.05	48958	Open	58.1	35
KFM06A	321.4	2448	1.05	16533	Open	57.4	101
KFM06A	327	5797	1.05	15634	Sealed	37.2	52
KFM06A	329.7	5645	1.05	21050	Sealed	32.5	67
KFM06A	332	1844	1.05	7559	Open	23.1	296
KFM06A	338.6	5751	1.05	19149	Sealed	48.5	43
KFM06A	341.7	5105	1.05	18884	Open	70.8	37
KFM06A	345.4	2435	1.05	14692	Sealed	57.5	99
KFM06A	354.2	1926	1.05	8874	Open	64.8	109
KFM06A	356.6	243	1.05	7742	Sealed	30.7	1882
KFM06A	384.6	5754	1.05	32850	Sealed	53.7	44
KFM06A	392.7	2575	1.05	23346	Sealed	51.4	108
KFM06A	449.4	4678	1.05	22620	Open	51.1	55
KFM06A	622.4	967	1.05	20159	Open	17.6	798
KFM06A	653.9	8385	1.05	24807	Sealed	23.8	60
KFM06A	743.3	1390	0.86	41295	Open	31.4	264
KFM06A	770.6	291	0.80	11567	Sealed	32.2	1149

Table A-2. Continued.

Borehole	Borehole length (m)	ρ (ohm·m)	ρ_w (ohm·m)	ρ_r (ohm·m)	Open/Sealed	α (°)	e_v (µm)
KFM07A	916.3	6981	0.18	13805	Open	31.4	8
KFM07A	970	109	0.17	2953	Open	13.3	1530
KFM08A	410.1	1574	1.46	30489	Open	42.1	300
KFM08A	411.6	768	1.45	1861	Open	49.5	385
KFM08A	431.7	5457	1.41	34051	Open	61.7	57
KFM08A	452	9062	1.36	33779	Open	50.2	35
KFM08A	480.5	1491	1.30	23643	Sealed	37.8	309
KFM08A	687	261	0.99	26463	Open	49.2	1122
KFM08C	454.7	1713	1.04	23456	Open	60.2	148
KFM08C	464	1970	1.03	7173	Open	41.8	145
KFM08C	470.7	4100	1.03	13686	Open	70.8	43
KFM08C	480	3612	1.02	13471	Sealed	39.1	83
KFM08C	499	449	1.00	12348	Sealed	38.3	787
KFM08C	518.8	3177	0.98	7661	Open	49.1	63
KFM08C	683.6	662	0.83	22641	Open	27	616
KFM10A	299.5	1131	2.04	58764	Open	32.3	751
KFM10A	308.8	1851	2.03	36035	Open	30.6	472
KFM10A	315.3	594	2.02	51838	Open	34.3	1350
KFM10A	322	4399	2.01	45225	Open	66.8	102
KFM10A	327.3	1267	2.01	20584	Open	54	418
KFM10A	328.1	4809	2.01	26119	Open	56.9	95
KFM10A	328.8	3531	2.00	29434	Open	47.9	157
KFM10A	332.9	3819	2.00	26914	Open	37.2	178
KFM10A	334.5	894	2.00	40632	Open	44	712
KFM10A	368.4	5754	1.96	59052	Open	47.1	97
KFM10A	373.6	2554	1.95	29902	Open	43.9	233
KFM10A	376	4511	1.95	21192	Open	49.2	108
KFM10A	431.9	212	1.89	9752	Open	46.4	2721
KFM10A	436.3	2857	1.88	34114	Open	9.2	915
KFM10A	437.3	2668	1.88	34114	Open	37.6	248
KFM10A	480.3	2493	1.84	21328	Open	45.7	212
KFM10A	483.8	351	1.83	9360	Open	57.7	1346
KFM10A	484.4	298	1.83	9360	Open	84	1349
KFM11A	256.9	1717	1.31	14244	Open	49.5	205
KFM11A	257.4	1747	1.31	14244	Open	52.4	192
KFM11A	261.5	2084	1.30	8159	Open	48.4	152
KFM11A	262	1574	1.30	8159	Open	51.7	202
KFM11A	266.8	1783	1.30	4282	Open	38.2	197
KFM11A	271.7	412	1.29	12633	Open	58.1	807
KFM11A	273.4	2145	1.29	17690	Open	58.4	143
KFM11A	275	868	1.29	20491	Open	49.5	425
KFM11A	276.5	1932	1.29	15393	Open	47.9	183
KFM11A	283.8	3098	1.28	12218	Open	38.3	126
KFM11A	285.2	4131	1.28	12047	Open	56.7	59
KFM11A	299.5	1582	1.26	11998	Open	45.4	228
KFM11A	333.9	1310	1.22	16528	Open	38.6	320
KFM11A	376.2	674	1.18	14369	Open	20	1134
KFM11A	379.3	642	1.18	2338	Open	38.3	552
KFM11A	395.3	2760	1.16	5570	Open	32.3	130
KFM11A	397.9	3088	1.16	13174	Open	52.8	86
KFM11A	400.8	1069	1.16	21051	Open	51.6	298
KFM11A	402.9	1383	1.16	7314	Open	39	263
KFM11A	403.6	1894	1.15	7314	Open	38.9	183
KFM11A	404.5	871	1.15	10655	Open	40.4	435

Table A-2. Continued.

Borehole	Borehole length (m)	ρ (ohm·m)	ρ_w (ohm·m)	ρ_r (ohm·m)	Open/Sealed	α (°)	e_v (µm)
KFM11A	409.1	1694	1.15	8863	Open	63.3	142
KFM11A	420.2	1333	1.14	10156	Open	29.8	362
KFM11A	426.1	316	1.13	8622	Open	52	996
KFM11A	427.2	1517	1.13	2830	Open	48.7	134
KFM11A	428	1326	1.13	4665	Open	49.1	200
KFM11A	432.5	1619	1.13	2543	Open	65.8	72
KFM11A	433.5	425	1.13	2807	Open	58.8	607
KFM11A	436.2	532	1.12	4528	Open	55.9	519
KFM11A	436.6	878	1.12	4528	Open	52.2	309
KFM11A	438.1	1183	1.12	2276	Open	38.7	231
KFM11A	440.7	1857	1.12	6027	Open	53.4	127
KFM11A	443.4	641	1.12	18660	Open	36.7	644
KFM11A	452.7	1129	1.11	17317	Open	37.6	348
KFM11A	467.6	2045	1.10	22086	Open	49	149
KFM11A	474.6	3164	1.09	28355	Open	19.8	221
KFM11A	475.7	1378	1.09	11072	Open	31.6	318

It should be noted that the borehole length coordinates of different logs and measurements mismatch somewhat, which has been corrected before prior to conducting this study. The borehole length shown is for the resistivity measurement, while the reported borehole lengths for the drip core mapping data may be slightly different.

A4 The effective diffusivity of salt

In the hydrogeological modelling, the matrix diffusion of salt is an integrated part of the calculations. To assess the diffusive transport of salt in an out of the rock matrix, the effective diffusivity D_e (m^2/s) is needed. The effective diffusivity is used both for the paleohydrogeological simulations including transport of salt and reference waters, and in the analytical calculations of salt transport.

A4.1 Effective diffusivity of salt in undisturbed rock matrix

The effective diffusivity of the undisturbed rock matrix is discussed in Section 6.8 of this report. This effective diffusivity is strictly estimated for rock at a distance from any open fracture, and not for the rock adjacent to the flow paths. This may seem peculiar, as the matrix diffusion of interest for safety assessment modelling occurs in the rock matrix surrounding flow paths. The explanation is that the effective diffusivities given in Section 6.8 are intended for radionuclide transport modelling, and that a pessimistic approach is taken. It is a common opinion that the capacity for matrix diffusion is generally enhanced in the rock adjacent to fractures. Furthermore, results from the site investigations clearly indicate that if a flow path is intersected by open or partly open fractures, which are water bearing but hydraulically non-conductive, this extra pore space adds to the diffusion capacity of the surrounding rock (e.g. Löfgren 2007). However, as it is difficult to demonstrate that every flow path is surrounded by rock of enhanced matrix diffusion capacity, the decision has been taken to pessimistically neglect this additional capacity in radionuclide transport modelling. In this type of modelling it is straightforward to see that such an approach is pessimistic, as increased matrix diffusion leads to increased radionuclide retention, which in turn reduces the radiological risk. However, in the case of salt diffusion in and out of the rock matrix, one cannot easily draw conclusion on whether a high of low value of D_e is the most pessimistic. This can be exemplified by the stability of the buffer, where at a certain groundwater composition the buffer is stable, but where buffer erosion may occur both as the water becomes more saline and more diluted. Because of this, a best estimate of the effective diffusivity in the fractured rock surrounding flow paths is needed (as discussed in Section A4.2).

In Section 6.8, the arithmetic mean of the formation factor F_f (-) for the undisturbed rock matrix at the Forsmark site is given as 2.1×10^{-5}. From the formation factor, the effective diffusivity can be obtained, in case there are no electrostatic effects such as anion exclusion, and in case the solute exists in trace amounts:

$$D_e = F_f \cdot D_w \qquad \text{A-7}$$

Where D_w (m^2/s) is the diffusivity in the unconfined pore water, which is often approximated by using the value for the diffusivity at infinite dilution (cf Section 6.8).

In the following, salt transport is approximated by NaCl transport. For Na^+ the D_w is 1.33×10^{-9} m^2/s and for Cl^- the D_w is 2.03×10^{-9} m^2/s at infinite dilution and at 25 °C (Brantley et al. 2008). Making a temperature correction to obtain D_w at the in situ temperature, which presently is about 12 °C at repository depth, is elementary (cf Section 6.8.5). When using Equation A-7 for anionic tracers, the resulting effective diffusivity should be reduced by a factor of $10^{0.5}$ (~3.16), as justified in Section 6.8. As stated above, Equation A-7 is valid for solutes at trace concentrations. In case of salt transport, one must account for ion-pair diffusion and the harmonic mean of the individual diffusivities of Na^+ and Cl^- should be taken:

$$D_{w,salt} = \frac{\left(z_+ + |z_-|\right) D_{w,+} \cdot D_{w,-}}{z_+ D_{w,+} + |z_-| D_{w,-}} \qquad \text{A-8}$$

where z is the charge number of the anion or cation. As can be seen, Equation A-8 applies in free water phase and assuming the equivalent equation for diffusion in the rock matrix, exchanging D_w for D_e, is somewhat speculative. As discussed in Section 6.8 and in the SR-Site Geosphere process report (SKB 2010h), Fickian diffusion theory has limitations in the applicability in the microporous system where electrostatic interactions are of major concern. If anyhow using the harmonic mean for calculating[23] the effective diffusivity of salt at the in situ temperature, $D_{e,salt}$ becomes 1.2×10^{-14} m^2/s.

A4.2 Effective diffusivity of salt in fractured rock surrounding flow paths

Under this heading we attempt to motivate a reasonable range of the effective diffusivity for use in salt transport calculation. Here, the fractured rock surrounding the flow paths is the focus of attention, as opposed to the undisturbed rock at distance from flow paths, as discussed above. The approach of obtaining the data is very similar to that presented in Section 6.8, although the background data somewhat differ and the scope of the study is limited to one borehole, KFM08C.

Figure A-6 shows site investigation result from the geophysical downhole tool (cf Figure A-1) used for assessing the in situ effective diffusivity by electrical methods. Here the rock resistivity is shown, which is (approximately) inversely proportional to the effective diffusivity.

As in Figure A-2, the triangles at the x-axis represent the locations of PFL anomalies, while the diamonds represent the locations of open fractures, as detected in the drill core logging. The solid grey line is the rock resistivity log obtained in the site investigations. The purple dots show data points obtained at a distance at least 0.5 m away from any open fracture. These data points are called rock matrix resistivities, which are used as a basis when assessing the effective diffusivity of the undisturbed rock (cf Section 6.8). The combination of grey and purple dots shows all data points obtained at a distance of at least 0.5 m away from any PFL-anomaly (for further descriptions, please turn to Löfgren (2007)). These data points are called fractured rock resistivities, and are used as a basis for assessing the effective diffusivity of salt in this work, for the fractured rock surrounding the flow paths. In doing this, a PFL-anomaly is assumed to represent a flow path, whereas the water

[23] Data used in temperature correction: Water viscosity $\eta = 1.24 \times 10^{-3}$ Ns/m^2 at 12 °C; $\mu = 0.89 \times 10^{-3}$ Ns/m^2 at 25 °C (Coulson et al. 1990). Temperature correction based on the Stoke-Einstein equation. Assumed $F_f = 2.1 \times 10^{-5}$. D_e of Cl^- calculated by (2.03×10^{-9} $m^2/s \times F_f \times$ temperature correction)/100.5. D_e of Na+ calculated by 1.33×10^{-9} $m^2/s \times F_f \times$ temperature correction.

in open fractures where no hydraulic response has been detected is assumed to be stagnant. This stagnant water is assumed to contribute to matrix diffusion in addition to the stagnant water of the microporous network of the rock matrix. It should be noted that we strictly do not know that these open fractures holds stagnant water. We only know that they are not sufficiently conductive to be detected with the Posiva flow log.

As can be seen in Figure A-6, the rock resistivity is on average smaller at the PFL anomalies around 520 m, than at the sparsely fracture rock, for example, between 550–560 m. In the borehole length interval 515–525 m the fractured rock resistivity is on average four times smaller than in the interval 550–560 m.

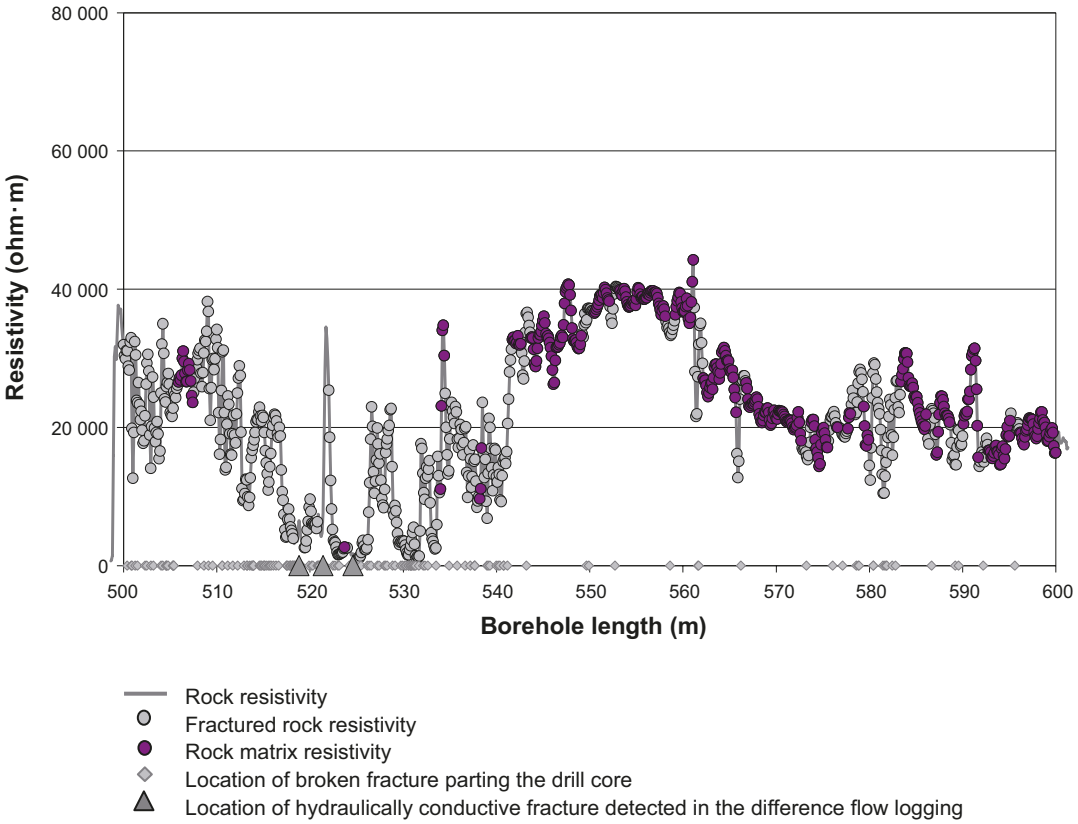

Figure A-6. *The rock resistivity of borehole section 500–600 m of KFM08C. Reproduced from Appendix A2 of Löfgren (2007).*

In the study presented in this appendix, the fracture rock formation factor is calculated exclusively for the rock within 5 m of, and at least 0.5 m away from, a detected PFL anomaly, in the borehole KFM08C. The value 5 m is set subjectively but should encompass the rock volume that has the greater impact on hydrogeological results. The locations of PFL-anomalies are taken from Appendix 7 of Väisäsvaara et al. (2006). The formation factors are obtained in the same manner as in Section 6.8, which includes making corrections for surface conduction. The resulting 982 data points are shown in Figure A-7, as a CDF.

The arithmetic mean of the fractured rock formation factors shown in Figure A-7 is 7.2×10^{-5}, which is a factor of 3.4 larger than for the undistributed rock matrix given Section 6.8. From this formation factor one can obtain the effective diffusivity. By performing the same operations as for the undisturbed bedrock (correcting for temperature and anion exclusion, and using the harmonic mean), the arithmetic mean of D_e becomes 4.3×10^{-14} m^2/s for the fractured rock surrounding flow paths.

For the fractured rock, it is uncertain to what degree anion exclusion should be accounted for, as the apertures of the open fractures likely are much larger than for the pores (cf discussion on anion exclusion in relation to constrictivity in Section 6.8). Therefore, the uncertainty range for D_e may need to be chosen so that it encompasses the assumption where anion exclusion is neglected. When disregarding anion exclusion, the arithmetic mean of D_e becomes 8.1×10^{-14} m^2/s for the fracture rock. It may also be justified to disregard the effect of surface conduction, at least in the fractures. This means that the apparent formation factor would equal the formation factor, and that no correction is needed (cf Section 6.6). When disregarding anion exclusion and surface conduction for both the rock matrix and the fractures, the arithmetic mean of D_e becomes 1.0×10^{-13} m^2/s for the fractured rock.

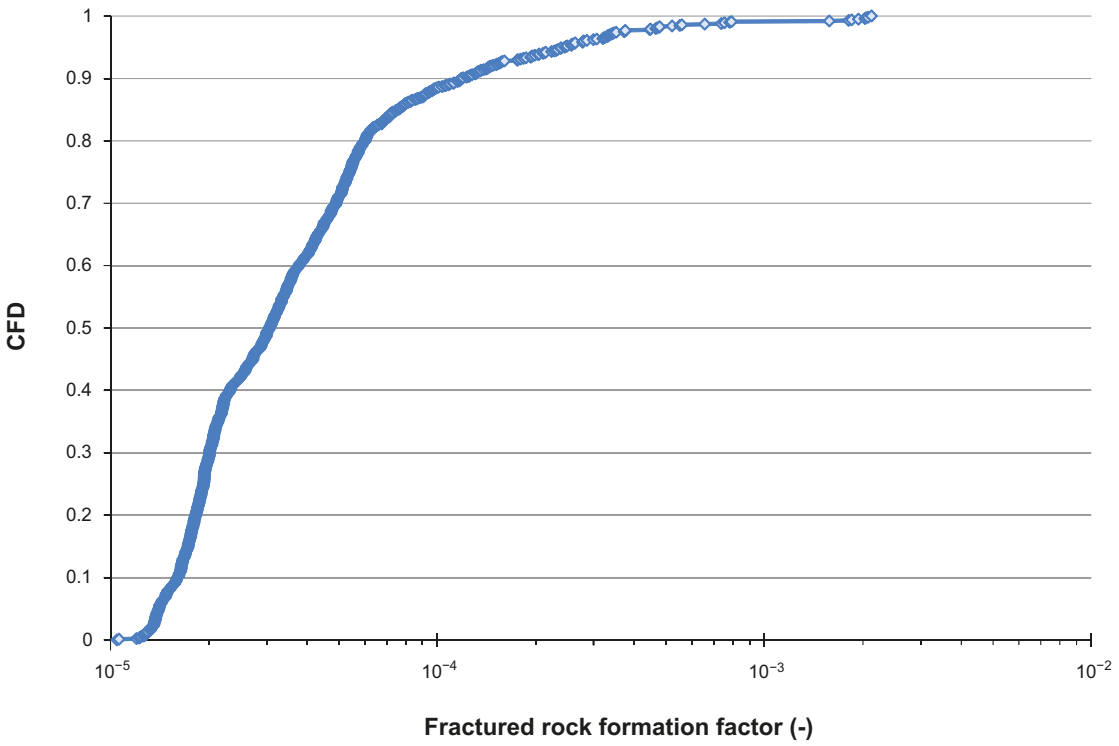

Figure A-7. *CDF of fracture rock formation factors obtained within 5 m of, and at least 0.5 m away from, any PFL anomaly in borehole KFM08C.*

Suggested effective diffusivity of rock surrounding flow paths

Based on the information above, a lower limit, best estimate, and upper limit are given for the D_e of salt diffusing in the fractured rock surrounding flow paths. For the lower limit, 1×10^{-14} m^2/s is suggested, which is the D_e for the undisturbed rock matrix.

As best estimate values, 4×10^{-14} m^2/s is suggested. This is the arithmetic mean of the D_e corresponding to the data points shown in Figure A-7. In Section 6.8 it is argued that the flow path averaged formation factors for the undisturbed rock is obtained by taking the arithmetic mean of available data points. In this study, formation factors around individual flow paths have been sampled. If the properties (e.g. the fracture intensity) along the flow path vary, and if one can estimate this variation by sampling rock surrounding many different flow paths, the arithmetic mean would also in this case represent the flow path averaged D_e. However, if the properties along the flow paths are relatively constant, one could argue that the median value would be more appropriate as best estimate. Considering these two choices, and also the fact that groundwater flow is conceptualised to occur in a fracture network, it seems somewhat more reasonable to propagate the arithmetic mean as the best estimate value.

For the upper limit we acknowledge the fact that the effective diffusivity of the rock surrounding a flow path may be consistently high. In Figure A-7, 90 % of the data ($0 < CFD < 0.9$) is contained within one order of magnitude. Therefore, the upper limit is assigned by multiplying the lower limit by one order of magnitude, giving an upper D_e of 1×10^{-13} m^2/s. This upper limit also encompasses the best estimate D_e obtained if one disregards anion exclusion, as well as surface conduction (see above). The lower, best estimate, and upper limit of D_e for salt diffusing in fractured rock surrounding flow paths are summarised in Figure A-2.

Table A-3. Suggested D_e for fractured rock surrounding flow paths.

Lower limit for D_e	1×10^{-14} m^2/s
Best estimate of D_e	4×10^{-14} m^2/s
Upper limit for D_e	1×10^{-13} m^2/s

It should be noted that for the rock directly adjacent to the flow path, the D_e may be even higher than this, in case the rock is altered. However, the rock directly adjacent to the flow path (PFL-anomaly) is by necessity excluded in this study, as the fracture water disturbs any attempt to measure the diffusive properties of the rock by electrical methods (cf Section A3.2).

Arkitektkopia AB, Bromma, 2022

SKB is responsible for managing spent nuclear fuel and radioactive waste produced by the Swedish nuclear power plants such that man and the environment are protected in the near and distant future.

skb.se